Transport Relationships in Porous Media as a Model for Oil Reservoir Rocks

Tanko, Nuradeen

Award date:
2011

Awarding institution:
University of Bath

Transport Relationships in Porous Media as a Model for Oil Reservoir Rocks

Nuradeen Labaran Tanko

A thesis submitted for the degree of Doctor of Philosophy

University of Bath

Department of Chemical Engineering

April 2011

For

Alhaji Labaran Tanko and Hajiya Barira Tanko

Abstract

There is growing fear that world oil reserves are depleting fast due to the current energy demand, and future energy needs. Recently, there has been a call for radical shifts in investment towards cleaner and more efficient energy technologies. However, most of these renewable energy alternatives are still at infant stages of research. Thus, the more conventional hydrocarbon oil is still the most logical option. Oil recovery efficiency is heavily influenced by the structure of void space that oil occupies within the reservoir rocks. In general, less than 50 % of oil is recoverable from the source rock, and thus the understanding of oil entrapment (bound volume index) is essential in prediction of economical potential of an oil reservoir. The bound volume index is the non-movable fluid volume in oil reservoirs. Reservoir rocks are chemically and geometrically heterogeneous. In this study, model catalyst support pellets with similar chemical and geometrical properties to oil reservoir rocks, but with more homogeneous chemistry were investigated.

In this thesis, novel multi-technique approaches have been used to understand the transport relationships in porous media. The mechanisms of entrapment and distribution of the irreducible non-wetting phase within porous media was investigated with mercury porosimetry. Mercury entrapment is strongly dependent on the structural (voidage fraction, pore size, and pore size distribution) as well as on topological (connectivity and tortuosity) properties of porous media. The pore size distribution (PSD), a measure of pore length, and pore connectivity were determined by gas sorption. PGSE NMR was used to study the heterogeneity and tortuosity of the samples. In addition, PSGE NMR was used to study the kinetics of adsorption in porous media, and thus elucidate the relationships of liquid connectivity, and molecular exchange between liquid and vapour phases.

In general, mercury entrapment occurred at larger mesopore radii, and was present at all experimental time-scales. In addition, mercury entrapment was found to increase with increased variance in the PSD. PGSE NMR kinetic studies revealed that tortuosity decreased with an increased liquid connectivity and there was enough evidence to suggest molecular exchange between the liquid and vapour phases. Furthermore, the tortuosity of fully saturated samples increased with an increased mercury entrapment.

Acknowledgements

I will like to express my sincere gratitude to Dr Sean Rigby for his invaluable supervision, support, and encouragement. This work would not have been possible without his guidance and knowledge. His dedication to research has given me the opportunity to contribute in my area of research interest. Once again, thank you for your efforts and patience with me.

I wish to acknowledge the help of the technicians in the Department of Chemical Engineering, particularly Mr Fernando Acosta and Mr Merv Newnes for their technical assistance during my experimental work. I will also like to thank Dr John Lowe (NMR spectroscopist), for PGSE NMR training and support.

I wish to thank Dr Irene Evbuomwan for running the mercury porosimetry characterisation of the P7129 and Q17/6 Silica gel spheres. I will also like to thank Ms Ann O'Reilly of the Department of Physics, University of Bath, for Atomic Force Microscopy (AFM) images of samples C10 and C30 at different magnifications.

My colleagues, especially Dr Peter Chigada, Dr Irene Evbuomwan, Dr Li Min, Mr Navin, Mr Firas, Ms Umi, Mr Iain, and Mr Yap thank you for supporting me with advice and guidance.

Finally, I am eternally grateful to my parents for their love and financial support; I could not have done this without you.

Contents

APPENDICES:

List of figures

List of tables

Glossary

Abbreviations

Acronym	Definition
AFM	Atomic force microscopy
ASAP	Accelerated surface area porosimeter
BC	Bulk condensation
BET	Brunauer Emmett Teller
BJH	Barret-Joyner-Halenda
BVI	Bound volume index
CPMG	Carr-Purcell-Meiboom-Gill
CPG	Controlled pore glasses
CPSM	Corrugated pore structure model
CW	Continuous wave
CXT	Computerised X-ray tomography
DFT	Density functional theory
EMI	Electron microscopy images
FFI	Free fluid index
FID	Free induction decay
HK	Horvath-Kawazoe
ICI	Industrial Chemical Industries
IOR	Improved oil recovery
IUPAC	International Union of Pure and Applied Chemistry
MC	Monte Carlo
MCM	Mobil crystalline material
MF-DFT	Mean-field density-functional theory
MD	Molecular dynamics
MRI	Magnetic resonance Imaging
NMR	Nuclear magnetic resonance
NS	Number of scans

PGSE	Pulsed gradient spin echo
PSD	Pore size distribution
r.m.s	Root mean square displacement, m
SAXS	Small-angle X-ray scattering
STP	Standard conditions for temperature and pressure
S:N	Signal to noise ratio
TEM	Transmission electron microscope
X-ray micro-CT	X-ray micro-computed tomography

Greek alphabets

Symbol	Definition	Unit
α	A constant in the power law correlation of Equation 3.26	_
α'	Nuclear spin at the upper energy level	J.s
β	Critical component of finite-size scale scaling equation	_
β^0	Compressibility of mercury	m^2/N
β'	Nuclear spin at the lower energy level in as illustrated in Figure 3.17	J.s
γ	Gyromagnetic ratio of the observed nucleus	_
γ_{HG}	Surface tension of mercury	N/m
γ_{SL}	Interfacial surface tension between solid and liquid in Figure 2.7	N/m
γ_{SV}	Interfacial surface tension between solid and vapour in Figure 2.7	N/m
γ_{LV}	Interfacial surface tension between liquid and vapour Figure 2.7	N/m
Δ	Diffusion time	s
δ	Length of gradient pulse	s
δ_a	Moles of nitrogen derived from bulk of liquid outside the pore	_
δG	The total increase free energy	J
δS	Decrease in the area of solid-liquid interface and an increase in solid-vapour interface and an increase in solid-vapour interface	m^2
ε	Porosity or voidage	_
ε_b	Bed voidage	_
ς_p	Pore neck to pore body diameter	_
η	Viscosity of mercury	Pa.s
θ	Contact angle between the liquid and the wall of the pore	°
λ	The total anisotropy of all the pores	_
μ	Mean of pore size distribution	_
μ_v	Viscosity as illustrated in Darcy's law [Equation 2.4]	Pa.s
ξ	As defined in the text, $\gamma^2 g^2 \delta^2 \left(\Delta - \frac{\delta}{3} \right)$	$s.m^2$
σ	Standard deviation of pore size distribution	

σ_a	Molecular area of the adsorbate molecule in the completed monolayer	m^2
σ_{so}	Interfacial tension between solid and lighter fluid phase in Figure 2.7	N/m
σ_{sw}	interfacial tension between solid and denser fluid phase in Figure 2.7	N/m
τ	Tortuosity	_
τ_e	Mesoscopic contribution to the tortuosity over length scales of a few pore diameters up to scales at which macroscopic heterogeneities become significant	_
τ_{mac}	Macrsocopic tortuosity	_
τ_{MRI}	Tortuosity measured by MRI	_
τ_{PGSE}	Tortuosity measured by PGSE	_
τ_p	Pulse duration	s
τ_h	Hydraulic tortuosity	_
τ_μ	Tortuosity over length scales of up to a few pore diameters	_
τ_1	Tortuosity of the fast component in a two component diffusion model	_
τ_2	Tortuosity of the slow component in a two component diffusion model	_
$\bar{\tau}$	Overall tortuosity in a two component diffusion model	_

Latin alphabets

Symbol	Definition	Unit
A	Cross sectional area	m^2
A_T	Adhesion tension	N/m
b	pore anisotropy	_
B_1	Superimposed field	Tesla
B_0	Magnetic flux density	Tesla
c	Affinity between the adsorbate and the adsorbent	_
d	Diameter of a pore	m
d_1	Diameter of a large pore in an ink bottle system	m
d_2	Diameter of a small pore in an ink bottle system	m
D	Diffusion coefficient	m^2/s
D_i	Diffusion coefficient of component i	m^2/s
D_{eff}	Effective self-diffusion coefficient	m^2/s
$D_{\text{int}ra}$	Intraparticle or pore diffusion coefficient	m^2/s
D_0	Molecular self-diffusion coefficient of the probing liquid	m^2/s
E	Energy illustrated in Figure 3.17	J
E_C	Amount of energy to separate a column of mercury	J
E_1	Energy of adsorption of the first layer	J
E_L	Liquefaction energy subsequent layers of molecules	J
f	Percolation factor as illustrated in Figure 3.8	_
F	Percolation probability as illustrated in Figure 3.8	_
g	Gradient strength as given in Equation 3.39	G/m
h	Scaling function as given in Equation 3.20	_
I	Echo intensity in the presence of the gradient	_
I_0	Echo intensity in the absence of the gradient	_
k	A constant in power law correlation of Equation 3.26	g
k'	Rock permeability	m^2
l	Length of cylindrical pore	m

l_{eff}	Effective pore length	m
l_p	Average linear flow path length	m
L	Characteristic dimension of the microparticles in Figure 3.11	_
N	Number of cylindrical pores	_
N_A	Avogadro number	mol^{-1}
N_1	Representative of the micro/mesopore network in Figure 3.11	_
N_2	Representative of the macropore networks in Figure 3.11	_
N_α	Population of nuclear spin at upper energy level in Figure 3.17	_
N_β	Population of nuclear spin at lower energy level in Figure 3.17	_
P	Partial vapour pressure	Pa
P_{CV}	The sum of pressure on the concave side of the meniscus	Pa
P_{CX}	The sum of the pressure on the convex side of the meniscus	Pa
P_0	Saturated vapour pressure	Pa
P_U	Upstream pressure	Pa
$P_U - d_P$	Downstream pressure	Pa
Q	Flow rate of a fluid as given in Darcy's law [Equation 2.6]	$m^3 s^{-1}$
R	Universal gas constant	J/mol.K
R'	Echo attenuation ratio as given in Section 3.4.2	_
s	Slope obtained from Equation 3.28	_
S	Surface area as stated in the text	m^2
r	Displacement of molecules undergoing Brownian motion	m
r_{cavity}	Cavity radius	m
r_{eff}	Effective hydraulic pore radius	m
r_k	Radius of condensate with a meniscus of hemispherical form	m
r_p	Radius of cylindrical pore	m
r_1, r_2	Radii of curvature of interface	m
t	Thickness of the adsorbed multilayer in Equation 3.19	m
t_0	Initial time of pulse duration	s
t_1	Final time of pulse duration	s

T	Temperature	K
U	Potential well of energy as given in Equation 3.34	J
v	Critical component of finite-size scale as given in Equation 3.20	_
v_f	Resonance frequency of a electromagnetic wave	Hz
V	Volume as stated in the text	m^3
v_1	Volume of large pore in an ink-bottle type pore system	cm^3
v_2	Volume of small pore in an ink-bottle type pore system	cm^3
V_C	Volume condensed in pores	cm^3
V_L	Molar volume	cm^3
V_l	Larmor frequency	Hz
V_M	Monolayer capacity	cm^3(STP)/g
x	Relative pressure	_
Z	Pore connectivity or mean coordination number	_

1.0 Introduction

1.1 Background

The 20th century saw the utilization of petroleum dominate the process industries. The World Oil Journal in its 2005 edition quotes ≈ 1.08 trillion barrels of petroleum reserves are left on the planet and only one new barrel is found for every four used. With over 31.03 billion barrels consumed worldwide annually and that amount rapidly increasing, there is apparently less than ≈ 25.4 years before these reserves are depleted (World Oil Journal, 2009). Thus the world's petroleum reserves are finite.

Because oil reservoirs are rapaciously being consumed, their costs are rising; drastic measures have to be taken to find more oil from existing oil reservoirs, e.g. application of different improved oil recovery (IOR) techniques. Although alternative forms of energy may grow rapidly, more hydrocarbon energy is essential in order to keep up with the rapidly growing demand and development needs. Therefore, new technologies and techniques, targeted to the exploration of complex oil reservoir systems are receiving great attention, and rightfully should, as they are essential in sustaining the current global energy supply (World oil Journal, 2005).

Oil recovery efficiency is heavily influenced by the structure of the void space occupied by oil within the reservoir rocks. In general, the amount of oil recovered from an existing oil reservoir is ≈ 20 to 40 % (Dandekar, 2006). The amount of oil remaining after different improved oil recovery techniques is called the Bound Volume Index (BVI). The BVI is traditionally characterised as the irreducible fluid saturation level. It may be used to quantify the economic potential of an oil reservoir and is an important parameter used in reservoir modelling of enhanced oil recovery. There are well known characterising techniques that can estimate the BVI. The BVI is strongly dependent on the structural (voidage fraction, pore size, and pore size distribution) as well as on topological (connectivity and tortuosity) properties of oil reservoir rocks.

1.2 Oil reservoir

Reservoirs are generally bodies of rocks that were laid down as sediments on the surface of the Earth million of years ago. These could have been sand dunes, beaches, deserts, or coral reefs. But as these sand bodies get buried, they tend to get compressed, and thus, the sand grains are cemented together, and eventually they get buried to depths of three to even thirty thousand feet. And that's where oil is found today (Dandekar, 2006). The rock containing this decayed matter is called source rock. These source rocks are either sandstones or carbonate rocks. These rocks are made up of sediments formed from the Earth's surface debris (mineral, animal and vegetable) or chemical precipitations (Dandekar, 2006).

1.3 Oil recovery

The amount of oil that is recoverable is determined by a number of factors. These factors include the permeability of the rocks, the strength of natural drives (the gas present, pressure from adjacent water or gravity), and the viscosity of the oil. When the reservoir rocks are tight, such as shale (carbonates), oil generally cannot flow through, but when they are permeable such as in sandstones, oil flows freely. This flow of oil is often pushed by natural pressures surrounding the reservoir rocks including natural gas that may be dissolved in the oil, natural gas present above the oil, water below the oil and the strength of gravity. There are three types of oils recoveries namely (Dandekar, 2006):

- **Primary recovery**: If the underground pressure in the oil reservoir is sufficient, then this pressure will force the oil to the surface. The presence of gaseous fuels, natural gas, and water, are the primary suppliers of the required underground pressure. Usually, about 20 % of the oil in a reservoir is extracted by the use of underground pressure.

- **Secondary recovery**: The decline in underground pressure makes it very hard to force oil out to the surface. Secondary oil recovery uses various techniques to aid in recovering oil from depleted pressure reservoirs. Pumps are generally used to bring the oil to the surface. However, other techniques are used to increase the

underground pressure. These techniques include brine injection, natural gas reinjection, air injection and carbon dioxide injection. The combination of primary and secondary recovery techniques, recovers 25 to 30 % of oil in reservoirs.

- **Tertiary recovery**: Oil viscosity is reduced in order to enhance oil production in tertiary oil recovery. Thermally enhanced oil recovery methods (TEOR) are tertiary recovery techniques that heat the oil and make it easier to extract. Steam injection is the most common form of TEOR. Tertiary recovery allows an extra 5 to 15 % of the reservoir's oil to be recovered.

1.4 Porosity

Porosity is defined as a ratio of the pore volume (void space) in a reservoir rock to the total volume (bulk volume) and it is expressed as a percentage (Dandekar, 2006). The pore structure is often considered as comprising a network of voids, or pores, with a distribution of sizes and an idealised shape such as cylinders (Sahimi *et al*., 1990). Techniques such as mercury porosimetry and gas sorption have been developed to characterise the structure of the pore space using parameters such as the overall voidage fraction, surface area, pore volume, pore size distribution (PSD), mercury entrapment and pore connectivity (Rigby *et al*., 2003).

1.5 Permeability

Permeability is a measure of the fluid conductivity of a particular porous material. Unlike porosity, which is a static property of the porous medium, permeability is a flow property (dynamic). It can only be characterised by conducting flow experiments on the rock (Dandekar, 2006). Several parameters of pore geometry are needed for estimating permeability which is a key parameter for the characterization of reservoir sandstones. Nuclear magnetic resonance (NMR) techniques are among the most powerful methods available for determining local dynamic properties of molecules in liquid, solid, and even gaseous phases of organic and inorganic molecules (Pape *et al*., 1999). The technique can also deliver estimates of radial profiling of fluid volumes, fluid saturations, and direct hydrocarbon characterization (Schlumberger limited annual report, 2008).

1.6 Scope of work

The understanding of how pore space properties of sedimentary rocks affect recovery and entrapment of oil is a vital requirement for the exploitation of hydrocarbon reservoirs. The total pore volume of a reservoir rock is considered to be comprised of movable and non-movable fluid volumes. The movable fluid is referred to as the free fluid index (FFI), whilst the non-movable fluid volume is called the bound volume index (BVI). These pore volumes (FFI and BVI) often expressed as a fraction, are typically used in formation evaluation as an indication of the economic potential of a reservoir (Appel *et al*., 1998). The standard method to determine FFI and BVI in laboratory measurements on reservoir core is by progressive centrifuge desaturation of the core plug, and thus, the capillary pressure is determined this way (Appel *et al*., 1998, Hirasaki and Mohanty, 2002). The BVI is the fluid volume remaining at a pre-selected capillary pressure, as determined by the centrifuge desaturation of the core plug. Alternatively, the BVI can be estimated with mercury porosimetry (Appel *et al*., 1998).

The FFI and BVI can also be predicted by Carr-Purcell-Meiboom-Gill (CPMG) NMR experiment (Miller *et al*., 1990). In the CPMG NMR measurement, the core plug is placed in a magnetic field and then by a long string of radio frequency pulses. Thus for a fluid in a single pore, isolated pore, and for condition known as the fast diffusion limit magnetization decays exponentially with time. The time constant, which is also known as transverse relaxation time, is related to the pore surface to volume ratio (Cohen and Mendelson, 1982). However, this method is limited to the fact that the pores are assumed to be isolated and other physical features such as the surface chemistry can affect the result. In a similar approach, Appel *et al*. (1998) used a pulsed gradient spin echo (PGSE) NMR technique for predicting the relative volumes of movable and non-movable fluid in core plugs. PGSE NMR is a well established method for measuring the root mean square (r.m.s) displacement of fluid molecules (Stejskal and Tanner, 1965; Karger *et al*., 1988; Callaghan, 1991). Appel *et al*. (1998) adopted a model similar to that of BVI and FFI analysis of the CPMG NMR data. These researchers assumed that the pores contributing to the FFI to be large and most likely well connected, thus, the mobility for fluid molecules in the pores should be free of any restriction, thereby restricting the r.m.s displacement. In contrast, the pores contributing to the BVI should be highly restrictive of fluid motion, and thus, the fluid molecules would make multiple collisions with the pore wall. Furthermore,

the model assumed that that there was hardly any exchange between the fluid volumes corresponding to the BVI and FFI. The values obtained for BVI and FFI were in good qualitative agreement with values obtained from mercury porosimetry, centrifuged gravimetric saturation measurements and CPMG NMR measurements.

In addition to FFI and BVI, the reservoir rock permeability is also an important parameter for economic evaluation potential of reservoir rocks. The rock permeability (k') allows estimation of the fluid flow. A fundamental expression for the permeability of a porous medium is given by the modified Kozeny–Carman equation (Pape *et al.*, 1999):

$$k' = \frac{1}{8}\frac{\varepsilon}{r_h} r^2 eff \qquad (1.1)$$

Where ε is the porosity, τ_h is the hydraulic tortuosity, and r_{eff} is the effective hydraulic pore radius. In general, the tortuosity (τ) of a porous medium describes the geometry of flow paths, and thus, a measure of the complexity of the material. Thus, it can be seen in Equation 1.1, that, depending on the geological history, for individual reservoir sandstones, relationships exist between porosity, tortuosity, and effective pore radius. These relationships, if tested on rock samples in the laboratory, can be used to understand diagenetic processes of compaction and derive a permeability–porosity relationship (Pape *et al.*, 1999). However, reservoir rocks are chemically and geometrically heterogeneous, and thus, the measurement and the relationships between both structural and topological might be difficult. In contrast, catalyst support pellets, with the same chemical components as sandstone reservoir rocks, can offer simplified analogy of these transport relationships.

As mentioned above, mercury porosimetry is widely used in the oil industry to estimate the BVI. This technique can provide information which is valuable in assessing the multiphase fluid behaviour of oil and gas in a strongly water-wetting system. It can estimate the trapping of oil or gas which is controlled mostly by capillary forces, and thus, a direct analogy with the air-mercury system is possible (Chatzis *et al.*, 1983). Mercury porosimetry has been used by various researchers to identify those aspects of pore systems which affect the trapping of non-wetting fluids such as mercury, or by analogy oil and gas, in strongly water-wet systems (Meyer, 1953; Wardlaw and McKellar, 1981; Tsakiroglou and Payatakes, 1990). Mercury porosimetry is often interpreted using the Washburn

equation and the assumption that pores are cylindrical, and, equally accessible to mercury. Therefore, the Washburn equation constitutes a special model that fails to take into account the real nature of pores that consist of a network of interconnected circular pores. Such a model may not represent the pores in reality but it's generally accepted as the practical means of dealing with complex pore structures (Moro and Bohni, 2002).

To address some of the limitations of mercury porosimetry raised above, Androutsopoulos and Mann (1979) developed a two-dimensional network model consisting of cylindrical pore segments assembled into square grids, and thus, introduced pore connectivity that is essential in determining the accessibility of the interior of porous materials. However, these workers simulation model was based on two-dimensional networks that were limited to fixed connectivity and pore length. Nevertheless, these researchers found that mercury entrapment increased as the variance of the PSD got wider and that mercury was preferentially entrapped in larger pores. Similar observations were made by Conner and Lane (1984), Lapidus *et al.* (1985), Carniglia (1986), and Tsakiroglou and Payatakes (1990). These independent research groups used a three dimensional bond network that offered a more realistic picture of a natural void structure. In a similar approach, Portsmouth and Gladden (1991; 1992) investigated the effects of PSD and pore connectivity on the features of mercury porosimetry experiments. These researchers used a three dimensional random pore bond network to determine tortuosity and the influence of this parameter on PSD and connectivity. It was found that entrapment increased with the variance of the PSD and decreased pore connectivity. In addition, the estimated tortuosities increased with decreased pore connectivity and increased variance of PSD. In recent years, similar observations were made by Friedman *et al.*, (1995), Vogel (1997; 2000), Salmas *et al.* (2003), Armatas and Pomonis (2004), and Armatas (2006). However, these significant transport relationships lack experimental verifications with real porous materials.

There are only limited successful experiments to support simulation findings on structural and topological properties of porous materials. Carniglia (1986) made an attempt to predict tortuosity factors by utilizing mercury porosimetry and gas adsorption data. This worker obtained a fair agreement between tortuosity factors computed by his method and those calculated from diffusion measurements from a variety of metal oxides and catalysts. In a

similar approach, Holt and Smith (1989) worked on the effect of surface roughness on effective diffusivities. These researchers used both mercury porosimetry and gas adsorption to obtain surface areas and effective diffusivities of different sphere packings. The geometry of the sample was obtained with the aid of transmission electron microscope (TEM). Holt and Smith (1989) correlated the fraction of effective diffusivities and porosity as a function of pore size. It was found that the Knudsen diffusion was independent of surface roughness. In a different approach, Reyes *et al.* (1991) used Monte Carlo simulation procedures to create random assemblages of micro-spheres and for the estimation of effective diffusivities in the model porous structures. The pore structures created by the Monte Carlo simulation closely resembled catalyst support pellets. It was found that the effective diffusivities increased with an increased porosity. In addition, the simulated diffusivities were in agreement with the experimental observation values.

In recent years, Salmas and Androutsopoulos (2001) presented a simplified empirical correlation for tortuosity prediction based on nitrogen sorption hysteresis data by fitting parameters of a corrugated pore structure model (CPSM). The CPSM is a statistical model which simulates gas adsorption and capillary condensation-evaporation phenomena. The correlation proposed by these researchers enabled the evaluation of low tortuosity factors (1-2) for porous materials that contained pores with a more or less cylindrical geometry. In addition, independent mercury porosimetry runs on catalysts showed a proportional increase in mercury entrapment with an increase in the corresponding tortuosity values, and thus, the tortuosity factor of porous media increases proportionally with the pore volume evolution. The work of Salmas and Androutsopoulos (2001) shared similar limitations to that of Carniglia (1986), Holt and Smith (1989), Reyes *et al.* (1991). These workers incorporated several techniques to estimate the tortuosities , and, in addition to the several assumptions made in the CPSM-nitrogen model, the tortuosity factors were only limited to materials exhibiting an H-2 Type gas sorption hysteresis. Thus, for random pore network models of unimodal/monodisperse porous media, simulation results suggest that the mercury entrapment increased as the variance of the PSD got wider; and decreased with increased pore connectivity. However, experimental studies are required to support these novel simulation findings. As mentioned above, mercury porosimetry can be used to estimate the mercury entrapment and PSD of porous media. Where as, the topological properties of porous media can be estimated with gas sorption and PGSE NMR techniques.

1.6.1 Objective

In this study, the transport relationships in catalyst support pellets will be investigated. Emphasis will be given to the relationships between PSD, pore connectivity, pore length, mercury entrapment, and tortuosities of these materials. The entrapment of oil in reservoir rocks, by analogy, is similar to the entrapment of mercury following porosimetry analysis of catalyst support pellets. Therefore, the entrapment translates to the BVI, which quantifies the irreducible hydrocarbon saturation. The fundamentals of how non-wetting fluids behave are consistent, and thus, validate the use of the mercury analogy to model oil. While the porosity may be sufficient to predict some macroscopic material properties, the analysis of the distribution of pore sizes and the connectivity of the pore structure is necessary for a deeper micro-structural understanding and the prediction of fluid transport. Mercury intrusion porosimetry and gas sorption techniques can be used to evaluate the porosity, pore size, PSD, pore connectivity and mercury entrapment.

As mentioned above, mercury porosimetry has been used extensively in pore structural characterisation in the oil and catalyst industries. The interpretation of the experiment is usually based on the intrusion data which is generally used to extract pore size, PSD, and pore volume. In general, much less use is made of the mercury retraction curve, which is generally associated with hysteresis and mercury entrapment. The mercury extrusion process is not well understood, and thus, this research intends to study the transport regime (mass transfer to and from the external surface) in detail, and, in particular the region of the onset of mercury retraction process and the pore connectivity related phenomena that can be described with aid of percolation theory. In addition, the transport properties of a porous solid depend very strongly on interconnectivity, and thus, materials with high tortuosity may involve a slow extrusion process of the non-wetting fluid. Therefore, the ability to measure tortuosity in fully and partially saturated porous media with PGSE NMR can elucidate the mechanism of mercury entrapment. The experimental techniques used in this work will include a combination of gas adsorption technique, mercury porosimetry, and PGSE NMR technique. The Experimental studies on these model materials used in place of reservoir rocks could reveal additional information towards achieving a better interpretation of the mechanisms of entrapment that could lead to more accurate predictions of BVI and FFI in the oil industry.

1.7 Thesis structure

The overall description of this project is divided into nine Chapters:

- The first Chapter introduces some of the familiar terms of the work. It offers an insight to the scope and general objective of the project.

- The second Chapter provides the literature review of petroleum reservoirs. It provides information to the general features of porous materials such as the porosity, permeability, interfacial tension and wettability. Finally, the rational selection of the adopted materials (catalyst support pellets) of this project is revealed in this section. In addition, the method of production and the characteristics of these materials are given in this Chapter.

- The third Chapter deals with the literature review of gas adsorption porosimetry, mercury porosimetry and PGSE (NMR) technique. It discusses the theories and applications of these novel techniques. Furthermore, the proposals for the research programmes are given under each relevant characterisation technique review.

- The fourth Chapter deals with the gas adsorption porosimetry and the characterisation of the materials in this project. A comprehensive study of the nitrogen adsorption and desorption isotherms is given this Chapter. The nitrogen adsorption and desorption isotherms are used to obtain traditional characteristics parameters such as the BET surface area, pore size, BJH pore size distribution, and pore volume. In addition, other less common parameters such as the pore connectivity and measure of pore length are given in this Chapter.

- The fifth Chapter deals with mercury porosimetry and the characterisation of the materials in this project. Mercury entrapment as a function of equilibration time is tested. In addition, the traditional characteristic parameters such as the pore size, pore size distribution, pore volume, porosity and surface area are obtained. Furthermore, the semi-empirical alternative equations to the Washburn equation are validated in this section to understand the origins of hysteresis in mercury porosimetry.

- The sixth Chapter is about the characterisation of the materials by using the PGSE technique. In this Chapter, diffusion as a function of time is investigated. In addition, the effect of restricted diffusion and heterogeneity in porous media are investigated. Finally, diffusion as a function of pore filling is investigated, and thus, the effects of vapour phase contribution to the overall diffusivity is elucidated.

- Chapter seven is an extension of Chapter six. The effect of diffusion as a function of pore loading is further investigated. Furthermore, this Chapter deals with the kinetic studies of the materials. The disposition and distribution of adsorbed water ganglia within partially-saturated samples is investigated as a function of pore loading in this Chapter.

- Chapter eight is the correlation part of this project. It combines all the results provided by the three characterisation methods to elucidate the mechanisms of transport phenomena in porous media, especially the correlation between entrapment and tortuosities that can help estimate the Bound Volume Index (BVI) parameter for oil reservoir rocks. In this Chapter, the simulation correlations discussed in Chapter one (see Section 1.6) and Chapter 3 (see Section 3.2.8) will be verified with experimental results reported in Chapters four to seven.

- Chapter nine offers the conclusion and future recommendations of the project.

1.8 References

Androutsopoulos, G.P. and Mann, R., 1979. Evaluation of mercury porosimeter experiments using a network pore structure model. *Chemical Engineering Science*, 34, 1203-1212.

Apple, M., Stallmach, F., Thomann, H., 1998. Irreproducible fluid saturation determined by pulsed field gradient NMR. *Journal of petroleum science and engineering*, 19, 45-54.

Armatas, G.S., and Pomonis, P.J., 2004. A Monte Carlo pore network for the simulation of porous characteristics of functionalized silica: pore size distribution, connectivity distribution and mean tortuosities. *Chemical engineering science*, 59, 5735-5749.

Armatas, G.S., 2006. Determination of the effects of the pore size distribution and pore connectivity distribution on the pore tortuosity and diffusive transport in model porous networks. *Chemical engineering science,* 61, 4662 – 4675.

Callaghan P.T., 1991. *Principles of nuclear magnetic resonance microscopy*. Oxford: University press.

Carniglia, S.C., 1986. Construction of the tortuosity factor from porosimetry. *Journal of catalysis*, 102 (2), 408-418.

Chatzis, I., Morrow, N.R., Lim, H.T., 1983. Magnitude and detailed structure of residual oil saturation. *SPE Journal*, 23, 311 – 326.

Cohen, M.H., Mendelson, K.S., 1982. Nuclear magnetic relaxation and internal geometry of sedmintry rocks. *Journal of applied physics*, 53 (2), 1127-1135.

Conner, W.C., and Lane, A.M., 1984. Measurement of the morphology of high surface area solids: effect of network structure on the simulation of porosimetry, J. Catal. 89, 217–225.

Dandekar, A.Y., 2006. *Petroleum reservoir rock and fluid properties.* Taylor & Francis group.

Friedman, S.P., Zhang, L., and Seaton, N.A., 1995. Gas and solute diffusion coefficients in pore networks and its description by a simple capillary model. *Transport in porous media*, 19, 281-301.

Hirasaki, G., and Mohanty K.K., 2002. *Fluid-rock characterisation and interactions in NMR well logging*. Thesis (PhD). Rice University, Houston.

Holt, T.E., and Smith, D.M, 1989. Surface roughness on Knudsen diffusion. *Chemical engineering science*, 44 (3), 779-781.

Lapidus, G.R., Lane, A.M., Conner, W.C., 1985. Interpretation of mercury porosimetry data using a pore-throat network model, *Chem. Engng Commun*. 38, 33–56.

Meyer, H.I., 1953. Pore distribution in porous media. *Journal of applied physics*, 24 (5), 510-512.

Miller, M.N., Paltiel, Z., Gillen, M.E., Ganot, J., Bouton, J.C., 1990. Spin echo magnetic resonance logging: porosity and free fluid index determination. *65TH Annual Technical conference and exhibition of the society of chemical engineers*, Richardson, TX, USA, 321-333.

Moro, F., and Bohni, H., 2002. Ink-bottle effect in mercury intrusion porosimetry of cement-based materials. *Journal of colloid and Interface Science*, 246, 135-149.

Karger, J., Pfeifer, H., Richter, R., Furtig, H., Roscher, W., Seidel, R., 1988. NMR-study of mass transfer in granulated molecular-sieves. *AICHE Journal*, 34 (7), 1185-1189.

Pape, H., Clauser, C., Iffland, J., 1999. Permeability prediction for reservoir sandstones based on fractal pore space geometry. *Geophysics*, 64 (5), 1447– 1460.

Portsmouth, R.L., and Gladden, L.F., 1991. Determination of pore connectivity by mercury porosimetry. *Chemical Engineering Science*, 46 (12), 3023-3036.

Portsmouth, R.L., and Gladden, L.F., 1992. Mercury porosimetry as a probe of pore connectivity. *Chemical Engineering Research and Design*, 70 (1), 63-70.

Reyes, S., Iglesia, E., Chiew, Y., 1990. Monte Carlo simulations of effective diffusivities in three-dimensional pore structures. *Proc. Mater. Res. Soc.*, 195, 553 -558.

Rigby, S.P., Fletcher, R.S., Riley, S.N., 2003. Determination of the cause of mercury entrapment during porosimetry experiments on sol-gel silica catalyst supports. *Appl. Catal. A*, 247, 27-39.

Sahimi, M., Gravels, G. R., and Tsotsis, T. T., 1990. Statistical and continuum models of fluid-solid reactions in porous media, *Chemical Engineering Science,* 45, 1443-1502.

Salmas C.E., and Androutsopoulos, G.P., 2001. A novel pore structure tortuosity concept based on nitrogen sorption hysteresis data. *Industrial engineering chemical research*, 40 (2), 721-730.

Salmas, C.E., Ladavos, A.K., Skaribas, S.P., Pomonis, P.J., Androutsopoulos, G.P. 2003. Evaluation of Microporosity, Pore Tortuosity, and Connectivity of Montmorillonite Solids Pillared with $LaNiO_x$ Binary Oxide. A Combined Application of the CPSM Model, the α_s-Plot Method and a Pore Percolation−Connectivity Model. *Langmuir*, 19 (21), 8777–8786.

Shlumberger limited annual report, 2008.

Stejskal, E.O., and Tanner, J.E., 1965. Spin diffusion measurements: Spin echoes in the presence of a time-dependent gradient. *Journal of chemical Physics*, 42, 1768-1777.

Tsakiroglou, C.D., and Payatakes, A.C., 1990. A new simulator of mercury porosimetry for the characterization of porous materials. *Journal of Colloid and Interface Science*, 137, 315-339.

Vogel, H.J., 1997. Morphological determination of pore connectivity as a function of pore size using serial sections. *European Journal of Soil Science*, 48, 365–377.

Vogel, H.J., 2000. A numerical experiment on pore size, pore connectivity, water retention, permeability, and solute transport using network models. *European Journal of Soil Science*, 51, 99–105.

Wardlaw, N.C., McKellar, M., 1981. Mercury porosimetry and the interpretation of pore geometry in sedimentary rocks and artificial models. *Powder Technology*, 29, 127 – 143.

World Oil Journal, 2005.

World Oil Journal, 2009.

2.0 Oil reservoir rocks and catalyst support pellets

2.1 Introduction

This Chapter provides a basic introduction to petroleum reservoir rocks. Different types of reservoirs rocks are discussed in Section 2.2. In addition, information is given in relation to the general features of oil reservoir rocks such as the porosity, permeability, interfacial and surface tension, and wettability. Oil reservoir rocks are chemically and geometrically heterogeneous, and thus, more chemically pure model materials for majority sandstone reservoir rocks have been adopted for this project. These are catalyst support pellets with the same chemical components as sandstone reservoir rocks. The formation and characteristics of these materials is summarised in Section 2.3.

2.2 Oil reservoir rocks

The majority of oil reservoir rocks are made up of sandstones and/or carbonates (about 99% of the total). These are sedimentary rocks; rocks that are made up of sediments formed at the Earth's surface from debris (mineral, animal and vegetable) or chemical precipitations. They are stratified in successive beds (Cosse, 1993). In general, sandstone reservoirs are by far the most widespread, accounting for 80% of all reservoirs and 60% of oil reserves. The rock is formed by grains of quartz (silica SiO_2). Free grains form sand and, if these grains are cemented, they form sandstone. Common types are shaly sandstone and carbonate sandstone (Cosse, 1993). The carbonate rocks consist of limestone ($CaCO_3$) and/or dolomite ($CaCO_3$, $MgCO_3$). A common type is shaly carbonates, but marls, which contain between 35 to 65% shale, are not reservoirs due to the small proportion of shale, binding the grains together, which considerably decreases the permeability (Cosse, 1993). A typical reservoirs rock is shown in Figure 2.1.

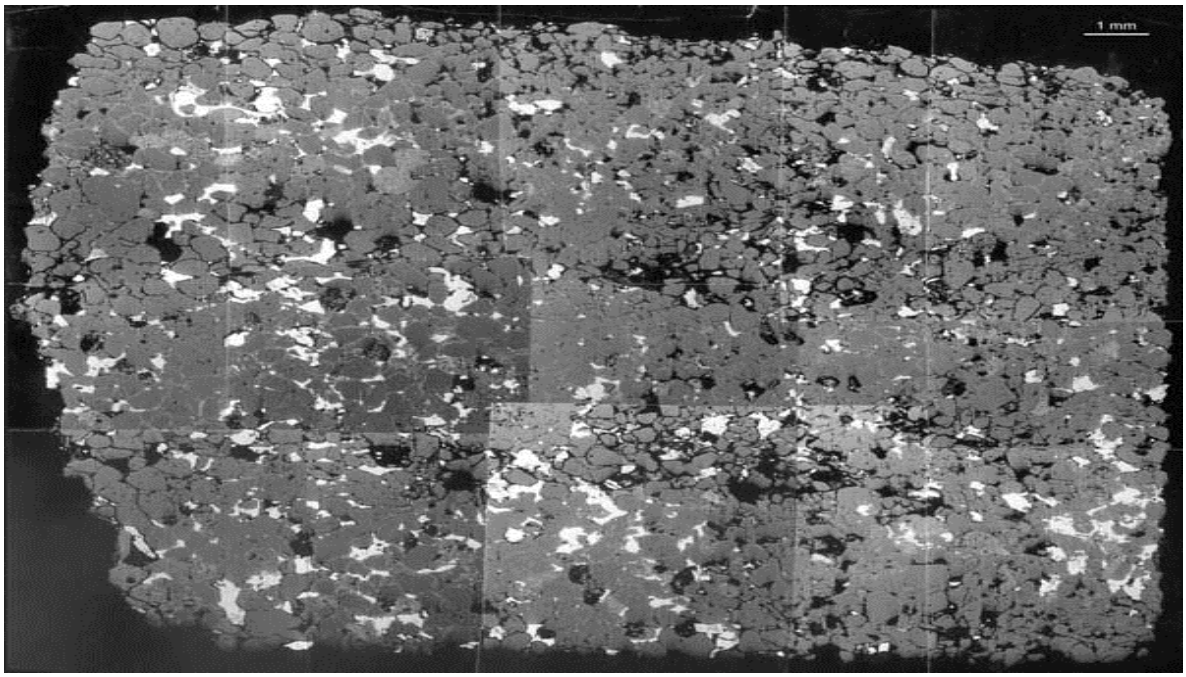

Figure 2.1

A montage of SEM images of a reservoir sandstone block (www.kpal.co.uk, 15/12/2010)

Petroleum reservoir fluids (oil and gas) are fossil fuels that were formed millions of years ago. They are found trapped within rocks in the Earth, in both offshore and onshore locations. Scientific data indicates that these fluids were formed million of years ago when animal and plant matter settled into the sea, together with sand, silt and rocks; consequently resulting in a build up of numerous layers along the coastline and on the sea bottom. These layers were buried deep in the Earth as a result of geological shifts. Variables such as geological time scales, pressure due to burial and depth, and temperature due to geothermal gradient related to depth resulted in the conversion of the organic material into petroleum reservoir fluids, and the mud, sand and silt into rock (Cosse, 1993; Dandekar, 2006).

Chemically, reservoir fluids are hydrocarbons with different molecular composition that gives each a unique identity. Physically, petroleum sources are fluids that can migrate, and the rocks that produced them are usually not the source rocks. In the absence of impermeable barriers, some of these fluids seep to the surface of the Earth. However, most

reservoir fluids were trapped by nonporous rocks or other barriers that did not allow any further migration (Dandekar, 2006). These underground traps of oil and gas are known as petroleum reservoirs. Oil reservoirs are made up of porous and permeable rocks that can hold significant amounts of oil and gas within pore spaces of those rocks (Cosse, 1993).

Oil reservoirs are created through three sequential steps, that is, deposition, conversion (migration), and trap. A trap is usually an anticline, where rocks have been buckled into the form of a dome. If this anticline has a seal of impermeable rock, hydrocarbons remain in this trap until they are drilled and brought up to the surface. These reservoirs can be found at depths as shallow as 40ft in West Africa, and as deep as 21,000ft at North Sea-UKCS (Dandekar, 2006). Most petroleum reservoirs contain at least two fluid phases, either gas and water, or oil and water. Nevertheless, some might contain all three phases, that is, gas, oil, and water. In principle, they are supposed to be separated by gravity segregation but parameters such as rock/fluid properties and solubility, restrict complete gravitational segregation as illustrated in Figure 2.2.

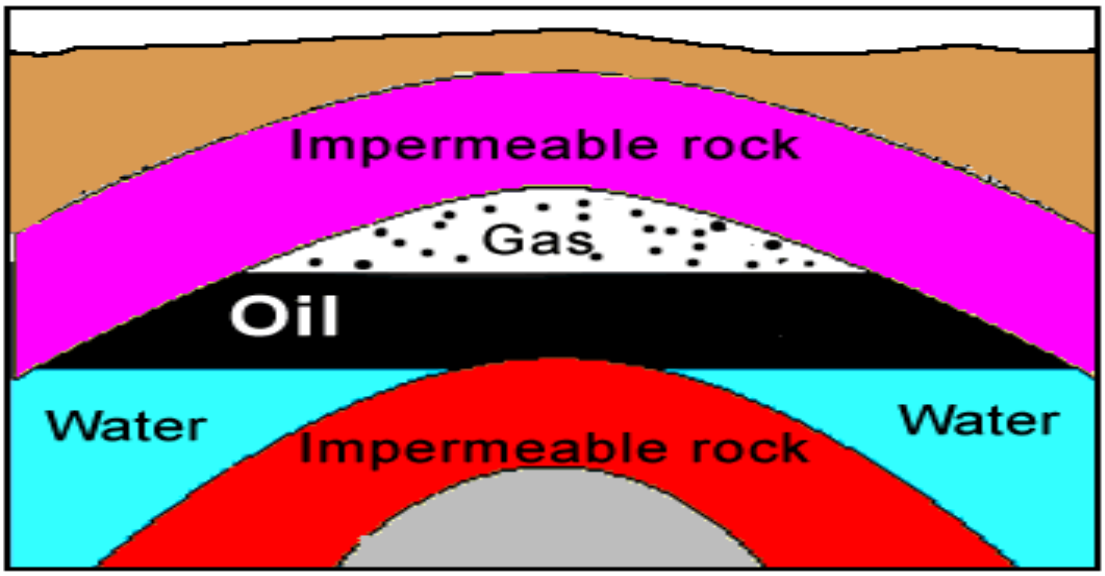

Figure 2.2

Schematic of an idealised petroleum reservoir (www.msnucleus.org, 4/3/2008)

2.2.1 Porosity

Sandstone started out as individual sand particles of varying grain sizes that were initially buried during the depositional process, resulting in spaces between the particles. These tiny spaces or pores (typically up to 300 μm) in petroleum reservoir rocks are the ones in which petroleum reservoir fluids are present, much like a sponge holding water. This particular storage capacity of reservoir rocks is called porosity (Dandekar, 2006). Porosity is defined as a ratio of the pore volume (void space) in a reservoir rock to the total volume (bulk volume) and it is expressed as a percentage. The void space is the summation or combined volume of all the pore spaces in a given reservoir rock. Porosity is donated by ϕ and expressed by the following relationship (Dandekar, 2006).

$$\phi = \text{Pore volume/Total or bulk volume} \tag{2.1}$$

In general, reservoir rocks are classified by the mode of origin, namely original or induced. Original or primary porosity is developed in the deposition of the material. Induced or secondary porosity on the other hand is developed by some geological process following the deposition of the rock such as the fractures commonly found in limestone. Reservoir rocks with original porosity are more uniform in their characteristics than those rocks in which a large part of the porosity is induced (Dandekar, 2006). The fact that reservoir rocks were formed as a result of deposition of sediments gives rise to different types of voids or pores. Some of these voids that developed were interconnected with other void spaces and as a result form a network, while some were connected with other void spaces but with a dead-end or cul-de-sac; and some pores became completely isolated or closed from other void spaces because of cementation (Dandekar, 2006).

Figure 2.3 shows a typical schematic representation of a porous material (Sing *et al.*, 1985). The first category of pores is those totally isolated from their neighbours, as in region (a), they are described as closed pores. These pores influence macroscopic properties such as bulk density, mechanical strength, and thermal conductivity, but are inactive in processes such as fluid flow and adsorption of gases. However, pores which have a continuous channel of communication with the external surface of the body, like (b), (c), (d), (e), and (f), are described as open pores. Some may be open only at one end

like (b), and (f); they are then described as blind pores. Others may be open at two ends (through pores), like around (e).

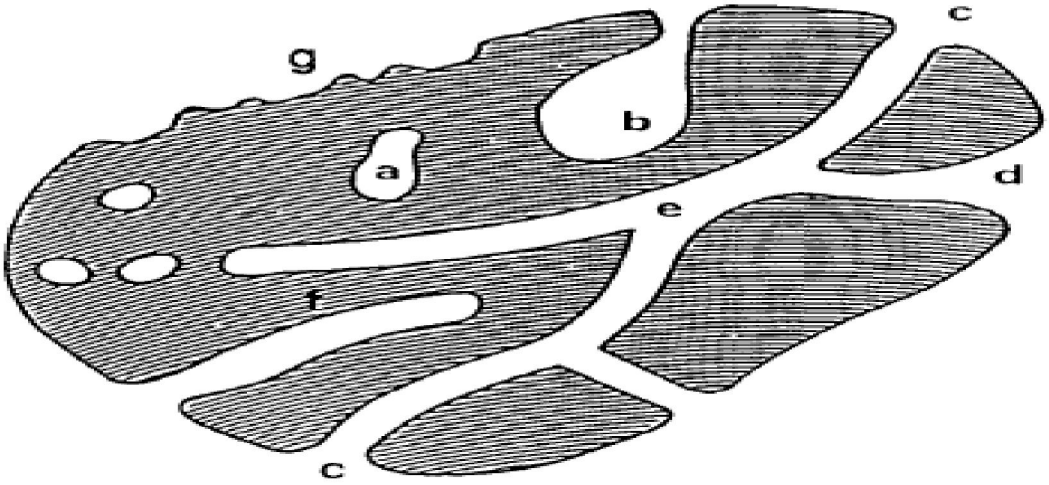

Figure 2.3
Schematic cross section of a porous solid (Sing *et al*., 1985)

In general, the internal structure of a porous material is often a complex one, with interconnected pores of a multiplicity of shapes and sizes (Sing *et al*., 1985). According to the International Union of Pure and Applied Chemistry (IUPAC) classifications, pores can be categorised into micropores (< 2 nm), mesopores (2-50 nm) and macropores (> 50 nm). In addition, pores can also be classified according to their shape (Sing *et al*., 1985). They may be cylindrical; either open (c) or blind (f), ink-bottle shaped (b), finnel shaped (d) or slit-shaped. Roughness is similar to porosity; this is normally found at the external surface, represented around (g). Based on these types of pores, the total or absolute porosity of a reservoir rock comprises effective and ineffective porosity (Dandekar, 2006).

- Absolute porosity is mathematically expressed by the following expression (Dandekar, 2006):

$$\text{Total or absolute porosity, } \phi = \text{Pore volume/Total or bulk volume} \qquad (2.2)$$

$$\phi = \frac{A}{B} \tag{2.3}$$

- Effective porosity is mathematically expressed by the following expression

$$\phi = \frac{C}{B} \tag{2.4}$$

- Ineffective porosity is mathematically expressed by the following expression

$$\phi = \frac{D}{B} \tag{2.5}$$

Where;

A = Vol. of interconnected pores + Vol. of dead-end pores + Vol. of isolated pores

B = Total or bulk volume

C = Vol. of interconnected pores + Vol. of dead-end pores

D = Vol. of completely disconnected connected pores

The effective porosity value is the quantitative value desired and it's used in almost all calculations because it represents the pore occupied by mobile fluids. The effective porosity of rocks varies between less than 1% to over 40%. The closed or isolated or completely disconnected pores are ineffective in producing any petroleum reservoir fluids due to their isolation. It is often stated that the porosity is (Dandekar, 2006):

- Low if $\phi < 5\%$.
- Mediocre if $5\% < \phi < 10\%$.
- Average if $10\% < \phi < 20\%$
- Good if $20\% < \phi < 30\%$
- Excellent if $\phi > 30\%$

2.2.2 Absolute Permeability

Permeability is a measure of the fluid conductivity of a particular porous material. By analogy to electrical conductance, permeability represents the reciprocal of the resistance

that the material medium offers to the fluid flow. It is the proportionality constant between fluid flow rate and potential gradient (applied pressure). Permeability can be determined experimentally according Darcy's law (Dandekar, 2006). For example, let us consider a sample length dx, and cross section area A, saturated with a fluid of dynamic viscosity μ_v, and crossed horizontally by a flow rate Q (measured in the conditions of section dx) as illustrated in Figure 2.4 (Cosse, 1993).

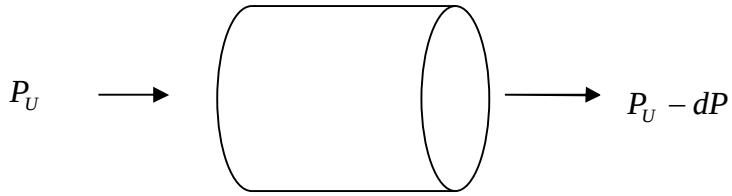

Figure 2.4
Schematic representation of permeability

In steady state conditions, the upstream pressure is P_U, and the downstream pressure is $P_U - dP$. The lateral sides are impervious to fluids. If the fluid doesn't react with the rock, then:

$$Q = A.\frac{k'}{\mu_v}\frac{dP}{dx} \tag{2.6}$$

Equation 2.6 is known as Darcy's law. k' is the permeability coefficient that describes the absolute or specific permeability in the direction considered. k' is expressed in meters square (m^2) but the customary unit is Darcy $(\mu m)^2$ (Cosse, 1993; Dandekar, 2006). Thus, permeability is a flow property (dynamic) that can only be characterised by conducting flow experiments of the rock. The follow pattern in a porous media is illustrated in Figure 2.5.

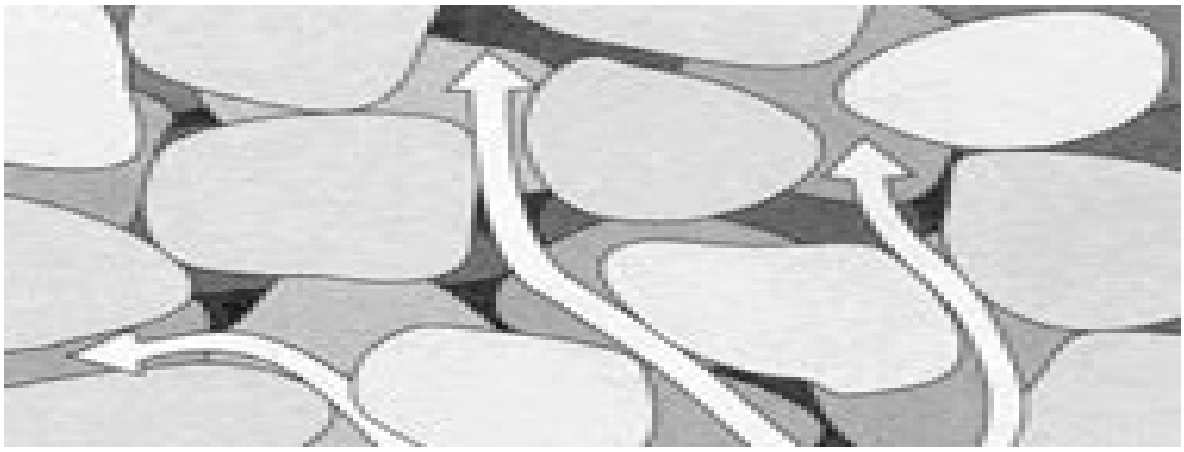

Figure 2.5
Illustration of flow patters in porous materials (www.mpgpetroleum.com, 04/03/2008)

2.2.3 Relative permeability

This is the permeability measure of a rock that contains two or more fluids. Reservoir rocks that are saturated with several phases are more common. The pore space or the pore volume of a reservoir rock does not contain one phase but multiple fluid saturations of gas, oil, and water. The concept of relative permeability provides a mechanism of quantifying the amount of flow for each phase in multiphase systems (Cosse, 1993; Dandekar, 2006).

2.2.4 Interfacial and surface tension

The multiple-phase fluid systems in petroleum reservoirs are normally immiscible and when they are in contact, these fluids are separated by a well-defined interface between gas-oil-water, and oil-water pairs. This interface is a few molecular diameters in thickness. Surface tension is normally used when characterizing the gas-liquid surface forces, whereas interface tension is used in characterizing two immiscible liquids (Dandekar, 2006). This is illustrated in Figure 2.6.

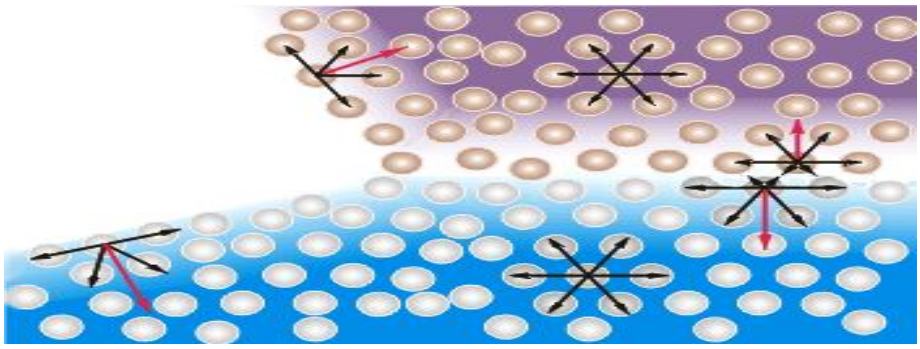

Figure 2.6
Illustration of contact between two immiscible liquids (www.igb.fraunhofer, 04/03/2008)

The attractive forces between the molecules of different kinds are considerably less than those between the molecules of the same kind which results in an interfacial tension. The surface tension generally decreases with an increase in pressure and temperature. An increase in temperature will ultimately increase the kinetic agitation of the molecules and speed of molecules increase, resulting in decrease in surface tension. The same behaviour is observed in interfacial tension (Dandekar, 2006).

2.2.5 Wettability

Wettability is the tendency of a fluid to spread on and preferentially adhere to wet a solid surface in the presence of other immiscible fluids, and thus, in a multiphase situation, one of the fluid phases has a greater degree of affinity towards the solid surface of the reservoir rock (Dandekar, 2006). For example, in a system comprising of oil, water (brine), and rock (sandstone or carbonate), one of these phases has a tendency to preferentially wet the rock. It is a key parameter that affects the petrophysical property of a reservoir rock. The knowledge of reservoir wettability is essential in determining reservoir rock properties such as the distribution of gas, oil, and water within reservoir rock, capillary pressure and relative permeability characteristics, and consequently the production of hydrocarbons (Cosse, 1993; Dandekar, 2006). The spreading tendency of a fluid can be expressed more conveniently as adhesion tension, A_T. Adhesion tension is a function of the interfacial tension and it determines which fluid preferentially wets the fluid. The concept of wettability is illustrated in the Figure 2.7.

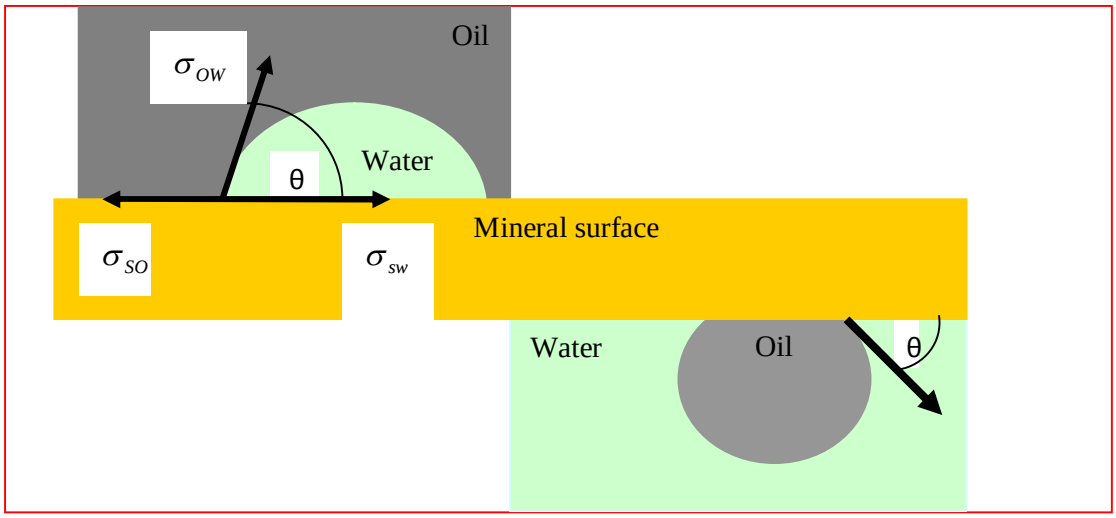

Figure 2.7

Schematic representation of a system of two immiscible liquids (oil and water) in contact with a mineral surface (Dandekar, 2006)

From the system shown above, the adhesion tension is defined by:

$$A_T = \sigma_{SO} - \sigma_{SW} \tag{2.7}$$

Where σ_{SO} is the interfacial tension between the solid and the lighter fluid phase (oil) and σ_{SW} is the interfacial tension between the solid and the denser fluid phase (water). The contact angle (θ), at the liquid-solid surface is measured through denser liquid phase and can range from 0 to 180°. Given that the cosine of the angle gives the following equation:

$$\cos\theta_{OW} = \frac{\sigma_{SO} - \sigma_{SW}}{\sigma_{OW}} \tag{2.8}$$

Therefore:

$$A_T = \sigma_{OW} \cos\theta_{OW} \tag{2.9}$$

According to Equation 2.9, the positive adhesion tension indicates that the denser phase liquid (water) preferential wets the solid surface, whereas negative value of adhesion tension indicates a wetting by lighter phase liquid (oil). Adhesion tension of zero indicates that both phases have equal wettability affinity for the solid surface (Dandekar, 2006).

2.3 Catalyst support pellets as models for oil reservoir rocks

As mentioned in Section 2.2, the vast majority of oil reservoir rocks are made up of sandstones (silica, SiO_2) and/or carbonates ($CaCO_3$). These are rocks made up of sediments formed at the Earth's surface from debris or chemical precipitations, and thus, reservoir rocks are chemically heterogeneous. As detailed in Section 2.2, contact angle is considered as one of the most important parameters of measuring the preferential affinity of reservoir rocks. However, the presence of numerous surface active compounds (e.g. minerals, organic matter) is known to display strong affinity for solid phases, and thus, makes it difficult to evaluate the reservoir wettability quantitatively using actual core samples (Dandekar, 2006). In addition, a large amount of mercury porosimetry work described in Section 3.3.2 has shown that the values of the surface tension and contact angle may vary with pore size (Kloubek, 1981), the nature of the surface (Moscou and Lub, 1981), or the direction the mercury is moving (Lowell and Shields, 1981). Therefore, as detailed in Sections 3.1 to 3.4, the characterising techniques adopted for this project require samples free of any impurities for accurate measurements and analysis.

Furthermore, oil reservoirs are physically heterogeneous, with layers of different permeabilities. Therefore, oil reservoirs can contain a network of high permeability fractures surrounded by matrix blocks of low permeability. In addition, oil reservoirs are heterogeneously macroscopic, and thus, a pore connectivity analysis is not applicable to oil core samples due to the limited pore size range of the sorption technique (0.002 to 0.4 μm). Therefore, the chemical and physical heterogeneity of oil reservoirs will make it difficult to estimate the structural and topological properties of a given oil core sample. As a result, purer forms of artificial simplified sandstone reservoir rocks have been adopted for this project. The adopted materials are chemically pure mesoporous silica and alumina catalyst support pellets with simplified pore sizes, pore size distribution, and surface chemistry. These materials are suitable for the proposed characterisation techniques as highlighted in Section 1.6.1. Summary and basic properties of adopted materials are given in Table 2.1.

The silica materials have the same chemical components as sandstone reservoir rocks, and thus a direct comparison could be made in terms of basic surface chemistry and wettability

effects. The alumina materials are formed by controlled heating of hydrated alumina that makes the crystal lattice ruptures along planes of structural weakness, and thus, a well defined pore structure results (Coulson and Richardson, 1999). Silica gel is prepared by the reaction between sodium silicate and acetic acid. When the gel is heated, water is expelled leaving a hard, glassy structure with voids between the micro-particles (Coulson and Richardson, 1999). The aerosil material is made from vaporized silicon tetrachloride oxidized in high-temperature flame with hydrogen and oxygen (Eisenlauer and Killmann, 1980). These treatment methods result in various pore size distributions that make silica materials more heterogeneous than the alumina materials. Silica alumina is made from precipitation of hydrous alumina on amorphous silica hydrogel (Froment, 1987). However, the pore size distribution of reservoir rocks is more complicated than the simplified forms of these catalyst support pellets. Nevertheless, there are reports of oil reservoir rocks, especially in carbonates, with similar pore sizes as the materials proposed in this study (Djevanshir, 1987; and Dandekar, 2006). Thus, these materials can offer a realistic analogy for the relationships structural and topological properties of oil reservoir rocks.

It can be seen in Table 2.1 that most of the materials have been studied previously, and thus some useful literature review can be found. However, a large amount of work described in the literature focused mainly on mercury entrapment and surface chemistry of these materials. In this project, emphasis will be given to the relationships between pore connectivity, pore length, mercury entrapment, and tortuosities of these materials. The materials were supplied by Industrial Chemical Industries (ICI) and Micromeritics. They have pore size lying in the range of 7-30 nm. The majority of the materials have unimodal structure with the exception of one bimodal structured material (AL3984T). Figures 2.8 to 2.11 show atomic force microscopy (AFM) images of C10 and C30 at different magnifications. The agglomerations of sol spheres are shown in these images. These images are typical of sol-gel silicas. Figure 2.12 shows electron microscopy images (EMI) of a typical sample from batch Q17/6. In addition, Figure 2.13 shows the X-ray micro-computed tomography of C30 containing entrapped mercury. The mercury entrapment observed in Figure 2.13 demonstrates that these materials have macroscopic heterogeneity over many different length scales as often observed in oil reservoirs rocks (see Figure 2.1).

Table 2.1

A range of porous catalyst support pellets considered for this study

Sample	Material	Pellet form	Voidage	Nominal diameter (mm)	Manufacturer/ Supplier	Selected past work
Aerosil	Silica (SiO_2)	Fumed sphere	N/D	3.5	ICI	Rigby and Chigada (2009)
AL3984T	Alumina (Al_2O_3)	Tablet	0.59	3	Engelhard cooperation	Hollewand and Gladden (1993; 1995a); Rigby and Gladden (1996; 1998)
AL3992E	Alumina (Al_2O_3)	Extrudate	0.65	3	Engelhard cooperation	Hollewand and Gladden (1993; 1995a); Rigby and Gladden (1996; 1998)
C10	Silica (SiO_2)	Gel sphere	0.66	3	Grace GMBH	Rigby and Gladden (1996, 1998); Evbuomwan (2009)
C30	Silica (SiO_2)	Gel sphere	0.69	3	Grace GMBH	Rigby and Gladden (1996; 1998); Rigby *et al*. (2008); Evbuomwan (2009)
P7129	Silica (SiO_2)	Gel sphere	0.67	3	ICI	Evbuomwan (2009)
Q17/6	Silica (SiO_2)	Gel sphere	0.49	3.5	ICI	Rigby *et al*. (2008); Evbuomwan (2009)
S980A	Silica (SiO_2)	Gel sphere	0.6	3	Shell chemicals	Hollewand and Gladden (1993; 1995a); Rigby and Gladden (1996; 1998); Evbuomwan (2009)
S980G	Silica (SiO_2)	Gel sphere	0.61	2.2	Shell chemicals	Hollewand and Gladden (1993; 1995a); Rigby and Gladden (1996); Evbuomwan (2009)
Silica Alumina	Silica and Alumina (Al_2O_5Si)	Extrudate	0.6	0.5	Micrometrics	-

Note

N/D– Not detected

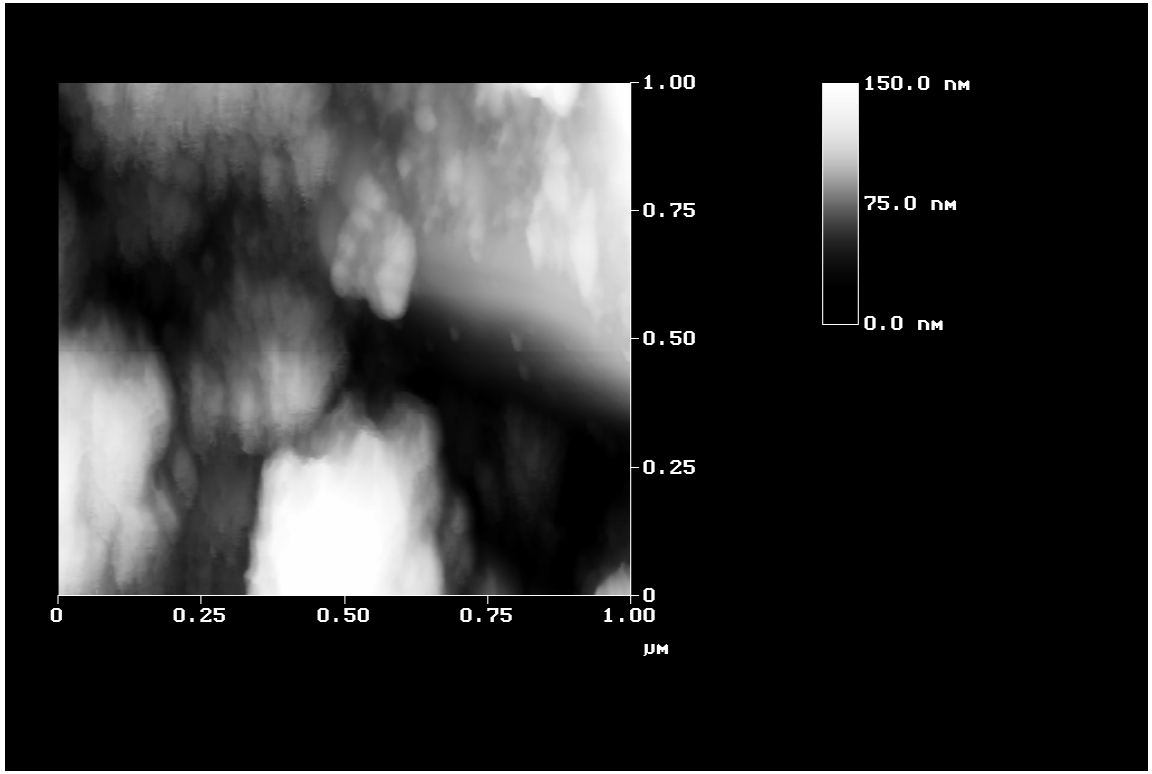

Figure 2.8

AFM images of C10 at 1 μm field of view. Images obtained courtesy of Ms Ann O'Reilly of the University of Bath.

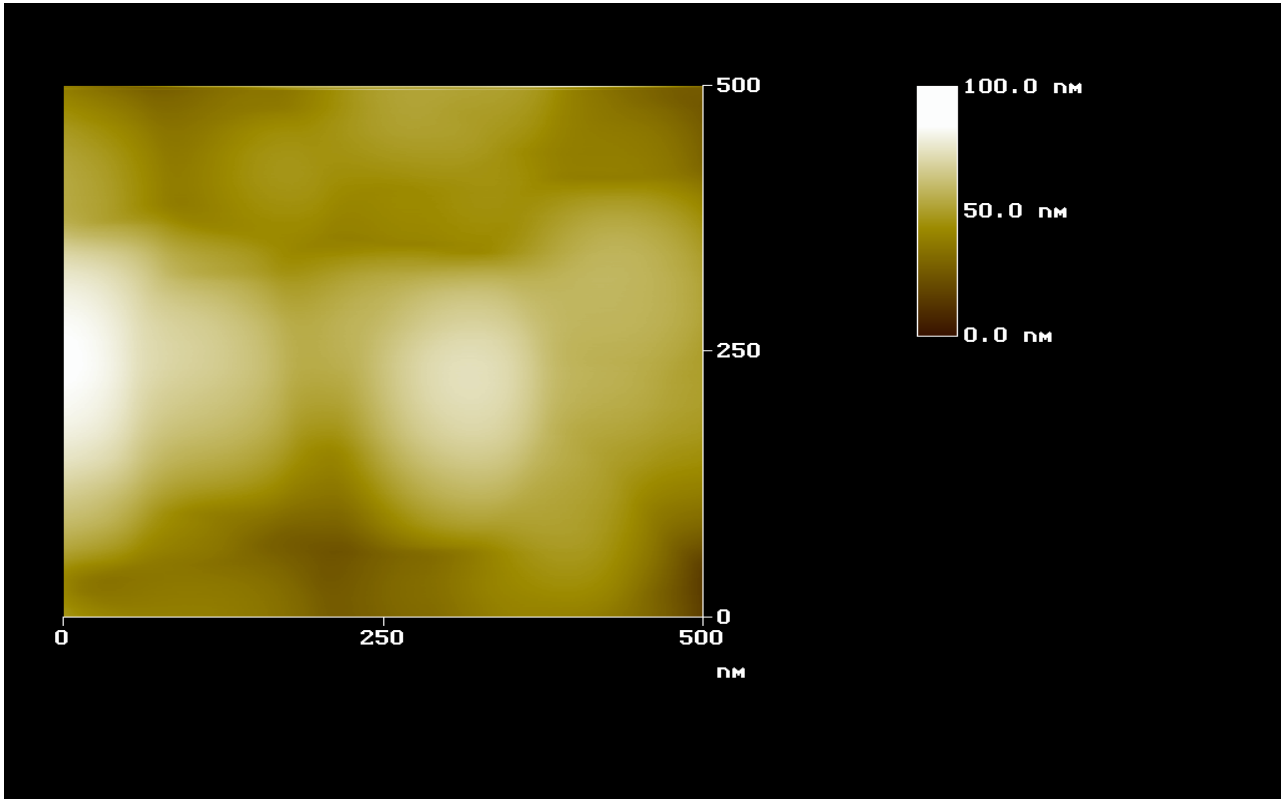

Figure 2.9

AFM images of C10 at 500 nm field of view. Images obtained courtesy of Ms Ann O'Reilly of the University of Bath.

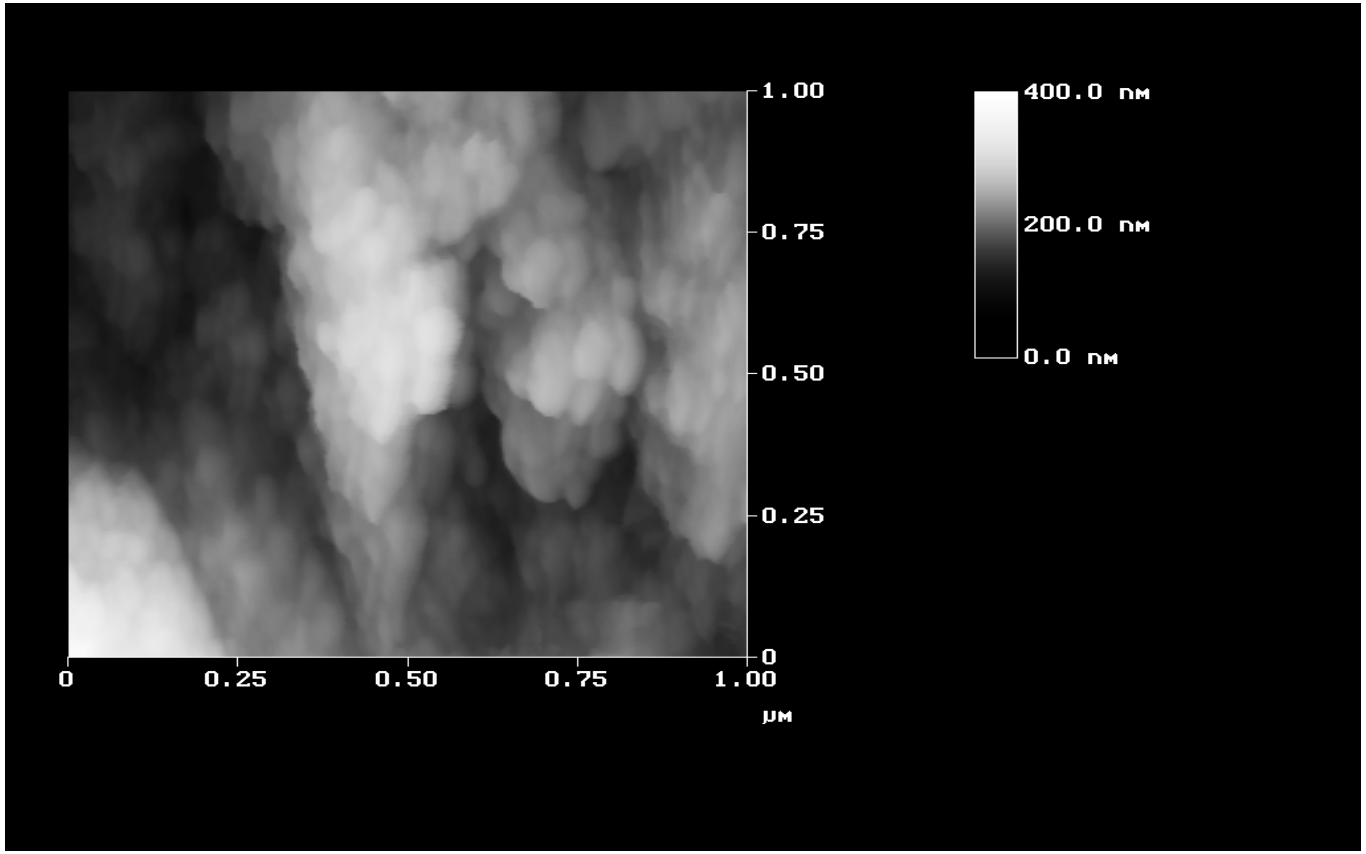

Figure 2.10

AFM images of C30 at 1 μm field of view. Images obtained courtesy of Ms Ann O'Reilly of the University of Bath.

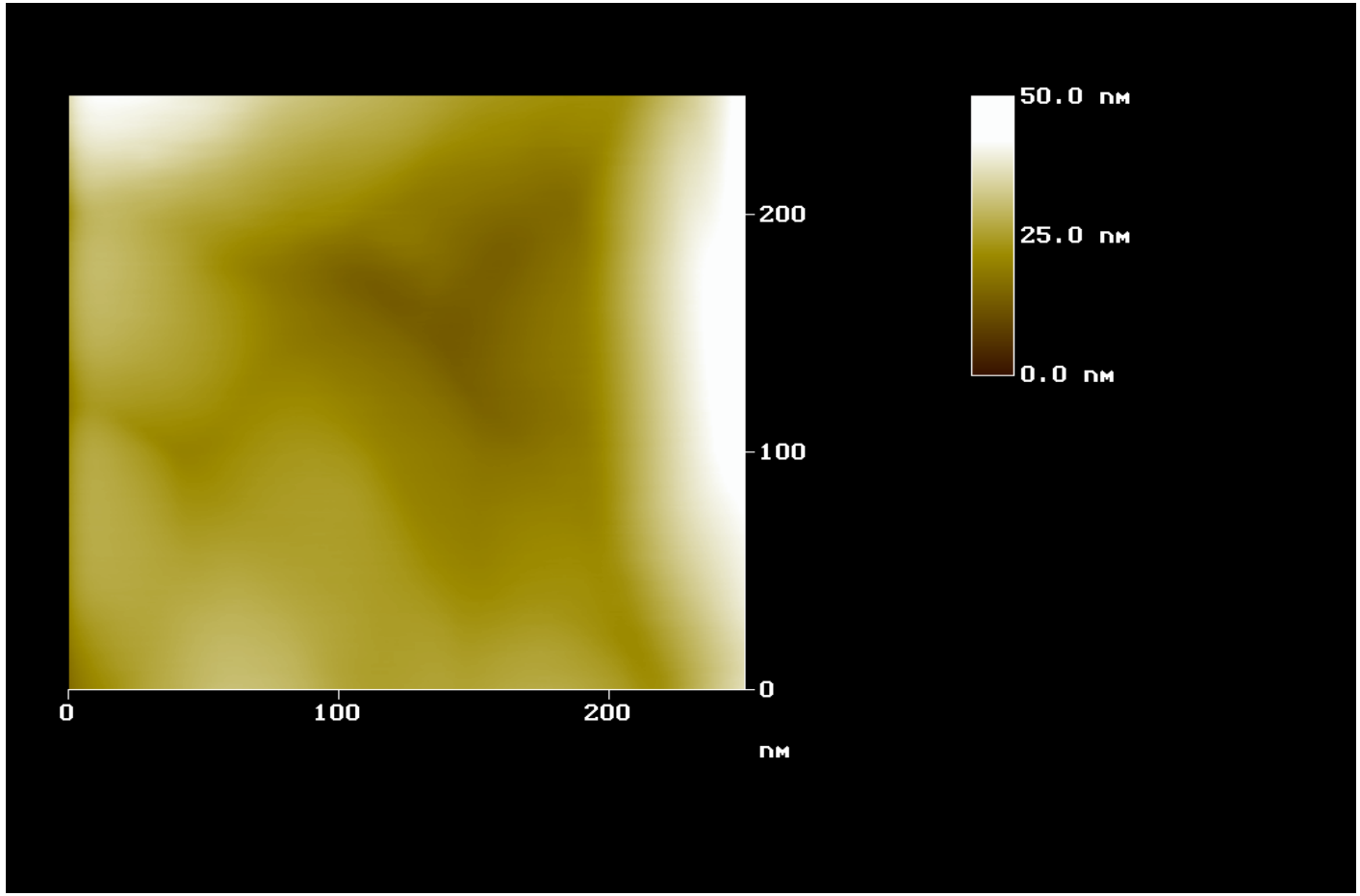

Figure 2.11

AFM images of C30 at 200 nm field of view. Images obtained courtesy of Ms Ann O'Reilly of the University of Bath.

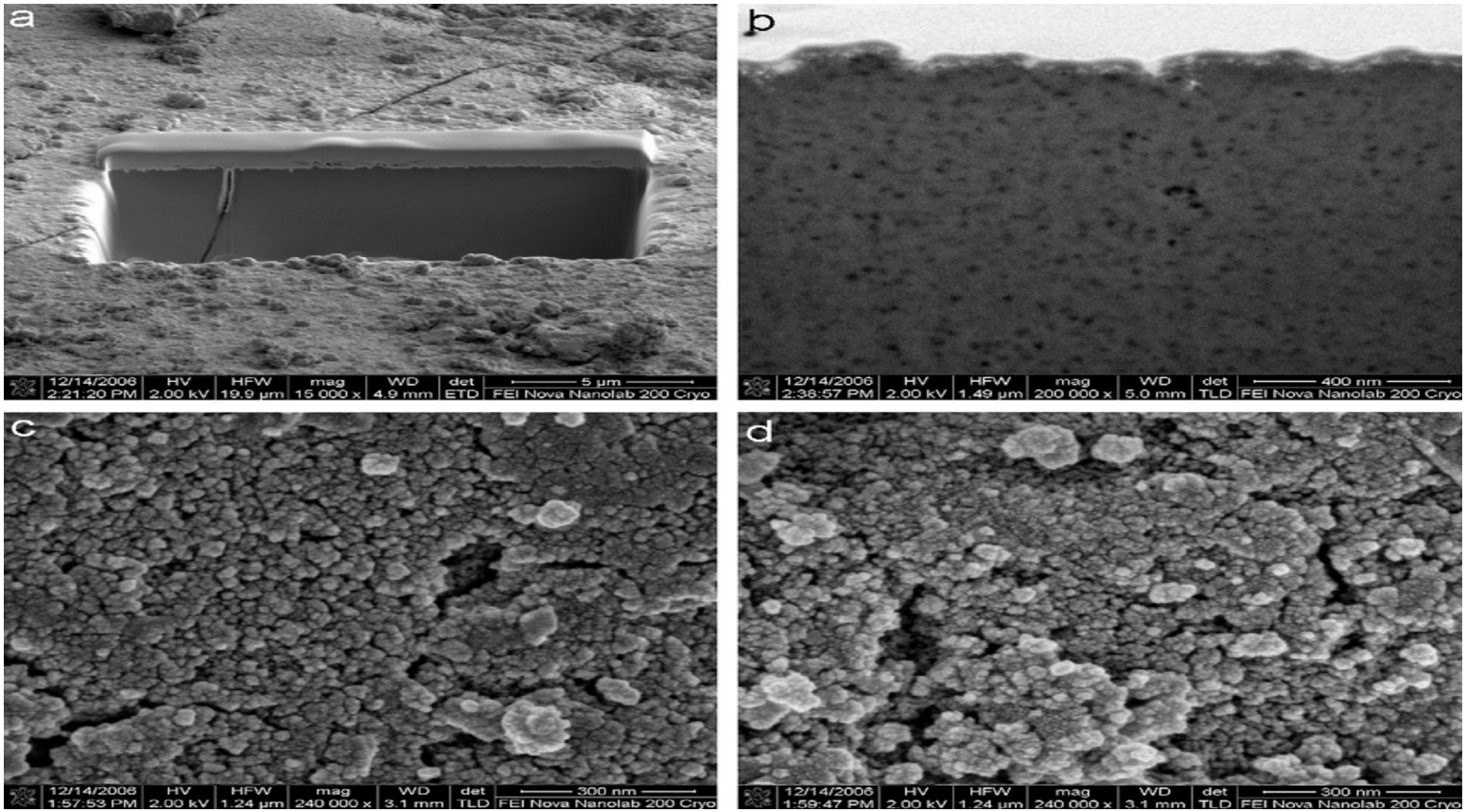

Figure 2.12

Low magnification EMI (a) of a trough cut in section of Q17/6. High magnification EMI (b) of a trough cut in section reveals the pores (black patches) located within the grey silica matrix. Additional high magnification EMI (c and d) suggest that the pore network within Q17/6 is made up of the void spaces left between a packing of single (roughly spherical particles) and/or between larger fused agglomerates of smaller particles (Rigby *et al.*, 2008).

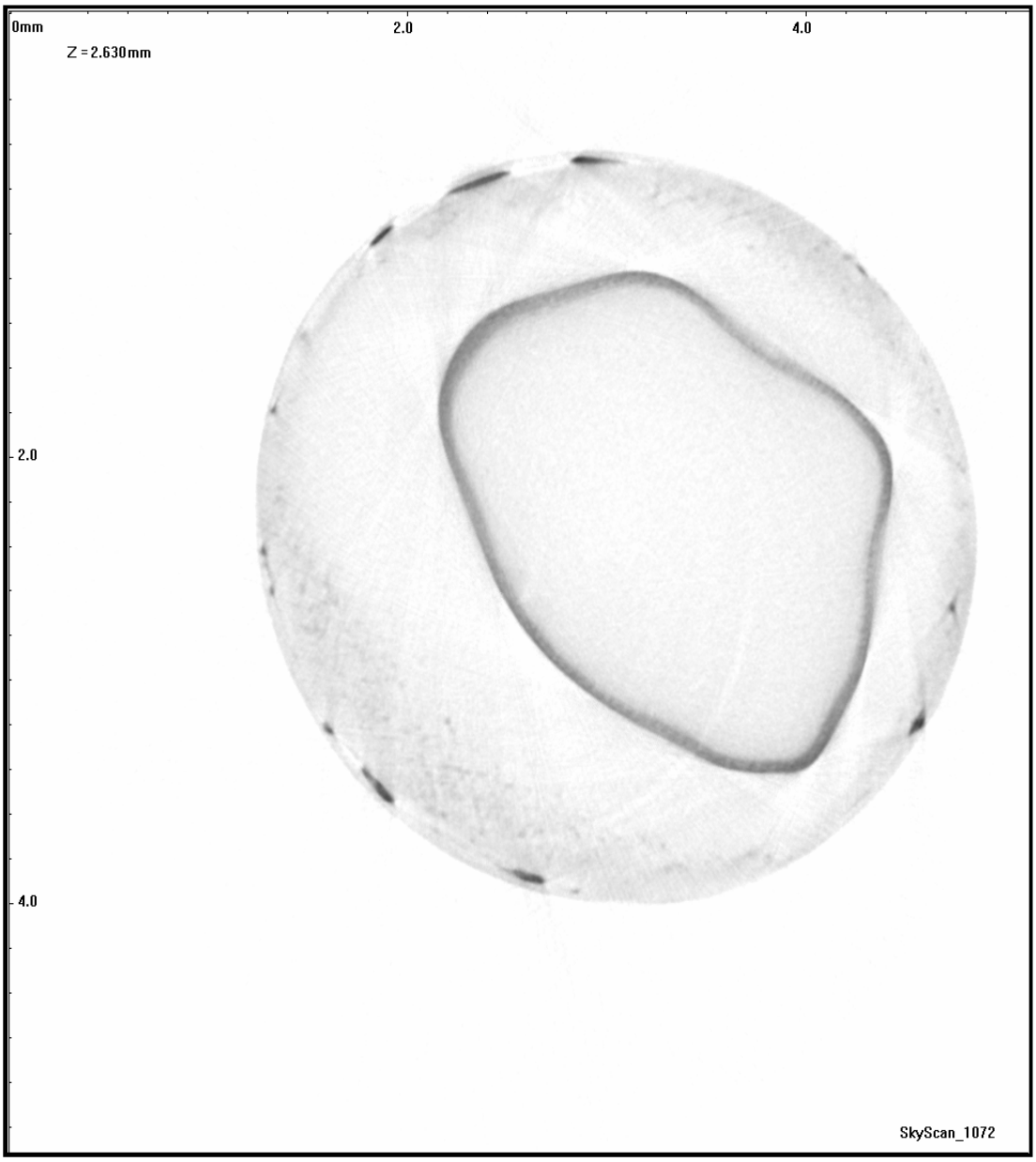

Figure 2.13

2D X-ray micro-CT image of a cross-section through a pellet from batch C30 following mercury porosimetry (Rigby *et al.*, 2008). The black regions of the image correspond to entrapped mercury, while the grey regions correspond to the silica matrix. The entrapment demonstrates the macrsocopic heterogeneity present in the sample.

2.4 References

Cosse', R., 1993. *Basics of reservoir engineering.* Paris: Editions Technip.

Coulson, J.M., and Richardson J.F., 1998. *Chemical Engineering: Particle technology, and Separation processes.* Butterworth-Heinemann.

Evbuomwan, O.E., 2009. *The structural characterisation of porous media for use as a model reservoir rocks, adsorbents and catalyst.* Thesis (PhD). University of Bath.

Fraunhofer IGB, 2008. *Contact between two immiscible liquids* [online]. Fraunhofer IGB: Stuttgart, Germany. Available from: http://www.igb.fraunhofer.de/start.en.html [Accessed 4 March 2008].

Froment, G.F., 1987. *Hydrocracking: science and technology.* Amsterdam: Elsevier.

Dandekar, A.Y., 2006. *Petroleum reservoir rock and fluid properties.* Taylor & Francis group.

Djevanshir, R.D., 1987. Relationships between clay minerals, low temperatures, high pore pressures, and oil, gas reservoirs at great depths in the Baku Archiphelago, U.S.S.R. *Journal of Petroleum Science and Engineering,* 1 (1987) 155-162.

Hollewand M.P., Gladden L.F., 1993. Heterogeneities in structure and diffusion within porous catalyst support pellets observed by NMR Imaging. *Journal of catalyst*, 144, 254-272.

Hollewand, M.P., and Gladden, L.F., 1995a. Transport heterogeneity in porous pellets-I. PGSE NMR studies, *Chemical Engineering Science,* 50, 309-326.

Kloubek, J., 1981. Hysteresis in porosimetry. *Powder Technol*., 1981, 29, 63 – 73.

KPAL, 2010. *A montage of SEM images of a reservoir of a sandstone block* [online]. KPAL: Berkshire, UK. Available from: http://www.kpal.co.uk/sem_montage2.jpg [Accessed 15 December 2010].

Lowell S., Shields J. E., 1981. Hysteresis, entrapment, and wetting angle in mercury porosimetry. *Journal of Colloid and Interface Science*, Vol. 83, No. 1.

Moscou, L. and S. Lub, 1981. Practical use of mercury porosimetry in the study of porous solids. *Powder Technology*, 29, 45-52.

MPG Petroleum, Inc., 2008. *Permeability* [online]. MPG Petroleum, Inc.: Houston, Texas, US Available from: http://www.mpgpetroleum.com/fundamentals.html [Accessed 4 March 2008].

Msn, 2008. *Gas, oil, and water in a reservoir rock* [online]. Msn: UK. Available from: http://www.msnucleus.org/.../lesson3/petroleum3a.html [Accessed 4 March 2008].

Rigby, S.P., and Gladden, L.F., 1996. NMR and fractal modelling studies of transport in porous media. *Chemical engineering science*, 51 (10), 2263-2272.

Rigby, S.P., Gladden, L.F., 1998. The use of magnetic resonance images in the simulation of diffusion in porous catalyst support pellets. *J. Catal*., 1998, 173, 484-489.

Rigby, S.P., Chigada, P.I., Evbuomwan, I.O., Chudek, J.A., Miri, T., Wood, J., Bakalis, S., 2008. Experimental and modelling studies of the kinetics of mercury retraction from highly confined geometries during porosimetry in the transport and the quasi-equilibrium regimes. C*hem. Engng. Sci*., 63 (24), 5771-5788.

Rigby, S.P., and Chigada, P.I., 2009. Interpretation of integrated gas sorption and mercury porosimetry studies of adsorption in disordered networks using mean-field DFT. *Adsorption-journal of the international adsorption society*, 15 (1), 31-41.

Sing, K.S.W., Everett, D.H., Haul, R.A.W., Moscou, L., Pierotti, R.A., Rouquerol, J. and Siemieniewska, T., 1985. Reporting physisorption data for gas solids systems with special reference to the determination of surface area porosimetry and porosity (recommendation 1984). *Pure and applied chemistry*, 57, 603-619.

3.0 Applications of porosimetry and PGSE NMR experimental methods to porous media

3.1 Introduction

The term "porosimetry" is often used to encompass the measurements of pore size, pore volume, pore size distribution, and other porosity-related characteristics of a porous material. The measurement of the size, geometry, and interconnectivity of mesopores and macropores in porous materials continues to be an important activity in oil and catalyst industries. Though it is sometimes possible to view pores with an electron microscope and to thereby obtain a measure of their diameter, it is difficult to measure the distribution of sizes, and impossible to representatively measure the associated surface area, particularly for a large sample. There are well-known and standard techniques from gas sorption that can determine key characteristic parameters of porous media, such as the BET surface area, BJH algorithm for pore size distribution, and pore connectivity by percolation analysis. Gas adsorption and mercury porosimetry are complementary methods with the latter covering a much wider size range (0.0035 to 500 μm).

Mercury porosimetry can give information that is valuable in assessing multiphase fluid behaviour of oil and gas in a strongly water-wetting system and the trapping of oil or gas that is controlled mostly by capillary forces, and thus, a direct analogy with the air-mercury system is possible (Chatzis *et al*., 1983). In general, mercury entrapment is strongly dependent on the structural (voidage fraction, pore size distribution) as well as on the topological (connectivity and tortuosity) properties of porous media. The PGSE NMR technique can be used to estimate the tortuosity of porous media. Thus, this Chapter discusses the theoretical aspects of the principles of porosimetry and PGSE NMR to elucidate mercury entrapment in porous media. Furthermore, the proposals for the research programmes are given under each relevant characterisation technique review. The experimental considerations and the results obtained are given in Chapters 4 to 7.

3.2 Applications of gas sorption technique to porous media

3.2.1 Principles of gas sorption technique

The process of adsorption involves separation of a substance from one phase accompanied by its accumulation on the surface of another of substance. Adsorption differs from absorption, where solute molecules diffuse from the bulk gas phase to the bulk of a liquid phase. In adsorption, the molecules diffuse from the bulk fluid to the surface of the solid adsorbent, forming a distinct adsorbed phase (Coulson and Richardson, 1998). Therefore, adsorption at a surface or interface is largely the result of binding forces between individual atoms, ions or molecules of an adsorbate and the surface, and all of which have their origin in electromagnetic interactions (Allen, 1998). A variety of adsorbatives, such as nitrogen, argon, carbon dioxide, helium and hydrocarbons can be used to characterize porous materials (Allen, 1998). However, nitrogen is the most widely used adsorbative for adsorption measurements. The choice of nitrogen is due to its richness of literature concerning its properties most particularly the small size of its molecule that can easily access the pores of most porous materials (Allen, 1998). In addition, nitrogen is easily available, and one of the cheapest adsorbatives for adsorption measurements.

Adsorption processes may be classified as either physical or chemical, depending on the nature of the forces involved. In physical adsorption, all the gas adsorbed can be removed by evacuation at the same temperature at which it was adsorbed due to the weak interaction between the adsorbent and adsorbate. Furthermore, no chemical bond is formed during physical adsorption. However, attraction between the adsorbate and adsorbent exists because of the formation of intermolecular electrostatic interactions, such as van der Waals forces, or London dispersion forces, from induced dipole-dipole interactions (Gregg and Sing, 1982). Chemical adsorption involves some degree of specific chemical interaction between the adsorbent and the gas (adsorbate). Consequently in chemical adsorption, the energies of adsorption might be quite large and comparable to chemical bond formation (Allen, 1998).

Physical adsorption occurs in three stages as the adsorbate concentration increases. The first stage is the build up of a single layer of molecules. More layers are formed by physical adsorption as the adsorbate concentration increases. The number of these layers

can be limited by the size of the pores. Finally, for adsorption from the gas phase, capillary condensation may occur in which capillaries become filled with condensed adsorbate, when its partial pressure reaches the critical value for the size of the pore. However, these stages can occur simultaneously in different parts of the adsorbent because conditions are not uniform throughout (Coulson and Richardson, 1998).

3.2.2 Adsorption equilibria

Adsorption equilibrium is a dynamic concept achieved when the rate at which molecules adsorb on to the surface is equal to the rate at which they desorb. Adsorption and desorption are used to indicate the direction from which the equilibrium states have been approached. In addition, adsorption hysteresis arises, when the amount adsorbed is not brought to the same level by desorption after at a given equilibrium pressure or bulk concentration. No single theory of adsorption has been put forward which explains all systems. Most theories have been developed for gas-solid systems because the gaseous state is better understood than the liquid (Coulson and Richardson, 1998).

Several adsorption isotherm equations have been developed to describe adsorption isotherm relationships but no single model has been found to be generally applicable. For example, Langmuir (1916) found that the equations derived for plane surfaces were not applicable to adsorption by highly porous adsorbents such as charcoal. This led Dubinin *et al*. (1960), to put forward additional evidence to show that the mechanism of physisorption in very narrow pores is not the same as that in wider pores. By experimenting on a wide range of activated carbons, Dubinin *et al*. (1960) identified three groups of pores of different width; micropores, transitional pores (also known as mesopores), and macropores. IUPAC now defines microporous (< 2 nm), mesoporous (2-50 nm) and macroporous (> 50 nm) regions (Gregg and Sing, 1982).

Gas sorption technique is accompanied by measuring the volume (V) of gas adsorbed/desorbed, at constant temperature over a wide range of pressures, to generate isotherms. For a gas at a pressure lower than the critical pressure (vapour pressure) the relative pressure, $x = \frac{P}{P_0}$, where P and P_0 are the partial vapour pressure of a component

and the saturated vapour pressure at the same temperature (T). There are 6 main types of isotherms according to the 1985 IUPAC classification in Figure 3.1 (Sing et *al*., 1985). The reversible Type I isotherm is characterised by a large amount adsorbed at low pressures followed by a flat region. The shape of the isotherm is concave with respect to relative pressure axis. Thus, the isotherm approaches a limiting value as x tends to unity and this region is characterised by micropore filling (Allen, 1998). Charcoal, with pores just a few molecular diameters wide, almost always give this type of isotherm (Coulson and Richardson, 1998). According to Rouquerol *et al.* (1999), the narrow range of relative pressure necessary to attain the plateau in Type 1, signifies the existence of a limited range of pore size. The appearance of a nearly horizontal plateau is an indication of a very small horizontal pore surface area and this is typical of microporous solids.

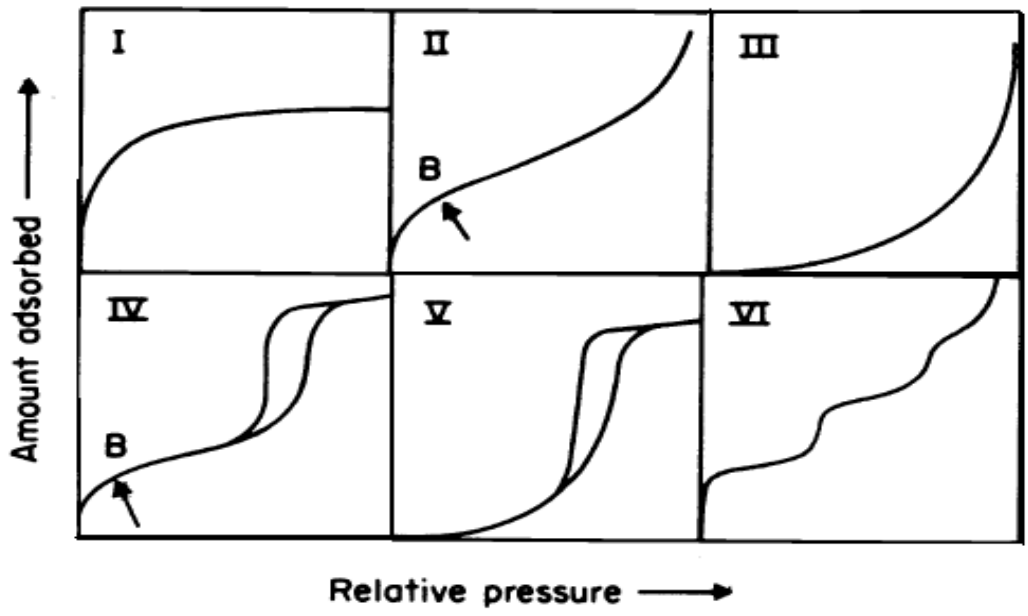

Figure 3.1
Classification of isotherms into six types (Sing et *al*., 1985)

The type II isotherm is associated with a non porous solid and macroporous adsorbents. It represents unrestricted monolayer-multilayer adsorption on a heterogeneous substrate (Allen, 1998). This type of isotherm is initially concave to the x-axis then it becomes almost linear, and finally convex to the x-axis. Although layers of different thickness might

exist simultaneously, Brunauer *et al*. (1938) assumed monolayer completion at the point of inflection of the isotherm. These researchers subsequently developed the point B method as illustrated in Figure 3.1, employing an equation containing a constant, c, to locate this point. Increasing c values indicate increasing affinity between the adsorbate and the adsorbent. A conventional method of determining the specific surface area of a porous media is to deduce the monolayer capacity (V_m) from the isotherm. The monolayer capacity is the quantity of adsorbate required to cover the adsorbent with a monolayer of molecules. However, a second layer may be forming before the monolayer is complete, but V_m is deduced irrespective of the formation of the second layer (Allen, 1998).

The reversible type III isotherm is convex to the relative pressure x-axis and exhibits an indistinct point B (Allen, 1998). This type of isotherm is characteristic of a non porous or macroporous solid with a weak adsorbent-adsorbate interaction (Coulson and Richardson, 1998). The shape of the type IV isotherm is similar to that of type II at the start but differs at the higher relative pressure region where it displays a hysteresis loop. The hysteresis is attributed to capillary cracks from which adsorbate molecules do not desorb as readily as they adsorb. This is due to vapour pressure lowering over the concave meniscus formed by condensed liquid in the pores (Sing et *al*., 1985). The majority of Type II or IV isotherms show an almost straight horizontal section at intermediate relative pressures. The more pronounced the section, the more complete is the adsorbed monolayer before multilayer adsorption begins (Coulson and Richardson, 1998).

The type V isotherms are characteristic of weak adsorbent-adsorbate interactions, as are type III isotherms, but exhibit a hysteresis loop. Type V isotherms represent mesoporous or microporous solids (Allen, 1998). Stepped isotherms are classified as type VI isotherm. The steepness of the steps depends on the system temperature. It represents stepwise multilayer adsorption on a non uniform non-porous surface. In general, one whole layer is completed before the next one starts (Coulson and Richardson, 1998). The Type VI isotherms are associated with non porous substrates. The isotherm is due to step rise adsorption multi-layer adsorption, and thus, the step height represents the monolayer capacity for each adsorbed layer (Allen, 1998).

3.2.3 Mechanisms of capillary adsorption and desorption

Adsorption begins at the wall of the pore and progresses towards the centre of the pore. When the adsorbed gas layer is sufficiently thick, such that the gap between opposing layers (gas-liquid) is small enough, capillary condensation occurs within the pore. Therefore, in capillary condensation, the gas-liquid meniscus travels along the axis of the pore to the pore surface where it eventually flattens with increasing pressure and the bulk gas becomes saturated (Rouquerol *et al.*, 1999). In addition, Neimark (1991) argued that condensation in a narrow pore might result in the formation of an unstable vapour-liquid interface in the adjacent wider pore that would cause spontaneous condensation. This effect of initiated capillary condensation or advanced condensation may trigger an avalanche filling of the pore network. Therefore, for a cylindrical pore with a narrower neck, capillary condensation could occur by two means. The first been, that both cylindrical meniscuses filling at the individual x, determined by the Kelvin equation (Equation 3.18), or in the case of advanced condensation effects, both body and throat filling at the filling pressure of the throat as this exceeds the pressure required to fill the body with a hemispherical meniscus.

In recent years, Rigby and Chigada (2009) carried out mean field density functional theory (MFDFT) simulations to enhance the interpretation of gas adsorption data. These researchers investigated the effects of the advanced condensation phenomenon on ink-bottle type pores. Two types of cylindrical pores; ink-bottle type one with neck diameter less than 0.5 × body diameter and the other with neck diameter greater than 0.5 × body diameter were examined. It was found that condensation in the neck and body occur independently in the first scenario. In the second scenario, following condensation in neck, at the pressure required for filling a cylindrical meniscus, the pore body automatically fills as the pressure exceeds the condensation pressure required for filling a hemispherical meniscus according to the Kelvin Equation (3.18). In addition, Rigby and Chigada (2009) defined the ratio of the pore neck to pore body diameter as ξ_p and concluded that adsorption will not detect pore-mouth blocking for $\xi_p > 0.9$, for short pore necks, advanced adsorption does not have sharp critical watershed at $\xi_p = 0.5$, as critical ξ_p depends on adsorbate-adsorbent interaction strength (surface chemistry) and pore neck length significantly affects condensation pressure. A similar conclusion was made earlier

by Rojas *et al*. (2002), and thus, supports the theory that if these ratios exist (neck diameter > 0.5 × body diameter) the following sequence can ensue: first, vapour condensation happens at the smaller of the two delimiting necks; next the central cavity fills with condensate (once the vapour pressure attains a critical value); finally the remaining empty neck is trespassed right away by the advancing liquid-vapour meniscus coming from the bulge. The mechanism of adsorption is illustrated in Figure 3.2.

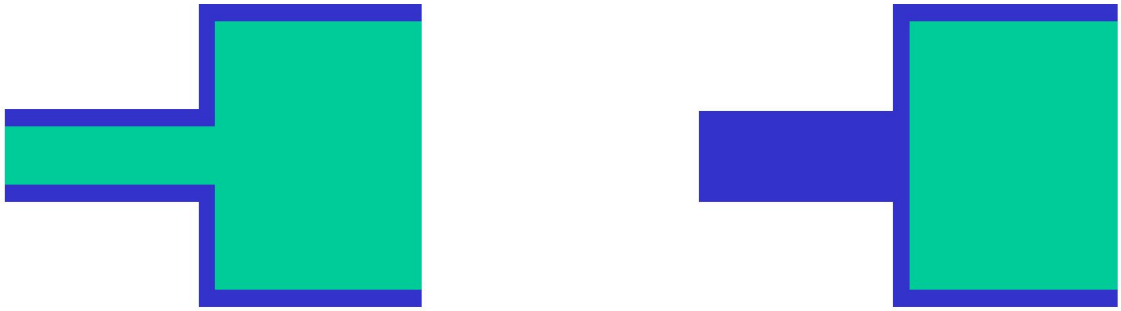

First scenario: Neck diameter < 0.5 × body diameter

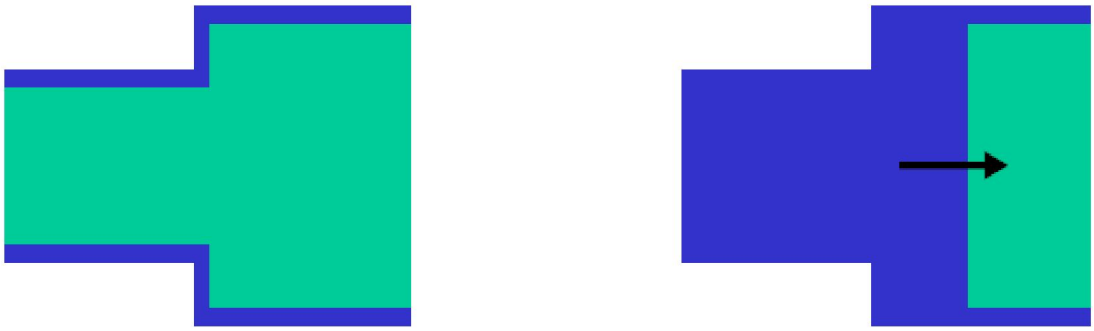

Second scenario: Neck diameter > 0.5 × body diameter

Figure 3.2

Schematic representation of advanced condensation in cylindrical pores of ink-bottle type (Rigby and Chigada, 2009)

In general, for desorption to occur, a curved meniscus must re-form between the condensed liquid in the pore and the gas phase of the bulk which requires a reduction in the bulk pressure (Sing et *al*., 1985). Therefore, for a curved meniscus in equilibrium, the forces on either side must balance, as illustrated in Figure 3.3. The sum of pressure on the concave side of the meniscus, P_{CV}, is equal to the sum of the pressure on the convex side of the meniscus, P_{CX}, and the surface tension, therefore, $P_{CX} \leq P_{CV}$.

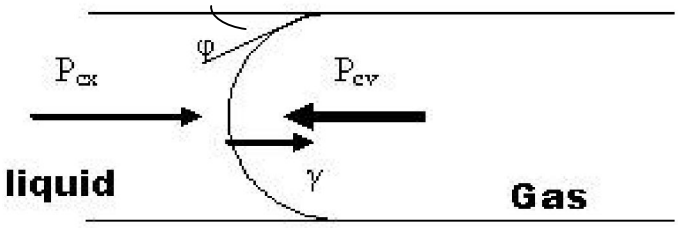

Figure 3.3
Diagram illustrating forces on a curved meniscus (Perkins, 2008)

The effect is more significant for a hemispherical meniscus. Therefore, during desorption, the pressure is reduced, and the meniscus at the surface of the pore begins to curve until it reaches a hemispherical dome protruding into the pore. The surface tension enables the pore to remain filled with liquid which is in equilibrium with the gas at pressures below the saturation pressure. After forming the meniscus, further decrease in pressure causes the adsorbent to evaporate according to the size of pore in which it is contained (Rouquerol *et al*., 1999). The pressure difference required to create the meniscus is inversely proportional to the radius of the pore, according to the Kelvin Equation (3.18). For ink-bottle style pores that are exposed to the bulk via smaller pores, the relative pressure required to form the meniscus is dominated by the outer pore. The adsorbed gas can only begin to evaporate when the pressure is sufficient to form a meniscus within the smaller outer pore, at which point the whole pore will empty. Therefore, desorption isotherm is shifted towards the smaller pore sizes and subject to pore shielding effects (Rigby and Fletcher, 2004).

Desorption conditions are hard to evaluate, due to two complications; namely, the classical pore blocking effect (McBain, 1935; and Cohan, 1938) and the more recently discovered

cavitation process (Burgess and Everett, 1970). The pore blocking effect implies the evaporation of a condensed liquid from a pore network is a cooperative process. As such, evaporation from a pore, which is connected to the bulk phase by narrower pores, is restricted by, and occurs spontaneously after emptying of one of the adjacent pores. This effect of pore blocking is a conventional explanation of the capillary condensation hysteresis of H2 type. The structure of these materials is disordered and represents a network of channels with prominent enlargements and constrictions as shown by high resolution microscopy and scattering data (Ravikovitch and Neimark, 2002). However, the pore blocking effect rests in the inability of a pore to evaporate its condensate if it has no direct access to the vapour phase, thus turning evaporation from pore entities into a percolation process, whereas cavitation implies the possibility that a condensate-filled pore could turn empty by means of bubble nucleation within the condensed liquid.

Recent cavitation studies have mainly focused on ink-bottle type pores, such as the work of Sarkisov and Monson (2000) which suggests that sometimes the shape of the desorption isotherm is mainly dictated by caviatation phenomenon rather than by the pore blocking effect. Burgess and Everett (1970) associated the lower closure point of adsorption hysteresis loops to the onset of cavitation in the stretched metastable liquid. Cavitation induced desorption is expected to occur in mesopores blocked by micropores. The cavitation effect was not considered in the classical theories of capillary condensation hysteresis in ink-bottle pores and pore networks. A detailed analysis of cavitation induced desorption is given by Ravikovitch and Neimark (2002). These researchers described a new physical mechanism of adsorption hysteresis in ink-bottle type pores confirmed by gas adsorption experiments of three different gases including N_2 in 3D cage-like structures of nanoporous templated silica with narrow PSD. The analysis revealed three mechanisms of evaporation including evaporation from blocked cavities controlled by the size of connecting pores, the spontaneous evaporation caused by the cavitation of a stretched metastable liquid, and the near equilibrium evaporation in the region of hysteresis from unblocked pore bodies that have access to the vapour phase. Ravikovitch and Neimark (2002) concluded that the pressure of cavitation depends on the pore geometry, and thus, questioning the conventional assumption by Burgess and Everett (1970) that the pressure of cavitation which determines the lower closure point of the hysteresis loop is a function of the adsorbate and temperature.

3.2.4 Hysteresis in gas sorption isotherms

During the desorption process, as the relative pressure is reduced, systems in which capillary condensation occurs, generally show hysteresis. Sing *et al*. (1985) classified several shape groups of hysteresis loops, which are shown in Figure 3.4. In Type H1 hysteresis loops, both adsorption and desorption branches are steep at intermediate relative pressures. Examples of pores that give such shapes include tubular capillaries open at both ends, tubular capillaries with slightly wider parts, wide ink bottle ores and wedged shaped capillaries (Allen, 1998). Also, Type H1 can be associated with agglomerates or compacts of uniform spheres in somewhat regular array that consequently have a narrow pore size distribution (Sing *et al*., 1985). Furthermore, the Type H1 loop could be a result of either condensation in independent capillaries within a narrow size distribution or by globular solids made of spherical particles of about the same diameter (Broekhoff and de Boer, 1968). In Type H2 hysteresis loops, the adsorption branch has a slopping character and the desorption branch is steep at intermediate relative pressures (Allen, 1998). The Type H2 hysteresis loop has been traditionally ascribed to a collection of ink-bottle type pores (Allen, 1998). However, this may well be an oversimplification since network effects that usually occur in a wide variety of adsorbents, can produce the same result (Sing *et al*., 1985). The dimensions responsible for the adsorption branch of the isotherm is heterogeneously distributed and the dimensions responsible for desorption are of equal size (Allen, 1998). This is a classic percolation shape.

In Type H3 hysteresis loops, the adsorption branch is steep at intermediate pressures whilst desorption branch is slopping. The ascending and descending boundary curves are sloping and usually the desorption branch also includes a steep region at which the remaining condensate comes out almost suddenly out of the pores as a consequence of the so-called tensile strength effect (Everett, 1967). Type H3 is normally associated with open-slit shaped capillaries with parallel walls (Allen, 1998). Aggregates of plate like particles give rise to slit shaped pores (Sing *et al*., 1985). Type H4 does not exhibit any limiting adsorption at high x which indicates that the adsorbent does not possess a well-defined mesopore structure similar to that of Type H3 (Allen, 1998).

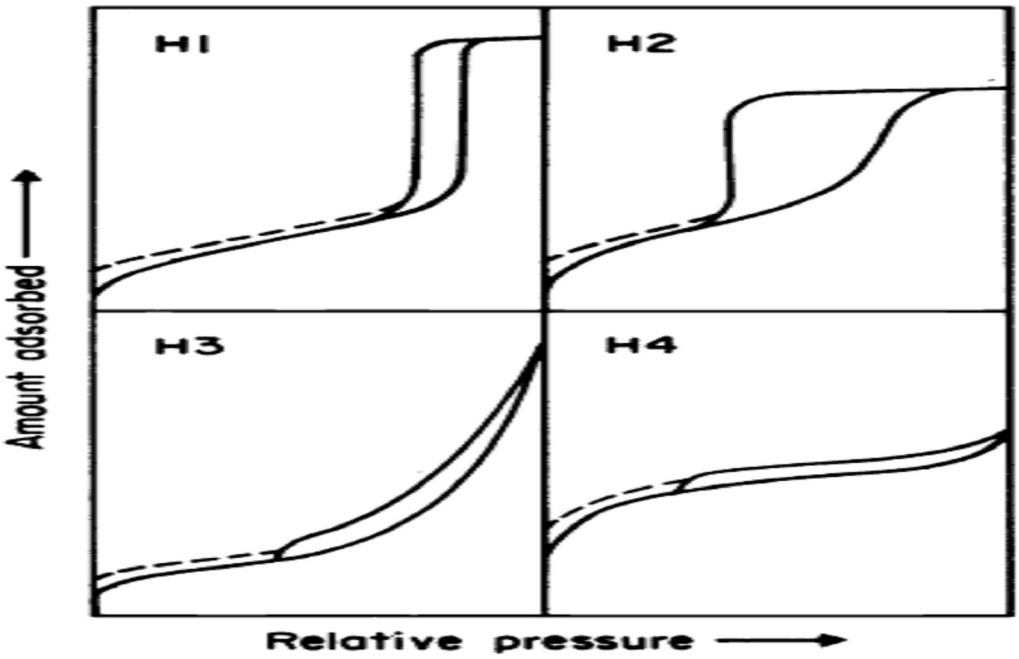

Figure 3.4

Types of hysteresis loops (Sing et *al.*, 1985)

The hysteresis of capillary condensable vapour has several possible origins. Most of the early theories of adsorption hysteresis made explicit use of the Kelvin Equation (3.18). Zsigmondy (1911) was the first to suggest the hysteresis phenomenon was due to a difference in the contact angles of the condensing and evaporating liquid. This explanation may account for some of the effects produced by the presence of surface impurities, but in its original form cannot explain the reproducibility of the majority of recorded loops. Other earlier explanation of hysteresis phenomena were based on ink-bottle theory that was developed by Mcbain (1935). It was based on the principle that the rate of evaporation of a liquid in a relatively large pore is likely to be retarded if there is only one narrow exit. This led Brunauer *et al.* (1938) to conclude that the liquid in the pore cannot be in true equilibrium with its vapour during the desorption process, and therefore, it is the adsorption branch of the loop which represents thermodynamic reversibility.

In contrast, network theory describes isotherms in terms of pore connectivity and pore size distribution. Therefore, at the end of adsorption, the adsorption isotherm forms a plateau and all accessible pores are filled. On reducing the pressure, liquid will evaporate from larger pores that are connected to surface area via narrow pores. Consequently, the

desorption process reflects the distribution of channels (pore necks) rather than the distribution of pores (Allen, 1998). The resulting hysteresis between the adsorption and desorption isotherm is therefore as a result of pore interconnectivity. As the pressure is reduced, a liquid-filled cavity cannot evaporate until at least one of the channels to the outside has evaporated. Therefore, the geometry of the network determines the shape of the adsorption branch of the isotherm.

A classic hysteresis theory is the 'independent pore model'. It regards the difference between the relative vapour pressures at which ink-bottle pores fill and empty as the primary cause of hysteresis (Sing *et al*., 1985). A single relative vapour pressure corresponding to the filling of the pore site with radius. However, there is a different single relative vapour pressure corresponding to the emptying of the pore connection with radius. The concept of pore blocking in ink-bottle type pores was successfully employed to describe the H2 hysteresis loops (Everett, 1967; and Ravikovitch *et al*., 2002), indicating exclusive dependence on the pore neck diameter. Pore blocking was reported to only take effect when the neck diameter is greater than a certain characteristic size of ~ 4 nm for nitrogen. These authors proposed a cavitation theory which states that for this critical 4 nm pore neck size and above pore blocking will take effect and for anything below there will be no pore blocking effects. Furthermore, the analysis of the hysteresis loops and scanning desorption isotherm on spherical pores of ~ 15 nm revealed three mechanisms of evaporation: evaporation from blocked cavities controlled by the size of connecting pores (classical ink-bottle or pore blocking effect); spontaneous evaporation caused by cavitation of the stretched metastable liquid; and finally that of near equilibrium evaporation in the region of hysteresis from unblocked cavities that have access to the vapour phase (Ravikovitch *et al*., 2002).

Sing *et al*., 1985 work on hysteresis loops was reviewed by Seaton (1991). This researcher proposed that for the Type H1 isotherm the formation of the hysteresis loop is governed by delayed condensation of nitrogen in the pores, whereas the H2 isotherm is dependent on network percolation effects. Similar observations were later made by Rajniak and Yang (1993), Soos and Rajniak (2001). The Type H3 and Type H4 are less common, and the reversibility depends on the adsorptive and operational temperature and parameters. Furthermore, Seaton (1991) determined pore connectivity based on the use of percolation

theory to analyse adsorption isotherms. The researcher illustrated the role of connectivity for three pores namely A, B, and C where only B has communication with the outside of the material as shown in Figure 3.5. As the pressure is increased during adsorption, nitrogen condenses into the pores in order of increasing pore size in the sequence of A, B and C. During desorption, the order in which the liquid in pores become thermodynamically unstable with respect to vapour phase is C, B, and A. However, the nitrogen condensed in contact with pore C is not in contact with the vapour phase which makes it difficult to vaporise at its condensation pressure. Consequently, metastable liquid nitrogen persists in pore C below its condensation pressure, until the liquid in B that is in contact with vapour phase, vaporises. Therefore, the nitrogen in Pore A is then in contact with its vapour and consequently able to vaporise at its condensation pressure. As a result, order of vaporisation during desorption in pore size is in the sequence of B and C together followed by A with the delay in C giving rise to the hysteresis.

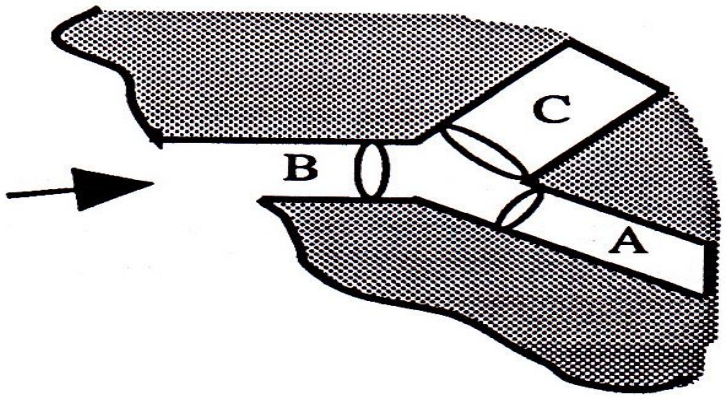

Figure 3.5
Network of three pores in porous solid (Seaton, 1991)

In recent years, Androutsopoulos and Salmas (2000) used a random corrugated pore concept to develop a new statistical model called the corrugated pore structure model (CPSM) to simulate capillary condensation-evaporation hysteresis. The pore structure was envisaged to be composed of a statistically large number of independent (non-intersected) corrugated pores. This corrugated pore was assumed to be made of a series of interconnected cylindrical elements (pore segments) of equal length with randomly distributed diameters of mesopore size. For capillary desorption or evaporation of the

condensate in a corrugated pore, which is fully saturated upon the termination of the condensation process $\left(\frac{P}{P^0} \to 1\right)$, a hemispherical interface is anticipated to be present at either pore necks. When the pressure is decreased gas desorption occurs, resulting in the retreat of the two interfaces in opposite directions and their convergence towards the pore centre. A continual film of liquid interface to the wide pore segments positioned in the interior parts of the corrugated pore was restricted by the intervention of smaller segments or throats where evaporation should occur prior to the interface motion toward the wider sections of the corrugated pore interior. Therefore, according to the work of Androutsopoulos and Salmas (2000), it is the restricted access of the vapour towards the wider segments that induces hysteresis during capillary desorption-evaporation.

In subsequent years, Monte Carlo (MC), and molecular dynamics (MD) simulations have been used to investigate pore blocking effects in capillary condensation hysteresis. The emphasis of these simulations is on disordered materials. Porous glasses and silica gels have been considered as case study systems for researching capillary hysteresis and networking effects. Sarkisov and Monson (2001) performed MC and MD simulations of capillary condensation in a single ink-bottle pore composed by a central rectangular cavity connected with the bulk phase by slit micropores half its size in width. The hysteresis observed in this model was not related to the classical pore blocking effect, as desorption from the central cavity occurred with the connecting pores remaining filled. During the desorption process, evaporation occurs from the pore throat into the bulk vapour phase and the molecules removed were then replaced by those coming from the pore body. Therefore, hysteresis arises when the pressure is decreased on desorption, and there is initially nothing to nucleate a large scale evaporation process in the large cavity until the pore liquid reaches a sufficiently expanded state such that spontaneous local density fluctuations lead to cavitation (spontaneous nucleation of a bubble). Furthermore, independent MC Simulations work on adsorption-desorption cycles in model porous glasses by Gelb and Gubbins (2002) and Pellenq *et al*. (2000) did not display any appreciable pore blocking effects.

In a subsequent report, Woo *et al*. (2001) developed density functional theory DFT models of sorption in disordered media and constructed hysteresis loops resembling the shape of experimental adsorption isotherms on porous glasses, without invoking pore-blocking

effects. Classical pore-blocking effects take place when the neck size is greater than a certain characteristic value (50 Å for nitrogen at 77 K, assuming that the neck can be considered as a cylindrical pore). Thommes *et al.* (2006) studied nitrogen and argon adsorption experiments performed at 77.4 and 87.3K on novel micro/mesoporous silica materials with morphologically different networks of mesopores embedded into microporous matrixes. These researchers showed that the type of hysteresis loop formed by adsorption/desorption isotherms is determined by different mechanisms of condensation and evaporation, and depends on the shape and sizes of featured pores (see Figure 3.6). This finding confirmed that cavitation-controlled evaporation occurs in ink-bottle pores with the neck size smaller than a certain value, and in this case, the pressure of evaporation does not depend upon the neck size. Therefore, desorption in a structure consisting of large mesopores occurs first by cavitation of the liquid in the large mesopores followed by desorption from smaller mesopores. In contrast, for pores with larger necks, they confirmed that percolation-controlled evaporation occurs, as observed for nitrogen and argon adsorption on porous Vycor glass. Hence, percolation effects contribute to hysteresis and hence information about the size of the pore necks can be obtained from the desorption branch.

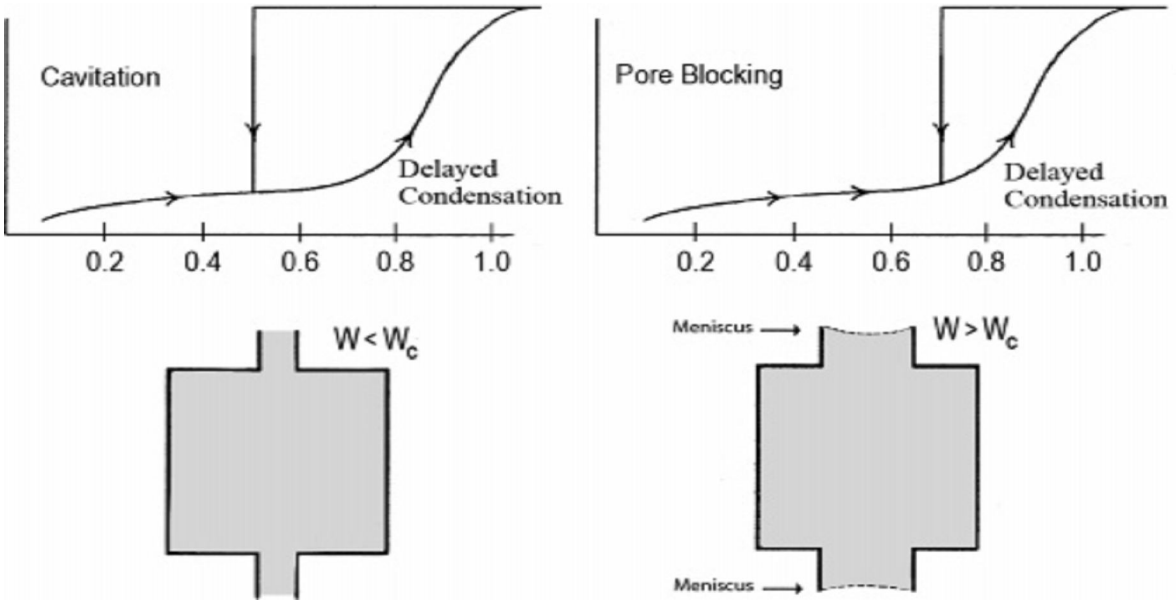

Figure 3.6

Schematic illustration of pore blocking and cavitation phenomena (Thommes *et al.*, 2006)

3.2.5 Determination of surface area by gas sorption technique

Accurate measurement of the surface area of porous solids presented a problem in early studies of adsorption. If the physical adsorption capacity were limited to a close packed monolayer, the determination of the saturation limit from an experimental isotherm, with a molecule of known size, would be straightforward, and hence lead to the specific surface area. However, this is not so, as chemisorption sites are usually widely spaced such that the saturation limit bears no obvious relationship to specific surface area, and physisorption usually involves multilayer adsorption (Coulson and Richardson, 1998). In multilayer adsorption, the multilayer commences at pressures well below that required for completion of the monolayer which leads to uncertainties as to how to extract the monolayer capacity from the experimental isotherm (Allen, 1998). Brunauer *et al*. (1938), solved this problem, by developing a simple model isotherm (BET), which accounted for multilayer adsorption, and was used to extract the monolayer capacity, and hence the specific surface area.

The multilayer adsorption theory, also known as BET equation, plays an important role in gas adsorption studies and surface area measurement. This BET isotherm theory is based on the concept of an adsorbed molecule that is not free to move over the surface and has no interaction between adjacent molecules on the surface (Brunauer *et al*., 1938). The main assumption in deriving the BET equation is that forces that produce condensation are responsible for the building up for multilayer adsorption. Therefore, it is assumed that the heat of adsorption is the same as the latent heat of vaporisation for all layers above the first. It should be noted that the isotherm equation derived by Brunauer *et al*. (1938) for multilayer adsorption was a modification of Langmuir's treatment of unimolecular adsorption. The generalization of the ideal localised monolayer treatment was achieved by assuming that each of the adsorbed molecules adsorbed in the first layer serves as a site for adsorption of a molecule into the second layer, and subsequent further layers to be formed. Therefore, the concept of localization prevails at all layers and forces of mutual interactions are neglected (Allen, 1998). In reality, these assumptions are not valid for a heterogeneous solid. Physical, structural or chemical heterogeneity is bound to exist and these factors can play a critical role in our ability to accurately evaluate the surface area. Nevertheless, the BET equation has been used as a standard technique for evaluating the surface area of catalysts. The BET equation derived by Brunauer *et al*. (1938) for multilayer adsorption is given by:

$$\frac{P}{V(P_0 - P)} = \frac{1}{cV_m} + \frac{c-1}{cV_m}\frac{P}{P_0} \tag{3.1}$$

A plot of $\frac{P}{V(P_0 - P)}$ against $\frac{P}{P_0}$ yields a line of slope $\frac{c-1}{cV_m}$ and intercept $\frac{1}{cV_m}$. The parameter c indicates the strength of the adsorbent-adsorbate interactions, with $c < 20$ and $c > 100$ representing low and high interaction strength respectively (Rouquerol *et al.*, 1999). The parameter, c, is related to the difference in the energy of adsorption of the first layer (E_1) and the liquefaction energy (E_L) of the subsequent layers of molecules, such that:

$$c \approx Exp\left(\frac{E_1 - E_L}{RT}\right), \tag{3.2}$$

where R and T are universal gas constant $\left(JK^{-1}mol^{-1}\right)$ and temperature (K) respectively (Rouquerol *et al.*, 1999).

The BET Equation (3.1) holds for Type I, Type II, Type III and Type IV isotherms, depending on the nature of the constant c. The selection of the range of relative pressures involving multilayer adsorption is most critical to the evaluation of the surface area of porous solids. Rouquerol *et al.* (1999) have stated that for many materials, the infinite form of the BET Equation (3.1) only fits over a narrow range of relative pressures (typically ~ 0.05 - 0.35). A coefficient of determination value (R^2) of 0.999 is recommended for most solids (Giesche, 1999). It should be noted that the failure of the BET plot at very low x (x < 0.05) is due to the influence of high adsorption potential in micropores and surface heterogeneity (Sing *et al.*, 1985). The BET plot of materials with high microporosity deviates from linearity. This deviation could lead to undesired negative values of the BET constant energy parameter value. Consequently, two criteria have been proposed for the selection of the x range. First, the pressure range must be in the region where $V(P - P_0)$ increases with an increase in x; and second the y - intercept of the linear region must be positive in order to give a meaningful value to BET constant, c (Rouquerol *et al.*, 2007). Also, Gregg and Jacobs (1948) doubt the adsorbed phase is liquid-like.

The BET surface area (a_{BET}) can be evaluated from monolayer capacity by using Equation 3.3, where σ_a is the molecular area of the adsorbate molecule in the completed monolayer and N_A is the Avogadro number. For nitrogen, σ_a is assumed to be 0.162 nm^2. An incorrect nitrogen molecular area can result in an error in the estimation of the surface area. Karnaukhov (1985) showed that the variation in nitrogen molecular area on different surfaces and quotes a value of 0.162 nm^2 for Al_2O_3 adsorbents.

$$(a_{BET}) = V_m \sigma_a N_A \tag{3.3}$$

The value of σ_a used for nitrogen is based on an assumption that the nitrogen molecules are spherical and rest on a plane surface with a packing similar to that in the bulk liquid. However, nitrogen molecules are in reality non-spherical. They tend to adsorb on the surface in a flat or upright position and also possess a quadrupole moment which causes the nitrogen molecules to adsorb specifically on certain surfaces (Gregg and Sing, 1982) masking the effect of the formation of a monolayer even though no monolayer has been formed in reality. In addition, the surface chemistry has a strong role in the apparent area projected by adsorbed molecules. Strong interactions can cause the area occupied by each molecule to decrease, and therefore adopt a denser packing relative to weaker interactions between the adsorbent and adsorbate.

3.2.6 Determination of pore size distribution by gas sorption technique

Adsorption pore size distribution analysis of mesoporous materials is based on an adopted interpretation of the mechanisms of capillary condensation, evaporation and the associated hysteresis phenomena (Sing et *al.*, 1985). The theory for condensation of vapour into a porous medium is derived from thermodynamic considerations. This is known as the Kelvin equation. Within a porous material, the gas layers continue to fill the pore until the pressure is sufficient that the gas condenses into a 'liquid-like phase'. The pressure at which the gas condenses can be related to the pore size according to the Kelvin equation. However, it becomes less accurate as the PSD becomes smaller because the Kelvin equation is purely thermodynamic, and thus, it does not take account at micropore region (Seaton *et al.*, 1989; and Lastoskie *et al.*, 1993). This model is usually applied for

diameters greater than 2 nm, because below this size the liquid cannot be considered a fluid with bulk properties due to forces exerted by the pore wall. Theoretical calculations suggest that the properties of fluids in microporous structures are highly sensitive to the size of the pores (Rouquerol *et al*., 1999).

In the case of mesopores, the Kelvin equation provides a useful model for the transformation of adsorption data into a PSD (Rouquerol *et al*., 1999). There established algorithms based on the Kelvin equation that are used for the determination of PSD such as the Barrett Joyner and Halenda (BJH) method by Barrett *et al*. (1951). However, there are other approaches that consider the fluid-solid interactions (Horvath Kawazoe, 1983). The Horvath-Kawazoe (HK) method is a novel technique for determining the micropore size distribution. The method was originally used to analyse nitrogen adsorption on molecular sieve carbons with slit shaped pores but has since been modified to account for cylindrical shaped pores as in the case of silica mesopores (Saito and Foley, 1991). The HK method is based on the general idea that the relative pressure required for the filling of micropores of a given shape and size, is directly related to the adsorbent-adsorbate interaction energy. Nevertheless, the BJH method is undoubtedly the most widely accepted method for the analysis of nitrogen adsorption/desorption PSD (Rouquerol *et al*., 1999), and thus, it has been adopted in this study.

When the BJH algorithm is used to determine the PSD, the pore size obtained from the Kelvin equation is generally corrected for the multi-layer film thickness using a universal t -layer equation. The empirical observation by Lowell and Shields (1984) have shown that, for many non-porous surfaces, the ratio of the volume adsorbed to the monolayer capacity $\left(\frac{V}{Vm}\right)$ plotted against relative pressure $\left(\frac{P}{P_0}\right)$ all approximately fit a common Type II curve above a relative pressure of 0.3. This implies for a given value of $\left(\frac{V}{Vm}\right)$ the adsorbed layer thickness will be the same regardless of the adsorbent. However, the data used to compile common t-curves was not comprehensive and the universality was only approximated (Rigby *et al*., 2008). Therefore, an individual porous solid may show a deviation from the common *t*-curves, as observed experimentally for nonporous templated silicas, such as the SBA-15 using neutron scattering (Schreiber *et al*., 2006).

The Kelvin equation can be derived as follows (Allen, 1998). Consider a liquid within a pore in equilibrium with its vapour. Let a small quantity, δa moles, be derived from bulk of liquid outside the pore, where its equilibrium pressure P_0, into pore where its equilibrium pressure is P. The total increase free energy δG is in three parts:

- Evaporation of ∂a moles of liquid at pressure $P_0(\delta G_1)$
- Expansion of ∂a moles of vapour from pressure P_0 to $P(\delta G_2)$
- Condensation of ∂a moles of vapour to liquid at pressure $P(\delta G_3)$

Since condensation and evaporation are equilibrium processes $\delta G_1 = (\delta G_3) = 0$. Therefore the change in free energy during expansion is given by:

$$\delta G_2 = RT \ln\left(\frac{P}{P_0}\right)\delta a \tag{3.4}$$

The vapour is assumed to behave like a perfect gas. The condensation of the vapour in the pores can result in a decrease in the area of solid-liquid interface and an increase in solid-vapour interface (δS). The change of energy during the process is:

$$\delta G^{'} = -\delta S(\gamma_{SL} - \gamma_{SV}) \tag{3.5}$$

where,

$$\gamma_{SL} - \gamma_{SV} = \gamma_{LV}\cos(\theta) \tag{3.6}$$

γ is the interfacial surface tension and the suffixes refer to solid-liquid (SL), solid-vapour (SV), and liquid vapour interface (LV); θ is the wetting contact angle which is taken as zero. since:

$$\delta G^{'} = \delta G_2 \tag{3.7}$$

then,

$$RT \ln\left(\frac{P}{P_0}\right)\delta a = -\gamma_{LV}\cos(\theta)\delta S \tag{3.8}$$

The volume condensed (V_C) in the pores is:

$$\delta V_C = V_L \delta a \tag{3.9}$$

where V_L is the molar volume. Therefore:

$$RT \ln\left(\frac{P}{P_0}\right)\frac{\delta V_C}{V_L} = -\gamma_{LV}\cos(\theta)\delta S \tag{3.10}$$

The limiting case being:

$$\frac{dV_C}{dS} = -\frac{V_L\gamma_{LV}\cos(\theta)}{RT\ln\frac{P}{P_0}} \tag{3.11}$$

For cylindrical pores of radius r_p and length l:

$$V_C = \pi r^2 l \tag{3.12}$$

$$S = 2\pi r l \tag{3.13}$$

Hence:

$$\frac{V_C}{S} = \frac{r}{2} \tag{3.14}$$

Therefore:

$$RT\ln x = \frac{-2\gamma_{LV}V_L\cos(\theta)}{r} \tag{3.15}$$

Where:

$$x = \frac{P}{P_0} \tag{3.16}$$

For non-cylindrical pores, having mutually perpendicular radii r_1 and r_2,

$$RT\ln x = -\gamma_{LV}V_L\left[\frac{1}{r_1}+\frac{1}{r_2}\right] \tag{3.17}$$

In general, the Kelvin equation is written as:

$$RT\ln x = \frac{-2\gamma_{LV}V_L\cos(\theta)}{r_K} \tag{3.18}$$

where r_K is the Kelvin radius.

For nitrogen at liquid nitrogen temperature:

γ_{LV} is the surface tension of the adsorbate in liquid form = 8.85×10^{-3} N m^{-2};

V_L = 34.6×10^{-6} m^{-3} mol^{-1};

R is the universal gas constant= 8.314 J mol^{-1} K^{-1};

T is the temperature = 77 K;

θ is the contact angle between the liquid and the wall of the pore = 0°.

In reality the contact angle changes as the pore fills and the pore shape varies (Gregg and Sing, 1982). Therefore, for a wide distribution of pore sizes, and possibly, quite separately developed pore systems, a mean size is not sufficient. For an ink-bottle type pore, the pressure required to fill a neck with a cylindrical meniscus exceeds the pressure required to fill a body via hemispherical meniscus, with neck radius that exceeds 0.5 times of the body. Ideally this should cause the neck and the pore body to be filled by condensed vapours at the same pressure. By the time the pressure for neck filling (considering cylindrical meniscus) is attained, the exerted pressure is more than sufficient to fill pore body (considering hemispherical meniscus) with condensed vapours (Rouquerol *et al*., 1999). Rouquerol *et al*. (1999) applied the Kelvin Equation (3.18) to the following diagrammatic model as illustrated in Figure 3.7. The radius (r_p) in the ideal and simplified situation of strict thermodynamic reversibility will be expected to have a vertical riser effect of pore filling in accordance with the above derived Kelvin Equation (3.18).

The work of Lastoskie *et al*. (1993) reports that the Kelvin Equation (3.18) probably underestimates pore size, and that its reliability may not extend below a pore size of ~ 7.5 nm. For a cylindrical pore shape, it seems reasonable to assume that the condensate has a meniscus of hemispherical form and radius (r_k), however as some physiosorption has already occurred on the mesopore walls, it is evident that (r_p) and (r_k) are not equal, as defined in Figure 3.7. If the thickness of the adsorbed multilayer is t, and has a finite contact angle, θ, which is assumed to be zero, the radius of the cylindrical pore can be written as:

$$r_p = r_k \cos\theta + t = r_k + t \tag{3.19}$$

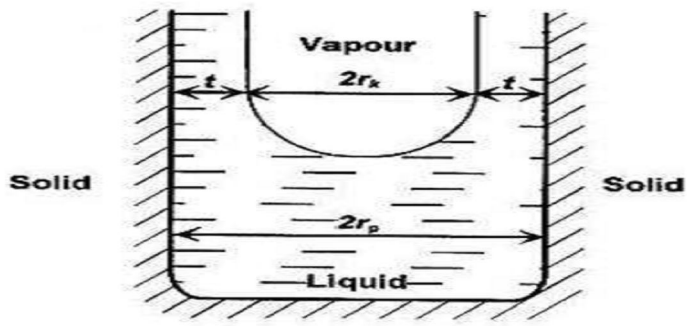

Figure 3.7

The relationship between the Kelvin radius and the pore radius (r_p) in a cylindrical mesopore (Rouquerol *et al*., 1999)

3.2.7 Determination of pore connectivity by gas sorption technique

As highlighted in Section 3.2.4, Seaton (1991) developed and tested a method for the determination of connectivity within pore networks. This method is based on the use of percolation theory to analyse the sorption hysteresis. Seaton (1991) viewed the hysteresis between the adsorption and desorption isotherms as a percolation phenomenon. Thus, the sharp decrease in the amount adsorbed at the knee of the desorption isotherm corresponds to the formation of a percolating network of vapour-filled pores. It was suggested by Seaton (1991), that a percolation cluster of pores, which are below their condensation pressures, is formed, and the metastable liquid nitrogen in these pores vaporises. As the pressure drops further, f (percolation factor) increases and the nitrogen in the rest of the pores vaporizes. Therefore, the primary desorption is a connectivity related phenomenon that can be described by percolation theory. Percolation theory is the theory of connected structures formed by random links on a lattice. The classical percolation theory focuses on two main problems, the bond percolation problem, and the site percolation problem. The primary adsorption process in the capillary condensation region can be treated as a classic site (cavity) percolation problem. Thus, desorption process for systems with hysteresis is the bond (connection) percolation problem.

Broadbent and Hammersley (1957) best described the percolation theory and explained, that the square lattice can be considered to consist of a number of bonds that can either be

occupied (denoted by a line) or unoccupied. The value f which is the fraction of occupied bonds represents the number of occupied bonds divided by the total number of bonds. Seaton (1991) modelled the solid as an array of three-dimensional lattices with each lattice corresponding to the pore network of a microparticle. The author defined a percolation threshold as the value of f where there are enough occupied bonds to span the length of the lattice. In addition, the worker defined the percolation probability (F) that a bond is part of the percolation cluster, and Z as coordination number. Seaton (1991) used this analogy to further investigate the percolation theory, and their resulting representation is shown in Figure 3.8, where the percolation threshold for the lattice is 0.5.

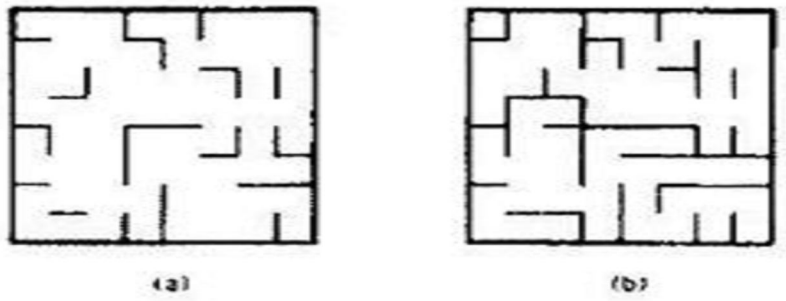

Figure 3.8

Percolation in a 2D lattice (a) f = 0.25, (b) f = 0.5, percolation threshold (Seaton, 1991)

The near percolation threshold, which is the number of occupied bonds per site in the percolation cluster, ZF, is an approximately universal function of the mean number of occupied bonds per site, Zf. The effect of system size on $F(f)$ is given by a modified finite-size scale scaling equation as:

$$L^{\frac{\beta}{\nu}} ZF = h\left[(Zf - 3/2) L^{\frac{1}{\nu}} \right], \tag{3.20}$$

where the critical components, β and ν have values 0.41, and 0.88, respectively, in three dimensions. The scaling function, h, has the same general shape for all 3D systems which vary from lattice to lattice. Figure 3.9 illustrates the generalised scaling function.

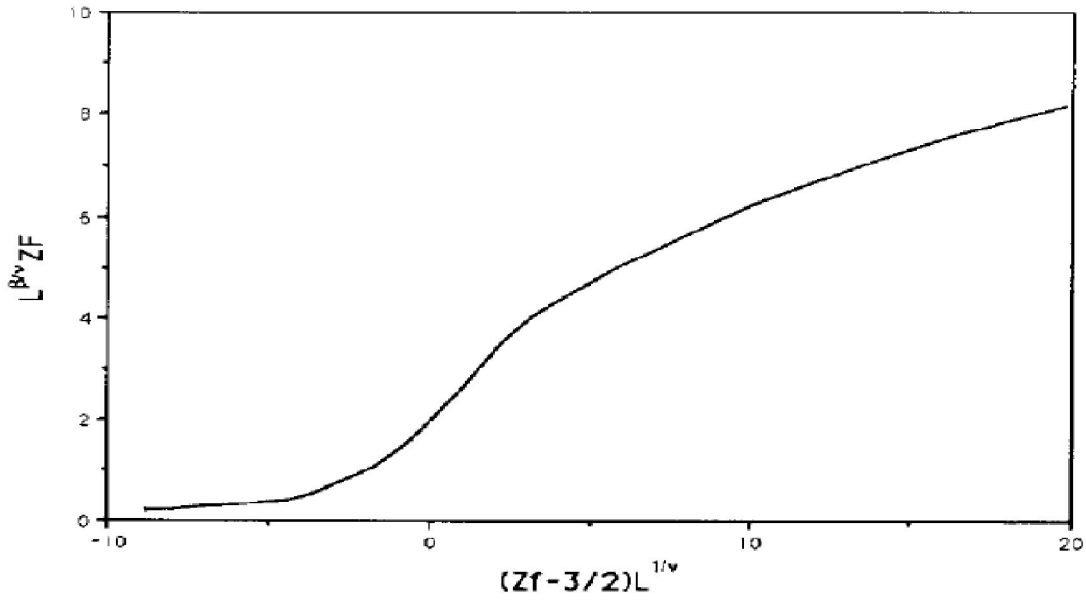

Figure 3.9

Illustration of the generalised scaling function (Seaton, 1991)

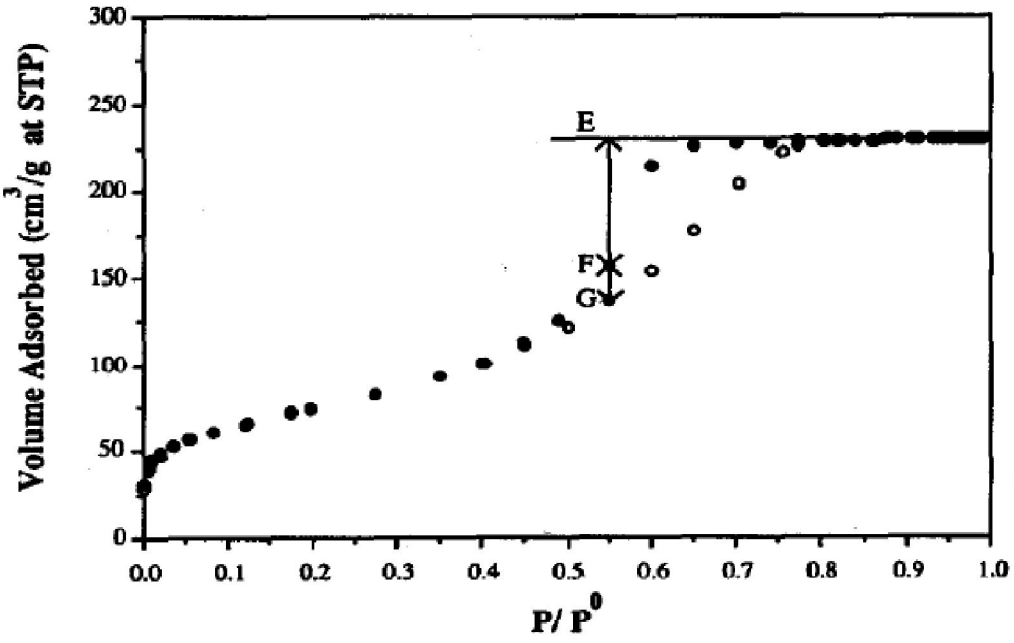

Figure 3.10

Schematic illustration of the calculation of $\frac{F}{f} = \frac{EF}{EG}$ **(Seaton, 1991)**

The procedure for the determination of pore network connectivity involves three stages:

- The pore size distribution is determined by using the method of Barrett *et al.* (1951). An appropriate pore shape must be assumed.
- $F(f)$ is determined from the adsorption and desorption data as illustrated in Figure 3.10.
- The size and shape of the hysteresis loop is dictated by the mean coordination number of the pore network, Z, and the number of pore lengths, L. The connectivity parameters, Z and L are obtained by fitting the quasi-universal curve of Equation 3.20 to $F(f)$.

The method was tested on several mesoporous solids which had hysteresis loops of the IUPAC types H1 and H2 classification (Seaton, 1991; Liu *et al.*, 1992; and Muray *et al.*, 1999). However, the physical significance of L is still difficult to understand. It reflects the aggregate behaviour of microparticles with different shapes and sizes. The microparticles contain pores that are typically in the microscope and mesopore size ranges. Consequently, it is not possible to equate L to any defined dimension, and thus it is regarded as a characteristic dimension of the microparticles (Seaton, 1991). It maps the linear dimension of lattices as illustrated by Seaton (1991) in Figure 3.11, and thus, it is often expressed as average number of pore lengths. Figure 3.11 (a) represents the part of a structure of a catalyst. Figure 3.11 (b) represents the pore structure of the catalyst as an array of lattices. N1 and N2 represent the micro/mesopore and macropore networks.

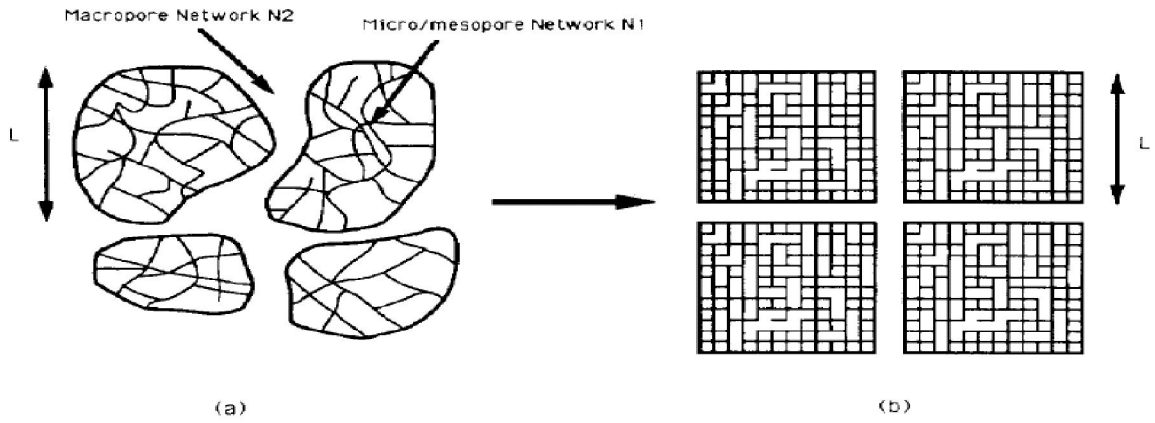

Figure 3.11

Mapping of the pore structure of a real solid to an array of lattices (Seaton, 1991)

3.2.8 Determination of pore length by gas sorption technique

In recent years, Rigby *et al*. (2004) presented an analytical method to determine the pore-length distribution from the results of novel experiments using the integrated nitrogen sorption and mercury porosimetry technique. These researchers analysed two sets of nitrogen sorption data, taken from integrated nitrogen sorption and mercury porosimetry experiments to derive the pore-length distribution by using the percolation theory developed by Seaton (1991). As in the original percolation method by Seaton (1991), the analysis presented by Rigby *et al*. (2004) was carried out in terms of percolation variables, the values of which were calculated from pore-diameter distributions (obtained from nitrogen adsorption isotherms). In the old version of Seaton's (1991) percolation theory, it was assumed that the average pore length is independent of pore diameter. In contrast, Rigby *et al*. (2004) assumed that the average pore length of pores is a function of the pore diameter, such that the distribution of average pore length for each pore diameter follows a power law. On the other hand, Dullien (1992) found from various micro-photographic images of solids with random porosity showed that that in many cases the length (l) of pores is very close to their diameter (d) of the pores $(l \sim d)$.

In a different approach, Pomonis and Armatas (2004) proposed a method for the estimation of pore anisotropy, *b*, in porous solids. The method is based on the pore size distribution and the surface area distribution, both calculated from nitrogen adsorption and desorption isotherms. The materials used for original testing of the method were aluminium containing Mobil crystalline materials (MCM) and silicas with different random porosity. However, Pomonis and Armatas (2004) left some important assumptions and parameters out of the correlation in their method that will be discussed later in this Section. Nevertheless, the resultant analysis was satisfactory for the materials they tested. This study intends to modify the correlation and include the missing assumptions in the original correlation, thus applying it to several materials. Let us first proceed based on the assumption, made by Pomonis and Armatas (2004), that in a collection of pores, for each pore i, or rather for each group of pores in a small interval of pore diameter, $d_i \pm \Delta d_i$, the length, l_i, is related to the diameter, d_i, via a relation of the form:

$$b_i = \frac{l_i}{d_i} = \frac{l_i}{2r_i} \tag{3.21}$$

If b_i is larger than unity $(b_i >> 1)$, those pores have a large anisotropy. Whilst, if $b_i \sim 1$ $(l_i \sim d_i)$, the pores are isotropic and, according to Dullien (1992), this should be the case in ordinary porous solids with a random porous network. However, if on the other hand $b_i < 1$, the pores are again anisotropic but assumed to be shallow cavities rather than typical pores (Pomonis and Armatas 2004). From the gas sorption experiments we can calculate at each $p_i\left(=\frac{P_i}{P_0}\right)$ the values corresponding to specific pore surface area S_{pi} and the specific pore volume V_{pi}. At each p_i we assume that a number N_i of cylindrical pores is filled up. Furthermore, Pomonis and Armatas (2004) assumed that:

$$S_{pi} = N_i(2\pi r_i)l_i = N_i(2\pi r_i)(2b_i r_i) = 4\pi N_i b_i r_i^2 \tag{3.22}$$

$$V_{pi} = N_i(\pi r_i^2)l_i = N_i(\pi r_i^2)(2b_i r_i) = 2\pi N_i b_i r_i^3 \tag{3.23}$$

Thus, dividing the cube of Equation (3.22) and the square of Equation (3.23) gives the dimensionless ratio:

$$S_i^3 / V_i^2 = \frac{N_i 8\pi l_i}{r_i}. \tag{3.24}$$

Substituting Equation (3.21) into Equation (3.24) will give the ratio of the cube of surface area S_i over the square of pore volume V_i, at each particular pressure:

$$S_i^3 / V_i^2 = 16\pi(N_i b_i) = 16\pi\lambda_i \tag{3.25}$$

where $N_i b_i$ is the number of pores having anisotropy, b_i, which are filled at each pressure$\left(\frac{P_i}{P_0}\right)$ and λ_i is the total anisotropy of all the pores N_i belonging to the group i of pores. Therefore, the plot of λ_i against $\left(\frac{P_i}{P_0}\right)$ provides a clear picture of the variation of the total pore anisotropy λ_i as the relative pressure $\left(\frac{P_i}{P_0}\right)$ increases. It should be noted

that N_i and b_i are constants. The particular values of N_i and b_i can be obtained by using the power law correlation:

$$l_i = kr_i^{\alpha_i} \tag{3.26}$$

Note that Pomonis and Armatas (2004) missed out the all important proportionality constant k (unit in grams) in the power law correlation (Equation 3.25). Finally, substituting Equation (3.26) into Equation (3.24) gives:

$$S_i^3 / V_i^2 = N_i 8\pi k r^{(\alpha-1)} \tag{3.27}$$

Taking the logarithm of Equation (3.27) gives:

$$\log\left(\frac{S^3}{V^2}\right) = \log(8\pi k) + \log(N_i) + \left[(\alpha_i - 1) \times \log r\right] \tag{3.28}$$

A plot of $\log\left(\frac{S^3}{V^2}\right)$ against $\log(r_i)$ should give rise to a line with slope, $s_i = \alpha_i - 1$. Note that Pomonis and Armatas (2004) left out the important assumption for Equation 3.28 to be valid for a straight line. Equation 3.28 can only be a straight line if α_i and N_i are constant for all d_i. The slope at each point i of the plot is equal to $s_i = \alpha_i - 1$, since:

$$l_i = b_i d_i = 2r_i b_i = kr_i^{\alpha_i - 1}, \tag{3.29}$$

Therefore:

$$b_i = 0.5kr_i^{\alpha_i - 1} = 0.5kr_i^{s_i} \tag{3.30}$$

In a subsequent report, Knowles *et al*. (2006) expanded the work of Pomonis and Armatas (2004) by applying the model to nanostructured ordered mesoporous solids. These researchers succeeded in estimating not only the anisotropy of pores in a mesoporous solid but also the related pore anisotropy distribution. Katsoulidis *et al*. (2007) also tested the model to nanostructured mesoporous silicate materials. However, as seen in the power correlation (Equation, 3.26), the pore anisotropy with corresponding pore anisotropy distribution cannot be obtained, and thus, the work of Knowles *et al*. (2006) and Katsoulidis *et al*. (2007) were incorrect. Pomonis and Armatas (2004) method can only

determine the slope of the Equation 3.28, which can tell some measure of the average pore length and perhaps the heterogeneity of the sample.

3.2.9 Scope of work by gas sorption technique

Mercury simulation works that are detailed in Section 3.3.3 suggest that mercury entrapment is a function of the coefficient of variance of the PSD, and pore connectivity (Androutsopoulos and Mann, 1979; Conner and Lane 1984; Portsmouth and Gladden, 1991; 1992). In addition, experimental data derived from mercury porosimetry showed enough evidence that entrapment can occur in long straight pores due to multiple snap-off in a porous material (Giesche, 2010). The retraction process in mercury porosimetry leads to the formation of collars around various mercury threads occupying long and narrow pores (throats). Thus, when a thread surface becomes unstable the mercury thread collapses (snap-off). Furthermore, Portsmouth and Gladden (1991; 1992) observed a positive correlation between tortuosity with pore connectivity and PSD in diffusion simulation work. These researchers found that tortuosity increases with an increased pore connectivity and the variance of PSD. Therefore, the estimation of pore connectivity, variance of the PSD, and the pore-length is a critical factor in understand the transport phenomena within porous materials. Various techniques have been developed to determine these parameters from gas sorption data as discussed in Sections 3.2.6 to 3.2.8.

It is the purpose of this study to check the applicability of the methods proposed by Seaton (1991) in Section 3.2.7, and that of Pomonis and Armatas (2004) in Section 3.2.8, to estimate the connectivity parameters and pore-length of a range of alumina and silica materials in this study. The PSD will be determined by using the method suggested by Barrett *et al.* (1951) in Section 3.2.6, and thus, the variance of the PSD can be estimated. In addition, other traditional characteristic parameters of the materials, such as the specific surface area will be estimated by BET Equation (3.1) as detailed in Section 3.2.5, and the total pore volume will be estimated by the Gurvitsch method as detailed by Gregg and Sing (1982). Finally, the ultimate objective of this study is to provide experimental verifications to the simulation results reported in Section 1.6. Therefore, in Chapter 8, the estimated pore connectivity, and width of the PSD will be correlated other aspects related to transportation in porous media such as the mercury entrapment, and tortuosity. In addition,

the estimated pore length parameter (α) of these materials will be correlated with mercury entrapment to experimentally verify Giesche's (2010) work on multiple snap-off in long straight pores. As detailed in Section 3.3, the mercury entrapment will be measured with mercury porosimetry. Also, detailed in Section 3.4, the tortuosity will be measured with PGSE NMR technique.

3.3 Applications of mercury porosimetry to porous media

3.3.1 Principles of mercury porosimetry

Mercury porosimetry is based on the capillary rise phenomenon whereby an excess pressure is required to cause a non-wetting fluid (mercury) to climb up a narrow capillary (Allen, 1999). The surface tension of mercury makes it difficult for it to enter small openings. Therefore, an external pressure is required to overcome this opposition and force the mercury into the void spaces of the material (Orr, 1969). Mercury porosimetry assessment of porous media covers mesoporosity (4 – 50 nm) and macroporosity (> 50 nm diameter). For the reasons stated above, mercury porosimetry has become the most favourite technique of characterising void spaces in porous media (Giesche, 2006). The conventional method of analysing the resultant data from a porosimetry experiment relies on the use of a parallel pore bundle model originally introduced by Washburn (1921). Most workers assumed cylindrical pore geometry as illustrated in Figure 3.12.

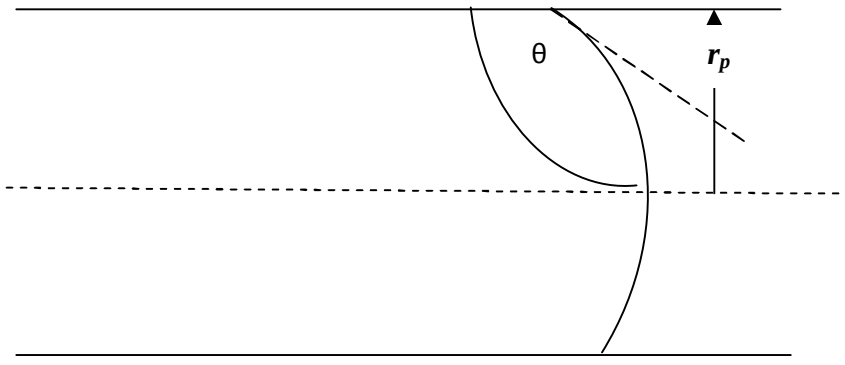

Figure 3.12

Schematic representation of a cylindrical pore assumed by most instruments

The Washburn equation, also known as the Laplace equation, can be employed to relate an applied pressure with a relevant pore diameter being intruded by the non-wetting liquid mercury.

$$\Delta P = \gamma_{HG}\left(\frac{1}{r_1}+\frac{1}{r_2}\right)=\frac{2\gamma_{HG}\cos\theta}{r_p} \tag{3.31}$$

The Washburn equation (Equation 3.31) relates the pressure difference across the curved mercury interface (r_1 and r_2 being the radii of curvature of that interface) to the corresponding pore size (r_p) using the surface tension of mercury (γ_{HG}) and the contact angle (θ) between the solid and mercury. The volume of mercury penetrating the pores is measured directly as a function of the applied pressure. According to Allen (1999), a value of 0.485 N/m at 25 $^{\circ}$C is generally accepted for surface tension and a fixed value of 130° for the contact angle (irrespective of the sample material). However, the surface or interfacial tension of mercury contributes greatly with respect to errors in the determination of the pore size distribution and can change with pore size (Allen, 1999).

The validity of the simplistic interpretation by Washburn (1921) has been questioned since the development of the method, as it fails to account for several features of porous media. Firstly, intrusion of mercury occurs within an interconnected network of pores that are not readily accessible to mercury at every stage of mercury penetration; and the second, the observed capillary hysteresis between the intrusion and extrusion curves cannot be predicted by capillary tube model (Ioannidis and Chatzis, 1993). Furthermore, the model fails to take into account that most porous media consist of a network of non-circular pores (Allen, 1999). Some of these pores do not empty to the surface as they have very small necks in comparisons to their big bodies. This can give rise to hysteresis and entrapment, where some mercury is retained within the sample. Nevertheless, no other porosity characterisation technique can achieve better presentation of porous media than mercury porosimetry due to its ability to cover a much wider pore size range (Giesche, 2006).

3.3.2 Hysteresis in mercury intrusion/extrusion curves

Hysteresis in mercury porosimetry is identified from the observation that, at a given pressure, the volume indicated on the extrusion curve is greater than that on the intrusion curve, and for a given volume, the pressure indicated on the intrusion curve is greater than that on the extrusion curve. Hysteresis between the intrusion and extrusion is observed in most samples during mercury porosimetry experiments (Ritter and Drake 1945; Giesche, 2006). Several explanations, although mostly from a mesoscopic or macroscopic perspective, have been proposed to explain the origin of hysteresis in mercury porosimetry such as the ink bottle theory, percolation-connectivity theory, and contact angle theory, (Giesche, 2006).

In ink-bottle hysteresis theory, the assumption about the special arrangement of pores in mercury porosimetry is mainly responsible for the hysteresis. In most samples, the throat opening to a pore is smaller than the actual cavity, which results in mercury entering the pore cavity at a pressure determined by the entrance size and not the actual cavity size. Therefore, during extrusion process, the mercury network would then break at throats between the pores leaving a large amount of mercury trapped inside the sample (Giesche, 2006). In addition, Levitz *et al.* (2002) explained the form of hysteresis caused by the effects of pore geometry as follows. Pore shape has a strong influence on the extrusion behaviour; the shape of a cylindrical pore closed at one end has no real effect on the intrusion behaviour. However, extrusion will occur at a lower pressure in the above type pore, in comparison to a cylindrical pore, which is open on both ends. The interconnectivity of pores plays an important role in mercury porosimetry, as, in order for a pore to become filled with mercury it must be equal to or larger than the corresponding "pore size" at the applied pressure, as long as a continuous path of mercury leads to that pore. Large internal voids will not be filled unless the pressure is sufficient to fill the smaller pores.

The network and percolation theories consider hysteresis as to be due to network effects that reflect the shape of the pores, their respective pore size distributions, and connectivity (Allen, 1998). The connectivity model is an extension of ink-bottle theory but it also considers the connection effects between the pores. Therefore, larger internal voids that are surrounded by smaller pores will not be filled unless the pressure is sufficient to fill a

pathway towards that pore. Consequently, during extrusion, the reverse occurs, and certain pores will remain filled with mercury if they do not have a continuous path towards the surface (Giesche, 2006). Rigby and Edler (2002), succeeded in employing percolation concepts to relate the hysteresis to network effects arising from the connectivity of the void space in the porous material. These researchers found that voids between the sample and the pores within them are interconnecting, and thus, these narrow inlets lead to wide pores. In addition to hysteresis, mercury remains contained in the porous network after extrusion (entrapment).

In the contact angle theory, differences in advancing and receding contact angles are frequently believed as the main cause of hysteresis. Liabastre and Orr (1978) were one of the earliest researchers to explain the hysteresis phenomenon and compressibility factors in porous media. These researchers examined a graded series of controlled pore glasses (CPG) and Nuclepore membranes by electron microscope and mercury porosimetry. These researchers used materials with low structural heterogeneity with independently measurable pore size as model materials. Liabastre and Orr (1978) measured the mercury intrusion and extrusion pressures for these materials and the pore sizes were measured directly with electron microscope. It was found that all the pore glasses and Nuclepore membranes exhibited hysteresis. However, Liabastre and Orr's (1978) work was limited by the cylindrical pore assumption they made. The real nature of pores in porous media consists of a network of interconnected circular pores but it's an acceptable practical means of dealing with the hysteresis of complex pore structures. In addition, Lowell and Shields (1981) observed a difference of contact angles as the main course of hysteresis. These researchers carried out extensive work to investigate the origin of hysteresis and entrapment by applying two cycles of mercury porosimetry to porous materials. It was found that hysteresis and entrapment were present in the first mercury intrusion/extrusion cycle. However, mercury entrapment was absent in the second cycle which suggests that entrapment and hysteresis are not both of same origin, and attributed the hysteresis to the difference of contact angle between intrusion and extrusion curves.

In a subsequent study, Kloubek (1981) used the data derived by Liabastre and Orr (1978) to obtain correlations for the apparent variation of the term $\gamma_{HG}\cos\theta$, in the Washburn Equation (3.31), with pore radius. Kloubek (1981) observed that the volume hysteresis in

mercury porosimetry is partially caused by the contact angle and the remaining is considered to be associated with structural hysteresis. In recent years, Rigby and Edler (2002) used the correlations by Kloubek (1981) to obtain semi-empirical alternatives to the Washburn Equation (3.31), to interpret raw mercury porosimetry intrusion and extrusion data. Rigby and Edler (2002) observed that the structural hysteresis and the overall level of mercury entrapment was caused by the macroscopic (> ~ 30 μm), and not the microscopic (< ~ 30 μm), properties of the porous medium. It was found that, when the raw mercury porosimetry data for various different silica materials were analyzed using these new correlations, a superposition of the transformed intrusion and extrusion curves was obtained. This finding was in agreement with original CPG materials used by Liabastre and Orr (1978) to obtain the $\gamma_{HG}\cos\theta$ correlations. In addition, Galarneau *et al*. (2008) observed similar results when they tested these correlations on templated porous silicas. In a subsequent report, Rigby (2002) suggested additional $\gamma_{HG}\cos\theta$ correlations for the use with alumina materials. It was found that the same set of correlations removed hysteresis for a range of different alumina materials.

The alternative expressions to the Washburn Equation (3.31) takes account of variations in both mercury contact angle and surface tension with pore size, for both advancing and retreating mercury menisci to pore radius, thus removing their contribution to the hysteresis (Rigby and Fletcher, 2004). For mercury intrusion into silica/alumina materials the pore radius (nm) for the alternative expressions is given by:

$$r_p = \frac{302.533 + \sqrt{91526.216 + 1.478P}}{P} \quad , \tag{3.32}$$

while for mercury retraction the pore radius (nm) is given by:

$$r_p = \frac{68.366 + \sqrt{4673.91 + 471.122P}}{P}, \tag{3.33}$$

where P is the pressure in MPa. Equations 3.32 and 3.33 remove the contact angle and surface tension hysteresis, and thus, the resultant observed hysteresis is due to structural effects. One of such effects is pore shielding which occurs when larger internal pores are

connected to the network or bulk by smaller pores (ink-bottles). The calibrations for Equations 3.32 and 3.33 are valid for pore radii in the ranges 6-99.75 and 4-68.5 nm, respectively (Rigby and Fletcher, 2004). Since Equations 3.32 and 3.33 are empirical in origin, their use leads to an experimental error in the pore sizes obtained, which is estimated to be ~ 4-5% (Kloubek, 1981).

Furthermore, various other models and theories have been employed to explain intrusion/extrusion hysteresis. In the energy barrier model, hysteresis is attributed to energy barriers associate with the formation of a liquid/vapour interface (which needs an extra amount of energy) during extrusion (Giesche, 2006). Van Brakel *et al.* (1981) proposed a different explanation of hysteresis. These researchers observed hysteresis at high pressure, where mercury atoms get pushed into the crystal lattice. It was also found that mercury wetting can be irreversible due to adhesion to the walls at high pressures, and as a result after retraction, part of the imbibed mercury remains distributed as a film on the wall of the large pores.

In a different approach, other researchers presented evidence, based on a lattice gas model, that the hysteresis loops observed during gas adsorption experiments for fluids in disordered materials involves two differential dynamic regimes (Woo and Monson, 2004). These researchers suggested that the first regime, also known as transport regime, is believed to be associated with mass transfer to and from the external surface. The experimental time is longer than the time scale covering this regime, which makes the width of the hysteresis insignificant to relative time. The second regime, which is also called the quasi-equilibrium regime, corresponds to the regime where fluid is redistributed within the sample. Equilibrium is very slow here, and the associated change is difficult to detect within an experimental time-scale, and thus explains why hysteresis is reproducible in gas adsorption (Woo and Monson, 2004). Many earlier researchers considered mass transport to occur by viscous flow processes (Wardlaw and McKellar, 1981; Tsakiroglou *et al.*, 1997; Tsakiroglou and Payatakes, 1998). Furthermore, this lattice gas model was applied to study penetration of a non-wetting liquid into disordered porous media (Porcheron and Monson, 2004; Porcheron and Monson 2005). The lattice model exhibits a symmetry that provides a direct relationship between intrusion/extrusion curves for non-wetting fluids and adsorption/desorption isotherms for wetting fluids. Therefore, the

symmetry of the lattice model means that arguments by Woo and Monson (2004) with regard to two dynamic regimes are also valid for mercury porosimetry.

In recent years, Porcheron *et al.* (2007) simulated mercury intrusion and retraction using mean-field density-functional theory (MF-DFT), in models of disordered porous materials such as a CPG and Vycor porous glass. The intrusion and extrusion curves were qualitatively similar to the experimental curves. These researchers' studies focused on the effects of larger scale structural heterogeneity on mercury porosimetry. It was also seen that hysteresis naturally arises during MF-DFT simulations of mercury intrusion and retraction. In a similar approach, Rigby *et al.* (2009) used MF-DFT simulations in conjunction with experimental work to investigate the origins of hysteresis in silica materials. Lattice-based MF-DFT simulations were performed on intrusion and retraction from pores with varying degrees of surface geometric roughness. The simulation work was compared with the experimental results (such as the surface roughness) obtained by gas adsorption, mercury porosimetry and Small-angle X-ray scattering (SAXS). It was found that the degree of hysteresis in raw mercury porosimetry data depends upon the degree of surface roughness of the material, and the width of the hysteresis increases with increased surface roughness. In a summary, these are some of the main factors responsible for hysteresis in mercury porosimetry:

- *Ink bottle pores.* These are pores with narrow necks and wide bodies. During extrusion, mercury is trapped in the ink bottle pores causing hysteresis. Meyer (1953) tried to correct the effect of ink bottle pores by a raw data using a probability theory and accidentally altered the measured distribution.

- *Network effects.* The voids between particles, and the pores within them, are interconnected and narrow inlets lead to wide voids (Allen, 1999). During extrusion, mercury is trapped in the wide voids causing hysteresis. Ioannidis *et al.* (1991) studied the network effects in glass-etched micromodels with the aid of an experimental apparatus that enabled the accurate measurement of capillary pressures and mercury saturations, as well as the observation of micro-displacement mechanisms at the pore level. These researchers concluded that intrusion is governed by the capillary resistance of the pore necks whilst the entrapment during extrusion is governed by the capillary resistance of pore bodies.

- *Contact angle*. The difference in the advancing and receding contact angle will result in the retraction curve being different from the penetration curve. The possible effect of contact angle hysteresis and its importance has been supported by several researchers, such as Kloubek (1981), and Liabastre and Orr (1978) showed contact angle hysteresis in mercury porosimetry of cylindrical pores.

- *Pore potential*. Mercury forced into a pore will interact with the pore walls and be trapped in a potential well of energy, U. During depressurization, a cylindrical pore of radius r_p will require an amount of energy E_C to separate the column such that (Allen, 1999):

$$E_C = 2\pi r_p{}^2 \gamma_{HG} \tag{3.34}$$

  If $U \geq E_C$, the column will break. Consequently, mercury will be trapped and thus cause the extrusion curve to intercept the volume axis above the zero. During pressurization the column is under tension, due to poor shielding, and can break if the pore potential is high and the pore radius is very small (Allen, 1999). In the case of hysteresis, it is that the pore potential that causes mercury to extrude from a pore at a lower pressure than it intrudes. Hence, any shape of pore can produce hysteresis and cause mercury entrapment in the initial intrusion (Allen, 1999).

- *Surface roughness*. This can cause the mercury to slip-stick so that mercury thread is broken (Allen, 1999).

3.3.3 Entrapment in mercury intrusion/extrusion curves

Entrapment of mercury is recognized from the observation that, at the completion of intrusion-extrusion cycle, the retraction curve does not give zero volume (Lowell and Shields, 1981). The size, shape, and arrangement of conducting spaces in porous materials, such as reservoir rocks, are known to affect the flow of fluids and the displacement of one fluid by another (Tsakiroglou and Payatakes, 1990). Various researchers (Meyer, 1953; Wardlaw and McKellar, 1981; Tsakiroglou and Payatakes, 1990) used mercury porosimetry to identify those aspects of pore systems that affect the trapping of non-

wetting fluids such as mercury, or, by analogy, oil and gas in strongly water-wetting systems.

One of the earliest studies aimed at explaining the origin of hysteresis and entrapment was conducted by Androutsopoulos and Mann (1979). These researchers developed a two-dimensional network model consisting of cylindrical pore segments assembled into square grids. This model was able to account for hysteresis and entrapment, but, more importantly, it allowed the extrusion curve and the extent of entrapment to contribute towards the determination of the pore size distribution (PSD). It was found that entrapment increased as the PSD got wider and that mercury was preferentially entrapped in larger pores. This proposal suggests that mercury retraction might involve a slower relaxation process as well as the more rapid, capillary flow process described by Washburn (1921). The slow retraction process was attributed to the formation of ganglia of entrapped mercury that, under a non-zero net force prior to equilibration, tend to move around slowly and may coalesce with the bulk. Therefore, it might be inaccurate to interpret mercury retraction solely on the basis of a piston-like withdrawal. In contrast to network effects, theoretical studies conducted by Kloubek (1981) suggested that mercury entrapment could arise in various pore geometries, such as conical dead-end pores, solely due to the difference between the advancing and retreating mercury contact angles.

Wardlaw and McKellar (1981) built on the simulation work of Androutsopoulos and Mann (1979) by conducting mercury porosimetry experiments on model porous media consisting of various different types of pore networks etched in glass. The mercury porosimetry experiments, conducted by these researchers suggested that non-random structural heterogeneity causes mercury entrapment. It was found that, for mercury experiments on micromodels consisting of grids of pore elements of uniform size, no mercury entrapment occurred. Furthermore, no mercury entrapment occurred in glass micromodels where the sizes of individual, neighbouring pore grid elements were slightly different. In a different approach, Wardlaw and McKellar (1981) constructed two different types of non-random model systems. The first type of glass micromodels consisted of clusters of smaller pores occurring in isolated domains amidst a continuous network of larger pores. In the second, the researchers constructed a model where isolated clusters of larger pores were located within a continuous network of smaller pores. It was found that mercury entrapment only

occurred in the second model as illustrated in Figure 3.13. Wardlaw and McKellar (1981) came to the conclusion that four aspects of pore systems may affect the movement of fluids and, in particular, the trapping of non-wetting phases during withdrawal from a pore system:

- **Pore and throat sizes**. Throats are small spaces linking pores (which are large spaces). The term pore system describes the total system of pores and throats. The amount of entrapment increases as pore to throat size ratio increases. Hence, excessive trapping of mercury will be seen in isolated pores that have large pore to throat size ratios.

- **Throat to pore coordination number**. The coordination number of a pore system is the average number of throats which connect with each pore. It is a measure of the connectivity of the network of throats and pores. It determines the number of different pathways between pores. In mercury-air system differences in coordination number cause insignificant entrapment but the local heterogeneities cause the majority of the entrapment.

- **Random and non-random heterogeneity**. Pores and throats of different sizes may be distributed randomly in a network (randomly heterogeneous) or they may be distributed non-randomly. In the latter case, the larger elements may be clustered together in domains and likewise the smaller elements are clustered together in other domains. Mercury preferentially saturates larger pores upon pressure increase but the opposite happens when pressure is reduced as the smaller pores empty in a uniform manner.

- **Surface roughness**. This is more common in reservoir rocks. The surface roughness of pores in reservoir rocks is different from the smooth crystal surfaces common in some dolomites and sandstones. Surface roughness affects advancing and receding angles.

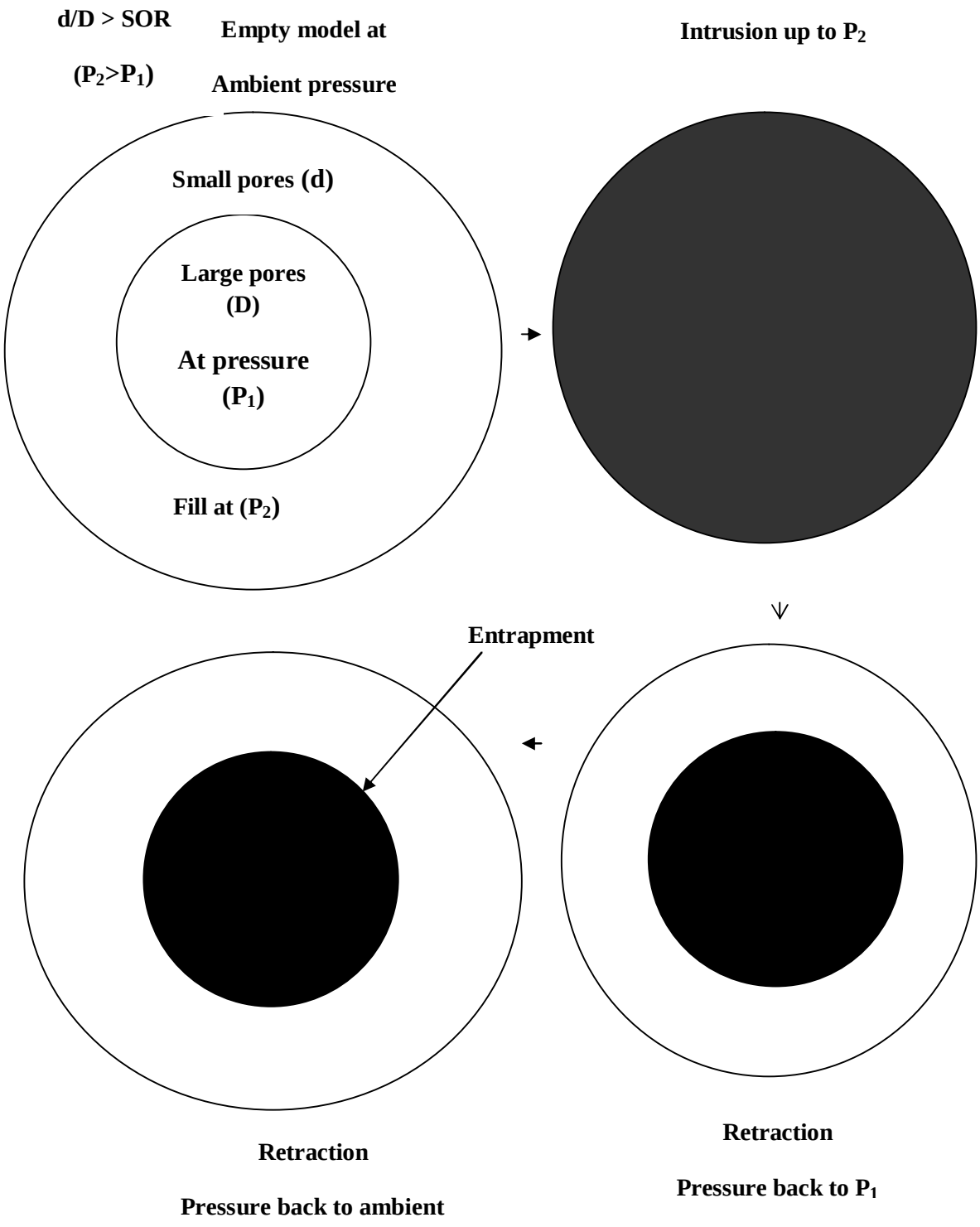

Figure 3.13

Schematic diagram illustrating the mechanism of mercury entrapment observed by Wardlaw and McKeller (1981) in a glass macromodels

In addition, the earliest studies of a network simulation model by Androutsopoulos and Mann (1979), and a glass micromodel by Wardlaw and McKellar (1981), proposed that the retraction of mercury may involve a slow relaxation process. The slow retraction process was attributed to the formation of isolated packages of entrapped mercury that, under the action of a non-zero net force prior to equilibration, tend to move around slowly and occasionally coalesce with the bulk. Once a meniscus is formed, Wardlaw and McKeller (1981) suggested that the time, for the meniscus to advance or retract down a cylindrical pore length (l) and radius (r_P), is given by:

$$t = \frac{4l^2\eta}{\Delta \mathrm{Pr}_P^2}, \tag{3.35}$$

where η is viscosity and ΔP is the pressure difference between the applied pressure and the equilibrium pressure required to maintain the mercury in the pore. These researchers stated that the volume of mercury leaving the pore space should be proportional to the square root of experimental time scale.

The micromodel experiments conducted by Wardlaw and McKellar (1981), and network model of Androutsopoulos and Mann (1979), still offer good explanations of the entrapment of mercury after retraction. However, both share similar limitations, where they failed to verify their findings by conducting mercury porosimetry experiments on real porous media. In addition, Wardlaw and McKellar (1981) failed to state the value of snap-off ratio that caused the entrapment between large pores surrounded by smaller pores. In a subsequent study, Wardlaw and McKellar (1982) reported multiple displacement experiments in the same pore-throat pair showing the amount of trapped oil to be a function of pore-throat geometry and wettability with little effect from viscosity or interfacial tension. In extending this discovery to a network of multiple pores and throats, Wardlaw and McKellar (1982) showed that for pore systems with relatively large size differences between larger pores and smaller adjoining throats, instability and snap-off occurs in the region of the junction of the pore with the exit throat, and is insensitive to the length of the throat which lies beyond. Snap-off usually occurs as a result of capillary instability, thus, it is one of several ways entrapment can occur. However, in the most common cases of strongly water-wetting rocks with high aspect ratios, snap-off may be the

most important mechanism of entrapment. Furthermore, Wardlaw and McKellar (1982) found that the narrow fluid interface in the region of the pore-neck junction would 'neck-down' further prior to snap-off.

Snap-off of unstable non-wetting phase in pores was extensively studied in relation to entrapment of non-wetting phase during imbibition process by Tsakiroglou and Payatakes (1990). In these researchers report mercury intrusion was defined as a drainage process in which mercury (non-wetting fluid) displaces air of very low pressure (wetting fluid) in proportion to the capillary resistance encountered at pore entrances; this is continued until the pore network becomes almost completely filled with mercury at the highest pressure value. At the end of intrusion, and as the mercury saturation tends to unity, there exist tiny pockets of compressed air sheltered in regions of pore wall roughness features that act as nuclei for mercury disconnection during retraction. Whereas, these researchers defined mercury retraction as an imbibition process in which low-pressure air (wetting fluid) displaces mercury (non-wetting fluid). As the external pressure reduces, the mercury menisci that occupy pore wall roughness features begin to retract. The retraction process leads to the formation of collars around various mercury threads occupying long and narrow pores (throats). When a thread surface becomes unstable, the mercury thread collapses. This mechanism is referred to as snap-off (Tsakiroglou and Payatakes, 1990). The retracting interfaces usually adopt saddle or collar shapes as illustrated in Figure 3.14.

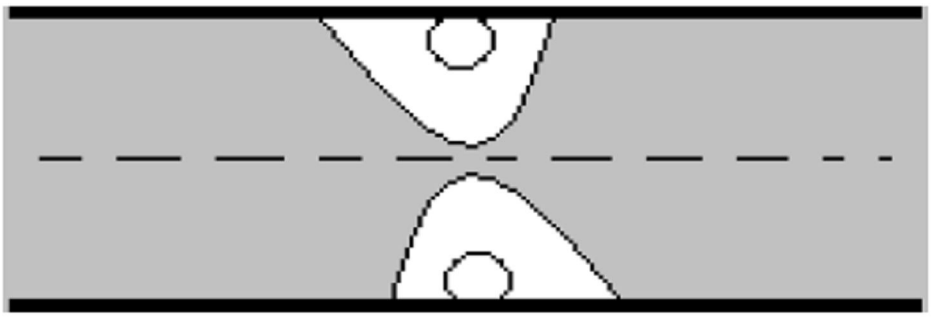

Figure 3.14

Illustration of thread snap-off occurring at a pore throat. The mercury phase is depicted in gray, while gas bubbles are shown in white (Felipe *et al.*, 2006).

In general, Tsakiroglou and Payatakes (1990) presented a detailed theoretical analysis of mercury porosimetry within a network model of spheres and capillaries that accounts for snap-off in cavity throats. It was found that the form of the retraction pressure curve is the results of two competing processes, namely, snap-off in throats and emptying of chambers. As snap-off intensifies with increasing ratio of the diameter of cavity to diameter of throat, the quantity of trapped mercury also increases, which is in accordance with the work of Wardlaw and McKeller (1981). However, the approach by Tsakiroglou and Payatakes (1990) lacked the ability to describe the network accessibility characteristics or state the snap-off ratio for mercury entrapment. In a subsequent report, Tsakiroglou and Payatakes (1997) investigated both experimental and theoretical aspects of the critical pressures for mercury intrusion and snap-off of mercury threads in long capillaries of uniform lenticular cross section, etched in glass. These researchers derived a mathematical expression for the pressure of mercury penetration in the lenticular pores in relation to pore width to pore depth aspect ratio. It was found that the critical pressures for intrusion and snap-off decrease as the pore aspect ratio increases. These findings are better than the glass micromodels presentations by the previous the work Wardlaw and McKeller (1981). To predict mercury entrapment, Tsakiroglou and Payatakes (1997) took into consideration of more realistic pores shapes for glass micromodels, such as the lenticular capillaries. Moreover, Tsakiroglou and Payatakes (1998) did further simulation work on lenticular throats. These researchers compared their simulation work with experimental intrusion and extrusion curves. It was found that cavities will empty not just only according to their pore size and the size of the connecting throats, but the specific geometric arrangement of the throats still filled with mercury is also important. Other models such as the conical and ellipsoidal pores have been considered (Cebeci, 1980; Jenkins and Rao, 1984). Nevertheless, no simple model of single pores can yield a realistic image of the relationship between the volume and the dimensions of pores when the porous structure is composed of network of cavities interconnected by narrow throats, which is the most frequent case (Smith and Stamer, 1987; Allen, 1999).

Tsetsekou *et al.* (1991) expanded the concept of mercury porosimetry hysteresis and entrapment, through the development of a probabilistic model simulating the mercury penetration-retraction operations. It was found that the breakage and entrapment of mercury in corrugated pores occurs if the constriction ratio is smaller than some critical

value. These researchers defined the constriction ratio as the diameter of the narrow pore divided by the diameter of the adjacent wide pore. This finding offers better advantage than the micromodels as it provided the typical pore throat diameters where snap off occurs. In a similar approach, Matthews *et al.* (1995) presented work aiming to expound on the snap-off phenomena by computer simulation. These researchers simulated a pore system with a 10 × 10 × 10 array of cubes (pores) joined by throats in a 3-D network. The software program (Pore-Cor) used snap-off and connectivity (pore blocking) factors to optimize the fit between the simulated and experimental data. It was found that mercury entrapment only arises once the ratio of the sizes of neighbouring pore bodies and necks exceeds a particular value. These researchers suggested that the ratio of the sizes of neighbouring large and small pore elements required to cause snap-off is > ~ 6. However, even though the model is limited to only 10 × 10 × 10 matrix, it still produced more general results than the previous works simulation such as the work Tsakiroglou and Payatakes (1990) where the model lacked the ability to describe the network accessibility of the system.

Furthermore, a three-dimensional pore bond network modelling approach was adopted by Portsmouth and Gladden (1991) to investigate the effects of pore size distribution and pore connectivity from the results of mercury porosimetry experiments. The inherent flexibility of this model facilitated the construction of networks with varying connectivities or distributions of connectivities. The results from simulations of standard intrusion/extrusion cycle porosimetry experiments suggested that there was a characteristic entrapment of mercury for a network comprising a Gaussian pore size distribution. It was also found that the mercury entrapment is dependent on the variance, $\frac{\sigma}{\mu}$, of the PSD, where σ is the standard deviation of the PSD and μ is the mean of PSD. This finding is in good agreement with the simulation work of Androutsopoulos and Mann (1979). Similar observations were also made by Conner and Lane (1984), Lapidus *et al.* (1985), Carniglia (1986), and Tsakiroglou and Payatakes (1990). In a subsequent, Portsmouth and Gladden (1992) investigated the effects of PSD and pore connectivity on the features of mercury porosimetry experiments. It was found that mercury entrapment increased with the variance of the PSD and decreased pore connectivity. In a similar approach, Ioannidis and Chatzis (1993) expanded the concept of mixed-percolation on cubic lattices, representing

pore bodies connected through pore throats, in a simulation to describe the phenomena of capillary pressure hysteresis and mercury entrapment. These researchers, model represented the pore structure of actual porous media in a 3-D regular cubic network consisting of pore bodies interconnected with pore throats. The pore bodies were modelled as cubes and pore throats as prisms. The key findings were that the pore size distribution, pore throat cross sectional shape, and contact angle were found to be very significant in determining the retraction and the magnitude of mercury entrapment; and consequently, the magnitude of mercury retention. However, these researchers assumption of pore bodies and throats as cubes and prisms is not generally compatible with all porous media even though it could be accepted for slit shaped pores such as sandstones and dolomites.

Most of the earlier mercury simulation work carried out previously used network models for void space structure and percolation processes to model the pore scale mercury displacement. Researchers such as Portsmouth and Gladden (1991; 1992) assumed a specific mercury entrapment mechanism without any experimental proof. Furthermore, these network models incorporated many adjustable parameters to permit the assumed mercury entrapment mechanism to give rise to correct comparisons of the model results and experiment. In recent years, Porcheron and Monson (2004) modelled mercury porosimetry experiments with an approach based on statistical thermodynamics and molecular simulations. In this approach, a Lattice Hamilton governed the system and the non-wetting nature of mercury was treated as a repulsive interaction between the fluid and the solid. The shapes of simulated curve were in good agreement with experimental results conducted. Also, the researchers found a correlation between mercury entrapment to the experimental time-scale.

In a subsequent report, Porcheron *et al.* (2005) extended their earlier approach to the treatment of dynamics to investigate the nature of mercury entrapment. These researchers performed dynamic Monte Carlo simulations using both Glauber dynamics and Kawasaki dynamics for a lattice gas model to study the behaviour of a non-wetting fluid within a porous material. Slit and ink-bottle pore geometries were tested in addition to the porous Vycor glass used in their previous work. The intrusion and extrusion data suggested that mercury entrapment is caused by a decrease in the rate of mass transfer attributed to the fragmentation of liquid during extrusion. Therefore, entrapment is believed to be

potentially associated with kinetic effects during mercury extrusion, coupled with the tortuosity of the disordered pore network and the surface chemistry of the material, as also seen by Moscou and Lub (1981). In addition, the primary mechanism of entrapment is believed to be snap-off of the liquid meniscus when extruding from narrow pore necks, leading to an isolated droplet of the liquid in the bottle pore. Porcheron *et al.* (2005) observations were in good agreement with the experimental work of Wardlaw and McKeller (1981) on glass micromodels. Lowell *et al.* (2004) had previously reported similar observations to those of Porcheron *et al.* (2005). Lowell and co-workers reported that often at the completion of the intrusion and extrusion cycle, mercury would slowly continue to extrude for hours. Recent simulation work on mercury porosimetry includes the use of lattice-Boltzmann (Hyvaluoma *et al.*, 2007), and statistical mechanics (Porcheron *et al.*, 2007) methods to simulate porosimetry on structural models obtained directly from full 3D X-ray tomographic reconstructions of void spaces (Hyvaluoma *et al.*, 2007), or statistical reconstructions based on scattering data (Porcheron *et al.*, 2007). The main drawback with these simulation techniques is that only a potentially unrepresentative microscopic fraction of the void space of a potentially macroscopically heterogeneous mesoporous solid can be represented on computer. However, the lattice- Boltzmann simulations conducted in the X-ray tomographic reconstructions validated the invasion percolation model for mercury intrusion into disordered materials (Hyvaluoma *et al*. 2007).

It is still unclear if the results from mercury simulations and micromodels can explain the cause of hysteresis and mercury entrapment in amorphous porous media. The pore structures of amorphous materials, such as oil reservoir rocks and heterogeneous catalyst support pellets, are considerably more complex than the micromodels investigated by researchers Wardlaw and McKellar (1981) and mercury simulations by Portsmouth and Gladden (199; 1992). Rigby and Edler (2002) provided the missing link by investigating heterogeneous catalyst support pellets. It was found that mercury entrapment is predominantly a macroscopic phenomenon, rather than being solely the microscopic process that was often assumed in many computer simulations. Rigby and Edler (2002) expanded on previous work by incorporation of other characterisation methods for porous media such as gas sorption. It was found that the entrapment was generally attributed to the presence of extended isolated macroscopic domains (>10 μm in size), within which the pore sizes are relatively similar, being shielded by other surrounding heterogeneity

domains with more disparate, and smaller, pore sizes. Subsequently, Rigby *et al.* (2006) investigated the mechanisms of entrapment, and the nanoscopic spatial distribution, of the residual mercury within nano-cast and amorphous porous media (pore sizes ~1-100 *nm*), following high-pressure penetration. These researchers came to the conclusion that entrapment occurs, either because of the presence of sufficiently narrow pore necks interspersed between larger voids, or due to non-random, longer-range structural heterogeneity. These findings agreed with the results of mercury porosimetry experiments conducted on glass micromodels by Wardlaw and McKellar (1981).

In recent years, Giesche (2006) carried out an investigation into the effects of intrusion rates on pore size and volume. This researcher analyzed five samples of an alumina extrudate using the scanning mode (equilibration time for 0 s), and equilibration – interval settings of 2, 10, and 30 seconds. The cumulative intrusion volume and the log-differential curves of the five experiments both showed an increasing trend in the value of pore volume and diameter in the order of increasing equilibration time. A difference of close to 10 % in pore volume and 40 to 50 % in pore size was reported between the fastest and the slowest analysis condition. Their observations of the intrusion/extrusion volume as a function of time by varying the equilibration time showed that reaching equilibrium during intrusion was achieved much faster than during extrusion for the same sample. These findings suggested that other factors besides the flow of mercury through the pore-network or temperature effects are responsible for the delay in reaching equilibrium.

In a similar approach, Rigby *et al.* (2008) studied the effects of extreme geometric confinement on mercury behaviour in order to understand the mercury retraction process from amorphous and mesoporous silica materials. These researchers used a variety of complementary experimental techniques, such as the mercury porosimetry, gas sorption, Magnetic resonance Imaging (MRI), computerised X-ray tomography (CXT), and electron microscopy, to characterise, in great detail, the pore network structures of the test materials. In order to elucidate the complex physical processes and mechanisms involved in mercury retraction itself, the quantities and spatial arrangements of mercury isolated packages within the chosen materials were examined over different time-scales, ranging from seconds to days, and over different length-scales, ranging from the pore-scale to the macroscopic scale of the whole pellet sample. In one material, the initiation of retraction

was found to be independent of the experimental time-scale because it was governed by the rapid equilibration of the narrowing of mercury necks, and subsequent snap-off of mercury connections at a small number of pore intersections. In the other material, it was shown that a combination of integrated gas sorption experiments and Monte-Carlo modelling of the relaxation process for entrapped mercury can be used to distinguish different models for mercury entrapment within nanopores.

3.3.4 Limitations of mercury porosimetry technique

The pore-size distribution is a key descriptor of the void space of mesoporous materials, such as heterogeneous catalyst pellets, is used in explaining their properties. In general, the measured pore-size distribution curves are frequently inclined towards small pore sizes as illustrated in Figure 3.14 (Allen, 1999). For the same reasons stated above, mercury porosimetry can not be used to analyse closed pores. Thus, the technique can only provide a valid estimate of pore structure, when the sample has pores directly accessible to mercury or that are easily reached by mercury through larger pores (Moro and Bohni, 2002). In addition, the Washburn equation (Equation 3.31) assumes contact angle value of mercury and the cylindrical pore shape. However, various observations made by electron microscopy have shown that many traditional porous materials such as the silicas and aluminas appear to be random collections of packed spherical and hemispherical particles, as well as cylinder (Drewry and Seaton, 1995).

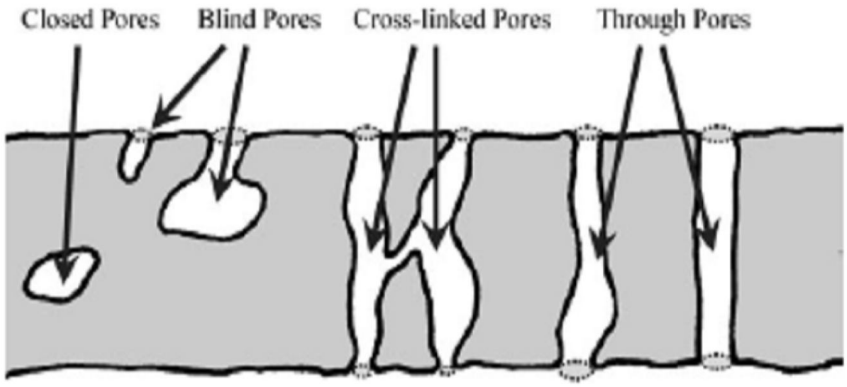

Figure 3.15

Schematic representation of pores (Giesche, 2006)

In addition, similar observations were made in cement-based materials where the pore size is randomly distributed and most pores are connected to the surface of the sample through a chain of pores with varying sizes and shapes. Therefore, with such a pore structure, mercury can not intrude into larger pores until the applied pressure is sufficient to force mercury to go through smaller throats. As a result, the standard mercury porosimetry results in an underestimate of large pores because of its intrinsic limitation due to ink-bottle type pores. These are pores that are connected to the surface by smaller neck entrances only, and thus, larger pores that are only accessible by smaller neck entrances will be underestimated in size and lead to hysteresis effects. The volume of these larger pores (ink-bottle pores) that is counted as the volume of smaller throats (pores) is referred to as the accessibility effect (Diamond, 2000). Therefore, the Washburn Equation (3.31) constitutes a special model that fails to take into account that real the real nature of pores media consist of a network of interconnected circular pores. Such a model may not represent the pores in actual materials but it's generally accepted as the practical means of dealing with complex pore structures.

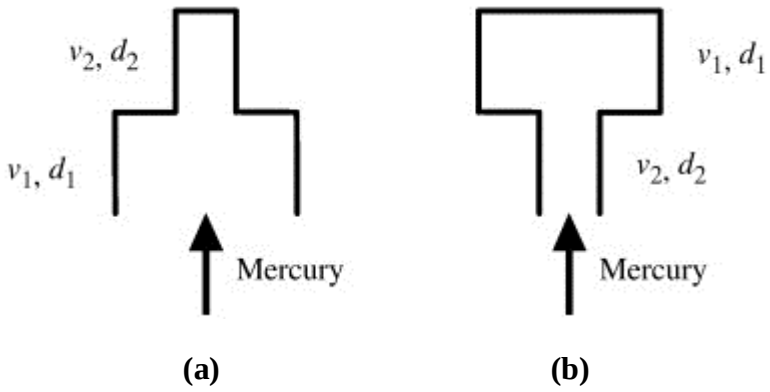

Figure 3.16

Schematic illustration of two imaginary pore systems with a large pore and a small pore (Zhou *et al*., 2010)

The accessibility effect is illustrated in Figure 3.16 with two imaginary pore systems each with a large pore (with a diameter of d_1 and a volume of v_1) and a small pore (with a diameter of d_2 and a volume of v_2). In the left pore system shown in Figure 3.16, the large pore is directly connected to mercury, and thus, during mercury porosimetry measurement, the large pore is filled with mercury when the applied pressure is increased

to P_1 and the small pore is filled with mercury when the applied pressure is increased to P_2. Therefore, for pore system in Figure 3.16 (a), the mercury porosimetry technique can reveal the real pore size distribution. In contrast, in Figure 3.16 (b), the large pore is connected to mercury through the small pore. An applied pressure of P_1 is not big enough to force mercury to intrude into the large pore, and thus, it is only when the applied pressure is increased to P_2 that mercury intrudes into both the large and small pores. Therefore in this case, the mercury porosimetry result shows that the volume of the large pore is zero, and the volume of the small pore becomes the sum equals to v_1 and v_2. As a result, the mercury porosimetry technique underestimates the volume of the large pore and overestimates the volume of the small pore.

Several researchers have spent effort on improving mercury porosimetry to eliminate the impact of the accessibility effect. One early unsuccessful attempt was made to correct for those pores that could fill at a given pressure but failed, because they were connected to the mercury source only by smaller pores (Meyer, 1953). This researcher tried to determine the actual distribution of the pore sizes in a porous rock from the cumulative distribution of mercury injected into the rock with increasing pressure against capillary forces but in the process altered the distribution of the large pores. In a different approach, Liu and Winslow (1995) worked with cement-based materials where mercury was intruded progressively up to the maximum pressure, then reduced the pressure progressively to the minimum pressure, and re-intruded to the maximum pressure. The minimum intruding pressure was 0.5 psia, and the maximum was 60,000 psia for the initial intrusion step, however, due to instrumental limitations, the extrusion and the re-intrusion steps had applied pressures of the range of 29 to 60,000 psia. It was found that the processes of mercury extrusion and re-intrusion were fully reversible when appropriate advancing and receding contact angles were used. In addition, these researchers suggested that the pore system of cement paste can be divided into two parts (reversibly and irreversibly intruded pores). It was concluded that the reversibly intruded pores were more accessible to mercury and more closely correlated with the transport properties of cement-based materials.

In recent years, Kaufmann (2010) studied pores of cement-based materials that were selectively filled with Wood's metal. Liquid Wood's metal is a non-wetting fluid that has contact angle and surface tension values similar to that of mercury (Abell *et al*. 1999). In

addition, wood's metal has low melting point, and thus can intrude at elevated temperatures and solidify in place by cooling at room temperature (Darot and Reuschle, 2003). Kaufmann (2010) used the Washburn Equation (3.31) to describe the relation between the applied pressure and the radius of the pores filled with Wood's metal. The liquid metal (at elevated temperature), was intruded into the samples by applying different pressure regimes and then re-solidified in place. Subsequent scanning electron microscopy, even at the highest pressure, showed no crack formation was caused by this impregnation. The partial impregnation with this metal allowed the analysis of non-ink-bottle type pore space in a subsequent nitrogen sorption experiment and its comparison with an empty pore system. It was found that the relative pore size distribution was similar to that of an empty pore system, and thus, not influenced by the metal impregnation of ink-bottle type or large pores. Previously, Kaufmann and Leemann (2009) showed that the size of the ink-bottle pores can be excluded from analysis in such multi-cycle mercury porosimetry analysis; thus, the sizes of their neck entrances can be estimated. In addition, Kaufmann and Leemann (2009) found that the pore size distribution obtained by nitrogen sorption agreed well with that obtained by second mercury intrusion (i.e. when mercury intrusion–extrusion cycle was repeated twice). Therefore, the accessibility effect was considered to be reduced in the second mercury intrusion, since the ink-bottle pores were already filled in the first intrusion–extrusion cycle. Although the work Meyer (1953). Liu and Winslow (1995), Kaufmann and Leemann (2009), and subsequent report by Kaufmann (2010) made a big progress in the characterization of pore structure in porous materials, especially in cement-based materials by using Mercury porosimetry, these researchers could not provide a valid estimate of pore size distribution.

Subsequent work by Zhou *et al*. (2010) developed a new mercury porosimetry method that can overcome the accessibility effect and provide a more accurate estimate of the pore size distribution in porous materials especially in cement-based materials. The new technique as conducted following a unique mercury intrusion procedure in which the applied pressure was increased from the minimum to the maximum by repeating pressurization–depressurization cycles instead of a continuous pressurization followed by a continuous depressurization. In every pressurization–depressurization cycle, the intrusion and extrusion pressure values were calculated using the Washburn Equation (3.31) with the different advancing and receding contact angles calculated with the pressures at which

mercury intrudes into and extrudes out of an artificial straight cylindrical pore with known diameter. Therefore, by repeating the pressurization–depressurization cycles, the volumes of throat pores and ink-bottle pores can be measured at each throat pore diameter. These values were used to calculate the pore size distribution. The new method offered a better estimation of pore size distribution that compared well to the standard mercury porosimetry result. In addition, the pore size distribution measured by this technique had a better agreement with that obtained from nitrogen sorption, scanning electron image analysis, and the numerical simulations.

The work of Kaufmann (2010) and Zhou *et al.* (2010) provided a way of addressing the accessibility effect and a measure of pore size distribution in cement based materials that was proven tricky with other porous materials such as catalyst support pellets. Mercury porosimetry is often affected by pore shielding effects. Pirard *et al.* (1997) studied role of pore shielding in mercury porosimetry analysis. It was found that in experiments up to relatively low pressures of mercury, the mercury intrusion and retraction curves seemed to show that substantial mercury entrapment was occurring within the material. However, a close inspection of the sample following porosimetry, using light microscopy, revealed that, in fact, no mercury had become entrapped at all and the overall sample size had decreased. As higher mercury pressure was used, it was shown that mercury was then actually intruded into the structure because the subsequent microscopy studies revealed many mercury droplets entrapped within the pore structure. These findings were explained by the proposal that the initial rise in mercury pressure caused the collapse of the larger pores in the material which was then followed by the actual intrusion of smaller pores. Therefore, the apparent mercury entrapment in porosimetry data may actually indicate that pore collapse is occurring instead of entrapment. As a result, the multiple pressurization–depressurization cycles in Zhou *et al.* (2010) method can alter the physical structures of other porous materials such as the catalyst support pellets.

In a different approach, Rigby and co-workers (2004; 2005) interfaced gas adsorption and mercury porosimetry to measure pore size distribution in catalyst supports pellets. The two independent techniques, namely nitrogen sorption and mercury porosimetry, were utilised completely separately, and then integrated into the same experiment to improve upon the information obtained from both methods, and thus, improve the knowledge of the internal

geometry and topology of the internal pore network of mesoporous materials. The initial nitrogen sorption experiment was carried out at 77 K, and then the sample was allowed to reach room temperature (298.9 K) before transferring to the mercury porosimeter. Following mercury porosimetry, the sample was transferred back to the nitrogen sorption apparatus. The sample was then cooled to 77 K to freeze the mercury in place and the final nitrogen sorption experiment was commenced. The linear expansion coefficient for solid metals is typically ~ 10^{-5} K^{-1}, and thus, the variation in the volume occupied by solid mercury between 234 and 77 K was expected to be miniscule. However, these kinds of approach carry a serious risk of contamination of the nitrogen porosimeter with mercury. Another drawback associated with this approach is the inability of the workers to tell if the mercury entrapped following mercury porosimetry has shifted to other parts of the sample. Nevertheless, it provides structural characterisations that are more statistically representative of a sample as a whole.

3.3.5 Scope of study by mercury porosimetry technique

In addition, to the issues raised in Section 3.3.4, another important parameter in obtaining the pressure-volume relationship for a sample is the equilibration time-scale. In general, much less use is made of the mercury retraction curve, which is generally associated with hysteresis and entrapment. In porosimetry simulation work, the retraction curve has been used to obtain information about pore connectivity (Portsmouth and Gladden, 1991), test models for the pore-scale mechanisms of meniscus retraction and snap-off (Tsakiroglou *et al*., 1997; Tsakiroglou and Payatakes, 1998), validate pore-bond network structural models obtained using the intrusion curve (Mata *et al*., 2001). At present, however, there has been few experimental works done to explain the cause of hysteresis and entrapment in the mercury retraction curve. In recent years, Rigby *et al.* (2006; 2008) examined the complex physical processes and mechanisms involved in mercury retraction by examining silica catalyst support pellets over different time-scales (see more details in Section 3.3.3). It was found that mercury entrapment in catalyst support pellets is a function of experimental time-scale. In addition, experimental data derived from mercury porosimetry showed enough evidence that entrapment can occur in long straight pores due to multiple snap-off in a porous material (Giesche, 2010). Therefore, mercury entrapment might be a function of the pore length parameter (α) of pores in a porous media.

It is the purpose of this study to generalize and expand the work of Rigby *et al.* (2006; 2008) on a range of alumina and silica materials. Emphasis will be made on the retraction curve, which is a potential source of useful information concerning mercury entrapment. A comparison will be made between the experimental results derived from mercury intrusion and retraction data and the lattice gas model penetration result of a non-wetting liquid into disordered porous media by Porcheron and Monson (2004). In addition, a comparison of the shapes of mercury retraction curves simulated using statistical mechanics with experimental data suggests that the simulations do not accurately re-create the shape of the initial knee in the high pressure region of the experimental retraction curves (Porcheron *et al*., 2007). This research intends to study the transport regime (mass transfer to and from the external surface) in detail, and, in particular the region of the onset of mercury retraction not accurately described by statistical mechanical models. Furthermore, this study will check the applicability of the semi-empirical alternatives by Rigby and Edler (2002) to the standard Washburn equation (Equation 3.31) for the interpretation of raw mercury porosimetry of the test materials.

In this study, the test materials will be examined over longer equilibration time-scales to study how mercury is redistributed (quasi-equilibrium regime) after retraction process. Therefore, by experimental observations of mercury porosimetry at varying relaxation times, the link between hysteresis, the equilibration time, and the varying amount of mercury entrapped can be explored, and thus improve the reliability of pore structure analysis. The data will be used to infer the initial spatial arrangement of entrapped mercury for heterogeneous, nanoporous materials, and thereby improve the understanding of the mechanism of mercury entrapment. Finally, the ultimate objective of this study is to provide experimental verifications to the simulation results reported in Section 1.6. Therefore, in Chapter 8, the estimated mercury entrapment will be correlated with other aspects of the materials such as the width of the PSD, pore connectivity, and tortuosity. In addition, the estimated mercury entrapment of these materials will be correlated with the pore length parameter (α) to experimentally verify Giesche's (2010) work on multiple snap-off in long straight cylindrical pores. As detailed in Section 3.1, the width of the pore size distribution, pore connectivity, and pore length parameter (α) will be estimated with gas sorption technique. Also detailed in Section 3.4, the tortuosity will be measured with the PGSE NMR technique.

3.4 Applications of PGSE NMR technique to porous media

3.4.1 Principles of PGSE NMR technique

Nuclear magnetic resonance (NMR) spectroscopy is one of the principal techniques of obtaining physical, chemical, electronic and structural information about molecules on the resonant frequencies of the nuclei present in the sample. NMR is observed if nuclei having magnetic properties are excited within a magnetic field, where a resonance signal is emitted as the nuclei relax. The observed resonance signal is dependent on the environment in which the nucleus is situated and can, therefore, be used to probe that environment. The pulsed field gradient sequence (PGSE) NMR diffusion studies can be used to determine the diffusion coefficient of a nucleus within a molecule based on the loss of signal detected due to the motion of the molecule over a given diffusion time. The relaxation behaviour of a nucleus in a solid is different to that of the liquid. Therefore, a change of state can be observed by either an increase or decrease in the observed signal intensity (Ullmann's Encyclopedia, 2008).

In NMR experiments, transitions are induced between different energy levels by irradiating the nuclei with a superimposed field (B_1) of the correct quantum energy that has an electromagnetic wave of appropriate frequency (v_f) to match the Larmor frequency (v_l). As a result, the nuclear spins (α' and β') can be forced to skip between different energy levels as illustrated in Figure 3.17. The Larmor frequency (v_l) is proportional to the magnetic flux density (B_0), such that (Friebolin, 1998):

$$v_l = \left|\frac{\gamma}{2\pi}\right| B_0 \tag{3.36}$$

where γ is called gyromagnetic ratio. The detection sensitivity of a nuclide depends on gyromagnetic ratio (γ). Thus, the condition enables the electromagnetic component of the radiation to interact with nuclear dipoles. The fundamental resonance conditions are (Friebolin, 1998) as:

$$\Delta E = h v_f \tag{3.37}$$

where h is the plank constant and (v_f) is the resonance frequency. The irradiation is such that $\Delta E = hv_f$, induces absorption (a) and emission (e) transition.

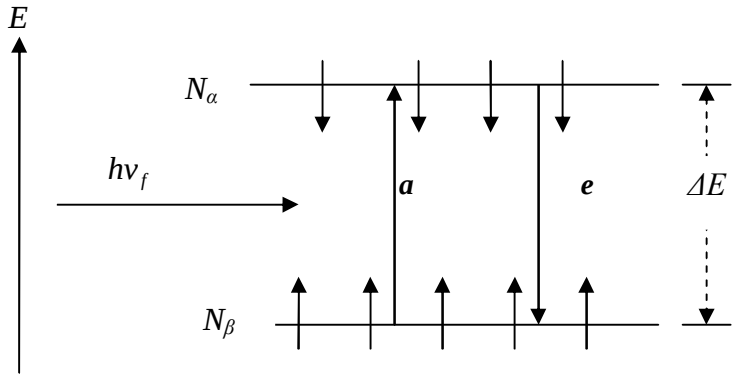

Figure 3.17

Energy level schemes for a system of nuclei with spin *I* = ½ (Friebolin, 1998)

Transition from lower to upper energy level corresponds to absorption of energy, and the ones in reverse direction to an emission of energy. Both transitions are equal and probable. The transitions are associated with spin orientation. Resonance absorption can only be detected if the spin levels involved differ in population (Friebolin, 1998). However, due to population excess in the lower level, the absorption of energy from irradiating field is the most dominant process. This is observed as a signal, whose intensity is proportional to the population difference $(N_\alpha - N_\beta)$ and the total number of spins in the system, and hence to the concentration (Friebolin, 1998). No signal is observed when the population is equal $(N_\alpha = N_\beta)$ as the absorption and emission processes cancel each other. This condition is known as saturation. When the resonance frequency matches the characteristic frequency of the nuclei, an electric signal is induced in the detector. The strength of the signal is plotted as a function of this resonance frequency in a diagram. The diagram is called the NMR spectrum (Ullmann's Encyclopedia, 2008).

Transitions in an analytical sample that can produce a signal in the receiver channel of the spectrometer can only occur when the resonance condition is satisfied (Friebolin, 1998). There are two ways to achieve this condition. They are field sweep method and frequency

sweep method (Keeler, 2005). These two methods are generally referred to as the continuous wave (CW) method because they use uninterrupted radiofrequency power. In the field sweep method, magnetic flux density (B_1) is varied and the transmitter frequency (ν_f) is kept constant. Whilst in the frequency sweep method, the transmitter frequency (ν_f) is varied and magnetic flux density (B_0) is kept constant. In either case the recorder drive is linked directly to the field or frequency sweep, so that the recorder pen progressively traces out the spectrum. The *CW* method was the basis of all NMR spectrometers before the invention of modern computers and has subsequently been superseded by new methods (Friebolin, 1998).

In the pulse NMR method, all the nuclei of one species are all excited simultaneously by a radiofrequency pulse. A radiofrequency generator usually operates at a fixed frequency (ν_f) as illustrated in Figure 3.18. However, if it is switched on for a short time (τ_p), the pulse contains not just the frequency (ν_f) but also a continuous band of frequencies symmetrical about a centre frequency (ν_f). Furthermore, only a part of the frequency band is effective in exciting transitions, and is approximately proportional to the inverse of the duration (τ_p^{-1}). The pulse duration (τ_p) is of order of a few seconds (μs). The choice of a generator frequency (ν_1) depends on the strength of the magnetic flux density (B_0) and the nuclide to be observed (Friebolin, 1998).

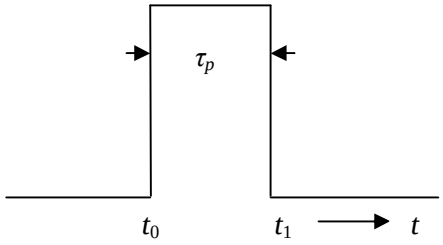

Figure 3.18

Radiofrequency generator (frequency, ν_f) switched on at time t_0 and off at t_1 (Friebolin, 1998)

In general, the NMR spectra usually suffer from a persistent artefact usually known as noise. It is a ridge that runs parallel to the frequency axis wherever there is a strong resonance peak in the spectrum (Freeman, 1988). It is usually in two parts; a random fluctuation of the baseline that is significantly larger than the true thermal noise and a direct current offset of the baseline that accounts for the tails of the strong resonance peak (Freeman, 1988). A common and often serious source of instability arises in the field/frequency regulation scheme which results from inadequate signal-to-noise ratio for the deuterium reference signal (Freeman, 1988). Another source of noise comes from poor reproducible phase or amplitude of the transmitter pulse. The solution to this problem is to employ a sufficient strong deuterium reference material and to restrict the bandwidth of the field/frequency regulation loop (Freeman, 1988).

The intensity of individual free induction decay (FID) is often weak such that even after Fourier transformation, the signals are smaller compared to the noise. Therefore, the FIDs of many pulses are added together (accumulated in the computer and only then transformed). In this accumulation, the random electronic noise becomes partly averaged out, while the contribution from the signal is always positive and builds up by addition. The signal to noise ratio, $S : N$, increases in proportion to the square root of the number of scans, such that (Friebolin, 1998):

$$S : N \sim \sqrt{NS} \tag{3.38}$$

The accumulation of many FID's needs very precise field-frequency stability and requires each data from FID to be stored in the exact corresponding memory addresses in the computer. Hence variation, such as temperature, can cause a line broadening and consequent loss of sensitivity (Friebolin, 1998). The device that ensures the necessary field frequency stability is called lock unit. This lock unit uses a separate radiofrequency channel to measure a nuclear resonance other than that of the actual NMR experiment. The lock unit can be used to optimize the magnetic field homogeneity, either manually or automatically. This is achieved by a shim unit and the procedure is called shimming (Friebolin, 1998).

3.4.2 Estimation of effective diffusivity by using PGSE NMR technique

In PGSE NMR, the echo attenuation $\left(R^{'}\right)$ is defined as the ratio of the echo intensity in the presence of the gradient $\left(I\right)$ to the echo intensity obtained in the absence of a gradient $\left(I_0\right)$. For unrestricted self-diffusion, where the random motion of the molecules is assumed to follow Gaussian behaviour, the echo intensity $\left(I\right)$ is given by (Stejskal and Tanner, 1965):

$$I = I_0 e^{-D\gamma^2 g^2 \delta^2 \left(\Delta - \frac{\delta}{3}\right)}, \tag{3.39}$$

where D is the diffusion coefficient, γ is called gyromagnetic ratio of the observed nucleus, g is the gradient strength, δ is length of the gradient pulse, and Δ is the diffusion time. A range of echo attenuations are obtained by varying g, δ or Δ. Equation 3.39 can be used to calculate diffusion coefficient of the observed nucleus in a homogeneous system. Therefore, in the case of isotropic bulk diffusion, a plot of $\ln\left[\frac{I}{I_0}\right]$ against the group $\xi = \left[\gamma^2 g^2 \delta^2 \left(\Delta - \frac{\delta}{3}\right)\right]$ yields the diffusion coefficient from the slope of the straight line obtained (Hollewand and Gladden, 1995a). The diffusion coefficient is obtained by labelling the position of the molecules at the start of the experiment through the use of a field gradient. After a certain period of time (diffusion time, Δ), during which the molecules will have moved to a different random position due to self-diffusion, the positions of the molecules are labelled again by a second gradient (Veith *et al.* 2004). The final signal observed will be a function of the diffusion coefficient D_0, the gradient strength g, δ, and the diffusion time Δ (Veith *et al.*, 2004). A typical pulse sequence is illustrated in Figure 3.19.

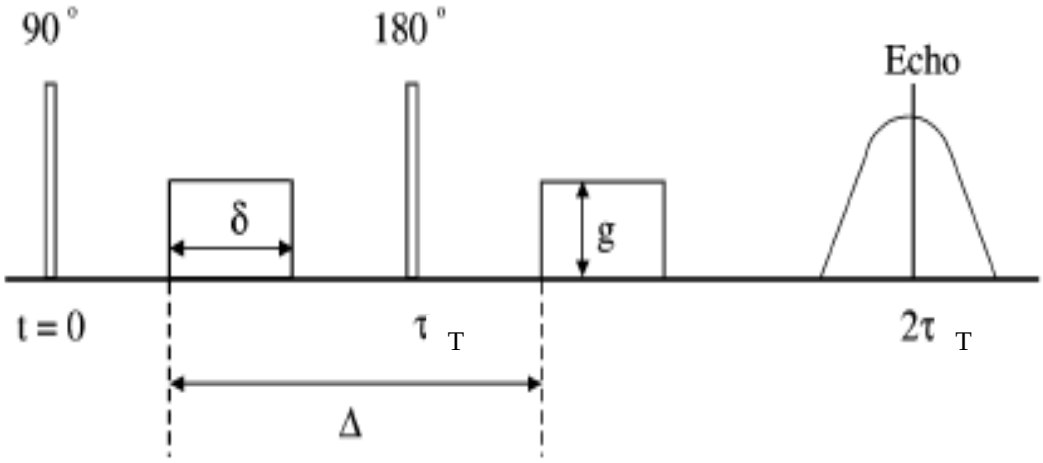

Figure 3.19

A schematic diagram of the pulse sequence that was first introduced by Stejskal and Tanner (1965)

In general, a linear log-attenuation plot suggests diffusion of a single component in a homogeneous environment and Equation 3.39 describes the relationship between signal attenuation and the diffusion coefficient. The effective diffusion coefficient calculated from a one component fit will be characteristic of the average motion of all molecules and, therefore, will be a combination of free diffusion and restricted diffusion. With a very small value of a short diffusion time (Δ) none of the molecules will be restricted as none of the molecules will have sufficient time to reach the walls of the pores. Therefore, the effective diffusion coefficient measured is that of molecule in free solution.

In contrast, if the diffusion time (Δ) is sufficiently large all the molecules contained within the pores will contact the pore walls and thus undergo restricted diffusion. As a result, non-linearity in the echo-attenuation plot will be observed if the molecules sample regions associated with largely varying diffusion coefficients. Therefore, the long-time behaviour of diffusion coefficient provides an indirect measure of the macroscopic structure (Veith *et al.*, 2004). A discrete multicomponent model was derived by Hollewand and Gladden (1995), Equation 3.40, where the heterogeneity in the apparent diffusion coefficient is attributed to i components, each containing the fraction, p_i, of observed nuclei, with the

actual diffusion coefficient, D_i, where ξ is characteristic of the experimental parameters $\left[\gamma^2 g^2 \delta^2 \left(\Delta - \frac{\delta}{3}\right)\right]$.

$$I = I_0 \Sigma p_i \exp\left(- D_i \xi\right) \tag{3.40}$$

In a PGSE NMR experiment, the diffusion time can be varied from a few milliseconds up to several seconds. Because of effects from the restricting geometry, the measured self-diffusion coefficient (D) depends on the diffusion time (Δ). The measured self-diffusion (D) is also sensitive to physical parameters like permeability and the volume fraction of the diffusing species. The measured self-diffusion (D) can be related to certain characteristics of the porous medium such as the surface-to-volume ratio and the tortuosity (τ). The measured self-diffusion (D) of a diffusing fluid is found to decrease with observation time (Δ) and reaches a plateau value. That plateau value represents the tortuosity (τ) of the system (Latour *et al.*, 1995).

The effective self-diffusion coefficient (D_{eff}) is a measure of how the water is diffusing within the porous network. Therefore, the tortuosity of a pore network (τ) is a measure of the potential deviation from a linear path that a diffusing molecule may experience. For the diffusion of a liquid in a porous solid, the effective diffusivity of the liquid in the material is related to the molecular self-diffusion coefficient (D_0) of the bulk liquid as follows (Hollewand and Gladden, 1995a):

$$D_{eff} = \frac{D_0 \varepsilon}{\tau}, \tag{3.41}$$

where ε voidage of the material. The voidage term is traditionally ignored since the observed signal contains spin density which is directly proportional to voidage. Therefore, Equation (3.50) can be written as:

$$D_{eff} = \frac{D_0}{\tau}, \tag{3.42}$$

where D_0 is the diffusion coefficient of the bulk liquid. Traditionally water is used as the bulk liquid. In general, tortuosity (τ) describes the geometry of flow paths, and thus, a measure of the complexity of a porous medium. It is as a conceptual, dimensionless number representing the departure of a porous system from being composed of straight pores. Since fluid travels along a tortuous path through the medium, the actual or effective pore length (l_{eff}) is greater than the average linear flow path length (l_p). The ratio of these two lengths defines tortuosity, such that (Scholes *et al.*, 2007):

$$\frac{\text{Effective flow path}}{\text{Average linear flow path}} = \frac{l_{eff}}{l_p} = \tau \tag{3.43}$$

In porous media, tortuosity depends on how well the pores are connected (Kleinberg *et al.*, 1995). In addition, the total tortuosity (τ) of a porous solid can be considered to have independent contributions from tortuosity on various length scales. The total tortuosity can considered as the product of these independent tortuosities since the effective diffusivity will decrease monotonically with scale (Rigby and Gladden, 1998). Therefore, the PGSE (NMR) experiment measures:

$$\tau = \tau_e \tau_\mu, \tag{3.44}$$

where τ_e is the mesoscopic contribution to the tortuosity over length scales of a few pore diameters up to scales at which macroscopic heterogeneities become significant, and τ_μ characterizes tortuosity over length scales of up to a few pore diameters (Rigby and Gladden, 1998). However, if the molecules diffuse between compact particles, the effective restricted interparticle diffusion coefficient is (Kleinberg *et al.*, 1995; and Veith *et al.*, 2004),

$$\frac{D_{eff}}{D_0} = \frac{D_{\text{int}er}}{D_0} = \frac{\varepsilon_b}{\tau}, \tag{3.45}$$

where ε_b is the particle bed porosity and τ the tortuosity that the molecules experience diffusion through the bed of particles. Whilst if the molecules diffuse inside the porous

particles, the intraparticle or pore diffusion coefficient, $D_{\text{int}ra}$, can be deduced as (Kleinberg *et al.*, 1995; Ek *et al.*, 1995; and Veith *et al.*, 2004):

$$\frac{D_{eff}}{D_0} = \frac{D_{\text{int}ra}}{D} = \frac{\varepsilon_b}{\tau} \tag{3.46}$$

The root mean square (r.m.s) displacement r of molecules undergoing Brownian motion can be derived from PGSE NMR data. The relationship for the molecular mean square displacement and the self-diffusion coefficient D and diffusion time Δ is given by the Einstein equation below (Seland *et al.*, 2001),

$$\langle r^2 \rangle = 6 D_{eff} \Delta \tag{3.47}$$

According to Equation 3.48, a plot of the measured diffusion coefficient (D_{eff}) against the square root of the diffusion time $(\Delta)^{0.5}$, gives an intercept value equivalent to the intra-particle diffusion coefficient (D_0) such that:

$$D_{eff} = D_0 - \frac{4 D_0^{\frac{3}{2}} S}{9\pi^{0.5} V} \Delta^{0.5}, \tag{3.48}$$

where S and V are the pore surface area and pore volume, respectively (Latour *et al.*, 1993). The time-dependent diffusion coefficient of fluid molecules in confining geometries was initially accepted to contain some information about restriction (Callaghan, 1991). However, the short time behaviour of the diffusion constant is independent of the restricting geometry and depends only on the surface-to-volume ratio $\left(\frac{S}{V}\right)$ of the pore space. At long diffusion time (Δ), diffusion molecules probe the connectivity of the pore space. Through the tortuosity, the diffusion coefficient is intimately connected to many important transport properties of fluids confined in porous media such as the permeability (Latour *et. al*, 1993). If a large fraction of the molecules are influenced by the restrictions during the diffusion time (Δ), or during the gradient pulse, the diffusion propagator might

not be Gaussian. Therefore, the attenuation plot will possibly be influenced by different degrees of restricted diffusion giving a non-linear attenuation, curving upward (Mitra and Halperin, 1995; Veith *et al.*, 2004).

Furthermore, for a spherical pore, the typical cavity radius $\left(r_{cavity}\right)$ in which the diffusion has been restricted can be calculated based on the diffusion time $\left(\Delta\right)$ and the length of the gradient pulse $\left(\delta\right)$ the nucleus is exposed to, as shown in Equation 3.49 (Callaghan *et al.*, 1983). However, for the relationship in Equation 3.49 to hold, diffusion time $\left(\Delta\right)$ must be sufficiently large for the diffusion of all molecules to be restricted.

$$r_{cavity} = \left[5D\left(\Delta - \frac{\delta}{3}\right)\right]^{0.5} \tag{3.49}$$

3.4.3 Diffusion in porous media

The work of Callaghan (1991) has greatly contributed to the development of diffusion models when the motion of the diffusing molecule is restricted (Callaghan *et al.*, 1979) or constrained within one or two dimensions (Callaghan *et al.*, 1983), and the influence of measurement of gradient field strength on diffusion within porous media (Callaghan *et al.*, 1991). Traditionally, the structure of a porous solid is characterised in terms of a pore-size distribution and the connectivity of the pore space. Any numerical model developed, based on these microscopic characteristics is then considered to be representative of the real material (Hollewand and Gladden, 1995a). It was also proven that the structure of the void space in a porous material constrains the fluid contained within it and as a result influences macroscopic transport properties, such as the effective diffusivity (Hollewand and Gladden, 1995a). These researchers used the pulsed field gradient (NMR) technique to estimate effective diffusivity of porous media. The study of diffusion by NMR began back in the early 1950s with the works of Hahn (1950) and Carr and Purcell (1954). Further developments included the use of spin echoes, (Stejskal and Tanner, 1965) and stimulated spin echo (Tanner, 1970) sequences for studying diffusion coefficients. Most subsequent diffusion sequences are derived from these two sequences (Callaghan, 1991). The PGSE NMR technique is now a well-established method for measuring diffusion coefficients in

systems ranging from catalyst supports (Rigby and Gladden, 1999) to sedimentary rocks (Kleinberg *et at.*, 1994).

In general, molecules probing a porous solid can encounter factors such as restriction and variation of domain within a given sample. Callaghan (1984) was one of the earliest pioneers of PGSE NMR technique that studied molecular translation in the liquids due to thermal energy (Brownian motion). For molecules undergoing Brownian motion, PGSE NMR is used to determine molecular self diffusion coefficients in liquids. In a different approach, Hollewand and Gladden (1993) have shown that NMR images of the spin density, spin-lattice relaxation time and self-diffusion of water imbibed within porous catalyst support pellets showed significant contrast indicating variations in voidage, pore structure and transport properties over macroscopic (0.05-1 mm) length scales. These researchers suggested that for a given image of the porous medium spatially resolving a property Q, regions of constant Q are observed (over length-scales of 0.05-1 mm). The region of constant Q value within the material is said to be 'homogeneous'. However, the total image consists of many such homogeneous clusters, each associated with a different value of Q, and thus, the material is said to be 'macroscopically heterogeneous'. By using the same definitions proposed by Hollewand and Gladden (1993), a material might be described as macroscopically homogeneous, even if it is associated with a wide pore-size distribution, if pores of various sizes are distributed homogeneously throughout the entire material. Under these circumstances, each macroscopic region of the material will be characterized by the same average voidage, pore-size distribution and transport processes as the whole sample (Hollewand and Gladden, 1993).

Hollewand and Gladden (1995a) expanded the scope of their work by considering the effect of macroscopic heterogeneities in diffusion coefficient within a porous catalyst support pellet, on the PGSE NMR measurement of the molecular self-diffusion coefficient of water imbibed within the pore structure. These researchers presented a method of analysis of PGSE NMR data that allows for the existence of macroscopic variations in the molecular self-diffusion coefficient of an imbibed fluid. As demonstrated in Section 3.4.2, the expressions derived can be used to estimate the effective diffusivity of such media from PGSE NMR data. In addition, degree of heterogeneity of diffusion present within a porous pellet was estimated. The result obtained confirmed that macroscopically heterogeneous

materials have a greater average tortuosity than more homogeneous materials. In a subsequent report, Hollewand and Gladden (1995b) used a different approach by acquiring a series of images during the course of a transient diffusion process in the catalysts support pellets. The researchers estimated the effective diffusivity of water within the pore space of the pellets. The NMR imaging produced two-dimensional images. The images clearly showed that porous catalyst support pellets contain significant heterogeneities. These images supported the spatially non-resolved PGSE NMR experiments presented in their previous work (Hollewand and Gladden 1995a).

Since then the PGSE NMR method has been widely applied to study various heterogeneous systems (Rigby and Gladden, 1996; Seland *et al.*, 2001; and Veith *et al.*, 2004). In addition, PGSE NMR has also been applied to porous media in an attempt to obtain both transport and structural information (Rigby and Gladden, 1998). However, due to Brownian motion, the root mean displacement of molecules is linearly proportional to time in bulk liquids. The proportionality constant is the bulk diffusion coefficient. Therefore, when a fluid is confined in a porous medium, diffusion is restricted by the solid surfaces bounding the void space, so the apparent diffusion becomes a function of observation time (Valiullin, 2001). According to Kleinberg *et al.* (1994), at short observation time, the diffusion coefficient is determined by the surface to volume ratio of the pore space. Whilst at longer observation time, diffusing molecules probe the connectivity of the probe space, and thus, the diffusion coefficient is determined.

3.4.4 Restricted diffusion in porous media

When the radius of the solute molecule is comparable to the pore radius, significant steric hindrance and hydrodynamic interactions with the pore wall might occur. This phenomenon is known as restricted diffusion or steric hindrance. It becomes more pronounced when the ratio of molecular to pore radius, exceeds 0.1 (Hollewand and Gladden 1995a). Therefore, solute transport is then retarded by the viscous drag of the solvent, which is a function of the pore wall and the partitioning between the pores and the bulk solution (Veith *et al.*, 2004). This sensitivity of PGSE NMR to structure was first demonstrated by Tanner and Stejskal (1968). The pair measured restricted diffusion of protons in colloidal systems by pulsed-gradient. A wide range of materials including thin

liquid layers, plant cells, and emulsions were studied. The results produced showed a clear indication of restricted diffusion in all the systems tested studied. The observed effects in these findings were consistent with the structural features of the materials.

In a similar approach, Callaghan *et al*. (1983) studied the diffusion of water and cheese in water. These researched observed non-liner log-attenuation plots of the samples studied. The non-linearity of the log-attenuation data for the diffusion of fat and water in cheese was attributed to the diffusion being restricted. These researchers suggested restricted diffusion as the ultimate cause of the deviation from linearity of the log-attenuation plots observed at longer diffusion times. The estimated root mean square displacement was of the same order or greater than the dimension of the restricting structure. Therefore, for heterogeneous systems, such as fluids in porous media, or molecules diffusing between compact spheres, the displacement of the diffusing species depends on interactions with the porous matrix and might be restricted by pore walls. In obstructed diffusion, restriction in the structure is reached as the diffusion time increases. As a result, the apparent diffusion rate decreases. In addition, the longer the molecules diffuse, the more restricting barriers will be encountered, and thus, the measured diffusion coefficient becomes time-dependent (Kleinberg *et al.*, 1994). Additionally, the long-time behaviour of the diffusion coefficient provides an indirect measure of the macroscopic structure (Veith *et al.*, 2004).

In recent years, Stallmach *et al.* (2001) used PGSE NMR to probe the propagation pattern of polar and non-polar liquids (benzene) in ordered mesoporous materials. It was found that the log-attenuation plots deviates from linearity behaviour. The result obtained supports the earlier work of Hollewand and Gladden (1995a) in heterogeneous systems where the average propagator is not Gaussian (not equally distributed). Therefore, the PGSE NMR spin echo attenuations in diffusion studies with nanoporous are found to exhibit non-exponential behaviour. In a similar approach, Karger *et al.* (1981) studied the molecular transport through assemblages of microporous particles. These researchers used PGSE NMR to determine long-range diffusivities. In addition, theoretical methods for mass transfer in heterogeneous media were considered and adapted to adsorbate-adsorbent systems. These researchers compared the experimental data for n-butane diffusion in NaX zeolites. It was found that the long-range diffusivities were predominantly determined by intercrystalline transport as opposed to molecular transport.

In an earlier report, Karger *et al.* (1983) studied adsorbed liquids in porous glasses with pore sizes in the range 0.8-50 nm. From variable temperature studies, it was found that the activation energy of diffusion did not vary significantly with pore size. These observed reductions of diffusivity in small pores were attributed to the stabilisation of liquid molecules by the pore wall. Fukuda *et al.* (1989) also noticed the effect of decreasing diffusivity in smaller pores for samples with pore sizes in the range 4-45 nm. These researchers measured the self diffusion process of water molecules with different pore diameters using PGSE (NMR). The diameter and the length of the pores were much larger than the mean free path of the water probing the sample. It was found that the diffusion process inside the micropores had a Gaussian distribution. In addition, these researchers concluded that the effective diffusivity constant is proportional to porosity of the samples.

The deviation from the simple behaviour for isotropic bulk diffusion was also observed for liquids in porous media such as porous alumina (Packer and Zelaya, 1989). Diffusion properties of water and n-decane in porous alumina were studied by PGSE NMR method. The samples were cylindrical, with a diameter of 7 mm and a length of 15 mm. Variation of the time between the gradient pulses allowed the technique to access molecular diffusion over a range of scales of translational displacements. The echo attenuations observed were non-exponential functions of the diffusion time. These researchers considered various models to represent the void space. In general, apparent non-linear behaviour was observed as a function of diffusion time. These researchers proposed that the abnormality observed as an evidence of either restricted, or some form of low dimensional anisotropic, or diffusion behaviour. This finding agreed with the work of Callaghan *et al.* (1991) in core rock samples.

Callaghan *et al.* (1991) observed similar deviations of behaviour for isotropic bulk diffusion in core rock samples with pore sizes in the range of 2-200 μm. The work of Callaghan, Packer and their co-workers involved pore sizes of the order of the root mean molecular displacement. Therefore, considering these circumstances, the diffusion behaviour observed depends on the pore size. The experimental data obtained was consistent with diffusion bounded by low-dimensionality barriers giving rise to anisotropic diffusion. These observations differ from those of Karger *et al.* (1981), Karger *et al.* (1983) and Fukuda *et al.* (1989), where the pore size was much smaller than diffusive

displacement. In a similar approach, Seland *et al.* (2001) measured restricted diffusion in more complex porous particles such as polyolefin particles to gain more information on diffusion resistance. The PGSE NMR technique was used to measure the diffusion of organic solvents in various systems of porous polymer particles. It was found that the effects from either restricted diffusion, domains having different diffusivity, and internal magnetic field gradients are always present in most porous particles.

In a subsequent report, Valiullin and Skirda (2001) and Vasenkov *et al.* (2001) showed that only two exceptional cases of determining the true self-diffusion coefficient are straightforward. These two cases are found in the free diffusion and the rapid diffusion regimes. In the free diffusion regime, the diffusional distance (molecular displacement) is relatively small compared to the barrier separation, and only a small fraction of molecules will be influenced by the barriers. Therefore, the diffusive motion of the molecules leads to a Gaussian distribution of the spin phases. In the rapid diffusion regime, the diffusional distance is relatively large compared to the barrier separation. All molecules of the ensemble are influenced by the restricting boundaries. The diffusive motion of the molecules hardly behaves like a Gaussian distribution of the spin phases.

3.4.5 Restricted diffusion as a function of pore loading in porous media

Self-diffusion of adsorbate molecules in small pores, which have large surface-to-volume ratios, can be strongly affected by interaction with the pore walls. This phenomenon becomes more evident upon variation of the pore loading (Valiullin *et al.*, 2005). At partial pore saturation by a liquid, two phases of molecules co-exist with each other. That is, those that are adsorbed on the surface and those that traverse the free space in the interior of the pores. Therefore, the equilibrium between these two phases and their dynamic properties are generally affected by the interaction with the pore walls. In addition, the impact of the surface interaction on the behaviour of a whole molecular ensemble becomes much more pronounced with decreasing pore loading and increasing surface-to-volume ratio (Valiullin *et al.*, 2005).

Earlier studies by D'Orazio *et al.* (1990) used self-diffusion and spin-relaxation NMR of deionized water in porous glass at different degrees of filling in order to characterize the

pore morphology. The result revealed linear behaviour with respect to the degree of fluid filling down to monolayer coverage, which was attributed to both a homogeneous pore space and an equal distribution of the water. These researchers observed that the self-diffusion of the liquid was markedly enhanced by an indirect process involving exchange with the vapour phase. However, a deviation was observed below a monolayer. D'Orazio *et al.* (1990) interpreted this deviation as a modification of the liquid-solid interface, which caused the water molecules to become less mobile. Therefore, the deviation was generally attributed to the crossover from bulk to surface transport of the molecules. As a result, the diffusion coefficient decreased more rapidly as the filling was reduced (D'Orazio *et al.*, 1990).

Valiullin *et al.* (2004) applied PGSE NMR to study the details of molecular motion of low-molecular-weight polar and non-polar organic liquids in nanoporous silicon crystals of straight cylindrical pore morphology at different pore loadings. It was found that the diffusion in the vapour phase is governed by the collisions with the pore walls or surface layers and by intermolecular collisions. Also, for the small pores considered, because of the low vapour densities (the molecular mean free path in a bulk vapour is much longer than the pore diameter) the influence of the intermolecular collisions was very negligibly. However, D'Orazio *et al.* (1990) observed that the effective self-diffusion coefficients of water have opposite tendencies with respect to changes in the water content in porous glasses. It was anticipated that, the smaller pore size leads to a suppression of vapour-phase diffusion proceeded by the Knudsen mechanism since the coefficient of Knudsen diffusion is proportional to the pore size. In a subsequent report, Valiullin *et al.* (2005) used PGSE NMR method to examine the self-diffusion of liquids in mesoporous materials with different pore sizes and morphologies as a function of pore loading. The result obtained suggested that the effective diffusivities of adsorbate molecules in mesopores at partial loadings are related to two mechanisms. These mechanisms are the Knudsen diffusion through the gaseous phase in the pore space and the diffusion within the layer of molecules adsorbed on the pore walls. The relative contributions of these modes change with variation of the pore loading which leads to a complex behaviour of the effective self-diffusion coefficient (Valiullin *et al.*, 2005).

In a different approach, other workers such as Valliullin *et al*. (1997) and Farrher *et al*. (2008) tried to check if there is any vapour phase contribution to the total diffusional displacements. Valliullin *et al*. (1997) studied the self-diffusion properties of hexane confined in porous glass with different filling fractions by means of pulsed field-gradient spin echo diffusometry. It was found that only for the partially filled sample that the shape of the echo attenuation curves depended on diffusion time. This observation indicates a vapour phase contribution to the total diffusional displacements, and was interpreted by molecular exchange between the liquid and vapour phases. Farrher *et al*. (2008) made similar observations with the aid of NMR microscopy and PGSE NMR study of silica glasses with micrometer pores that were partially filled with water or cyclohexane. The images produced revealed a heterogeneous distribution of liquid on a length-scale much longer than the pore dimension. For the PGSE NMR section, these researchers used four decades of the diffusion time from 100 ms to 1 s. The data obtained was compared with Monte Carlo simulations of a model structure showing a qualitatively equivalent behaviour in the common time window. It was found that the self-diffusion in partially filled porous systems was strongly affected by a vapour phase.

In general, all porous materials usually exhibit a certain pore-size distribution. Therefore, variation of the relative pressure of adsorbate may lead to a situation where some pores (those of smaller diameter) to be completely filled by the liquid, while others (those of bigger diameter) to consist of the vapour and the adsorbed phases. The equilibrium between these two types of pores at a certain pressure is governed by the pore-size distribution function. At relatively high pressures, all the pores will be completely filled by the liquid. The value of effective self-diffusion coefficient (D_{eff}) is slightly smaller than the bulk self-diffusion coefficient (D_0). Furthermore, most liquids and solids have a tendency to evaporate into a gaseous phase. However, gases have a tendency to condense back to their liquid or solid form. The amount of physically adsorbed molecules is associated with the relative pressure, x.

In recent years, Pimenov *et al*. (2003) used PGSE NMR method to study the kinetics of hexane adsorption, from a vapour phase, by porous glasses with mean pore radii from 20 to 400 Å. These researchers revealed two stages of adsorption. The first stage, which had a high rate of adsorption ended by the formation of a monolayer on a pore surface, and, the

second stage was slow, and in addition, the rate of adsorption was inversely proportional to the pore radius of the glass at this stage. In a subsequent report, Pimenov and Skirda (2005) linked the first stage to monolayer adsorption and the second stage to capillary condensation. Therefore, the rate of adsorption was limited by the rate of adsorbate transfer to the adsorbent surface, with the latter rate being described by the classical diffusion flux. In a similar approach, Nechifor *et al*. (2009) investigated the relationship between liquid morphology and relaxation time distribution in partially saturated pores of a silica glass. These researchers could not find a general explanation for the distribution of adsorbate molecules on the pore surface at low saturation degrees, and thus, attributed the spatial distribution to the instability between the liquid and vapour phases as a consequence of the competition between the adhesion and cohesion forces.

3.4.6 Scope of work by PGSE NMR technique

The movement of water within a matrix may provide information on transport properties that can indicate the ability of constrained or restricted molecules to move within a porous media. For heterogeneous systems, such as fluids in catalyst support pellets, or molecules diffusing between compact spheres, the displacement of the diffusing species depends on interactions with the porous matrix and might be restricted by pore walls. In obstructed diffusion, restriction by the structure is reached as the diffusion time increases. The longer the molecules diffuse, the more restricting barriers will be encountered, and thus, the measured diffusion coefficient becomes time dependent (Packer and Zelaya, 1989; Kleinberg *et al.,* 1994). Therefore, the long-time behaviour of the diffusion coefficient provides an indirect measure of the macroscopic structure of a porous medium (Veith *et al.,* 2004). In recent years, mercury simulation work has indicated that entrapment increases with an increase in tortuosity (Salmas and Androutsopoulos, 2001). Therefore, samples with high tortuosity may involve a slow extrusion process of the non-wetting fluid higlighted in Section 3.3.3. In addition, the mercury porosimetry experiment, conducted by Wardlaw and McKellar (1981) suggests that non-random structural heterogeneity causes mercury entrapment.

In this study, the effects from restricted diffusion, and or various domains having different diffusivities, will be investigated. By examining the diffusion behaviour of water within a

porous medium, it may be possible to see the changes in tortuosity effects as a function of diffusion time. In the case of slow exchange between two diffusion domains, multi-exponential echo decay will be observed as each domain would possess its own diffusion coefficient (Hollewand and Gladden, 1995a). As detailed in Section 1.6, Appel *et al*. (1998) used PGSE NMR to estimate the relative volumes of movable (FFI) and non-movable (BVI) fluid in oil core plugs. These researchers suggested that the pores contributing to the FFI are large and most likely well connected, and thus, the mobility for fluid molecules in the pores should be free of any restriction. In contrast, the pores contributing to the BVI should be in a strongly restricted limit, and thus, the fluid molecules make multiple collisions with the pore wall. Therefore, the slow diffusion component in a two diffusion domain can elucidate the mechanisms of mercury entrapment and distribution of the irreducible non-wetting phase within a porous medium. As a result, the correlation between tortuosity of the slow component in a two component diffusion model with the corresponding mercury entrapment will be investigated.

Furthermore, the effect of vapour phase contribution to the total diffusional displacements will be studied. There is a lot of work where PGSE NMR method was used to examine the self-diffusion of liquids in pore-filled mesoporous materials with different pore sizes. At present, however, there are few works on self-diffusion of liquids in porous media as a function of pore loading that can offer better explanation of fluid distribution within the pore network of a material. In recent years, molecular exchange between the liquid and vapour phases was observed in porous glass (Valliullin *et al*., 1997; 2005; and Farrher *et al*., 2008). In addition, computer simulations on artificial porous materials have shown increased tortuosities with decreased pore connectivity (Friedman et *al*., 1995; Vogel, 2000; and Armatas, 2006). In this study, the effects from restricted diffusion, and or various domains having different diffusivities, potentially rising from partial saturation of the materials will investigated. Therefore, the liquid connectivity within the samples will be deliberately reduced in order to study the liquid distribution and the effect of vapour phase contribution to the total diffusional displacements.

At present, however, no practical method exists for the determination of the connectivity of the pore network from PGSE NMR data. In general, more investigations are necessary in order to fully elucidate the liquid morphology under partially saturated conditions. As a

result, a new robust method of understanding the behaviour of fluids in systems with either restricted or constrained geometry at different pore loading will be provided in Chapter 7. The rate of mass transfer and the adsorbed ganglia morphology, such as the tortuosity can be estimated over a period of time. This study will check the ability of PGSE NMR methods to quantitatively elucidate the absorption phenomenon under different pore filling conditions of the internal pore surfaces. The rate of mass transfer and subsequent distribution of water at different degree of pore loading will be elucidated, and thus, a better of understanding of restricted diffusion, liquid connectivity, and vapour phase contribution to the total diffusional displacements might be achieved.

Finally, it was reported in Section 1.6, that several researchers used two and three dimensional bond networks to determine the relationships between structural and transport properties in artificial porous materials. In general, for random pore network models of unimodal/monodisperse porous media, simulation results suggest that the mercury entrapment decreased with increased pore connectivity (Portsmouth and Gladden 1991; 1992). In addition, the simulation results suggest that tortuosity for molecular diffusion increases with decreasing pore connectivity, and increasing width of PSD (Friedman *et al.*, 1995; and Armatas, 2006). Furthermore, Salmas and Androutsopoulos (2001) observed a positive correlation between mercury entrapment obtained by experiment and tortuosity obtained from CPSM. The ultimate objective of this study is to provide experimental verifications to the simulation results reported in Section 1.6. Therefore, in Chapter 8, tortuosity will be correlated with pore connectivity, width of the PSD, and mercury entrapment. As detailed in Section 3.1, the width of the PSD, and pore connectivity will be measured with gas sorption technique. Also, detailed in Section 3.5, the mercury entrapment will be measured with the mercury porosimetry.

3.5 References

Abell, A., Willis, K., Lange, D., 1999. Mercury intrusion porosimetry and image analysis of cement-based materials. *J Colloid Interface Sci,* 211, 39–44.

Allen, T., 1999. *Particle size measurement.* Dordretch, The Netherlands: Kluwer Academic publishers.

Akpa, B.S., Holland, D.J., Sederman, A.J., Johns, M.L., Gladden, L.F., 2007. Enhanced C-13 PFG for the study of hydrodynamic dispersion in porous media. *Journal of magnetic resonance*, 186 (1), 160-165.

Allen, T., 1999. *Particle size measurement.* Dordretch, The Netherlands: Kluwer Academic publishers.

Androutsopoulos, G.P. and Mann, R., 1979. Evaluation of mercury porosimeter experiments using a network pore structure model. *Chemical Engineering Science*, 34, 1203-1212.

Apple, M., Stallmach, F., Thomann, H., 1998. Irreproducible fluid saturation determined by pulsed field gradient NMR. *Journal of petroleum science and engineering,* 19, 45-54.

Armatas, G.S., 2006. Determination of the effects of the pore size distribution and pore connectivity distribution on the pore tortuosity and diffusive transport in model porous networks. *Chemical engineering science,* 61, 4662 – 4675.

Barrett, E. P., Joyner, L. G., Halenda, P. P., 1951. The determination of pore volume and area distributions in porous substances. I. Computations from nitrogen isotherms, *J. Am. Chem. Soc*., 73, 373–380.

Brakel, J. V., Modry, S., Svata, M., 1981. Mercury porosimetry: state of the art. *Powder Technol*., 29, 1 – 12.

Brunauer, S., Emmett, P. H., and Teller, E. 1938. Adsorption of Gases in Multimolecular Layers. *Journal of the American Chemical Society*, 60, 309-319.

Broadbent, S.R. and Hammersley, J.M., 1957. Percolation processes, I and II, *Proc. Cambridge Philos. Soc.*, 53, 629.645.

Broekhoff, J.C.P., and de Boer, J.H., 1968. Studies on pore systems in catalysts XI: Pore distribution calculations from the adsorption branch of a nitrogen adsorption isotherm in the case of “ink-bottle” type pores. *Journal of Catalysis*, 10, 153-165.

Burgess, C. G. V., and Everett, D. H., 1970. The lower closure point in adsorption isotherms of the capillary condensation type. *Journal of Colloid Interface Science*, 33, 611–614.

Callaghan, P., Jolley, K.W., and Lelievre, J. 1979. Diffusion of water in the endosperm tissue of wheat grains as studied by pulsed field gradient nuclear magnetic resonance. *Biophysical Journal*, 28:133–142.

Callaghan, P.T., Jolley, K.W., and Humphrey, R.S., 1983. Diffusion of fat and water in cheese as studied by pulsed field gradient nuclear magnetic-resonance. *Journal of Colloid and Interface Science*, 93 (2), 521–529.

Callaghan, P. T., 1984. Pulsed field gradient nuclear magnetic resonance as a probe of liquid state molecular organisation. *Aust. J. Phys.*, 37, 359-387.

Callaghan, P.T., 1991. *Principles of nuclear magnetic resonance microscopy*. Oxford: University press.

Callaghan, P., Macgowan, D., Packer, K.J., and Zelaya, F.O., 1991. Influence of field gradient strength in nmr-studies of diffusion in porous-media. *Magnetic Resonance Imaging*, 9 (5), 663–671.

Carniglia, S.C., 1986. Construction of the tortuosity factor from porosimetry. *Journal of catalysis*, 102 (2), 408-418.

Carr, H.Y., and Purcell, E.M., 1954. Effects of Diffusion on Free Precession in Nuclear Magnetic Resonance Experiments. *Phys. Rev.*, 94, 630–638.

Cebeci, Omer Z., 1980. The Intrusion of Conical and Spherical Pores in Mercury Intrusion Porosimetry, *Journal of Colloid and Interface Science*, 78, 383-388.

Chatzis, I., Morrow, N.R., Lim, H.T., 1983. Magnitude and detailed structure of residual oil saturation. *SPE Journal*, 23, 311–326.

Cohan, L.H., 1938. Sorption hysteresis and the vapor pressure of concave surfaces. *Journal of American society*, 60, 43.

Conner, W.C., and Lane, A.M., 1984. Measurement of the morphology of high surface area solids: Effect of network structure on the simulation of porosimetry. *Journal of Catalysis*, 89 (2), 217-225.

Coulson, J.M., and Richardson J.F., 1998. *Chemical Engineering: Particle technology, and Separation processes*. Butterworth-Heinemann.

Coulson, J.M., and Richardson, J.F., 1999. *Chemical Engineering; Fluid flow, Heat transfer and Mass transfer, Volume 1*. 6TH edition. Butterworth-Heinemann.

Coulson, J.M., and Richardson J.F., 1998. *Chemical Engineering: Particle technology, and Separation processes*. Butterworth-Heinemann.

Cussler, E. L., 2009. *Diffusion: Mass transfer in fluid systems*. Cambridge: University Press.

D'Orazio, F., Bhattacharja, S., and Halperin W.P., 1990. Molecular self diffusion and nuclear magnetic resonance relaxation of water in unsaturated porous silica glass. *Physical review*, 42, 9810-9818.

Darot, M., Reuschle, T., 2003. Wood's metal dynamic wettability on Quarz, granite and limestone. *Pure Appl Geophys*, 160, 1415–27.

Diamond, S., 2000. Mercury porosimetry an inappropriate method for the measurement of pore size distributions in cement-based materials. *Cement and Concrete Research*, 30, 1517-1525.

Drewry, H. P. G., and Seaton, N. A., 1995. Continuum random walk simulations of diffusion and reaction in catalyst particles. *AIChE Journal*, 41: 880–893.

Dubinin, M.M., 1960. The potential theory of adsorption of gases and vapors for adsorbents with energetically nonuniform surfaces. *Chem. Rev*., 60 (2), 235-241.

Dullien, F.A.L., 1992. *In porous media; Fluid transport and pore structure*. 2nd edition. New York: Accademic press.

Ek, R., Lennholm, H., Davidson, R., Nystrom, C., & Ragnarsson, G. 1995. Pore swelling in beads made of cellulose fibers and fiber fragments. *International Journal of Pharmaceutics*, 122, 49–56.

Evbuomwan, O.E., 2009. *The structural characterisation of porous media for use as a model reservoir rocks, adsorbents and catalyst.* Thesis (PhD). University of Bath.

Farrher, G., Ardelean, I., Kimmich, R., 2008. Time-dependent molecular diffusion in partially filled porous glasses with heterogeneous structure. *Applied magnetic resonance*, 34 (1-2), 85-99.

Felipe C., Cordero S., Kornhauser I., Zgrablich G., López R., Rojas F., 2006. Domain Complexion Diagrams Related to Mercury Intrusion-Extrusion in Monte Carlo-Simulated Porous Networks. P*art. Part. Syst. Characteristics*, 23, 48–60.

Fordham, E.J., Gibbs, S., and Hall, L., 1994. Partially restricted diffusion in a permeable sandstone: observations by stimulated echo pfg nmr. *Magnetic Resonance Imaging*, 12 (2), 279–284.

Freeman, R., 1988. *A handbook of nuclear magnetic resona*nce. Longman-Wiley.

Frevel, L. K., Kressley, L. J., 1936. Modifications in mercury porosimetry. *Anal. Chem.*, 35, 1492-1502.

Friebolin, H., 1998. *Basic one- and two- dimensional NMR spectroscopy*. Translated by Jack Becconall. Wiley-vch.

Friedman, S.P., Zhang, L., and Seaton, N.A., 1995. Gas and solute diffusion coefficients in pore networks and its description by a simple capillary model. *Transport in porous media*, 19, 281-301.

Galarneau, A., Lefevre, B., Cambon, H., Coasne, B., Vallange, S., Gabelica, Z., Bellat, J-P., Di Renzo, F., 2008. Pore-Shape effects in determination of pore size of ordered mesoporous silicas by mercury intrusion. *J.* Phys. Chem. C, *112* (33), 12921–12927.

Giesche H., 2006. Mercury porosimetry: A general (practical) overview. *Particle and particles system characterisation*, 23, 9–19.

Gane, P.A.C., Ridgway, C.J., Lehtinen, E., Valiullin, R., Furo, I., Schoelkopf, J., Paulapuro, H., and Daicic., J., 2004. Comparison of NMR Cryoporometry, Mercury intrusion porosimetry, and DSC thermoporosimetry in characterizing pore size distributions of compressed finely ground calcium carbonate structures. *Ind. Eng. Chem. Res.*, 43 (24), 7920–7927.

Gelb, L. D., Gubbins, K. E., Radhakrishnan, R., and Sliwinskabtkowiak, M., 1999. Phase separation in confined systems. *Reports on Progress in Physics*, 62, 1573-1659.

Giesche, H., 1999. *Surface area and porosity characterisation by gas adsorption: an overview IN JILLAVENKATESA*. A. & ONODA, G. Y. (Eds.) Advances in process measurements for the ceramic industry: John Wiley & Sons, Inc.

Giesche, H., 2006. Mercury porosimetry: A general (practical) overview. Particle and particles system characterisation, 23, 9-19.

Giesche H., 2010. Multiple snap-off in long cylindrical pores. Thesis: Department of Ceramic Engineering and Material science, Alfred University.

Gregg, S. J., and Jacobs, J. 1948. An examination of the adsorption theory of Brunaeur, Emmett & Teller and Brunaeur, Deming, Deming & Teller. *Trans. Faraday Soc*. 44, 575.

Gregg, S.J., and Sing, K.S.W., 1982. *Adsorption, Surface Area and Porosity*. London: Academic Press.

Hahn, E.L., 1950. Spin echoes. *Physical review*, 80 (4).

Horvath, G., and Kawazoe, K., 1983. Method for calculation of effective pore size distribution in molecular sieve carbon. *J. chem. Engng Japan*, 16, 470-475.

Hollewand, M.P., and Gladden, L.F., 1992. Modelling of diffusion and reaction in porous catalysts using a random three-dimensional network model. *Chemical Engineering Science* 47, 1761-1770.

Hollewand M.P., Gladden L.F., 1993. Heterogeneities in structure and diffusion within porous catalyst support pellets observed by NMR Imaging. *Journal of catalyst*, 144, 254-272.

Hollewand, M.P., and Gladden, L.F., 1995a. Transport heterogeneity in porous pellets-I. PGSE NMR studies. *Chemical Engineering Science*, 50, 309-326.

Hollewand, M.P., and Gladden, L.F., 1995b. Transport heterogeneity in porous pellets-II. NMR imaging studies under transient and steady-state conditions. *Chemical Engineering Science*, 50, 327-344.

Hyvaluoma, J.; Turpeinen, T.; Raiskinmaki, P.; Jasberg, A.; 2007. Koponen, A.; Kataja, M.; Timonen, J. and Ramaswamy, S., Intrusion of nonwetting liquid in paper, *Physical Review E*, 75, 036301.

Ioannides, M.A., Chatzis, I., and Payatakes, A.C., 1991. A mercury porosimeter for investigating capillary phenomena and microdisplacement mechanisms in capillary networks," *J. Colloid and Interface Sci.*, 143, 22-36.

Ioannidis, M. A., & Chatzis, I. 1993. Network modeling of pore structure and transport properties of porous media. *Chemical Engineering Science*, 48, 951-972.

Jenkins, R.G., and Rao, M.B., 1984. The effect of elliptical pores on mercury porosimetry results. *Powder Technol.*, 38, 177-180.

Karger, J., Lenzer, J., Pfeifer, H., Schwabe, H., Heyer, W., Janowski, F., Wolf, F. and Zdanov, S. P., 1983. NMR study of adsorbate self-diffusion in porous glasses. *J. Am. Ceram. Soc.*, 66, 69-72.

Karger, J., Lenzner, J., Pfeifer, H., Schwabe, H., Heyer, W., Janowski, F., Wolf, F., Zdanov, S.P., 1984. NMR-STUDY of adsorbate self-diffusion in porous glasses. *Journal of the American ceramic society*, 66 (1), 69-72.

Keeler, J., 2005. *Understanding NMR spectroscopy*. Wiley.

Kleinberg, R.L., Kenyon W.E., and Mitra P.P., 1994. Mechanism of NMR relaxation of fluids in rock. *Journal of magnetic resonance series A*, 108, 206-214.

Kloubek, J., 1981. Hysteresis in porosimetry. *Powder Technol*., 1981, 29, 63 – 73.

Langmuir, I., 1916. The evaporation, condensation and reflection of molecules and the mechanism of adsorption. Phys. Rev., 8, 149-176.

Lapidus, G. R., Lane, A. M., Ng, K. M. and Conner, W. C., 1985. Interpretation of mercury porosimetry data using a pore-throat network model. *Chem. Engng Commun*. 38, 33-56.

Lastoskie, C., Gubbins, K.E., Quirke, N., 1993. Pore size distribution analysis of microporous carbons: a density functional theory approach. *J. Phys. Chem.*, 97 (18), 4786–4796.

Leon, C.E., 1998. New perspectives in mercury porosimetry. Advances in colloids and interface science, 76-77, 341-372.

Levitz, P.E., 2002. *Handbook of Porous Solids, Schuth, F., Sing, K.S.W., Weitkamp, J., Eds, Wiley–VCH*. Weinheim.

Liu, H., Zhang, L., Seaton, N.A., 1992. Determination of the connectivity of porous solids from nitrogen sorption measurements-II. Generalisation. *Chemical Engineering Science*, 47(17-18), 4393-4404.

Liu, Z., and Winslow, D., 1995. Sub-distribution of pore-size-A new approach to correlatex pore structure with permeablity. *Cem. Concr. Res.*,25, 769-778.

Lowell S., Shields J. E., 1981. Hysteresis, entrapment, and wetting angle in mercury porosimetry. *Journal of Colloid and Interface Science*, Vol. 83, No. 1.

Lowell, S., and Shields, J.E., 1984. *Powder Surface Area and Porosity*. London: Chapman and Hall.

Lowell S., Shields J.E., Thomas, M. A., Thommes, M., 2004. *Characterisation of porous solids and powders; Surface area, pore size and density*. Springer.

Liabastre, A.A., Orr, C., 1978. An evaluation of pore structure by mercury penetration. J. *Colloid Interface Sci*. 1978, 64, 1 – 18.

Mata, V.G., Lopes, J.C.B. and Dias, M.M., 2001. Porous Media Characterisation Using Mercury Porosimetry Simulation; Description of the Simulator and Its sensitivity to Model Parameters. *Industrial and Engineering Chemical Research*, 40, 3511 – 3522.

McBain, J.W., 1935. An explanation of hysteresis in the hydration and dehydration of gels. Journal of American society, 57, 4, 699-700.

Matthews G.P., Ridgway C.J., Spearing M.C., 1995. Void space modeling of mercury intrusion hysteresis in sandstone, paper coating, and other porous media. *J. Colloid Interface Sci*., 171, 8-27.

Meyer, H.I., 1953. Pore distribution in porous media. *Journal of applied physics*, 24 (5), 510-512.

Mills R., 1973. Self- diffusion in normal and heavy water in the range 1-45'. *The Journal of Physical Chemistry*, 77(5), 685–688.

Mitra, P.P., and Halperin, B.I., 1995. Effects of finite gradient-pulse widths in pulsed-field-gradient diffusion measurements. *Journal of magnetic resonance series A*, 113 (1), 94-101.

Moro, F., Böhni, H., 2002. Ink-bottle effect in mercury intrusion porosimetry of cement-based materials. *Journal of Colloid and Interface Science*, 246, 135–149.

Moscou, L. and S. Lub, 1981. Practical use of mercury porosimetry in the study of porous solids. *Powder Technology,* 29, 45-52.

Murray, K.L., Seaton, N.A., and Day, M.A., 1998. Analysis of the spatial variation of the pore network coordination number of porous solids using nitrogen sorption measurements. *Langmuir,* 14, 4953-4954.

Neimark, A.V., 1991. Percolation theory of capillary hysteresis phenomena and its applications for characterization of porous solids. *Studies in surface science catalysis*, 62, 67-74.

Nechifor, R., Badea, C., and Ardelean, I., 2009. Nuclear magnetic resonance studies of liquids morphology inside partially saturated porous media. *Journal of physics: conference series*, 182 (1).

Orr, C., 1969. Application of mercury penetration to materials analysis. *Powder Technol.*, 3, 117-123.

Packer, K. J. and Zelaya, F. O., 1989. Observations of diffusion of fluids in porous solids by pulsed field gradient NMR. *Colloids Surfaces,* 36, 221 227.

Pellenq, R.J., Rodts, S., Pasquier, V., Delville, A., and Levitz, D.P., 2000. A grand canonical Monte-Carlo simulation study of xenon adsorption in a Vycor-likeporous matrix. *Adsorption*, 6, 241-249.

Perkins, E.L., 2009. *Nuclear magnetic resonance studies of drug release devices.* Thesis (PhD). University of Bath.

Perry, R.H., and Green, D.W., 1998. *Perry's Chemical Engineers' Handbook.* The McGraw Hill.

Pimenov, G.G., Kortunov, P.V., and Dvoyashkin, M.N., 2003. Structure and Dynamics of Molecular Systems, Kazan: *Kazan. Gos. Univ*., 10(3), 84.

Pimenov, G.G., and Skirda, V.D., 2005. NMR Study of the Kinetics of Butane and Hexane Adsorption from Vapour Phase by Porous Glasses. *Colloid Journal*, Vol. 67(6), 746–750.

Pirard R., Heinrichs B., Pirard J.P. in: McEnaney B., Mays T.J., Rouquerol J., Reinoso R.F., Sing K.S.W., Unger (Eds.) K.K., 1997. *Characterisation of Porous Solids IV, Royal Society of Chemistry*. Cambridge.

Pomonis, P.J., and Armatas, G.S., 2004. A method of estimation of pore anisotropy in porous solids. *Langmuir*, 20, 6719-6726.

Porcheron F., Monson P. A., 2004. Modeling mercury porosimetry using statistical mechanics. *Langmuir*, 20 (15), 6482-6489.

Porcheron F., Monson P. A., 2005. Dynamic aspects of mercury porosimetry: A lattice model study. *Langmuir*, 21, 3179-3186.

Porcheron, F., Monson, P.A., 2005. Molecular modeling of mercury porosimetry. adsorption, *Langmuir*, 11, 325–329.

Porcheron, F., Thommes, M., Ahmad, R., and Monson, P.A., 2007. Mercury porosimetry in mersoporous glasses: A comparison of experiments with results from a molecular model. *Langmuir*, 23,372-3380.

Portsmouth, R.L., and Gladden, L.F., 1991. Determination of pore connectivity by mercury porosimetry. Chemical Engineering Science, 46 (12), 3023-3036.

Portsmouth, R.L., and Gladden, L.F., 1992. Mercury porosimetry as a probe of pore connectivity. *Chemical Engineering Research and Design*, 70 (1), 63-70.

Rana, M. S., Ancheyta, J., Maity, S. K. and Rayo, P., 2005b. Maya crude hydrodemetallization and hydrodesulfurization catalysts: An effect of TiO_2 incorporation in Al_2O_3. *Catalysis Today*, 109, 61-68.

Rajniak, P., and Yang, R.T., 1993. A simple model and experiment for adsorption–desorption hysteresis: water vapor on silica gel. *AIChE Journal*, 39, 774–780.

Ravikovitch, P. I., and Neimark, A. V., 2002. Experimental confirmation of different mechanisms of evaporation from Ink bottle type Pores: equilibrium, pore blocking and cavitation, *Langmuir*, 18, 9830-9837.

Rigby, S.P., and Gladden, L.F., 1996. NMR and fractal modelling studies of transport in porous media. *Chemical engineering science*, 51 (10), 2263-2272.

Rigby, S.P., Gladden, L.F., 1998. The use of magnetic resonance images in the simulation of diffusion in porous catalyst support pellets. *Journal of Catalysis*, 173 (2), 484-489.

Rigby, S.P., 1999. NMR and modelling studies of structural heterogeneity over several lengthscales in amorphous catalyst supports. *Catalysis Today*, 53 (2), 207-223.

Rigby, S.P., 2000. A Hierachical Model for the Interpretation of Mercury Porosimetry and Nitrogen Sorption. *J. Colloid and Interface Sci.*, 224, 382–396.

Rigby, S.P., Fletcher, R.S., Riley, S.N., 2001. Characterization of macroscopic structural disorder in porous media using mercury porosimetry. *J. Colloid Interface Sci.*, 240, 190-210.

Rigby, S.P., 2002. New methodologies in mercury porosimetry. *Stud. Surf. Sci. Catal.*, 144, 185 – 192.

Rigby S.P., Edler K.J., 2002. The influence of mercury contact angle, surface tension, and retraction mechanism on the interpretation of mercury porosimetry data. *Journal of Colloid Interface Science*, 250, 175-190.

Rigby, S.P., Fletcher, R.S., Raistrick, J.H., Riley, S.N., 2002. Characterisation of porous solids using a synergistic combination of nitrogen sorption, mercury porosimetry, electron microscopy and micro-focus x-ray imaging techniques. *Phys. Chem. Chem. Phys.*, 4, 3467-3481.

Rigby, S.P., Fletcher, R.S., Raistrick, J.H., Riley, S.N., 2002. Characterisation of porous solids using a synergistic combination of nitrogen sorption, mercury porosimetry, electron microscopy and micro-focus x-ray imaging techniques. *Phys. Chem. Chem. Phys.*, 4, 3467-3481.

Rigby, S.P., Fletcher, R.S., Raistrick, J.H., Riley, S.N., 2002. Characterisation of porous solids using a synergistic combination of nitrogen sorption, mercury porosimetry, electron microscopy and micro-focus x-ray imaging techniques. *Phys. Chem. Chem. Phys.*, 4, 3467-3481.

Rigby, S.P., Fletcher, R.S., Riley S.N., 2002. Determination of the multiscale percolation properties of porous media using mercury porosimetry. *Industrial and engineering chemistry research.* 41 (5), 1205-1226.

Rigby S. P., Fletcher R.S., Riley S. N., 2003b. Determination of the cause of mercury entrapment during porosimetry experiments on sol–gel silica catalyst supports. *Applied Catalysis (A),* 247, 27–39.

Rigby, S.P., Fletcher, R.S., 2004. Interfacing mercury porosimetry with nitrogen sorption. *Part. Part. Syst. Charac.*, 21, 138-148.

Rigby S. P., Fletcher, R. S., Riley S. N., 2004. Characterisation of porous solids using integrated nitrogen sorption and mercury porosimetry. Chem. Engng. Sci., 59, 41 – 51.

Rigby, S.P., Watt-Smith, M.J., Fletcher, R.S., 2005. Integrating gas sorption with mercury porosimetry. *Adsorption*, 11, 201-206.

Rigby, S.P., Watt-Smith, M.J., Fletcher, R. S., 2004. Simultaneous determination of the pore-length distribution and pore connectivity for porous catalyst supports using integrated nitrogen sorption and mercury porosimetry. *Journal of catalysis*, 227 (1), 68-76.

Rigby, S.P., and Fletcher, R.S., 2004. Experimental Evidence for pore blocking as a mechanism for nitrogen sorption hysteresis in a mesoporous material. *J. Phys.Chem. B.*,108, 4690-4695.

Rigby, S.P., Evbuomwan, I.O., Watt-Smith, M.J., Edler, K.J., Fletcher, R.S., 2006. Using nano-cast model porous media and integrated gas sorption to improve fundamental understanding and data interpretation in mercury porosimetry. *Part. Part. Syst. Charac.*, 23, 82-93.

Rigby, S.P., Chigada, P.I., Evbuomwan, I.O., Chudek, J.A., Miri, T., Wood, J., Bakalis, S., 2008. Experimental and modelling studies of the kinetics of mercury retraction from highly confined geometries during porosimetry in the transport and the quasi-equilibrium regimes. *Chem. Engng. Sci*., 63 (24), 5771-5788.

Rigby, S.P., Chigada, P.I., Perkins, E.L., Lowe, J., Edler, K.J., 2008. Fundamental studies of gas sorption within mesopores situated amidst inter-connected, irregular network. *Adsorption-journal of the international adsorption society*, 14 (2-3), 289-307.

Rigby, S.P., and Chigada, P.I., 2009. Interpretation of integrated gas sorption and mercury porosimetry studies of adsorption in disordered networks using mean-field DFT. *Adsorption-journal of the international adsorption society*, 15 (1), 31-41.

Ritter, H. L. and Drake, L. C., 1945. Pore-size distribution in porous materials. *Ind. Engng Chem. Anal*. Ed., 17, 782-786.

Rojas, F., Kornhauser, I., Felipe, C., Esparza, J.M., Cordero, S., Dominguez, A., and Ricardo, J.L., 2002. Capillary condensation in heterogeneous mesoporous networks consisting of variable connectivity and pore-size correlation. *Phys. Chem. Chem. Phys.*,4, 2346 – 2355.

Rootare, H.M., and Prenzlow C.F., 1967. Surface areas from mercury porosimeter measurements. *J. Phys. Chem.*, 71, 2733-2736.

Rouquerol, F., Rouquerol, J., and Sing, K., 1999. *Adsorption By Powders And Porous Solids Principles, Methodology And Applications*. London: Academic Press.

Rouquerol, J., Llewellyn, P., and Rouquerol, F., 2007. *Is the BET Equation Applicable to Microporous Adsorbents?*. Amsterdam: Elsevier.

Salmas C.E., and Androutsopoulos, G.P., 2001. A novel pore structure tortuosity concept based on nitrogen sorption hysteresis data. *Industrial engineering chemical research*, 40 (2), 721-730.

Saito, A., and Foley, H.C., 1991. Curvature and parametric sensitivity in models for adsorption in micropores, *AIChE Journal*, 37 (3), 429 – 436.

Sarkisov, L., and Monson, P.A., 2000. Hysteresis in Monte Carlo and molecular dynamics simulations of adsorption in porous materials. *Langmuir*, 16, 9857-9860.

Scholes, O.N., Clayton, S.A., Hoadley, A.F.A, and Tiu, C., 2007. Permeability anisotropy due to consolidation of compressible porous media. *Transport porous media*. 68 365-387.

Seland, G.J., Ottaviani, M., and Hafskjold. K., 2001. A PFG-NMR Study of restricted diffusion in heterogeneous polymer particles, *Journal of Colloid and Interface Science*, 239, 168–177.

Sen, P.N., Schwartz, L.M., Mitra, P.P., 1994. Probing the structure of porous media using NMR Spin echoes. *Magnetic resonance imaging*, 12 (2), 227-230.

Schreiber, J.F., Grüner, F., Schramm, U., Geissler, M., Schnürer, M., Ter-Avetisyan, S., Hegelich, M., Cobble, J., Brambrink, E., Fuchs, J., Audebert, P., and Habs, D., 2006. Analytical Model for Ion Acceleration by High-Intensity Laser Pulses. *Phys. Rev. Lett*. 97

Schreiber, A., Ketelsen, I., Findenegg, G. H., and Hoinkis, E., 2007. Thickness of adsorbed nitrogen films in SBA-15 silica from small-angle neutron diffraction. *Stud. Surf. Sci. Catal.*, 160, 17-24.

Seaton, N.A., Walton, J.P.R.B., and Quirke N., 1989. A new analysis method for the determination of the pore size distributions of porous carbons from nitrogen adsorption measurements. *Carbon*, 27, 853–861.

Seaton, N.A., 1991. Determination of the connectivity of porous solids from nitrogen sorption measurements. *Chemical engineering science*, 46 (8), 1895-1909.

Sing, K.S.W., Everett, D.H., Haul, R.A.W., Moscou, L., Pierotti, R.A., Rouquerol, J. and Siemieniewska, T., 1985. Reporting physisorption data for gas solids systems with special reference to the determination of surface area porosimetry and porosity (recommendation 1984). *Pure and applied chemistry*, 57, 603-619.

Smith, D.M., and Stermer, D.L., 1987. Particle size analysis via mercury intrusion measurements. *Powder Technol*., 53, 23-30.

Stallmach, F., Graser, A., Karger, J., Krause, C., Jeschke, M., Oberhagemann, U., and Spange, S., 2001. Pulsed Field Gradient NMR Studies of Diffusion in MCM-41 Mesoporous Solids. *Microp. Mesop. Mat.*, 44/45, 745–753.

Stejskal, E. O., and Tanner J.E., 1965. Spin diffusion measurements: spin echoes in the presence of a time dependent field gradient. *Journal of Chemical Physics*, 42,288 -292.

Soos, M., and Rajniak, P., 2001. Percolation model of adsorption-desorption equilibria with hysteresis. *Chemical Papers-Chemickezsti*, 55 (6), 391-396.

Soos, M., Rajniak, P., and Stepanek, F., 2007. Percolation model of adsorption-desorption equilibria with hysteresis. *Colliods and surfaces A-Physicochemical and engineering aspects*, 300(1-2), 191-203.

Tanner, J. E., 1970. Use of the stimulated echo in NMR diffusion studies. *J. Chem. Phys.*, 52, 2523–2526.

Tsakiroglou, C.D., and Payatakes, A.C., 1990. A new simulator of mercury porosimetry for the characterization of porous materials. *Journal of Colloid and Interface Science*, 137, 315-339.

Tsakiroglou C. D., Kolonis G. B., Roumeliotis T. C., Payatakes A. C., 1997. Mercury Penetration and Snap-off in Lenticular Pores, *J. Colloid Interf. Sci.*, 193, 259–272.

Tsakiroglou C. D., Payatakes A. C., 1998. Mercury Intrusion and Retraction in Model Porous Media, *Adv. Colloid Interf. Sci*., 75, 215–253.

Tsetsekou, A., Androutsopoulos, G., and Mann, R., 1991. Mercury hysteresis and entrapment predictions based on a corrugated random pore model. *Chem. Eng. Commun.*, 110, 1-29.

Thommes, M., Smarsly, B., Groenewolt, M., Ravikovitch, P.I., Neimark, A.V., 2006. Adsorption hysteresis of nitrogen and argon in pore networks and characterization of novel micro- and mesoporous silicas. *Langmuir*, 22, 756 -764.

Ullmann's Encyclopedia of Industrial Chemistry, (2008) . John Wiley & Sons.

Van Brakel, J., S. Modry, and M. Svata. 1981. Mercury Porosimetry: State of the Art. *Powder Technology*, 29, 1–12.

Valiullin, R.R., Skirda, V.D., Stapf, S., Kimmich, R., 1997. Molecular exchange processes in partially filled porous glass as seen with NMR diffusometry. *Physical review E*, 55 (3), Part A, 2664-2671.

Valiullin, R., and Skirda, V., 2001. Time dependent self-diffusion coefficient of molecules in porous media *Journal of chemical physics*, 114 (1). 452-458.

Valiullin, R., Kortunov, P., Karger, J., and Timoshenko, V., 2004. Concentration-dependent self-diffusion of liquids in nanopores: a nuclear magnetic resonance study. *J. Chem. Phys.*, 120, 11804–11814.

Valiullin, R., Korunov, P., Karger, J., and Timoshenko, V., 2005. Concentration-dependent self-diffusion of adsorbates in mesoporous materials. *Magnetic resonance imaging*, 23, 209-214

Vasenkov, S., Galvosas P., Geier O., Nestle N., Stallmach F., Karger, J., 2001. Determination of genuine diffusivities in heterogeneous media using stimulated echo pulsed field gradient NMR. *Journal of magnetic resonance*, 149 (2), 228-233.

Veith, S.R, Hughes, E., Vuataz, G., and Pratsinis, S.E., 2004. Restricted diffusion in silica particles measured by pulsed field gradient NMR. *Journal of Colloid and Interface Science*, 274, 216–228.

Wardlaw, N.C., McKellar, M., 1981. Mercury porosimetry and the interpretation of pore geometry in sedimentary rocks and artificial models. *Powder Technology*, 29, 127 – 143.

Wardlaw, N.C., 1982. The effects of geometry, wettability, viscosity and interfacial tension on trapping in single pore-throat pairs. *Journal of Canadian Petroleum Technology*, 21, 21-27.

Washburn, E. W., (1921). The dynamics of capillary flow. Phys. Rev. 17, 273-283.

Woo, H.J., Sarkisov, L., and Monson. P.A, 2001. Mean-field theory of fluid adsorption in a porous glass. *Langmuir*, 17 (24), 7472-7475.

Woo, H.J., F. Porcheron, and P.A. Monson, 2004. Modeling Desorption of Fluids from Disordered Mesoporous Materials. *Langmuir*, 20, 4743–4747.

Zhou, J., Ye, G., and Breugel, K.V., 2010. Characterization of pore structure in cement-based materials using pressurization–depressurization cyclin mercury intrusion porosimetry (PDC-MIP). *Cement and concrete research*, 40, 1120-1128.

Zsigmondy, R., 1911. Structure of gelatinous silicic acid: Theory of dehydration. *Zeitschrift Anorganic Chemistry*, 71, 356–377.

4.0 Gas sorption experimental method to porous media

[Study of pore size distribution, pore connectivity, and pore anisotropy]

4.1 Introduction

The principles and the applications of gas sorption technique have been discussed in Section 3.2. The proposal for the research programme can be found in Section 3.2.9. This Chapter introduces the gas sorption porosimetry and the experimental conditions. The ASAP 2010 porosimeter used in this section covers pore size ranging from approximately 0.002 to 0.4 μm. As detailed in Section 3.2.9, much less use is made of the nitrogen adsorption/desorption isotherm data, to estimate the connectivity of a pore space, and pore length. In this Chapter, pore connectivity, and a measure of pore length (α) of porous media were estimated from nitrogen isotherm data. In addition, other traditional pore structure parameters, such as the BET surface area, pore volume, and pore size, and variance of the PSD, were estimated from nitrogen isotherm data. Furthermore, a comprehensive study of the nitrogen adsorption and desorption isotherms was made to elucidate the nature of the pores, advanced condensation, and cavitation processes.

4.2 Gas sorption porosimetry and experimental considerations

The accelerated surface area porosimeter (ASAP 2010) system, performs automatic analyses, collects, and reports analysis data. The status of the system was constantly monitored by the control module and could also be viewed manually on the status/control screen. The equipment has two sample preparation ports and a single analysis port. The analysis bath fluid Dewar resides on an automatically operated elevator. Controls and indicators located on the front panel operate the vacuum systems; degas valves, and heating mantles. A sliding shield can be lowered to provide safety or raised to access to the sample analysis port and preparation ports.

Initially, the sample tube was rinsed with acetone followed by water, and then placed in a drying oven overnight. The weight of the sealed sample tube was recorded prior to

introduction of any sample. Then, about 0.2 g (~ five pellets) of the sample was introduced into the tube. The initial weight of the sample was calculated by determining the weight of the sample and sample tube. In addition, the cold trap Dewar was filled with liquid nitrogen.

The sample-containing plugged tube was then screwed tightly into the degassing port of the system with a connector nut and o-ring. The loaded sample tube was first filled with the backfill gas (nitrogen) to atmospheric pressure. Once vacuum was reached, a heating mantle was applied to the sample tube, and the contents were heated, under vacuum, to a temperature of 250 °C. The sample was left under vacuum for 4 hours at a pressure of 0.27 Pa. The sample tube and its contents were re-weighed after cooling to room temperature. Thus, the dry weight of the sample before being transferred to the analysis port for the automated analysis procedure was measured. The purpose of the thermal pre-treatment for each particular sample was to drive any physisorbed water on the sample while leaving the morphology of the sample itself unchanged.

A thermo-heating jacket was inserted around the sample flask which was placed in the analysis port. The flask was fixed at the top with a nut and o-ring, together with the sample tube. The liquid nitrogen Dewar at the analysis port was filled to the required volume and placed in the elevator. Foam supplied by the manufacturer was used to cover the Dewar to prevent the liquid nitrogen from evaporating. A sample information file was created where the sample's dry mass and the analysis conditions were entered. A full adsorption/desorption micro/mesoporous was carried out since the sample characteristics were unknown.

The calculation of the dead volume of flask, also known as free space analysis, was carried out by using helium. The dead space was the volume of the sample tube excluding the sample itself. Once the vacuum condition was reached, the thermo heating jacket was removed and replaced with a heating mantle which was applied to the sample tube, and the contents were then heated, under vacuum, to a temperature of 250 °C for 2 hours. The liquid nitrogen Dewar at the analysis port was filled to the required volume and placed in the elevator. A free space information file was created where the sample's dry mass and the conditions were entered for analysis

4.3 Results and analysis

A range of porous alumina and silica pellets of spherical or cylindrical geometry was investigated. In order to allow for the variation of support structure between pellets from the same batch and to test the reproducibility of measurements, replicate measurements were made. Sets 1 and 2 represent the replicate measurements. Therefore, the reported parameters in this section are the mean of the sets used. During the course of the experiment, the relative pressure was either increased or decreased in small steps, and a small volume of nitrogen, either entered, or left, the sample. After each relative pressure change, the volume of nitrogen within the sample was allowed to come to equilibrium over a period of time. It should be noted that a previous worker (Evbuomwan**,** 2009) within this research group determined the absolute values for different pre-treatment conditions, and the equilibration time suitable for these materials. Evbuomwan (2009) suggested a pre-treatment condition of 250 °C for 4 hours, and 45 seconds equilibration time for the diffusion of nitrogen molecules to access most of the pores present in these materials. This researcher observed that the lower point of the hysteresis loop in most nitrogen isotherms closed at ~ 0.7 to 0.8 with the above conditions. This observation was in good agreement with the accepted literature of near equilibration by Gregg and Sing (1982). Therefore, the same pre-treatment conditions, and equilibration time were adopted in Section 4.2. In the Kelvin Equation (3.18), the adsorbate property factor was taken to be 9.53×10^{-10} m. Furthermore, it was assumed that, the fraction of pores open at both ends was zero, for both adsorption and desorption. Thus, capillary condensation commenced at the closed end of a pore to form a hemispherical meniscus, and the process of evaporation commenced at a hemispherical meniscus.

The estimated values of BET surface area, c constant, monolayer capacity, pore volume, pore size, variance of the PSD, and connectivity parameters of the materials investigated are given in Table 4.1. The reported uncertainties indicate the spread of the results over samples from the same batch, and the error associated with the technique. It can be seen from Table 4.1 that most of the samples have strong interactions between the adsorbate and adsorbents $(c > 100)$. As detailed in Section 3.2.5, the surface area of porous media may be determined by using the Brunauer, Emmett and Teller (BET) Equation 3.1. The following pressure range, $0.1 < x \leq 0.3$, was used for the BET plots. For each data set, the BET

plots yielded a coefficient of determination with linear regression (R^2) greater than 0.999. Figure 4.1 shows the BET surface area plot of Aerosil. The rest of the BET plots for the rest of the samples can be found in Appendix A4. The BET surface area (a_{BET}) was evaluated from the monolayer capacity by using Equation 3.3. The pore volume was determined from the quantity adsorbed at the plateau by assuming the adsorbate density to be the liquid density of the adsorbate at the temperature of adsorption. Therefore, the pore volume was obtained according to the Gurvitsch rule at $x = 0.99$ as detailed by Gregg and Sing (1982). The plateau in the isotherm at high relative pressure corresponds to near complete filling of the mesopores and micropores. The average hydraulic radius of pores was obtained by taking the ratio of pore volume from the Gurvitsch rule, and the BET surface area of the sample. As detailed in Section 3.2.6, the pressure at which the gas condenses can be related to the pore size according to the Kelvin equation (Equation 3.18). Therefore, the variance of PSD was estimated from the BJH algorithm data.

The connectivity estimations in Table 4.1 were carried out in terms of percolation variables as described in Section 3.2.7. These values were calculated from the PSD using the method of Barrett *et al*. (1951). The hysteresis loop was used to determine the number fraction of pores that would have emptied in a perfectly connected network, f, and the fraction of pores that would have emptied in a perfectly connected network (F), as illustrated by Seaton (1991) in Figure 3.10 (see Section 3.2.7). The mean coordination number, Z, and the number of pore lengths, L, were obtained by fitting the quasi-universal curve of Equation 3.20 to $F(f)$. The mean coordination number of the pore network (Z) is the average number of pores which intersect at a pore junction. The characteristic dimension L often refers to typical microparticle size. It maps the linear dimension of the lattices, and thus, it is expressed as a number of pore lengths (Seaton, 1991). The fits of the generalised scaling faction $F(f)$ for the Aerosil data is shown in Figure 4.2. The generalised scaling faction for the rest of the data samples can be found in Appendix A4. It should be noted that the connectivity analysis suggested by Seaton (1991) requires an isotherm where pores are full of condensed nitrogen at the top of the hysteresis loop, thereby corresponding to H1 or H2 hysteresis loop. However, samples such as AL3984T had an incomplete adsorption isotherm due to the limitation of the machine, and thus, still contained vapour in the largest pores that makes the connectivity analysis unfeasible.

Table 4.1

The average result and standard error obtained from nitrogen adsorption isotherms of the samples

Sample	BET Surface area m^2/g	BET constant (c) _	Monolayer capacity (V_m) $cm^3(STP)/g$	Pore volume cm^3/g	Pore diameter Nm	Variance $\left(\frac{\sigma}{\mu}\right)$ _	Pore connectivity (Z) _	Lattice size (L) _
Aerosil	162 ± 24	328 ± 108.47	37.68 ± 5.57	0.67 ± 0.01	16.95 ± 2.42	0.9 ± 0.23	6.35 ± 2.65	5.8 ± 0.8
AL3984T	103 ± 9.04	143 ± 28.43	23.92 ± 2.1	0.36 ± 0.03	13.87 ± 0.08	0.722 ± 0.05	6.25 ± 1.75	5 ± 1
AL3992E	159 ± 29.02	162 ± 23.93	15.14 ± 6.75	0.56 ± 0.11	14.46 ± 0.16	0.585 ± 0.04	N/S	N/S
C10	287 ± 6.96	155 ± 31.56	66.69 ± 1.62	1.06 ± 0.01	14.74 ± 0.43	0.356 ± 0.11	2 ± N/A	4 ± N/A
C30	101 ± 2.22	100 ± 1.2	23.47 ± 0.52	1.03 ± 0.08	40.83 ± 0.6	0.19 ± 0.02	N/S	N/A
Q17/6	153 ± 0.86	433 ± 14.22	35.63 ± 0.2	0.52 ± 0.04	13.68 ± 1	0.46 ± 0.09	2.7 ± 0.3	5 ± 1
S980A	130 ± 44.54	270 ± 66.84	30.27 ± 10.36	1 ± 0.18	36.81 ± 18.02	0.511 ± 0.16	4.3 ± N/A	3.6 ± N/S
S980G	64 ± 2.22	456 ± 99.19	14.77 ± 0.55	0.78 ± 0.02	49.01 ± 0.46	0.143 ± N/A	N/S	N/S
Silica Alumina	198 ± 2.34	321 ± 130.88	45.97 ± 0.55	0.86 ± 0.28	11.27 ± 5.55	1.25 ± 0.5	N/S	N/S

Note

L **- Number of detectable changes in characteristics pore dimension (measured by gas adsorption technique) in traversing the sample from one side to another. It reflects the aggregate behaviour of microparticles with different shapes and sizes. The microparticles contain pores that are typically in the microscope and mesopore size ranges. As a result, it is not possible to equate** L **to any defined dimension, and thus it is regarded as a characteristic dimension of the microparticles (Seaton, 1991).**

N/A – Not applicable due to lack of sample (stock ran out)

N/S – Model not suitable for the set of data

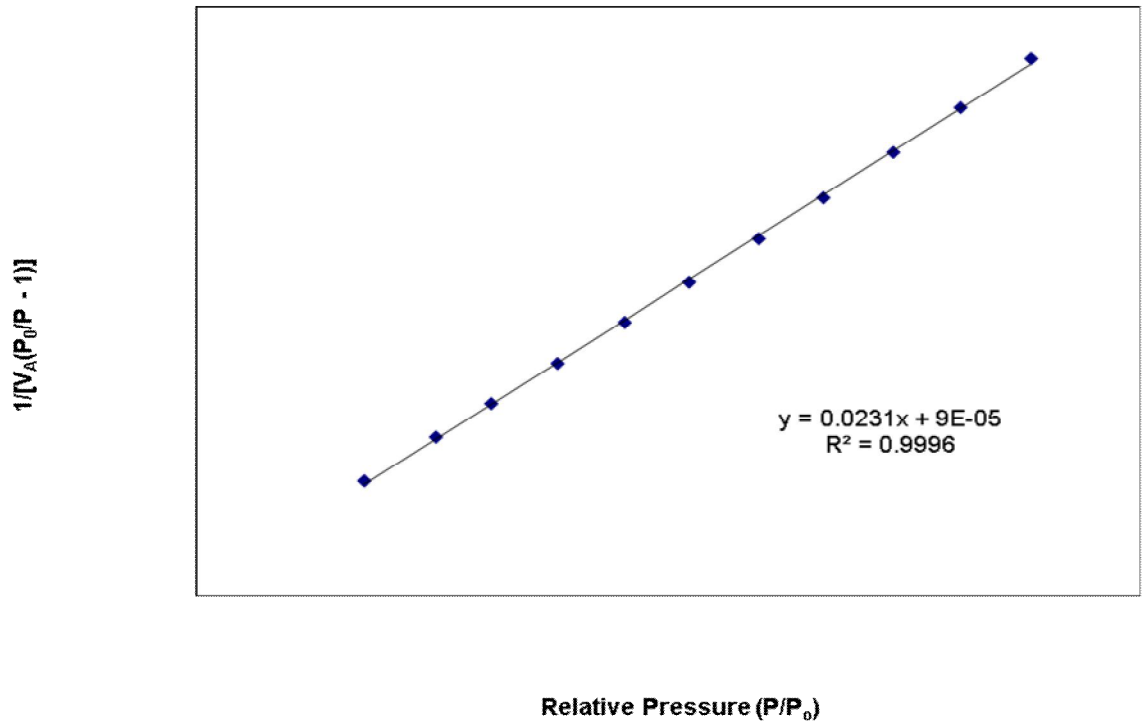

Figure 4.1

The BET plot for Nitrogen adsorption at 77 K of Aerosil

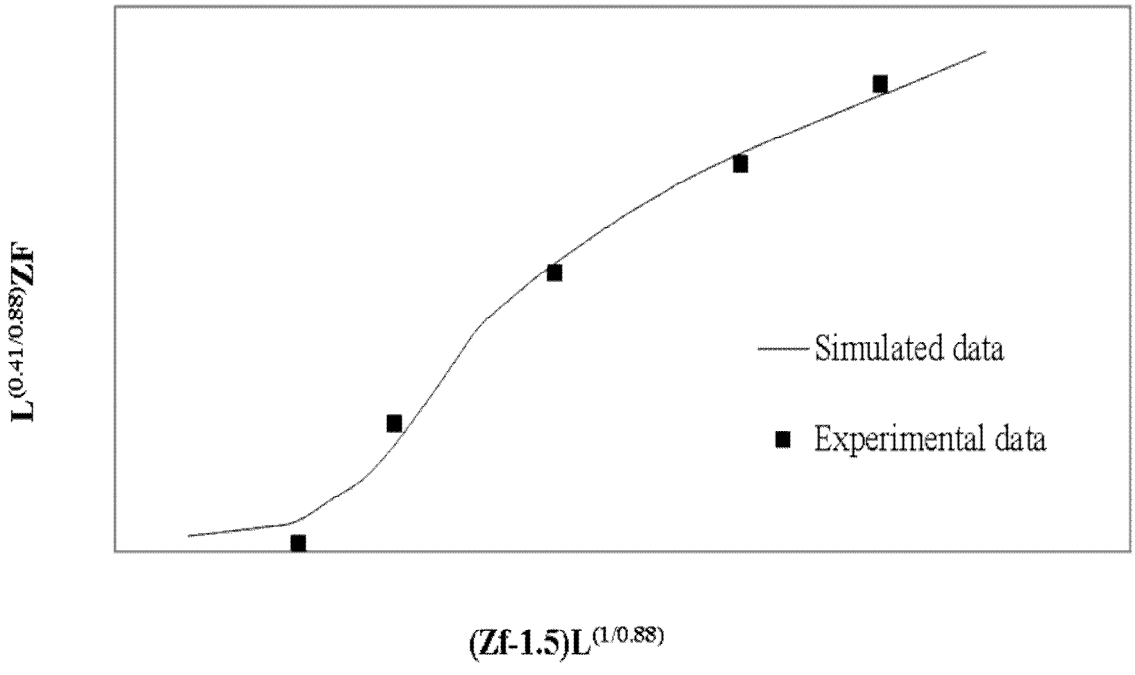

Figure 4.2

Generalised accessibility plot of Aerosil showing the experiemental and simulated data for $Z = 9$ **and** $L = 6.6$

Figures 4.3 to 4.7 show the full nitrogen adsorption and desorption isotherms for the samples investigated. The data is presented as the volume of gas adsorbed (at STP) against the relative pressure. The relative pressure is related to the pore size according to the Kelvin equation (Equation 3.18). All isotherms plotted are of type IV classification according to the IUPAC, which is typical of the monolayer–multilayer coverage to capillary condensation pattern. It can be seen in Figures 4.3 to 4.7 that reproducible type H2 hysteresis loops are produced, which are typical of mesoporous materials. Thus, the hysteresis loops observed indicate the presence of a mesopore network that allows capillary condensation to take place. Figure 4.3 indicates that for the different pellets studied from the same batch (within the experimental error), the nitrogen adsorption and desorption isotherms do not overlay each other for Aerosil sample. This can be attributed to batch variability as a result of slight differences in manufacturing conditions. The mass uptake ($cm^3\ g^{-1}$) of the samples in increasing order is AL3984T < AL3984T < Q17/6 < Silica Alumina < Aerosil < S980A < S980G < C30 < C10. The high uptake at relative pressures close to unity could be a result of high interaction strength between the adsorbent and adsorbate. Therefore, it can be assumed that the high uptake observed in sample C10 sample is as a result of either bulk condensation or the big macropores, in the form of cracks that exists in the material.

Furthermore, it can be seen in Figures 4.3 to 4.7 that adsorption takes place with the filling of the smallest pores. The sudden rise after multilayer adsorption corresponds to capillary condensation. Above relative pressures, $x > 0.9$, the upper closure point of the hysteresis loop, most of the pores become filled with capillary condensate. The adsorption curves show some tendency for the cumulative nitrogen volume to level off to a plateau at the top of the adsorption curve, thereby indicating near complete mesopore filling in most samples. However, due to machine limitations on achieving relative pressures close to unity, it was not possible to cause the capillary condensation of liquid nitrogen in pores of sizes greater than mesoporosity, particularly in samples AL3992E, S980G, and Silica Alumina. During desorption, the amount desorbed does not follow the same path due to the change in the radius of curvature of the meniscus, phase transition effect, pore blocking or network effects as detailed in Section 3.2.4 (Gregg and Sing, 1982; Gelb *et al.*, 1999). Those effects were the likeliest cause of hysteresis in these isotherms which result in the creation of a threshold after which the amount desorbed decreases with reduction in

pressure finally meeting the adsorption isotherm at relative pressure, $x > 0.75$. This was followed by a desorption mechanism back to the lowest pressure possible.

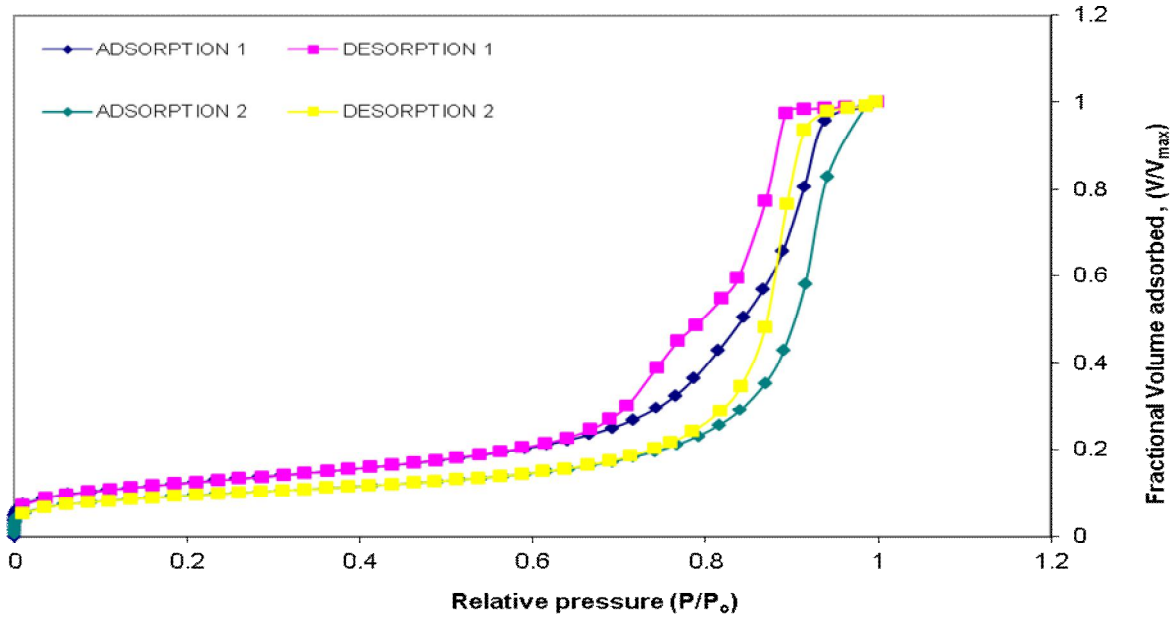

Figure 4.3

Nitrogen adsorption and desorption isotherms for Aerosil at 77 K

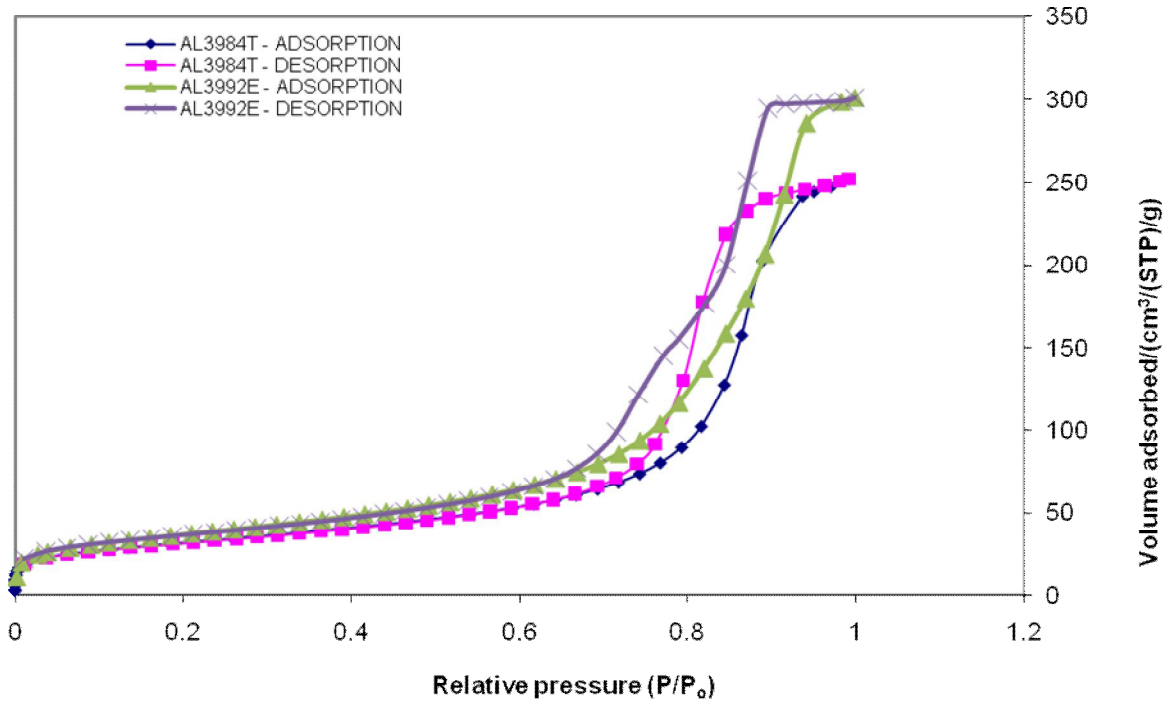

Figure 4.4

Nitrogen adsorption/desorption isotherms for AL3984T and AL3992E at 77 K

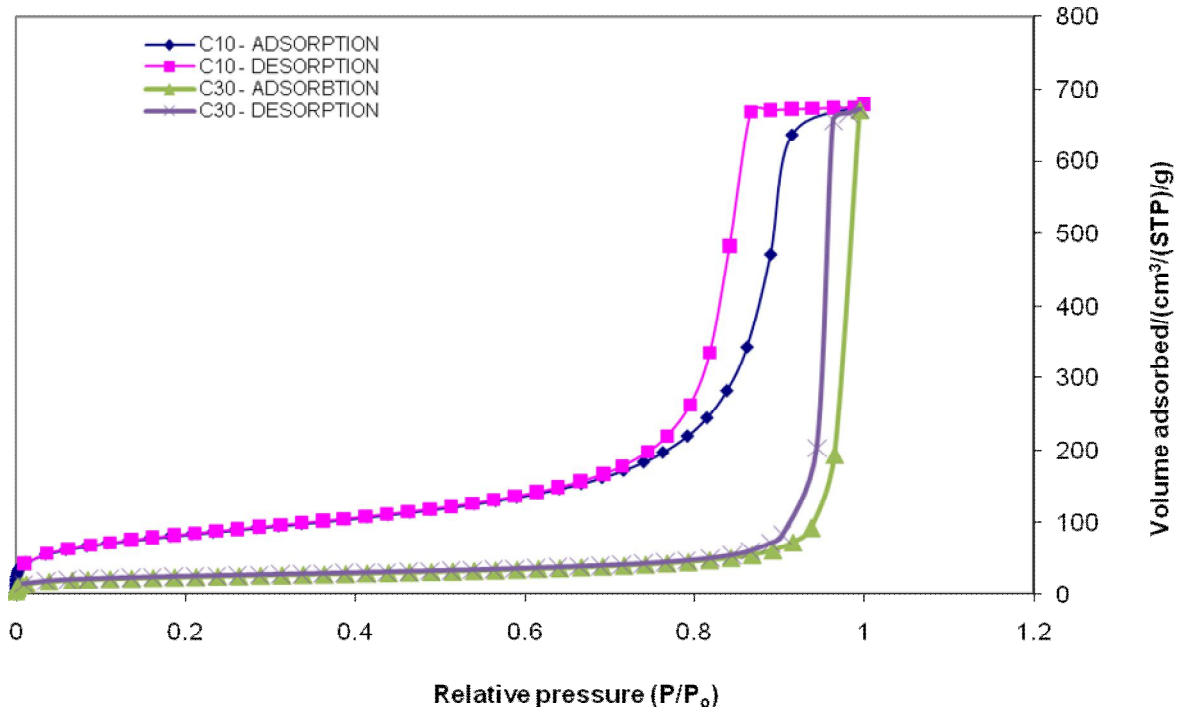

Figure 4.5

Nitrogen adsorption and desorption isotherms for C10 and C30 at 77 K

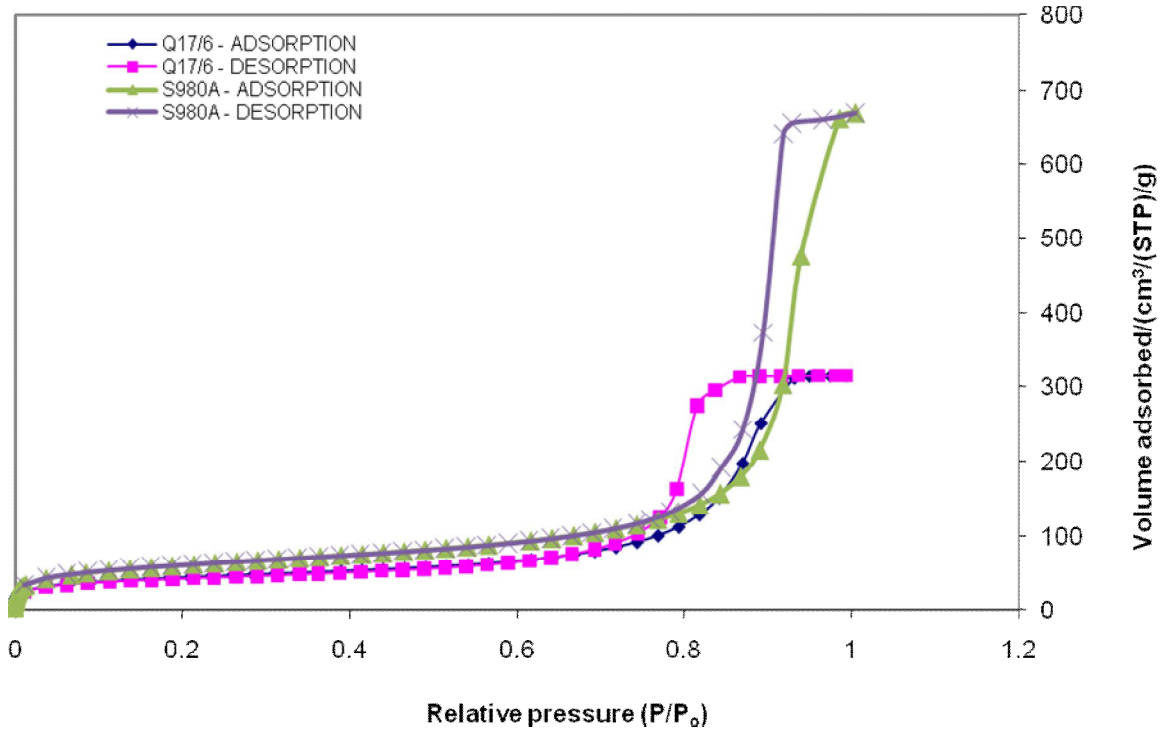

Figure 4.6

Nitrogen adsorption and desorption isotherms for Q17/6 and S980A at 77 K

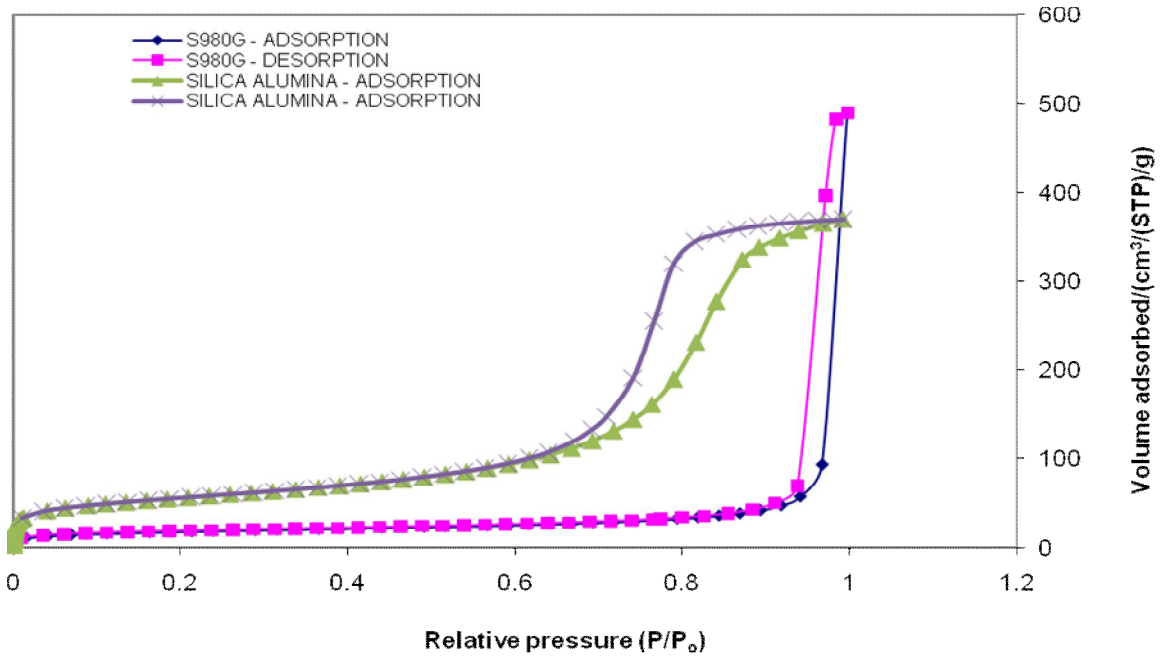

Figure 4.7

Nitrogen adsorption and desorption isotherms for S980G and Silica Alumina at 77 K

Finally, the method of measuring pore length that was proposed by Pomonis and Armatas (2004) was tested in all samples. The summary of the key findings is provided in Table 4.2. The reported uncertainties in Table 4.2 indicate the spread of the results over samples from the same batch, and the error associated with the technique. It can be seen in Table 4.2 that the slope $(\alpha - 1)$ for most of the samples is negative with the exception of samples C30 and S980G. Pomonis and Armatas (2004) method has already been discussed in Section 3.2.8. As detailed Section 3.2.8, the method cannot be used to determine the pore length. However, it can be used to determine a parameter (α) which likely demonstrates the degree of pore length. This parameter can be determined directly from the slope $(\alpha - 1)$ of Equation 3.28. Thus, according to Equation 3.28, the plot of $\log\left(\frac{S^3}{V^2}\right)$ against $\log(r_i)$ provides a line, with a slope $(\alpha - 1)$, and an intercept $(8\pi kN)$. It can be seen Figures 4.8 to 4.15, the plots for this study are suitable for the following pore size range, 6.485 - 106.18 nm. A respectable degree of linearity was obtained for these plots. For simplification, a coefficient of determination $(R^2) \geq 0.95$ has been adopted for the analysis of the slope $(\alpha - 1)$ values. The rest of the plots of the samples can be found in Appendix A4.

Table 4.2

The average anisotropy parameters and standard error obtained from nitrogen BJH adsorption algorithm of the samples

Sample	Pore size range (nm)		Coefficient of determination, R^2		Slope		Intercept	
	_		_		α-1		8πkN	
	Set 1	Set 2	Set 1	Set 2	Set 1	Set 2	Set 1	Set 2
Aerosil	6.485 - 106.18	6.485 - 106.18	0.9827	0.9575	-3.855 ± 0.26	-3.824 ± 0.4	21.44 ± 0.32	21.51 ± 0.48
AL3984T	6.26 - 29.05	6.385 - 31.62	0.9559	0.9586	-4.069 ± 0.44	-5.055 ± 0.52	20.68 ± 0.48	22.32 ± 0.59
AL3992E	N/S	N/S	N/S	N/S	N/S	N/S	N/S	N/S
C10	N/S	0.86 - 5.95	N/S	0.9701	N/S	-2.059 ± 0.08	N/S	19.77 ± 0.03
C30*	N/S	5.805 - 26.89	N/S	0.9749	N/S	1.249 ± 0.12	N/S	15.6 ± 0.13
Q17/6	6.33 - 27.18	N/S	0.9651	N/S	-4.635 ± 0.44	N/S	22.22 ± 0.48	N/S
S980A	N/S	0.09 - 0.45	N/A	0.9798	N/S	-0.29 ± 0.01	N/S	18.63 ± 0.01
S980G*	N/S	6.405 - 29.43	N/A	0.9649	N/S	1.514 ± 0.14	N/S	14.47 ± 0.2
Silica Alumina	0.545 - 3.08	6.805 - 120.13	0.978	0.9655	-4.609 ± 0.31	-3.641 ± 0.31	17.21 ± 0.08	20.83 ± 0.41

Note

Set 1 and 2 represent the replicate measurements

*** Samples with positive slopes**

N/S – Model not suitable for the set of data

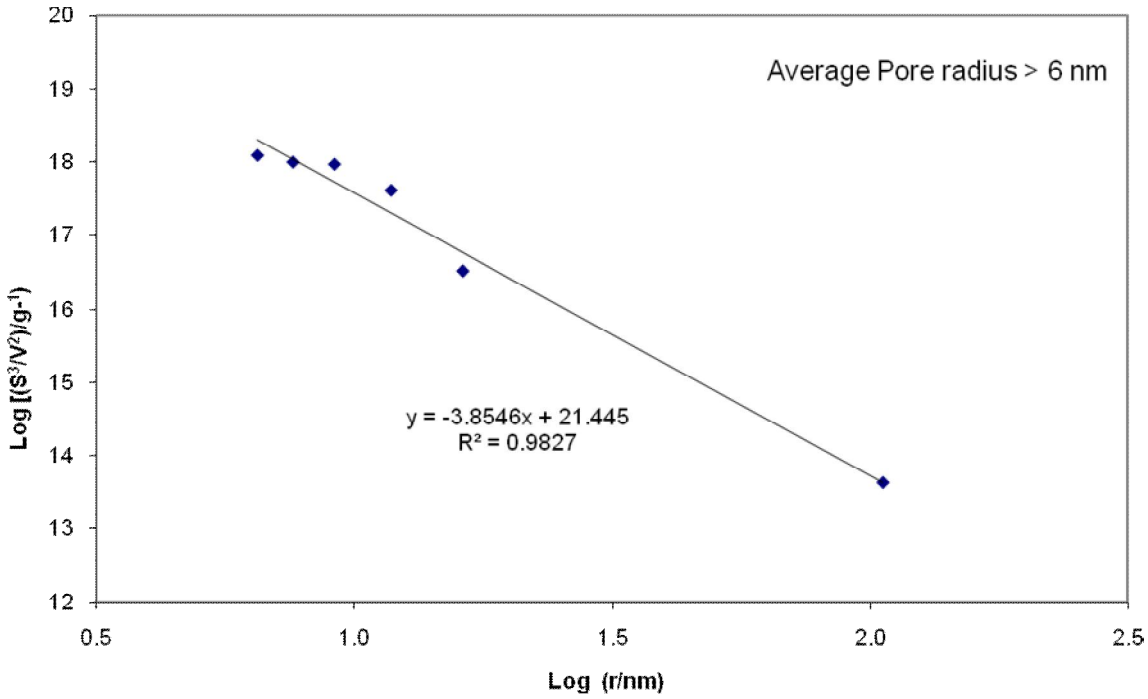

Figure 4.8

Variation of the parameter $\log(\lambda_i)$ as a function of pore radius $\log(r_i)$ for Aerosil

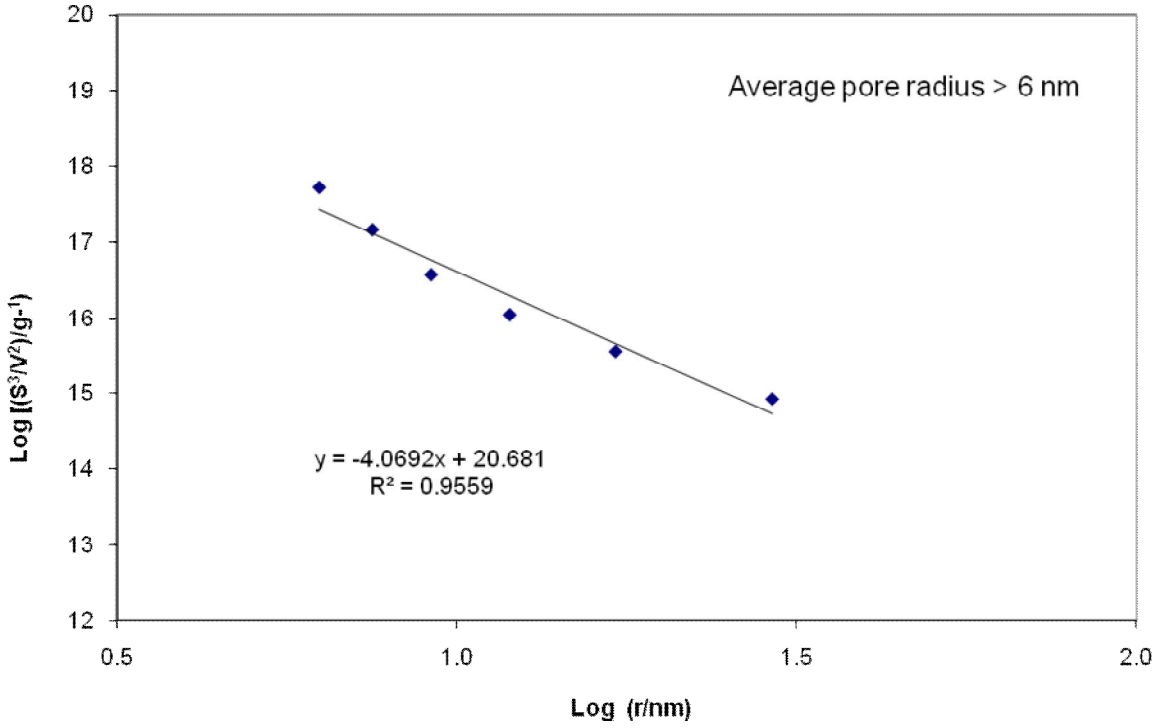

Figure 4.9

Variation of the parameter $\log(\lambda_i)$ as a function of pore radius $\log(r_i)$ for AL3984T

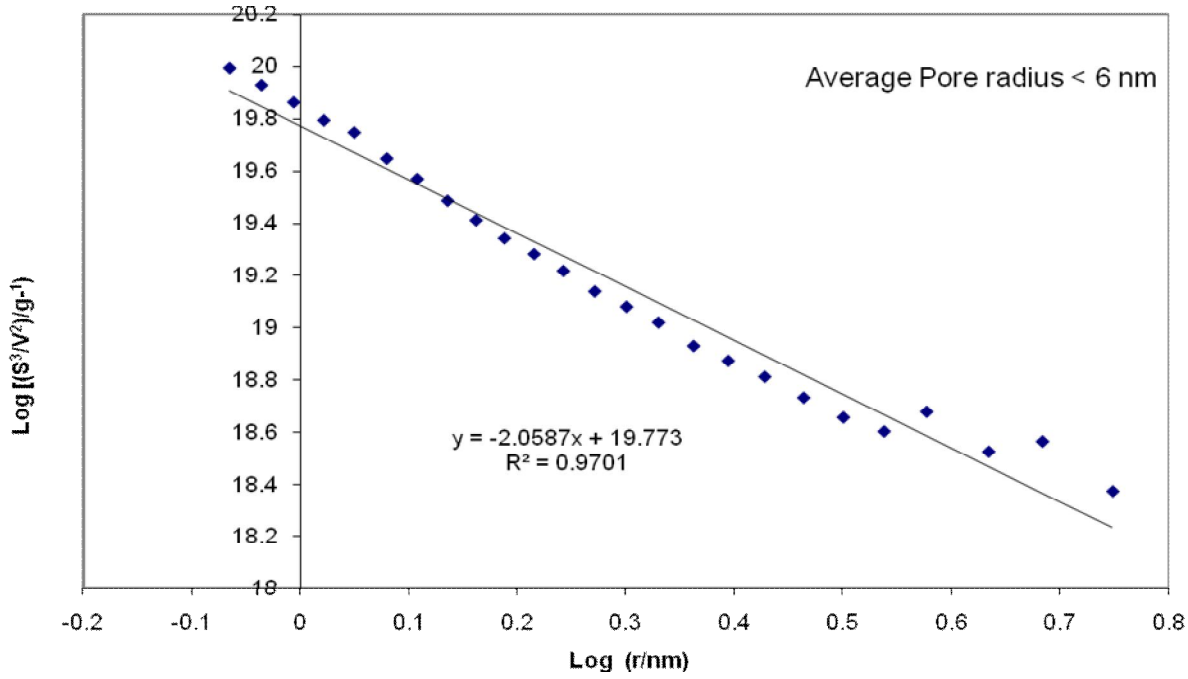

Figure 4.10

Variation of the parameter $\log(\lambda_i)$ as a function of pore radius $\log(r_i)$ for C10

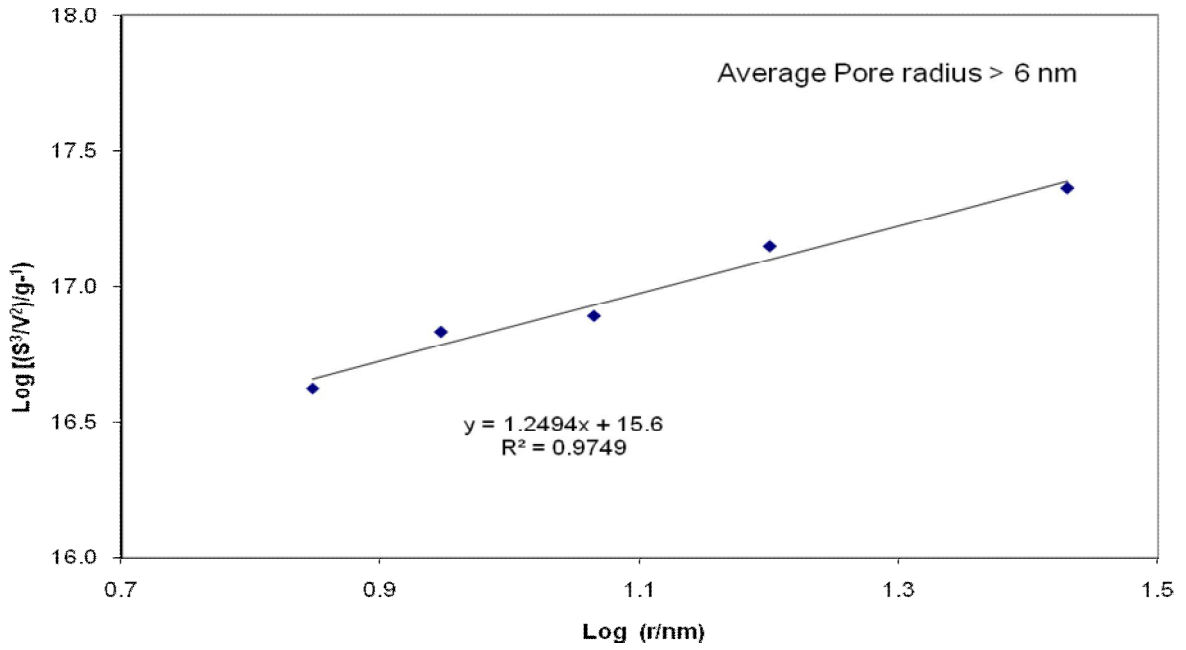

Figure 4.11

Variation of the parameter $\log(\lambda_i)$ as a function of pore radius $\log(r_i)$ for C30

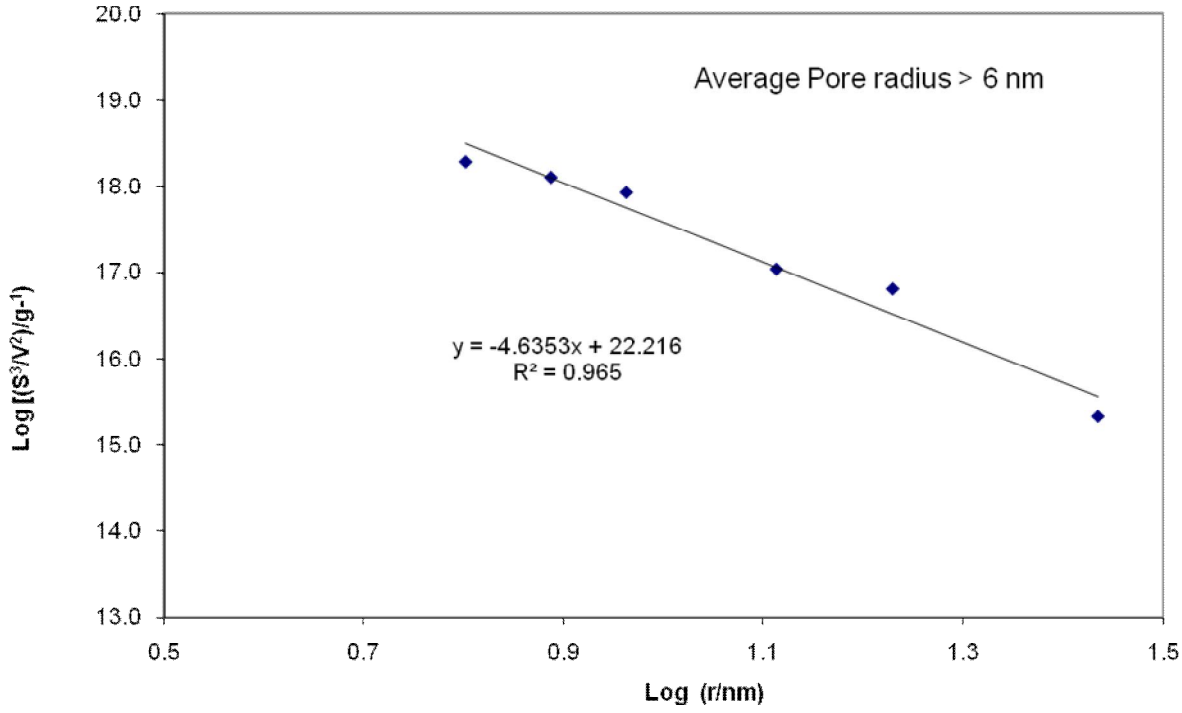

Figure 4.12

Variation of the parameter $\log(\lambda_i)$ as a function of pore radius $\log(r_i)$ for Q17/6

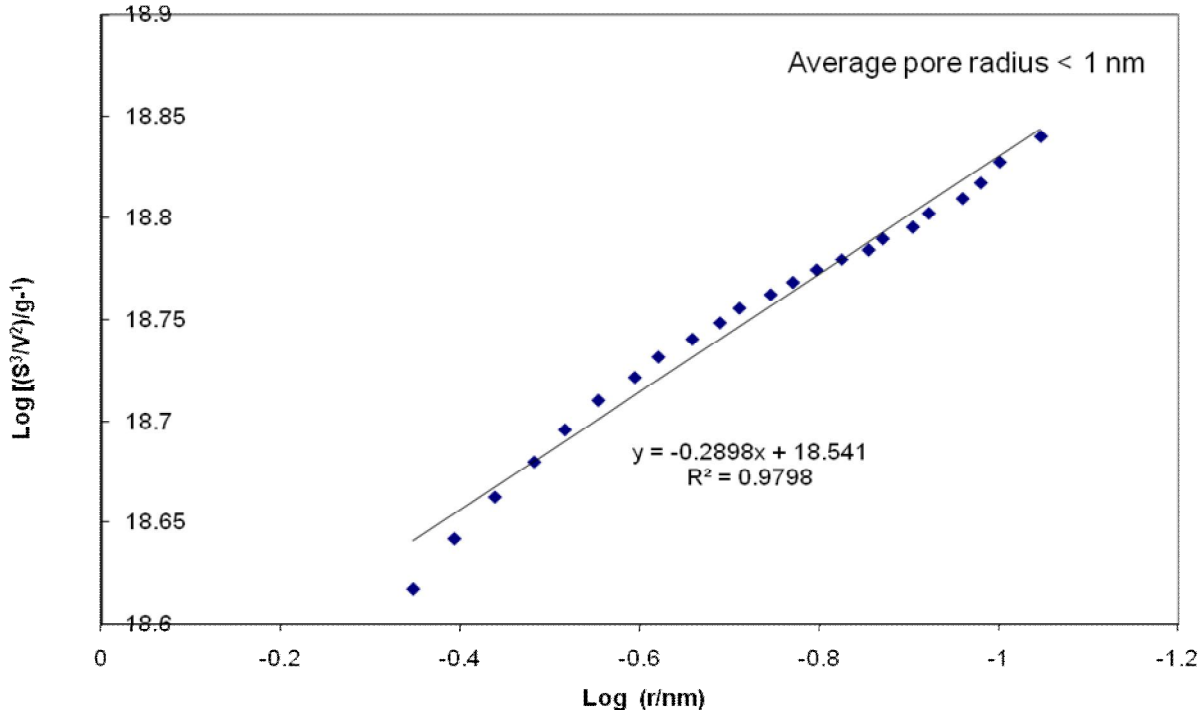

Figure 4.13

Variation of the parameter $\log(\lambda_i)$ as a function of pore radius $\log(r_i)$ for S980A

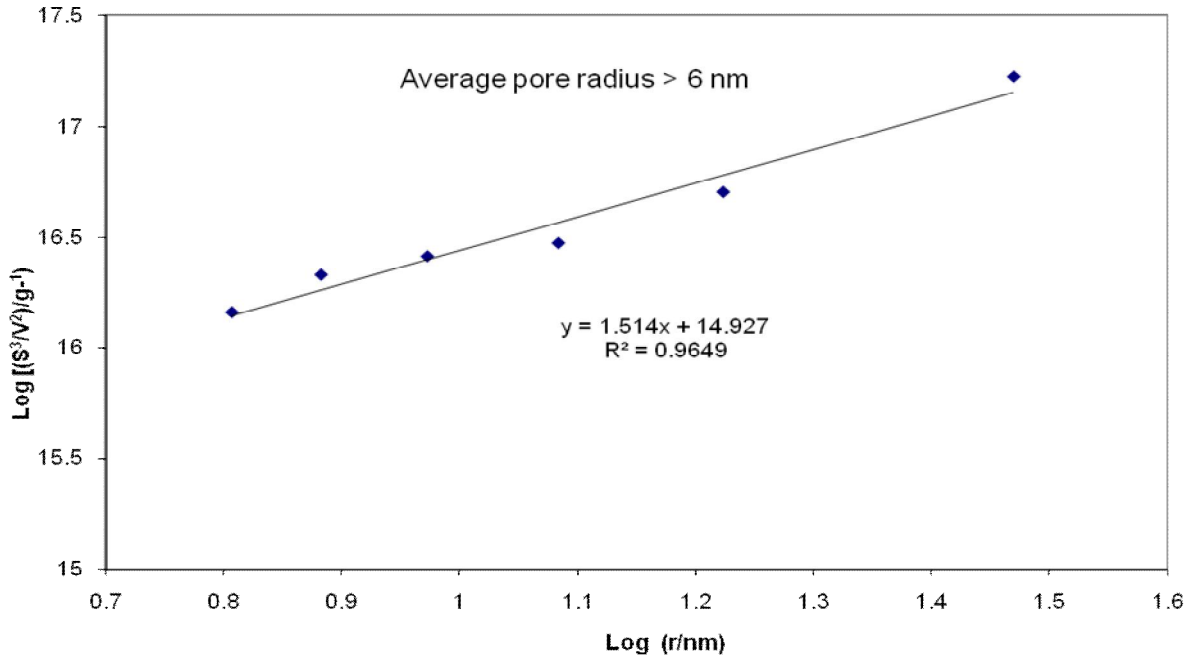

Figure 4.14

Variation of the parameter $\log(\lambda_i)$ as a function of pore radius $\log(r_i)$ for S980G

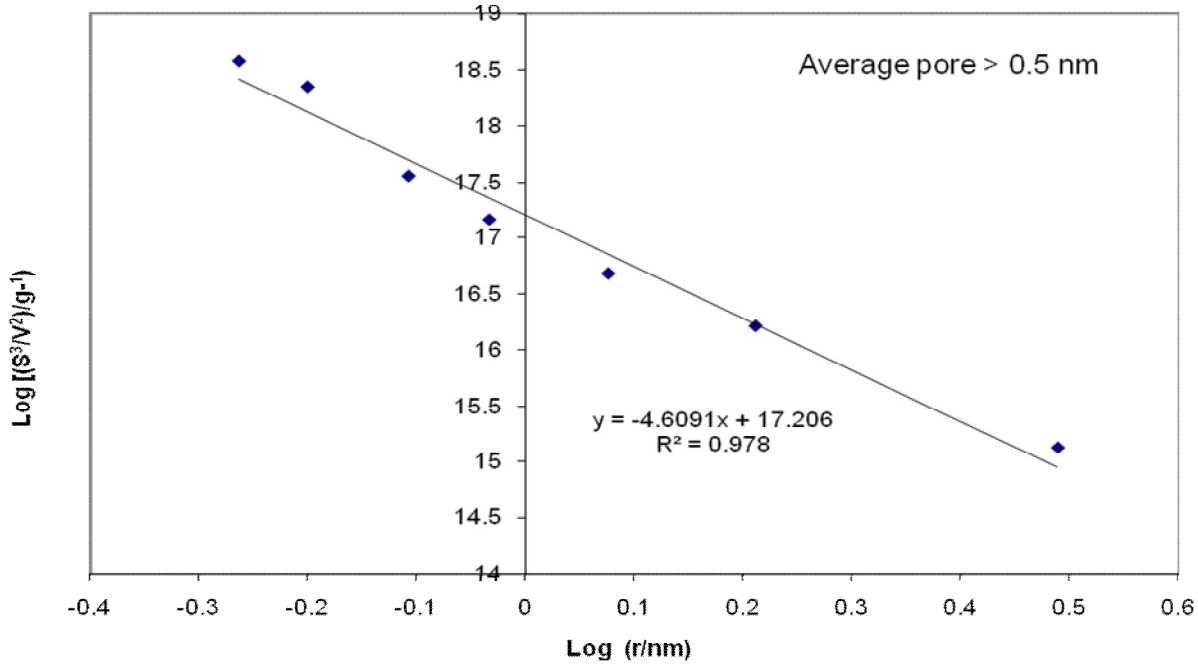

Figure 4.15

Variation of the parameter $\log(\lambda_i)$ as a function of pore radius $\log(r_i)$ for Silica Alumina

4.4 Discussion

In general, within the experimental error, for the different pellets studied from the same batch, the isotherms plotted are of type IV classification according to the IUPAC. This is typical of monolayer–multilayer coverage to capillary condensation pattern, with reproducible type H2 hysteresis loops with mesoporous materials. It should be noted that samples C30 and S980G have type H2 hysteresis loop, however, due to machine limitations; it was not possible to cause the capillary condensation of liquid nitrogen in pores of sizes greater than mesoporosity. The average pore sizes of samples C30 and S980G are considerably large and thereby explaining the observed narrower hysteresis loop with very steep and nearly parallel adsorption and desorption branches. This can be explained by the pockets of vapours left in mesopores in samples C30 and S980G at relative pressures close to unity.

As detailed in Section 3.2.4, the characteristic feature of the hysteresis loops is associated with certain pore structures (Sing *et al*., 1985; Allen, 1998; Rouquerol *et al*., 1999). Therefore, most of the pore structures, of the samples examined, have interconnected network of pores with different sizes and shapes, such as the ink-bottle type pores. As detailed in Section 3.2.3, the concept of pore blocking in ink-bottle type pores was successfully employed to describe the type H2 hysteresis loops (Everett, 1967; Ravikovitch *et al*., 2002; Soos *et al*., 2007). Pore blocking was reported to only take effect when the neck diameter is greater than a certain characteristic size of ~ 4 nm. In contrast, Ravikovitch *et al*. (2002) and Thommes *et al*. (2006) revealed spontaneous evaporation caused by cavitation of the stretched metastable liquid in spherical pores of ~ 15 nm. In this study, the desorption branch of the isotherm meet desorption isotherm at relative pressures, $x > 0.7$, and as result, rules out the possibility of cavitation-controlled evaporation process. However, for Silica Alumina sample, the desorption branch of the isotherm, meet desorption isotherm at relative pressures, $x < 0.7$, and thus, there is a possibility of cavitation-controlled evaporation process in this sample.

It can be seen in Table 4.1 that most of the samples have strong interactions between the adsorbate and adsorbents $(c > 100)$. It is likely the surface of these samples exhibit high polarity causing nitrogen molecules to adsorb strongly due to its quadruple moment on

certain sites relative to others masking the effect of monolayer formation. As detailed in Section 3.2.3, Rigby and co-workers (2004; 2009) observed similar findings for some of the samples investigated in this study. Therefore, for a cylindrical pore with a narrower neck, capillary condensation could occur by two means. The first being, both cylindrical meniscuses filling at the individual x, determined by the Kelvin equation (Equation 3.18). In the case of advanced condensation effects, both body and throat filling at the filling pressure of the throat exceeds the pressure required to fill the body with a hemispherical meniscus. As detailed in Section 3.2.3, Neimark (1991) argued that condensation in a narrow pore might result in the formation of an unstable vapour-liquid interface in the adjacent wider pore that would cause spontaneous condensation in the latter prior to achievement of the limit of metastability of adsorption films. This effect of initiated capillary condensation or advanced condensation may trigger an avalanche filling of the pore network. As a result, the observed PSD is narrower than it exists in reality for most of the samples investigated in this study.

The connectivity characterization method developed by Seaton (1991) was successfully tested on these samples. As detailed in Section 3.2.7, Liu *et al*. (1992) showed that the assumption of pore geometry has a significant effect on the mean coordination number (Z). As the exact pore shapes of the samples are unknown, a cylindrical shaped pore model was assumed in this study. It should be noted that Seaton (1991) assumed the same pore shape for connectivity analysis. As mentioned earlier in this Section, the isotherm plots are of type IV with reproducible type H2 hysteresis loops according to the IUPAC classification. However, some of the samples isotherms were incomplete, and thus, the largest pores still contained vapour at x = 1. As detailed in Section 3.2.7, the connectivity characterization method developed by Seaton (1991) requires an isotherm that has all the characteristics necessary for calculating the PSD by a Kelvin equation based method such as the one suggested by Barrett *et al*. (1951). Seaton's (1991) method was particularly robust for samples Aerosil, AL3984T, C10, Q17/6, and S980A. Similar connectivity parameters were obtained for a range of silica and alumina materials investigated by Seaton (1991), Liu *et al*. (1992), and Rigby *et al*. (2004). It should be noted that the connectivity parameters in conjunction with the variance of the PSD will be used to elucidate the transport phenomena, especially the mechanism of mercury entrapment that will be investigated in Chapter 5.

The Pomonis and Armatas (2004) method for estimating the pore length of porous solids was initially developed and tested on MCM materials. These MCM materials generally have long cylindrical pores with well defined length and diameter (Kresge *et al*., 1992). In contrast, the samples tested in this study are probably associated with a random pore network, and thus, it might be difficult to measure the cylindrical geometrical parameters. However, microphotograhic images showed that traditional porous materials such as the silica and alumina have pores with diameters that are nearly close to their length (Dullien, 1992). In addition, various observations made by electron microscopy have shown that many traditional porous materials appear to be random collection of packed spherical and semi-spherical particles as well as cylinders (Drewry and Seaton, 1995). Therefore, it is safe to suggest that the method proposed by Pomonis and Armatas (2004) for measuring the pore length parameter (α) is suitable for the samples tested in this study.

The method proposed by Pomonis and Armatas (2004) was successfully tested on the samples in this study. The BJH adsorption algorithm was used to obtain the PSD of the samples. The plot of $\log\left(\frac{S^3}{V^2}\right)$ against $\log(r_i)$ produced a straight line with a slope, $(\alpha - 1)$, and intercept, $8\pi kN$. In general, the plots were robust for a particular pore size range (6.485 - 106.18 nm). However, as detailed in Section 3.2.8, the method cannot be used to estimate the pore anisotropy, *b*, in porous solids, and thus the pore-length cannot be determined from the power law correlation in Equation 3.29. The failure of the method to estimate the pore anisotropy, *b*, is due to the fact that, the intercept, $8\pi kN$, has an unknown parameter, k. The unknown parameter k (unit in grams) is from the power law correlation in Equation 3.29. As detailed in Section 3.2.8, Rigby *et al*. (2004) also encountered similar problems with power law correlation in their pore length determination approach. The typical pore lengths obtained by Rigby *et al*. (2004) were of the order of several micrometres. Rigby *et al*. (2004) thought the values were unrealistically large for a single mesopore in an amorphous material. Therefore, it is safe to connect the failure for estimating pore length of these samples from nitrogen sorption data to the power law correlation in Equation 3.29. However, the pore length parameter (α) obtained from the power law in Equation 3.29 can be used for the pore length analysis of these samples.

It can be seen in Table 4.2 that the pore length parameters (α) obtained for the silica samples are close to or greater than zero. As detailed in Section 2.3, the manufacturing conditions of silica materials make them highly heterogeneous with different pore shapes and wide pore size distributions. Therefore, these materials might have a combination of several long cylindrical pores and ink-bottle type pores. For example, the pore length parameter (α) of samples C30 and S980G are 2.249 and 2.514, respectively. By using the power correlation in Equation 3.29, it can be said that these samples would have long cylindrical pores depending on the size of k. As detailed in Section 3.2.8, Dullien (1992) observed similar findings in samples with random porous network with $b_i \sim 1$ $(l_i \sim d_i)$, and thus, the pores were assumed to be isotropic by these researchers. In contrast, Dullien (1992) observed shallow cavities rather than typical pores in samples with random porous network with $b_i < 1$. For example, the pore length parameter (α) of sample AL3984T is -4.055. By using the power correlation in Equation 3.29, it can be said that this sample would have short pores depending on the size of k. As detailed in Section 2.3, the manufacturing conditions of alumina materials results in a well defined pore structure forms, and thus, alumina materials are less heterogeneous than silica materials. Therefore, it can be concluded that the pore length parameter (α) is sensitive to the method of production of these materials. In general, the heterogeneous silica materials, such as samples C30 and S980G have large positive slope values. In contrast, the alumina materials such as samples AL3984T have a very negative slope values. As a result, it is safe to deduce that pore length parameter (α) is suitable for measuring heterogeneity of porous materials such as the silica and alumina materials investigated in this study.

4.5 Conclusion

Gas adsorption studies carried out on all samples revealed isotherms of type IV classification, according to the IUPAC, which is typical of the monolayer–multilayer coverage to capillary condensation pattern, with reproducible type H2 hysteresis loops. In general, the Type H2 hysteresis loop has been traditionally ascribed to a collection of ink-bottle type pores which are susceptible to pore-blocking phenomena. Most of the samples have strong interactions between the adsorbate and adsorbent, and thus are susceptible to advanced condensation phenomena that will result in a narrow PSD than it exists in reality.

The connectivity parameters estimated using Seaton's (1991) method was found to be robust on porous alumina and silica materials. These values were in the range of 2.7± 0.3 to 6.35 ± 2.65. In contrast, a consideration of the method of estimating pore length proposed by Pomonis and Armatas (2004) suggested had severe limitations due to the inability to measure pore length of the samples. Nevertheless, a measure of the pore length (α) was derived from the method. It was concluded that slope (α) from the power law correlation in Equation 3.29 can be used to estimate the degree of pore length and heterogeneity of the samples in this study.

4.6 References

Allen, T., 1999. *Particle size measurement.* Dordretch, The Netherlands: Kluwer Academic publishers.

Barrett, E. P., Joyner, L. G., Halenda, P. P., 1951. The determination of pore volume and area distributions in porous substances. I. Computations from nitrogen isotherms, *J. Am. Chem. Soc*., 73, 373–380.

Brunauer, S., Emmett, P. H., and Teller, E. 1938. Adsorption of Gases in Multimolecular Layers. *Journal of the American Chemical Society*, 60, 309-319.

Dullien, F.A.L., 1992. *In porous media; Fluid transport and pore structure.* 2nd edition. New York: Accademic press.

Drewry, H. P. G., and Seaton, N. A., 1995. Continuum random walk simulations of diffusion and reaction in catalyst particles. *AIChE Journal*, 41: 880–893

Evbuomwan, O.E., 2009. *The structural characterisation of porous media for use as a model reservoir rocks, adsorbents and catalyst.* Thesis (PhD). University of Bath.

Everett, D.H., 1967. *The Solid-Gas Interface*. Edited by E. A. Flood. New York: Marcel Decker

Gelb, L. D., Gubbins, K. E., Radhakrishnan, R., and Sliwinskabtkowiak, M., 1999. Phase separation in confined systems. *Reports on Progress in Physics*, 62, 1573-1659.

Gregg, S. J., and Jacobs, J. 1948. An examination of the adsorption theory of Brunaeur, Emmett & Teller and Brunaeur, Deming, Deming & Teller. *Trans. Faraday Soc*. 44, 575.

Kresge, C.T., Leonowicz, M.E., Roth, W.J., Vartuli, J.C., Beck, J.S., 1992. Ordered mesoporous molecular sieves synthesized by a liquid crystal template mechanism. *Nature*, 359, 710-712.

Liu, H., Zhang, L., Seaton, N.A., 1992. Determination of the connectivity of porous solids from nitrogen sorption measurements-II. Generalisation. *Chemical Engineering Science*, 47(17-18), 4393-4404.

Neimark, A.V., 1991. Percolation theory of capillary hysteresis phenomena and its applications for characterization of porous solids. *Studies in surface science catalysis*, 62, 67-74.

Pomonis, P.J., and Armatas, G.S., 2004. A method of estimation of pore anisotropy in porous solids. *Langmuir*, 20, 6719-6726.

Ravikovitch, P. I., and Neimark, A. V., 2002. Experimental confirmation of different mechanisms of evaporation from Ink bottle type Pores: equilibrium, pore blocking and cavitation, *Langmuir*, 18, 9830-9837.

Rigby, S.P., Gladden, L.F., 1998. The use of magnetic resonance images in the simulation of diffusion in porous catalyst support pellets. *Journal of Catalysis*, 173 (2), 484-489.

Rigby, S.P., Watt-Smith, M.J., Fletcher, R. S., 2004. Simultaneous determination of the pore-length distribution and pore connectivity for porous catalyst supports using integrated nitrogen sorption and mercury porosimetry. *Journal of catalysis*, 227 (1), 68-76.

Rouquerol, F., Rouquerol, J., and Sing, K., 1999. *Adsorption By Powders And Porous Solids Principles, Methodology And Applications*. London: Academic Press.

Seaton, N.A., 1991. Determination of the connectivity of porous solids from nitrogen sorption measurements. *Chemical engineering science*, 46 (8), 1895-1909.

Sing, K.S.W., Everett, D.H., Haul, R.A.W., Moscou, L., Pierotti, R.A., Rouquerol, J. and Siemieniewska, T., 1985. Reporting physisorption data for gas solids systems with special reference to the determination of surface area porosimetry and porosity (recommendation 1984). *Pure and applied chemistry*, 57, 603-619.

Soos, M., Rajniak, P., and Stepanek, F., 2007. Percolation model of adsorption-desorption equilibria with hysteresis. *Colliods and surfaces A-Physicochemical and engineering aspects*, 300(1-2), 191-203.

Thommes, M., Smarsly, B., Groenewolt, M., Ravikovitch, P.I., Neimark, A.V., 2006. Adsorption hysteresis of nitrogen and argon in pore networks and characterization of novel micro- and mesoporous silicas. *Langmuir*, 22, 756 -764.

5.0 Mercury porosimetry technique

[Study of entrapment of non-wetting fluids within porous media]

5.1 Introduction

The principles and the applications of mercury porosimetry have been discussed in Section 3.3. In addition, the proposal for the research programme can be found in Section 3.3.5. This Chapter introduces mercury porosimetry and the experimental conditions. The AutoPore III 9420 mercury porosimeter used in this section covers the pore size ranging from approximately 0.003 to 360 μm. As detailed in Section 3.3.3, recent studies on silica catalyst support pellets have shown that the physical processes and mechanisms involved in mercury retraction are sensitive to the equilibration time-scale used (Rigby *et al.*, 2006; 2008). In this Chapter, the variation in quantities and spatial arrangements of entrapped mercury ganglia, within a range of porous alumina and silica samples, was examined over different equilibration time-scales. The experiments were performed in the stepwise experimental mode with various equilibration time-scales ranging from 0 to 100 s at each pressure value. Therefore, traditional pore structure parameters such as the pore size, pore volume, surface area, porosity, and mercury entrapment were obtained over different equilibration time-scales. Furthermore, in order to understand the origin of entrapment and hysteresis, the semi-empirical alternative correlations to the standard Washburn equation were used for the interpretation of raw mercury porosimetry data.

5.2 Mercury porosimetry and experimental considerations

The AutoPore III 9420 mercury porosimeter is designed to perform low pressure analysis of four samples at one time. The equipment is designed to perform two high pressure analyses at the same time. The equipment measures the intruded volume in relation to the mass of the sample at a specific pressure; this pressure can be converted to an equivalent Laplace diameter according to Equation 3.31. The amount of mercury intruded is determined by the fall in the level of the interface between the mercury and the compressing fluid. A value of 0.485 Nm^{-1} at 25 $^{\circ}C$ is generally accepted for surface tension

and a fixed value of 130° for the contact angle, and thus, these values were adopted in this study. If less than four samples were to be analysed, a blank rod must be installed in the unused low pressure ports. Vacuum conditions cannot not be achieved if penetrometers or blank rods are not installed in an unused pressure ports.

Porous materials are prone to adsorb water or other chemicals, and therefore the sample has to be cleared of these contaminants before the analysis by heating. The purpose of the thermal pre-treatment for each particular sample was to drive any physisorbed water on the sample leaving the morphology of the sample itself unchanged. As detailed in Section 4.3, a pre-treatment condition of 250 °C for 4 hours used by Evbuomwan (2009) was adopted for this study. For analysis, a powder penetrometer (3cc powder) was used due to the small physical size of the materials. The weight of the empty sample flask was registered prior to introducing the sample. The sample (~ 0.7 g) was loaded into the penetrometer, which consisted of a sample cup connected to a metal-clad, precision-bore, and glass capillary stem. A vacuum tight seal (Apiezon H) was used to fill the inevitable roughness of the ground glass lip and polished surface. Care was taken when applying the grease as too much grease exposes the sample to an unwanted coating, whilst too little grease results in an imperfect seal.

The penetrometers were sealed with spacers over the stem and placed in low pressure ports, where the sample was evacuated to remove air and moisture. The sample cell was evacuated and filled with mercury while the entire system was still under reduced pressure. The first data point was taken at a pressure of 3000 to 4000 Pa or higher. At the end of the low pressure analysis, the weight of the penetrometer filled with mercury and sample was determined by the machine. The measured value determines the bulk density of the sample by using corresponding blank-runs as a reference. Once the pre-weighed sample from the low pressure analyses port was transferred to the high pressure system, the sample and the injected mercury from the low pressure system was surrounded by hydraulic fluid and pressurised up to 414 MPa. Both chambers were tightly closed and had sufficient high pressure fluid drawn into the vent valve. If the fluid was above the visible ledge level, excess fresh fluid was removed to bring the level to the ledge.

In order to calculate the true volume intrusion of mercury into the pores of a sample, a correction was made to account for the compression of mercury, sample cell and sample. Compressibility $\left(\beta^0\right)$ is the fractional change in volume per unit pressure change and therefore a major effect that has to be addressed (Giesche, 2006). Ideally, this problem can be corrected by a corresponding blank run using a non-porous sample of the same material. However, the blank run does not always solve the problem as encountered in the course of the experiments. One of the adjustments made in this study was to create separate blank runs with the same respective equilibration time as those used in the sample analysis.

5.3 Results and analysis

A range of porous alumina and silica pellets of spherical or cylindrical geometry was investigated. In order to allow for the variation of support structure between pellets of the same batch and to test the reproducibility of measurements, replicate measurements were made for all samples. Sets 1 to 4 represent the replicate measurements in each case. Therefore, the reported parameters in this section are the mean of the sets used. In order to determine whether the length of this equilibration time-scale had any effect on the shapes of the intrusion and/or extrusion curves, and the level of mercury entrapment, separate mercury porosimetry experiments were conducted on different samples from the same batch with different equilibration time-scales, but always using the same pressure table. After each pressure change, the volume of mercury within the sample was then allowed to come to equilibrium over a period of time. The equilibration time at each of the increasing applied pressures of mercury was set at 0 s, 10 s, 30 s, 50 s, and 100 s, respectively.

The mercury porosimetry results of samples obtained from the intrusion and extrusion curves at different equilibration time-scales are presented in Tables 5.1 to 5.9. The reported uncertainties indicate the spread of the results over pellets from the same batch and the error associated with the technique. It can be seen from the results obtained at each successive equilibration time, that there is a little batch variability within the pellets investigated. In addition, it can be seen from Tables 5.1 to 5.4, that there was no significant difference to the entrapment found at different equilibration time-scales for the samples AL3984T, AL3992E, P7129, and Silica Alumina. In contrast, it can be seen in Tables 5.5 to 5.8 that the entrapment decreased with an increased equilibration time-scales in samples

C10, C30, Q17/6, S980A, and S80G. Furthermore, it can be seen from Tables 5.6 and 5.7 that there was a great deal of variability occurring with respect to equilibration time-scales in samples C30 and Q17/6. The mercury entrapment found in these particular samples was the highest and varied substantially with equilibration time-scales.

The pore diameter was obtained by using the Washburn equation (Equation 3.31). An estimate of the total pore volume of the sample accessible to mercury porosimetry may be obtained from the mercury intrusion curve. The total pore volume is the total volume of intruded mercury at high pressure and the total surface area was calculated by performing integration over the intrusion curve as illustrated by Rootare and Prenzlow (1967). The intruded mesopore volume in the intrusion/extrusion curves is the difference of volume of mercury entering the sample between the end of the low flat plateau (separating interparticle and intraparticle intrusion) and the ultimate intrusion volume. An estimate of the total mercury trapped following depressurization was found from the mercury retraction curve. The volume of entrapped mercury determines the level of remaining open porosity. The entrapped mercury is the difference between the volume at the end of the retraction curve and corresponding pressure point on intrusion curve (separating interparticle and intraparticle intrusion).

Figures 5.1 to 5.10 show examples of raw mercury intrusion and retraction curves for the various equilibration times. It appears that most samples have a unimodal structure, with the exception of one bimodal structure material (AL398T). The ultimate intrusion volume is the maximum possible with the apparatus used (~ 414 MPa), which corresponds to the smallest pore diameter (~ 3.2 nm) by Washburn equation (Equation 3.31). The relatively small initial intrusion for the pellets in each data set corresponds to inter-particle intrusion. The intrusion curves for both sets of pellets exhibit a generally flat plateau, following the initial inter-particle intrusion, before intra-particle intrusion begins. The intrusion curves show some tendency for the cumulative mercury volume to level off to a plateau at the top of the intrusion curve, thereby indicating near complete mesopore filling. This was followed by retraction back to nearly atmospheric pressure (~ 0.2 MPa), which corresponds to the largest pore diameter in each data sets. It can be seen that, within the experimental error, for the different pellets studied from the same batch of different samples, the mercury intrusion and extrusion curves overlay each other at smaller mesopore radii.

Table 5.1

The average mercury porosimetry results of AL3984T data at different equilibration times. The error quoted is the standard error

Equilibration time (s)	Intrusion volume (mL/g)	Entrapment (%)	Porosity (%)	Pore diameter (nm)	Surface area (m^2/g)
10	0.397 ± 0.03	13.41 ± 0.69	54.95 ± 2.04	11.85 ± 0.15	147 ± 14.63
30	0.394 ± 0.04	15.44 ± 0.84	52.89 ± 1.81	12.25 ± 0.25	142 ± 10.13
50	0.443 ± 0.02	15.51 ± 0.80	56.50 ± 1.85	12.60 ± 0.20	154 ± 3.13

Table 5.2

The average mercury porosimetry results of AL3992E data at different equilibration times. The error quoted is the standard error

Equilibration time (s)	Intrusion volume (mL/g)	Entrapment (%)	Porosity (%)	Pore diameter (nm)	Surface area (m^2/g)
10	0.647 ± 0.03	15.30 ± 1.10	66.10 ± 18.841	9.55 ± 0.05	292 ± 14.62
30	0.656 ± 0.03	13.23 ± 0.68	66.82 ± 1.817	9.77 ± 0.12	293 ± 13.69
50	0.615 ± 0.01	12.23 ± 2.94	66.60 ± 0.815	9.50 ± 0.20	285 ± 4.87

Table 5.3

The average mercury porosimetry results of P7129 data at different equilibration times. The error quoted is the standard error

Equilibration time (s)	Intrusion volume (mL/g)	Entrapment (%)	Porosity (%)	Pore diameter (nm)	Surface area (m^2/g)
0	1.003 ± 0.07	52.788 ± 1.28	67.71 ± 4.61	8.05 ± 0.05	540 ± 31.06
10	1.045 ± 0.08	49.409 ± 1.98	69.15 ± 3.09	8.80 ± 0.01	525 ± 30.49
30	1.040 ± 0.07	50.128 ± 3.04	65.54 ± 0.00	9.10 ± 0.20	499 ± 45.89

Table 5.4

The average mercury porosimetry results of Silica Alumina data at different equilibration times. The error quoted is standard error.

Equilibration time (s)	Intrusion volume (mL/g)	Entrapment (%)	Porosity (%)	Pore diameter (nm)	Surface area (m^2/g)
10	0.498 ± 0.02	23.11 ± 0.33	60.54 ± 2.14	7.45 ± 0.05	293.399 ± 6.27
30	0.489 ± 0.03	20.04 ± 1.01	58.45 ± 4.71	7.60 ± 0.10	283 ± 11.87
50	0.489 ± 0.01	20.69 ± 2.53	60.79 ± 0.35	7.90 ± 0.01	281 ± 1.73

Table 5.5

The average mercury porosimetry results of C10 data at different equilibration times. The error quoted the standard error

Equilibration time (s)	Intrusion volume (mL/g)	Entrapment (%)	Porosity (%)	Pore diameter (nm)	Surface area (m^2/g)
0	0.978 ± 0.02	14.55 ± 0.36	66.67 ± 1.88	8.15 ± 0.05	529 ± 14.17
10	0.995 ± 0.04	11.83 ± 0.47	67.81 ± 2.16	9.00 ± 0.01	492 ± 22.60
30	0.977 ± 0.07	12.33 ± 0.85	68.37 ± 5.36	9.17 ± 0.12	471 ± 36.75
100	1.029 ± 0.05	9.46 ± 1.23	69.70 ± 3.13	9.00 ± 0.01	502 ± 26.42

Table 5.6

The average mercury porosimetry results of C30 data at different equilibration times. The error quoted the standard error

Equilibration time (s)	Intrusion volume (mL/g)	Entrapment (%)	Porosity (%)	Pore diameter (nm)	Surface area (m^2/g)
0	1.031 ± 0.04	66.49 ± 1.57	68.83 ± 3.06	27.08 ± 1.77	173 ± 19.65
10	1.033 ± 0.04	26.76 ± 4.12	70.51 ± 3.06	27.90 ± 2.07	167 ± 18.89
30	1.042 ± 0.04	16.14 ± 2.71	67.94 ± 0.70	28.10 ± 1.81	166 ± 16.50
50	0.853 ± 0.16	26.46 ± 6.45	56.45 ± 10.24	32.45 ± 2.25	119 ± 30.62
100	1.078 ± 0.05	3.45 ± 0.23	70.51 ± 3.43	26.80 ± 2.37	148 ± 24.02

Table 5.7

The average mercury porosimetry results of Q17/6 data at different equilibration times. The error quoted is the standard error

Equilibration time (s)	Intrusion volume (mL/g)	Entrapment (%)	Porosity (%)	Pore diameter (nm)	Surface area (m^2/g)
10	0.447 ± 0.01	52.14 ± 6.26	49.06 ± 1.49	6.70 ± 0.10	293 ± 9.30
30	0.457 ± 0.01	39.49 ± 5.66	50.69 ± 5.99	7.57 ± 0.03	269 ± 3.79
50	0.461 ± 0.02	20.26 ± 5.21	48.53 ± 1.73	7.65 ± 0.07	272 ± 61.67

Table 5.8

The average mercury porosimetry results of S980A data at different equilibration times. The error quoted is the standard error

Equilibration time (s)	Intrusion volume (mL/g)	Entrapment (%)	Porosity (%)	Pore diameter (nm)	Surface area (m^2/g)
30	0.794 ± 0.05	14.026 ± 0.68	62.547 ± 2.88	11.60 ± 0.30	300 ± 8.84
50	0.818 ± 0.05	12.549 ± 1.16	63.424 ± 0.55	12.00 ± 0.50	298 ± 4.47
100	1.070 ± 0.05	9.361 ± 0.89	72.345 ± 3.95	12.60 ± 0.30	373 ± 28.90

Table 5.9

The average mercury porosimetry results of S980G data at different equilibration times. The error quoted is the standard error

Equilibration time (s)	Intrusion volume (mL/g)	Entrapment (%)	Porosity (%)	Pore diameter (nm)	Surface area (m^2/g)
10	0.769 ± 0.05	18.15 ± 1.91	60.25 ± 1.42	38.15 ± 2.15	90 ± 5.48
30	0.958 ± 0.05	6.09 ± 1.16	77.24 ± 5.11	22.50 ± 3.30	192 ± 29.81
50	0.903 ± 0.05	15.18 ± 0.73	72.41 ± 0.26	26.75 ± 0.95	144 ± 1.03

It can be seen from Figures 5.1 to 5.10 that the initial part of the mercury retraction curves all exhibit a similar, almost horizontal plateau. There is virtually no change in mercury volume until after ~ 50 MPa (~ 22 nm), which was followed by a steep decrease in mercury volume in most samples. The hysteresis between the intrusion and extrusion curves occurs at larger mesopore radii, and some mercury entrapment is observed for all equilibration time-scales used. It can be seen from Figures 5.3, 5.4, 5.5, 5.8 and 5.10 that the hysteresis and entrapment are slightly sensitive to the variation in equilibration time in samples C10, S980A, S980G, C30 and Q17/6. At lower pressures, the amount of entrapped mercury decreases slightly as the sample equilibration time is increased. Figure 5.9 shows the raw mercury intrusion and retraction curves for the various equilibration times used for sample C30 analysed by using the semi-empirical correlations of Rigby and Edler (2002). It can be seen from Figure 5.9 that, within the experimental error, for the different pellets studied from the same batch of sample C30, the correlation leads to superposition of the intrusion and retraction curves at low pore sizes, within the residual of ~ 4-5 %, due to the experimental error in the correlation. The same superposition of the intrusion and retraction curves at low pore sizes were obtained in the rest of the samples. The semi-empirical correlations plots of the rest of the samples can be found in the Appendix (A5).

Figures 5.8 and 5.10 show the raw mercury intrusion and retraction curves for samples C30 and Q17/6 indicating the pressure steps where the volumes extruded became sensitive to equilibration time-scales. The vertical lines define the pressure steps featured in Figures 5.8 and 5.10. Figure 5.11 shows the variation of the volume of mercury lost with the square root of the experimental equilibration time for step 1 in Figure 5.10, and it also shows a best fit straight line to these data. Rigby *et al.* (2008) have previously investigated sample C30, and thus, only sample Q17/6 was investigated in this study. The initial part of the retraction curve, particularly the first sharp knee in Figures 5.8 and 5.10 are all independent of experimental time scales. It can be seen in Figure 5.11 for step 1, that the average variation of the volume of mercury leaving sample Q17/6 during step 1 with the square root of equilibration time gives rise to a good fit to a straight line. The pressure step for step size, ΔP, for step 1 was typically 44 MPa and the average radius of the pores emptying during step 1 was 2.7 nm, which were determined by using the semi-empirical correlation by Rigby and Edler (2002). The viscosity at 25 °C is 1.5×10^{-3} Pa s, and thus, from Equation 4.5, the distance moved by a mercury meniscus in 30 s is 1.27 mm.

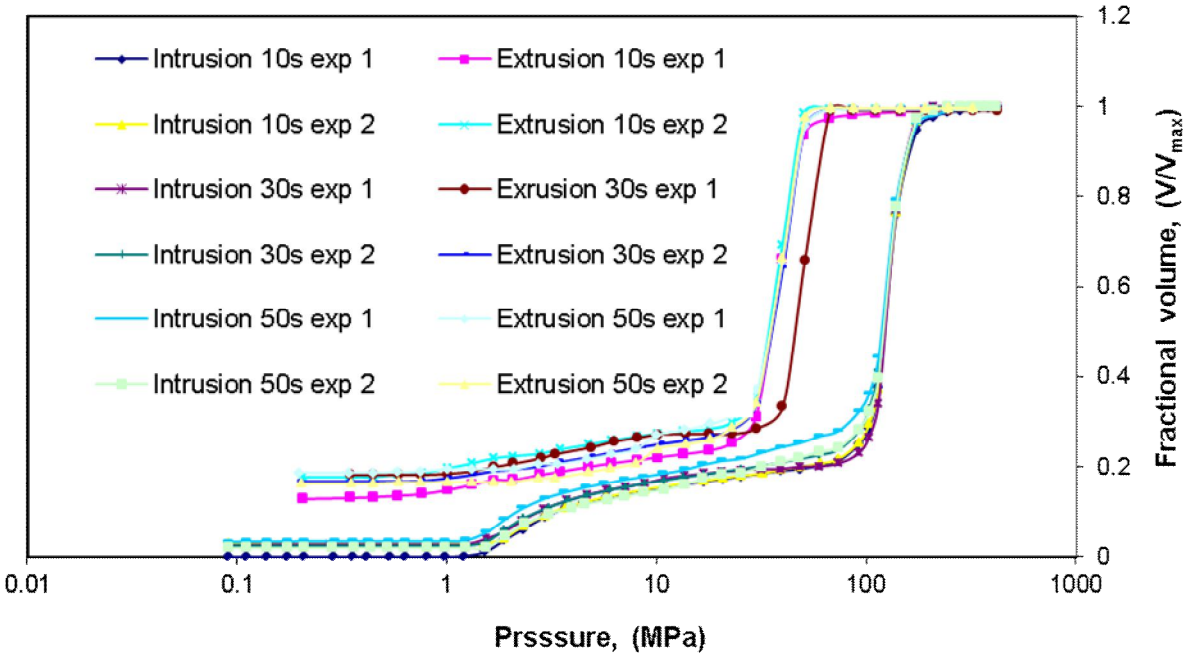

Figure 5.1

Mercury intrusion and extrusion curves of AL3984T for different equilibration times

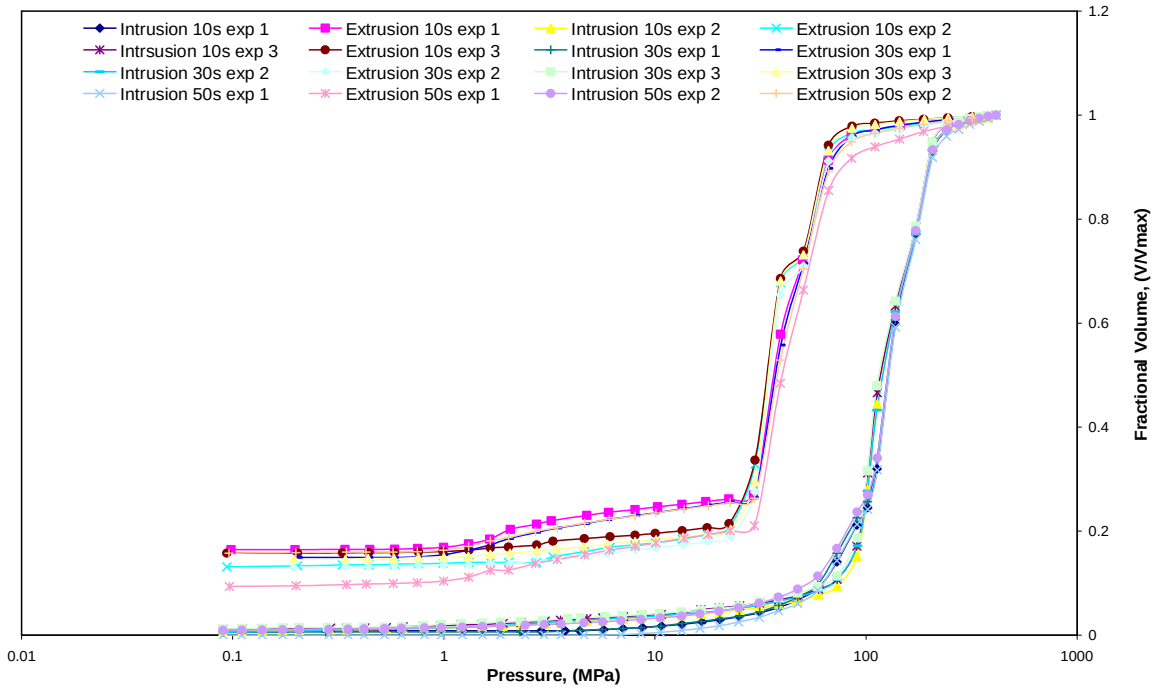

Figure 5.2

Mercury intrusion and extrusion curves of AL3992E for different equilibration times

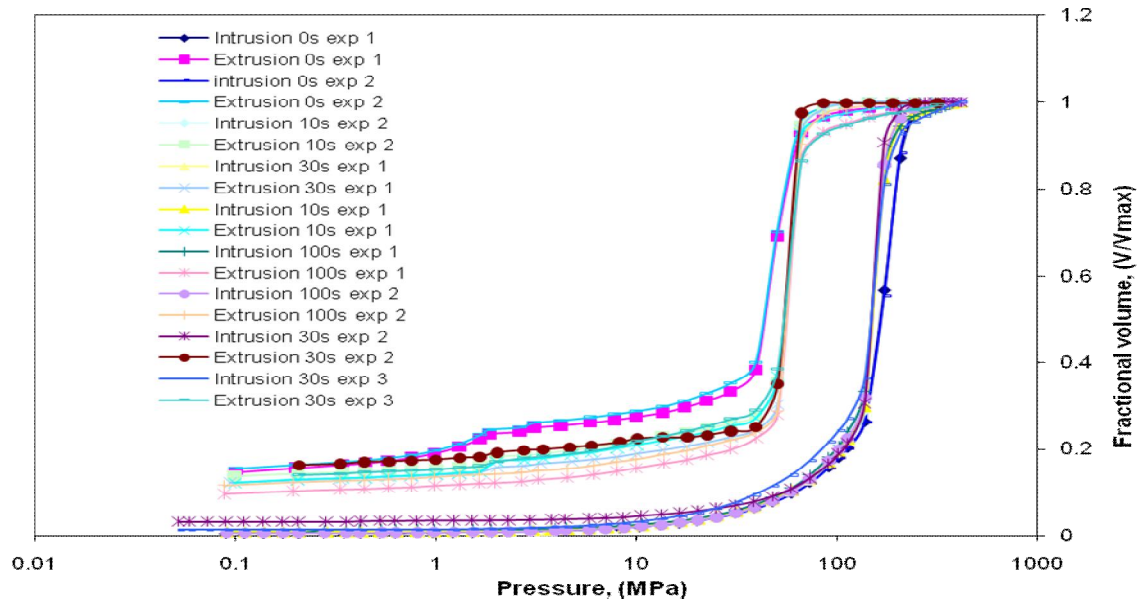

Figure 5.3

Mercury intrusion and extrusion curves of C10 for different equilibration times

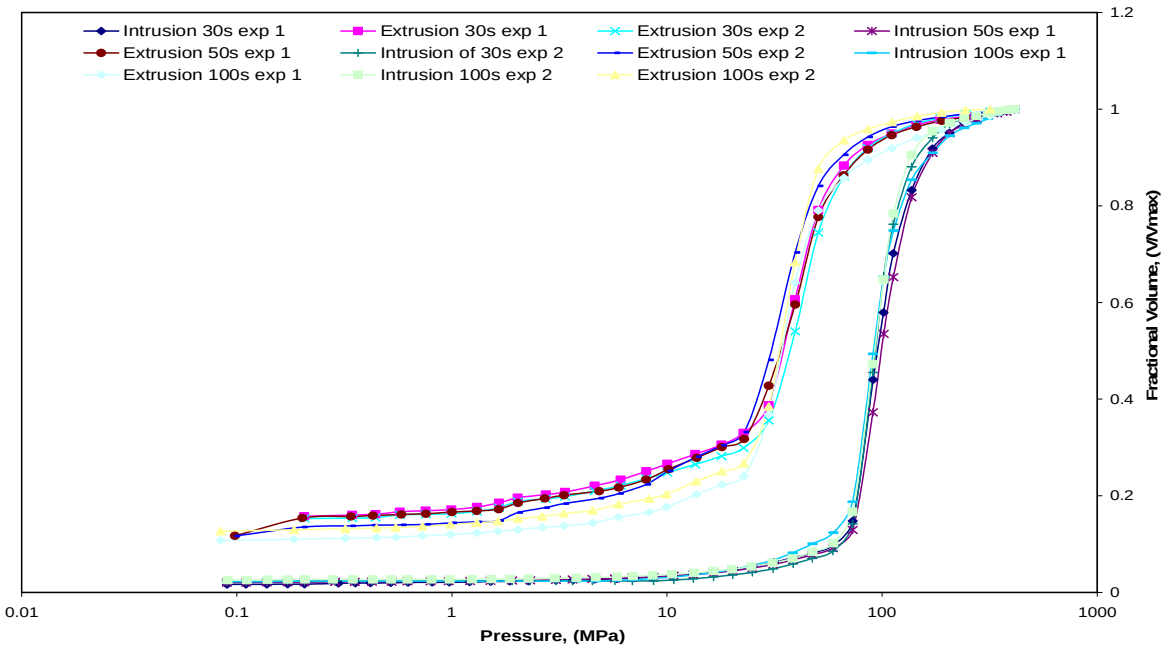

Figure 5.4

Mercury intrusion and extrusion curves of S980A for different equilibration times

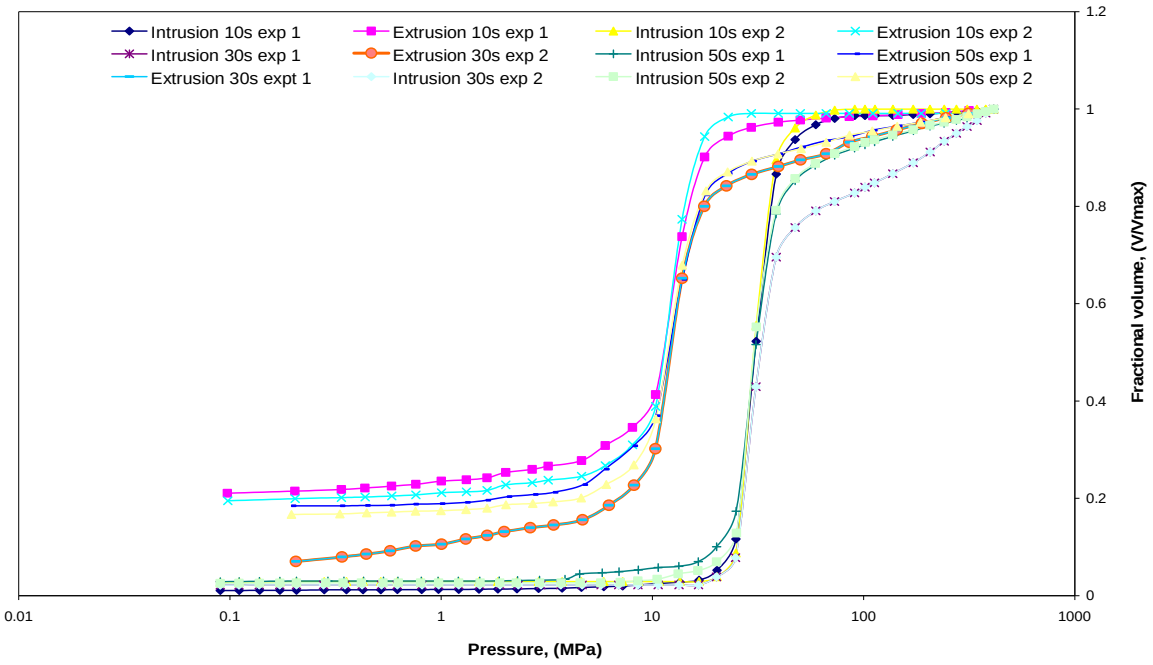

Figure 5.5

Mercury intrusion and extrusion curves of S980G for different equilibration times

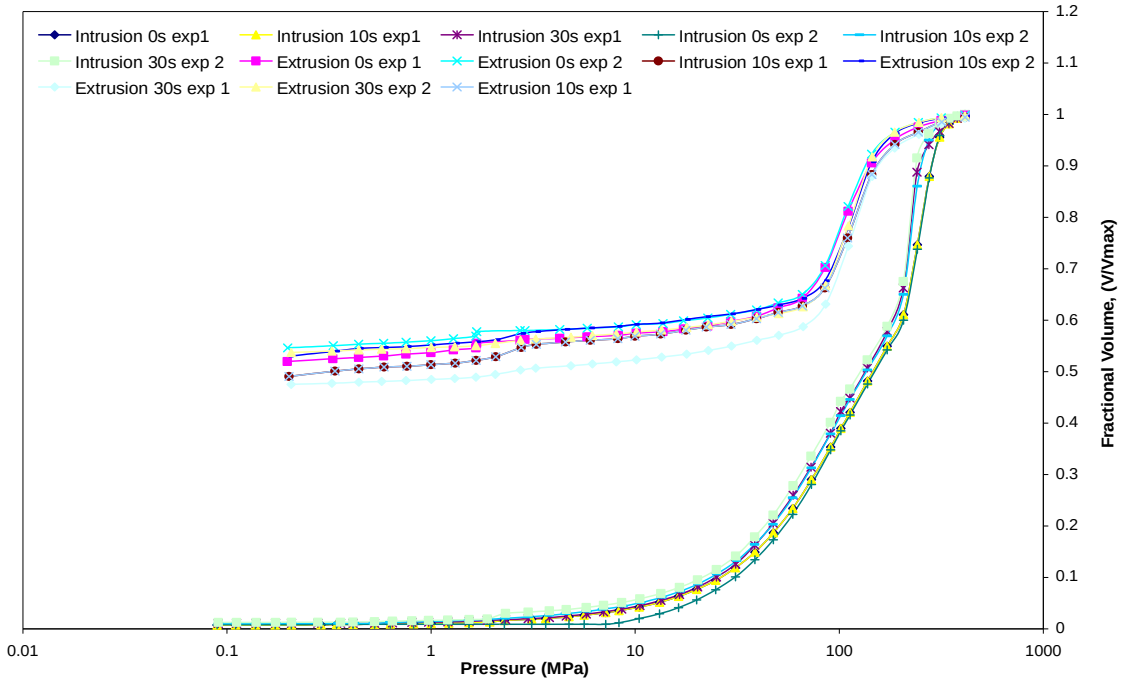

Figure 5.6

Mercury intrusion and extrusion curves of P1729 for different equilibration times

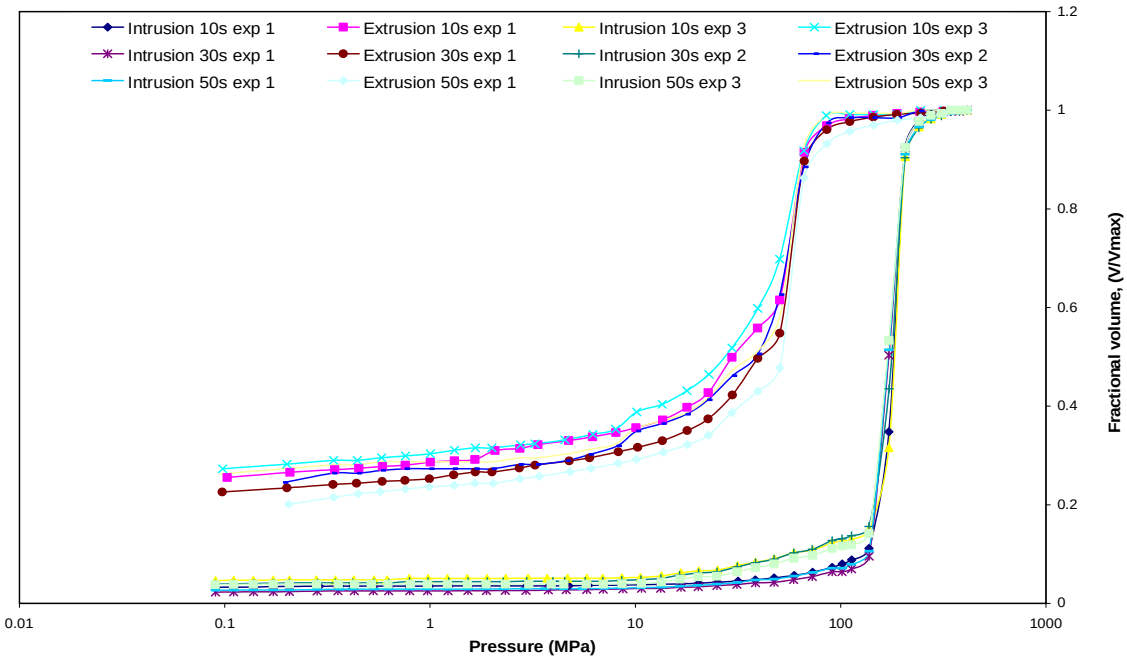

Figure 5.7

Mercury intrusion and extrusion curves of Silica Alumina for different equilibration time

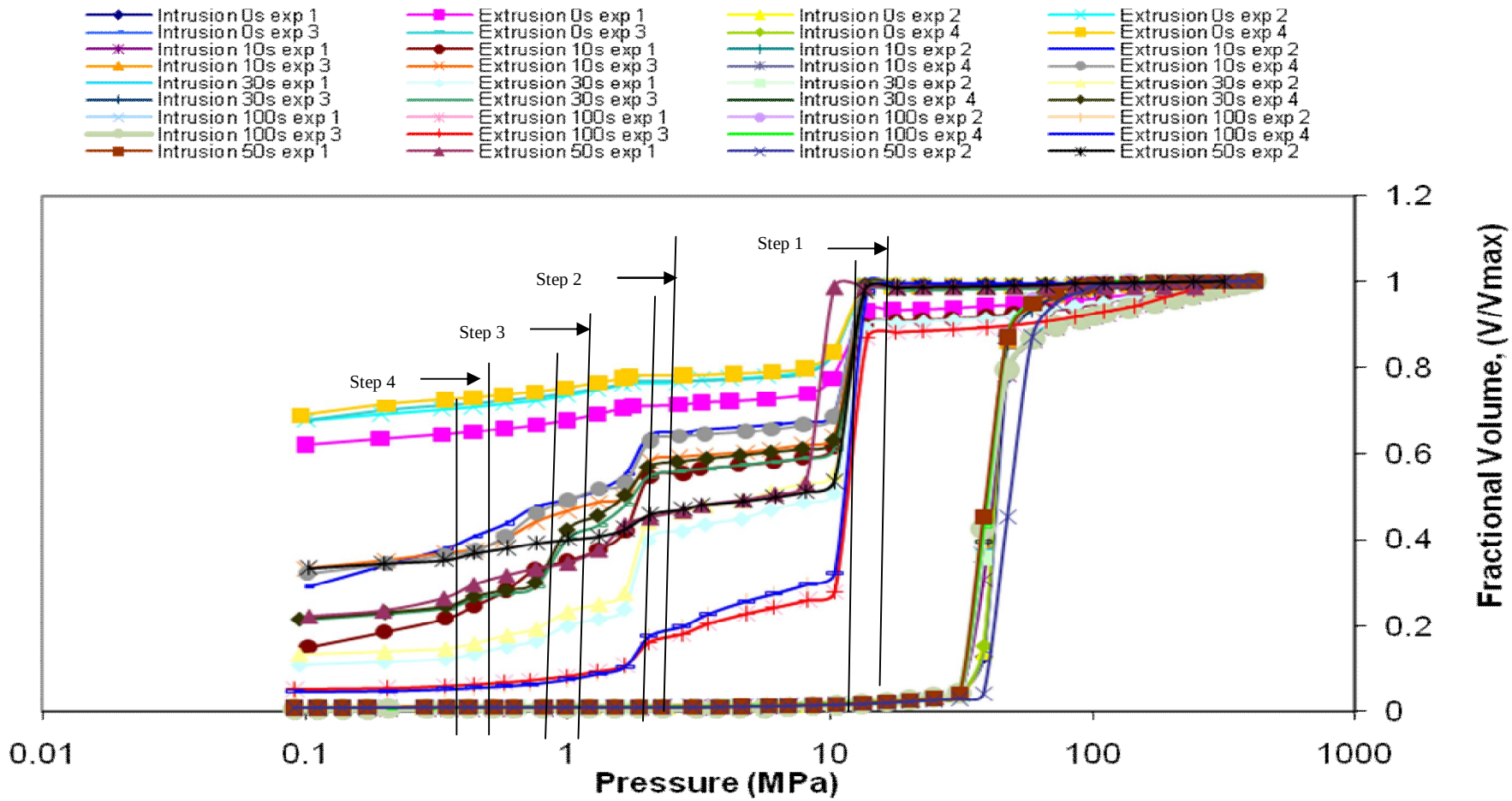

Figure 5.8

Mercury intrusion and extrusion curves of C30 for different equilibration times showing different pressure steps

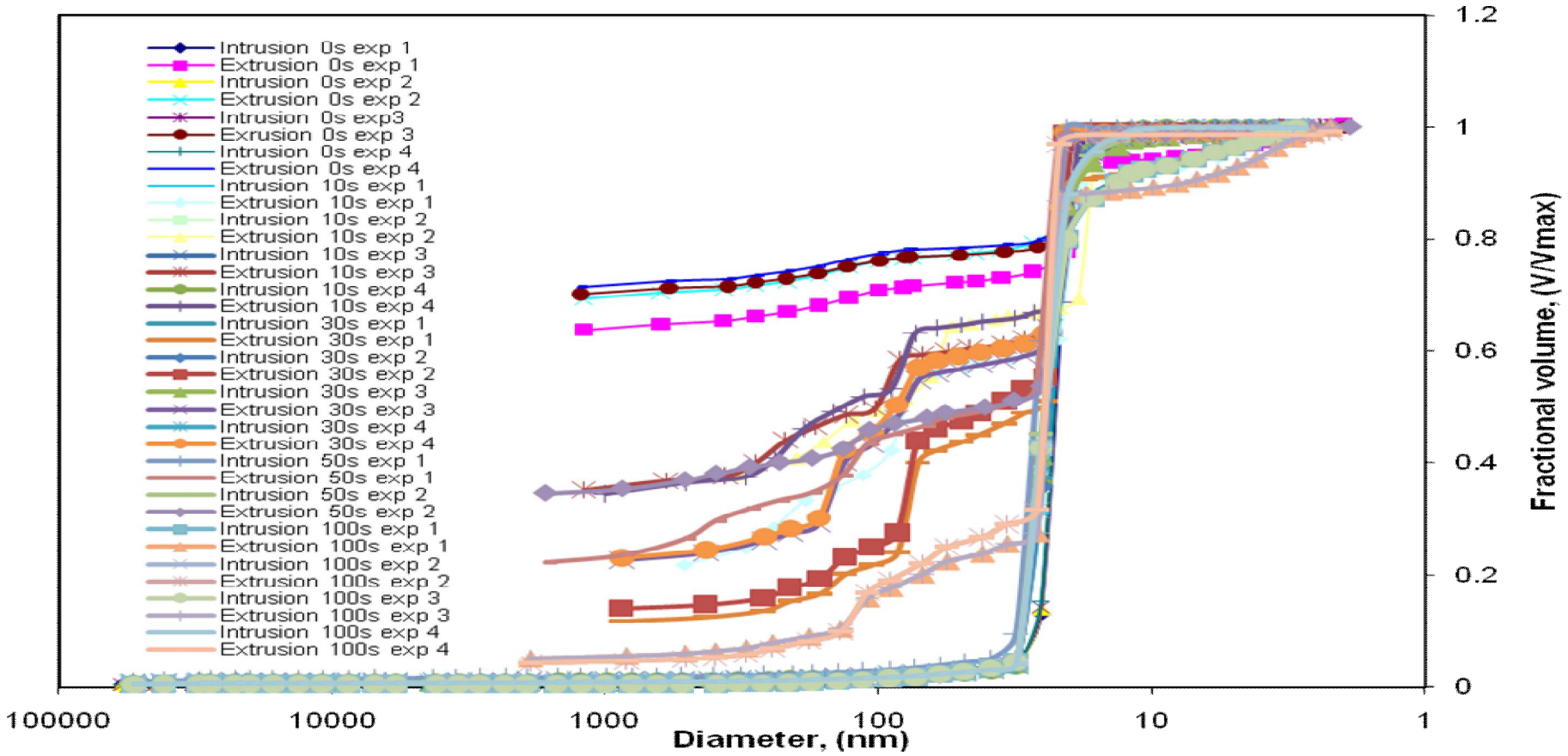

Figure 5.9

Mercury intrusion and extrusion curves by using semi empirical correlation of C30 with different equilibration times

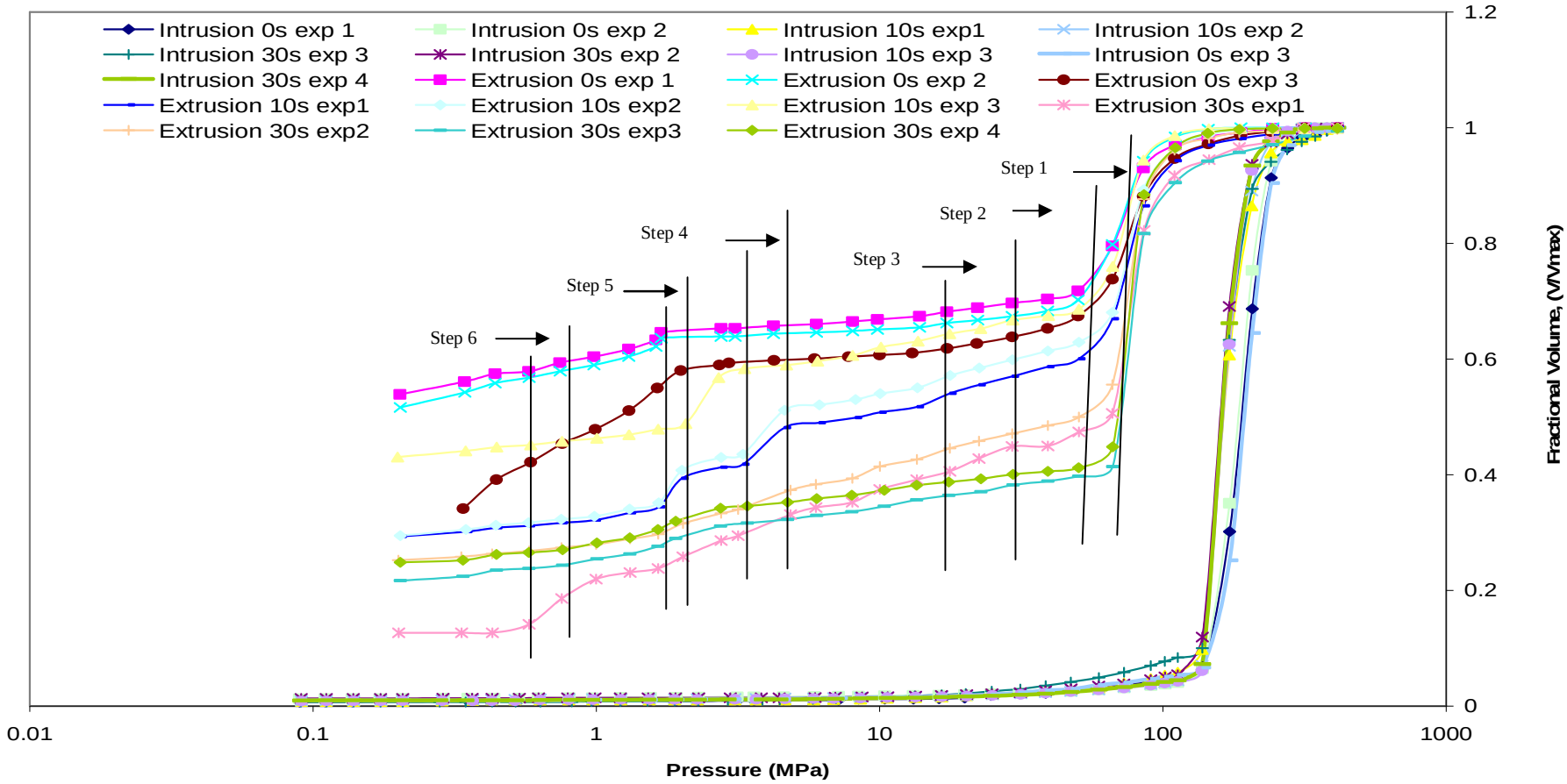

Figure 5.10

Mercury intrusion and extrusion curves of Q17/6 for different equilibration times showing different pressure steps

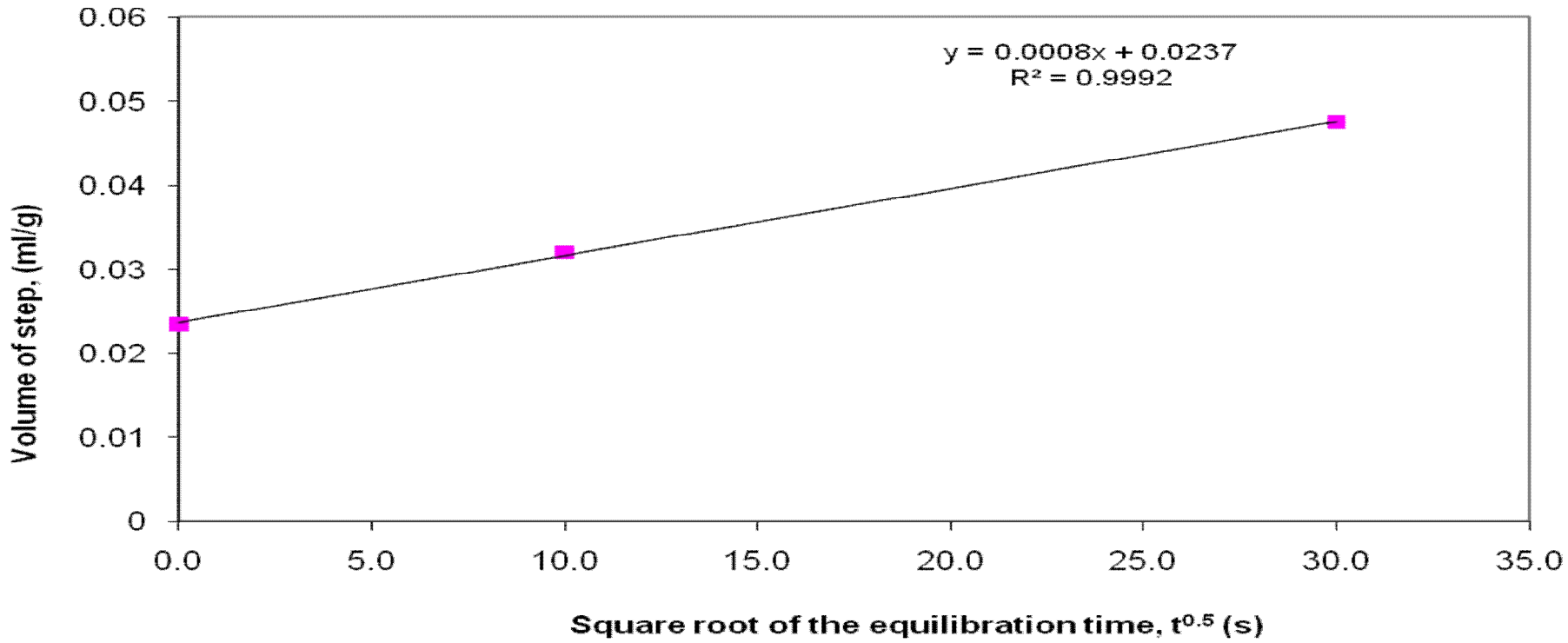

Figure 5.11

Best line fit straight line for the variation of the average volume of mercury lost in sample Q17/6 with the square root of the experimental equilibration time for step 1 in Figure 5.10. The volume step error bars are too small to show on the data points.

5.4 Discussion

During the course of the mercury porosimetry experiments, the pressure was either increased or decreased in small steps, and thus, this might have affected the pore network of the samples. As detailed in Section 3.3.4, the effect of high hydraulic pressure applied on materials during intrusion can sometimes lead to partial collapsing of the pore network or alteration of the sample during the experiments (Pirard *et al*., 1997). Therefore, these pressures may also give rise to potential collapse of the unoccupied pores. Consequently, this will reduce the number of large pores and give false entrapment values. This research has been altered to avoid such limitations, such as the mechanical damage of samples. In this study, all samples were visually observed after the experiments to ensure that the high hydraulic pressure applied on the materials did not cause elastic or permanent structural changes. It was found that the majority of the samples retained their external structural stability except for samples C10, AL3992E, and Silica Alumina. However, the presence of pore shielding in these materials was studied previously by Rigby *et al*. (2003b). It was found that no structural deformation or collapse occurred for these samples. Therefore, the traditional pore structure parameters such as the pore size, pore volume, surface area, porosity, and mercury entrapment were free of pore shielding over the different equilibration time-scales used.

In general, within the experimental error, for the different pellets studied from the same batch, the mercury intrusion and extrusion curves overlay each other at smaller mesopore radii. Hysteresis was observed between the intrusion and extrusion curves at larger mesopore radii, and mercury entrapment was present at all experimental time-scales. As detailed in Section 3.3.2, the hysteresis observed between the intrusion and extrusion curves could be as a result of ink-bottle type pores, differences of the contact angle, percolation-connectivity effects, pore potential, and surface roughness. From the raw mercury intrusion data, it can be deduced that samples have a pore network that exists over a wide range. In recent years, Giesche (2006) reported equilibration time-scale sensitivity to the intrusion branch of mercury porosimetry. As detailed in Section 3.3.3, Giesche (2006) observed a difference of up to 10 % in pore volume and 40 to 50 % in pore size between the fastest and the slowest analysis conditions. This equilibration time-scale sensitivity was investigated in Section 5.3. It was found that the intrusion branch was spontaneous, and thereby insensitive to the spatial arrangement within the pore network,

and independent of the experimental time-scale, as also observed by Lowell and Shields (1982). Therefore, the small discrepancies observed in the data derived from the intrusion curve could be attributed to batch variability as a result of slight differences from manufacturing conditions. In addition, they could be attributed to the deviation from flat plateaus at the top of their intrusion curves due to the heating effect encountered by the penetrometers at the highest pressure. Alternatively, the small discrepancies could be attributed to issues surrounding the blank corrections within experimental error (due to intrabatch variability) or the test samples could contain some small pores that required pressures higher than that attainable by the machine (414 MPa).

In recent years, the lattice-based MF-DFT simulations performed on intrusion and retraction data have shown that hysteresis depends upon the degree of surface roughness of the materials, and the width of the hysteresis increases with increased surface roughness (Rigby *et al.*, 2009). The materials investigated in this study are commercially based catalyst support pellet, and thus, although surface roughness is usually undesirable, it is difficult and expensive to control it during manufacturing. Therefore, the effect of surface roughness will contribute to overall hysteresis observed in this study. The semi-empirical correlations suggested by Rigby *et al*. (2002) were applied to the comprehensive study of these materials. These correlations led to superposition of the intrusion and retraction curves at low pore sizes, within the residual of ~ 4-5 % (Kloubek, 1981), due to the experimental error in the correlation. These alternative expressions to the Washburn equation have successfully removed the contact angle and surface tension contribution to the overall hysteresis. Therefore, the pressures at which intrusion and retraction processes occurred are controlled by different aspects of pore structure. Nevertheless, structural hysteresis and mercury entrapment were still observed at larger pore sizes. As detailed in Section 3.3.3, Rigby *et al*. (2002) and Galarneau *et al*. (2008) reported similar observations with alumina and templated silica materials.

It can be seen from Figures 5.1 to 5.10, the initial part of the retraction curves were insensitive to the equilibration time-scales. This suggests that the initiation part of retraction mechanism was caused by the thinning of the mercury connection at the intersections of large and small pressure as the pressure was decreased. As detailed in Section 3.3.3, Wardlaw and McKellar (1981) reported similar observations in glass

micromodels. Therefore, the very small decrease in the retraction curve could be attributed to the narrowing of mercury connections at pore intersections. In addition, an experimental work by Rigby *et al*. (2006) reported that mercury entrapment is sensitive to the number of free menisci generated, thus, the small volume change suggests that narrowing of mercury ganglia at an intersection only occurs at limited places. Therefore, in this study, the onset of retraction is independent of the experimental time-scale, as it appeared to be governed by the rapid equilibration of the narrowing of mercury necks, to form a connecting meniscus. The mercury entrapment observed occurred at larger mesopore radii, and was present in all experimental time-scales. Similar observations were reported by the experimental work of Rigby *et al*. (2006; 2008), and (Giesche, 2006). Thus, this finding supports the simulation work of Androutsopoulos and Mann (1979) detailed in Section 3.3.3 where mercury was preferentially entrapped in larger pores. In general, mercury intrusion process is associated with pore throats of a system, whilst the retraction process probes the pore body. Therefore, in this study, the ink-bottle snap-off, and network effects are considered to be the most likely cause of mercury entrapment observed in these materials. As detailed in Section 3.3.3, Moscou and Lub (1981) made a similar observation where they argued that, the pore shape determines the mercury retraction because mercury that has been retracted from ink-bottle shaped pores will only leave these pores through small entrances/exits. Furthermore, in recent years, simulation work by Porcheron and Monson (2004), have proposed a similar explanation, where the primary mechanism of entrapment was believed to be snap-off of the liquid meniscus when extruding from narrow pore necks, leading to an isolated droplet of the liquid in the bottle pore.

Moreover, the initial part of the mercury retraction curves for all equilibration time-scales exhibit a similar, almost horizontal plateau. As stated earlier in this Section, the onset of retraction is believed to be independent of the experimental time-scale, as it appeared to be governed by the rapid equilibration of the narrowing of mercury necks, to form a connecting meniscus. Although the shapes of the subsequent mercury retraction curves are very similar, it is apparent that for several downward pressure steps, the amount of mercury lost is a function of experimental time-scale used in most of the silica materials. This sensitivity to the equilibration time-scale was much larger in samples C10, C30, Q17/6, S980A, and S980G. This finding supports the work of Lowell and Shields (1981) that is detailed in Section 3.3.3, who stated that often, at the completion of

intrusion/extrusion cycle, mercury would slowly continue to extrude for a long time. Therefore, the energy stored by the mercury due to the work of compression prior to breakthrough into the pore was available to increase the interfacial free surface energy once breakthrough occurred. Under such conditions, extrusion involves vapour phase transport with a low flux and consequently slows down the dynamics of the transport regime. Therefore, the amount of mercury entrapment is also potentially associated with kinetic effects during mercury extrusion, coupled with the tortuosity of the disordered pore network, and the surface chemistry of these materials. As highlighted in Section 2.3, a 2D X-ray micro-CT image of a cross-section through sample C30 following mercury porosimetry was investigated by Rigby *et al*. (2008). The image showed that the mercury entrapment remained stationary in the centre of the sample. Moscou and Lub (1981) suggested a similar explanation, where an examination of samples of gel spheres, using light microscopy, following mercury porosimetry experiments showed that mercury entrapment occurred in heterogeneously distributed, macroscopic domains within the samples. In addition, it was found that once mercury is entrapped within a region of the sample, the mercury will remain stationary within the pore space for a long period of time.

In contrast, the mercury entrapment observed in alumina materials was independent of the experimental time-scales used. As stated earlier in this Section, the mercury entrapment observed in most silica materials was sensitive to the experimental time-scales used. The silica made materials in this study are samples C10, C30, P7129, Q17/6, S980A, and S980G. Therefore, perhaps, the production method of these materials can offer an explanation to the observed sensitivity. As detailed in Section 2.3, the manufacturing conditions of silica materials make them more heterogeneous than alumina materials. The silica materials have a much wider pore size distributions, and several pore shapes that are randomly distributed. Therefore, the mercury entrapment observed in most silica materials is due to their non-random longer-range structural heterogeneity effects. These experimental observations are in good qualitative agreement with the experimental work of Wardlaw and McKellar (1981) on glass micromodels, where clusters of large pores were connected to clusters of smaller pores. These researchers stated that mercury entrapment is either due to the presence of sufficiently narrow pore necks interspersed between larger voids, or due to non-random, longer-range structural heterogeneity.

In addition, the mercury entrapment observed in samples C30 and Q17/6 was the highest and varied substantially with equilibration time-scales used. The initial part of the retraction curves, particularly, the first sharp knee is independent of experimental time scale in these samples. However, subsequent analysis of the volume of mercury lost as a function of square root of experimental time in Figure 5.11 revealed a linear correlation for sample Q17/6. This observation suggests that retraction is a flow-rate controlled process. The estimated distanced that the mercury moved in the time required to achieve equilibrium for step 1 was 1.27 mm for Q17/6, and thus suggesting that, the mercury mass transport was by viscous flow in that region. As detailed in Section 3.2.4, Rigby *et al.* (2008) made a similar finding for sample C30. Therefore, based on these experimental findings, it can be deduced that samples C30 and Q17/6 exhibit a much more pronounced heterogeneity compared to the other group of silica materials studied. The shape of pores in samples C30 and Q17/6 can offer some explanation to the exceptional volume of mercury observed between the fastest and slowest analysis conditions.

In the original Washburn hypothesis, the intrusion into and extrusion out of uniformly sized pores of cylindrical shape should happen at the same pressure. However, this is not observed in most real samples, and thus, explains the hysteresis displayed in mercury porosimetry. Therefore, during the extrusion process new mercury interfaces are created as the mercury retracts from the pore system. This process requires additional energy; as a result, an energy-barrier is to be expected. Giesche (2006) expressed this energy barrier as a snap-off factor that describes the degree to which the extrusion pressure has to be lowered, relative to the corresponding intrusion pressure until the mercury network breaks apart and mercury can retreat from a specific pore. In a subsequent report, Giesche (2010) observed multiple snap-off following porosimetry on five different straight cylindrical pores of cut silica tubes open at both ends. Giesche (2010) reported that the snap-off factor for long cylindrical pores of uniform diameter is relatively small. However, when the snap-off factor was increased as the pore length was increased, reduced snap-off was observed. Therefore, the large amount of mercury entrapment observed in sample Q17/6 can be attributed to the presence of long cylindrical pores. In contrast, the mercury entrapment observed in sample C30 was the most affected by the equilibration time-scale used, and thus, rules out the possibility of multiple snap-off due to long cylindrical pores. The structural and topological properties of the sample were the likely cause of the entrapment.

5.5 Conclusion

Mercury porosimetry studies carried out on all samples revealed that the initiation part of mercury retraction curve, particularly the first sharp knee, was independent of experimental time-scale. The likeliest cause of this insensitivity to experimental time-scale is rapid equilibration of the necking-down process and subsequent breaking of the mercury ganglia at the boundaries of the region of smallest pores within the materials. This theory can be supported by the earlier glass micromodel work of Wardlaw and McKellar (1981) and recent experimental work of Rigby *et al.* (2006). In general, mercury entrapment occurred at larger pore radii, and was present for all experimental time-scales used. The semi-empirical alternatives to the Washburn Equation (3.31), suggested by Rigby *et al.* (2002), were applied to the comprehensive study of the hysteresis phenomena of the materials. The correlation led to superposition of the intrusion and retraction curves at low pore sizes, within the residual of ~ 4-5 % (Kloubek, 1981), due to the experimental error in the correlation. Thus, these alternative expressions have successfully removed the contact angle and surface tension contribution to the overall hysteresis. Nevertheless, hysteresis and entrapment were still observed at larger pore size.

In addition, it was found that, the intrusion branch of the isotherms was insensitive to the spatial arrangement within the pore network, and thus, independent of the experimental time-scale. Similar conclusions were made by Lowell and Shields (1981). In contrast, this finding deviates from recent work of Giesche (2006) where the intrusion curve was seen to be sensitive to the experimental time-scale. In this study, the mercury entrapment occurred at larger mesopore radii Therefore, depending on the pore geometry of the material, the ink-bottle snap-off, network effects, non-random longer-range structural heterogeneity effects, and multiple snap-off due to the presence of long cylindrical pores are considered the likely cause of mercury entrapment observed in these materials. The effect of experimental time-scales in silica materials was significantly large in sample C30 and Q17/6. A subsequent analysis of the volume of mercury lost as a function of square root of experimental time revealed a liner correlation for sample Q17/6. The estimated distanced that the mercury moved in the time required to achieve equilibrium for step 1 was 1.27 mm for Q17/6. This suggests that the retraction is a viscous flow-rate controlled process in Q17/6. A similar conclusion was made by Rigby *et al.* (2008) for sample C30.

5.6 References

Androutsopoulos, G.P. and Mann, R., 1979. Evaluation of mercury porosimeter experiments using a network pore structure model. *Chemical Engineering Science*, 34, 1203-1212.

Allen, T., 1999. *Particle size measurement.* Dordretch, The Netherlands: Kluwer Academic publishers.

Evbuomwan, O.E., 2009. *The structural characterisation of porous media for use as a model reservoir rocks, adsorbents and catalyst.* Thesis (PhD). University of Bath.

Galarneau, A., Lefevre, B., Cambon, H., Coasne, B., Vallange, S., Gabelica, Z., Bellat, J-P., Di Renzo, F., 2008. Pore-Shape effects in determination of pore size of ordered mesoporous silicas by mercury intrusion. *J.* Phys. Chem. C, *112* (33), 12921–12927.

Giesche H., 2006. Mercury porosimetry: A general (practical) overview. *Particle and particles system characterisation*, 23, 9-19.

Giesche H., 2010. *Multiple snap-off in long cylindrical pores.* Thesis: Department of Ceramic Engineering and Material science, Alfred University.

Kloubek, J., 1981. Hysteresis in porosimetry. *Powder Technol*., 1981, 29, 63 – 73.

Lowell S., Shields J. E., 1981. Hysteresis, entrapment, and wetting angle in mercury porosimetry. *Journal of Colloid and Interface Science*, Vol. 83, No. 1.

Moscou, L. and S. Lub, 1981. Practical use of mercury porosimetry in the study of porous solids. *Powder Technology*, 29, 45-52.

Pirard R., Heinrichs B., Pirard J.P. in: McEnaney B., Mays T.J., Rouquerol J., Reinoso R.F., Sing K.S.W., Unger (Eds.) K.K., 1997. *Characterisation of Porous Solids IV, Royal Society of Chemistry*. Publisher: Cambridge Press.

Porcheron F., Monson P. A., 2004. Modeling mercury porosimetry using statistical mechanics. *Langmuir*, 20 (15), 6482-6489.

Rigby, S.P., 2002. New methodologies in mercury porosimetry. *Stud. Surf. Sci. Catal.*, 144, 185 – 192.

Rigby S.P., Edler K.J., 2002. The influence of mercury contact angle, surface tension, and retraction mechanism on the interpretation of mercury porosimetry data. *Journal of Colloid Interface Science*, 250, 175-190.

Rigby S. P., Fletcher R.S., Riley S. N., 2003b. Determination of the cause of mercury entrapment during porosimetry experiments on sol–gel silica catalyst supports. *Applied Catalysis (A)*, 247, 27–39.

Rigby S. P., Fletcher, R. S., Riley S. N., 2004. Characterisation of porous solids using integrated nitrogen sorption and mercury porosimetry. *Chem. Engng.*, Sci., 59, 41 – 51.

Rigby, S.P., Evbuomwan, I.O., Watt-Smith, M.J., Edler, K.J., Fletcher, R.S., 2006. Using nano-cast model porous media and integrated gas sorption to improve fundamental understanding and data interpretation in mercury porosimetry. *Part. Part. Syst. Charac.*, 23, 82-93.

Rigby, S.P., Chigada, P.I., Evbuomwan, I.O., Chudek, J.A., Miri, T., Wood, J., Bakalis, S., 2008. Experimental and modelling studies of the kinetics of mercury retraction from highly confined geometries during porosimetry in the transport and the quasi-equilibrium regimes. *Chem. Engng. Sci.*, 63 (24), 5771-5788.

Rigby, S.P., and Chigada, P.I., 2009. Interpretation of integrated gas sorption and mercury porosimetry studies of adsorption in disordered networks using mean-field DFT. *Adsorption-journal of the international adsorption society*, 15 (1), 31-41.

Rootare, H.M., and Prenzlow C.F., 1967. Surface areas from mercury porosimeter measurements. *J. Phys. Chem.*, 71, 2733-2736.

Wardlaw, N.C., McKellar, M., 1981. Mercury porosimetry and the interpretation of pore geometry in sedimentary rocks and artificial models. *Powder Technology*, 29, 127 – 143.

6.0 NMR pulsed gradient spin echo technique I

[Study of the equilibrium adsorption in porous media]

6.1 Introduction

The principles and the applications of the PGSE NMR technique have been discussed in Section 3.4. The proposal for the research programme is given in Section 3.4.6. This Chapter introduces the PGSE NMR experiment with its particular considerations. In this study, potential explanation of non-linearity of the log-attenuation plots were explained over two diffusion time-scales (Δ = 50 ms and Δ = 100 ms). Thus, the interpretation of diffusion studies for linear and non-linear log-attenuation plots are discussed in Section 6.5. In cases I and II, the diffusion behaviour of water within the fully saturated materials was investigated. As detailed in Section 3.4.5, recent studies on partially saturated porous glasses have shown evidence of molecular exchange between liquid and vapour phases (Valliullin *et al*., 1997; 2005; and Farrher *et al*., 2008). In cases III and IV, the disposition and distribution of adsorbed water ganglia within a range of porous alumina and silica partially-saturated samples was investigated as a function of pore loading. In addition, the effect of molecular exchange between the liquid and vapour phase was investigated.

6.2 Preparation of the samples

6.2.1 Fully saturated samples prepared by immersion (Case I)

In this study, tortuosity as a function of diffusion time was investigated. The samples were prepared by imbibing them with deionised water, under ambient conditions, in a beaker for at least 24 hours. However, before any imbibitions, the big pellets, such as Aerosil and Q17/6 tablets, were sliced into appropriate sizes that could readily fit into an NMR sample tube. It was essential to allow the liquid to fully imbibe the porous network. However, excess water was removed from the pellet's external surface by contacting it with pre-soaked tissue paper as demonstrated by Hollewand and Gladden (1993). The pre-soaked tissue paper was necessary in order to prevent any liquid being removed from within the pores of the pellets. Finally, with the aid of a small tong, the pellets were gently ushered

into a sample tube at a height of around 5 cm as illustrated in Figure 6.1. A small piece of soaked filter paper was inserted into the sample tube cap and closed. Excess deionised water was removed from the soaked filter paper by squeezing. The wet cap was necessary in order to prevent unwanted evaporation of the sample in the course of the experiments.

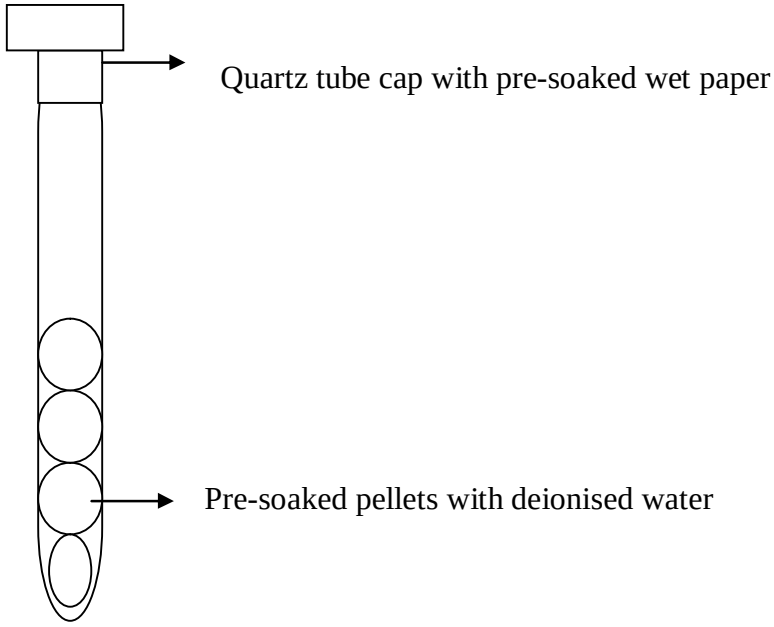

Figure 6.1
A schematic of quartz tube filled pre-soaked pellets to a height of around 5 cm

6.2.2 Fully saturated samples prepared by adsorption (Case II)

In this study, the effect of intra batch (intraparticle), and extra film thickness of water, to the overall diffusional displacement was investigated. Therefore, the diffusion coefficients measured in this study refer to the molecular self-diffusion coefficient of the imbibed water within the pore space of a single pellet. The samples were heated with the aid of ASAP 2010. As described in Section 4.2, the purpose of the thermal pre-treatment for each particular sample was to drive any physisorbed water on the sample and leave the morphology of the sample unchanged. The adsorption process set up was prepared in a closed system in order to establish the equilibrium. The closed system contained the adsorbate (250 mL of water) in equilibrium with the adsorbent (samples) as illustrated in Figure 6.2. It can be seen in Figure 6.2, that a single pellet of each sample was suspended

over a reservoir of deionised water with the aid of weir gauze in a plastic container. The large reservoir, in Figure 6.2, was to ensure a sufficient volume of water, such that, any eventual loss due to the water molecules uptake by the samples was negligible. The container was then properly sealed (airtight) with a packaging tape to prevent any fluid invasion inside the container. Finally, the sealed container was clamped and lowered into a water bath operating at 25 °C. The pore network of the samples was allowed to be imbibed by the adsorbate (water) for at least one week to achieve full saturation. It should be noted that the operational temperature inside the PGSE NMR machine was also maintained at 25 °C to mimic similar adsorption equilibrium conditions. Thus, this would reduce the effect of evaporation of the sample in the course of the PGSE NMR experiments.

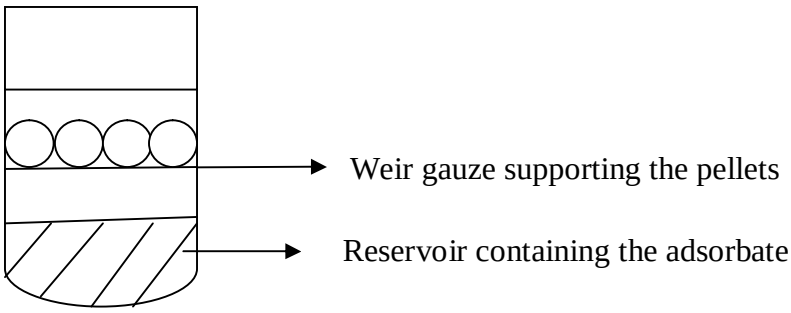

Figure 6.2

A schematic of a closed system containing the adsorbate in equilibrium with the adsorbent

For the sample tube set up, a pipette was used to introduce water into the quartz tube to form a reservoir of ~ 1 cm height. The quartz tube was then left for a minimum of 168 hours under room temperature (~ 25 °C) to lose any water traces above the reservoir. A doty susceptibility plug (~ 1 cm in height), with the aid of a small plastic capillary (~ 1.5 cm in height) were used to support the pellet above the water reservoir inside the quartz tube. A single fully saturated pellet from the container was gently ushered into the quartz tube as illustrated in Figure 6.3. It was necessary ensure that there was no contact between the reservoir inside the quartz tube and the saturated pellet.

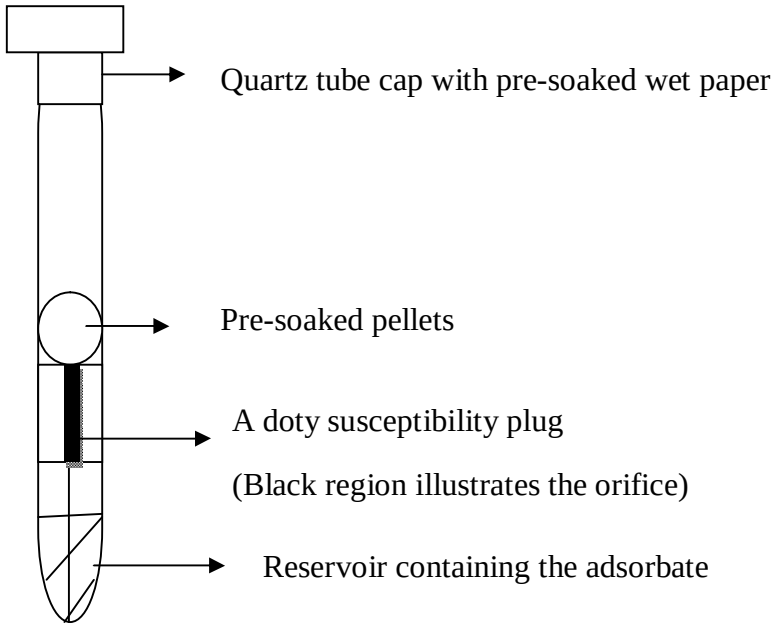

Figure 6.3

A schematic of quartz tube filled pre-soaked pellet suspended over a reservoir of the adsorbate to a height of around 5 cm

6.2.3 Partially saturated samples prepared by adsorption over a 0.5 M Na_2CO_3 reservoir (Case III)

In this study, the liquid connectivity was reduced in order to study the effects from restricted diffusion, and or various domains having different diffusivities, potentially rising from partial saturation of the samples. In addition, the effect of molecular exchange between the liquid and vapour phase was investigated. The sample preparation and the quartz tube set up in Section 6.2.2 (Case II) were adopted. However, in this study, the adsorbate used in the reservoir was 0.5 M Na_2CO_3 solution. The amount of water vapour in equilibrium with the reservoir was lowered by the presence of salt in the solution. Thus, the amount of physically adsorbed water molecules was associated with the low relative pressure of the solution, x = 0.982. For each sample analysis, the same pellet probed in Section 6.2.2 (Case II) was used. The choice of adopting the same pellet was essential in understanding the transport mechanism of the pellet at different saturation conditions.

6.2.4 Partially saturated samples prepared by adsorption over a 1.5 M Na_2CO_3 reservoir (Case IV)

In this study, the liquid connectivity was further reduced, in order to study the effects from restricted diffusion, and or various domains having different diffusivities, molecular exchange between the liquid and vapour phase, potentially rising from partial saturation of the samples. The sample preparation and the quartz tube in Section 6.2.2 (Case II) were adopted. However, in this study, the adsorbate used in the reservoir was 1.5 M Na_2CO_3 solution. The relative pressure of the solution was 0.931. Therefore, the amount of physically adsorbed water molecules was further reduced. For the same reasons stated in Section 6.2.3 (Case III), the same sets of pellets probed in Section 6.2.2 (Case II) were adopted for this study.

6.3 PGSE NMR spectrometry and experimental considerations

All PGSE NMR experiments were performed by using a Bruker AV400 NMR spectrometer, with a broadband multinuclear probe equipped with z – gradient coils. The magnet has static field strength of 9.4 T, yielding a proton resonant frequency of 400.13 MHz for ^1H nucleus. The gradients were supplied by a Bruker Grasp II unit, and the maximum attainable gradient strength was 53.5 Gcm^{-1}. The maximum sample length was constrained by the region over which uniform linear gradients could be produced and it was 15 ± 1 mm. In this study, it was assumed that the magnetic field was uniform and there was no cross-relaxation with the sample. All experiments were conducted at temperatures of 25 ± 0.5 °C. The acquisition parameters used in this study are given in Table 6.1. The data acquisition was controlled by a computer. For the bulk liquid diffusion analysis, acqusition Set 1 was used; where as in the case of sample diffusion analysis, both acquision Sets 1 and 2 were used. A series of eight spectra were taken at increasing gradient strengths and the number of scans for each spectrum was 16. As discussed in Section 3.4.2, signal attenuation was used to calculate the diffusion coefficient and comparative tortuosities of the water confined within the samples.

As detailed in Section 3.4.2, PGSE NMR technique is sensitive to the chemical and physical environments of a molecule such as temperature in particular (Hollewand and

Gladden, 1995a). Therefore, the diffusion coefficient of bulk liquid was measured before and after sample analysis. This was necessary in order to detect any slight temperature difference in the course of experiment. A quartz tube filled with deionised water to a height of around 5 cm was used for estimating the diffusion coefficient, D_0, of the bulk liquid.

Table 6.1

Experimental acquisition parameters used for the PGSE NMR analysis

Parameters	Acquisition set	
_	**1**	**2**
Gradient strenght, g (G cm^{-1})	0.674 to 32.030	0.674 to 32.030
Diffusion time, Δ (s)	0.05	0.1
Gyromagnetic ratio, γ (radT^{-1}s^{-1})	2.765	2.765
Duration of the gradient, δ (s)	0.02	0.02
Bi polar correction delay, τ_T (s)	0.0001	0.0001

6.4 Results and analysis

Repeat measurements were made on the bulk probing liquid sample on the same day at constant temperature and yielded diffusion coefficients agreeing to within 0.8 %. For each data set of the probing bulk liquid, the coefficient of determination $\left(R^2\right)$ yielded a correlation coefficient greater than 0.999. The self-diffusion coefficient of water at 25 °C was nearly 2.5 $\times 10^{-9}$ ($\pm$ 3.29$\times 10^{-11}$) m^2/s in each analysis. The average diffusion coefficient of bulk liquid was considered for calculations. A range of porous alumina and silica pellets of spherical and cylindrical geometry were investigated. In order to allow for the variation of support structure between pellets from the same batch and to test the reproducibility of measurements, replicate measurements were made for all batches. The apparent tortuosity of the samples were calculated by using the diffusion correlation in Equation 3.42. The relative mean square displacement of molecules in the samples was calculated by using the Einstein equation (Equation 3.47). The complete results of these fits, and the data obtained can be found in Appendix A6. In the case of suspected deviation from linear behaviour of the log-attenuation plot, further replicate measurements (up to two repeats) were made to confirm the true nature of the sample. The number of scans was also doubled. The increased number of was to the effect of signal to noise ratio, and as a

result, reduce the effect of errors associated with measurement. A two-component diffusion models was considered for macroscopic heterogeneous samples. The Microsoft Excel Solver was used to estimate the model parameters such as the intensity, diffusivities and their respective fraction in each diffusion domain within the sample. These model parameters from Solver were then used as the first guess in Origin 6.1 software to generate better parameters, along with their respective errors.

The total intraparticle pore volume of the sample accessible to water was estimated by gravimetric method. Water was imbibed into the sample for at least 24 hours under ambient conditions. Thus, the water molecules should be able to enter all of the meso- and macro-porosity which are accessible from the surface. This imbibitions procedure has been shown to give rise to complete pore filling, equivalent to that performed under vacuum conditions (Hollewand and Gladden 1993). The mass uptake of molecules of water by the sample was measured and the volume deduced using the known density of water. The total intraparticle pore volume of the samples accessible to water and the pore diameter along with the respective porosity of the samples are presented in Table 6.2. In addition, the average total water adsorbed for each case investigated is presented in Table 6.3.

Table 6.2

The average total intraparticle pore volume of the samples accessible to water, the pore diameter, and porosity of the samples

Sample	Characterisation technique		
	Gravimetric method	Mercury porosimetry	
	Pore volume (mL/g)	Pore diameter (nm)	Porosity (%)
Aerosil	0.690 ± 0.04	N/A	N/A
AL3984T	0.417 ± 0.01	11.85 ± 0.15	54.95 ± 2.04
AL3992E	0.554 ± 0.07	9.55 ± 0.05	66.10 ± 18.84
C10	0.667 ± 0.25	9.00 ± 0.01	67.81 ± 2.16
C30	1.027 ± 0.01	27.90 ± 2.07	70.51 ± 3.06
Q17/6	0.531 ± 0.07	6.70 ± 0.10	49.06 ± 1.49
S980A	0.648 ± 0.48	11.60 ± 0.30	62.55 ± 2.88
S980G	0.934 ± 0.01	38.15 ± 2.15	60.25 ± 1.42
Silica Alumina	0.524 ± 0.01	7.45 ± 0.05	60.54 ± 2.14

Table 6.3

The average total water adsorbed in each case investigated (Seven pellets were investigated in each case)

Sample	Fully saturated						Partially saturated					
	H_2O			H_2O Reservoir			0.5M Na_2CO_3 Reservoir (x = 0.981)			1.5M Na_2CO_3 Reservoir (x = 0.931)		
	Mass (g)			Mass (g)			Mass (g)			Mass (g)		
_	Initial	Final	Adsorbed	Initial	Final	Adsorbed (M_0)	Initial	Final	M/M_0	Initial	Final	M/M_0
Aerosil	0.084	0.14	0.056	0.084	0.137	0.053	0.084	0.134	0.943	0.084	0.132	0.906
AL3984T	0.064	0.294	0.23	0.064	0.293	0.229	0.064	0.285	0.961	0.064	0.282	0.952
AL3992E	0.275	0.454	0.179	0.275	0.451	0.175	0.275	0.449	0.994	0.275	0.447	0.983
C10	0.064	0.127	0.063	0.064	0.129	0.064	0.064	0.126	0.969	0.064	0.125	0.953
C30	0.074	0.148	0.073	0.074	0.148	0.074	0.074	0.147	0.986	0.074	0.080	0.081
Q17/6	0.293	0.437	0.144	0.293	0.441	0.148	0.293	0.44	0.993	0.293	0.439	0.986
S980A	0.031	0.061	0.03	0.031	0.074	0.043	0.031	0.061	0.698	0.031	0.047	0.372
S980G	0.038	0.054	0.015	0.038	0.054	0.015	0.038	0.052	0.933	0.038	0.040	0.133
Silica Alumina	0.089	0.137	0.048	0.089	0.136	0.048	0.089	0.131	0.896	0.089	0.125	0.750

Note

N/A – Not available (The sample was not enough for analysis)

***x* = Relative pressure of the solution**

M/M_0 = Amount adsorbed (g)/ Amount adsorbed when fully saturated (g)

6.4.1 Estimating the tortuosity of the samples in case I

In this study, tortuosity as a function of diffusion time was investigated. A minimum of seven fully saturated pellets were probed in each analysis. The data of each sample was subsequently averaged. Therefore, the sample mean error for the tortuosities and displacements are given in Table 6.4. The reported uncertainties are the 95% confidence intervals that indicate the spread of the results over samples from the same batch and the error associated with the PGSE NMR measurement. In general, these uncertainties indicate the reliability of tortuosity estimates for the diffusion times used in this study.

It can be seen from Table 6.4, the magnitude of the tortuosities in increasing order is C30 < S980g < C10 < Aerosil < AL3984T < S980A < AL3992E < Silica Alumina < Q17/6. The error bars for measurements obtained at Δ = 50 ms and Δ = 100 ms overlapped for most samples, and thus, there was no significant effect of the diffusion time used on tortuosity in most of the samples. In contrast, Aerosil and C30 (the least tortuous sample is C30) were sensitive to the diffusion time. Therefore, Aerosil and C30 are the only samples where the tortuosity varied with length scale for the range of values studied. It can be seen from Table 6.4, the magnitude of displacement increases in the order C10 < C30 < S980A < Q17/6 < Aerosil < AL3992E < S980G < Silica Alumina < AL3984T. The displacement of molecules undergoing Brownian motion increased with diffusion time. In addition, it can be seen from Table 6.2 that the displacements reported in Table 6.4 were far greater than the average pore sizes in all samples. Therefore, any deviation from linearity of the log-attenuation plot observed at long diffusion time was not associated with restricted diffusion but macroscopic heterogeneity of the sample.

Furthermore, it can be seen from Table 6.5, a simple linear behaviour ($R^2 \geq 0.999$) was exhibited in most data sets at short diffusion time (Δ = 50 ms). However at long diffusion time (Δ = 100 ms), there were signs of deviation from simple linear behaviour in most data sets ($R^2 \leq 0.998$). In contrast, the log-attenuations plots of samples C30 and Q17/6 showed a reasonable degree of linearity ($R^2 = 0.999$) at long diffusion time. An example of a log attenuation plot for one of the samples (S980G) with the most deviation from linear behaviour is shown in Figure 6.4. In the absence of restricted diffusion, Figure 6.4 fits a concave curve characteristic of a macroscopically heterogeneous sample (Hollewand and Gladden, 1995a).

Table 6.4

Tortuosities and molecular mean square displacements for the samples in case I for one-component fits (The error quoted is 95 % confidence intervals)

Sample	Average Tortuosity		Average displacement (μm)	
	(Δ = 50 ms)	**(Δ = 100 ms)**	**(Δ = 50 ms)**	**(Δ = 100 ms)**
Aerosil	1.59 ± 0.06	1.86 ± 0.09	23.00 ± 0.29	31.71 ± 0.46
AL3984T	1.75 ± 0.03	1.81 ± 0.04	25.07 ± 0.21	35.90 ± 6.51
AL3992E	1.76 ± 0.02	1.85 ± 0.03	23.38 ± 0.20	26.62 ± 0.37
C10	1.57 ± 0.01	1.63 ± 0.04	20.70 ± 0.20	28.27 ± 0.51
C30	1.41 ± 0.01	1.49 ± 0.05	21.49 ± 0.48	29.79 ± 0.57
Q17/6	2.38 ± 0.03	2.42 ± 0.05	22.48 ± 0.70	30.81 ± 0.89
S980A	1.75 ± 0.02	1.81 ± 0.04	21.92 ± 0.49	29.85 ± 1.04
S980G	1.54 ± 0.02	1.57 ± 0.04	23.83 ± 0.41	32.70 ± 0.78
Silica Alumina	2.05 ± 0.04	2.19 ± 0.07	24.58 ± 0.34	32.79 ± 1.39

Table 6.5

Coefficients of determination for the log attenuation plots of the samples in case I for one-component fit

Sample	Coefficient of determination, R^2							
_	(Δ = 50 ms)				(Δ = 100 ms)			
_	Number of scans = 16		Number of scans = 32		Number of scans = 16		Number of scans = 32	
Aerosil	0.9956	0.9996	0.9963	0.9958	0.9916	0.9973	0.9961	0.9995
AL3984T	0.9991	0.9996	_	_	0.9984	0.9989	_	_
AL3992E	0.9996	0.9997	_	_	0.9996	0.9992	_	_
C10	0.9999	0.9997	_	_	0.9983	0.9994	_	_
C30	_	_	0.9999	0.9998	_	_	0.9999	0.9995
Q17/6	0.9994	0.9994	_	_	0.9989	0.9990	_	_
S980A	0.9995	0.9998	_	_	0.9984	0.9994	_	_
S980G	0.9999	0.9997	0.9998	0.9990	0.9995	0.9982	0.9993	0.9996
Silica Alumina	0.9990	0.9985	_	_	0.9979	0.9977	_	_

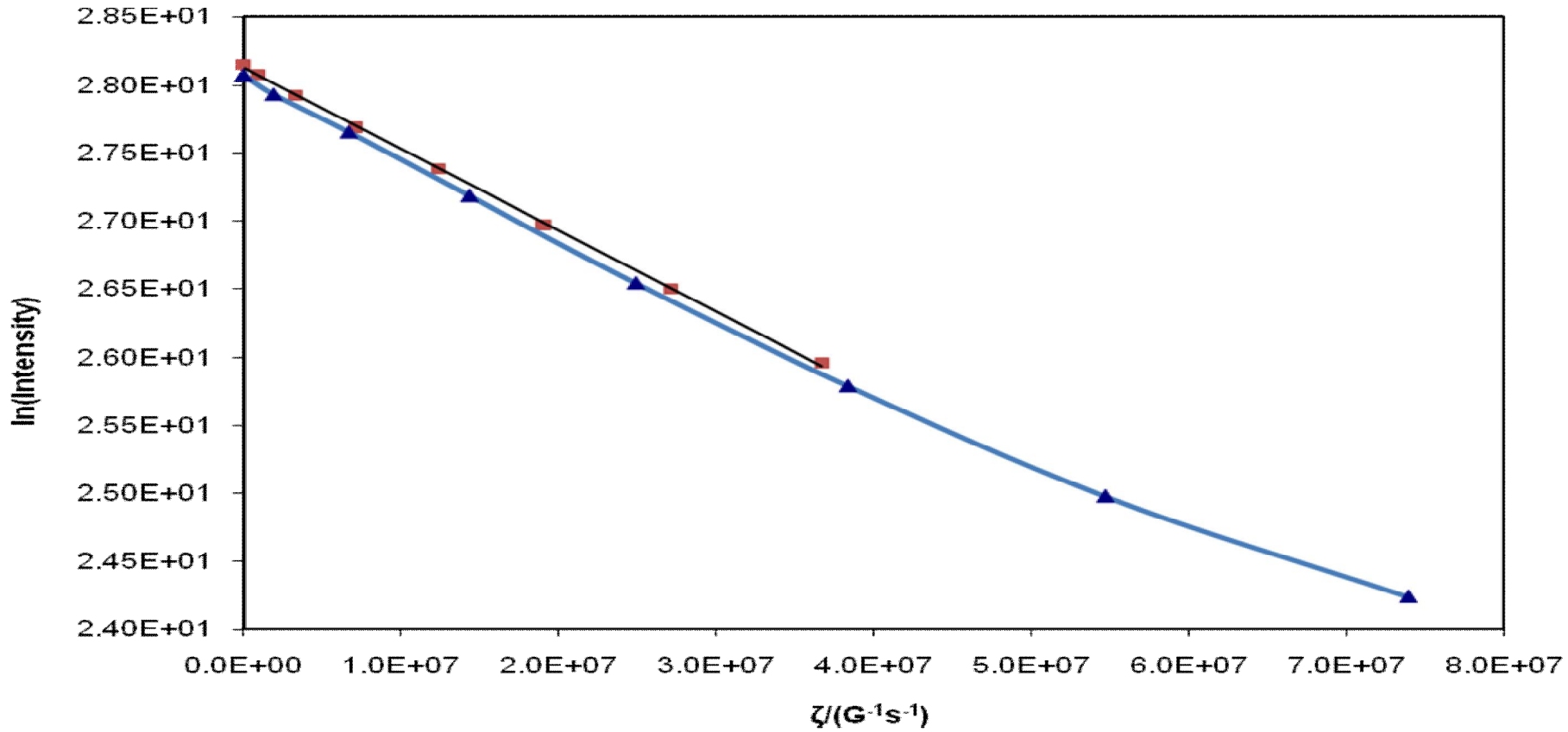

Figure 6.4

Echo log-attenuation results from simulated echo PFG experiments on fully saturated support pellet (S980G, Set 2) showing the combined deviation of linearity of the sample. The square and triangle blocks represent the 50 ms and 100 ms diffusion times, respectively

6.4.2 Estimating the tortuosity of samples in case II

In this study, tortuosity as a function of diffusion time was also investigated. However, a single fully saturated pellet was used for each analysis. The sample mean error for the tortuosities and displacements are given in Table 6.6. The reported uncertainties are the 95% confidence intervals. It can be seen from Table 6.6, that the magnitude of the tortuosities increases in the order AL3984T < Silica Alumina < S980G < Aerosil < Q17/6 < AL3992E < C30 < C10 < S980A. There was no significant difference to the diffusivity with varying diffusion time used in Aerosil, C10, C30, S980A, S980G, and Silica Alumina (error bars over-lapped). In contrast, the error bars for measurements, where Δ = 50 ms and Δ = 100 ms, did not overlap for AL3984T, AL3992E, Q17/6 and S980A. In the case of AL3922E, a significant difference was seen in diffusivity with an increase of diffusion time (error bars did not over-lap). Where as, the errors at long diffusion time for AL3984T and S980A are considerably large, and thus, the error bars over-lapped even though the quoted mean tortuosities differed; hence, there is no trend with regards to diffusion time. The magnitude of displacement increases in the order C10 < S980A < C30 < Q17/6 < Aerosil < S980G < AL3992E < Silica Alumina < AL3984T. The displacements in Table 6.6 were far greater than the average pore sizes reported from Table 6.2.

Table 6.9 shows the coefficient of determination for the log-attenuation plots. A simple linear ($R^2 \geq 0.998$) behaviour was exhibited in most data sets at short diffusion time. At long diffusion time, deviation from simple linear behaviour was seen in Aerosil, AL3984T and S980A. In contrast, the log-attenuation plots of AL3992E, C10, C30, Q17/6 and S980G showed a reasonable degree of linearity ($R^2 \geq 0.998$). Signs of deviation from simple linear behaviour were exhibited in the following samples; Aerosil, AL3984T, AL3992E, C10, C30 and Q17/6. However, for Aerosil and AL3992E, non-linearity was confirmed after careful repetition of the experiments, and by increasing the number of scans to 32 (see Figures 6.5 and 6.6). Tables 6.7 and 6.8 show the two-component model parameters with their respective tortuosities; and displacements. The first component is defined as the component showing greater movement during the diffusion time. The second component is the slow component, where diffusion is comparatively slower than the first component. The two diffusion coefficients for the two components are denoted as D_1 and D_2 respectively, thus, $\overline{D}$ is the overall diffusion coefficient. The fraction of water in the first component is P_w, and the fraction of water in the second component is $(1 - P_w)$.

Table 6.6

Tortuosities and molecular mean square displacements for the samples in case II (The error quoted is 95 % confidence intervals)

Sample	Average Tortuosity		Average displacement (μm)	
	(Δ = 50 ms)	**(Δ = 100 ms)**	**(Δ = 50 ms)**	**(Δ = 100 ms)**
Aerosil	1.51 ± 0.03	1.55 ± 0.05	22.1 ± 0.28	30.9 ± 0.69
AL3984T*	1.16 ± 0.02	1.11 ± 0.41	25.07 ± 0.21	35.90 ± 6.51
AL3992E	1.44 ± 0.02	2.05 ± 0.04	23.38 ± 0.20	26.62 ± 0.37
C10	1.70 ± 0.02	1.82 ± 0.05	17.97 ± 0.06	22.22 ± 0.30
C30	1.54 ± 0.02	1.60 ± 0.02	21.49 ± 0.48	29.79 ± 0.57
Q17/6	1.51 ± 0.07	1.86 ± 0.08	21.89 ± 0.69	27.86 ± 0.89
S980A*	1.52 ± 0.06	1.2 ± 0.28	21.92 ± 0.49	31.61 ± 3.18
S980G	1.27 ± 0.03	1.35 ± 0.05	23.83 ± 0.41	32.70 ± 0.78
Silica Alumina	1.20 ± 0.03	1.35 ± 0.08	24.58 ± 0.34	32.79 ± 1.39

Note

*** Double component fits of one of the pellets at long diffusion time (Δ = 100 ms)**

Table 6.7

Two-component model parameters derived from Origin Software [Long diffusion time (Δ = 100 ms)] in case II. The error quoted is 95 % confidence intervals.

Sample	Intensity	Fraction	Effective diffusivity/($4\pi^2 \times 10^{-8}$ m^2 s^{-1})		
	$I_0 \times 10^8$	P_w	D_1	D_2	$\overline{D}$
AL3984T, Pellet 2	1683 ± 9.78	0.949 ± 0.07	8.027 ± 0.52	1.685 ± 2.23	7.706 ± 2.86
S980A, Pellet 1	102 ± 1.05	0.946 ± 0.12	8.283 ± 0.95	1.746 ± 3.60	7.928 ± 1.29

Table 6.8

Tortuosities and molecular mean square displacements for the two-component model parameters [Long diffusion time (Δ = 100 ms)] in case II. The error quoted is 95 % confidence intervals.

Sample	Tortuosity			Average displacement (μm)		
	τ_1	τ_2	$\bar{\tau}$	r_1	r_2	$\bar{r}$
AL3984T, Pellet 2	1.19 ± 0.08	5.68 ± 7.50	1.24 ± 0.46	34.93 ± 2.25	16.03 ± 21.15	34.22 ± 12.70
S980A, Pellet 1	1.15 ± 0.13	5.55 ± 11.25	1.20 ± 0.20	35.48 ± 4.07	16.29 ± 33.60	34.71 ± 5.64

Table 6.9

Coefficients of determination of the log attenuation plots for the samples in case II for one-component fits

Sample	Coefficient of determination, R^2							
_	(Δ = 50 ms)				(Δ = 100 ms)			
_	Number of scans = 16		Number of scans = 32		Number of scans = 16		Number of scans = 32	
Aerosil	0.99959	0.99844	_	_	0.999141	0.99614	_	_
AL3984T*	_	_	0.99964	0.99818	_	_	0.99928	_
AL3992E	0.99997	0.99899	_	_	0.99899	0.99874	_	_
C10	0.99968	0.99995	_	_	0.99790	0.99820	_	_
C30	_	_	0.99918	0.99946	_	_	0.99896	0.99929
Q17/6	_	_	0.99201	0.99993	_	_	0.99342	0.99993
S980A*	0.99966	0.99086	_	_	0.99052	_	_	_
S980G	0.99887	0.99743	_	_	0.99946	0.99191	_	_
Silica Alumina	0.99931	0.99823	_	_	0.98924	0.99109	_	_

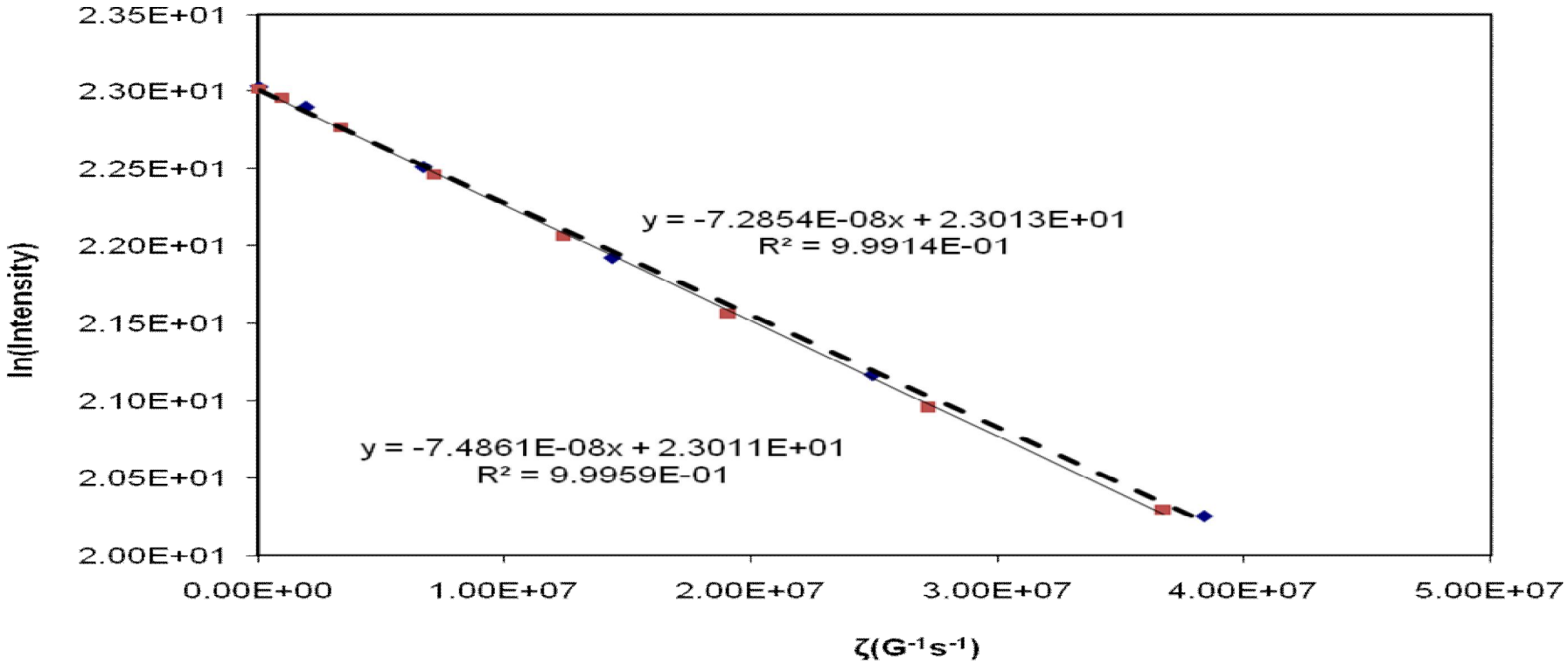

Figure 6.5

Echo log-attenuation results from simulated echo PFG experiments on fully saturated support pellet (Aerosil, Pellet 1) showing signs of deviation of linearity at short diffusion time (Δ = 50 ms) and long diffusion time (Δ = 100 ms). The square and diamond blocks represent the 50 ms and 100 ms diffusion times, respectively.

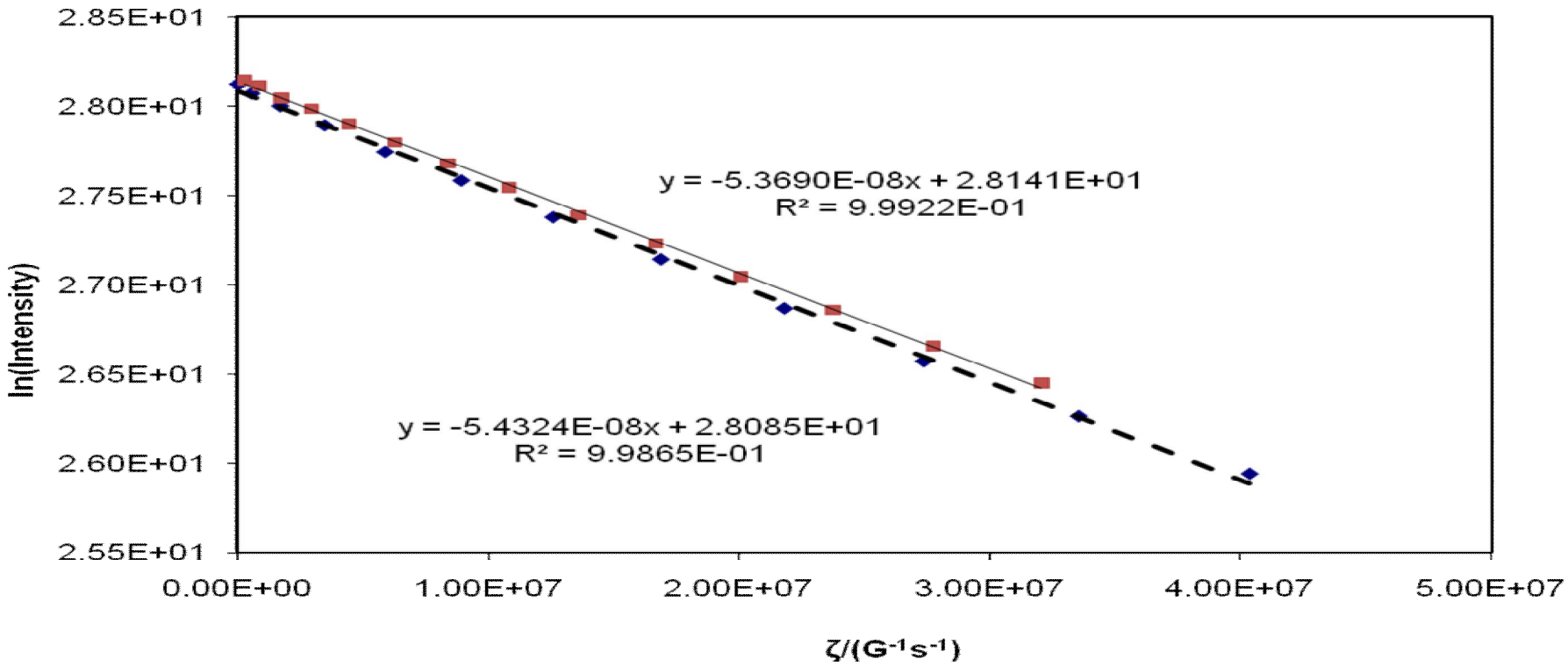

Figure 6.6

Echo log-attenuation results from simulated echo PFG experiments on fully saturated support pellet (Aerosil, Pellet 1) showing confirmed signs of deviation of linearity at short diffusion time (Δ = 50 ms) and long diffusion time (Δ = 100 ms). The square and diamond blocks represent the 50 ms and 100 ms diffusion times, respectively.

6.4.3 Estimating the tortuosity of samples in case III

A single pellet was used for each analysis. The same pellet probed in case II was used for each PGSE NMR experiment. The samples were partially saturated with water by suspending over 0.5M Na_2CO_3 solution until saturation equilibrium was reached. The potential effects from restricted diffusion, or various diffusion domains which have potentially different diffusivities and molecular exchange between liquid and vapour were investigated. The values of sample mean and error for the tortuosities, and displacements are given in Table 6.10. The reported uncertainties are the 95% confidence intervals. The magnitude of displacement increased in the order AL3992E < Aerosil < S980G < AL3984T < C10 < C30 < Q17/6 < S980A < Silica Alumina. There is no evidence of restricted diffusion. It can be seen in Table 6.10, the magnitude of the tortuosities increased in the order Silica Alumina < S980A < Q17/6 < C30 < C10 < AL3984T < S980G < Aerosil < AL3992E. There was no significant difference in diffusivity with diffusion time used in Aerosil, AL3984T, AL3992E, C30, S980A, S980G, and Silica Alumina.

The quoted mean tortuosities for C10 and Q17/6 reduced with increased diffusion time but by a value less than the errors, and thus, the trends are not statistically significant. It should be noted that a two-component diffusion model was used to plot the log-attenuation curve for those samples. The reported errors for these samples (C10 and Q17/6) are greater than 0.5. Therefore, the reported errors were not only due to the spread of the results over samples from the same batch and the error associated with the PGSE NMR measurement but also the fit of the plot by the Origin Software. This could be due to insufficient data to constrain the fit, thus, the Origin Software had too many parameters (5) to fit a small number of data points. Table 6.13 shows the coefficient of determination of the log-attenuation plots. A simple linear ($R^2 \geq 0.998$) behaviour was exhibited in most data sets at short diffusion time (Δ = 50 ms). At long diffusion time (Δ = 100 ms), deviation from simple linear behaviour was exhibited in most data sets. The data sets were now fitted to a two-component diffusion model in Equation 3.40 (see Tables 6.11 and 6.12). In contrast, the log-attenuations plots of C30 and Q17/6 showed a reasonable degree of linearity ($R^2 \geq$ 0.998) at long diffusion time. An example of a log-attenuation plot for one of the samples (C10) with the most deviation from linearity behaviour is shown in Figures 6.7 and 6.8. The product of effective diffusivity and diffusion time is not constant which rules out the possibility of restricted diffusion in these samples.

Table 6.10

Tortuosities and molecular mean square displacements for the samples in case III (The error quoted is 95 % confidence intervals)

Sample	Average Tortuosity		Average displacement (μm)	
_	(Δ = 50 ms)	(Δ = 100 ms)	(Δ = 50 ms)	(Δ = 100 ms)
Aerosil	1.81 ± 0.05	2.03 ± 0.09	20.05 ± 0.36	26.82 ± 0.81
AL3984T	1.41 ± 0.03	1.48 ± 0.05	22.70 ± 0.31	31.42 ± 0.71
AL3992E	2.06 ± 0.02	2.16 ± 0.03	18.42 ± 0.12	25.40 ± 0.24
C10*	1.40 ± 0.03	1.05 ± 0.52	22.89 ± 0.29	39.10 ± 15.31
C30	1.32 ± 0.01	1.50 ± 0.07	23.26 ± 0.12	32.12 ± 0.50
Q17/6*	1.26 ± 0.06	1.19 ± 0.77	23.53 ± 0.76	33.51 ± 11.93
S980A	1.28 ± 0.03	1.54 ± 0.11	23.70 ± 0.38	32.29 ± 0.97
S980G	1.47 ± 0.03	1.56 ± 0.05	22.13 ± 0.27	30.43 ± 0.63
Silica Alumina*	1.27 ± 0.02	1.23 ± 0.37	23.81 ± 0.21	34.17 ± 5.08

Note

*** Double component fits of one of the pellets at long diffusion time (Δ = 100 ms)**

Table 6.11

Two-component model parameters derived from Origin Software [Long diffusion time (Δ = 100 ms)]. The error quoted is 95 % confidence intervals

Sample	Intensity	Fraction	Effective diffusivity/($4\pi^2 \times 10^{-8}$ m^2 s^{-1})		
	$I_0 \times 10^8$	P_w	D_1	D_2	$\overline{D}$
C10, Pellet 1	109 ± 4.91	0.847 ± 0.01	10.507 ± 2.19	0.819 ± 1.18	9.028 ± 3.14
C10, Pellet 2	113 ± 5.84	0.543 ± 0.13	17.783 ± 6.46	3.271 ± 0.87	11.146 ± 4.81
Q17/6, Pellet 1	101 ± 1.69	0.909 ± 0.17	9.131 ± 1.74	1.128 ± 3.53	8.398 ± 5.41
Silica Alumina, Pellet 2	1E-6 ± 4.7E-9	0.960 ± 0.04	7.647 ± 0.35	1.057 ± 1.18	7.400 ± 2.19

Table 6.12

Tortuosities and molecular mean square displacements for the two-component model parameters [Long diffusion time (Δ = 100 ms)]. The error quoted is 95 % confidence intervals

Sample	Tortuosity			Average displacement (μm)		
	τ_1	τ_2	$\bar{\tau}$	r_1	r_2	$\bar{r}$
C10, Pellet 1	0.91 ± 0.19	11.61 ± 16.71	1.05 ± 0.37	28.26 ± 5.90	7.89 ± 11.36	37.04 ± 12.87
C10, Pellet 2	0.54 ± 0.20	2.92 ± 0.78	0.86 ± 0.37	28.26 ± 5.90	37.76 ± 13.34	41.16 ± 17.76
Q17/6, Pellet 1	1.06 ± 0.20	8.57 ± 26.81	1.15 ± 0.74	26.34 ± 5.03	9.26 ± 28.98	35.73 ± 23.00
Silica Alumina, Pellet 2	1.21 ± 0.06	8.77 ± 9.79	1.25 ± 0.37	32.20 ± 0.40	1.34 ± 9.53	33.54 ± 9.93

Table 6.13

Coefficients of determination of the log attenuation plots for the samples in case I for one-component fit

Sample	Coefficient of determination, R^2							
_	(Δ = 50 ms)				(Δ = 100 ms)			
_	Number of scans = 16		Number of scans = 32		Number of scans = 16		Number of scans = 32	
Aerosil	0.99590	0.99930	_	_	0.99456	0.99551	_	_
AL3984T	0.99910	0.99877	_	_	0.99987	0.99877	_	_
AL3992E	_	_	0.99893	0.99980	_	_	0.99844	0.99980
C10*	0.99941	0.99872	_	_	_	_	_	_
C30	0.99989	0.99981	_	_	0.99922	0.99827	_	_
Q17/6*	0.99299	0.99742	_	_	_	0.99700	_	_
S980A	0.99646	0.99967	_	_	0.99346	0.99717	_	_
S980G	0.99916	0.99926	_	_	0.99806	0.99761	_	_
Silica Alumina*	0.99965	0.99936	_	_	_	0.99435	_	_

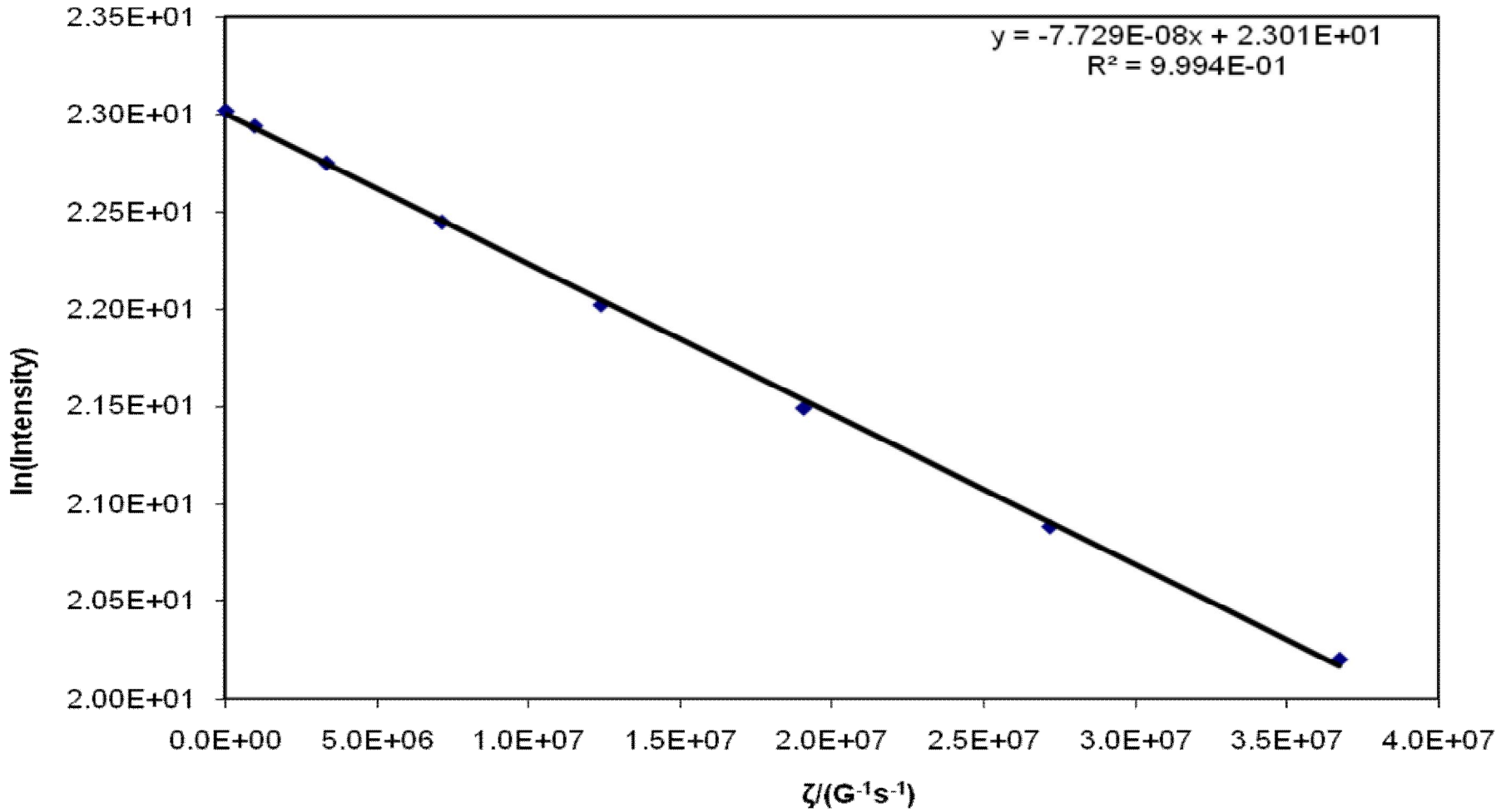

Figure 6.7

Echo log-attenuation results from simulated echo PFG experiments of partially water saturated support pellet (C10, Pellet 1) showing signs of deviation of linearity at short diffusion time (Δ = 50 ms)

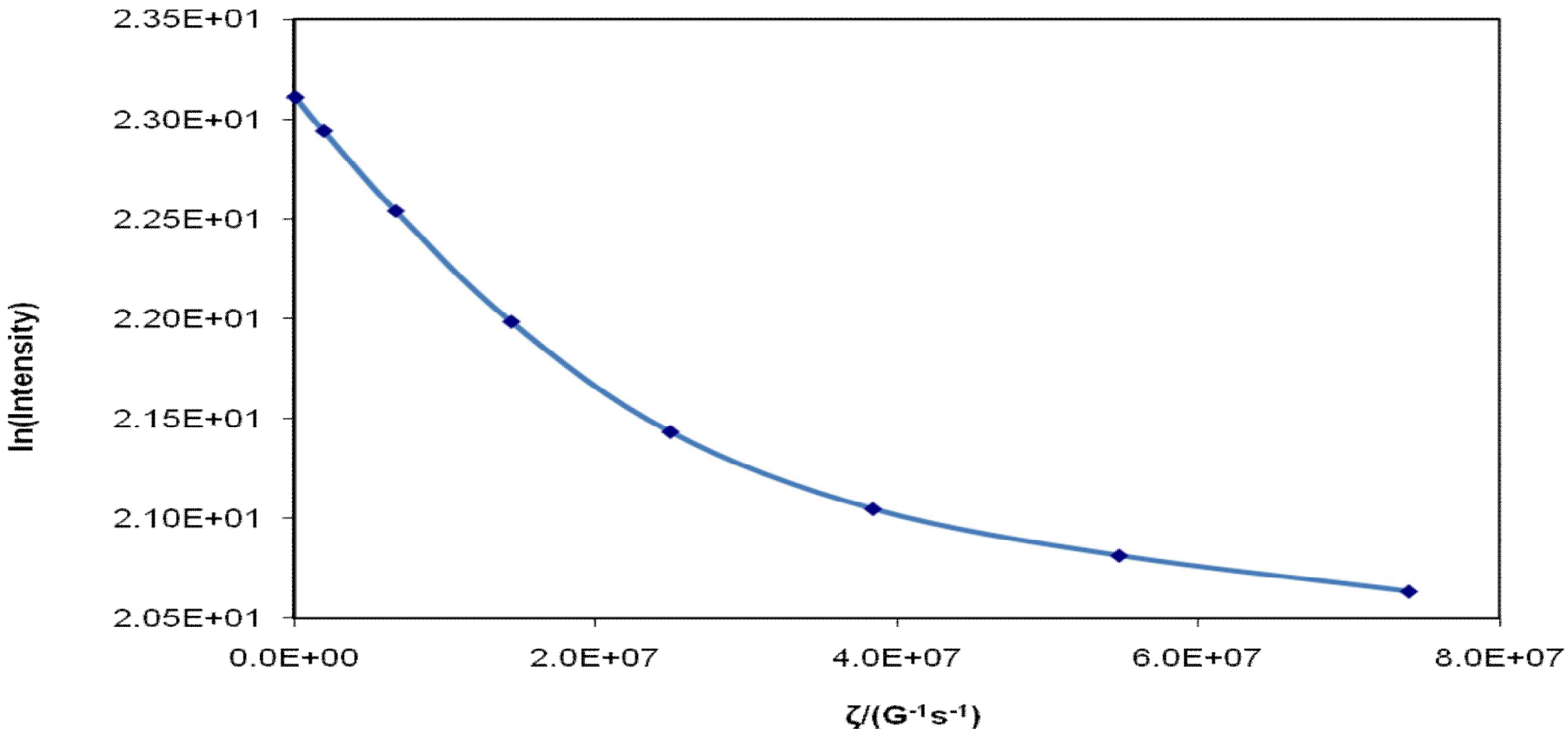

Figure 6.8

Echo log-attenuation results from simulated echo PFG experiments of partially water saturated support pellet (C10, Pellet 1) showing confirmed signs of deviation of linearity at long diffusion time. The solid line is a two-component model (Microsoft Excel and Origin Software were used to derive data)

6.4.4 Estimating the tortuosity of samples in case IV

A single pellet was used for each analysis. The same pellet probed in case II was used for each of the PGSE NMR experiment. The samples were partially saturated with water by suspending over 1.5M Na_2CO_3 solution until saturation equilibrium was reached. In this study, the effects from partially saturated pellets will be due to the lower adsorbate loading were investigated. The values of sample mean and error for the tortuosities, and displacements are given in Table 6.14. The reported uncertainties are the 95% confidence intervals.

It can be seen from Table 6.14, that the magnitude of the tortuosities increased in the order AL3992E < C30 < S980A < C10 < Silica Alumina < S980G < Q17/6 < AL3984T < Aerosil. There was no significant difference of diffusivity with time in most samples. From the displacement obtained in Table 6.14, it can be seen that there is no evidence of restricted diffusion in this case; the displacements are far greater than the average pore sizes in all samples shown in Table 6.2. The magnitude of displacement is increased in these order Aerosil < AL3984T < Q17/6 < S980G < Silica Alumina < C10 < S980A < C30 < AL3992E.

Table 6.15 shows the coefficient of determination of the log-attenuation plots. In general, there was difficulty in the assessments of log-attenuation plots even though the coefficients of determination were good. There were too many scattered points in the log-attenuation plots. Nevertheless, some of the samples that produced a good signal such as C10 have shown suspected signs of deviation from linearity at long diffusion times. However, after careful examination, such as increasing the number of scans to twenty, there was still no clear sign of possible double component diffusion model. As a result, after increasing the number of scans on two different occasions, it was decided to accept the linearity of the log-attenuation plot of samples. An example of such log-attenuation plot is shown in Figures 6.9 and 6.10.

Table 6.14

Tortuosities and molecular mean square displacements for the samples in case IV (The error quoted is 95 % confidence intervals)

Sample	Average Tortuosity		Average displacement (μm)	
	(Δ = 50 ms)	**(Δ = 100 ms)**	**(Δ = 50 ms)**	**(Δ = 100 ms)**
Aerosil	2.44 ± 0.02	2.69 ± 0.02	16.94 ± 0.08	22.72 ± 0.08
AL3984T	2.23 ± 0.14	2.20 ± 0.07	18.03 ± 0.68	25.75 ± 0.52
AL3992E	1.68 ± 0.03	1.70 ± 0.04	20.82 ± 0.20	29.21 ± 0.47
C10	1.84 ± 0.07	2.16 ± 0.08	19.92 ± 0.47	25.96 ± 0.64
C30	1.81 ± 0.06	1.91 ± 0.05	20.01 ± 0.38	27.56 ± 0.48
Q17/6	2.23 ± 0.03	2.34 ± 0.03	18.08 ± 0.16	24.93 ± 0.25
S980A	1.83 ± 0.05	1.97 ± 0.05	19.98 ± 0.39	27.24 ± 0.49
S980G	2.05 ± 0.05	2.16 ± 0.03	18.63 ± 0.32	25.67 ± 0.25
Silica Alumina	1.90 ± 0.06	1.96 ± 0.04	19.30 ± 0.39	26.91 ± 0.35

Table 6.15

Coefficients of determination of the log attenuation plots for the samples in case IV for one-component fit

Sample	Coefficient of determination, R^2			
_	(Δ = 50 ms)		(Δ = 100 ms)	
_	Number of scans = 24		Number of scans = 24	
Aerosil	0.99973	0.99976	0.99982	0.99982
AL3984T	0.96577	0.99832	0.99270	0.99838
AL3992E	0.99892	0.99925	0.99572	0.99925
C10	0.99830	0.98907	0.99446	0.99580
C30	0.98883	0.99977	0.99396	0.99881
Q17/6	0.99922	0.99916	0.99916	0.99902
S980A	0.99651	0.99609	0.99800	0.99510
S980G	0.99829	0.99584	0.99915	0.99887
Silica Alumina	0.99935	0.99025	0.99802	0.99861

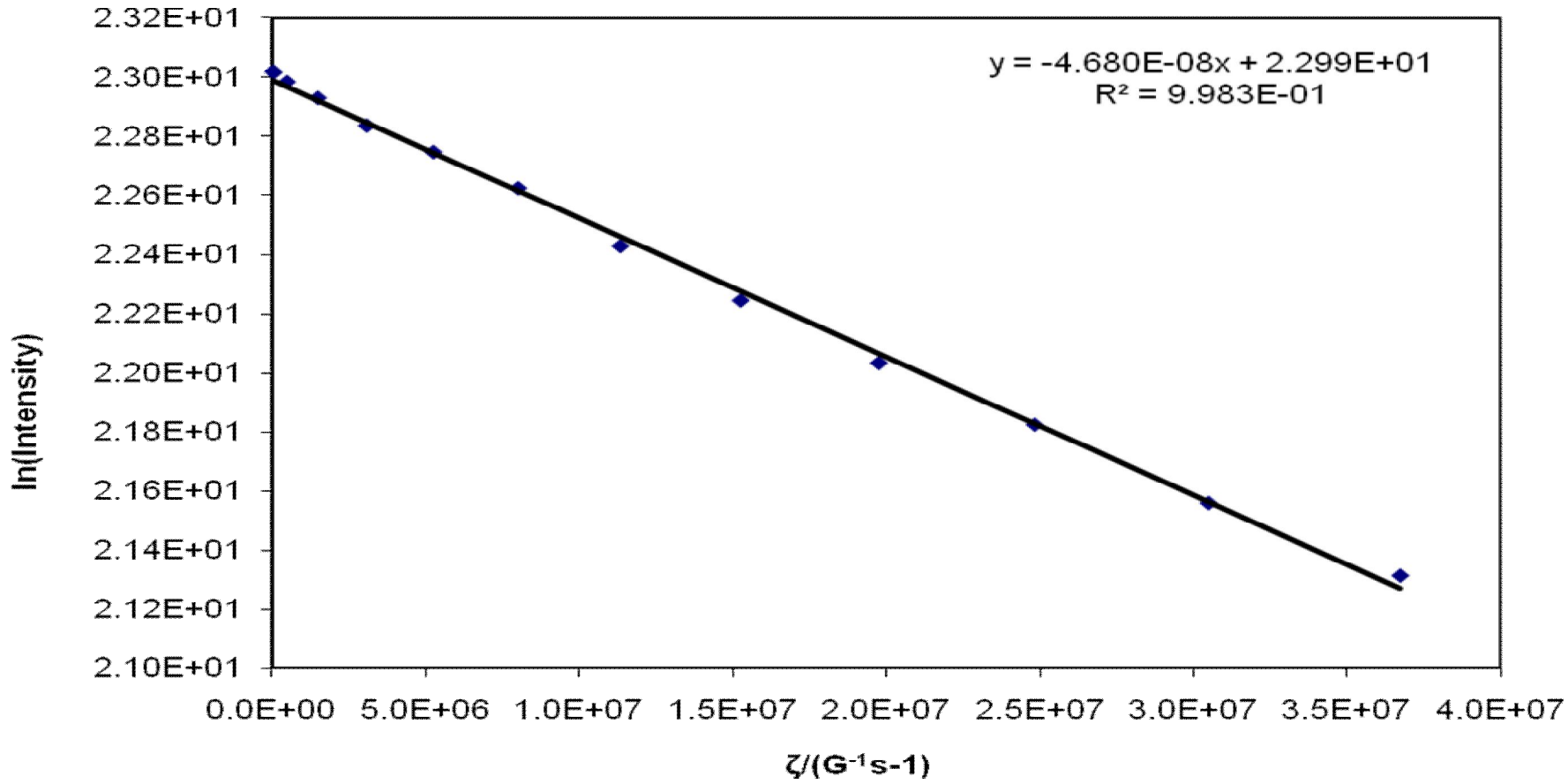

Figure 6.9

Echo log-attenuation results from simulated echo PFG experiments on partially water saturated pellet (C10, Pellet 1) showing scattered points at short diffusion time (Δ = 50 ms)

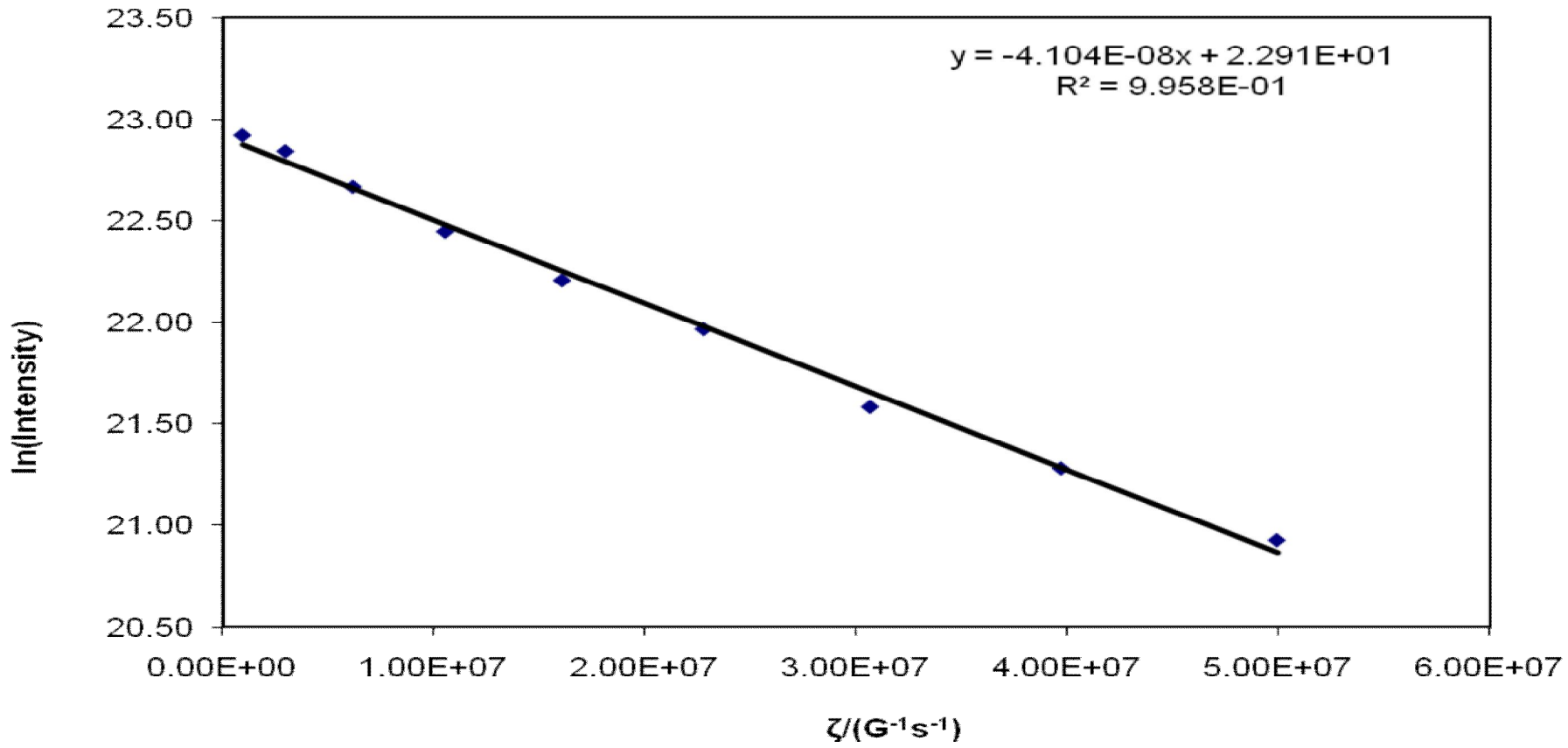

Figure 6.10

Echo log-attenuation results from simulated echo PFG experiments on partially water saturated pellet (C10, Pellet 1) showing signs deviation from non linearity at long diffusion time (Δ = 100 ms)

6.4.5 Comparisons of tortuosities obtained in cases I to IV

This section provides a comparison between the respective estimated tortuosities with the different experimental set up and conditions in each case. Samples were fully saturated with water in cases I and II. However, a single pellet was suspended over a water reservoir for imbibition in case II. The same set pellets probed in case II was considered for the analysis in cases III and IV. The samples were partially saturated with water by suspending over sodium carbonate solution (Na_2CO_3) until saturation equilibrium was reached. However, the concentration of the solution in case IV was three times higher than that of case III. Therefore, PGSE NMR technique was used to investigate the distribution of water ganglia within these samples. In general, a range of echo attenuations were obtained by varying the gradient duration. The diffusion times used for each analysis were 50 and 100 ms, respectively. It was found that the estimated tortuosities for most samples were not affected by diffusion time. Therefore, for this Section and Section 6.5, the tortuosities at short diffusion time will be considered for analysis. The estimated tortuosity and fractional saturation values are summarised in Table 6.16.

It can be seen from Table 6.16, the tortuosities for most of the samples in case I were of values ≥ 0.2 and higher than the tortuosities of the same samples in case II. This was much significant in AL3984T, Q17/6, and Silica Alumina. The estimated tortuosities of C10 and S980A were roughly the same in cases I and II. It should be noted that the estimated tortusities in case I describe the interparticle and intrapellet tortuosities. Thus, there was a high possibility of bulk film on the outside of the pellets in case I. For case III, the estimated tortuosities for most samples were of values ≥ 0.2 and higher than the tortuosities of the same samples in case II. This was much significant in Aerosil and S980A. However, the estimated tortuosities in Q17/6 and Silica Alumina were roughly the same in cases II and III. In contrast, the estimated tortuosities of C10, C30, and S980A in case II were of values ≥ 0.2 and higher than the tortuosities of the same samples in case III. Finally, the tortuosities in case IV were of values ≥ 0.4 and higher than the tortuosities of the same samples in case III. This was much significant in AL3984T. In contrast, the estimated tortuosities for AL3992E in case III were of values ≥ 0.4 and higher than the tortuosities in case IV. Therefore, the estimated tortuosities for pellets of Aerosil, AL3984T, Q17/6, S980G, and Silica Alumina generally increased with decreased saturation levels. The rest of the samples showed advanced complex variability.

Table 6.16

Comparison of tortuosities for samples in cases I to IV

Sample	Average of fourteen pellets (Case I)		Average of two pellets (Case II)		Average of two pellets (Case III)		Average of two pellets (Case IV)	
	Tortuosity	Amount Adsorbed	Tortuosity	Amount adsorbed (M_0)	Tortuosity	Fractional saturation	Tortuosity	Fractional saturation
_	(Δ = 50 ms)	(g)	(Δ = 50 ms)	(g)	(Δ = 50 ms)	M/M_0	(Δ = 50 ms)	M/M_0
Aerosil	1.59 ± 0.06	0.056	1.39 ± 0.03	0.053	1.81 ± 0.05	0.943	2.44 ± 0.02	0.906
AL3984T	1.75 ± 0.03	0.230	1.16 ± 0.02	0.229	1.44 ± 0.04	0.961	2.23 ± 0.14	0.952
AL3992E	1.76 ± 0.02	0.179	1.44 ± 0.02	0.175	2.06 ± 0.02	0.994	1.68 ± 0.03	0.983
C10	1.57 ± 0.01	0.063	1.70 ± 0.02	0.064	1.40 ± 0.03	0.969	1.84 ± 0.07	0.953
C30	1.41 ± 0.01	0.073	1.54 ± 0.02	0.074	1.32 ± 0.01	0.986	1.81 ± 0.06	0.081
Q17/6	2.38 ± 0.03	0.144	1.33 ± 0.02	0.148	1.31 ± 0.06	0.993	2.23 ± 0.03	0.986
S980A	1.75 ± 0.02	0.030	1.75 ± 0.10	0.043	1.28 ± 0.03	0.698	1.83 ± 0.05	0.372
S980G	1.54 ± 0.02	0.015	1.27 ± 0.03	0.015	1.47 ± 0.03	0.933	2.05 ± 0.05	0.133
Silica Alumina	2.05 ± 0.04	0.048	1.20 ± 0.03	0.048	1.27 ± 0.02	0.896	1.90 ± 0.06	0.750

Note

M/M_0 = Amount adsorbed (g)/ Amount adsorbed when fully saturated (g)

6.5 Discussion

PGSE NMR diffusion measurements are sensitive to the structure of a medium over a scale comparable to the r.m.s displacement of molecules during the experimental time scale of 10^{-3} to 1 s (Callaghan, 1984). The PGSE NMR studies of liquid self-diffusion within a porous medium can give information on the pore structure itself. Unlike NMR relaxometry, no ancillary technique is required to derive the target parameter from raw PGSE NMR data. Therefore, the diffusion measurements provide absolute values of diffusivities, with respect to the probe liquid (deionised water) used. In addition, the effect of structural damage was limited by cutting the big samples (Aerosil and Q17/6) with a small hand saw. In general, the PGSE NMR technique does not probe length scale equivalent to the dimension of the whole pellet. Unlike MRI, PGSE NMR method is limited to the length scale of the probe, and thus, the effect of structural damage in those big samples was negligible. Furthermore, the presence of pore shielding and structural damage in these materials was studied previously by Rigby *et al*. (2003b). It was found that no structural deformation or collapse occurred for these samples.

The main objective of this study was to investigate the potential effects from restricted diffusion, or various diffusion domains having different diffusivities. In addition, the effects of different diffusion time-scales in the estimated tortuosities were observed by examining the diffusion behaviour of water within these samples. Therefore, in order to elucidate transport phenomena in porous media, the interconnectivities of the pore system of a wide range of porous alumina and silica pellets were examined by diffusion over two diffusion time-scales (Δ = 50 and Δ = 100 ms). The total intraparticle pore volume of the samples accessible to water was estimated by gravimetric method. It was found that the pore volume accessed by the adsorbate decreased with a decrease of relative pressure. Therefore, the liquid connectivity within these samples was successfully reduced as intended. The quoted tortuosities of the samples previously studied by Hollewand and Gladden (1995a) and Rigby and Gladden (1998) are in good agreement with the estimated tortuosities of fully saturated samples in Table 6.4. Furthermore, it was found that, for different pellets studied from the same batch of different samples, the estimated tortuosities were in close agreement with minor intra-batch variability in most samples. This observation was in good agreement with the accepted literature of accurate sample mean of tortuosity values equilibration by Karger and Ruthven (1992). The observed intra-batch

variability in this study could be attributed to slight differences from manufacturing conditions of the material.

The log-attenuation plots obtained allowed for a high precision determination of diffusivity in bulk liquid (deionised water) and self-diffusion of deionised water imbibed within these samples. The self-diffusion coefficient of water obtained at 25 °C was nearly 2.34 ± 0.03 $\times 10^{-9}$ m^2/s in each analysis. This value is similar to the quoted value of 2.3×10^{-9} m^2/s obtained by Mills (1973) at 25 °C. However, some of the collected data at the long diffusion time produced non-linear log-attenuation plots. The cause of this non-linearity observed must be determined for accurate interpretation of the samples. As detailed in Section 3.4.4, restricted diffusion can cause non-linearity in log-attenuation plots (Callaghan *et al.*, 1983). In addition, Hollewand and Gladden (1995a) investigated some of the samples in this study. These researchers observed non-linearity in log-attenuation plots the samples investigated. Hollewand and Gladden (1995a) attributed the non-linearity of the log-attenuation plots to molecules in different environments diffusing at different rates. Therefore, the non-linearity of log-attenuation plots observed can be attributed to restricted diffusion by solid boundaries and/or the contributions from different diffusion domains (macroscopic heterogeneity). However, these samples are amorphous oxide supports, and thus, in the absence of structural order, anisotropic diffusion behaviour is not expected.

The estimated displacements were far greater than the average pore sizes, and thus, this rules out the possibility of restricted diffusion for the length scales studied. In addition, if restricted diffusion was present, then from the Stokes-Einstein relation, Equation 3.47, by the same factor for an increase in diffusion time, there would be a decrease in diffusion coefficient. Furthermore, there was no evidence of a sample having pores with a radius greater than $1\,\mu m$. According to Perry and Green (1998), the average radius of a water molecule is 1.9 Å for a water density of 997 kg/m^3 at 25 °C. When the radius of the solute molecule is comparable to the pore radius, significant steric hindrance and hydrodynamic interactions with the pore wall might occur (restricted diffusion). This effect becomes more pronounced when the ratio of molecular to pore radius, exceeds 0.1 (Hollewand and Gladden, 1995a). In this study, the ratio of molecular radius to pore radius was less than 0.1, and thus confirms the absence of restricted diffusion from solid boundaries. Therefore, the non-linearity observed in log-attenuation plots is due the macroscopic heterogeneity.

As detailed in Section 3.4.4, the log-attenuation plots of a macroscopic heterogeneous sample might have various diffusional domains which have different diffusivities (for example, diffusion of water between and within the material). In the case of slow exchange between two diffusion domains, multi-exponential echo decay would be observed with each domain possessing its own diffusion coefficient (Kärger *et al*., 1983). However, when the exchange between the different domains is fast, an average diffusion coefficient would be observed (Hollewand and Gladden, 1995a). In this study, a simple linear ($R^2 \geq 0.997$) behaviour from the log-attenuation plots was exhibited in most data sets at short diffusion time. This further supports the theory of fast exchange between bulk and surface water in pore space of a porous glass by Kärger *et al*. (1983) and D'Orazio *et al*. (1990). In addition, the r.m.s displacement during the diffusion time probed is of order of $10\,\mu m$. The mean pore size of the samples investigated is in the range of 7.45 – 27.9 nm. Therefore, the PGSE NMR technique gave information about the structural contribution from a given region at short diffusion time. The average of that region produced a single component diffusion coefficient given by the effective diffusivity of that specified volume. However, at long diffusion time, the r.m.s displacement traced environments averaged over several pores, reflecting the average medium properties in the whole sample, and thus, revealing the heterogeneous nature of the system. Therefore, the deviation from simple linear behaviour observed in most data sets indicates the presence of several diffusion domains. This further supports the theory of slow exchange between two or more diffusion domains observed in silica and alumina materials by Hollewand and Gladden (1995a). Figure 6.6 illustrates the combined effect of such a macroscopic heterogeneous system. In contrast, the log-attenuations plots of some samples have shown a reasonable degree of linearity ($R^2 = 0.999$) irrespective of the diffusion time used, and thus, suggests the PGSE technique probed the homogenous part of the system.

In addition, the majority of fluid molecules held within a saturated porous medium at short diffusion time would experience free diffusion (Davies *et al*., 2007). However, at long diffusion time, the diffusing molecules would explore the connectivity of the porous medium and the ratio of the apparent diffusion coefficient to the free diffusion coefficient approaches an asymptote equal to the inverse of tortuosity (Sen *et al.*, 1994). Therefore, the results obtained in this study support the findings of Sen *et al.* (1994) and Davies *et al*. (2007). Moreover, the displacement of molecules undergoing Brownian motion increased

with diffusion time, and thus, the increased molecular displacement suggests that diffusing molecules explored the connectivity of the porous medium. At short diffusion time, the length scale allowed the molecules to probe the diffusion domains present at that scale. However, at increased diffusion time, the length scale allowed for additional diffusion domains to be probed by the water molecules. The increased displacement confirms the non existence of resistance of water molecules probing these materials.

The estimated tortuosities of the samples at short diffusion time are of order of 1.85 ± 0.50 in case I. At first glance, the estimated tortuosities of most samples varied with diffusion time. Then, 95 % confidence intervals were used to evaluate the reliability of the estimated tortuosities. It was found that the estimated tortuosities did not vary with diffusion time in most samples. As detailed in Section 3.4.5, Farrher *et al*. (2008) observed similar findings for fully saturated silica glasses. However, Aerosil and C30 showed more complex behaviour that the rest of the samples. The estimated tortuosities of Aerosil and C30 varied with the diffusion time. The complex behaviour of these samples can be attributed to high degree of heterogeneity they possessed than the rest of the samples. In case II, the estimated tortuosities at short diffusion time are of order of 1.50 ± 0.30. It was found that only AL3922E was sensitive to the diffusion time. Therefore, there are minor discrepancies between the estimated tortuosities in case I and II. The estimated tortuosity for most of the samples in case I was of values ≥ 0.2 and higher than the tortuosity of the same samples in case II. It should be noted that the samples were fully saturated with water in cases I and II. However, a single pellet was suspended over a water reservoir for imbibition and PGSE NMR experiment in case I. Nevertheless, there was an evidence of complete saturation in case II. This complete saturation was supported by the impregnation and adsorption test results in Table 6.3. Therefore, the reduced tortusities observed in case II could be attributed to the absence of additional film thickness of water, reduced sample batch variability, and interparticle path of the pellets that were present in the samples used in case I. An average of seven pellets in the NMR sample tube in case I.

The same set pellets probed in case II were used for each PGSE NMR experiment in cases III and IV. The choice of adopting the pellets was considered in order to make comparison of estimaed tortuosities at different equilibrium saturations. As detailed in Sections 6.2.3 and 6.2.4, the pellets were partially saturated with water. It was found that the saturation

levels decreased with a decrease in relative pressure of the solution. Thus, the partially saturated samples would have clusters of air pockets that were absent with fully saturated pellets in case II. These clusters air pockets would ultimately block paths accessible to water molecules. Subsequently, the water molecules would be forced to go some extra length that could increase the overall tortuosities of the samples. The estimated tortuosities of the samples at short diffusion time are of order of 1.70 ± 0.40 in case III. Where as, in case IV, the estimated tortuosities at short diffusion time are 2.10 ± 0.40. It can be seen the estimated tortuosities of most samples, increased with the decreased relative pressure of the solution. Therefore, increased estimated tortuosities suggest the absence of vapour phase contribution to the total diffusional displacements. This finding can be interpreted as an absence of molecular exchange between the liquid and vapour phases within these samples. However, as detailed in Section 3.4.5, molecular exchange between liquid and vapour phases was observed within partially saturated porous glass by Valliullin *et al*. (1997) and Farrher *et al*. (2008). Therefore the finding in this study disagreed with the work of Valliullin *et al*. (1997) and Farrher *et al*. (2008) on partially saturated porous glass.

The distribution and mass transfer mechanisms within porous materials can be explained by the pore size of these samples. As detailed in Section 3.4.5, D'Orazio *et al.* (1990) investigated of distribution of water molecules in partially saturated porous glasses. It was found that the smaller pore size lead to a suppression of vapour-phase diffusion proceeded by the Knudsen mechanism since the coefficient of Knudsen diffusion is proportional to the pore size. Therefore, perhaps the small pores in these samples, which are generally the path ways, were completely filled by capillary condensation and the bigger pores consist of the water vapour and the multi-layered adsorbed phases. Subsequently, this would reduce the vapour phase contribution to the total diffusion rate. In addition, Karger *et al*. (1983) investigated liquid confided in porous glasses with pore sizes within the range of 0.8-50 nm. These researchers observed reduction of diffusivity in small pores which was attributed to stabilisation of liquid molecules by pore walls. Similar observations were made by Fakuda *et al*. (1989) for porous glases with pore sizes in the range of 4-45 nm.

Furthermore, the estimated diffusion coefficients for the fast and slow components of the samples in cases II and III at long diffusion time were examined for restricted diffusion behaviour. The r.m.s displacement of a water molecule estimated for water contained in

both the fast and moving components were far greater than the average pore size of the samples. Therefore, there was no evidence of restricted diffusion in both fast and slow moving components. In addition, most of the transport phenomena investigated in these samples was a product of the fast diffusion component. The effect of vapour phase contribution to the total diffusional displacements was observed when the diffusion time was doubled. Also, the estimated tortuosities of most of the samples with double component models were lower than the tortuosities of the same samples at short diffusion time. This finding can be interpreted as molecular exchange between the liquid and vapour phases, between the fast and slow components. Similar observation was made in porous glasses by Valliullin *et al*. (1997), and Farrher *et al*. (2008). Moreover, in case III, the tortuosities observed in C10 in the first and second pellet were 0.91 ± 0.19 and 0.54 ± 0.20, respectively. This finding can be interpreted as the presence of vapour phase contribution to the total diffusional displacements.

6.6 Conclusion

PGSE NMR studies carried out on fully and partially saturated samples revealed similar tortuosities for the range of length scales studied. A simple linear behaviour ($R^2 \geq 0.999$) was exhibited in most data sets at short diffusion time (Δ = 50 ms). However, a deviation from linearity was observed at long diffusion time (Δ = 100 ms) in most data sets. The relative molecular displacements estimated were far greater than the average pore sizes of samples, and thus, any deviation seen was associated with the macroscopic heterogeneity of the sample. The apparent linearity of the log-attenuation plot at short diffusion time was due to the relatively restricted range of values of ξ possible, when compared with longer diffusion time. Therefore, the linearity observed at short diffusion time produced a single component diffusion coefficient given by the effective diffusivity of that specified volume. Similar tortuosities were obtained for the range of length scales studied. In partially saturated samples, the tortuosities of most samples increased with a decrease of relative pressure of the vapour. These increased tortuosity values ruled out the possibility of vapour phase contribution to the total diffusional displacements, and can therefore be interpreted as no molecular exchange between liquid and vapour phases within the samples. However, there was evidence of vapour phase contribution to the total diffusional displacements in partially saturated samples with two component diffusion models.

6.7 References

Callaghan, P.T., Jolley, K.W., and Humphrey, R.S., 1983. Diffusion of fat and water in cheese as studied by pulsed field gradient nuclear magnetic-resonance. *Journal of Colloid and Interface Science,* 93(2), 521–529.

D'Orazio, F., Bhattacharja, S., and Halperin W.P., 1990. Molecular self diffusion and nuclear magnetic resonance relaxation of water in unsaturated porous silica glass. *Physical review,* 42, 9810-9818.

Davies, C.J., Griffith, J.D., Sederman, A.J., Gladden, L.F., Johns, M.L., 2007. Rapid surface-to-volume ratio and tortuosity measurement using Diffirain. *Journal of magnetic resonance*, 187 (1). 170-175.

Fakuda, K., Kasuga, T., Mizusaki, T., Hirai, A., Eguchi, K., 1989. Study of self-diffusion process of water molecules in porous glass by simulated spin echo method with pulsed field gradients. *Journal of physical society of Japan*, 58 (5), 1662-1666.

Farrher, G., Ardelean, I., Kimmich, R., 2008. Time-dependent molecular diffusion in partially filled porous glasses with heterogeneous structure. *Applied magnetic resonance,* 34 (1-2), 85-99.

Hollewand M.P., Gladden L.F., 1993. Heterogeneities in structure and diffusion within porous catalyst support pellets observed by NMR Imaging. *Journal of catalyst,* 144, 254-272.

Hollewand, M.P., and Gladden, L.F., 1995a. Transport heterogeneity in porous pellets-I. PGSE NMR studies. *Chemical Engineering Science*, 50, 309-326.

Kärger, J., Lenzer, J., Pfeifer, H., Schwabe, H., Heyer, W., Janowski, F., Wolf, F. and Zdanov, S.P., 1983. NMR study of adsorbate self-diffusion in porous glasses. *J. Am. Ceram. Soc.*, 66, 69–72.

Kärger, J. and Ruthven, D.M., 1992. *In: Diffusion in Zeolites and other Microporous Solids*. New York: Wiley.

Mills R., 1973. Self- diffusion in normal and heavy water in the range 1-45'. *The Journal of Physical Chemistry*, 77(5), 685–688.

Perry, R.H., and Green, D.W., 1998. *Perry's Chemical Engineers' Handbook*. The McGraw Hill.

Rigby, S.P., and Gladden, L.F., 1998. The use of magnetic resonance images in the simulation of diffusion in porous catalyst support pellets. *Journal of Catalysis*, 173 (2), 484-489.

Sen, P.N., Schwartz, L.M., Mitra, P.P., 1994. Probing the structure of porous media using NMR Spin echoes. *Magnetic resonance imaging*, 12 (2), 227-230.

Valiullin, R.R., Skirda, V.D., Stapf, S., Kimmich, R., 1997. Molecular exchange processes in partially filled porous glass as seen with NMR diffusometry. *Physical review E*, 55 (3), Part A, 2664-2671.

7.0 NMR pulsed gradient spin echo technique II

[Study of the kinetics of adsorption in porous media]

7.1 Introduction

The principles and the applications of PGSE NMR technique have been discussed in Section 3.4. The proposal for the research programme can be found in Section 3.4.6. In addition, the description of the PGSE NMR spectrometry and the experimental considerations are given in Section 6.3. In order to understand the process underlying water adsorption, the disposition and distribution of adsorbed water ganglia within partially-saturated samples was investigated as a function of pore loading in this Chapter. The rate of mass transfer and the adsorbed ganglia morphology, as characterised by the tortuosity, was studied over a period of time. Thus, the PGSE NMR technique was used quantitatively to study absorption phenomenon under different pore filling conditions.

7.2 Sample preparation and experimental considerations

The sample preparation and the quartz tube set up in Section 6.2.4 was adopted for this study. The samples were partially saturated with water by suspending over 1.5M Na_2CO_3 solution until saturation equilibrium was reached. The pellets probed in Section 6.4.2 were used for each sample preparation and PGSE NMR experiment. In Section 6.2.4, the pellets were allowed to reach saturation equilibrium without any disturbance. In this study, the pellets were disturbed periodically to take a mass uptake reading before any PGSE NMR experiment. The mass uptake of water by the pellets was measured by an electronic mass balance after every 24 hours. The diffusion coefficients were quickly measured with PGSE NMR technique after each mass of uptake reading. The duration of the period of the PGSE NMR experiments depended on the saturation equilibrium of the pellets. All experiments were conducted at 25 ± 0.5 °C, and the acquisition parameters used in Section 6.3 were adopted. A series of eight spectra was taken at increasing gradient strengths and the number of scans for each spectrum was 16. Signal attenuation was used to calculate the confined water diffusion coefficient and its tortuosity as described in Section 3.4.2.

7.3 Results and analysis

PGSE NMR technique was used to probe the liquid distribution within the pellet during the course of adsorption. For each sample, the daily mass uptake and diffusional displacements were measured. The reported uncertainties are the 95% confidence intervals that indicate the spread of the results over samples from the same batch and the error associated with the PGSE NMR measurement. The complete set of results for these fits and the data obtained are given in Appendix A7. Furthermore, the rate limiting step for the mass transfer was determined by calculating the Biot number. The Biot number represents the ratio of the external convective to internal diffusive mass transport. For low Biot numbers (< 0.1) the resistance to adsorption within the sample is much higher than the resistance to convection by the external fluid (air). It can be seen in Table 7.1 that the rate limiting step is the convective mass transfer. It was found that the Biot number of the samples increases with an increase in concentration of the solution.

Table 7.1

Average Biot number estimated in fully and partially saturated samples

Sample	Biot number		
	H_20 Reservoir (x = 1)	**0.5M Na_2CO_3 Reservoir (x = 0.981)**	**1.5M Na_2CO_3 Reservoir (x = 0.931)**
Aerosil	5.19 ± 0.28	7.31 ± 0.49	9.71 ± 0.49
AL3984T	4.13 ± 1.55	5.71 ± 0.40	8.16 ± 0.48
AL3992E	3.37 ± 3.62	6.49 ± 0.37	5.32 ± 2.71
C10	8.22 ± 0.43	4.31 ± 1.53	6.34 ± 0.37
C30	4.62 ± 0.17	4.31 ± 0.26	5.51 ± 0.24
Q17/6	5.72 ± 0.75	5.24 ± 3.44	9.46 ± 1.21
S980A	5.32 ± 0.43	4.65 ± 0.47	5.96 ± 0.46
S980G	3.86 ± 0.31	4.76 ± 0.40	6.17 ± 0.44
Silica Alumina	4.31 ± 0.66	4.28 ± 0.62	6.24 ± 0.89

Note

***x* = Relative pressure of the solution**

7.3.1 Tortuosity as a function of pore filling and time in Aerosil

The daily mass uptake of the sample is given in Table 7.2. The mass transfer was relatively fast for both pellets, with minor intra-bath variability. However, pellet 1 attained saturation equilibrium after 48 hours. In contrast, pellet 2 attained saturation equilibrium after 96 hours. The evolution of tortuosity with time can be seen in Table 7.3. It can be seen in Table 7.3, that in the first three days, the error bars for measurements where $\Delta = 50$ ms and $\Delta = 100$ ms did not over-lap in most data. Therefore, a significant difference was observed due the different diffusion time used.

Table 7.2

The daily mass uptake (by adsorption) of Aerosil in a period of four days

	Pellet 1			**Pellet 2**		
Time	**weight of sample**	**Amount adsorbed (M)**	**Fractional saturation (M_t/M_∞)**	**weight of sample**	**Amount adsorbed (M)**	**Fractional saturation (M_t/M_∞)**
(Hours)	**(g)**	**(g)**	**_**	**(g)**	**(g)**	**_**
0	0.0087	0	0	0.0105	0	0
24	0.0114	0.0027	0.5786	0.0140	0.0053	0.6208
48	0.0124	0.0037	0.7991	0.0155	0.0068	0.7911
72	0.0129	0.0042	0.9214	0.0165	0.0078	0.9067
96	0.0133	0.0046	1	0.0173	0.0086	1

Note

M_t = Amount adsorbed at some time, *t*

M_∞ = Amount adsorbed at equilibrium

The spectrum obtained from the PGSE NMR spectrometer after 24 hours was noisy though there was a reasonable linearity of the log-attenuation plot shown in Figures 7.2 to 7.3. It should be noted that there was a limit to the number of scans that could be used to reduce the noise as the system evolved rapidly. The tortuosity of the system as a function of fractional saturation is shown in Figure 7.1. The high tortuosity observed in Figure 7.1 after 24 hours can be attributed to low liquid connectivity. The difference between the short and long diffusion time suggests that the structure of adsorbed water ganglia was

heterogeneous over length-scales of the order of the r.m.s displacement. The tortuosities of the pellets significantly dropped after 48 hours. This sudden of tortuosity can be interpreted as increased liquid connectivity. Finally, there was a general stability of the tortuosities after 72 hours. In addition, the further water uptake of the sample removed the heterogeneity over length-scales of the order of the r.m.s displacement. The average tortuosity estimated at saturation equilibrium for Δ = 50 ms and Δ = 100 ms diffusion time were 1.51 ± 0.03 and 1.55 ± 0.05, respectively. Higher tortuosities were estimated in Section 6.4.4. The average estimated tortuosities in an undisturbed set up at Δ = 50 ms and Δ = 100 ms diffusion time were 2.44 ± 0.02 and 2.69 ± 0.02, respectively.

Table 7.3

The daily tortuosity values of Aerosil in a period of one week. The error quoted represents 95 % confidence intervals

Time	Tortuosity (Pellet 1)		Tortuosity (Pellet 2)	
Hours	(Δ = 50 ms)	(Δ = 100 ms)	(Δ = 50 ms)	(Δ = 100 ms)
24	6.40 ± 0.29	9.29 ± 0.45	7.21 ± 0.60	9.57 ± 0.39
48	1.18 ± 0.02	1.48 ± 0.07	1.56 ± 0.04	1.49 ± 0.04
72	1.41 ± 0.01	1.74 ± 0.06	1.39 ± 0.03	1.55 ± 0.05
96	1.41 ± 0.02	1.48 ± 0.03	1.60 ± 0.02	1.62 ± 0.04

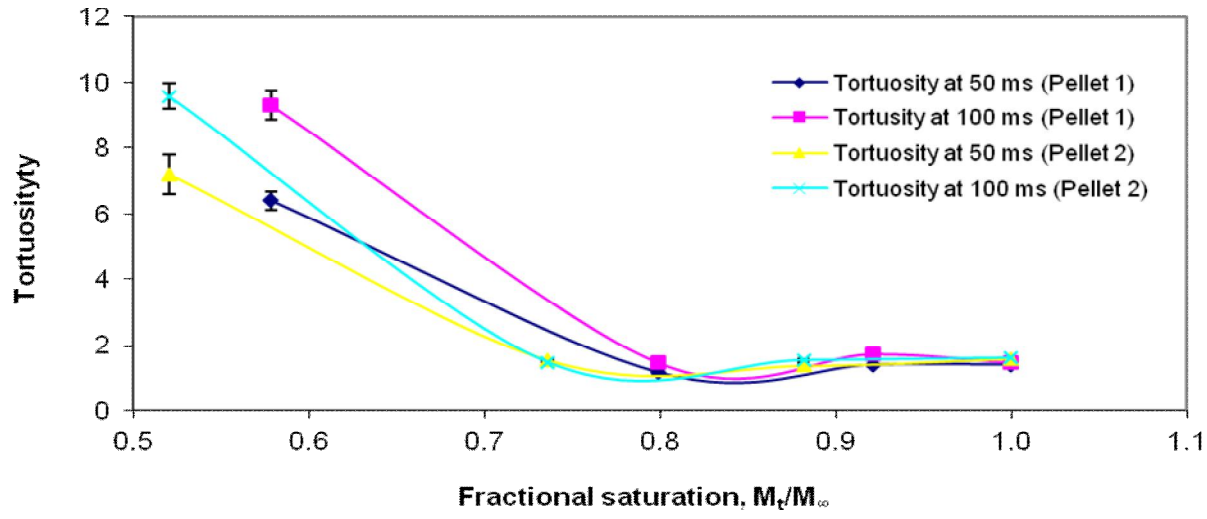

Figure 7.1

Tortuosity as a function fractional saturation of Aerosil

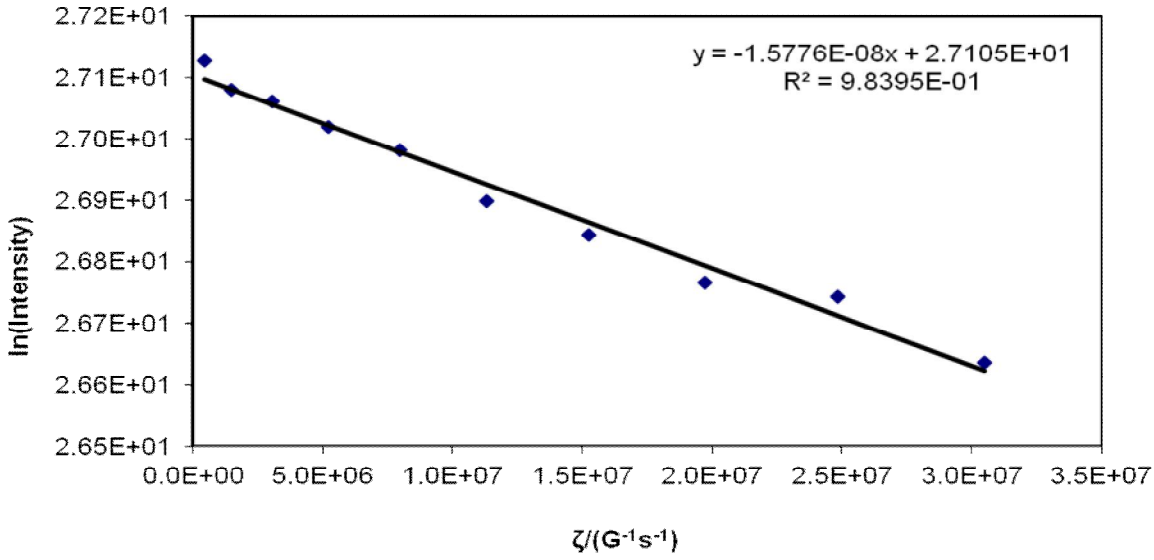

Figure 7.2

Echo log-attenuation results from simulated echo PGSE experiments on partially saturated support pellet 1 showing signs of noise at 50 ms diffusion time after 24 hours

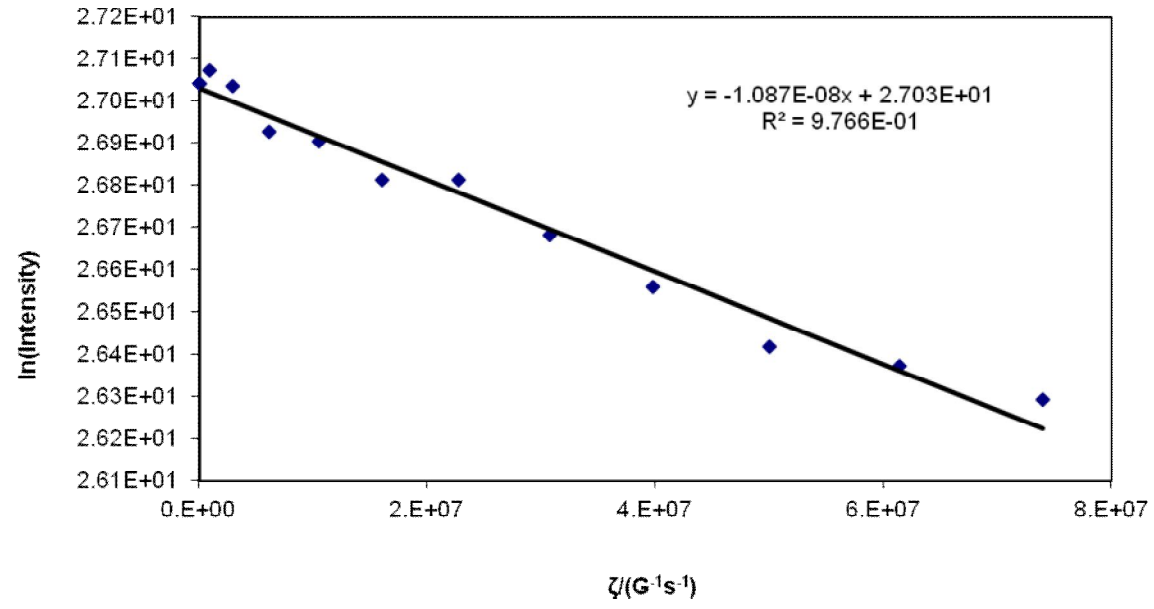

Figure 7.3

Echo log-attenuation results from simulated echo PGSE experiments on partially saturated support pellet 1 showing signs of noise at 100 ms diffusion time after 24 hours

7.3.2 Tortuosity as a function of pore filling and time in AL3984T

The daily mass uptake by the sample is given in Table 7.4. The mass transfer was relatively the same for both pellets, with minor batch variability. The daily values of sample mean, and error, for the tortuosities are given in Table 7.5. A good intensity signal was obtained after 48 hours as shown in the log-attenuation plots in Figures 7.5 and 7.6. A simple linear ($R^2 \geq 0.999$) behaviour was observed in the log-attenuation plot of pellet 1 at short diffusion time ($\Delta = 50$ ms). In contrast, deviation from simple linear behaviour was observed in pellet 2. However, at long diffusion time ($\Delta = 100$ ms), deviation from simple linear behaviour was exhibited in the log-attenuation plot for both pellets.

Table 7.4

The daily mass uptake (by adsorption) of AL3984T in a period of one week

	Pellet 1			Pellet 2		
Time	**weight of sample**	**Amount adsorbed (M)**	**Fractional saturation (M_t/M_∞)**	**weight of sample**	**Amount adsorbed (M)**	**Fractional saturation (M_t/M_∞)**
(Hours)	**(g)**	**(g)**	**_**	**(g)**	**(g)**	**_**
0	0.0343	0	0	0.0295	0	0
24	0.0384	0.0041	0.2880	0.0331	0.0036	0.2447
48	0.0464	0.0121	0.8451	0.0389	0.0094	0.6387
72	0.0470	0.0127	0.8865	0.0403	0.0108	0.7369
96	0.0477	0.0134	0.9396	0.0407	0.0112	0.7641
120	0.0486	0.0143	1	0.0442	0.0147	1

Table 7.5

The daily tortuosity values of AL3984T in a period of one week. The error quoted represents 95 % confidence intervals

Time	**Tortuosity (Pellet 1)**		**Tortuosity (Pellet 2)**	
Hours	**($\Delta = 50$ ms)**	**($\Delta = 100$ ms)**	**($\Delta = 50$ ms)**	**($\Delta = 100$ ms)**
24	1.49 ± 0.02	1.76 ± 0.05	1.48 ± 0.02	1.48 ± 0.02
48	1.67 ± 0.02	1.83 ± 0.03	1.40 ± 0.01	1.62 ± 0.05
72	1.25 ± 0.03	1.58 ± 0.07	1.18 ± 0.02	1.60 ± 0.11
96	1.25 ± 0.02	1.27 ± 0.03	1.52 ± 0.03	1.57 ± 0.06

The tortuosity of the sample as a function of fractional saturation is shown in Figure 7.4. For pellet 1, there was a continuous increase of tortuosity after 24 hours. The tortuosity reached its peak and declined after 48 hours and 72 hours, respectively. The high tortuosity observed for the first 48 hours can be attributed to low liquid connectivity. Where as, the peak at 48 hours indicates water ganglia shift to sections with low liquid connectivity. The sudden decline in tortuosity after 48 hours can be attributed to better liquid connectivity between different diffusion domains. In addition, further water uptake removed the heterogeneity over length-scales of the order of the r.m.s displacement. A similar tortuosity trend was observed in pellet 2. However, a sudden increased tortuosity was observed for 50 ms after 72 hours. This can be attributed to low liquid connectivity between different diffusion domains at this length-scale that was equivalent to the r.m.s displacement. The average tortuosity obtained at saturation equilibrium for Δ = 50 ms and Δ = 100 ms diffusion time were 1.39 ± 0.03 and 1.42 ± 0.06, respectively. Higher tortuosities were estimated in Section 6.4.4. The average tortuosities obtained in an undisturbed set up at Δ = 50 ms and Δ = 100 ms diffusion time were 2.23 ± 0.01 and 2.20 ± 0.07, respectively.

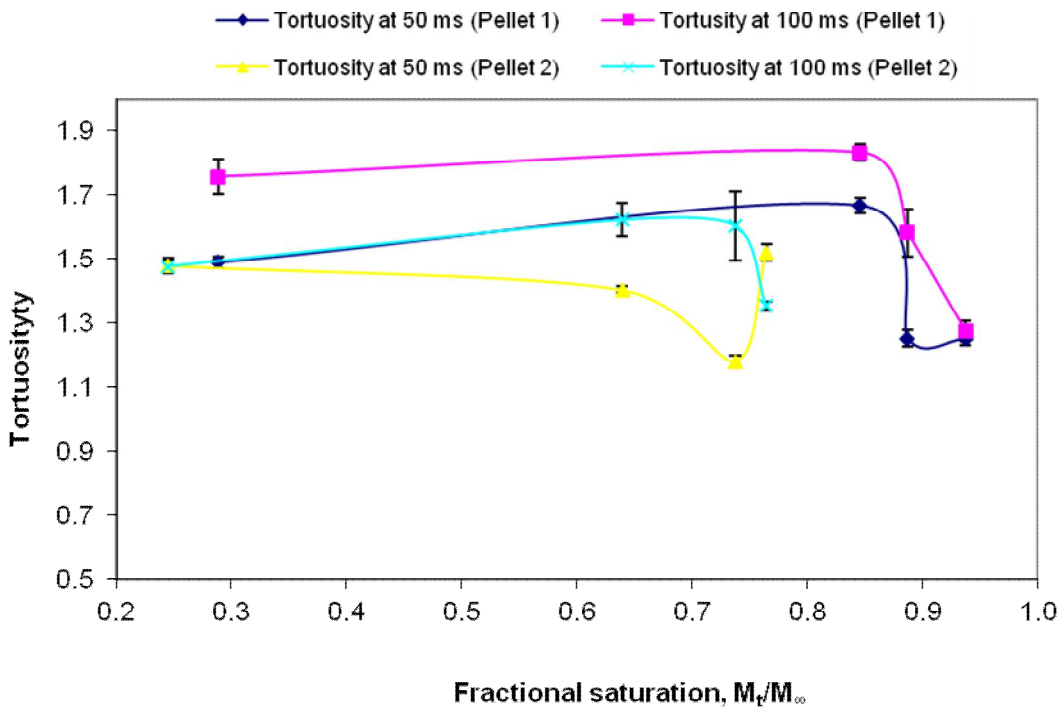

Figure 7.4

Tortuosity as a function of fractional saturation of AL3984T

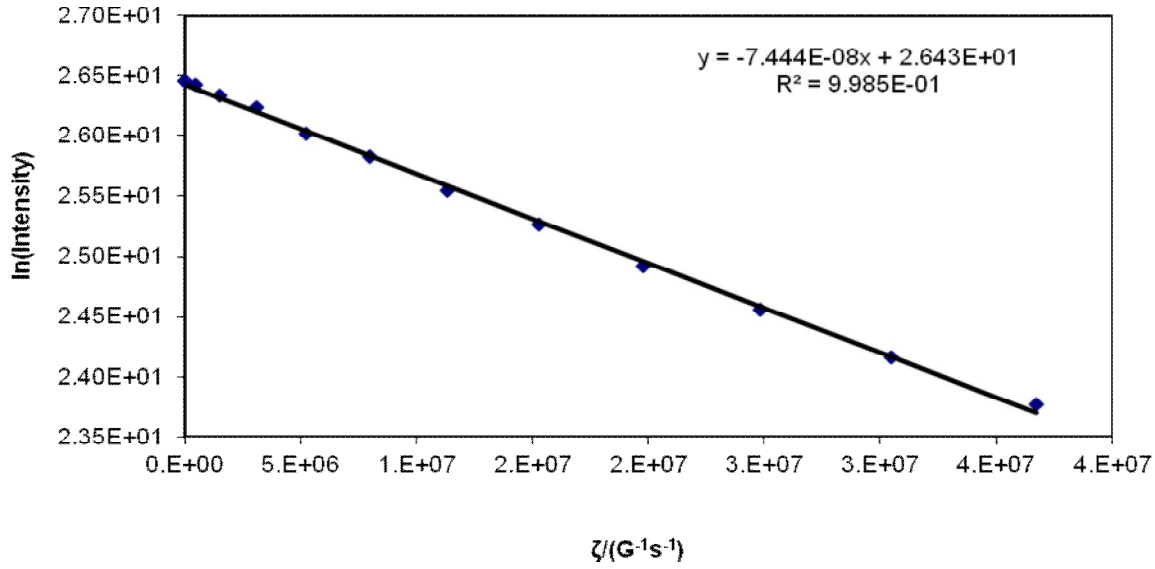

Figure 7.5

Echo log-attenuation results from simulated echo PGSE experiments on partially saturated support pellet 1 showing signs of noise at 50 ms diffusion time after 24 hours

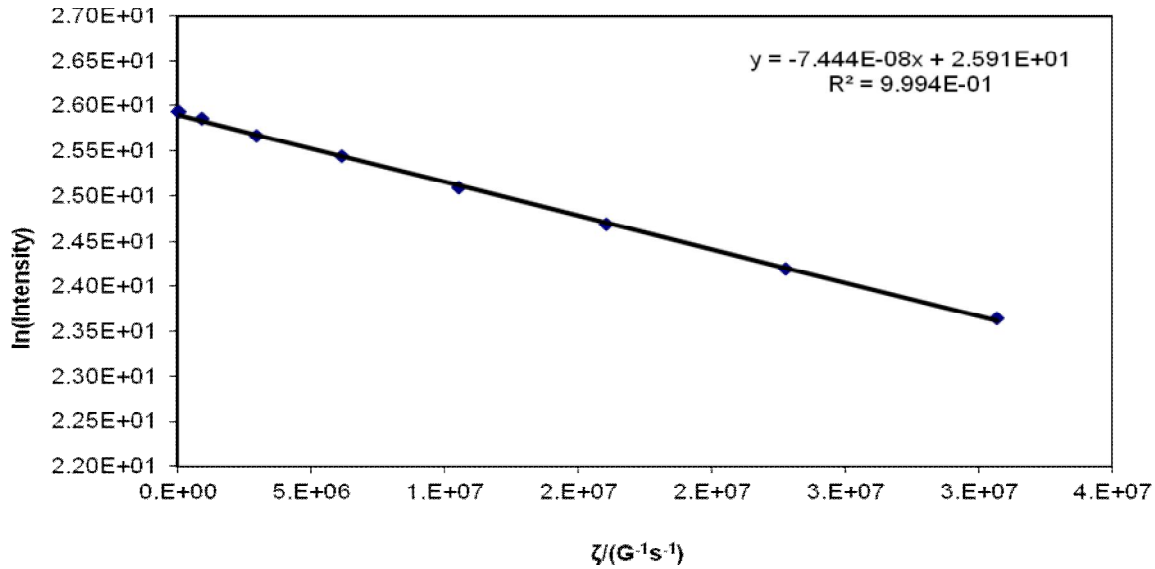

Figure 7.6

Echo log-attenuation results from simulated echo PFG experiments on partially water saturated support pellet 1 showing signs of noise at 100 ms diffusion time after 24 hours

7.3.3 Tortuosity as a function of pore filling and time in AL3992E

The daily mass uptake by the sample is given in Table 7.6. The mass transfer was relatively the same for both pellets. The daily values of sample mean, and error, for the tortuosities is given in Table 7.7. A good intensity signal was obtained after 24 hours. It can be seen in Figures 7.8 and 7.9 that a simple linear ($R^2 \geq 0.998$) behaviour was observed at short and long diffusion time.

Table 7.6

The daily mass uptake (by adsorption) of AL3992E in a period of one week

Time	Pellet 1			Pellet 2		
	weight of sample	Amount adsorbed (M)	Fractional saturation (M_t/M_∞)	weight of sample	Amount adsorbed (M)	Fractional saturation (M_t/M_∞)
(Hours)	(g)	(g)	_	(g)	(g)	_
0	0.0541	0	0	0.0672	0	0
24	0.0821	0.0280	0.7289	0.0979	0.0307	0.5971
48	0.0902	0.0361	0.9399	0.1104	0.0432	0.8390
72	0.0922	0.0381	0.9917	0.1158	0.0486	0.9444
96	0.0923	0.0382	0.9948	0.1174	0.0502	0.9765
120	0.0925	0.0384	0.9982	0.1186	0.0514	0.9988
144	0.0925	0.0384	0.9992	0.1186	0.0514	0.9996
168	0.0925	0.0384	1	0.1186	0.0514	1

Table 7.7

The daily tortuosity values of AL3992E in a period of one week. The error quoted represents 95 % confidence intervals

Time	Tortuosity (Pellet 1)		Tortuosity (Pellet 2)	
(Hours)	(Δ = 50 ms)	(Δ = 100 ms)	(Δ = 50 ms)	(Δ = 100 ms)
24	1.69 ± 0.03	1.78 ± 0.03	1.42 ± 0.72	1.53 ± 0.77
48	1.68 ± 0.02	1.77 ± 0.04	1.74 ± 0.88	1.76 ± 0.89
72	1.90 ± 0.02	2.11 ± 0.05	1.83 ± 0.89	2.16 ± 1.05
96	1.71 ± 0.03	1.98 ± 0.05	1.87 ± 0.90	2.18 ± 1.06
120	1.66 ± 0.03	1.73 ± 0.04	1.74 ± 0.89	2.09 ± 1.07

The tortuosity of the sample as a function of fractional saturation is shown in Figure 7.7. For pellet 1, similar tortuosity was observed for the first 48 hours. This was followed by a sudden rise of the tortuosity with its maxima at 72 hours (M_t/M_∞ = 0.9917) before declining after 96 hours (M_t/M_∞ = 0.9948). The constant tortuosity observed for the first 48 hours can be interpreted as filling regions with similar tortuosities. Alternatively, the pellet might have had the same liquid connectivity even though the fractional saturations were different. A different tortuosity trend was observed in pellet 2. For pellet 2, there was a continuous increase of tortuosity after 24 hours. The tortuosity reached its peak and declined after 96 hours and 120 hours, respectively. At the beginning, there was a possibility of vapour phase contribution to the total diffusional displacements that is if the water ganglia adsorbed were well distributed pervasively within the pellet. Further addition of water reduced the influence of vapour phase transport and the low liquid connectivity of the different diffusion domains was revealed after 96 hours. The sudden decline of tortuosity after 120 hours can be attributed to better liquid connectivity between those diffusion domains.

The tortuosity at 120 hours was much higher than the tortuosity after 24 hours adsorption, and thus provides proof of molecular exchange between liquid and vapours phases after 24 hours. In addition, the further water uptake removed the heterogeneity over length-scales of the order of the r.m.s displacement. It should be noted that the error quoted for the tortuosity in pellet 2 were uncharacteristically high. This suggests the possibility of a two component model. However, this possibility was ruled out in Section 6.4.4., and thus the data was represented as a one component model due to the uncertainty surrounding the log-attenuation plots. The final average tortuosity obtained at saturation equilibrium for Δ = 50 ms and Δ = 100 ms diffusion time were 1.70 ± 0.87 and 1.91 ± 0.98, respectively. Similar tortuosities were obtained in Section 6.4.4. The average tortuosities obtained in an undisturbed set up at Δ = 50 ms and Δ = 100 ms diffusion time were 1.68 ± 0.03 and 1.77 ± 0.04, respectively.

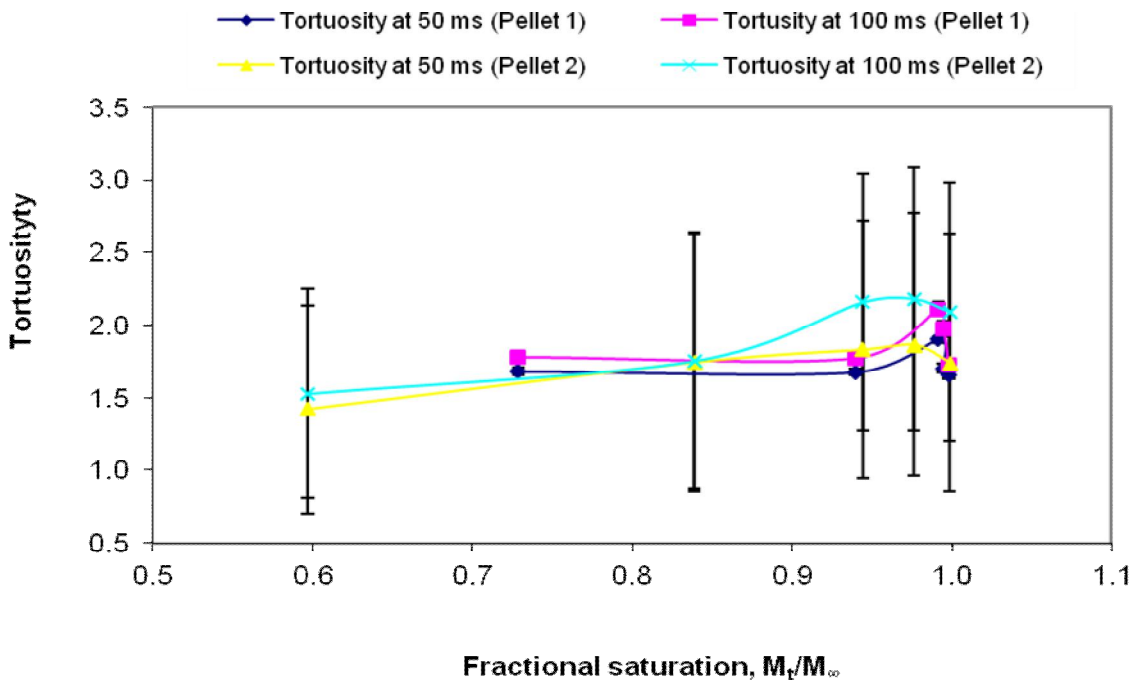

Figure 7.7

Tortuosity as a function of fractional saturation of AL3992E

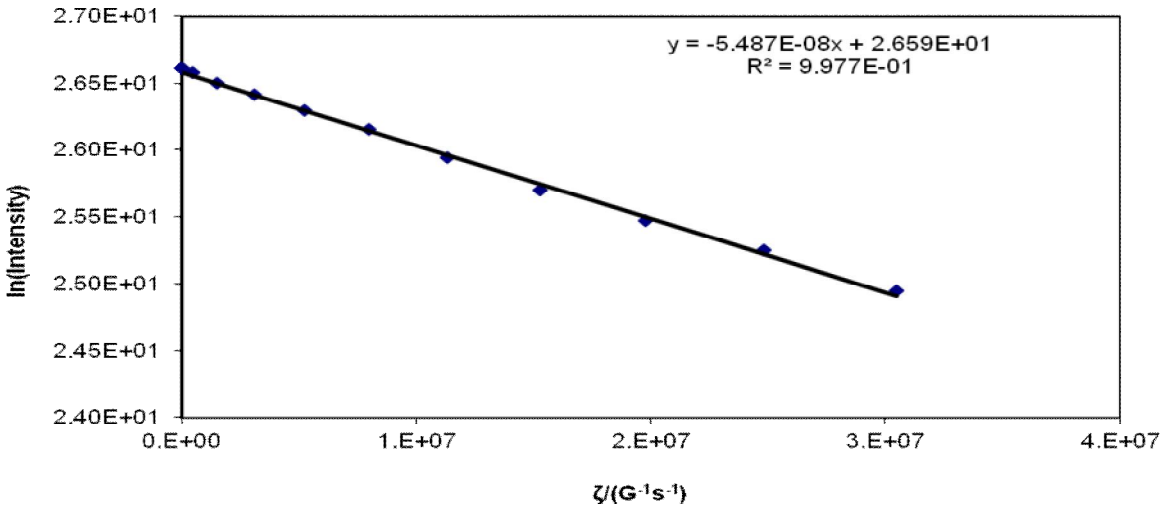

Figure 7.8

Echo log-attenuation results from simulated echo PFG experiments on partially saturated support pellet 1 showing signs of noise at 50 ms diffusion time after 24 hours

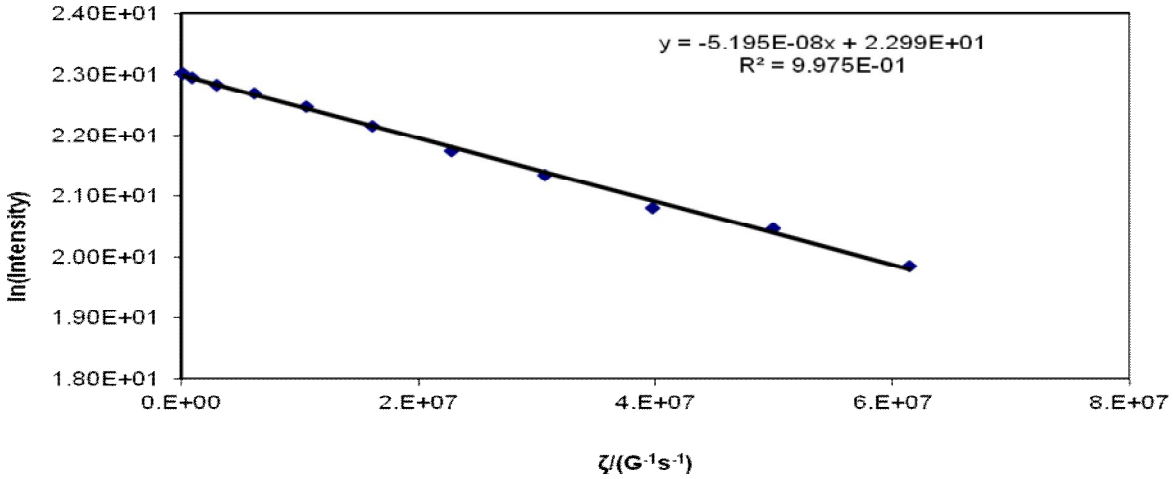

Figure 7.9

Echo log-attenuation results from simulated echo PFG experiments on partially water saturated support pellet 1 showing signs of noise at 100 ms diffusion time after 24 hours

7.3.4 Tortuosity as a function of pore filling and time in C10

The daily mass uptake by the sample is given in Table 7.8. The mass transfer was relatively the same for both pellets. The daily values of sample mean, and error, for the tortuosities are given in Table 7.9. It can be seen Figures 7.11 and 7.12 that a simple linear ($R^2 \geq 0.997$) behaviour was observed at short and long diffusion time. The tortuosity of the sample as a function of fractional saturation is also shown in Figure 7.10.

For pellet 1, there was an increase in tortuosity after 24 hours. The tortuosity reached its peak and declined after 48 hours and 72 hours, respectively. This was followed by two successive peaks at 144 hours (M_t/M_∞ = 0.9946) and 168 hours (M_t/M_∞ = 1). The low tortuosity observed can be interpreted as filling regions with very high liquid connectivity. Further addition of water introduced regions with low liquid connectivity, and thus the low tortuosity which was observed after 24 hours adsorption. The sudden declined tortuosity after 120 hours can be attributed to a better liquid connectivity between different diffusion domains. Finally, the difference between the short and long diffusion time suggests that the structure of adsorbed water ganglia was heterogeneous over the length-scales equivalent to

r.m.s displacement. A similar tortuosity trend was observed in pellet 2. The final average tortuosity obtained at saturation equilibrium for Δ = 50 ms and Δ = 100 ms diffusion time were 1.42 ± 0.04 and 1.52 ± 0.08, respectively. Higher tortuosities were obtained in Section 6.4.4. The average tortuosities obtained in an undisturbed set up at Δ = 50 ms and Δ = 100 ms diffusion time were 1.84 ± 0.07 and 2.16 ± 0.08, respectively.

Table 7.8

The daily mass uptake (by adsorption) of C10 in a period of one week

Time	Pellet 1			Pellet 2		
	weight of sample	Amount adsorbed (M)	Fractional saturation (M_t/M_∞)	weight of sample	Amount adsorbed (M)	Fractional saturation (M_t/M_∞)
(Hours)	(g)	(g)	_	(g)	(g)	_
0	0.0067	0	0	0.0056	0	0
24	0.0123	0.0056	0.5040	0.0090	0.0034	0.5128
48	0.0168	0.0101	0.9076	0.0109	0.0053	0.7964
72	0.0168	0.0102	0.9103	0.0111	0.0055	0.8281
96	0.0169	0.0102	0.9139	0.0111	0.0055	0.8296
120	0.0175	0.0108	0.9722	0.0114	0.0058	0.8748
144	0.0178	0.0111	0.9946	0.0120	0.0064	0.9653
168	0.0178	0.0112	1	0.0122	0.0066	1

Table 7.9

The daily tortuosity values of C10 in a period of one week. The error quoted represents 95 % confidence intervals.

Time	Tortuosity (Pellet 1)		Tortuosity (Pellet 2)	
Hours	(Δ = 50 ms)	(Δ = 100 ms)	(Δ = 50 ms)	(Δ = 100ms)
24	1.53 ± 0.01	1.54 ± 0.02	1.11 ± 0.02	1.59 ± 0.10
48	1.97 ± 0.03	2.08 ± 0.04	1.69 ± 0.02	1.74 ± 0.03
72	1.56 ± 0.01	1.64 ± 0.03	2.02 ± 0.04	2.11 ± 0.02
96	1.70 ± 0.01	1.77 ± 0.02	2.00 ± 0.02	2.23 ± 0.03
120	2.30 ± 0.04	2.58 ± 0.10	1.88 ± 0.02	2.18 ± 0.06
144	1.30 ± 0.03	1.34 ± 0.04	1.53 ± 0.02	1.78 ± 0.07

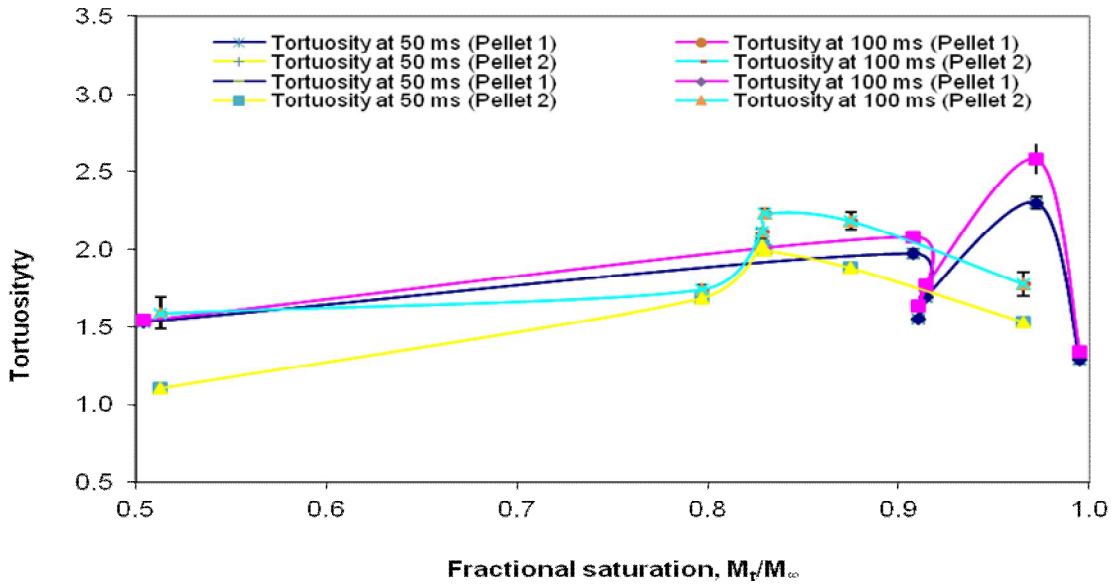

Figure 7.10

Tortuosity as a function of fractional saturation of C10

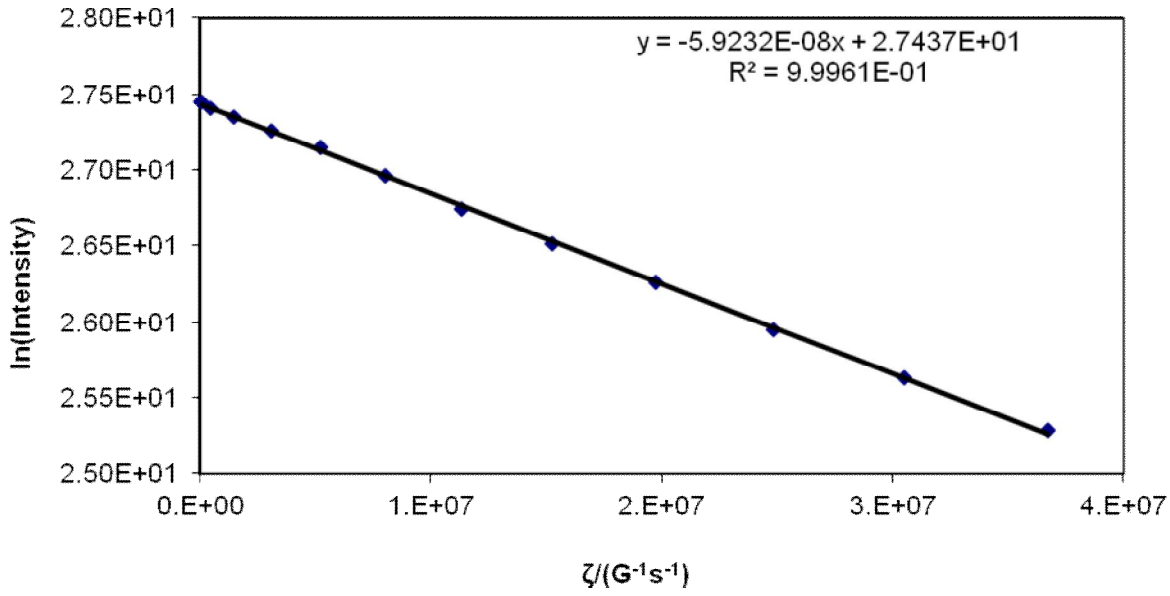

Figure 7.11

Echo log-attenuation results from simulated echo PFG experiments on partially water saturated support pellet 1 showing signs noise at 50 ms diffusion time after 24 hours

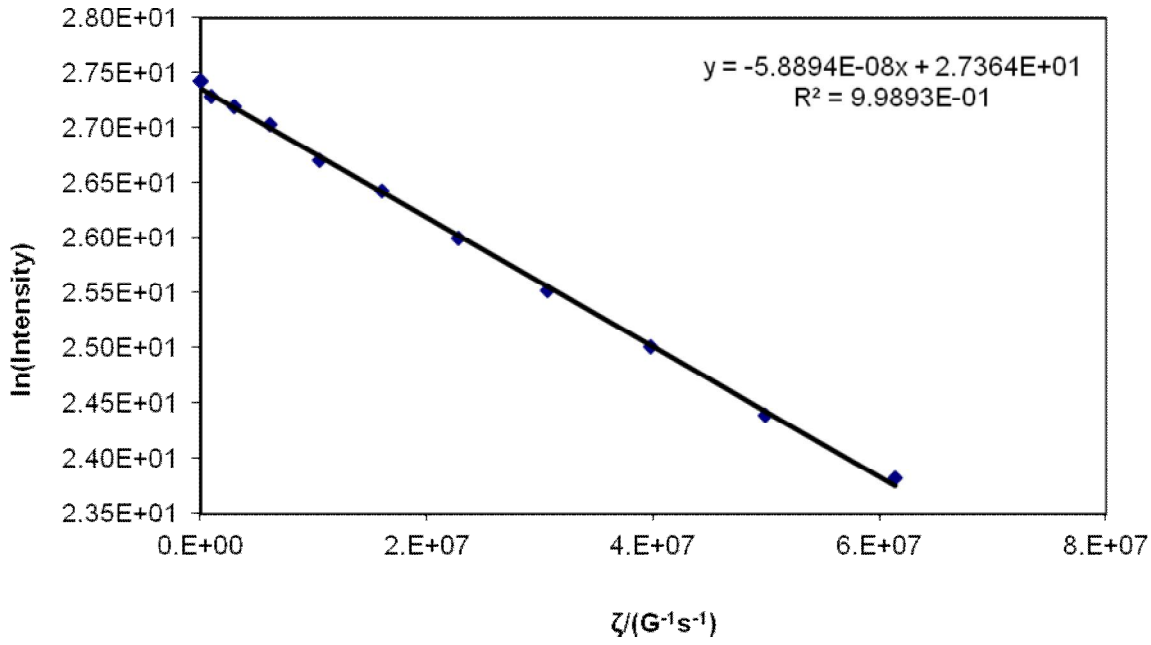

Figure 7.12

Echo log-attenuation results from simulated echo PFG experiments on partially water saturated support pellet 1 showing signs noise at 100 ms diffusion time after 24 hours

7.3.5 Tortuosity as a function of pore filling and time in C30

The daily mass uptake by the sample is given in Table 7.10. The mass transfer was relatively fast in the first pellet (115 % percentage change in the first day as opposed to only 5 % in the second pellet). Nevertheless, both pellets achieved some degree of stability of mass uptake after 72 hours. The daily values of sample mean, and error, for the tortuosities are given in Table 7.11. A good intensity signal was obtained after 24 hours.

The tortuosity as a function of fractional saturation is shown in Figure 7.13. For pellet 1, there was a continuous increase of tortuosity after 24 hours. The low tortuosity observed after 24 hours can be attributed to the filling of regions with high liquid connectivity. The difference between the short and long diffusion time suggests that the structure of adsorbed water ganglia was heterogeneous over length scales equivalent to the r.m.s displacement. Further addition of water introduced regions with low liquid connectivity, and thus the low tortuosity observed after 24 hours adsorption. The similar tortuosity observed after 24

hours can be interpreted as filling of regions with similar tortuosities. Alternatively, the pellet might have had the same liquid connectivity even though the fractional saturations were different. The difference between the short and long diffusion time suggests that the structure of adsorbed water ganglia was heterogeneous over the length-scales equivalent to r.m.s displacement. A similar trend of tortuosity was observed in pellet 2. The average tortuosity obtained at saturation equilibrium for Δ = 50 ms and Δ = 100 ms diffusion time were 1.94 ± 0.04 and 1.92 ± 0.05, respectively. Similar tortuosities were obtained in Section 6.4.4. The average tortuosities obtained in an undisturbed set up at Δ = 50 ms and Δ = 100 ms diffusion time were 1.81 ± 0.06 and 1.91 ± 0.05, respectively.

Table 7.10

The daily mass uptake (by adsorption) of C30 in a period of one week

	Pellet 1			**Pellet 2**		
Time	**weight of sample**	**Amount adsorbed (M)**	**Fractional saturation (M_t/M_∞)**	**weight of sample**	**Amount adsorbed (M)**	**Fractional saturation (M_t/M_∞)**
(Hours)	**(g)**	**(g)**	**_**	**(g)**	**(g)**	**_**
0	0.0092	0	0	0.0069	0	0
24	0.0199	0.0106	0.9117	0.0073	0.0004	0.0431
48	0.0204	0.0112	0.9571	0.0135	0.0066	0.7646
72	0.0203	0.0111	0.9494	0.0147	0.0078	0.9091
96	0.0209	0.0117	1	0.0155	0.0086	1

Table 7.11

The daily tortuosity values of C30 in a period of one week. The error quoted represents 95 % confidence intervals

Time	**Tortuosity (Pellet 1)**		**Tortuosity (Pellet 2)**	
Hours	**(Δ = 50 ms)**	**(Δ = 100 ms)**	**(Δ = 50 ms)**	**(Δ = 100 ms)**
24	1.59 ± 0.01	1.74 ± 0.04	1.58 ± 0.02	1.70 ± 0.02
48	2.25 ± 0.02	2.44 ± 0.04	2.12 ± 0.02	2.09 ± 0.06
72	2.31 ± 0.03	2.49 ± 0.03	1.76 ± 0.02	1.54 ± 0.03
96	2.11 ± 0.02	2.29 ± 0.03	1.77 ± 0.03	1.54 ± 0.03

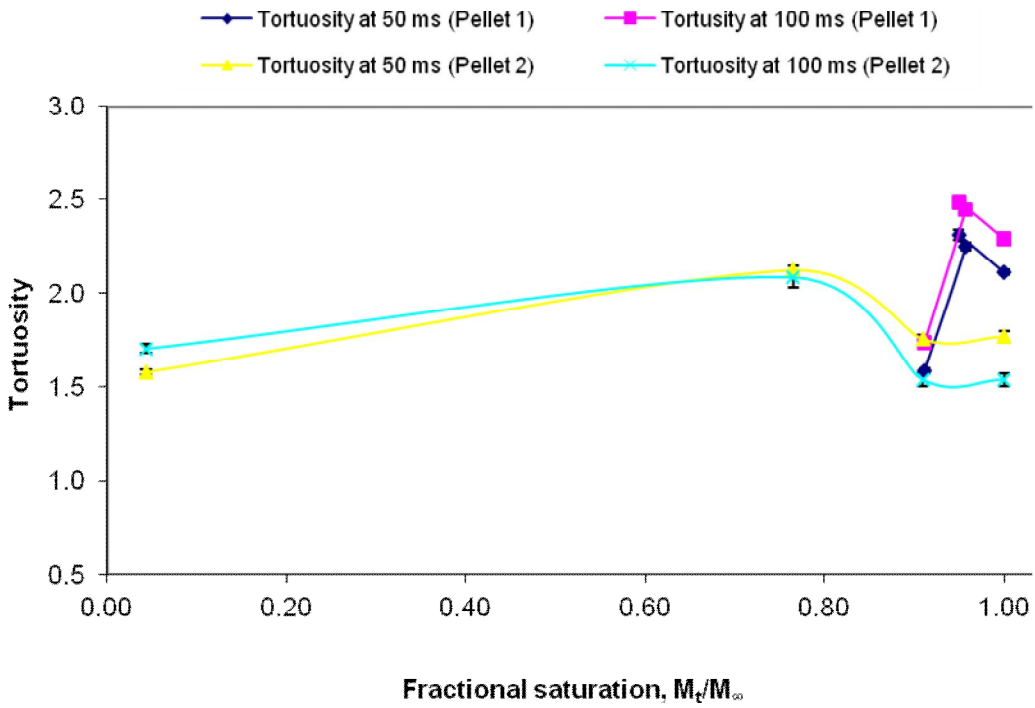

Figure 7.13

Tortuosity as a function of fractional saturation of C30

7.3.6 Tortuosity as a function of pore filling and time in Q17/6

The daily mass uptake by the sample is given in Table 7.12. The mass transfer was relatively similar and fast for both pellets. The daily values of sample mean, and error, for the tortuosities are given in Table 7.13. A good intensity signal was obtained after 24 hours. In pellet 1, the tortuosity for short diffusion time is similar in the first 48 hours. The constant tortuosities observed for the first 48 hours can be interpreted as filling regions with similar tortuosities. Alternatively, the pellet might have had the same liquid connectivity even though the fractional saturations were different. A significant difference was observed in the diffusivity with an increased diffusion time, and thus suggests heterogeneity of the liquid distribution over the length-scales equivalent to the r.m.s displacement. A different trend was observed in pellet 2. The tortuosity after 24 hours (M_t/M_∞ = 1.015) was low at the beginning and then suddenly increased to a higher value after 48 hours (M_t/M_∞ = 1.015). It should be noted that equilibrium saturation was achieved just after 24 hours, and thus, the low tortuosity can be the product of high liquid

connectivity within the pellet. However, perhaps after 48 hours, the distribution of water shifted to other parts of the tortuosity with low liquid connectivity, and thus, the high tortuosity observed. The difference between the short and long diffusion time suggests that the structure of adsorbed water ganglia was heterogeneous over length-scales equivalent to the r.m.s displacement. The average tortuosity obtained at saturation equilibrium for Δ = 50 ms and Δ = 100 ms diffusion time were 1.05 ± 0.02 and 1.19 ± 0.05, respectively. Higher tortuosities were observed in Section 6.4.4. The average tortuosities obtained in an undisturbed set up at Δ = 50 ms and Δ = 100 ms diffusion time were 2.23 ± 0.03 and 2.34 ± 0.03, respectively.

Table 7.12

The daily mass uptake (by adsorption) of Q17/6 in a period of two days

	Pellet 1			**Pellet 2**		
Time	**weight of sample**	**Amount adsorbed (M)**	**Fractional saturation (M_t/M_∞)**	**weight of sample**	**Amount adsorbed (M)**	**Fractional saturation (M_t/M_∞)**
(Hours)	**(g)**	**(g)**	**_**	**(g)**	**(g)**	**_**
0	0.0064	0	0	0.0074	0	0
24	0.0094	0.0029	0.9274	0.0106	0.0032	0.9848
48	0.0096	0.0032	1	0.0107	0.0033	1

Table 7.13

The daily tortuosity values of Q17/6 in a period of two days. The error quoted represents 95 % confidence intervals

Time	**Average Tortuosity (Pellet 1)**		**Average Tortuosity (Pellet 2)**	
Hours	**(Δ = 50 ms)**	**(Δ = 100 ms)**	**(Δ = 50 ms)**	**(Δ = 100 ms)**
24	1.09 ± 0.02	1.36 ± 0.06	1.86 ± 0.02	1.97 ± 0.02
48	1.05 ± 0.01	1.23 ± 0.04	1.05 ± 0.02	1.14 ± 0.03

7.3.7 Tortuosity as a function of pore filling and time in S980A

The daily mass uptake by the sample is given in Table 7.14. The mass transfer was relatively fast for both pellets. The daily values of sample mean, and error, for the tortuosities are given in Table 7.15. The high tortuosity observed at M_t/M_∞ = 0.381, for pellet 1, can be attributed to low liquid connectivity. However, as the saturation was increased at M_t/M_∞ = 0.985, better liquid connectivity was revealed, and thus, the reduced tortuosity was observed. A similar trend was observed in pellet 2 at Δ = 50 ms, with increased liquid connectivity due to the saturation level. It should be noted that tortuosity in pellet 2, after 24 hour adsorption, at Δ = 100 ms diffusion time, was uncharacteristically low. This suggests the possible molecular exchange between the liquid and gas phases at that length scale that was equivalent to the r.m.s displacement. The average tortuosity obtained at saturation equilibrium for Δ = 50 ms and Δ = 100 ms diffusion time were 1.48 ± 0.07 and 1.67 ± 0.01, respectively. Higher tortuosities were obtained in Section 6.4.4. The average tortuosities obtained in an undisturbed set up at Δ = 50 ms and Δ = 100 ms diffusion time were 1.83 ± 0.05 and 1.97 ± 0.05, respectively.

Table 7.14

The daily mass uptake (by adsorption) of S980A in a period of three days

	Pellet 1			**Pellet 2**		
Time	**weight of sample**	**Amount adsorbed (M)**	**Fractional saturation (M_t/M_∞)**	**weight of sample**	**Amount adsorbed (M)**	**Fractional saturation (M_t/M_∞)**
(Hours)	**(g)**	**(g)**	**_**	**(g)**	**(g)**	**_**
0	0.0049	0	0	0.0077	0	0
24	0.0079	0.0031	0.3806	0.0096	0.0019	0.2339
48	0.0128	0.0079	0.9851	0.0155	0.0078	0.9848
72	0.0129	0.0080	1	0.0156	0.0079	1

Table 7.15

The daily tortuosity values of S980A in a period of three days. The error quoted represents 95 % confidence intervals.

Time	Tortuosity (Pellet 1)		Tortuosity (Pellet 2)	
Hours	(Δ = 50 ms)	(Δ = 100 ms)	(Δ = 50 ms)	(Δ = 100 ms)
24	3.13 ± 0.10	7.16 ± 0.30	2.42 ± 0.08	1.43 ± 0.04
48	1.44 ± 0.06	1.66 ± 0.07	1.52 ± 0.05	1.68 ± 0.07

7.3.8 Tortuosity as a function of pore filling and time in S980G

The daily mass uptake by the sample is given in Table 7.16. The mass transfer was relatively fast for both pellets. The daily values of sample mean, and error, for the tortuosities are given in Table 7.17. The tortuosities were affected by the diffusion time used. It was difficult to assess the true nature of the log-attenuation plots due to the scattering of the data, and thus, the error bars of the measurement are big in pellet 2. A fairly good intensity signal was observed after 48 hours.

Table 7.16

The daily mass uptake (by adsorption) of S980G in a period of two days

	Pellet 1			Pellet 2		
Time	weight of sample	Amount adsorbed (M)	Fractional saturation (M_t/M_∞)	weight of sample	Amount adsorbed (M)	Fractional saturation (M_t/M_∞)
(Hours)	(g)	(g)	_	(g)	(g)	_
0	0.0058	0	0	0.0061	0	0
24	0.0063	0.0005	0.0958	0.0066	0.0005	0.0642
48	0.0110	0.0052	1	0.0133	0.0072	1

At the beginning, there was a possible vapour phase contribution to the total diffusional displacements that is if the water ganglia adsorbed were well distributed pervasively within the pellet. However, as the saturation was increased at $M_t/M_\infty = 1$, the influence of molecular exchange between the liquid and vapour phases was reduced, and thus, the

increased tortuosity was observed due to low liquid connectivity. The difference between the short and long diffusion time suggests that the structure of adsorbed water ganglia was heterogeneous over length-scales of the order of the r.m.s displacement. It should be noted that tortuosity in pellet 1, after 48 hour adsorption, at Δ = 100 ms diffusion time, was uncharacteristically low. This suggests a possible molecular exchange between the liquid and gas phases at that length scale that was equivalent to the r.m.s displacement. A similar tortuosity trend was observed in pellet 2. The average tortuosity obtained at saturation equilibrium for Δ = 50 ms and Δ = 100 ms diffusion time were 2.24 ± 1.12 and 1.67 ± 0.84, respectively. The average tortuosities obtained in an undisturbed set up at Δ = 50 ms and Δ = 100 ms diffusion time were 2.44 ± 0.02 and 2.69 ± 0.02, respectively. The error associated with the measurement is substantially high, and thus the comparison between the disturbed and undisturbed case is not feasible. The error associated with the tortuosity in pellet 2 indicates possible two component model. However, the possibility of two component models was ruled out in section 6.4.4 due to the uncertainty of the nature of the log-attenuation plots.

Table 7.17

The daily tortuosity values of S980G in a period of one week. The error quoted represents 95 % confidence intervals

Time	Tortuosity (Pellet 1)		Tortuosity (Pellet 2)	
Hours	(Δ = 50 ms)	(Δ = 100 ms)	(Δ = 50 ms)	(Δ = 100 ms)
24	1.12 ± 0.01	1.30 ± 0.02	1.08 ± 0.53	1.54 ± 0.75
48	2.88 ± 0.13	1.67 ± 0.09	1.60 ± 0.80	1.67 ± 0.83

7.3.9 Tortuosity as a function of pore filling and time in Silica alumina

The daily mass uptake by the sample is given in Table 7.18. The mass transfer was relatively the same for both pellets, with minor batch variability. The daily values of sample mean, and error, for the tortuosities are given in Table 7.19. A good intensity signal was obtained after 24 hours. The tortuosity of the sample as a function of fractional saturation is shown in Figure 7.14. In pellet 1, the tortuosity was not sensitive to the saturation for the first 48 hours. The constant tortuosities observed for the first 48 hours

can be interpreted as filling regions with similar tortuosities. Alternatively, the pellet might have had the same liquid connectivity even though the fractional saturations were different. This was followed by a steep increase that reached its maximum after 144 hours (M_t/M_∞ = 1). The decreased tortuosity at M_t/M_∞ = 0.844 is a clear example of a molecular exchange between the liquid and vapour phases. As the saturation was gradually increased, the effect of gas phase transport was reduced, and thus low liquid connectivity was observed. However, the tortuosity observed at M_t/M_∞ = 1, was uncharacteristically big. This can be interpreted as regions of the sample with low connectivity. In pellet 2, the trend for the first 48 hours is similar to that of pellet 1, reaching its maxima after 72 hours (M_t/M_∞ = 0.857). In contrast, the tortuosity in pellet 1 declined after its maximum to a value similar to the tortuosity obtained after 48 hours. Therefore, the maxima at M_t/M_∞ = 0.857 can be interpreted as the presence of several diffusion domains with low liquid connectivity. The increased saturation level, improved the liquid connectivity between those domains, and thus, low liquid tortuosity was observed at saturation equilibrium. The average tortuosity obtained at saturation equilibrium for 50 ms and 100 ms diffusion time were 1.90 ± 0.06 and 1.96 ± 0.04, respectively. Higher tortuosities were obtained in Section 6.4.4. The average tortuosities obtained in an undisturbed set up at 50 ms and 100 ms diffusion time were 2.55 ± 0.12 and 2.92 ± 0.10, respectively.

Table 7.18

The daily mass uptake (by adsorption) of Silica Alumina in a period of one week

	Pellet 1			**Pellet 2**		
Time	**weight of sample**	**Amount adsorbed (M)**	**Fractional saturation (M_t/M_∞)**	**weight of sample**	**Amount adsorbed (M)**	**Fractional saturation (M_t/M_∞)**
(Hours)	**(g)**	**(g)**	**_**	**(g)**	**(g)**	**_**
0	0.0097	0	0	0.0104	0	0
24	0.0145	0.0048	0.7643	0.0150	0.0046	0.7496
48	0.0149	0.0052	0.8280	0.0151	0.0047	0.7792
72	0.0150	0.0053	0.8439	0.0156	0.0052	0.8567
96	0.0153	0.0056	0.8901	0.0157	0.0053	0.8666
120	0.0157	0.0059	0.9459	0.0164	0.0060	0.9951
144	0.0160	0.0063	1	0.0165	0.0061	1

Table 7.19

The daily tortuosity values of Silica Alumina in a period of one week. The error quoted represents 95 % confidence intervals

Time	Tortuosity (Pellet 1)		Tortuosity (Pellet 2)	
Hours	(Δ = 50 ms)	(Δ = 100 ms)	(Δ = 50 ms)	(Δ = 100 ms)
24	1.20 ± 0.01	1.33 ± 0.04	1.13 ± 0.01	1.38 ± 0.06
48	1.15 ± 0.01	1.29 ± 0.03	1.16 ± 0.01	1.21 ± 0.03
72	0.90 ± 0.02	1.11 ± 0.04	1.22 ± 0.05	1.65 ± 0.09
96	1.45 ± 0.03	1.65 ± 0.05	3.08 ± 0.05	3.36 ± 0.05
120	1.51 ± 0.08	2.37 ± 0.09	0.90 ± 0.04	1.65 ± 0.13
144	4.29 ± 0.18	4.31 ± 0.11	1.52 ± 0.02	1.52 ± 0.04

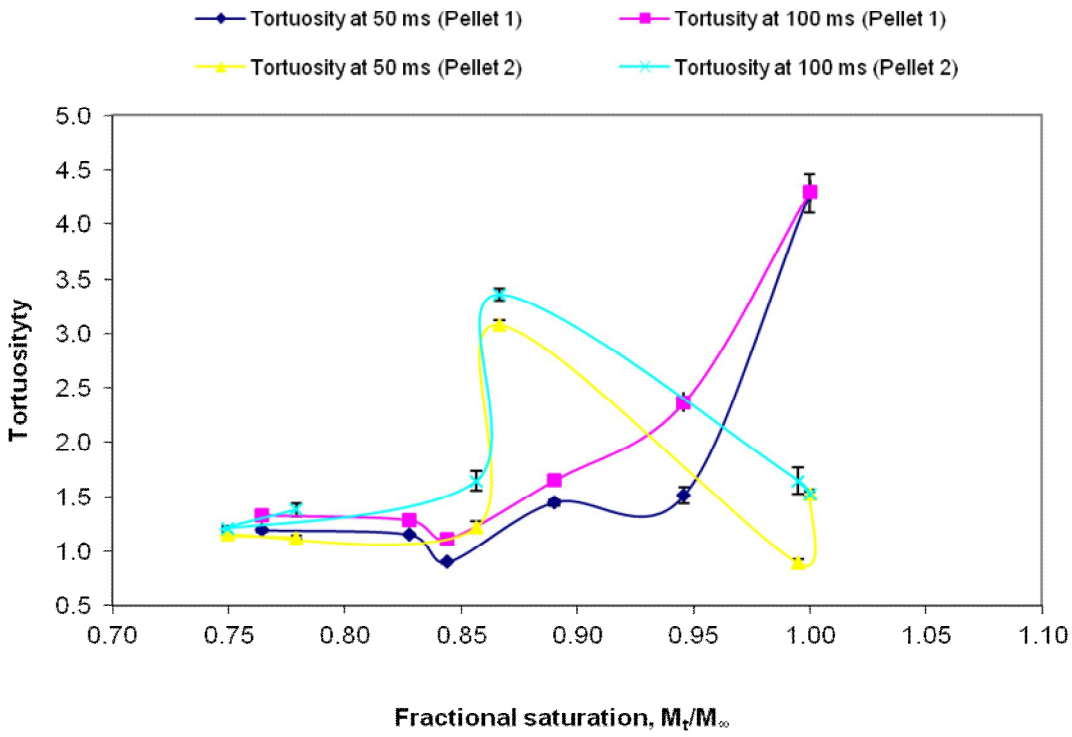

Figure 7.14

Tortuosity as a function of fractional saturation of Silica Alumina

7.4 Discussion

In general, within the experimental error, for the different samples studied from the same batch, the estimated water mass uptake by adsorption and the tortuosities were in close agreement. The rate limiting step of the mass transfer was estimated by calculating the Biot number. It was found that the convective mass transfer was the most dominant process. As detailed in Section 3.4.5, Pimenov and co-workers (2003; 2005) reported similar findings for porous glasses. The magnitude of mass uptake, increases in the order Q17/6 (2 days) < S980A (3 days) < Aerosil (4 days) < S980G (5 days) < AL3984T (5 days) < AL3992E (5 days) < Silica Alumina (6 days) < C10 (7 days) < C30 (7 days). It can be seen that samples with large external surface area such as samples Q17/6 and Aerosil reached equilibrium saturation under a short period of time. Nevertheless, other samples such as samples S980A and S980G that have small external surface area also reached saturation equilibrium under a short period time. It is likely that the surfaces of these samples are composed of hydroxyl groups which can conveniently form hydrogen bonds with highly polar water molecules. This can cause water molecule to adsorb strongly on certain sites relative to others masking the effect of monolayer formation.

The log-attenuation plot allows a high precision determination of diffusivity in bulk liquid (deionised water) and self-diffusion of deionised water imbibed within porous media. There was a general difficulty in the analysis of log-attenuation plots even though the number of scans (16) was relatively high. The high number was necessary for reduced influence of the associated noise due to the relative dryness of the pellets. However, there was a limit to the number of scans that was used. The systems evolved rapidly in the course of the PGSE NMR experiments. Therefore, the log-attenuation plots were proven less valuable in the analysis of restricted diffusion and heterogeneity of the samples at initial stage of pore filling. Nevertheless, the log-attenuation plots, after 48 hours adsorption, were fairly good. The influence and effect of noise on the log-attenuation plots was 48 hours adsorption. In general, a simple linear behaviour ($R^2 \geq 0.993$) was observed in most samples at short diffusion times. However, a deviation from linearity was observed in most data sets at long diffusion times. The possibility of anisotropic diffusion or restricted diffusion contributing to the observed non-linearities in the log-attenuation plots was ruled out in Section 6.5, and thus, the deviations from linear log-attenuation behaviour reported here are analysed in terms of macroscopic variations in the samples.

In most samples, the tortuosity observed after 24 hours was considerably low despite the low liquid connectivity. Therefore, the majority of the samples had extra dimension to the overall self-diffusion of deionised water adsorbed. It was reported in earlier studies that the distribution of water is not always isolated in one particular region of porous media (D'Orazio *et al.*, 1989). As detailed in Section 3.4.5, Valliulin *et al*. (1997) showed a strong dependence of exchange processes on temperature, filling fraction, and type of liquid. In addition, Farrher *et al*. (2008) used PGSE NMR in conjunction with SEM micrograph to study the effect of molecular exchange between liquid and vapour in porous materials. The SEM micrograph showed that spatial distribution of water does not depend on preparation history. Even extended annealing periods (up to six weeks) of the investigated samples did not change the coarse grain distribution of the liquid phase. Therefore, the spatial distribution depends on the instability between the liquid and vapour phases as a consequence of the competition between the adhesion and cohesion forces. These researchers came to the same conclusion as Valliulin *et al*. (1997) that vapour phase contributes to the overall effective diffusivity seen in partially saturated porous glasses. Similar conclusion can be about the findings in this study. There was enough evidence to suggest that vapour phase contributes to the total diffusion displacement which is interpreted by molecular exchange between the liquid and vapour phases, particularly in the 24 hours of this study. The influence of vapour phase transport was reduced by increased saturation within the sample, and thus, the influence of liquid connectivity was revealed. In general, the high tortuosity observed was followed by sudden decline in tortuosity. The high tortuosity was due to low liquid connectivity and the declined tortuosity was associated with uniform water distribution with improved liquid connectivity.

The rest of the samples, such as Aerosil, revealed high tortuosity after 24 hours. This was followed by sudden declined tortuosity. The high tortuosity was due to low liquid connectivity and the declined tortuosity was associated with uniform water distribution with improved the liquid connectivity. Therefore, the liquid connectivity is inversely proportional to the tortuosity. As detailed in Section 1.6, similar observations were reported in two and three dimensional bond networks for artificial porous materials (Friedman *et al.*, 1995; Vogel, 1997; 2000; Salmas and Androutsopoulos, 2001; Armatas and Pomonis, 2004; and Armatas, 2006). Nevertheless, there were some samples such as

AL3992E where a constant tortuosity was observed for the first 48 hours. The observed tortuosity can be attributed to either filling regions with similar tortuosities or similar liquid connectivity despite different fractional saturations. This was followed by high tortuosity and finally a lower tortuosity value was observed at saturation equilibrium, and thus, suggests uniform water distribution with improved liquid connectivity.

Finally, the average estimated tortuosities in an undisturbed set up in Section 6.4.4 were higher than the values observed in this study. It should be noted that the same pellets and preparation that were used in Section 6.4.4 were adopted in this study. However, in Section 6.4.4, the samples were allowed to reach saturation equilibrium for one week without any disturbance. In contrast, the samples in this study were disturbed periodically to take water mass readings. Therefore, the lower tortuosities observed in this study can be attributed to a better exchange between the different domains and vapor phase contribution that will increase the total diffusion displacement of the sample. This was possible as the position of the pellet in the water bath set up was constantly changed on daily basis when taking the readings. As a result, this would improve the mass transfer to the surface of the samples. In contrast, the position of the pellets in Section 6.4.4, were unchanged for a period of one week, and thus, the side facing the reservoir was exposed to most of the mass transfer. Nevertheless, the rest of the samples got relatively the same tortuosities in this study and the previous estimated tortuosities in Section 6.4.4. This further supports the theory detailed in Section 3.4.5, that the spatial distribution depends on the instability between the liquid and vapour phases as a consequence of the competition between the adhesion and cohesion forces (Farrher *et al.,* 2008 and Nechifor *et al.,* 2009). Furthermore, the effect connectivity and variance of the PSD on the tortuosity will be tested in Chapter 8.

7.5 Conclusion

The distribution of adsorbate molecules within the pores surface at different saturation degrees was successfully studied with PGSE NMR technique. In addition, a gravimetric method was used to determine the rate limiting step. It was found that the rate limiting step was the convective mass transfer. This finding is in good agreement with the result of Pimenov and co-workers (2003; 2005). The PGSE NMR technique has shown that, at low saturation level, the structure of adsorbed water ganglia was heterogeneous over length-

scales of the order of the r.m.s displacement. Further increased saturation level removed the heterogeneity over length-scales of the order of the r.m.s displacement. In general, the tortuosity decreased with an increased liquid saturation, and thus presumably increased connectivity. These findings are in good agreement with the computer simulation results of Friedman (1995), Vogel (1997; 2000), Salmas and Androutsopoulos (2001), Salmas *et al.* (2003) Armatas and Pomonis (2004), and Armatas (2006). However, the tortuosities of some of the samples were uncharacteristically low at low saturation levels, and thus were attributed to molecular exchange between the liquid and vapour phases. This finding is in good agreement with the results of Valliullin *et al*. (1997) and Farrher *et al*. (2008).

7.6 References

Armatas, G.S., and Pomonis, P.J., 2004. A Monte Carlo pore network for the simulation of porous characteristics of functionalized silica: pore size distribution, connectivity distribution and mean tortuosities. *Chemical engineering science*, 59, 5735-5749.

Armatas, G.S., 2006. Determination of the effects of the pore size distribution and pore connectivity distribution on the pore tortuosity and diffusive transport in model porous networks. *Chemical engineering science*, 61, 4662 – 4675

Farrher, G., Ardelean, I., Kimmich, R., 2008. Time-dependent molecular diffusion in partially filled porous glasses with heterogeneous structure. *Applied magnetic resonance*, 34 (1-2), 85-99.

Friedman, S.P., Zhang, L., and Seaton, N.A., 1995. Gas and solute diffusion coefficients in pore networks and its description by a simple capillary model. *Transport in porous media*, 19, 281-301.

Nechifor, R., Badea, C., and Ardelean, I., 2009. Nuclear magnetic resonance studies of liquids morphology inside partially saturated porous media. *Journal of physics: conference series*, 182 (1).

Pimenov, G.G., Kortunov, P.V., and Dvoyashkin, M.N., 2003. Structure and Dynamics of Molecular Systems, Kazan: *Kazan. Gos. Univ*., 10(3), 84.

Pimenov, G.G., and Skirda, V.D., 2005. NMR Study of the Kinetics of Butane and Hexane Adsorption from Vapour Phase by Porous Glasses. *Colloid Journal*, Vol. 67(6), 746–750.

Salmas C.E., and Androutsopoulos, G.P., 2001. A novel pore structure tortuosity concept based on nitrogen sorption hysteresis data. *Industrial engineering chemical research*, 40 (2), 721-730.

Valiullin, R.R., Skirda, V.D., Stapf, S., Kimmich, R., 1997. Molecular exchange processes in partially filled porous glass as seen with NMR diffusometry. *Physical review E*, 55 (3), Part A, 2664-2671.

Valiullin, R., Korunov, P., Karger, J., and Timoshenko, V., 2005. Concentration-dependent self-diffusion of adsorbates in mesoporous materials. *Magnetic resonance imaging*, 23, 209-214.

Vogel, H.J., 1997. Morphological determination of pore connectivity as a function of pore size using serial sections. *European Journal of Soil Science*, 48, 365–377.

Vogel, H.J., 2000. A numerical experiment on pore size, pore connectivity, water retention, permeability, and solute transport using network models. *European Journal of Soil Science*, 51, 99–105.

8.0 The relationships between structural and topological properties of porous media

8.1 Introduction

The pore size distribution (PSD) is one of the most important requirements for predicting diffusivity and mercury entrapment. In addition, mercury entrapment is strongly dependent on the topological (pore connectivity and tortuosity) properties of porous media. As detailed in Section 1.6, the significant effect of PSD on mercury entrapment, tortuosities, and pore connectivity was described by Androutsopoulos and Mann (1979), Conner and Lane (1984), Lapidus *et al.* (1985), Carniglia (1986), Tsakiroglou and Payatakes (1990), Portsmouth and Gladden (1991; 1992), and Friedman *et al.* (1995). In general, for random pore network models of unimodal/monodisperse porous media, simulation results suggest that the mercury entrapment increased as the variance of the PSD got wider, and decreased with increased pore connectivity (except for $Z = 2$). Also, the simulation results suggest that tortuosity for molecular diffusion increases with decreasing pore connectivity, and increasing width of PSD. Similar observations were made by Vogel (1997; 2000), Salmas *et al.* (2003), Armatas and Pomonis (2004), and Armatas (2006). Thus, based on these simulations, it is safe to conclude that a correlation should exist between mercury entrapment and tortuosity since they both depend on the same network parameters. Salmas and Androutsopoulos (2001) observed a positive correlation between mercury entrapment obtained by experiment and tortuosity obtained from corrugated pore structure model (CPSM). However, these simulation correlations lack experimental evidence to support them. In this Chapter, these simulation correlations will be checked with experimental results reported in previous Chapters.

The pore connectivity, mercury entrapment, PSD, and tortuosity were determined experimentally in previous Chapters. However, the experimental methods of measuring PSD (BJH method), pore connectivity (percolation analysis), and tortuosity all have limitations. For example, to obtain PSD, one must assume the pore geometry (cylinder, slit, etc.) of the sample. For percolation analysis, in addition to the pore geometry assumption,

one must assume that pore diameter is independent of the pore length which may not be true for some samples in this study. The PGSE NMR diffusion measurements are sensitive to the structure of the medium over a scale comparable to the r.m.s displacement of molecules ($\leq 10\ \mu m$) during the experimental time scale (10^{-3} to 1 s). In contrast, the MRI experiments probe the length scale of the dimension of the pellet ($\geq 10\ \mu m$), and thus will be used to address the length scale limitations of the PGSE NMR diffusion measurements. Also, despite the limitations of the methods of analysis in the previous Chapters, the materials investigated in this study might not be like random pore bond networks of the simulation correlations. Therefore, in this Chapter, novel multi-technique approaches will be used to check the simulation correlations. Furthermore, an alternative explanation of the cause of mercury entrapment was proposed by Giesche (2010). As detailed in Section 5.4, Giesche (2010) suggested that multiple snap-off (a major cause of mercury entrapment) can occur for long straight cylindrical pores open at both ends. To test this prediction, a measure of pore length was derived from the gas adsorption data with the aid of Pomonis and Armatas (2004) method. Therefore, mercury entrapment will be correlated with the measure of pore length to check Giesche's theory.

8.2 Influence of connectivity and width of PSD on entrapment

It can be seen in Table 8.1 that similar pore volume values, within the quoted errors, were obtained by all these characterisation techniques used here. This work supports Rigby *et al*. (2003b) finding that elastic or permanent structural changes due to the application of high hydraulic pressures during intrusion was negligible in these materials. The gas adsorption studies carried out on all samples revealed isotherms of type IV classification with reproducible type H2 hysteresis loops. The PSD of the materials was obtained by using the Barrett *et al*. (1951) method. The variance of the PSD distribution of the samples is shown in Table 8.2. In addition, the connectivity analysis suggested by Seaton (1991) requires an isotherm where pores are completely filled by condensed nitrogen, and thus, corresponding to H1 or H2 hysteresis loop. However, due to machine limitations on achieving relative pressures close to unity, only limited numbers of connectivity parameters were obtained in Table 8.2. The mercury entrapment quoted in Table 8.2 was barely affected by the experimental equilibration time-scale, and thus, was considered as the BVI of the samples.

Table 8.1

Comparisons of average key pore geometry characteristics obtained by various different methods. The error quoted is the standard error

Sample	Characterisation technique					
	Gravimetric method	Mercury porosimetry			Gas adsorption	
	Pore volume	Pore volume	Pore diameter	Surface area	BET Surface area	Pore volume
	(mL/g)	(mL/g)	(nm)	(m^2/g)	(m^2/g)	(mL/g)
Aerosil	0.69 ± 0.04	0.822 ± N/A	15.55 ± N/A	212 ± N/A	162 ± 24	0.67 ± 0.01
AL3984T	0.417 ± 0.01	0.443 ± 0.02	12.6 ± 0.2	154 ± 3.13	103 ± 9.04	0.36 ± 0.03
AL3992E	0.554 ± 0.07	0.615 ± 0.01	9.5 ± 0.2	285 ± 4.87	159 ± 29.02	0.56 ± 0.11
C10	0.667 ± 0.25	1.029 ± 0.05	9 ± 0.01	502 ± 26.42	326 ± 32.56	1.2 ± 0.15
C30	1.027 ± 0.01	1.078 ± 0.05	26.8 ± 2.37	148 ± 24.02	81 ± 4.15	1.03 ± 0.01
P7129	N/A	1.04 ± 0.07	9.1 ± 0.2	499 ± 45.89	N/A	N/A
Q17/6	0.531 ± 0.07	0.461 ± 0.02	7.65 ± 0.07	272 ± 61.67	156 ± 3.9	0.52 ± 0.04
S980A	0.648 ± 0.48	1.07 ± 0.05	12.6 ± 0.3	373 ± 28.9	192 ± 15.44	0.52 ± 0.04
S980g	0.934 ± 0.01	0.903 ± 0.05	26.75 ± 0.95	144 ± 1.03	63 ± 2.56	0.78 ± 0.02
Silica Alumina	0.524 ± 0.01	0.489 ± 0.01	7.9 ± 0.01	281 ± 1.73	198 ± 2.34	0.86 ± 0.28

Note

N/A – Not applicable due to limited samples for experimental analysis

Table 8.2

Average key pore geometry characteristics obtained by various different methods. The error quoted is the standard error

	Characterization technique					
	Mercury porosimetry		Gas adsorption			
	Porosity	Entrapment	Connectivity parameters		Variance of PSD	Pore anistropy
Sample	(%)	(%)	*Z*	*L*	σ/μ	slope $(\alpha)_{avg}$
Aerosil	66.99 ± N/A	13.66 ± N/A	6.35 ± 2.65	5.80 ± 0.8	0.9 ± 0.23	-2.84 ± N/A
AL3984T	56.5 ± 1.85	15.51 ± 0.8	6.25 ± 1.75	5.00 ± 1	0.722 ± 0.05	-3.56 ± N/A
AL3992E	66.6 ± 0.82	12.23 ± 2.94	N/S	N/S	0.585 ± 0.04	N/S
C10	69.7 ± 3.13	9.46 ± 1.23	2 ± N/A	4 ± N/A	0.356 ± 0.11	-1.06 ± N/A
C30	70.51 ± 3.43	3.45 ± 0.23	N/S	N/S	0.19 ± 0.02	2.25 ± N/A
P7129	65.54 ± 0.01	50.13 ± 3.04	N/A	N/A	N/A	N/A
Q17/6	48.53 ± 1.73	20.26 ± 5.21	2.7 ± 0.3	5 ± 1	0.46 ± 0.09	-3.64 ± N/A
S980A	72.35 ± 3.95	9.361 ± 0.89	4.3 ± N/S	3.6 ± N/S	0.511 ± 0.16	0.71 ± N/A
S980g	72.41 ± 0.26	15.18 ± 0.73	N/S	N/S	0.143 ± N/A	2.51 ± N/A
Silica Alumina	60.79 ± 0.35	20.69 ± 2.53	N/S	N/S	1.25 ± 0.5	-3.13 ± N/A

Note

The mercury entrapment quoted above was obtained at the highest experimental time-scales.

***L* and *Z* – Reflect the aggregate behaviour of microparticles with different shapes and sizes; and pore connectivity, respectively**

N/S – Not suitable for the method

As stated in Section 8.1, for random pore network models of unimodal/monodisperse porous media, simulation results suggested that the mercury entrapment increased as the variance of the PSD got wider and decreased with increased pore connectivity (except for $Z = 2$). It can be seen in Figure 8.1 that the amount of ultimate entrapment increased with an increase in variance of the PSD. To support this correlation, static analysis was carried out in order to rule out any possibility of random chance. A common alpha level for research is 0.10 (Chatfield, 1983), and was thus adopted in this study. The correlation coefficient obtained for the correlation was 0.566, and the number of data points is nine. Therefore, by using the critical value table for Pearson's correlation coefficient (Chatfield, 1983), it can be concluded that the correlation is statistically significant. Furthermore, the effect of pore connectivity on mercury entrapment was tested (see Appendix A8). The correlation coefficient was 0.166. Thus by using the critical value table for Pearson's correlation coefficient (Chatfield, 1983), it can be concluded that the correlation is statistically insignificant. Thus there was no trend between mercury entrapment and the connectivity data obtained by using the percolation analysis of Seaton (1991).

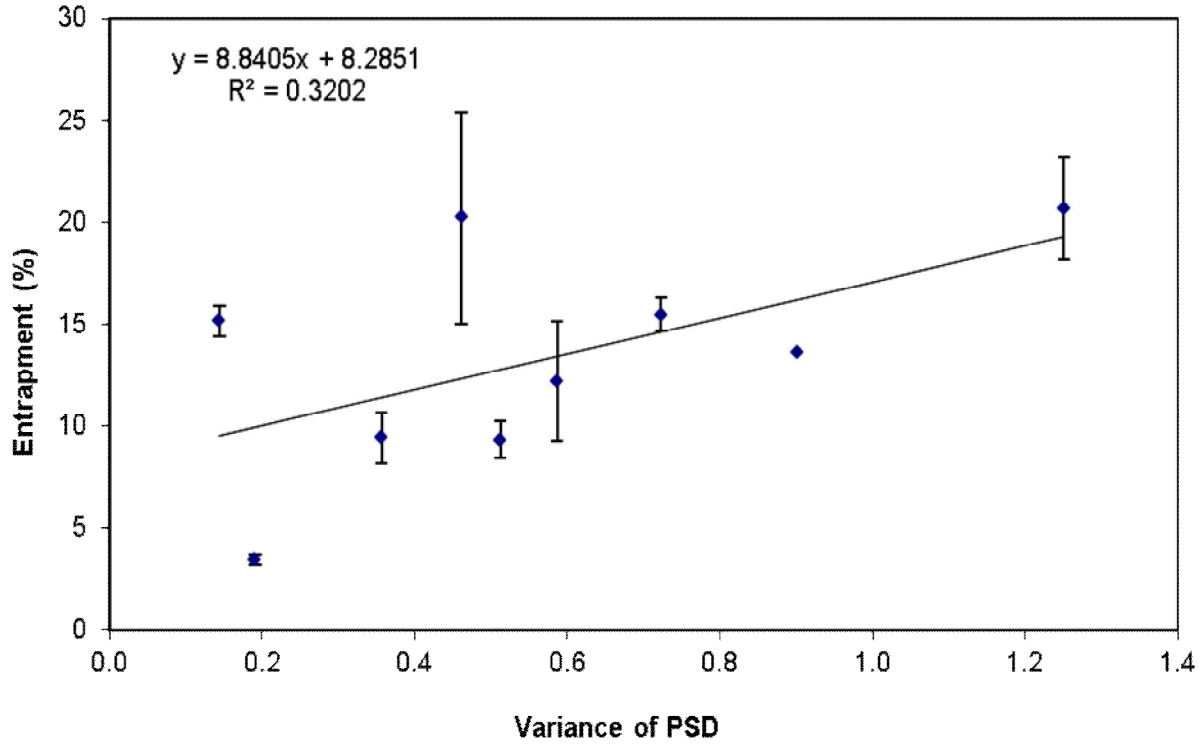

Figure 8.1

Relating the ultimate entrapment with the variance of the PSD

8.3 Influence of pore length on entrapment

Giesche (2010) observed multiple snap-off in long straight cylindrical pores open at both ends. As discussed in Section 4.4, Pomonis and Armatas (2004) method cannot measure the absolute pore length of porous materials. However, a parameter (α) which indicates the likely magnitude of the pore length was obtained. The slopes (α) of the fits to Pomonis and Armatas (2004) in Equation 3.28 for each sample are shown in Table 8.2. As discussed in Section 4.4, samples with very positive slope (α) would likely have long pores depending on the size of the constant k in the power law correlation of Equation 3.29, and thus, the opposite trend can be said for samples with very negative slopes (α). It can be seen in Figure 8.2 that the amount of ultimate entrapment decreased with an increase of pore length parameter, α. The correlation coefficient obtained for the correlation was 0.68. Therefore, by using the critical value table for Pearson's correlation coefficient (Chatfield, 1983), the correlation can be considered statistically significant.

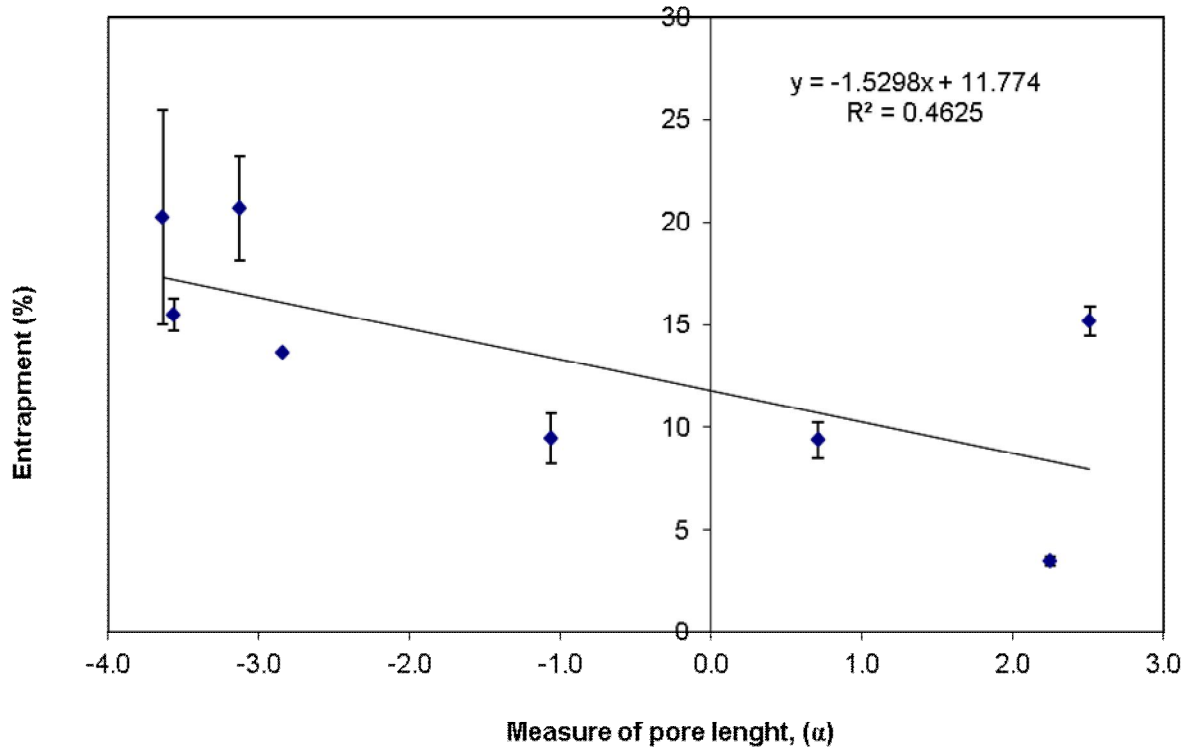

Figure 8.2

Relating the ultimate entrapment with the measure of pore length (α)

8.4 Influence of connectivity and width of PSD on tortuosity

It can be seen in Table 8.3 that the PGSE NMR results for each type of material carried out on fully saturated samples have similar tortuosities for the range of length scales studied. However, the tortuosity of Aerosil varied with length scale for the range of values studied for case I. Sample AL3992E was sensitive to the diffusion time for case II, and thus its tortuosity varied with the length scale that is equivalent to the r.m.s displacement. As detailed in Section 6.5, the relative molecular displacements estimated were far greater than the average pore sizes of the samples, and thus, any deviation seen in the log-attenuation plot was associated with the macroscopic heterogeneity of the sample.

As stated earlier in Section 8.1, for random pore network models of unimodal/monodisperse porous media, simulation results suggest that the tortuosity for molecular diffusion increased with decreased pore connectivity (except for $Z = 2$), and increased width of PSD. For case I, the tortuosity at short diffusion time was correlated with the pore connectivity (see Appendix A8). The correlation coefficient was 0.352, and thus, by using the critical value table for Pearson's correlation coefficient (Chatfield, 1983), the correlation is therefore statistically insignificant. For verification, this study correlated the tortuosity at long diffusion time with the pore connectivity (see Appendix A8). The correlation coefficient obtained was 0.118, and thus considered statistically insignificant. In addition, the correlations of pore connectivity and tortuosities for case II were also statistically insignificant (see Appendix A8).

Furthermore, the effect of PSD on tortuosity was tested in this Section. Figure 8.3 shows that the tortuosity for case I at short diffusion time increased with an increased variance of PSD. The correlation coefficient was 0.419, and thus, considered statistically insignificant. It can also be seen in Figure 8.4 that the tortuosity for case I at long diffusion time increased with the variance of PSD. The correlation coefficient was 0.582, and thus considered statistically insignificant according to Pearson's correlation table (Chatfield, 1983). For verification, this study correlated the tortuosities at different diffusion time for case II with the variance of PSD (see Appendix A8). The correlations observed were statistically insignificant for case II.

Table 8.3

Tortuosity and molecular mean square displacement of fully saturated samples. The error quoted is 95 % confidence intervals

	Characterization technique							
	PGSE NMR							
	H_2O Imbibition (Case I)[a]				Adsorption by H_2O Reservoir (Case II)[b]			
	Average Tortuosity		Average displacement (μm)		Average Tortuosity		Average displacement (μm)	
Sample	(Δ = 50 ms)	(Δ = 100 ms)	(Δ = 50 ms)	(Δ = 100 ms)	(Δ = 50 ms)	(Δ = 100 ms)	(Δ = 50 ms)	(Δ = 100 ms)
Aerosil	1.59 ± 0.06	1.86 ± 0.09	23.00 ± 0.29	31.71 ± 0.46	1.51 ± 0.03	1.55 ± 0.05	23.00 ± 0.29	31.71 ± 0.46
AL3984T*	1.75 ± 0.03	1.81 ± 0.04	25.07 ± 0.21	35.90 ± 6.51	1.16 ± 0.02	1.11 ± 0.41	25.07 ± 0.21	35.90 ± 6.51
AL3992E	1.76 ± 0.02	1.85 ± 0.03	23.38 ± 0.20	26.62 ± 0.37	1.44 ± 0.02	2.05 ± 0.04	23.38 ± 0.20	26.62 ± 0.37
C10	1.57 ± 0.01	1.63 ± 0.04	20.70 ± 0.20	28.27 ± 0.51	1.70 ± 0.02	1.82 ± 0.05	17.97 ± 0.06	22.22 ± 0.30
C30	1.41 ± 0.01	1.49 ± 0.05	21.49 ± 0.48	31.06 ± 0.72	1.54 ± 0.02	1.60 ± 0.02	21.49 ± 0.48	29.79 ± 0.57
Q17/6	2.38 ± 0.03	2.42 ± 0.05	22.48 ± 0.70	30.81 ± 0.89	1.51 ± 0.07	1.86 ± 0.08	21.89 ± 0.69	27.86 ± 0.89
S980A*	1.75 ± 0.02	1.81 ± 0.04	21.92 ± 0.49	29.85 ± 1.04	1.55 ± 0.06	1.20 ± 0.28	21.92 ± 0.49	31.61 ± 3.18
S980g	1.54 ± 0.02	1.57 ± 0.04	23.83 ± 0.41	32.70 ± 0.78	1.27 ± 0.03	1.35 ± 0.05	23.83 ± 0.41	32.70 ± 0.78
Silica Alumina	2.05 ± 0.04	2.19 ± 0.07	24.58 ± 0.34	32.79 ± 1.39	1.20 ± 0.03	1.35 ± 0.08	24.58 ± 0.34	32.79 ± 1.39

Note

*** Two component model in case II (see Table 8.4 for more details)**

[a] The tortuosity quoted is an average of fourteen pellets

[b] The tortuosity quoted is an average of two pellet

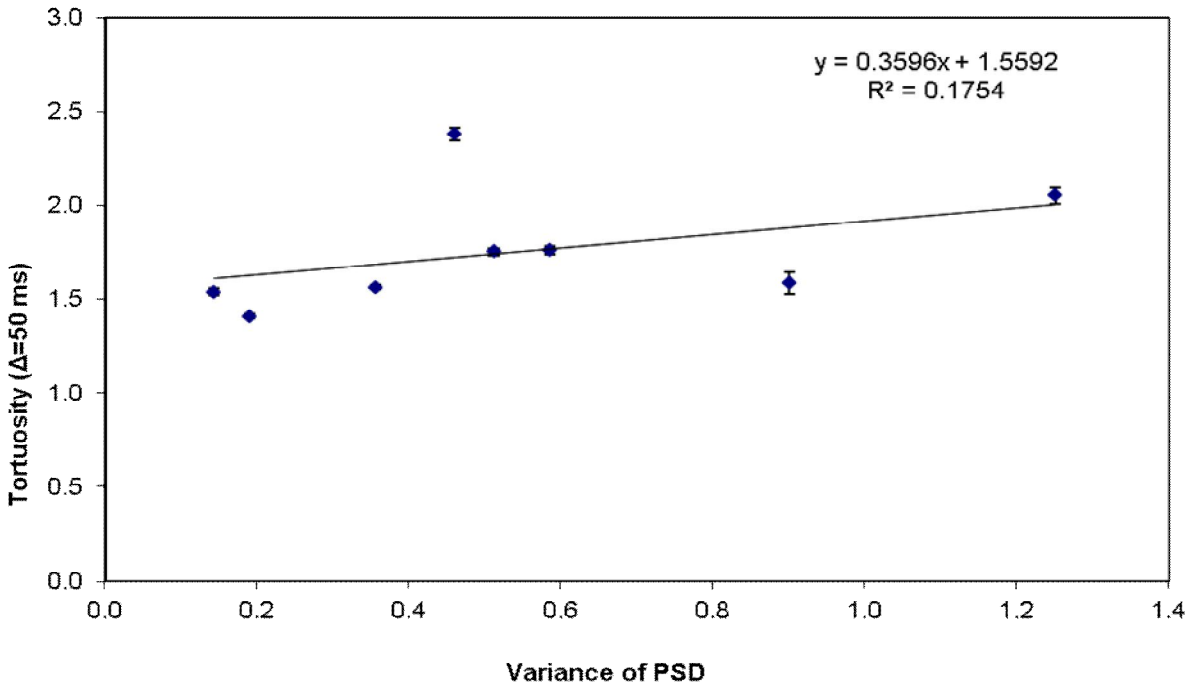

Figure 8.3

Relating tortuosity at short diffusion time with the variance of PSD for case I

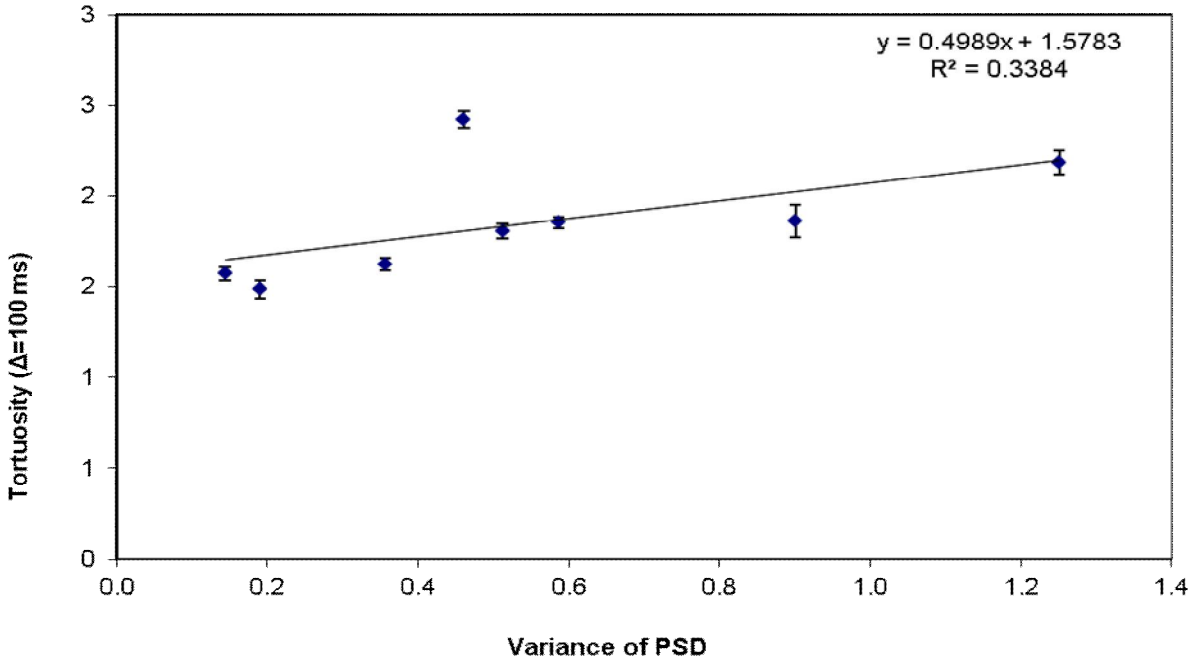

Figure 8.4

Relating tortuosity at long diffusion with the variance of PSD for case I

8.5 Influence of tortuosity on entrapment

Data consistent with two-component diffusion models were observed at long diffusion time for case II. The two tortuosities for the two components are denoted as τ_1 and τ_2 respectively, thus, $\bar{\tau}$ is the overall tortuosity. The fraction of water in the first component is P_W and the fraction of water in the second component is $(1-P_W)$. The estimated tortuosities and molecular mean square displacement of the two-component models for case II are summarised in Table 8.4. It was found that transport was dominated by the fast diffusion component. It can be seen in Table 8.4 that the displacement was far greater than the average pore size of the sample. Therefore, there is no evidence of restricted diffusion in fast and slow components. In contrast, Appel *et al*. (1998) thought the pores that contribute to the BVI are strongly restricted, and thus, the fluid molecules make multiple collisions with the pore wall. It was intended to correlate the tortuosity of the slow component with the corresponding ultimate mercury entrapment. However, the idea was not feasible due to the limited PGSE NMR data for samples with the two-component diffusion models.

In addition, this Section intends to check the prediction of Salmas and Androutsopoulos (2001) on entrapment and tortuosity. These researchers stated that entrapment increases with an increased tortuosity. It can be seen in Figure 8.5 that the amount of mercury trapped in pores upon the termination of the retraction process, increases proportionally with the corresponding tortuosity values at short diffusion time for case I. The tortuosity quoted for case I in Table 8.3 represents an average for fourteen fully saturated pellets. A similar number of pellets were investigated with mercury porosimetry, and, thus, the entrapment quoted was an average of fourteen pellets. The correlation coefficient obtained was 0.791. By using the critical value table from Pearson's correlation coefficient (Chatfield, 1983), it can be concluded that the correlation is statistically significant. Also, the entrapment increased with an increase in tortuosity at long diffusion time for case I. A correlation coefficient of 0.824 was obtained in Figure 8.6, and thus considered to be statistically significant.

Table 8.4

Tortuosities and molecular mean square displacement of the two-component model parameters [Long diffusion time (Δ = 100 ms)].

Sample	Fraction	Tortuosity			Average displacement (μm)		
	P	τ_1	τ_2	$\bar{\tau}$	r_1	r_2	$\bar{r}$
AL3984T, Pellet 2	0.949 ± 0.07	1.19 ± 0.08	5.68 ± 7.50	1.24 ± 0.46	34.93 ± 2.25	16.03 ± 21.15	34.22 ± 12.70
S980A, Pellet 1	0.946 ± 0.12	1.15 ± 0.13	5.55 ± 11.25	1.20 ± 0.20	35.48 ± 4.07	16.29 ± 33.60	34.71 ± 5.64

Table 8.5

Macroscopic contribution to the tortuosity determined by experimental measurements in this study[+] and Rigby and Gladden (1998)*

Sample	Characterisation technique			Macroscopic Tortuosity	
	Tortuosity				
	PGSE (NMR)		MRI		
	Fully saturated pellets[+]	Fully saturated Pellets[*]	Fully saturated Pellets[*]	Fully saturated pellets[+]	Fully saturated Pellets[*]
	H_2O Imbibed	H_2O Imbibition	H_2O Imbibition	H_2O Imbibition	H_2O Imbibition
AL3992E	1.76 ± 0.02	1.80 ± 0.20	2.30 ± 0.30	1.28 ± 0.22	1.24 ± 0.22
AL3984T	1.75 ± 0.03	1.84 ± 0.12	2.40 ± 0.30	1.3 ± 0.18	2.16 ± 0.27
C10	1.57 ± 0.01	2.04 ± 0.06	2.30 ± 0.10	1.15 ± 0.06	1.42 ± 0.07
C30	1.41 ± 0.01	1.65 ± 0.35	1.80 ± 0.30	1.09 ± 0.30	1.21 ± 0.20

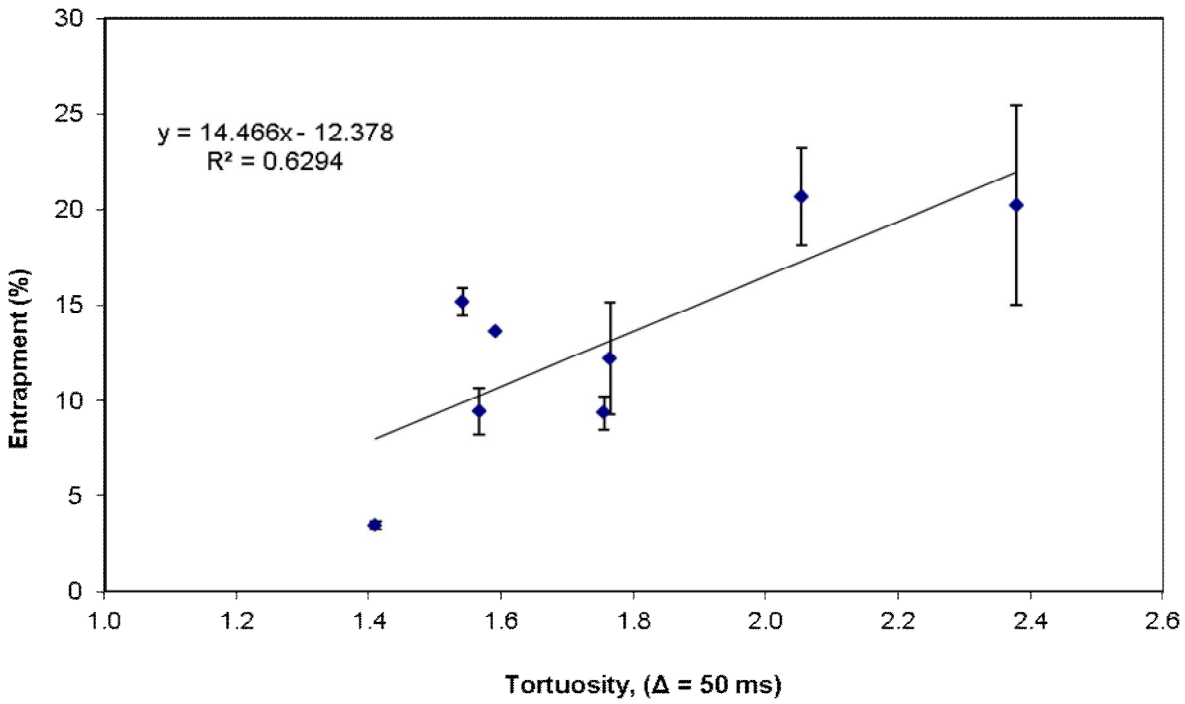

Figure 8.5

Relating ultimate entrapment with tortuosity at short diffusion time for case I

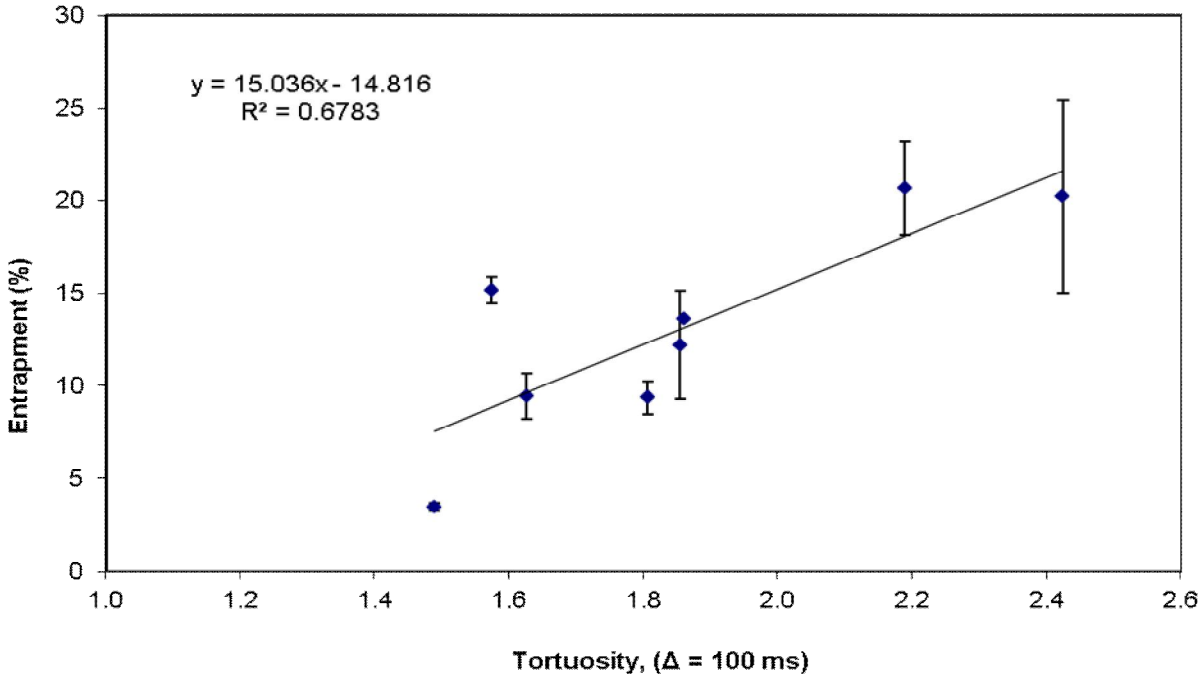

Figure 8.6

Relating ultimate entrapment with tortuosity at long diffusion time for case I

Furthermore, the mercury entrapment quoted in Table 8.2 was correlated with the tortuosity for case II. The mercury entrapment decreased with an increased tortuosity at short diffusion time (see Appendix A8). The correlation coefficient obtained was 0.591, and thus considered to be statistically insignificant. Similarly, the mercury entrapment was correlated with the tortuosities at long diffusion time (see Appendix A8). A correlation coefficient of 0.022 was obtained for the correlation, and thus considered to be statistically insignificant. It should be noted that the tortuosity quoted for case II represents an average of two pellets, and thus is susceptible to significant batch variability. Moreover, the tortuosity obtained by the PGSE NMR technique was limited to the length scale probed. This research intends to address such limitations, and thus, the ultimate entrapment was correlated with the macroscopic tortuosity quoted in Table 8.5. The PGSE NMR and MRI studies by Rigby and Gladden (1998) provided a more comprehensive study of tortuosity. The combination of these two NMR methods can provide a measure of the macroscopic tortuosity describing the pore structure over length scales of the whole pellet. These researchers investigated some of the samples for case I. The quoted tortuosities in Table 8.5 by Rigby and Gladden are the average values of the fitted distribution diffusivity values. Rigby and Gladden (1998) expressed the macroscopic tortuosity (τ_{Mac}) as a ratio of the tortuosities from the two NMR techniques, and thus, $\tau_{Mac} = \tau_{MRI} / \tau_{PGSE}$. Where τ_{Mac} and τ_{PGSE} are the estimated tortuosities obtained by MRI and PGSE NMR techniques, respectively.

It can be seen in Figure 8.7 that the amount of mercury trapped in pores upon the termination of the retraction process, increases proportionally with the corresponding macroscopic tortuosity values obtained by Rigby and Gladden (1998). The correlation coefficient obtained was 0.918 and by using the critical value table for Pearson's correlation coefficient (Chatfield, 1983), it can be concluded that the correlation is statistically significant. In addition, the mercury entrapment quoted in Table 8.2 was correlated with the macroscopic tortuosity obtained for case I (see Appendix A8). The correlation coefficient obtained was 0.333, and thus the correlation was statistically insignificant. A similar correlation coefficient (0.383) was obtained with the tortuosities at long diffusion time (see Appendix 8). For verification, this study correlated the mercury entrapment with the macroscopic tortuosities for case II (see Appendix A8). Mercury entrapment increases with an increased tortuosity. However, the correlation was only

significant with the macroscopic tortuosity at short diffusion time. It should be noted that Rigby and Gladden (1998) used the same materials for the τ_{MRI} and τ_{PGSE} measurements.

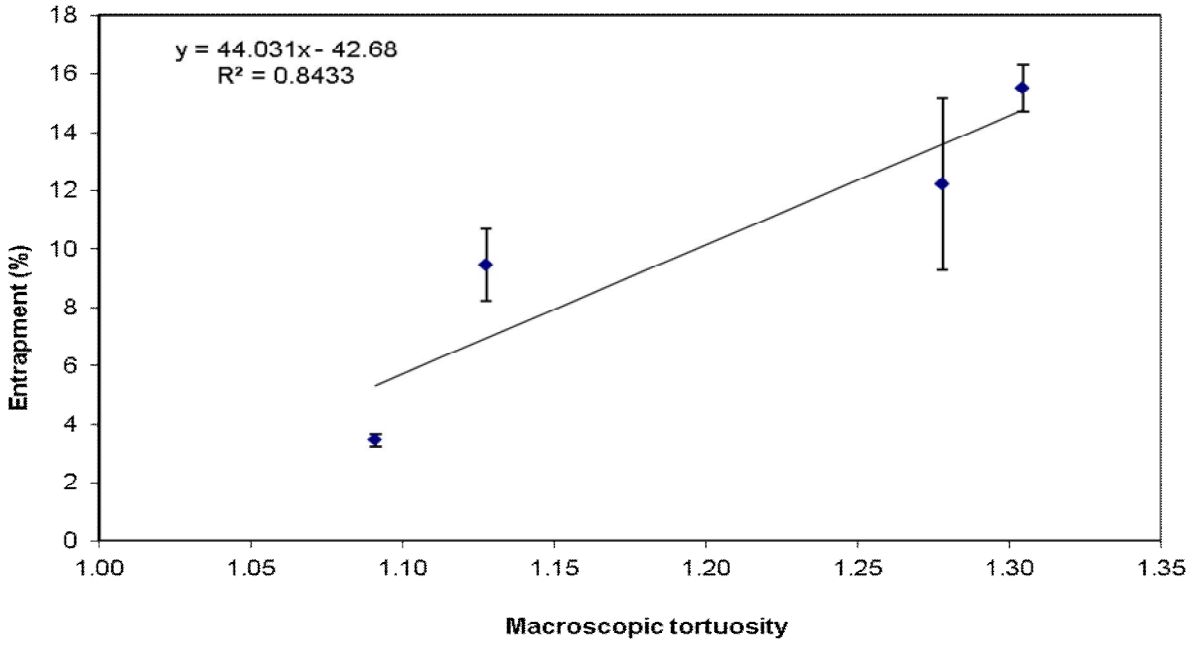

Figure 8.7

Relating ultimate entrapment with macroscopic tortuosity

Table 8.6

Summary of the experimental correlations in this study

Correlations	Trend	Statistical significance
Mercury entrapment against variance of PSD	✓	✓
Mercury entrapment against pore connectivity	×	×
Tortuosity against variance of PSD	✓	×
Tortuosity against pore connectivity	✓	×
Mercury entrapment against measure of pore length	✓	✓
Mercury entrapment against tortuosity at short diffusion time for case I	✓	✓
Mercury entrapment against tortuosity at long diffusion time for case I	✓	✓
Mercury entrapment against tortuosity at short diffusion time for case II	✓	×
Mercury entrapment against tortuosity at long diffusion time for case II	✓	×
Mercury entrapment against macroscopic tortuosity	✓	✓

8.6 Discussion

A novel multi-technique approach has been used to derive structural-topological relationships in order to understand the mechanism of mercury entrapment in porous materials. As stated in Section 1.6, several researchers used two and three dimensional bond networks to determine the relationships between structural and transport properties in artificial porous materials. As a result, these simulation correlations are expected to work reasonably well for materials with random pore network. In a different approach, there is evidence that linked mercury entrapment in long cylindrical pores to their respective pore length (Giesche, 2010). In this study, these correlations for structural-topological relationships were tested with experimental results for a range of porous alumina and silica pellets of spherical or cylindrical geometries. The main findings are summary in Table 8.6. This Section will discuss the experimental correlations observed in this study.

As detailed in Section 5.4, Giesche (2010) reported multiple snap-off in long straight cylindrical pores open at both ends. This was observed following mercury porosimetry on five different straight cylindrical pores of cut silica tubes. To check Giesche's (2010) findings, this study correlated the amount of ultimate mercury entrapment with the measure of pore length (α) obtained by Pomonis and Armatas (2004) method. It was found that the amount of ultimate mercury entrapment decreased with the measure of pore length (α). The finding in this study is at odds with the work of Giesche (2010). Thus, the ultimate mercury entrapment occurs by conventional structural mechanisms. In addition, if the estimated pore length (α) parameters were accurate, then this finding suggests that the materials in this study are dominated by a random collection of pore shapes such as the ink-bottle type pores that are traditionally associated with mercury entrapment. This can be supported by the Type H2 hysteresis loops observed in adsorption/desorption isotherms discussed in Section 4.4.

In a different approach, the simulation results of Androutsopoulos and Mann (1979) suggest that mercury entrapment increased as the variance of the PSD got wider. In this study, the mercury entrapment of some of the samples was sensitive to the experimental time-scales. Thus, the mercury entrapment obtained at the highest experimental time-scale was correlated with the variance of the PSD obtained by Barrett *et al.* (1951) method. It

was found that the amount of ultimate mercury entrapment increased with an increased variance of the PSD. This finding is in good agreement with the mercury simulation works of Androutsopoulos and Mann (1979), Conner and Lane (1984), Lapidus *et al.* (1985), Tsakiroglou and Payatakes (1990), and Portsmouth and Gladden (1991; 1992). In addition, the effect of variance of PSD on the estimated tortuosity was investigated in Section 8.3. The correlation was statistically insignificant even though the tortuosity increased with an increased variance of PSD. This finding is surprising given the expectations arising from the aforementioned results from simulation of diffusion on pore bond networks. This thus begs the question why the simulation results were not confirmed experimentally. Possible explanations are described as follows. The length-scales probed by PGSE NMR greatly exceed those that can be feasibly studied on computer simulation for random pre bond networks. In addition, real materials may not be random in the sense of random pore bond networks.

In a similar approach, the effect of pore connectivity on mercury entrapment was tested by Portsmouth and Gladden (1991; 1992). These simulation results that the amount of mercury entrapment decreases with increased pore connectivity. In this study, the amount of ultimate mercury entrapment was correlated with the pore connectivity estimated with the aid of Seaton's (1991) method. It was found that the correlation is statistically insignificant. Similarly, the estimated tortuosity in fully saturated samples was correlated with the pore connectivity estimated by Seaton's (1991) method. The correlation was statically insignificant even though the tortuosity decreased with an increased tortuosity. Thus there was no trend between either mercury entrapment or tortuosity and the connectivity data obtained by using the percolation analysis of Seaton (1991). As detailed in Section 3.2.7, the connectivity analysis suggested by Seaton (1991) requires an isotherm where pores are fully filled by condensed nitrogen at the top of the isotherm. Therefore, with limited pore connectivity values obtained Seaton's (1991) method; it was difficult to experimentally explore the effect of pore connectivity on either mercury entrapment or tortuosity.

In a different approach, the significance of pore connectivity on tortuosity was investigated in Chapter 7. As detailed in Section 7.4, the disposition and distribution of adsorbed water ganglia within partially-saturated samples was investigated as a function of pore loading

and time. It was found that when the effect of vapour phase contribution to the total diffusion displacement was reduced by increased saturation, the tortuosity decreased with increased liquid connectivity. This finding is in good agreement with the work of Friedman *et al.*, (1995), Vogel (1997; 2000), Salmas *et al.* (2003), Armatas and Pomonis (2004), and Armatas (2006). It should be noted that, none of the correlations with pore connectivity worked in this study. Thus perhaps the fault lies in the Seaton' (1991) percolation analysis of porous materials. For percolation analysis, in addition to the pore geometry assumption of cylindrical pore, one must also assume that pore diameter is independent of the pore length. However, in Sections 3.2.8 and 4.4, it was reported that this might not be true for some samples in this study.

Furthermore, the effect of tortuosity on mercury entrapment was investigated in Section 8.4. Salmas and Androutsopoulos (2001) simulation work found that mercury entrapment increases with an increased tortuosity. In this study, the amount of ultimate mercury entrapment increases with the tortuosity from case I. The correlation coefficients with the tortuosities at both diffusion times were statically significant. Thus these findings are in good agreement with the simulation work of Salmas and Androutsopoulos (2001). However, the correlations with ultimate mercury entrapment and the tortuosities from case II were statistically insignificant. It should be noted that the estimated tortuosity from case I represented an average of fourteen fully saturated pellets. A similar number of pellets were investigated with mercury porosimetry, and, thus, the entrapment quoted was an average of fourteen pellets. However, the tortuosity estimates for case II were an average of only two pellets, and thus more susceptible to batch variability.

For verification, the ultimate mercury entrapment was correlated with the macroscopic tortuosity. It was found that the ultimate mercury entrapment increases with the macroscopic tortuosity estimates from Rigby and Gladden (1998) work. This finding is similar to the pore scale phenomena simulation work by Salmas and Androutsopoulos (2001). In addition, the ultimate entrapment increases with the macroscopic tortuosity from cases I and II. However, only the correlation of coefficient with the macroscopic tortuosity from case II at short diffusion time was statistically significant. Nevertheless, by using the findings of the correlations in Figures 8.5, 8.6, and 8.7, it is safe to conclude that the mercury entrapment is significantly correlated with tortuosity. Thus, this finding suggests

macroscopic structure has a contribution to mercury entrapment. This is in line with the results from X-ray tomography described by Rigby *et al*. (2008) on sample C30 in Figure 2.13 that shows macroscopic heterogeneity in spatial distribution of entrapped mercury. Also detailed in Section 3.3.3, Moscou and Lub (1981) have suggested a similar explanation, where an examination of samples of gel spheres, using light microscopy, following mercury porosimetry experiments showed that mercury entrapment occurred in heterogeneously distributed, macroscopic domains within the sample.

Furthermore, the positive correlation obtained between mercury entrapment and the tortuosity obtained by PGSE NMR suggests that there was no problem with the tortuosity measurement used for the correlations in Section 8.4. In contrast, the correlation trend between tortuosity and the variance of PSD was statistically insignificant even though the tortuosity increases with an increased variance of PSD. As stated earlier in this Section, the simulation correlations highlighted in Section 8.1 were expected to work reasonably well for materials with random pore network. However, there was no trend between either mercury entrapment or tortuosity and the connectivity data obtained by using the percolation analysis of Seaton (1991). Therefore, some of the correlations for structural-topological relationships tested with experimental results were not successful in this Section. As a result, it can be concluded that the pore structures of materials in this study might not have a random pore network. The presence of random pore network in most of these materials was studied previously by Rigby and Gladden (1996). It was found that like most real materials, the materials do not have a random pore network.

In addition, for the simulation correlations to work in this study, other structural factors of the materials have to be considered. These structural factors include the pore size, pore constriction ratio, and uniformity/heterogeneity of the pores. The cylindrical pore model often assumed in porosimetry will reduce the tortuosity of the sample, and thus the chances of thinning of mercury menisci are reduced as shown in Figure 8.2. The pore constriction ratio is large, for a wide pore size range, and thus, the respective tortuosity and mercury entrapment increases. Furthermore, if the pore size are similar, then the pore constriction ratio is reduced which will give a less tortuous pore network with a chance of reduced mercury entrapment. In the case of pore uniformity, the average distance that molecules will move in pores with similar shape reduces, and therefore, mercury entrapment reduces.

8.7 Conclusion

A novel multi-technique approach has been used to predict the relationships between PSD pore connectivity, pore length, tortuosity, and mercury entrapment. A range of porous alumina and silica pellets of spherical or cylindrical geometries were investigated. It was found in Section 4.4 that these samples had strong interactions between the adsorbate and adsorbent, and thus is susceptible to advanced condensation phenomena that will result in a narrow PSD than it exists in reality. In addition, the assumed cylindrical pore shape by the porosimetry techniques ought to have an effect on the structural-topological relationships. Nevertheless, good statistical correlations were obtained in this study. Thus the effect of advanced condensation and the assumed pore shape did not have any effect on the correlations. It was found that mercury entrapment increases with an increase in variance of the PSD, despite limitations on the measurement of this descriptor. This finding is in good agreement with the simulation works of Androutsopoulos and Mann (1979), Conner and Lane (1984), Lapidus *et al.* (1985), Carniglia (1986), Tsakiroglou and Payatakes (1990), Portsmouth and Gladden (1991; 1992). However, with limited pore connectivity values, it was difficult to experimentally predict the effect of pore connectivity on mercury entrapment and tortuosity. In contrast to Giesche's (2010) finding, the mercury entrapment decreased with an increase of pore length. Furthermore, the variance of PSD on the estimated tortuosity correlation was statically insignificant even though the tortuosity increases with an increased variance of PSD. Finally, it was found that the tortuosity is directly proportional to the mercury entrapment. This finding is in good agreement with the works of Moscou and Lub (1981), and Salmas and Androutsopoulos (2001).

8.8 References

Androutsopoulos, G.P. and Mann, R., 1979. Evaluation of mercury porosimetery experiments using a network pore structure model. *Chemical Engineering Science*, 34, 1203-1212.

Apple, M., Stallmach, F., Thomann, H., 1998. Irreproducible fluid saturation determined by pulsed field gradient NMR. *Journal of petroleum science and engineering*,19,45-54.

Armatas, G.S., and Pomonis, P.J., 2004. A Monte Carlo pore network for the simulation of porous characteristics of functionalized silica: pore size distribution, connectivity distribution and mean tortuosities. *Chemical engineering science*, 59, 5735-5749.

Armatas, G.S., 2006. Determination of the effects of the pore size distribution and pore connectivity distribution on the pore tortuosity and diffusive transport in model porous networks. *Chemical engineering science*, 61, 4662 – 4675

Barrett, E. P., Joyner, L. G., Halenda, P. P., 1951. The determination of pore volume and area distributions in porous substances. I. Computations from nitrogen isotherms. *J. Am. Chem. Soc*., 73, 373–380.

Carniglia, S.C., 1986. Construction of the tortuosity factor from porosimetry. *Journal of Catalysis*, 102, 401–418.

Chatfield, C., 1983. *Statistics for technology: A course in applied statistics*. Chapman & Hall/CRC.

Conner, W.C., and Lane, A.M., 1984. Measurement of the morphology of high surface area solids: effect of network structure on the simulation of porosimetry, *J. Catal*., 89, 217–225.

Friedman, S.P., Zhang, L., and Seaton, N.A., 1995. Gas and solute diffusion coefficients in pore networks and its description by a simple capillary model. *Transport in porous media*, 19, 281-301.

Giesche H., 2010. *Multiple snap-off in long cylindrical pores*. Thesis (PhD). Alfred University.

Lapidus, G.R., Lane, A.M., Conner, W.C., 1985. Interpretation of mercury porosimetry data using a pore-throat network model. *Chem. Engng Commun.*, 38, 33–56.

Moscou, L. and S. Lub, 1981. Practical use of mercury porosimetry in the study of porous solids. *Powder Technology*, 29, 45-52.

Pomonis, P.J., and Armatas, G.S., 2004. A method of estimation of pore anisotropy in porous solids. *Langmuir*, 20, 6719-6726.

Portsmouth, R.L., and Gladden, L.F., 1991. Determination of pore connectivity by mercury porosimetry. *Chemical Engineering Science*, 46 (12), 3023-3036.

Portsmouth, R.L., and Gladden, L.F., 1992. Mercury porosimetry as a probe of pore connectivity. *Chemical Engineering Research and Design*, 70 (1), 63-70.

Rigby, S.P., and Gladden, L.F., 1996. NMR and fractal modelling studies of transport in porous media. *Chemical engineering science*, 51 (10), 2263-2272.

Rigby, S.P., and Gladden, L.F., 1998. The use of magnetic resonance images in the simulation of diffusion in porous catalyst support pellets. *Journal of Catalysis*, 173 (2), 484-489.

Rigby S. P., Fletcher R.S., Riley S. N., 2003b. Determination of the cause of mercury entrapment during porosimetry experiments on sol–gel silica catalyst supports. *Applied Catalysis (A),* 247, 27–39.

Salmas C.E., and Androutsopoulos, G.P., 2001. A novel pore structure tortuosity concept based on nitrogen sorption hysteresis data. *Industrial engineering chemical research,* 40 (2), 721-730.

Seaton, N.A., 1991. Determination of the connectivity of porous solids from nitrogen sorption measurements. *Chemical engineering science,* 46 (8), 1895-1909.

Tsakiroglou, C.D., and Payatakes, A.C., 1990. A new simulator of mercury porosimetry for the characterization of porous materials. *Journal of Colloid and Interface Science,* 137, 315-339.

Vogel, H.J., 1997. Morphological determination of pore connectivity as a function of pore size using serial sections. European Journal of Soil Science, 48, 365–377.

Vogel, H.J., 2000. A numerical experiment on pore size, pore connectivity, water retention, permeability, and solute transport using network models. *European Journal of Soil Science*, 51, 99–105.

9.0 Conclusion and future work

9.1 Conclusion

Oil recovery efficiency is heavily influenced by the structure of void space that oil occupies within the reservoir rocks. Therefore, characterisation of porous materials such as the catalyst supports pellets, which have similar chemical and physical properties to those of reservoir rocks can be used to aid understanding of the transport relationships in oil reservoir rocks. The total pore volume of a reservoir rock is generally considered to be comprised of movable and non-movable fluid volumes (FFI and BVI). The non-movable fluid volume is often associated with the entrapment of oil after successive methods of recovery. As reservoir rocks are chemically and geometrically heterogeneous, understanding fluid transport processes occurring in them is difficult. However, catalyst support pellets can offer simplified models for reservoir rocks.

In this thesis, a novel multi-technique approach has been used to predict the transport phenomena in a range of porous alumina and silica pellets with different pore geometries. The entrapment of non-wetting fluid within the samples was investigated with mercury porosimetry at different experimental time-scales. Also, the pore connectivity, measure of pore length (α), and PSDs were obtained with gas adsorption. In addition, PGSE NMR technique was used to study the heterogeneity of diffusion within the samples over different diffusion time-scales. Furthermore, PSGE NMR was used to study the kinetics of adsorption in porous media, and thus elucidate the relationships of liquid connectivity and molecular exchange between liquid and vapour phases.

In general, mercury entrapment occurred at larger mesopore radii, and was present in all experimental time-scales of the materials investigated. The effect of experimental time-scales in silica materials was significantly greater in samples C30 and Q17/6, and thus suggests that the retraction is a flow-rate controlled process. The PGSE NMR studies revealed macroscopic heterogeneity of the samples. In this study, similar tortuosities were obtained for the range of length scales studied. In addition, PGSE NMR studies of kinetics of adsorption revealed that the tortuosity of the adsorbed liquid ganglia decreased with an

increased liquid connectivity within the materials. Furthermore, there was enough evidence to suggest molecular exchange between the liquid and vapour phases. Finally, the combination of the novel characterisation techniques findings are highlighted below:

- The amount of ultimate mercury entrapment increases with an increase in variance of the PSD.
- The amount of ultimate mercury entrapment decreases with an increase in pore length, contrary to the theory of Giesche (2010).
- The amount of ultimate mercury entrapment increases with increasing tortuosity.
- The amount of ultimate mercury entrapment increases with an increase of macroscopic tortuosity.

9.2 Future work

The ultimate objective of this research was to improve predictions of BVI of oil reservoir rocks. In this study three novel techniques have been used to characterise the transport relationships of industrial catalysts support pellets. It was the intension of this research to expand the traditional characterisation technique and use advanced simulation packages. There are many options for future work which could be incorporated into this study. However, these proposed options are considered to be the most significant:

- **Gas sorption studies**

  The samples have strong interactions between the adsorbate and adsorbent, and thus are susceptible to advanced condensation phenomena. This might have resulted in a narrower PSD being measured than existed in reality. Therefore, for more accurate estimate of PSD it is essential to check the possibility of advanced condensation in these samples. In addition, limited numbers of connectivity parameters were obtained due to machine limitations on achieving relative pressures close to unity that can cause capillary condensation of liquid nitrogen with pores of sizes. Aukett and Jessop (1996) developed a method to the conventional nitrogen experiment that involved bulk

condensation (BC) to obtain better estimation for the PSD and connectivity parameters. Therefore this BC method is recommended for further investigation of the materials.

- **Mercury porosimetry studies**

  Mercury intrusion was known to be spontaneous process, and thus independent of equilibration time (Lowell and Shields, 1981). In this study, different values of key characteristic parameters (such as pore size, and pore volume) were obtained at different experimental time-scales in some of the materials. Therefore, mercury intrusion was slightly affected by experimental time-scale. Similar observations were reported by Giesche (2006). Therefore, longer experimental time-scales are recommended to elucidate the sensitivity of mercury intrusion curve to experimental time.

- **PGSE NMR studies of partially saturated samples**

  The kinetics of adsorption in porous media was successfully studied with PGSE NMR technique. Several other researchers used diffusimetry and relaxometry of polar/nonpolar at different degrees of filling in order to characterize the pore morphology in porous media (D'Orazio *et al.*, 1990; Valliullin *et al.*, 1997; 2005; and Farrher *et al.*, 2008). However, not much emphasis was given to the kinetics of desorption in porous media. Therefore, it is recommended that kinetics of desorption in porous media are investigated with the PGSE NMR technique.

- **Computer simulation studies of mercury entrapment**

In recent years, multiple snap-off was observed in long cylindrical pores with uniform diameters (Giesche, 2010). The above research was conducted in the light of such claims, and thus, the effect of pore length on mercury entrapment was investigated. It was found that the amount of ultimate entrapment decreased with increased pore length. However, this research was limited by the accuracy of estimated pore length parameter (α). The effect of pore length on mercury entrapment can be tested with computer simulations. In recent years, computer simulation of mercury intrusion and retraction has been performed with mean-field density-functional theory (MF-DFT) in models of disordered porous materials (Porcheron *et al.*, 2007; Rigby *et al.*, 2009). MF-DFT could be used to further elucidate the claim of Giesche's (2010) work, and its limitations.

9.3 References

Aukett, P. N.; Jessop, C. A., 1996. *In Fundamentals of Adsorption*. LeVan, M. D., Ed.; Kluwer: Boston.

D'Orazio, F., Bhattacharja, S., and Halperin W.P., 1990. Molecular self diffusion and nuclear magnetic resonance relaxation of water in unsaturated porous silica glass. Physical review 42, 9810-9818.

Farrher, G., Ardelean, I., Kimmich, R., 2008. Time-dependent molecular diffusion in partially filled porous glasses with heterogeneous structure. *Applied magnetic resonance*, 34 (1-2), 85-99.

Giesche H., 2010. *Multiple snap-off in long cylindrical pores*. Thesis (PhD). Alfred University.

Lowell S., Shields J. E., 1981. Hysteresis, entrapment, and wetting angle in mercury porosimetry. *Journal of Colloid and Interface Science*, Vol. 83, No. 1.

Porcheron, F., Thommes, M., Ahmad, R., and Monson, P.A., 2007. Mercury porosimetry in mersoporous glasses: A comparison of experiments with results from a molecular model. *Langmuir*. 23,372-3380.

Rigby, S.P., and Chigada, P.I., 2009. Interpretation of integrated gas sorption and mercury porosimetry studies of adsorption in disordered networks using mean-field DFT. *Adsorption-journal of the international adsorption society*, 15 (1), 31-41.

Valiullin, R.R., Skirda, V.D., Stapf, S., Kimmich, R., 1997. Molecular exchange processes in partially filled porous glass as seen with NMR diffusometry. Physical review E, 55 (3), Part A, 2664-2671.

Valiullin, R., Korunov, P., Karger, J., and Timoshenko, V., 2005. Concentration-dependent self-diffusion of adsorbates in mesoporous materials. *Magnetic resonance imaging*, 23, 209-214.

Appendix (A4)

(Gas sorption technique appendix figures)

Nitrogen adsorption and desorption isotherms for the rest of the samples

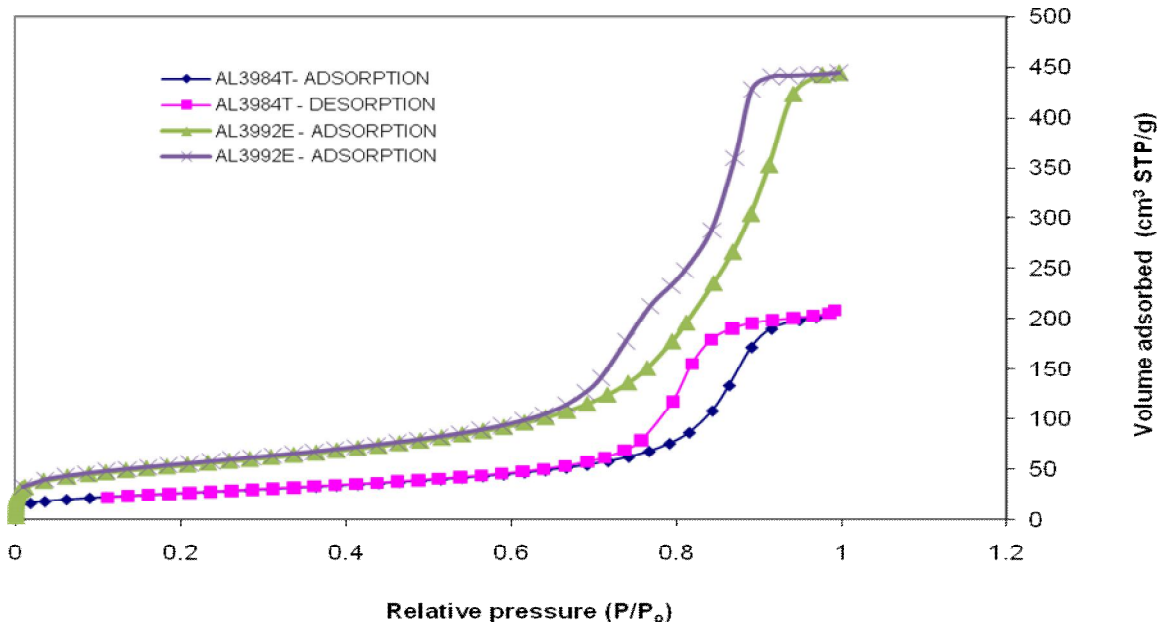

Figure A3-1

Nitrogen adsorption/desorption isotherms for AL3984T and AL3992E at 77 K

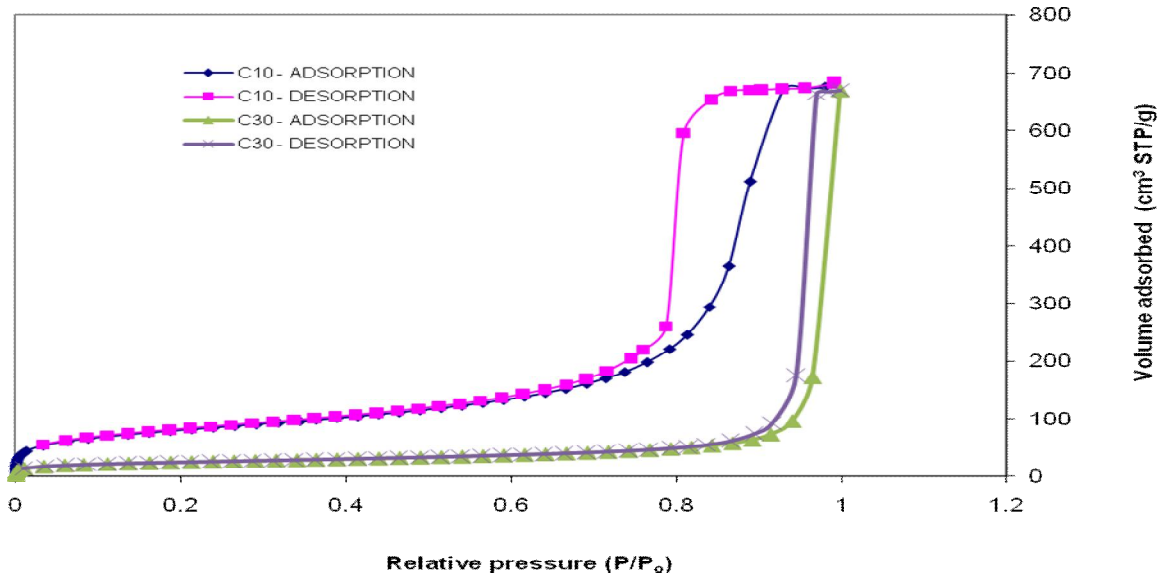

Figure A3-2

Nitrogen adsorption and desorption isotherms for C10 and C30 at 77 K

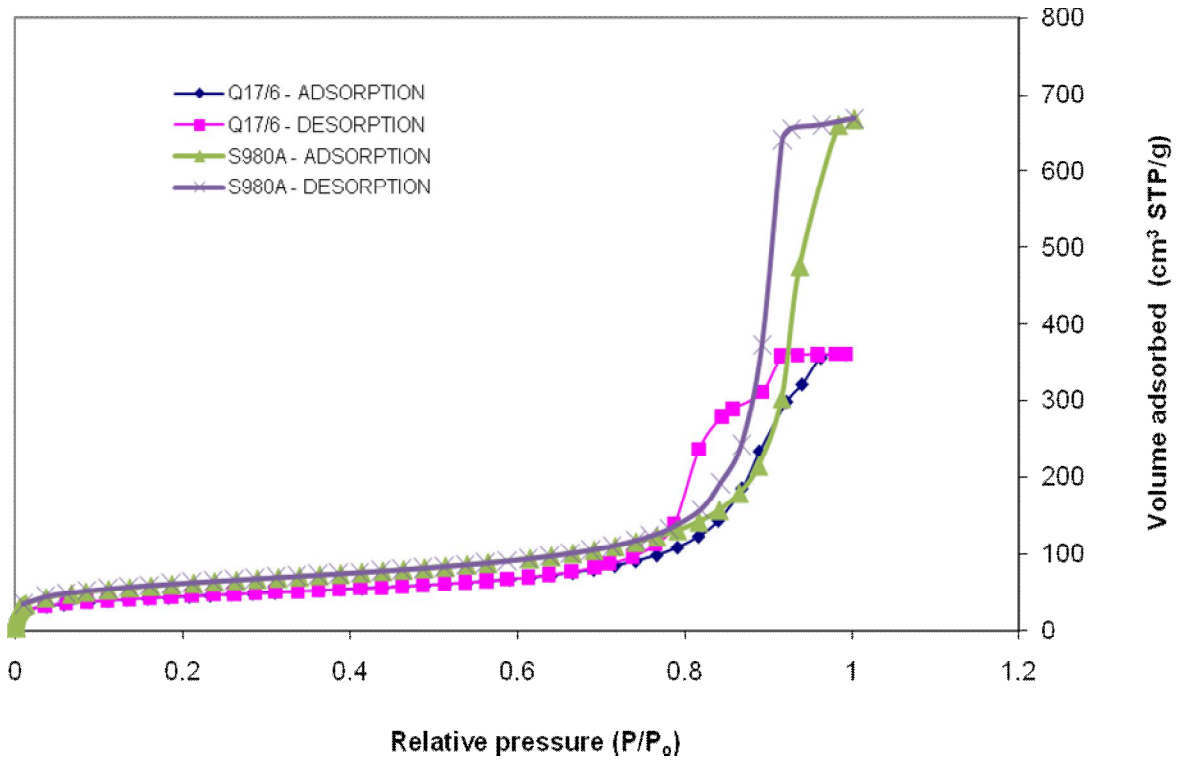

Figure A3-3

Nitrogen adsorption and desorption isotherms for Q17/6 and S980A at 77 K

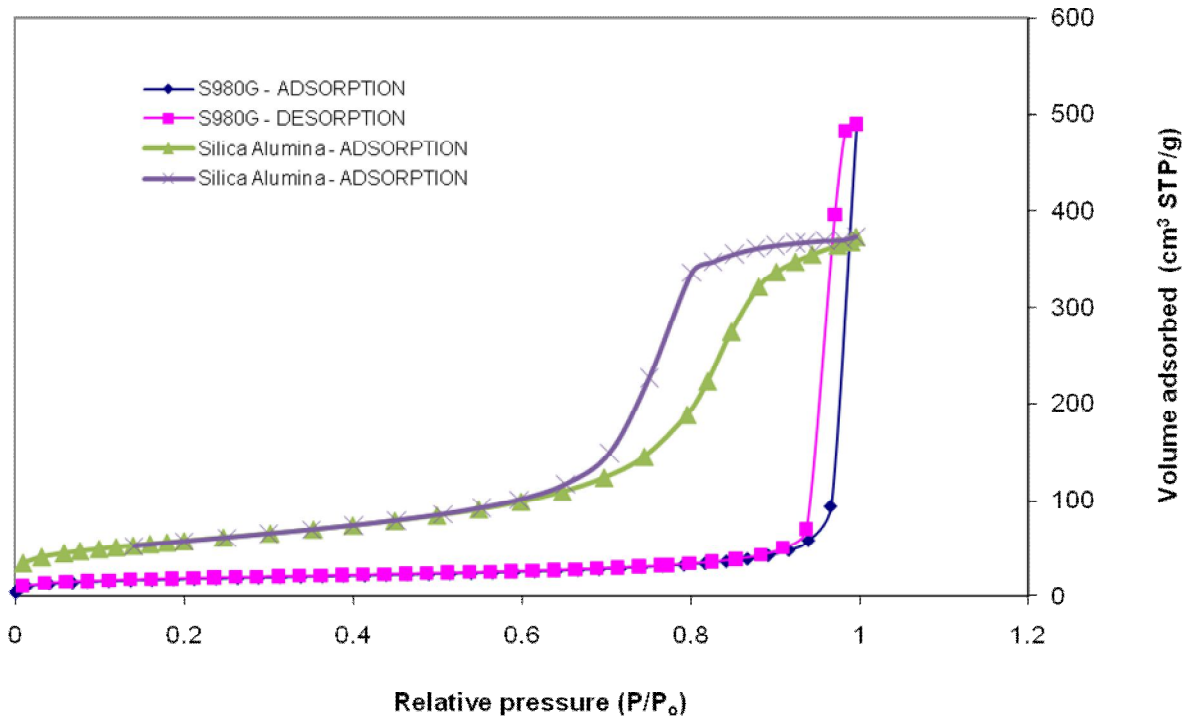

Figure A3-4

Nitrogen adsorption and desorption isotherms for S980G and Silica Alumina at 77 K

BET Surface area for the rest of the samples

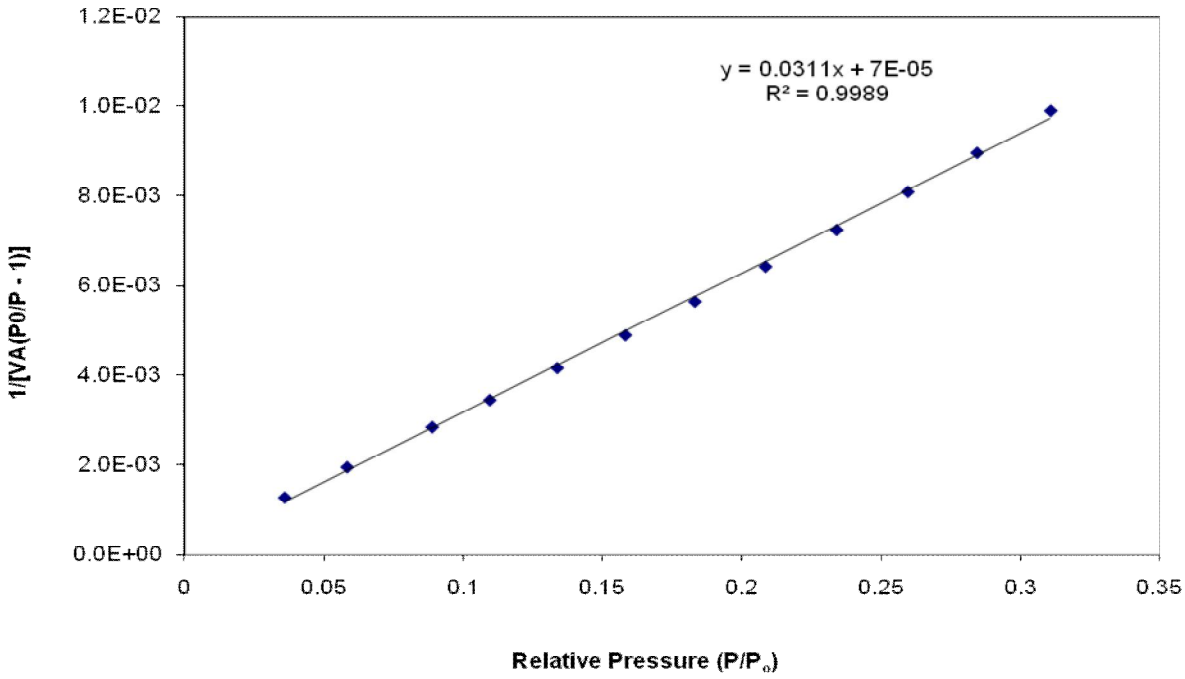

Figure A3-5

The BET plot for Nitrogen adsorption at 77 K of Aerosil

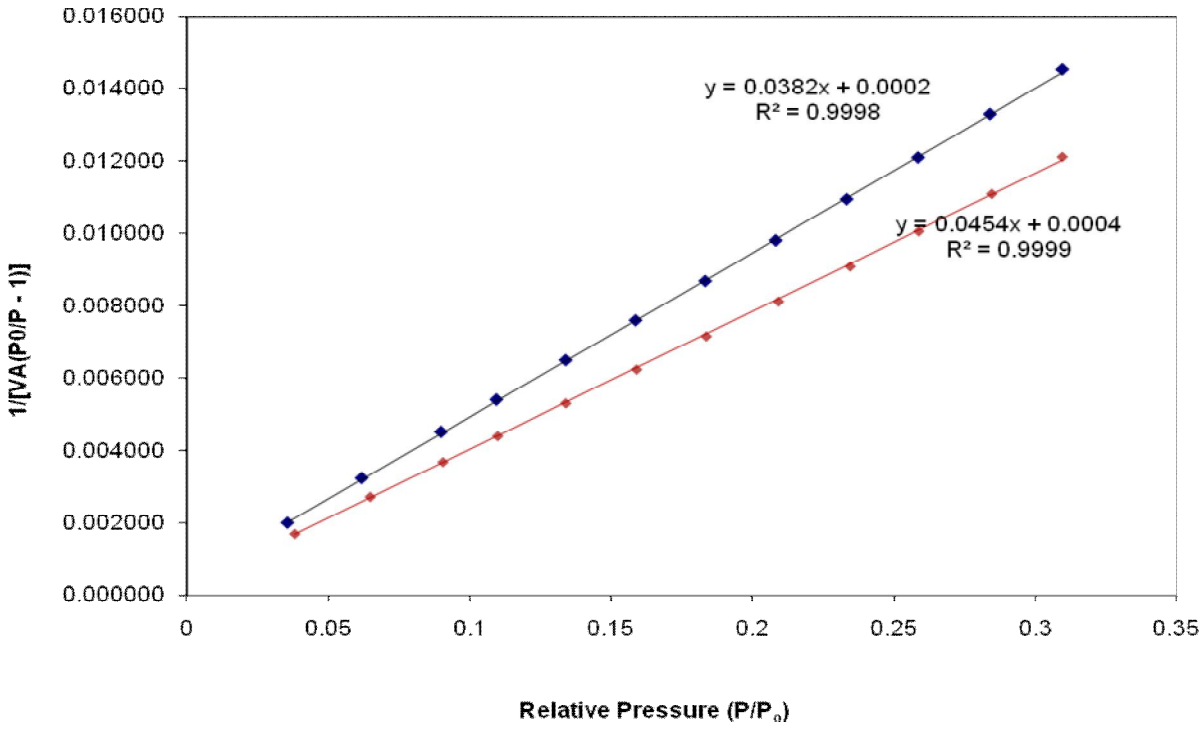

Figure A3-6

The BET plot for Nitrogen adsorption at 77 K of AL3984T

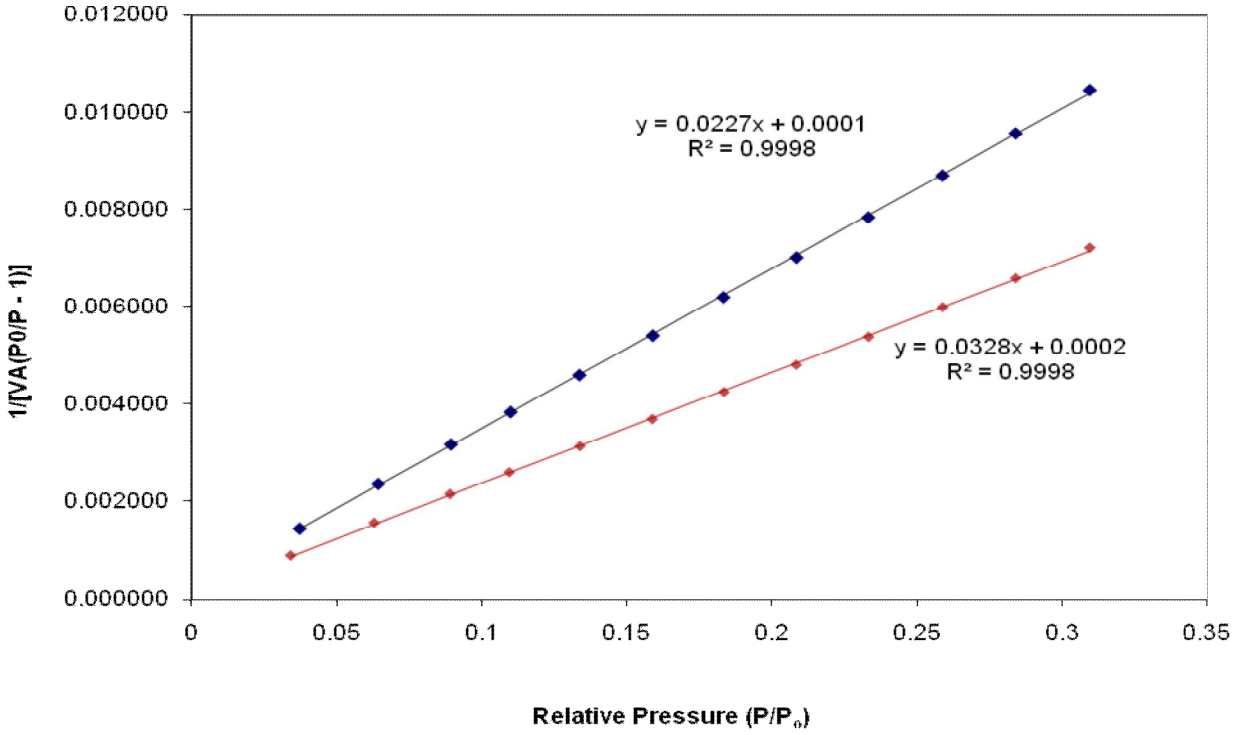

Figure A3-7

The BET plot for Nitrogen adsorption at 77 K of AL3992E

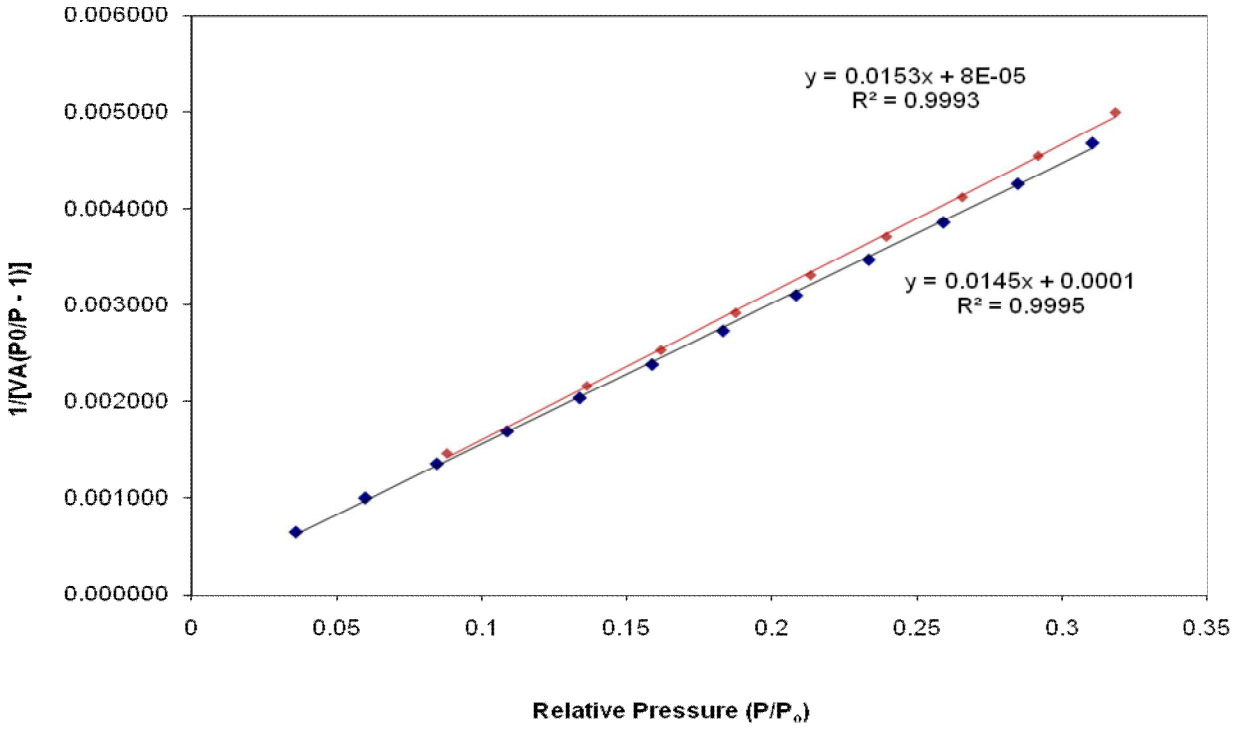

Figure A3-8

The BET plot for Nitrogen adsorption at 77 K of AL3992E

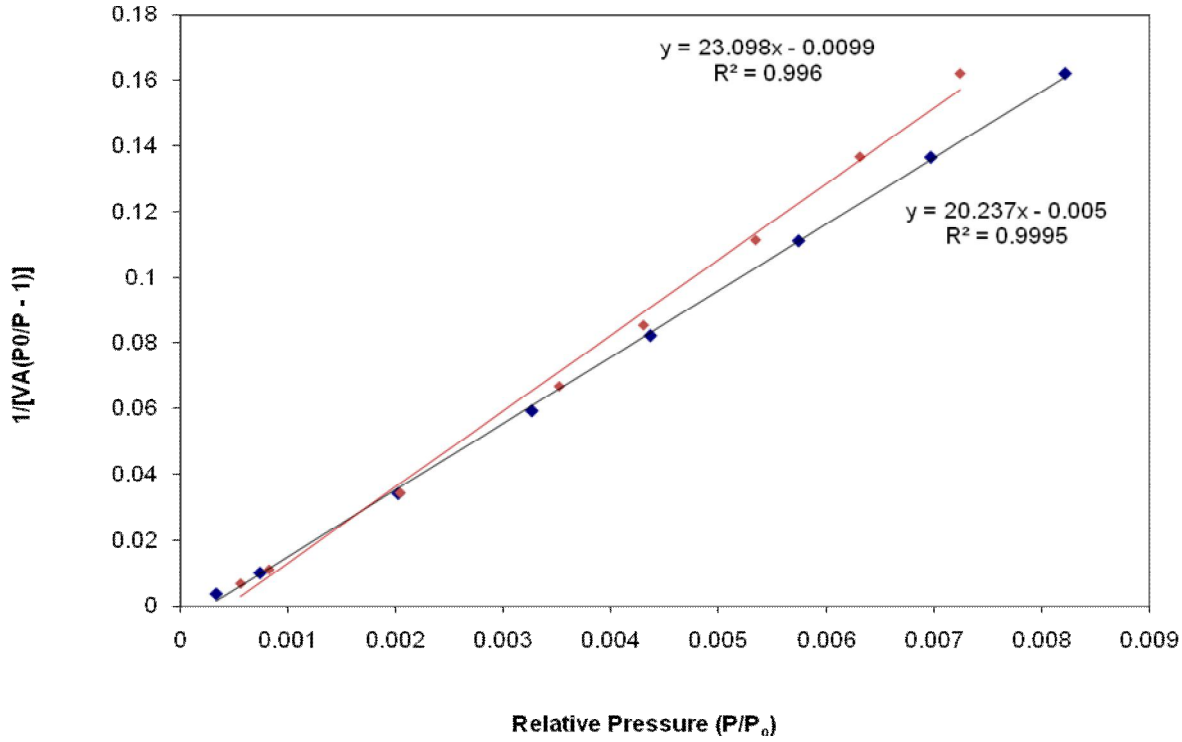

Figure A3-9

The BET plot for Nitrogen adsorption at 77 K of C30

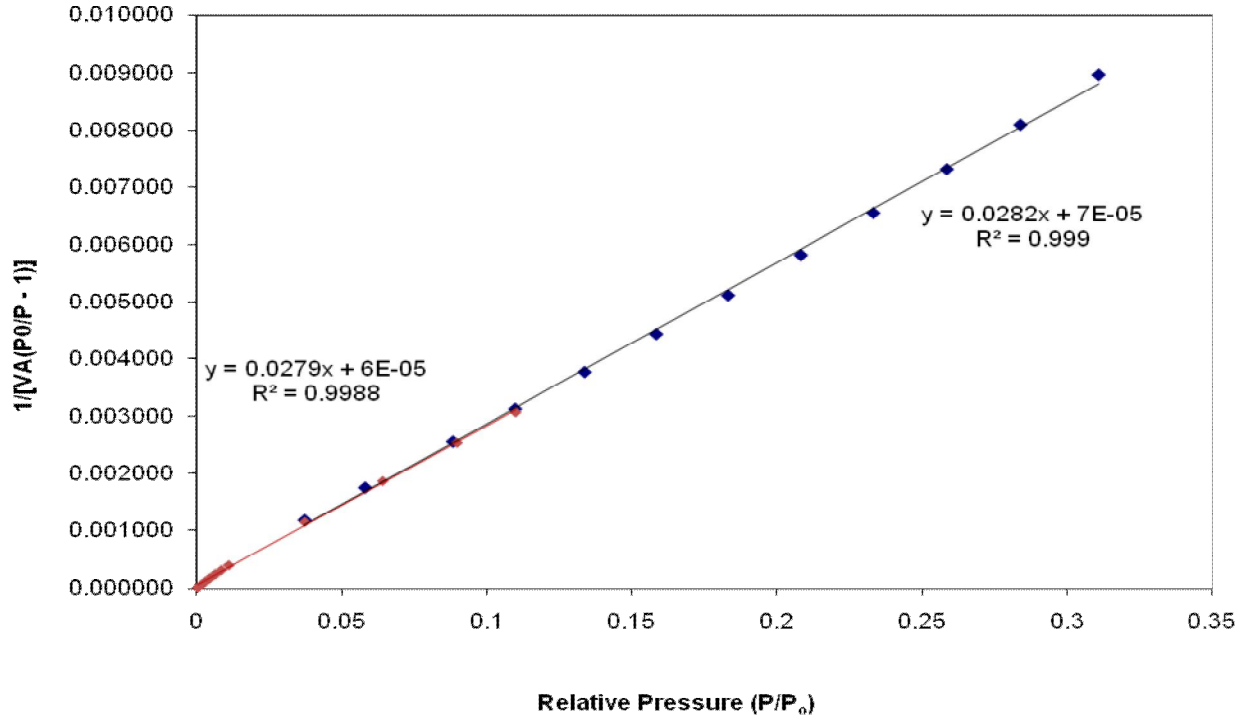

Figure A3-10

The BET plot for Nitrogen adsorption at 77 K of Q17/6

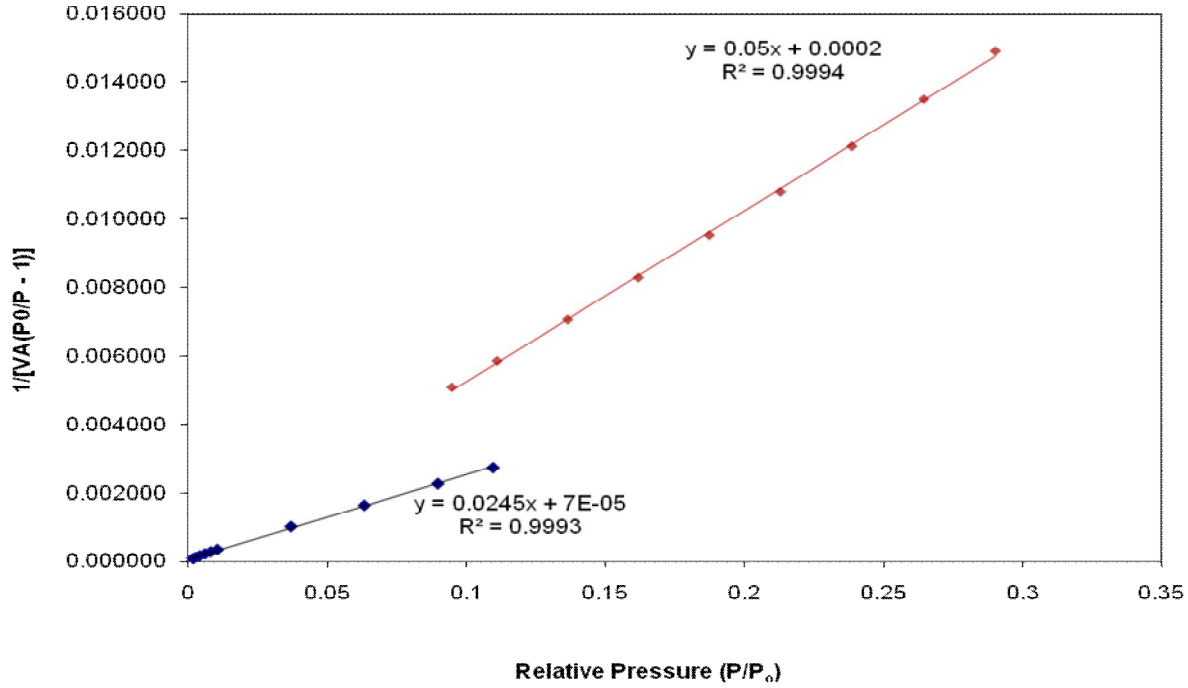

Figure A3-11

The BET plot for Nitrogen adsorption at 77 K of S980A

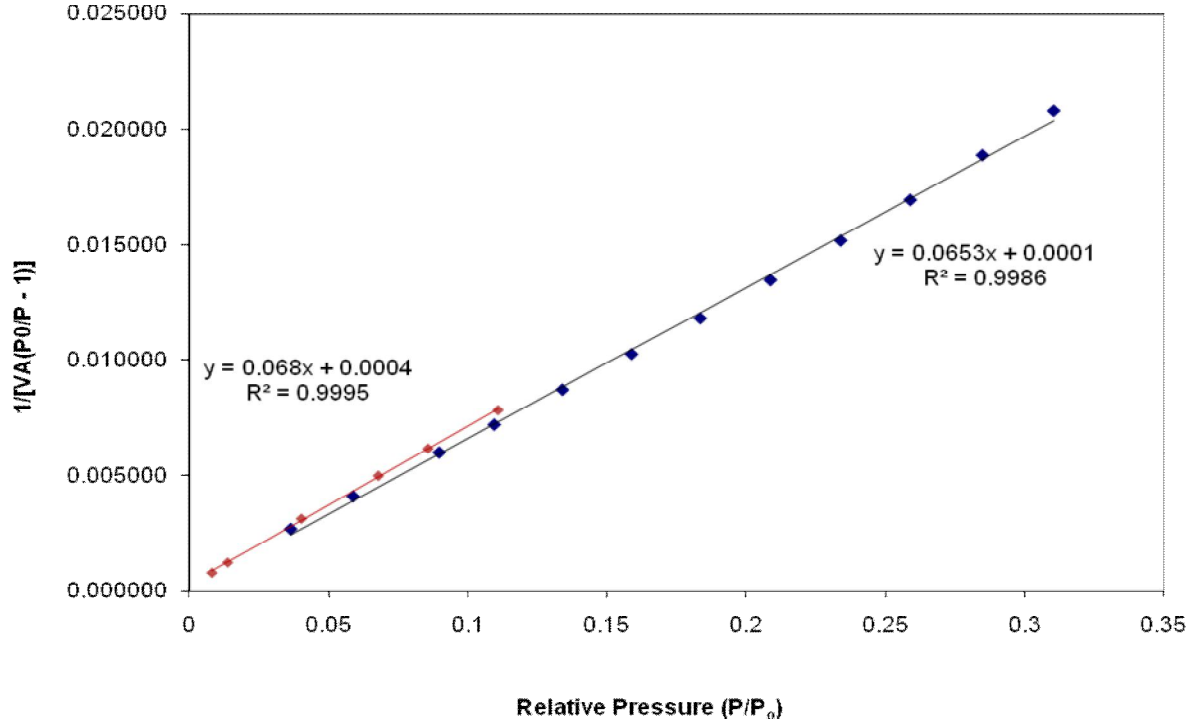

Figure A3-12

The BET plot for Nitrogen adsorption at 77 K of S980G

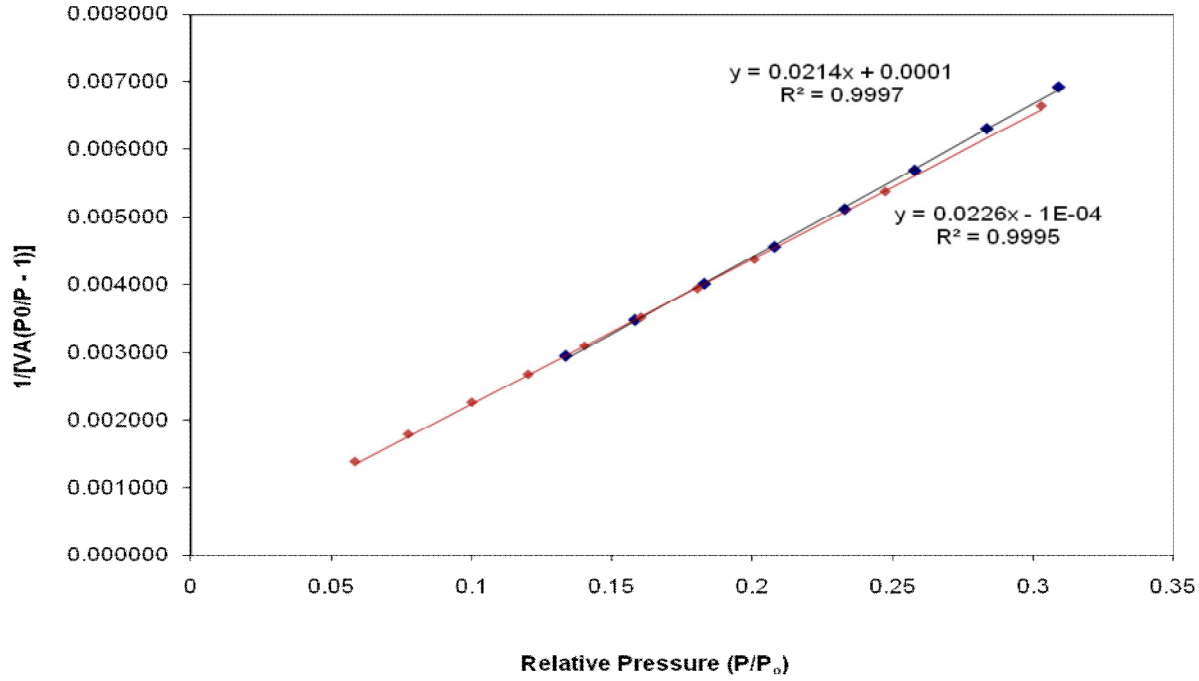

Figure A3-13

The BET plot for Nitrogen adsorption at 77 K of Silica Alumina

Connectivity parameters for the rest of the samples

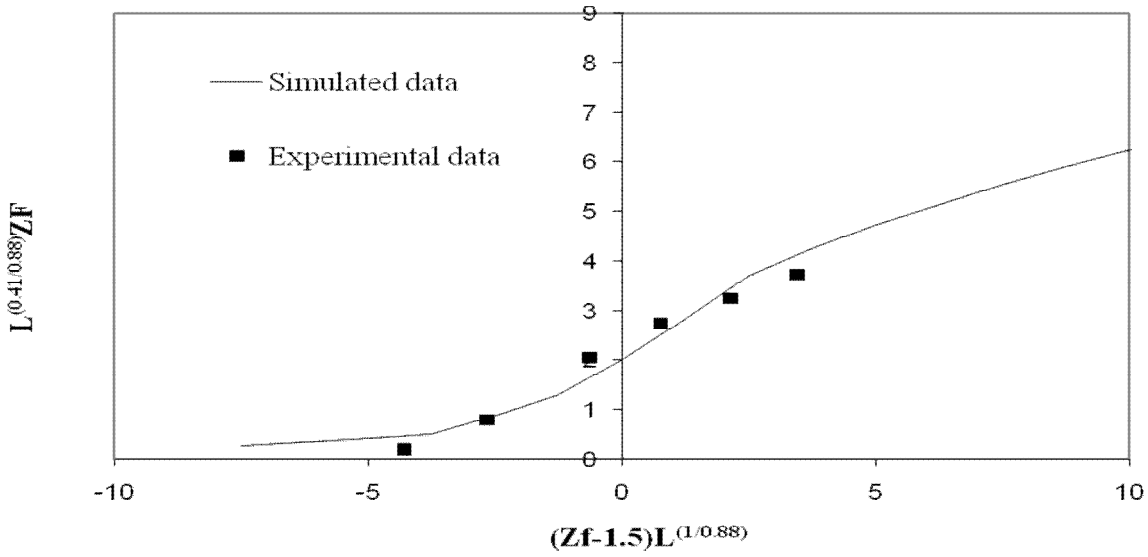

Figure A3-14

Generalised accessibility plot of Aerosil showing the experiemental and simulated data for $Z = 3.7$ **and** $L = 5$

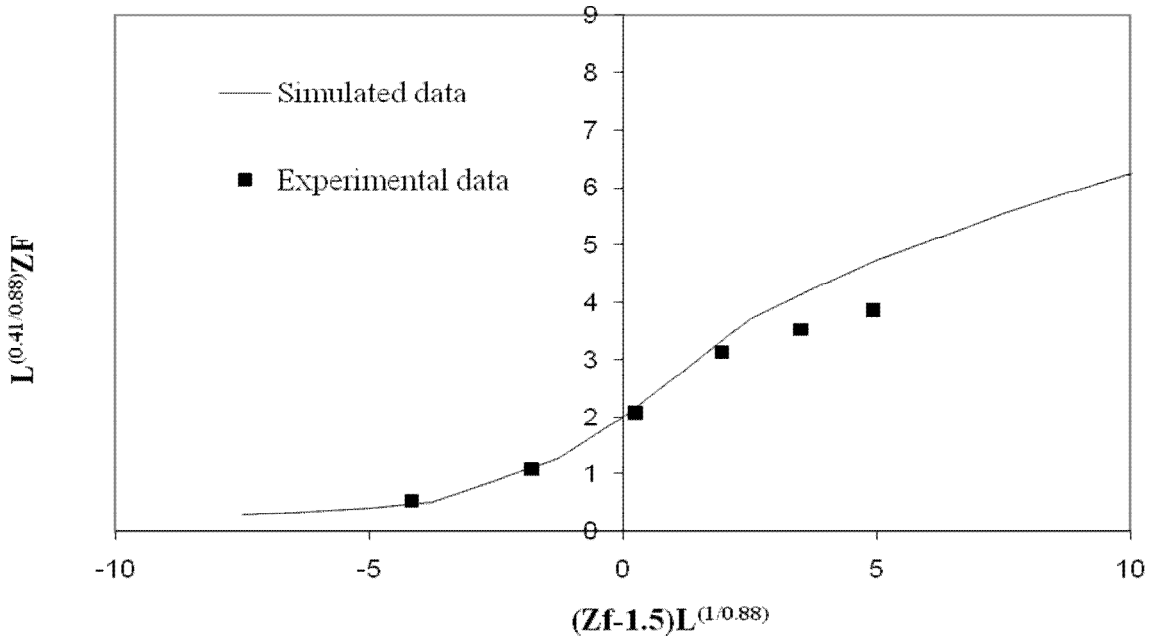

Figure A3-15

Generalised accessibility plot of AL3984T showing the experiemental and simulated data for $Z = 4.5$ **and** $L = 8$

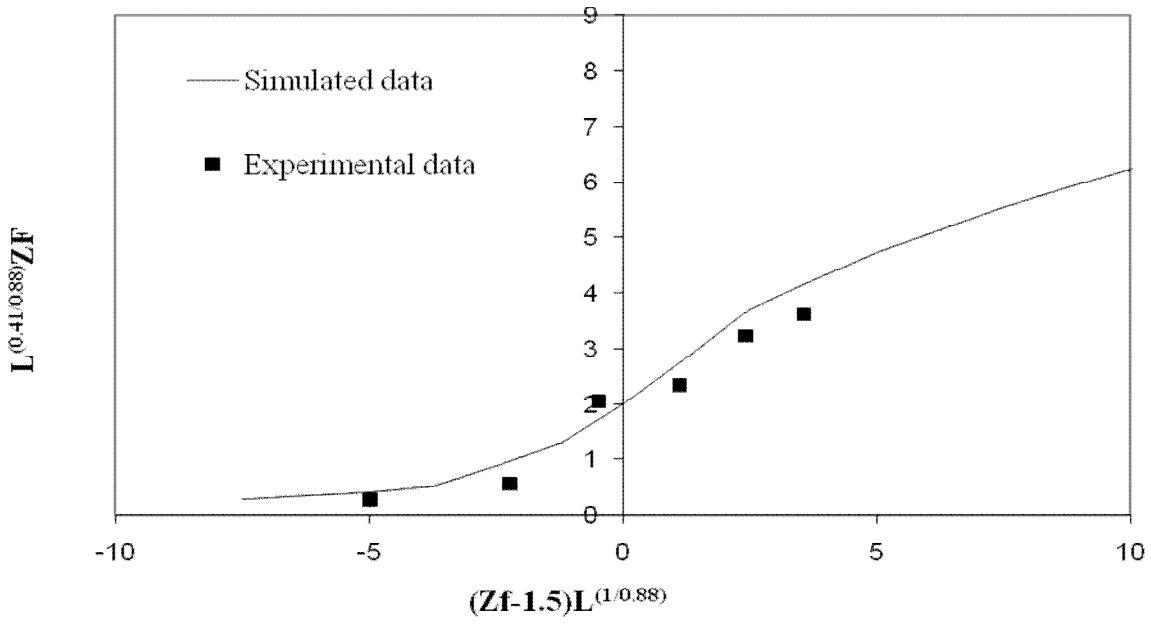

Figure A3-16

Generalised accessibility plot of AL3984T showing the experiemental and simulated data for $Z = 4$ **and** $L = 6$

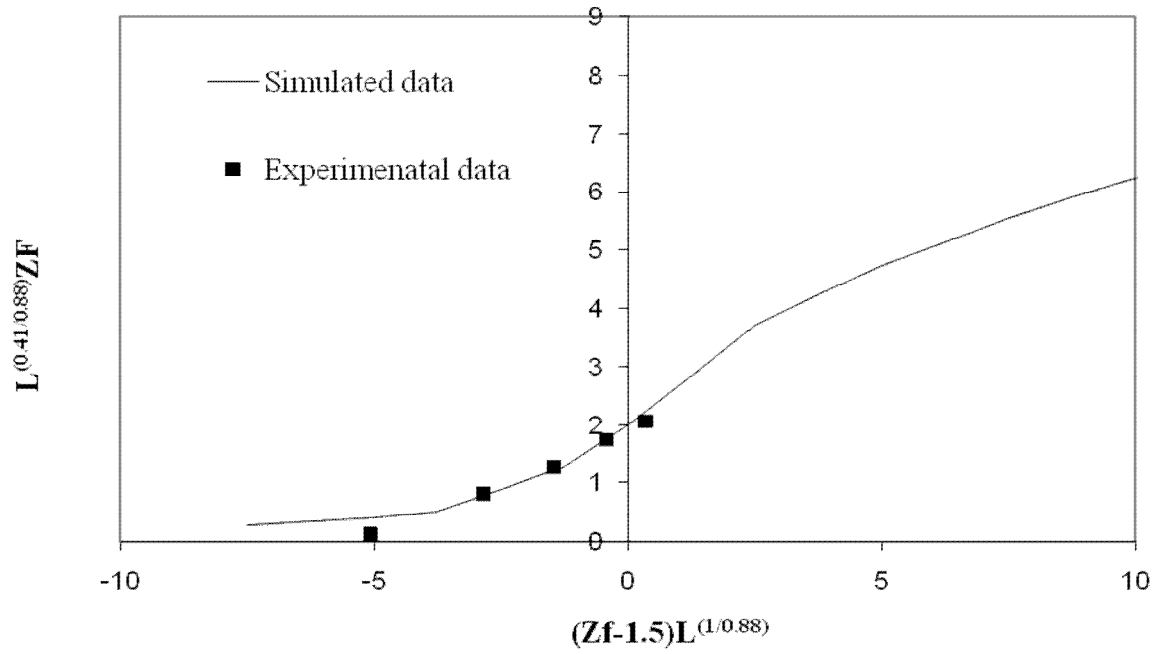

Figure A3-17

Generalised accessibility plot of C10 showing the experiemental and simulated data for $Z = 2$ **and** $L = 4$

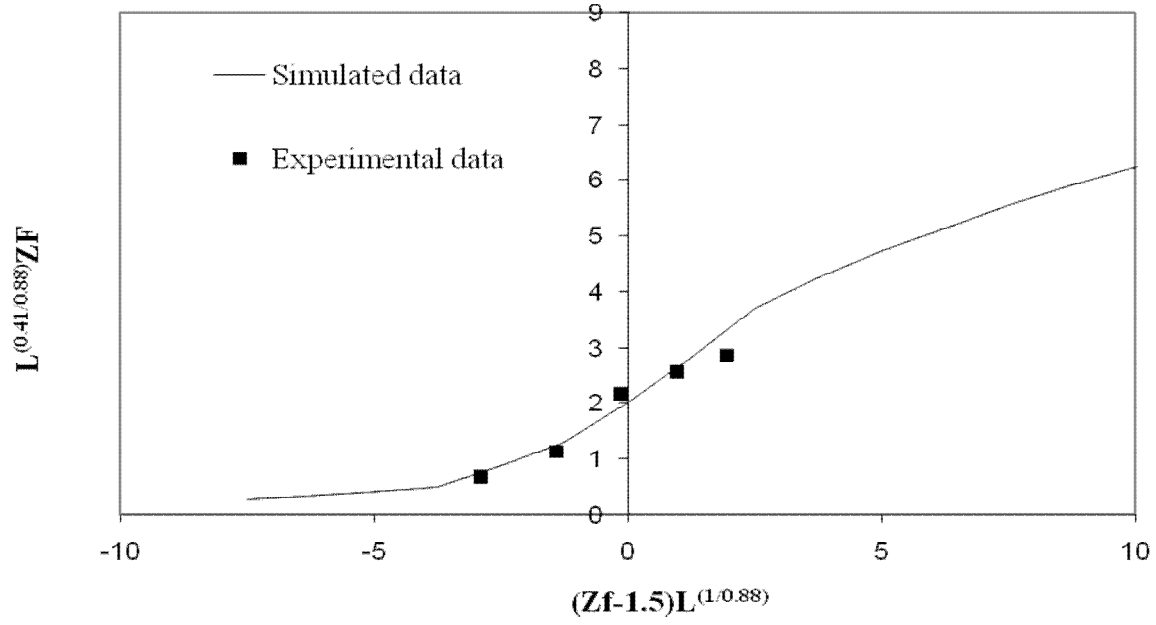

Figure A3-18

Generalised accessibility plot of Q17/6 showing the experiemental and simulated data for $Z = 3$ **and** $L = 6$

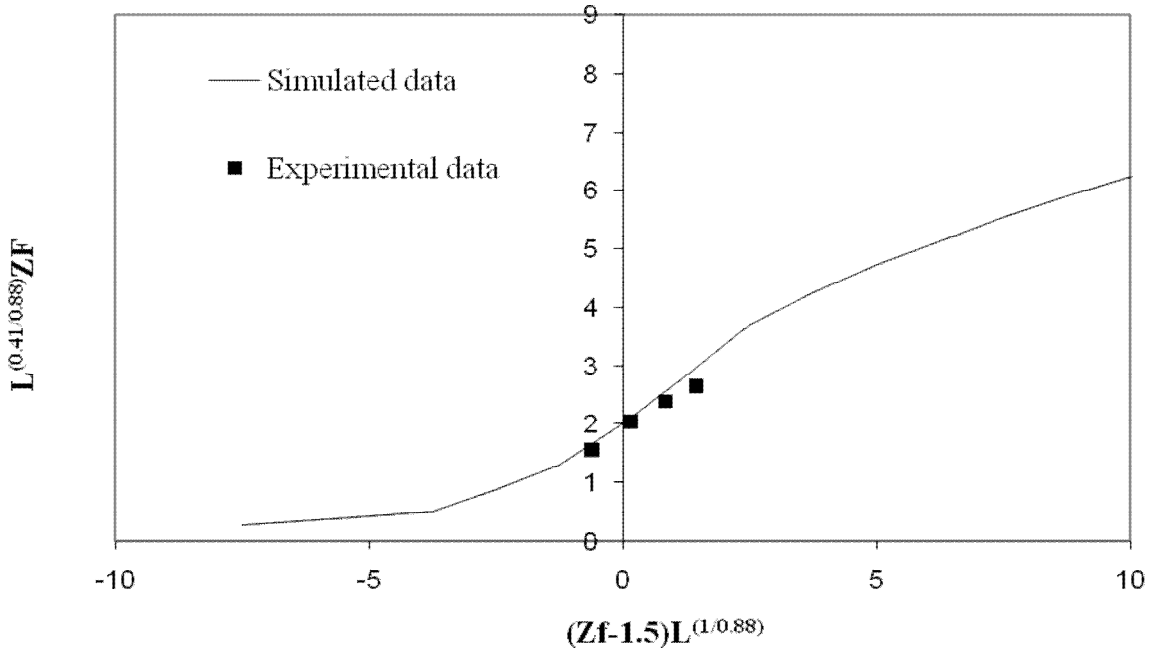

Figure A3-19

Generalised accessibility plot of Q17/6 showing the experiemental and simulated data for $Z = 2.4$ **and** $L = 4$

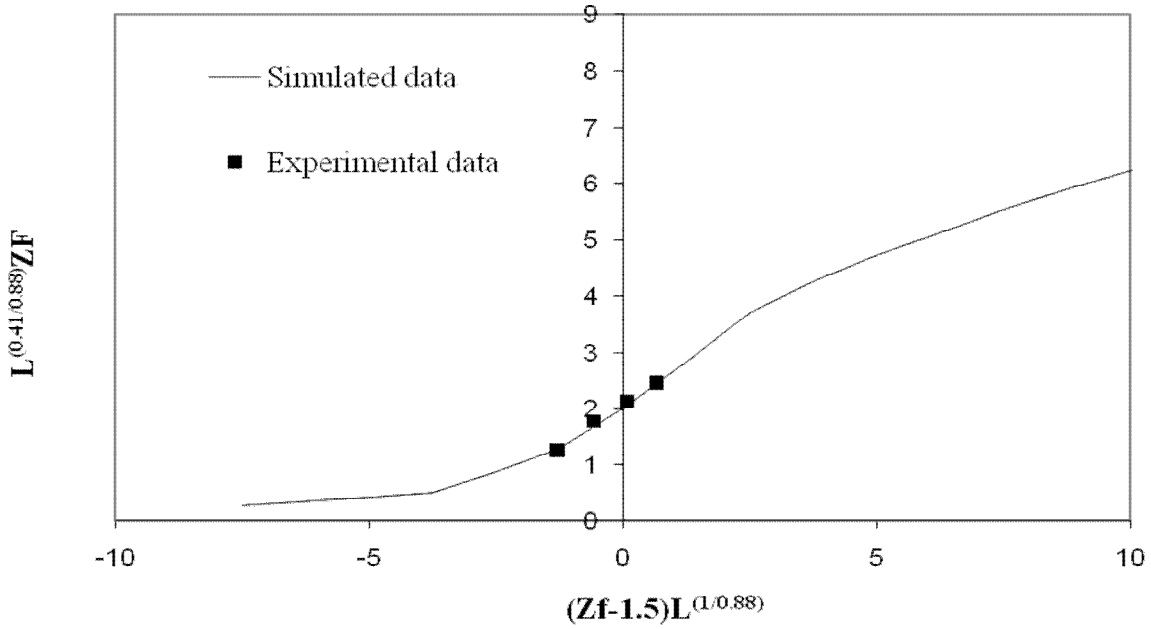

Figure A3-20

Generalised accessibility plot of Q17/6 showing the experiemental and simulated data for $Z = 5$ **and** $L = 3.6$

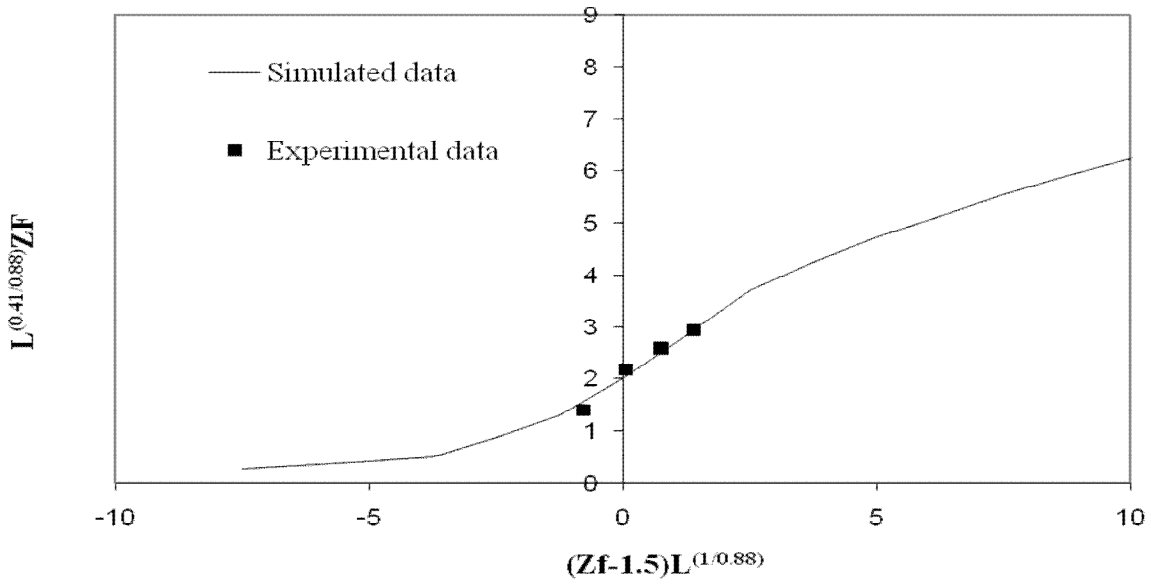

Figure A3-21

Generalised accessibility plot of Q17/6 showing the experiemental and simulated data for $Z = 4.3$ **and** $L = 3.6$

Pore length parameters for the rest of the samples

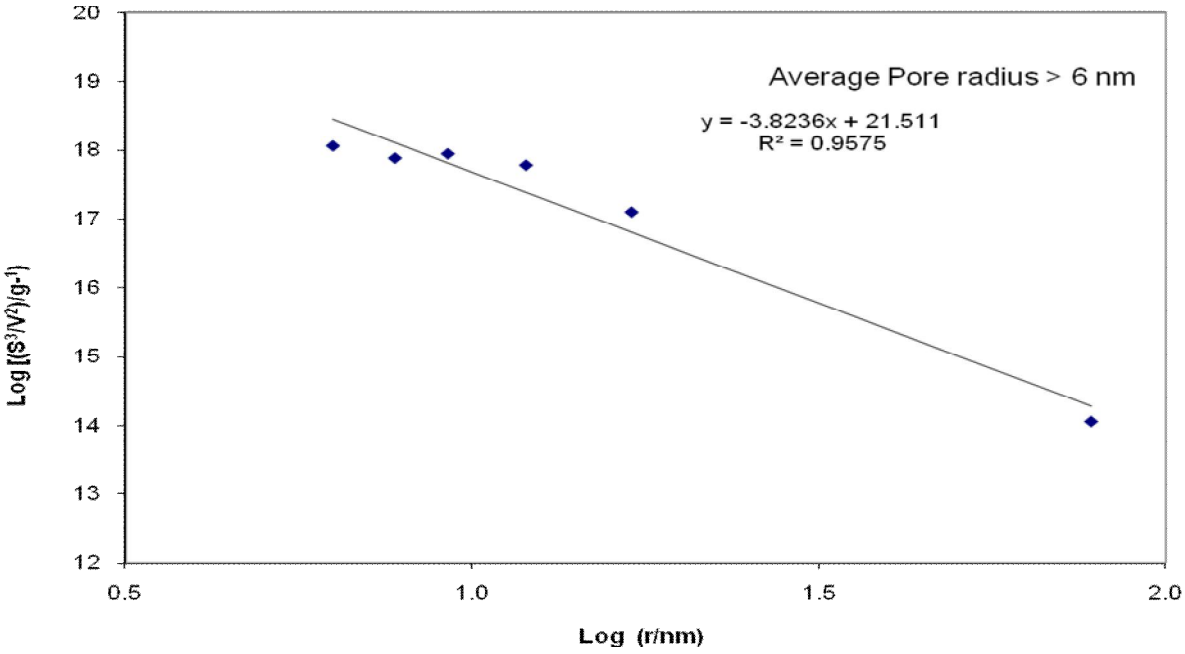

Figure A3-22

Variation of the parameter $\log(\lambda_i)$ **as a function of pore radius** $\log(r_i)$ **for Aerosil**

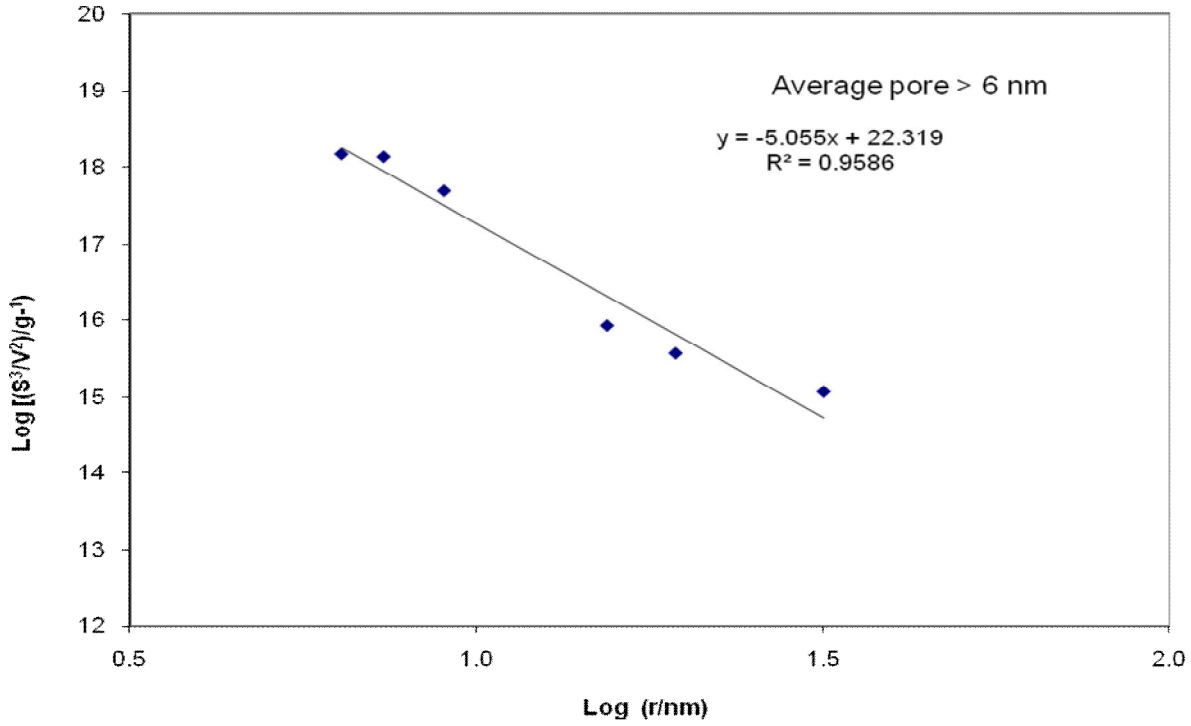

Figure A3-23

Variation of the parameter $\log(\lambda_i)$ as a function of pore radius $\log(r_i)$ for AL3984T

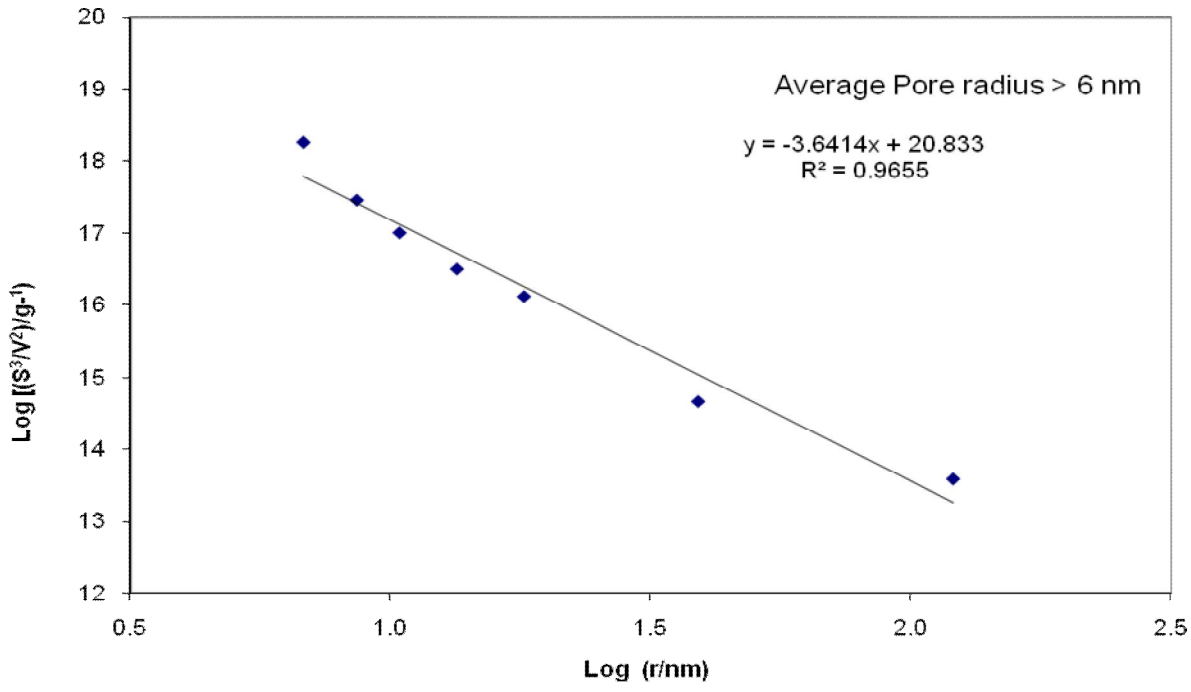

Figure A3-24

Variation of the parameter $\log(\lambda_i)$ as a function of pore radius $\log(r_i)$ for Silica Alumina

Appendix (A5)

(Mercury porosimetry appendix figures)

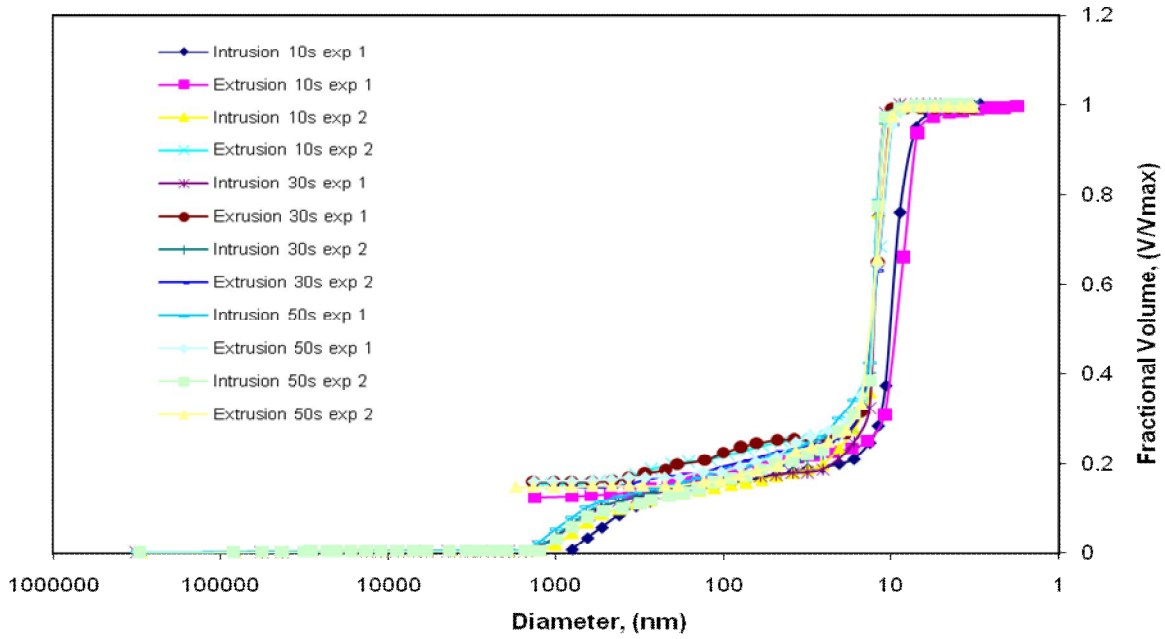

Figure A4-1

Mercury intrusion/extrusion curves for AL3984T by using semi-empirical correlation

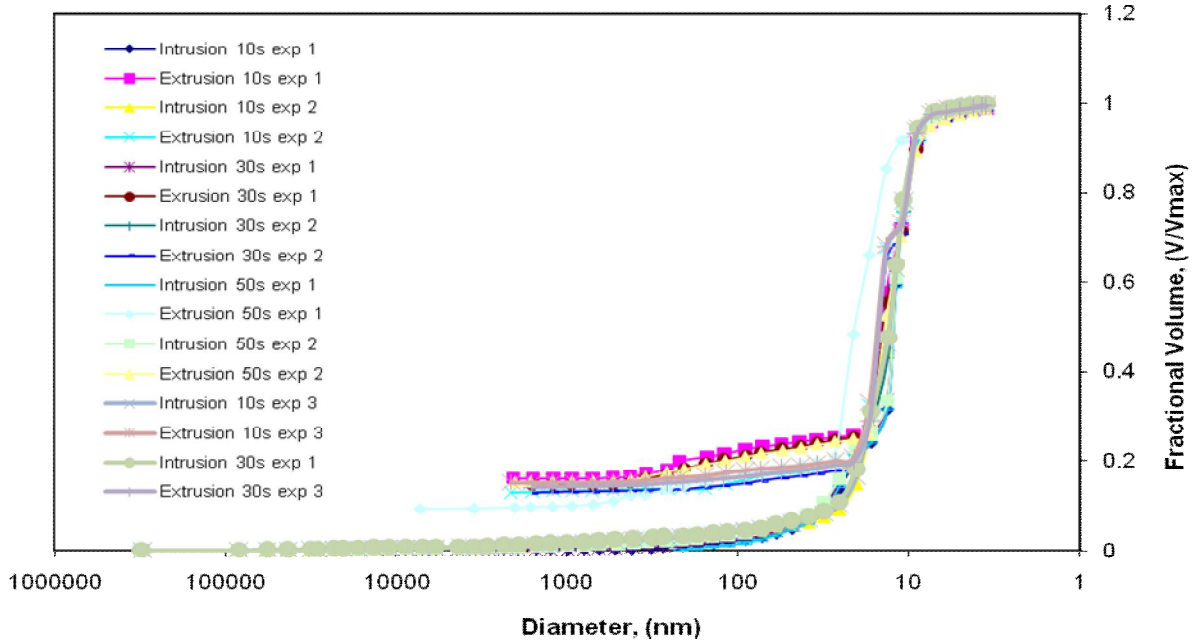

Figure A4-2

Mercury intrusion/extrusion curves for AL3992E by using semi-empirical correlation

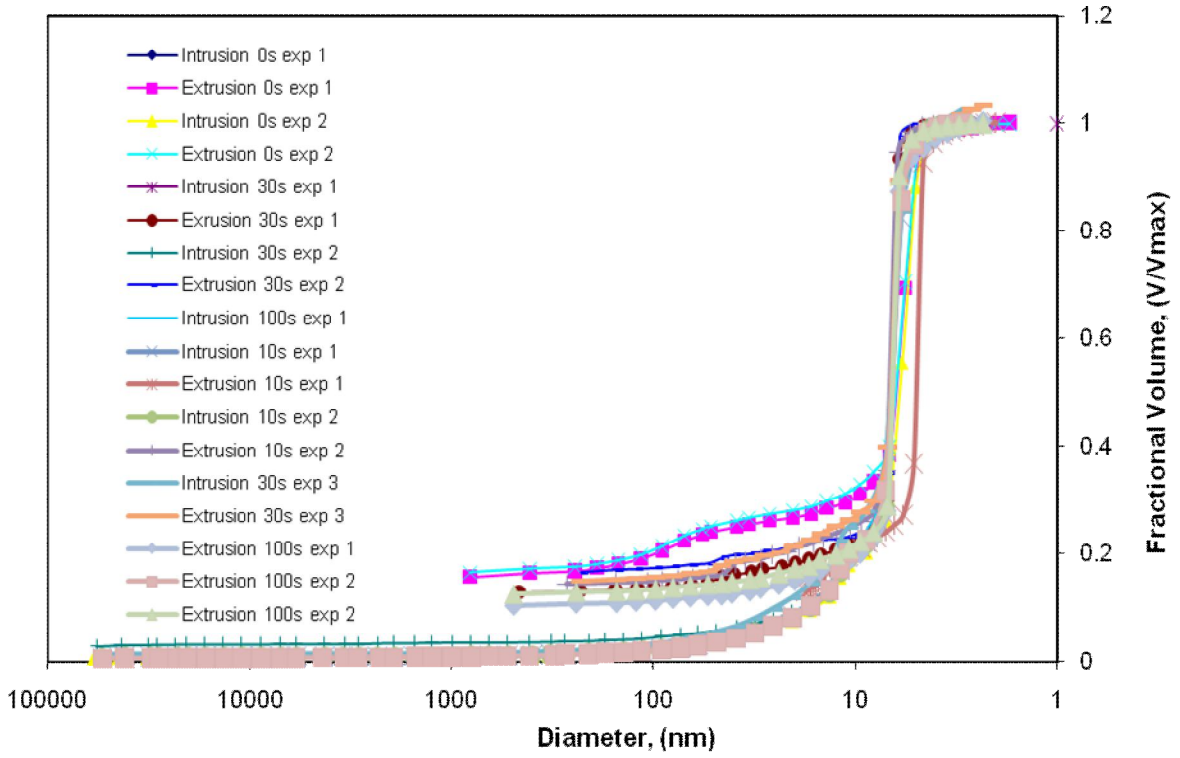

Figure A4-3

Mercury intrusion/extrusion curves for C10 by using semi-empirical correlation

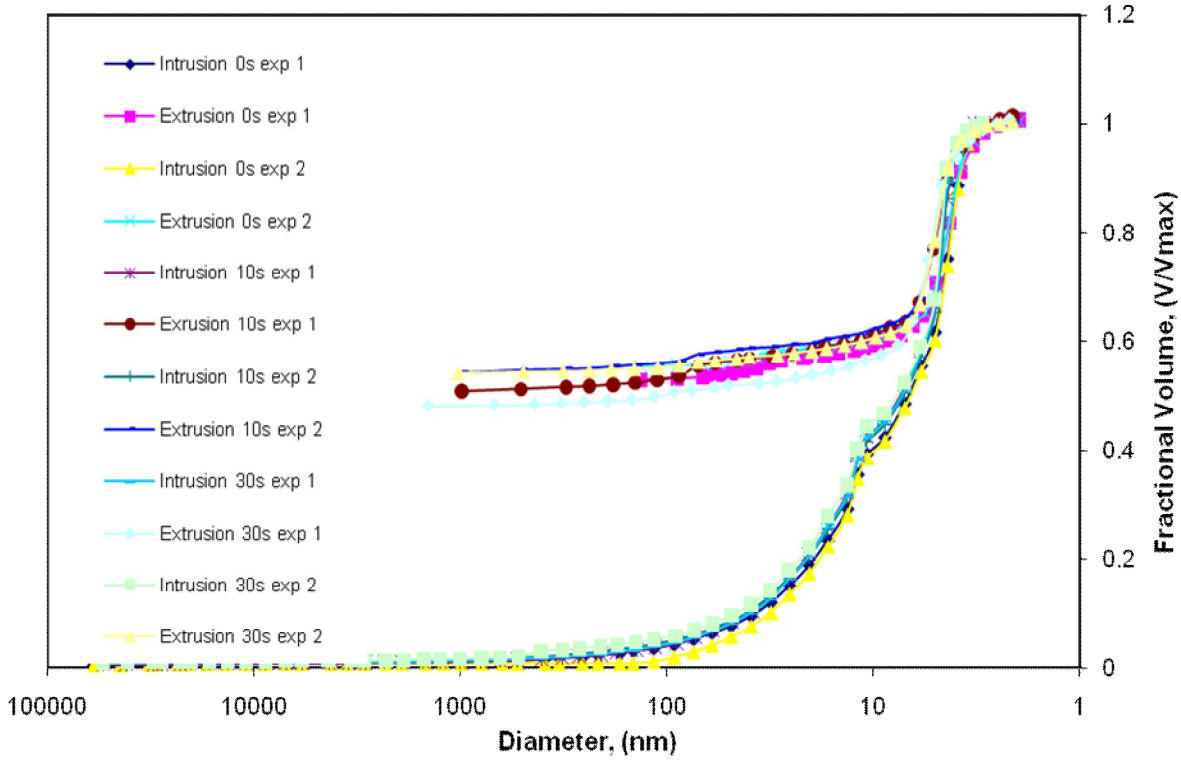

Figure A4-4

Mercury intrusion/extrusion curves for P7129 by using semi-empirical correlation

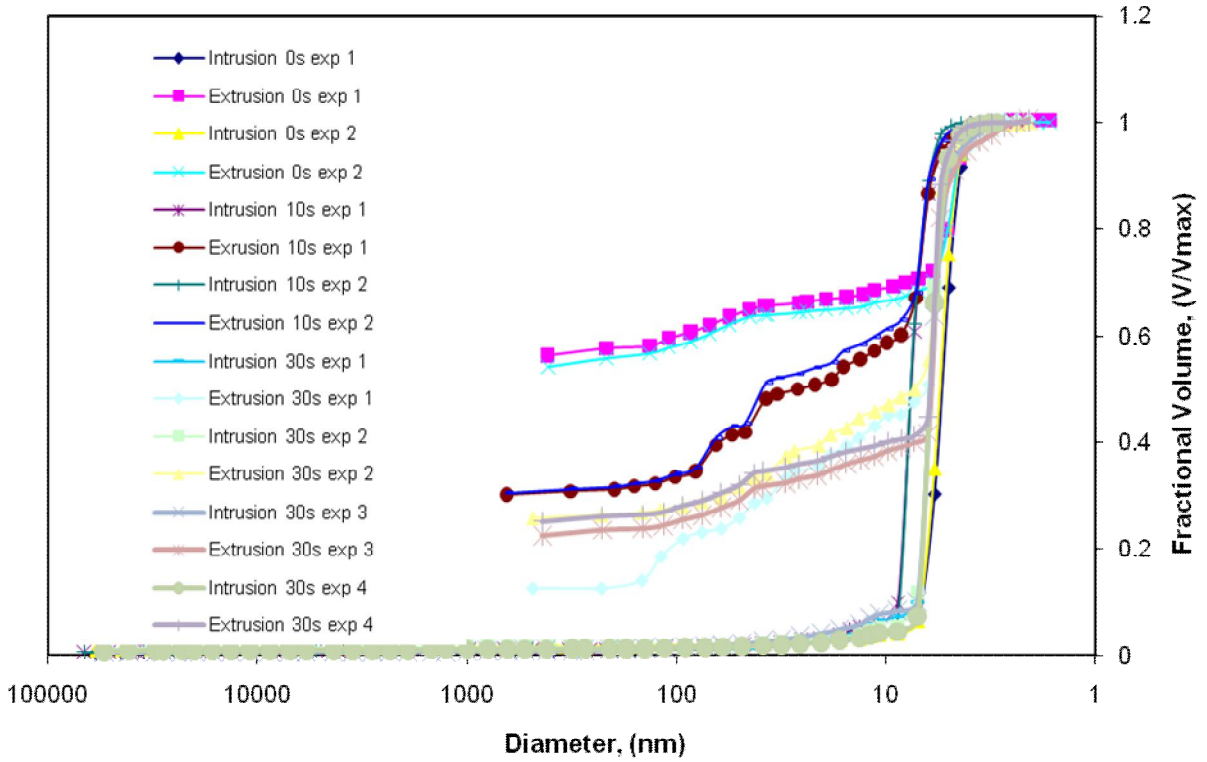

Figure A4-5

Mercury intrusion/extrusion curves for Q17/6 by using semi-empirical correlation

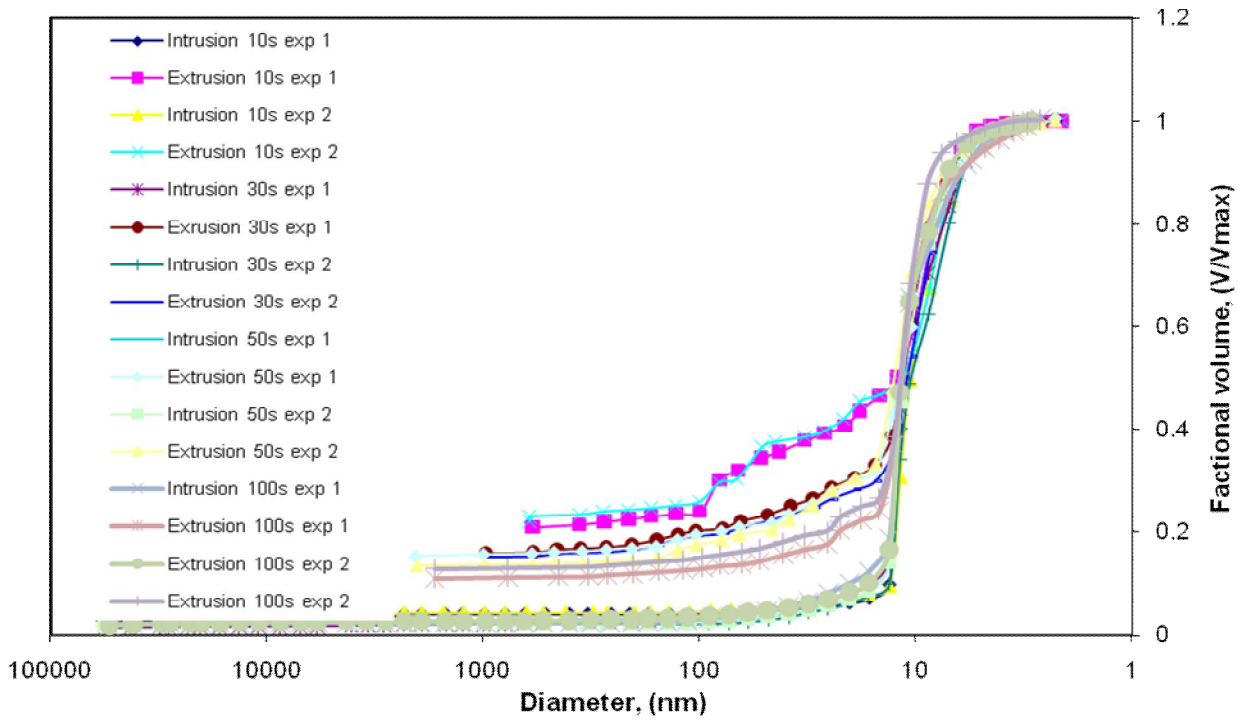

Figure A4-6

Mercury intrusion/extrusion curves for S980A by using semi-empirical correlation

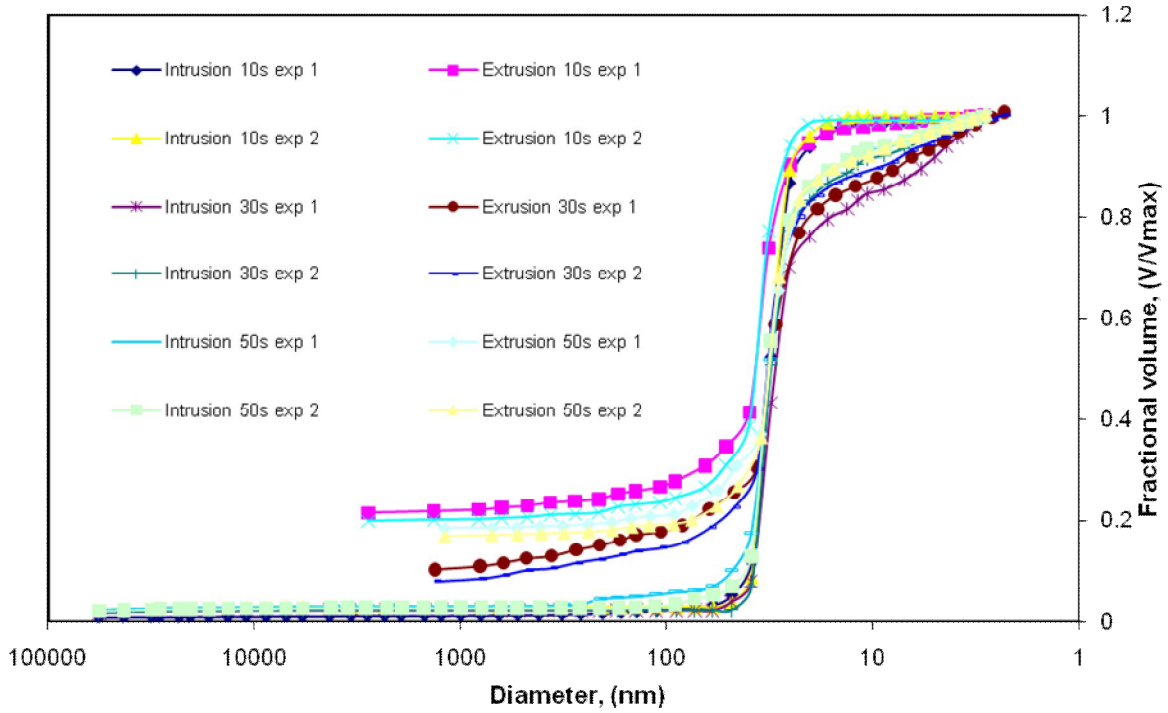

Figure A4-7

Mercury intrusion/extrusion curves for S980G by using semi-empirical correlation

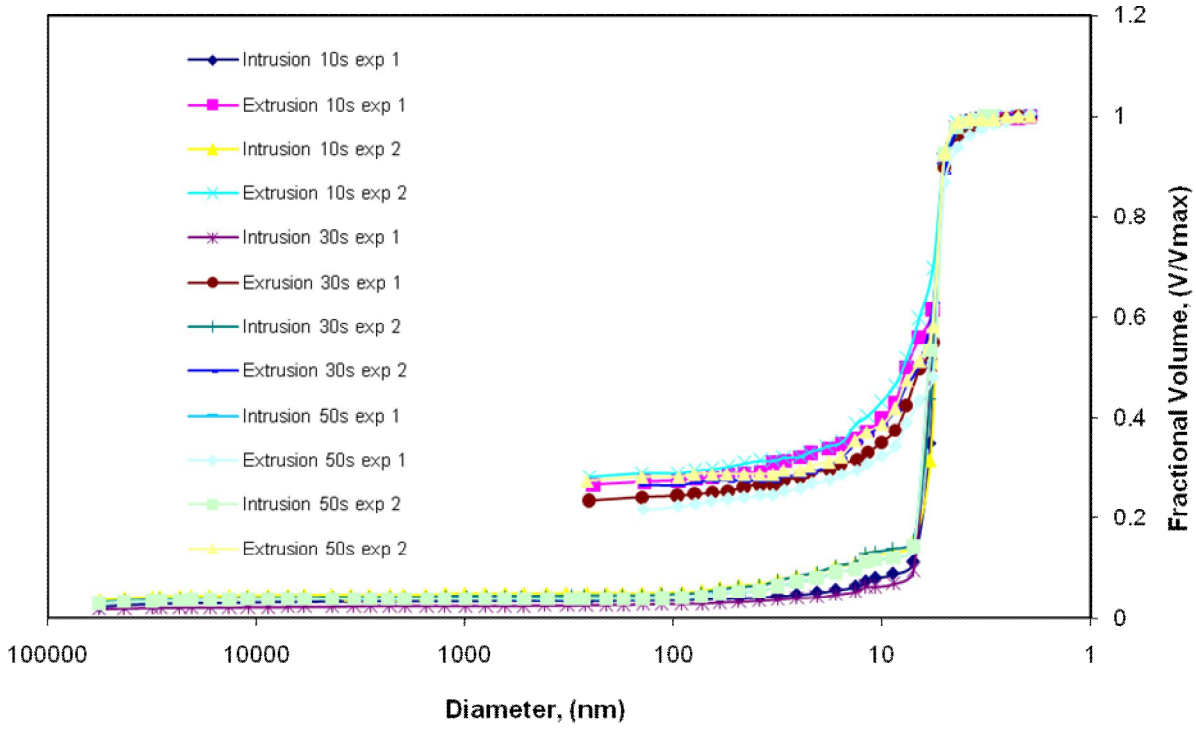

Figure A4-8

Mercury intrusion/extrusion curves for Silica Alumina by using semi-empirical correlation

Appendix (A6)

(NMR pulsed gradient spin echo technique I appendix figures)

Fully saturated samples (Case I)

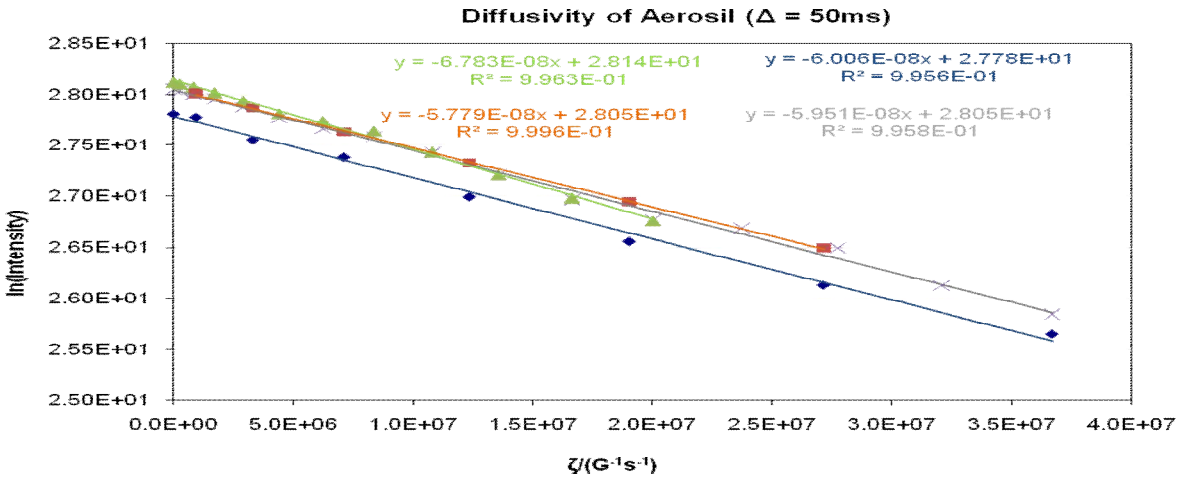

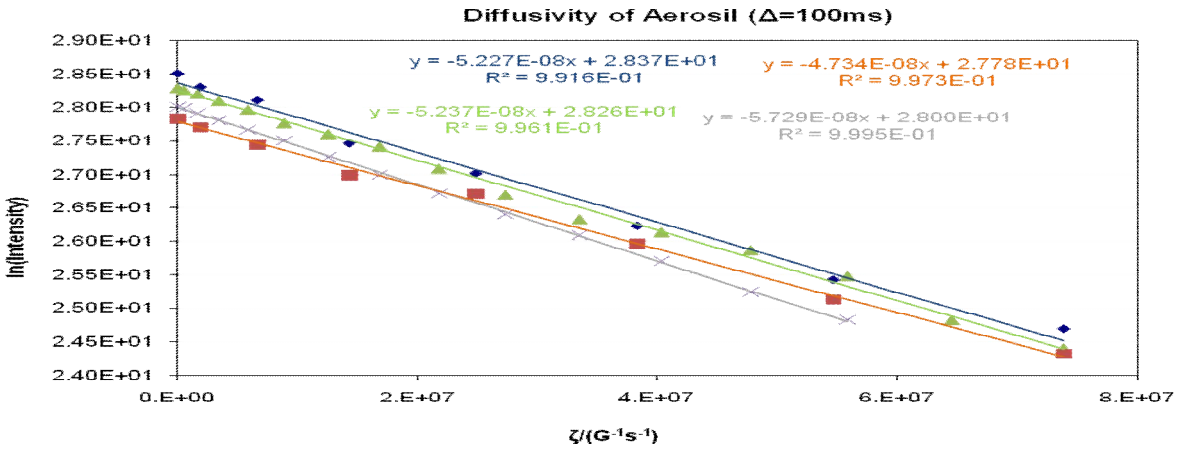

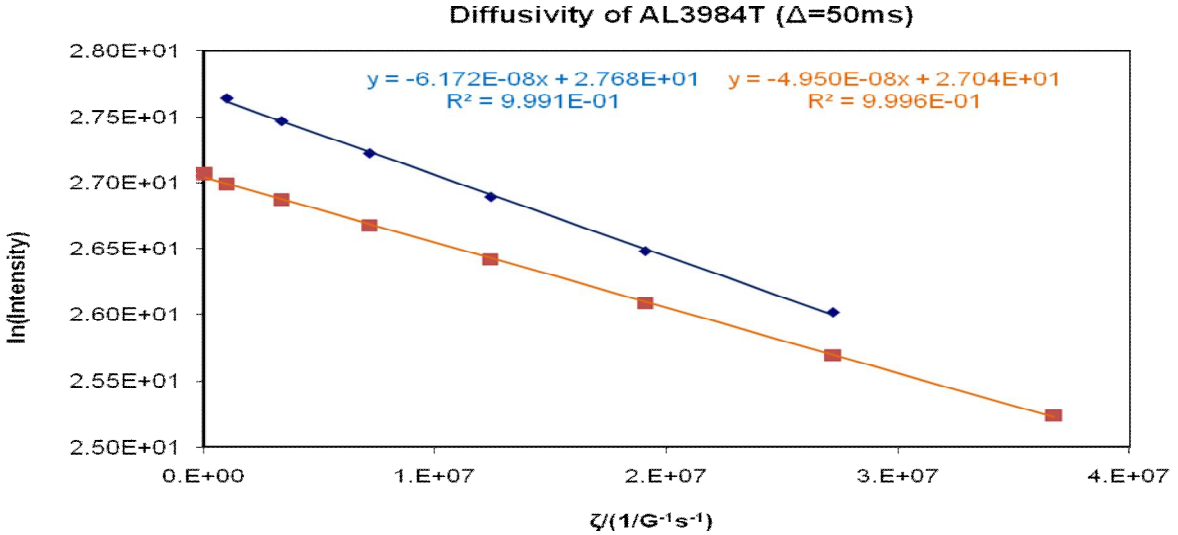

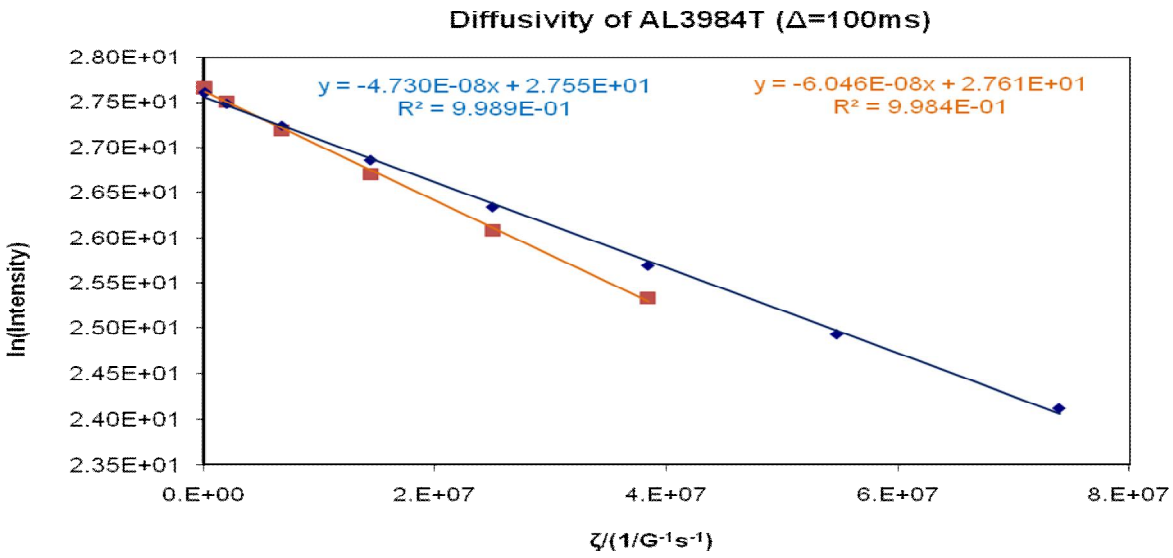
Diffusivity of AL3984T (Δ=100ms)
y = -4.730E-08x + 2.755E+01
R² = 9.989E-01
y = -6.046E-08x + 2.761E+01
R² = 9.984E-01
ln(Intensity)
ζ/(1/G⁻¹s⁻¹)

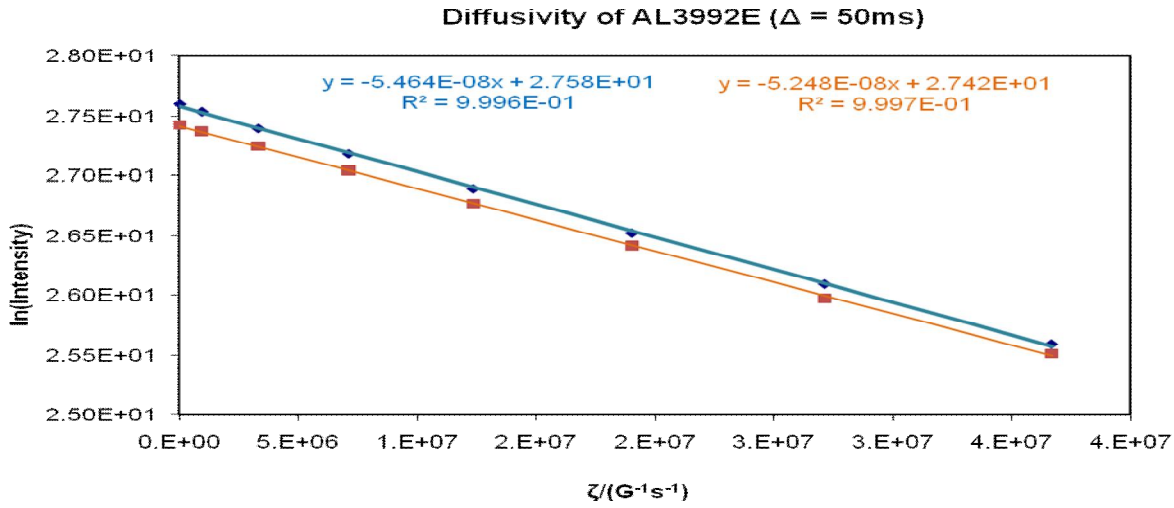
Diffusivity of AL3992E (Δ = 50ms)
y = -5.464E-08x + 2.758E+01
R² = 9.996E-01
y = -5.248E-08x + 2.742E+01
R² = 9.997E-01
ln(Intensity)
ζ/(G⁻¹s⁻¹)

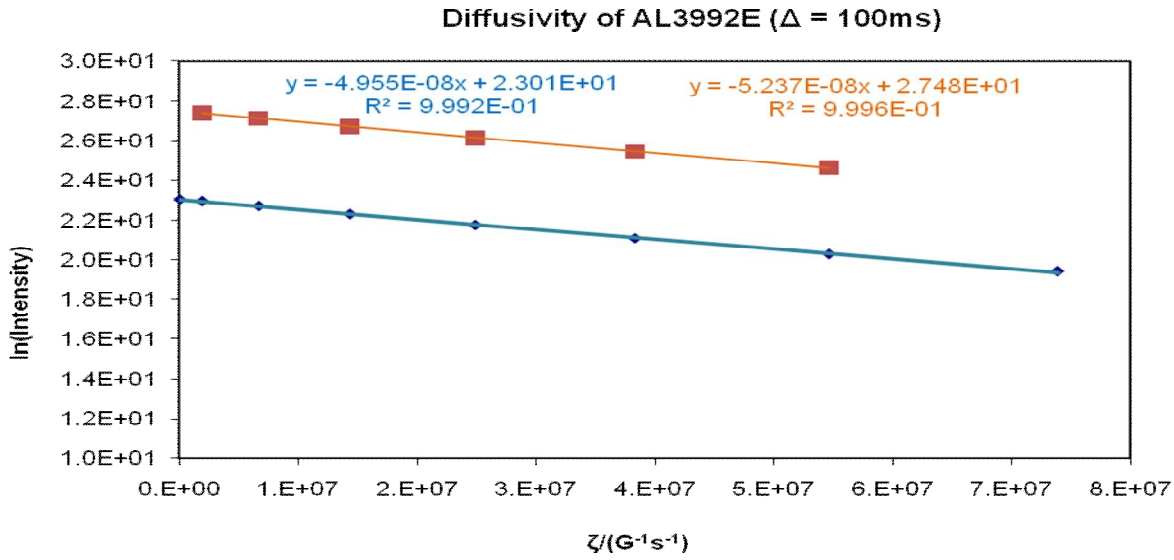
Diffusivity of AL3992E (Δ = 100ms)
y = -4.955E-08x + 2.301E+01
R² = 9.992E-01
y = -5.237E-08x + 2.748E+01
R² = 9.996E-01
ln(Intensity)
ζ/(G⁻¹s⁻¹)

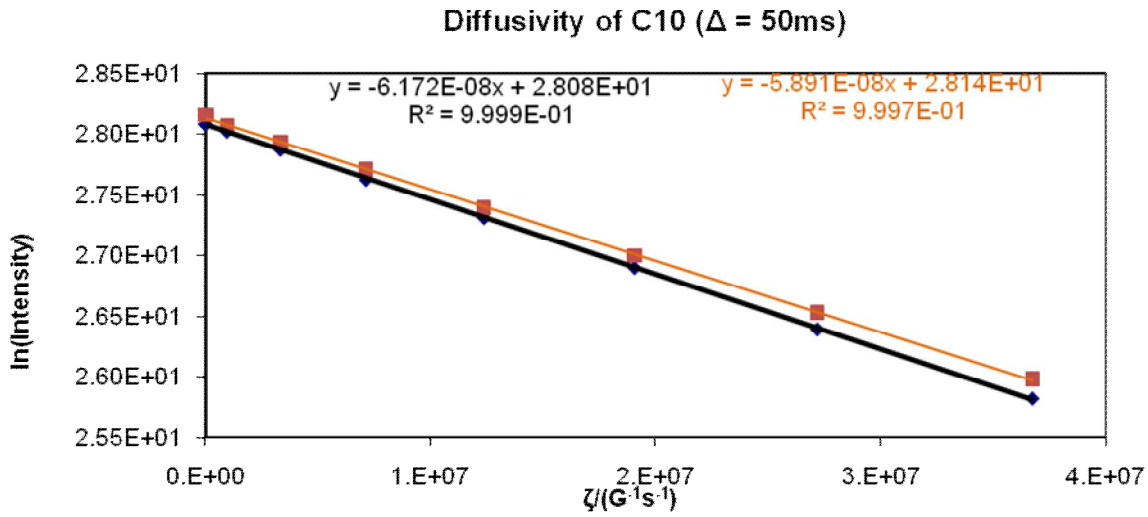
Diffusivity of C10 (Δ = 50ms)
y = -6.172E-08x + 2.808E+01
R² = 9.999E-01
y = -5.891E-08x + 2.814E+01
R² = 9.997E-01
ln(Intensity)
ζ/(G⁻¹s⁻¹)

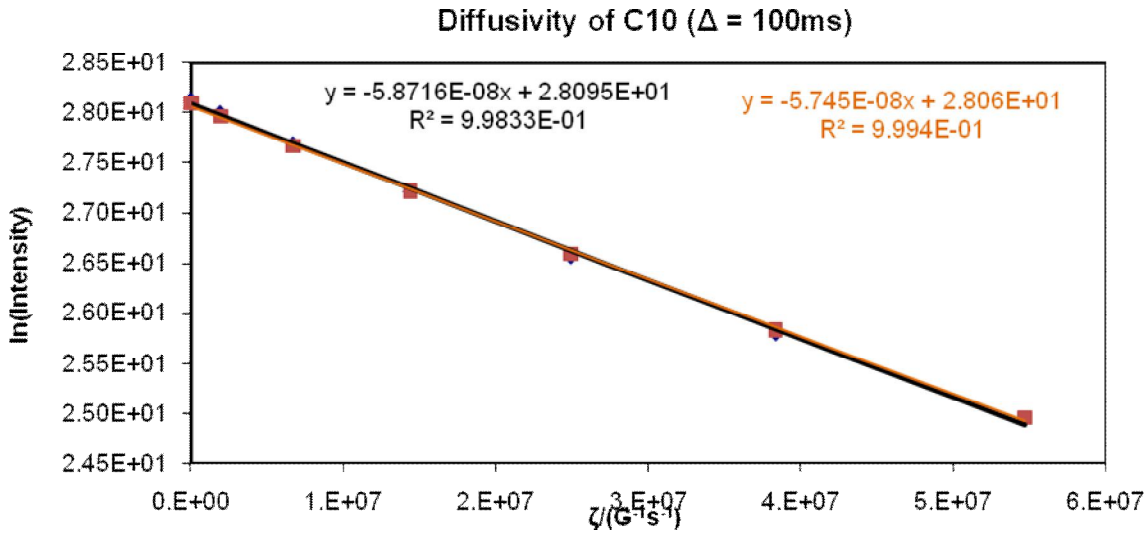
Diffusivity of C10 (Δ = 100ms)
y = -5.8716E-08x + 2.8095E+01
R² = 9.9833E-01
y = -5.745E-08x + 2.806E+01
R² = 9.994E-01
ln(Intensity)
ζ/(G⁻¹s⁻¹)

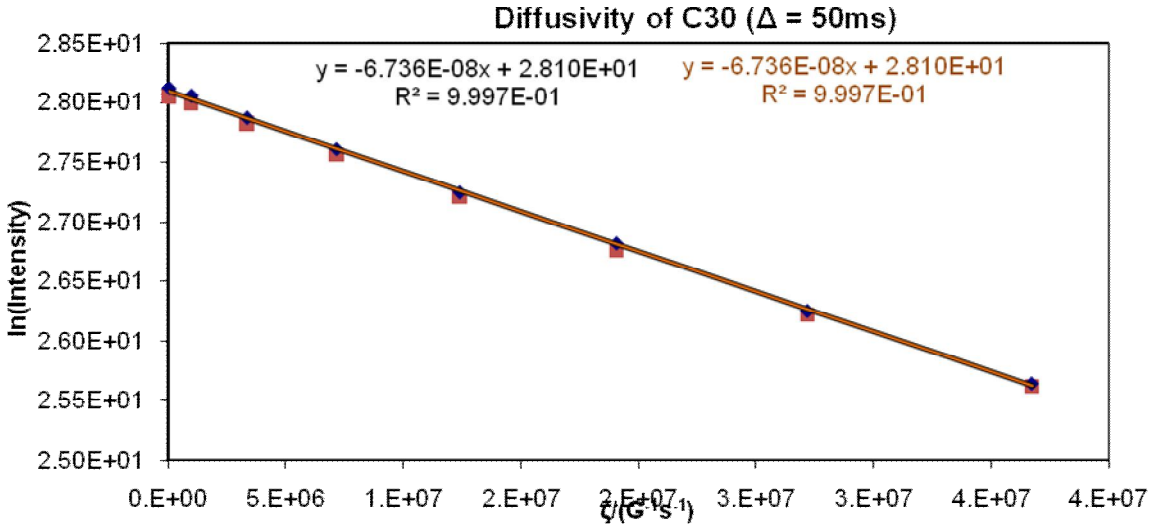
Diffusivity of C30 (Δ = 50ms)
y = -6.736E-08x + 2.810E+01
R² = 9.997E-01
y = -6.736E-08x + 2.810E+01
R² = 9.997E-01
ln(Intensity)
ζ/(G⁻¹s⁻¹)

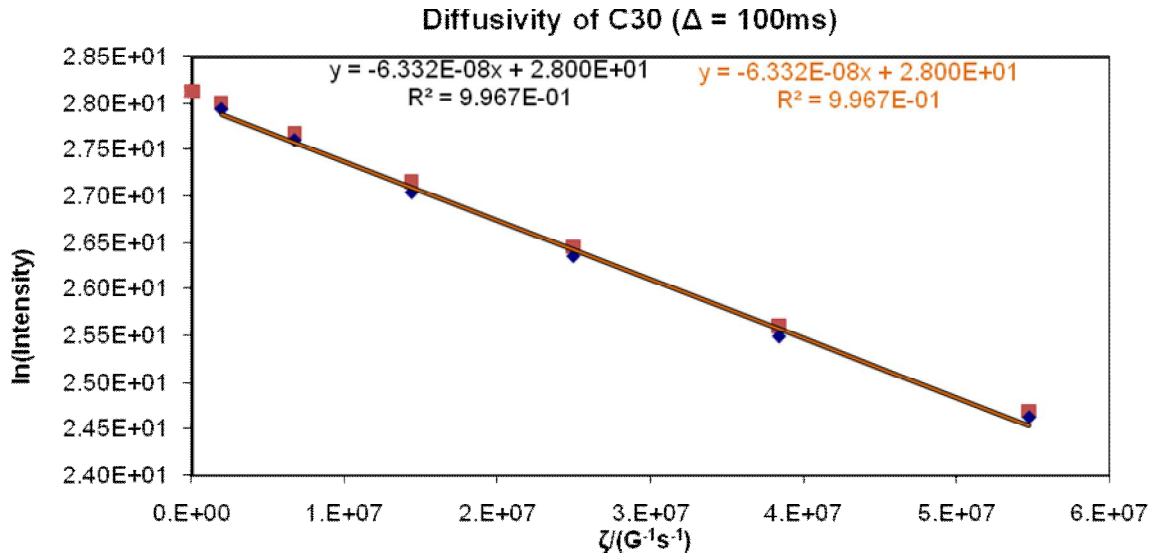
Diffusivity of C30 (Δ = 100ms)
y = -6.332E-08x + 2.800E+01
R² = 9.967E-01
y = -6.332E-08x + 2.800E+01
R² = 9.967E-01
ln(Intensity)
ζ/(G⁻¹s⁻¹)

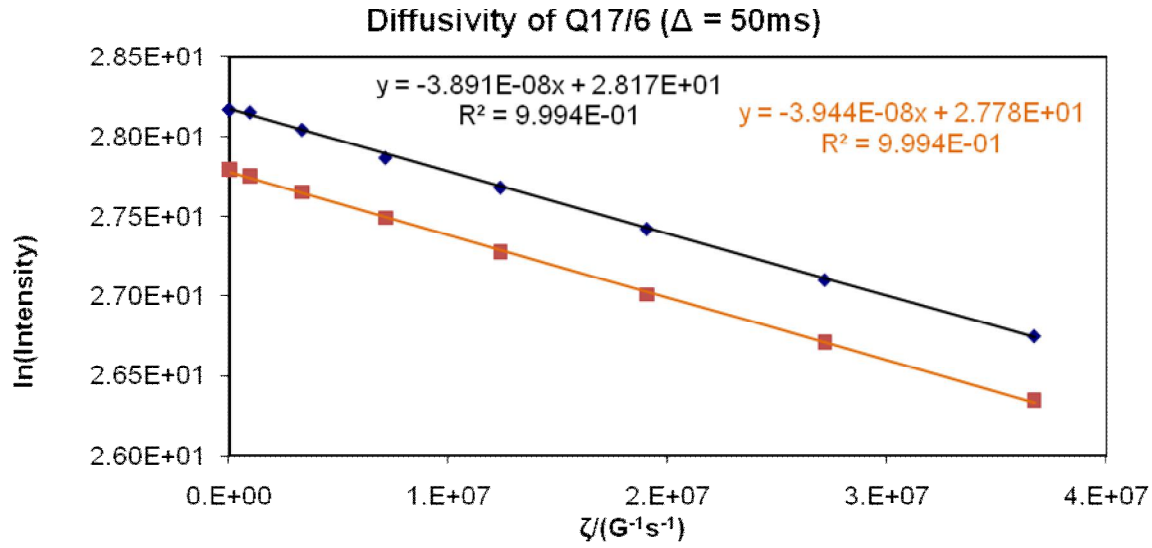
Diffusivity of Q17/6 (Δ = 50ms)
y = -3.891E-08x + 2.817E+01
R² = 9.994E-01
y = -3.944E-08x + 2.778E+01
R² = 9.994E-01
ln(Intensity)
ζ/(G⁻¹s⁻¹)

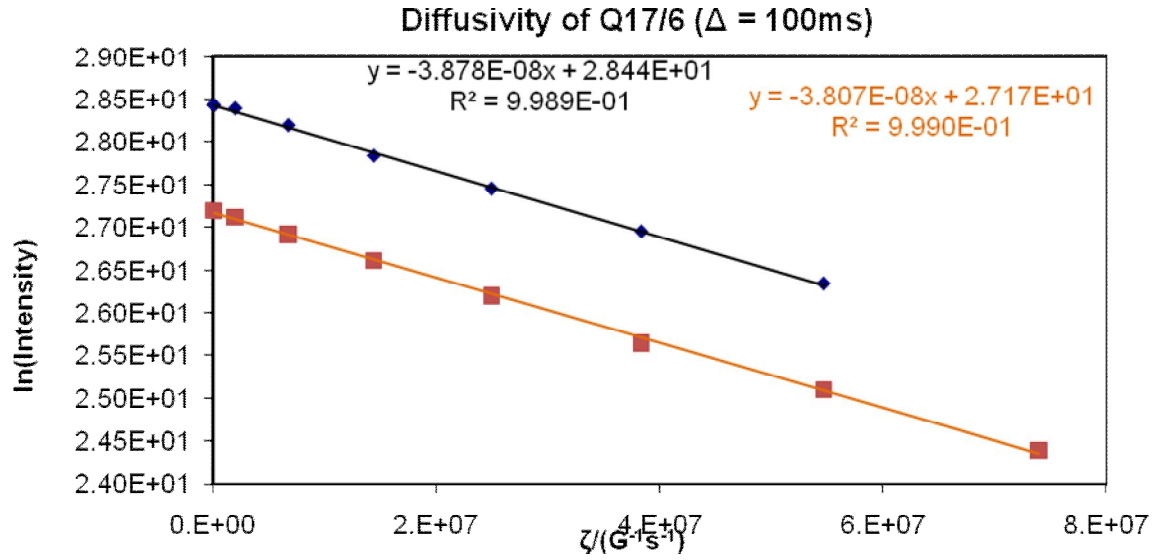
Diffusivity of Q17/6 (Δ = 100ms)
y = -3.878E-08x + 2.844E+01
R² = 9.989E-01
y = -3.807E-08x + 2.717E+01
R² = 9.990E-01
ln(Intensity)
ζ/(G⁻¹s⁻¹)

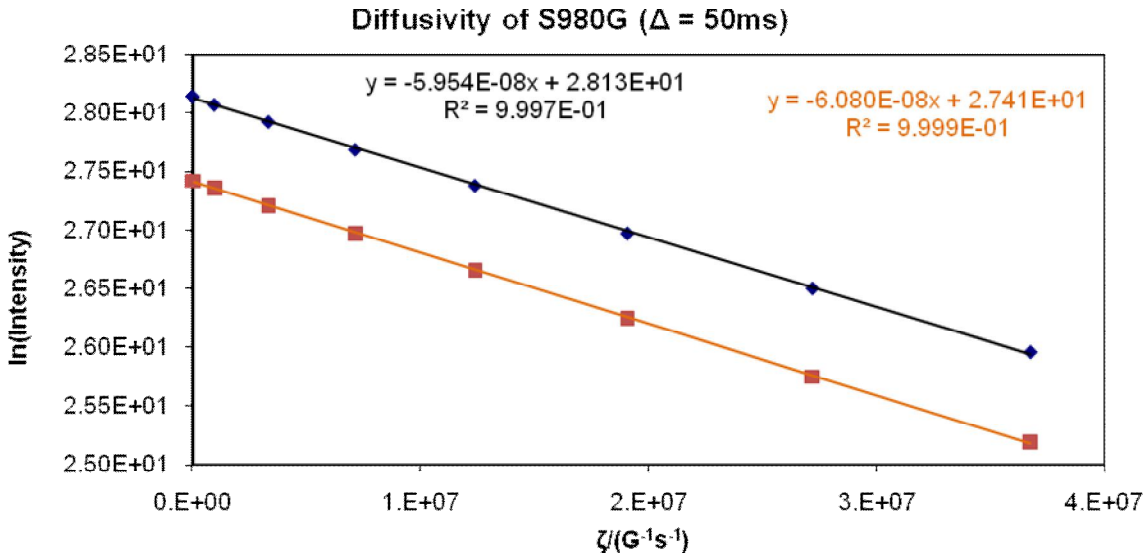
Diffusivity of S980G (Δ = 50ms)
y = -5.954E-08x + 2.813E+01
R² = 9.997E-01
y = -6.080E-08x + 2.741E+01
R² = 9.999E-01
ln(Intensity)
2.85E+01
2.80E+01
2.75E+01
2.70E+01
2.65E+01
2.60E+01
2.55E+01
2.50E+01
0.E+00
1.E+07
2.E+07
3.E+07
4.E+07
ζ/(G⁻¹s⁻¹)

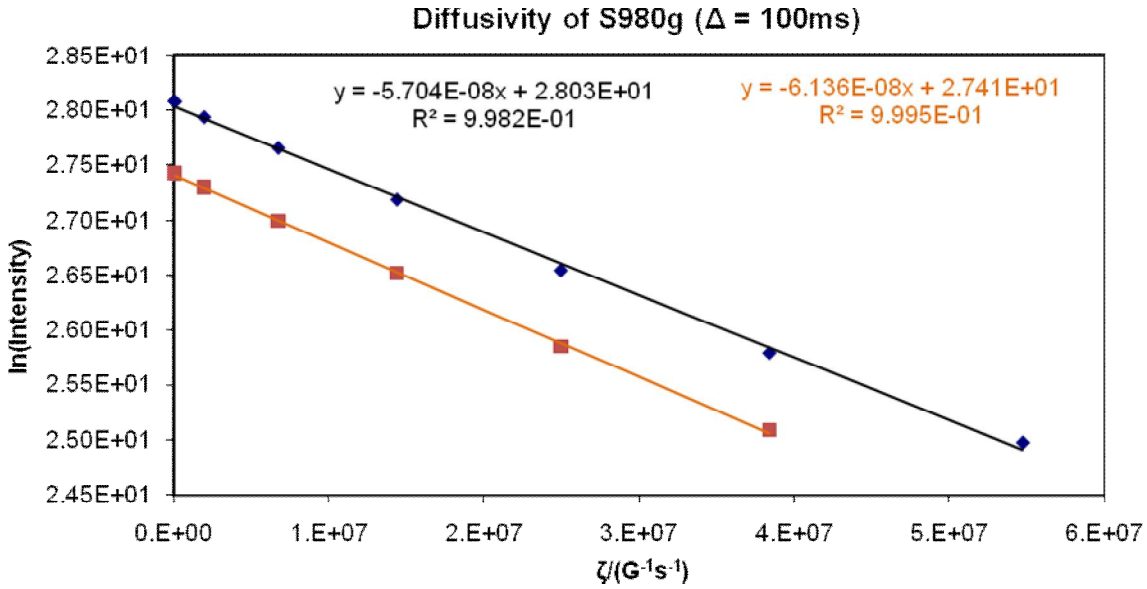
Diffusivity of S980g (Δ = 100ms)
y = -5.704E-08x + 2.803E+01
R² = 9.982E-01
y = -6.136E-08x + 2.741E+01
R² = 9.995E-01
ln(Intensity)
2.85E+01
2.80E+01
2.75E+01
2.70E+01
2.65E+01
2.60E+01
2.55E+01
2.50E+01
2.45E+01
0.E+00
1.E+07
2.E+07
3.E+07
4.E+07
5.E+07
6.E+07
ζ/(G⁻¹s⁻¹)

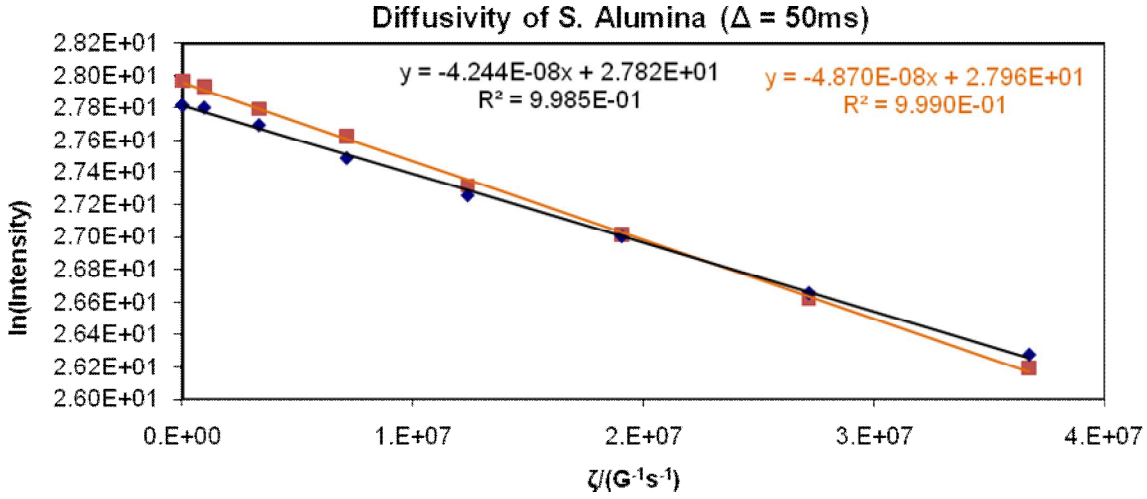
Diffusivity of S. Alumina (Δ = 50ms)
y = -4.244E-08x + 2.782E+01
R² = 9.985E-01
y = -4.870E-08x + 2.796E+01
R² = 9.990E-01
ln(Intensity)
2.82E+01
2.80E+01
2.78E+01
2.76E+01
2.74E+01
2.72E+01
2.70E+01
2.68E+01
2.66E+01
2.64E+01
2.62E+01
2.60E+01
0.E+00
1.E+07
2.E+07
3.E+07
4.E+07
ζ/(G⁻¹s⁻¹)

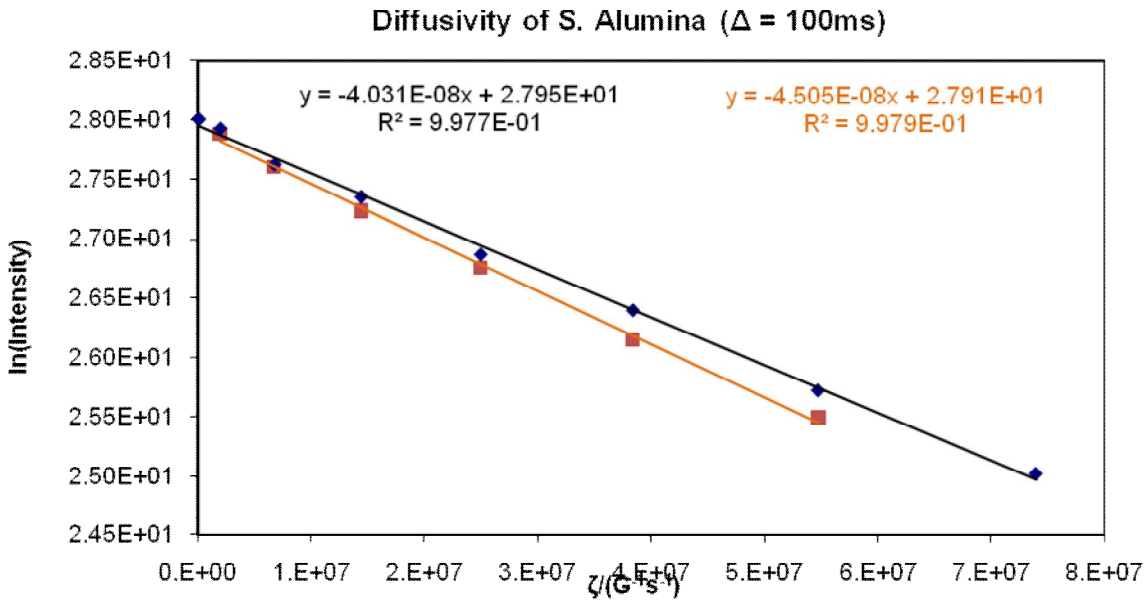

Fully saturated samples with deionised water reservoir (Case II)

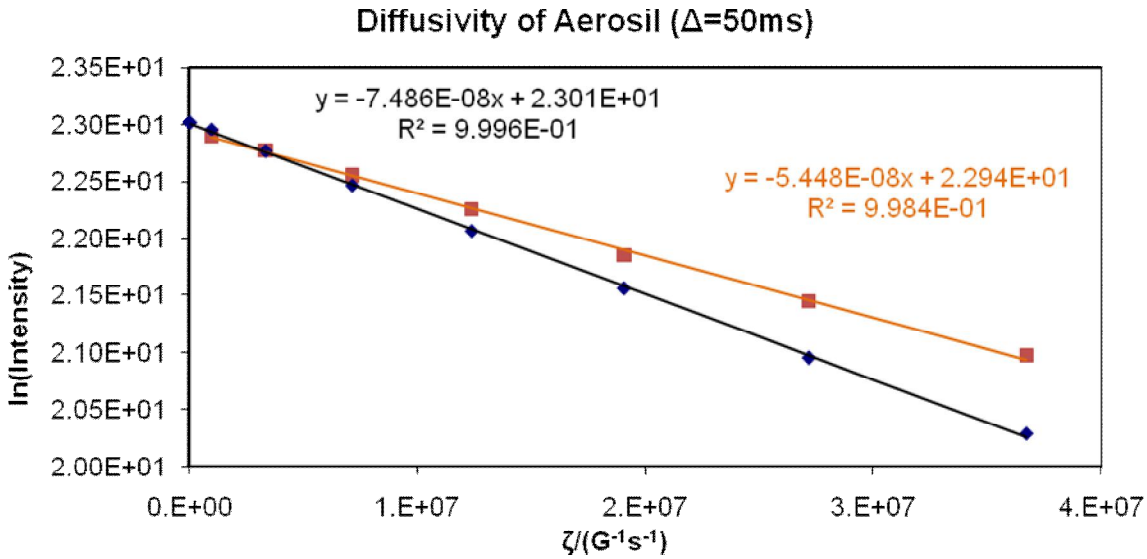

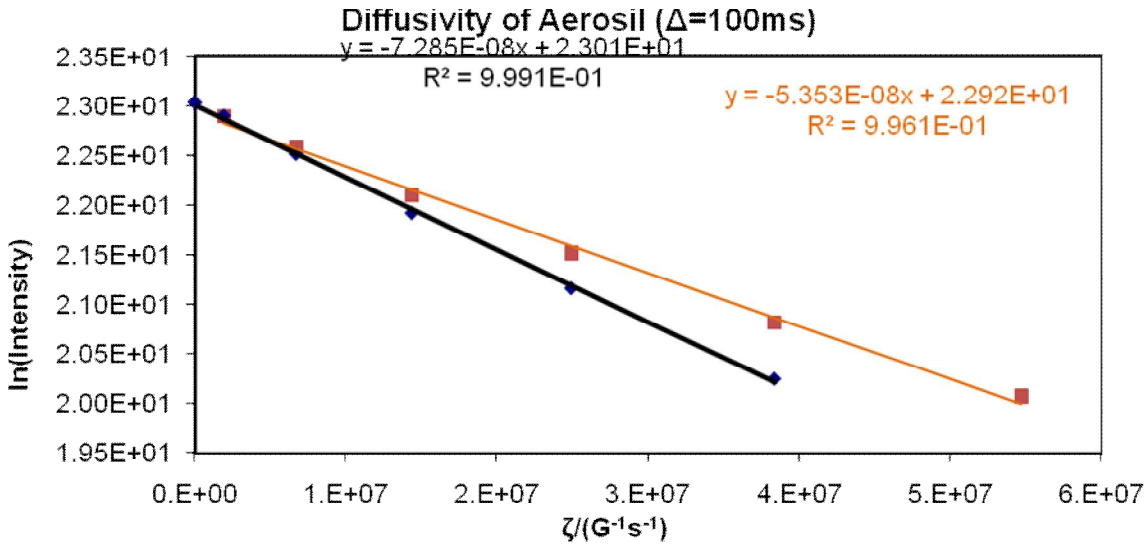
Diffusivity of Aerosil (Δ=100ms)
y = -7.285E-08x + 2.301E+01
R² = 9.991E-01
y = -5.353E-08x + 2.292E+01
R² = 9.961E-01
ln(Intensity)
2.35E+01
2.30E+01
2.25E+01
2.20E+01
2.15E+01
2.10E+01
2.05E+01
2.00E+01
1.95E+01
0.E+00
1.E+07
2.E+07
3.E+07
4.E+07
5.E+07
6.E+07
ζ/(G⁻¹s⁻¹)

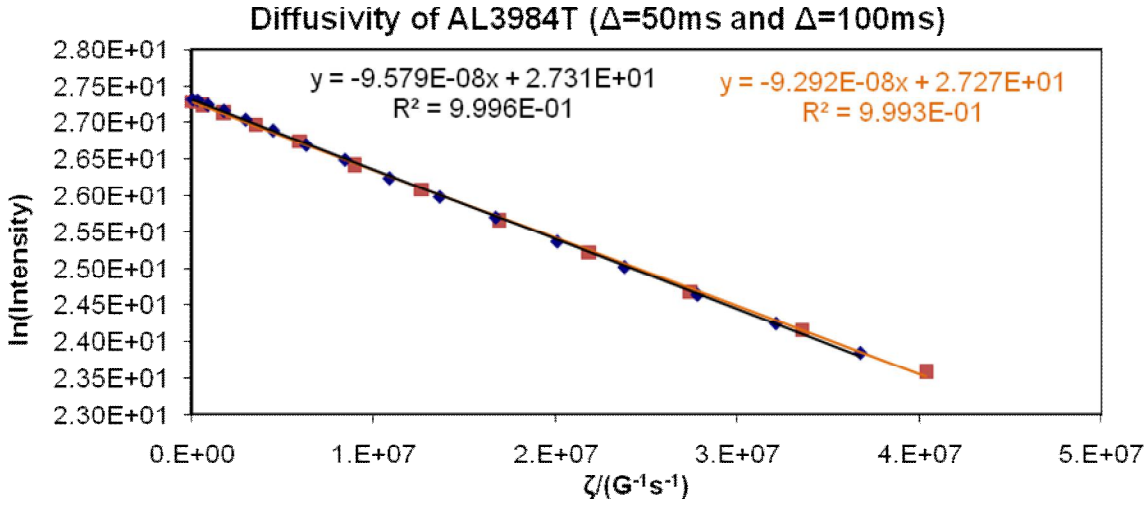
Diffusivity of AL3984T (Δ=50ms and Δ=100ms)
y = -9.579E-08x + 2.731E+01
R² = 9.996E-01
y = -9.292E-08x + 2.727E+01
R² = 9.993E-01
ln(Intensity)
2.80E+01
2.75E+01
2.70E+01
2.65E+01
2.60E+01
2.55E+01
2.50E+01
2.45E+01
2.40E+01
2.35E+01
2.30E+01
0.E+00
1.E+07
2.E+07
3.E+07
4.E+07
5.E+07
ζ/(G⁻¹s⁻¹)

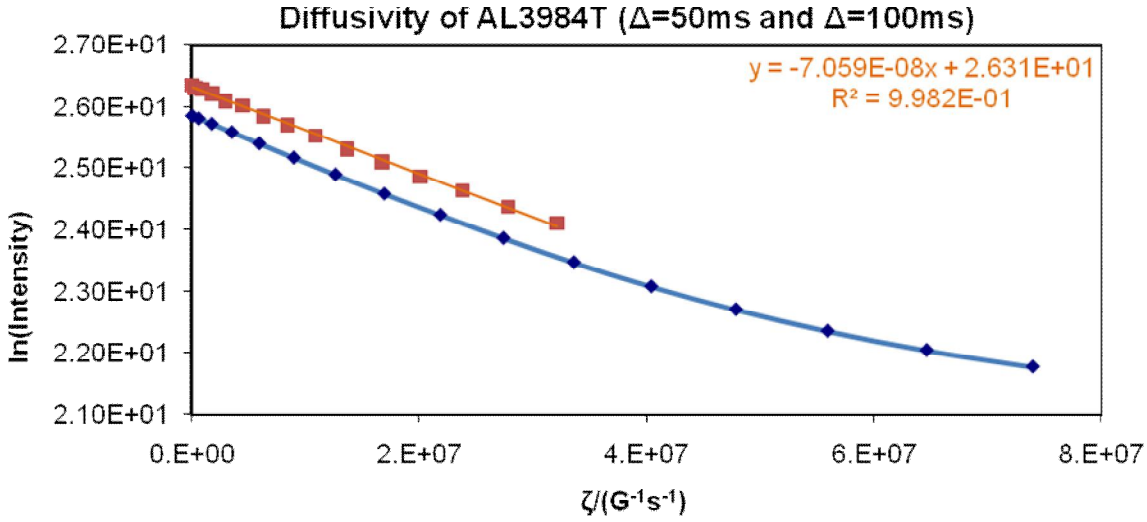
Diffusivity of AL3984T (Δ=50ms and Δ=100ms)
y = -7.059E-08x + 2.631E+01
R² = 9.982E-01
ln(Intensity)
2.70E+01
2.60E+01
2.50E+01
2.40E+01
2.30E+01
2.20E+01
2.10E+01
0.E+00
2.E+07
4.E+07
6.E+07
8.E+07
ζ/(G⁻¹s⁻¹)

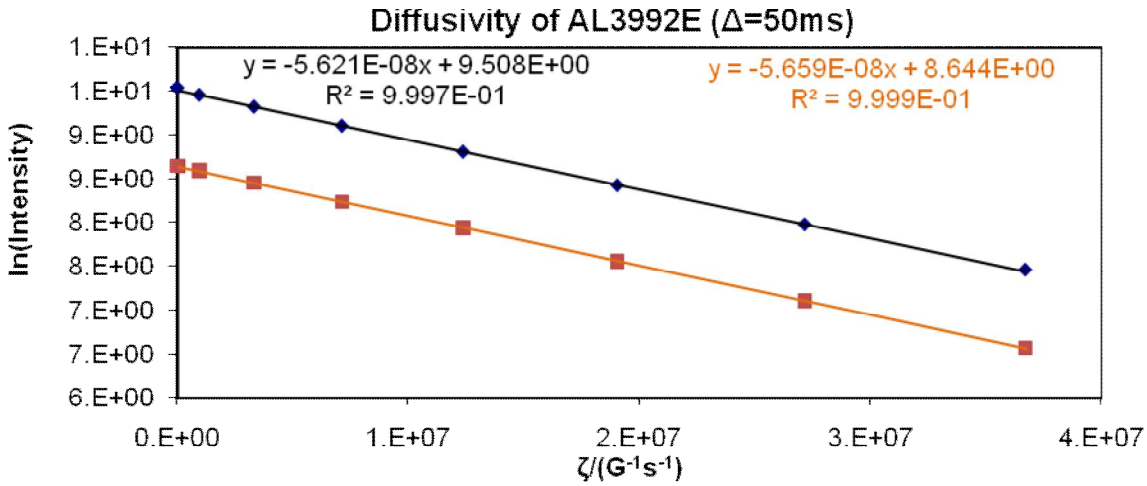
Diffusivity of AL3992E (Δ=50ms)
y = -5.621E-08x + 9.508E+00
R² = 9.997E-01
y = -5.659E-08x + 8.644E+00
R² = 9.999E-01
ln(Intensity)
ζ/(G⁻¹s⁻¹)

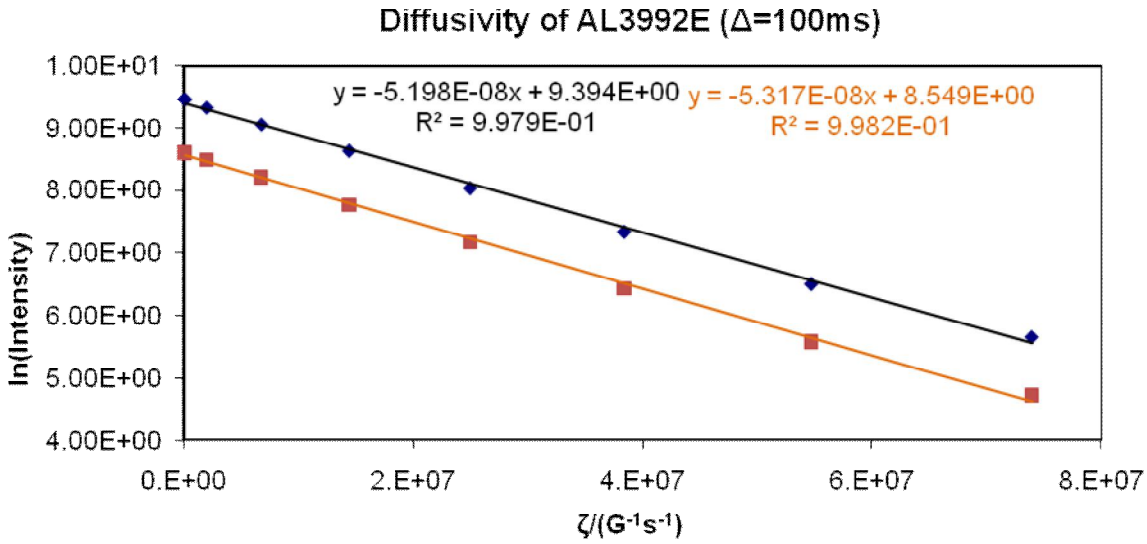
Diffusivity of AL3992E (Δ=100ms)
y = -5.198E-08x + 9.394E+00
R² = 9.979E-01
y = -5.317E-08x + 8.549E+00
R² = 9.982E-01
ln(Intensity)
ζ/(G⁻¹s⁻¹)

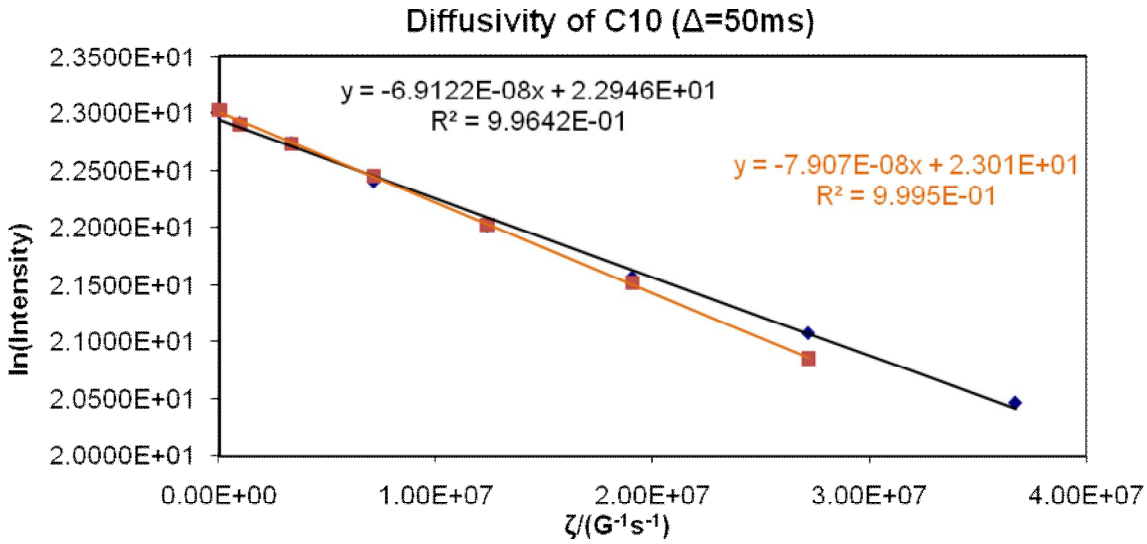
Diffusivity of C10 (Δ=50ms)
y = -6.9122E-08x + 2.2946E+01
R² = 9.9642E-01
y = -7.907E-08x + 2.301E+01
R² = 9.995E-01
ln(Intensity)
ζ/(G⁻¹s⁻¹)

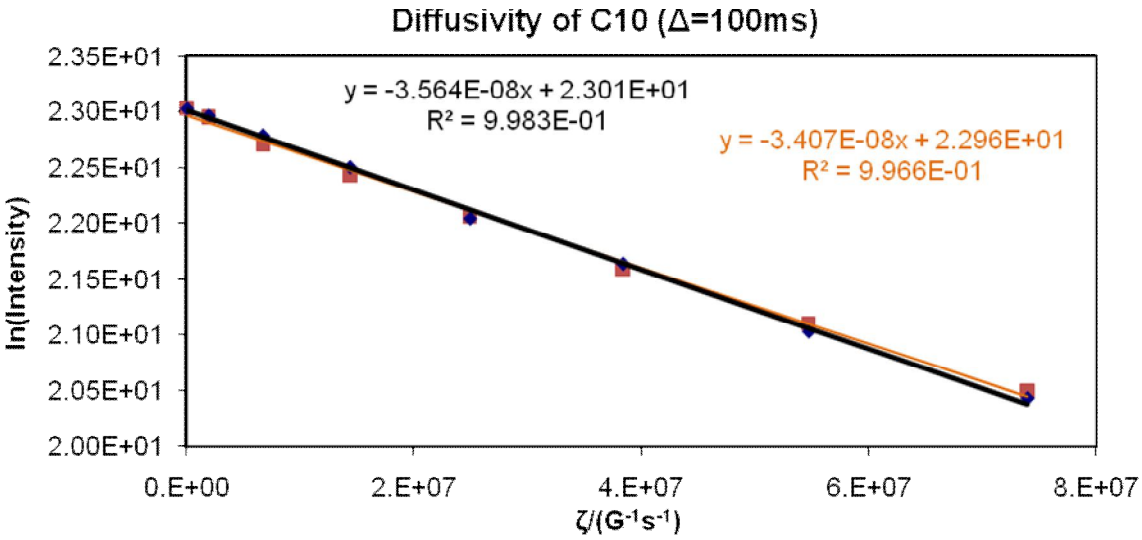
Diffusivity of C10 (Δ=100ms)
y = -3.564E-08x + 2.301E+01
R² = 9.983E-01
y = -3.407E-08x + 2.296E+01
R² = 9.966E-01
ln(Intensity)
2.35E+01
2.30E+01
2.25E+01
2.20E+01
2.15E+01
2.10E+01
2.05E+01
2.00E+01
0.E+00
2.E+07
4.E+07
6.E+07
8.E+07
ζ/(G⁻¹s⁻¹)

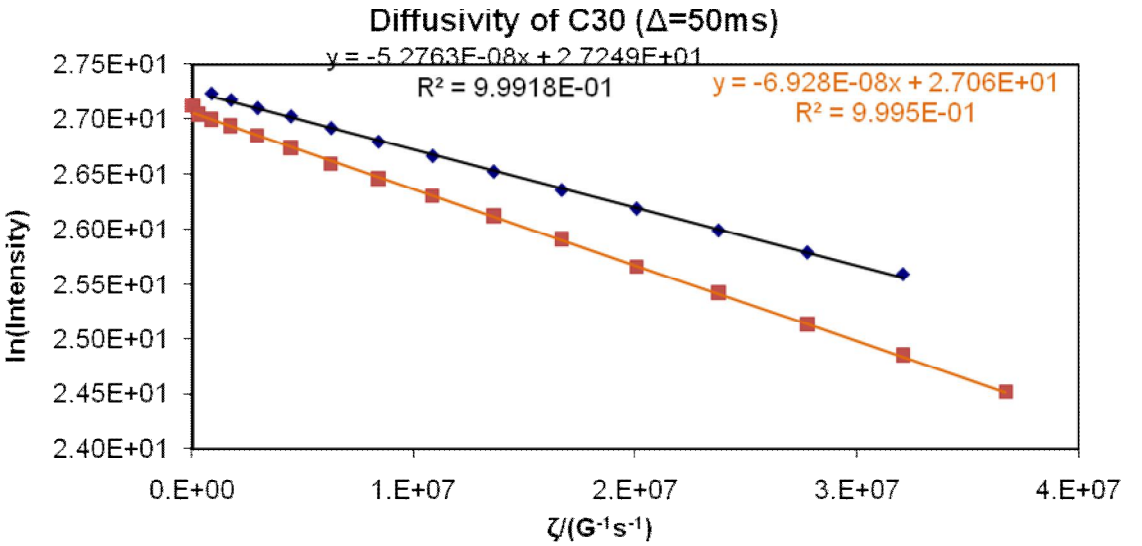
Diffusivity of C30 (Δ=50ms)
y = -5.2763E-08x + 2.7249E+01
R² = 9.9918E-01
y = -6.928E-08x + 2.706E+01
R² = 9.995E-01
ln(Intensity)
2.75E+01
2.70E+01
2.65E+01
2.60E+01
2.55E+01
2.50E+01
2.45E+01
2.40E+01
0.E+00
1.E+07
2.E+07
3.E+07
4.E+07
ζ/(G⁻¹s⁻¹)

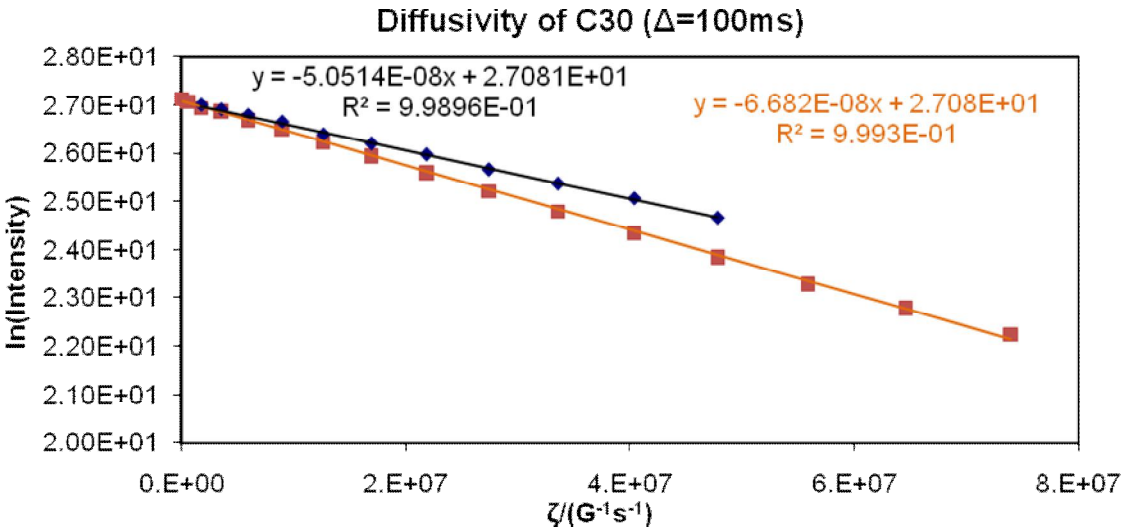
Diffusivity of C30 (Δ=100ms)
y = -5.0514E-08x + 2.7081E+01
R² = 9.9896E-01
y = -6.682E-08x + 2.708E+01
R² = 9.993E-01
ln(Intensity)
2.80E+01
2.70E+01
2.60E+01
2.50E+01
2.40E+01
2.30E+01
2.20E+01
2.10E+01
2.00E+01
0.E+00
2.E+07
4.E+07
6.E+07
8.E+07
ζ/(G⁻¹s⁻¹)

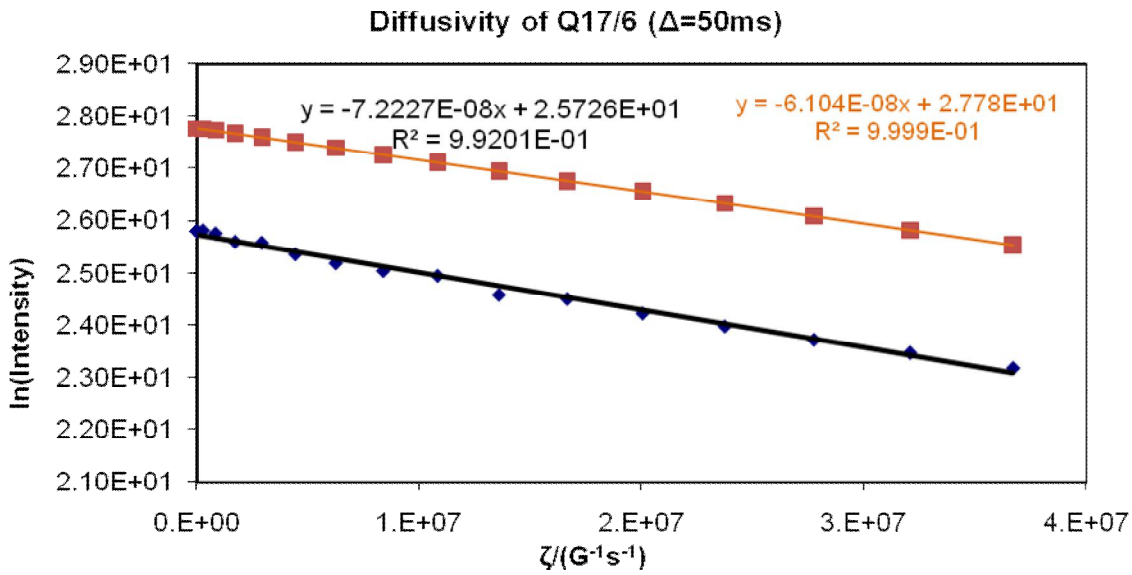
Diffusivity of Q17/6 (Δ=50ms)
y = -7.2227E-08x + 2.5726E+01
R² = 9.9201E-01
y = -6.104E-08x + 2.778E+01
R² = 9.999E-01
ln(Intensity)
ζ/(G⁻¹s⁻¹)
2.90E+01
2.80E+01
2.70E+01
2.60E+01
2.50E+01
2.40E+01
2.30E+01
2.20E+01
2.10E+01
0.E+00
1.E+07
2.E+07
3.E+07
4.E+07

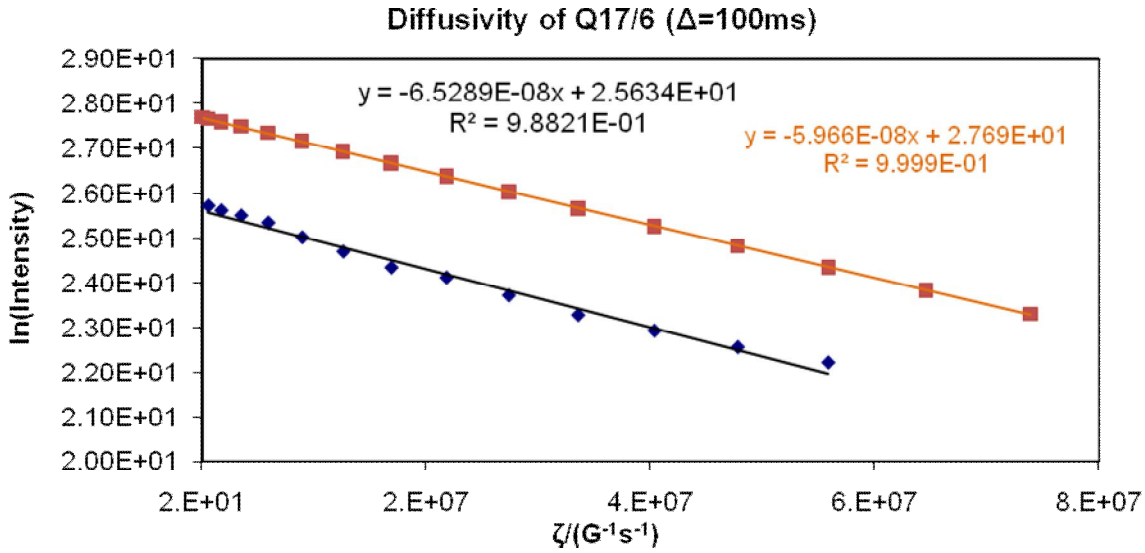
Diffusivity of Q17/6 (Δ=100ms)
y = -6.5289E-08x + 2.5634E+01
R² = 9.8821E-01
y = -5.966E-08x + 2.769E+01
R² = 9.999E-01
ln(Intensity)
ζ/(G⁻¹s⁻¹)
2.90E+01
2.80E+01
2.70E+01
2.60E+01
2.50E+01
2.40E+01
2.30E+01
2.20E+01
2.10E+01
2.00E+01
2.E+01
2.E+07
4.E+07
6.E+07
8.E+07

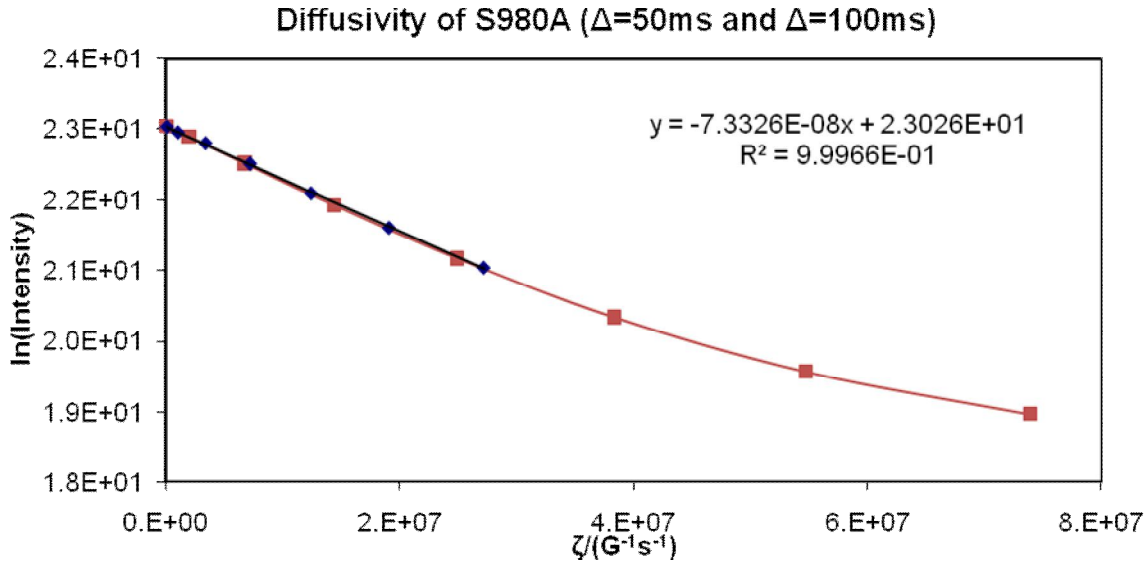
Diffusivity of S980A (Δ=50ms and Δ=100ms)
y = -7.3326E-08x + 2.3026E+01
R² = 9.9966E-01
ln(Intensity)
ζ/(G⁻¹s⁻¹)
2.4E+01
2.3E+01
2.2E+01
2.1E+01
2.0E+01
1.9E+01
1.8E+01
0.E+00
2.E+07
4.E+07
6.E+07
8.E+07

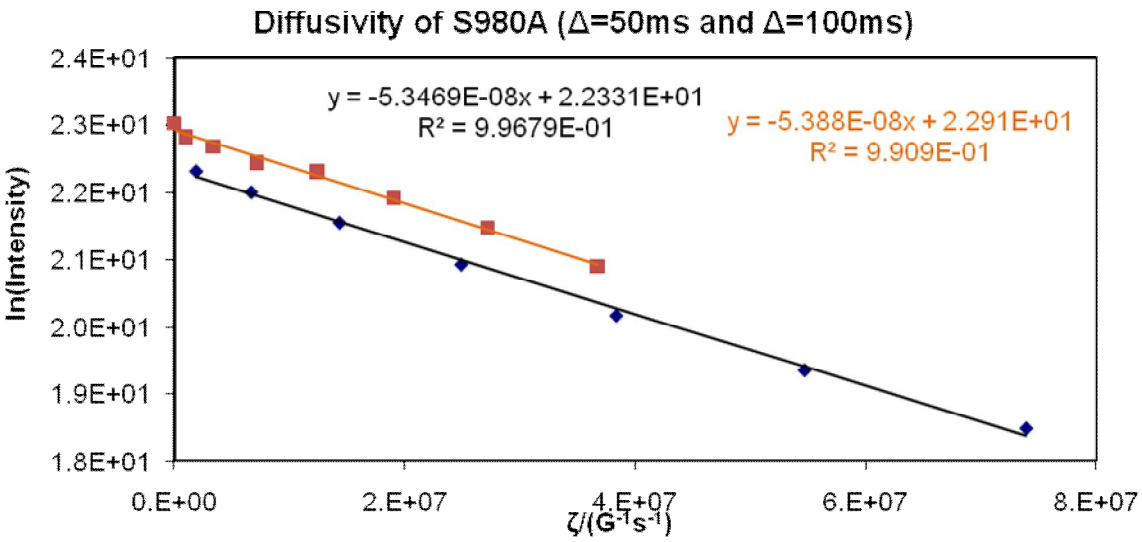
Diffusivity of S980A (Δ=50ms and Δ=100ms)
y = -5.3469E-08x + 2.2331E+01
R² = 9.9679E-01
y = -5.388E-08x + 2.291E+01
R² = 9.909E-01
ln(Intensity)
2.4E+01
2.3E+01
2.2E+01
2.1E+01
2.0E+01
1.9E+01
1.8E+01
0.E+00
2.E+07
4.E+07
6.E+07
8.E+07
ζ/(G-1s-1)

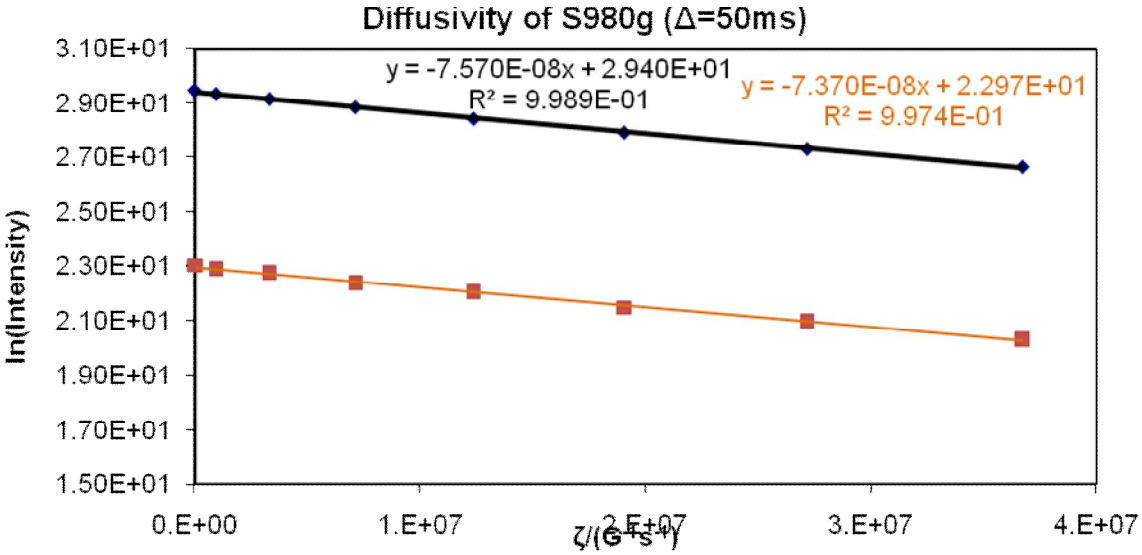
Diffusivity of S980g (Δ=50ms)
y = -7.570E-08x + 2.940E+01
R² = 9.989E-01
y = -7.370E-08x + 2.297E+01
R² = 9.974E-01
ln(Intensity)
3.10E+01
2.90E+01
2.70E+01
2.50E+01
2.30E+01
2.10E+01
1.90E+01
1.70E+01
1.50E+01
0.E+00
1.E+07
2.E+07
3.E+07
4.E+07
ζ/(G-1s-1)

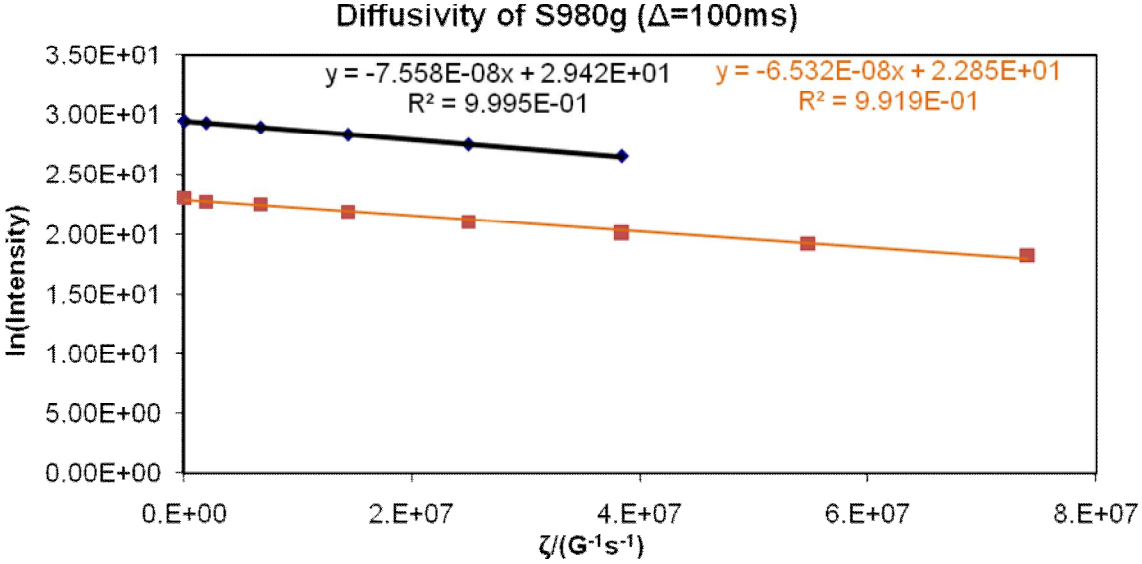
Diffusivity of S980g (Δ=100ms)
y = -7.558E-08x + 2.942E+01
R² = 9.995E-01
y = -6.532E-08x + 2.285E+01
R² = 9.919E-01
ln(Intensity)
3.50E+01
3.00E+01
2.50E+01
2.00E+01
1.50E+01
1.00E+01
5.00E+00
0.00E+00
0.E+00
2.E+07
4.E+07
6.E+07
8.E+07
ζ/(G-1s-1)

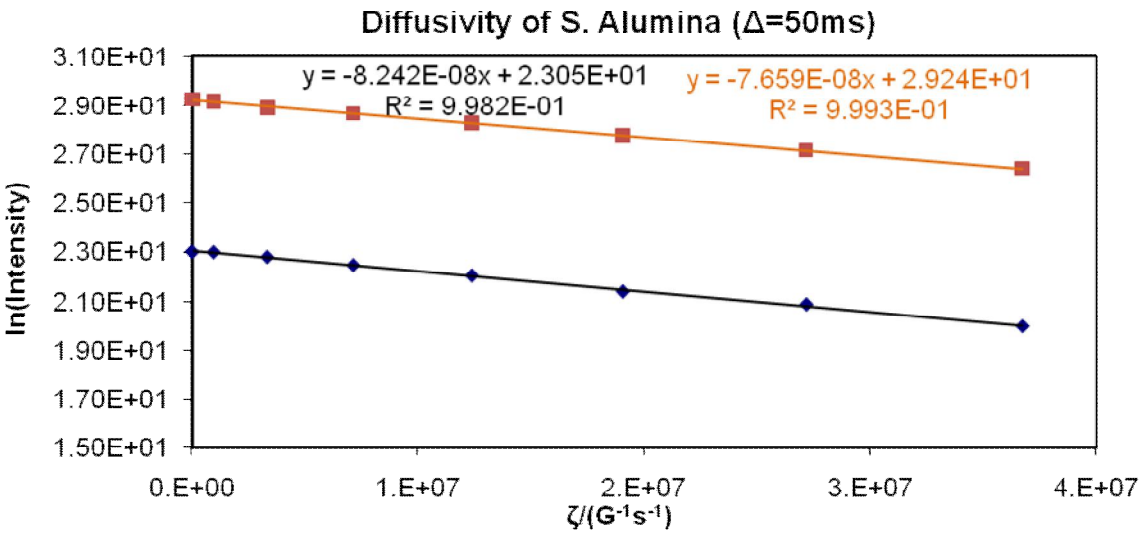

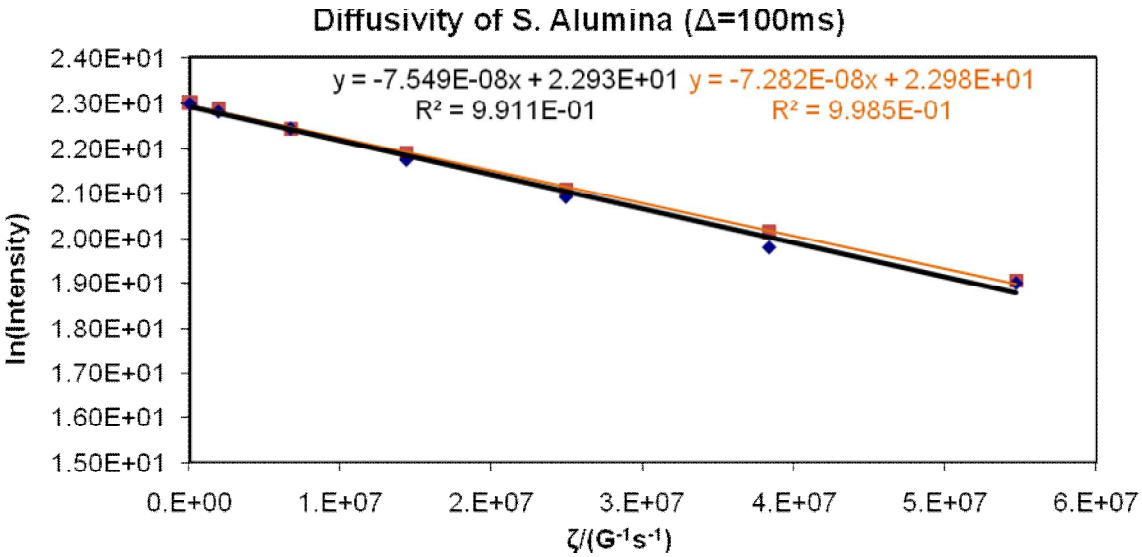

Partially saturated samples with 0.5M Na_2CO_3 reservoir (Case III)

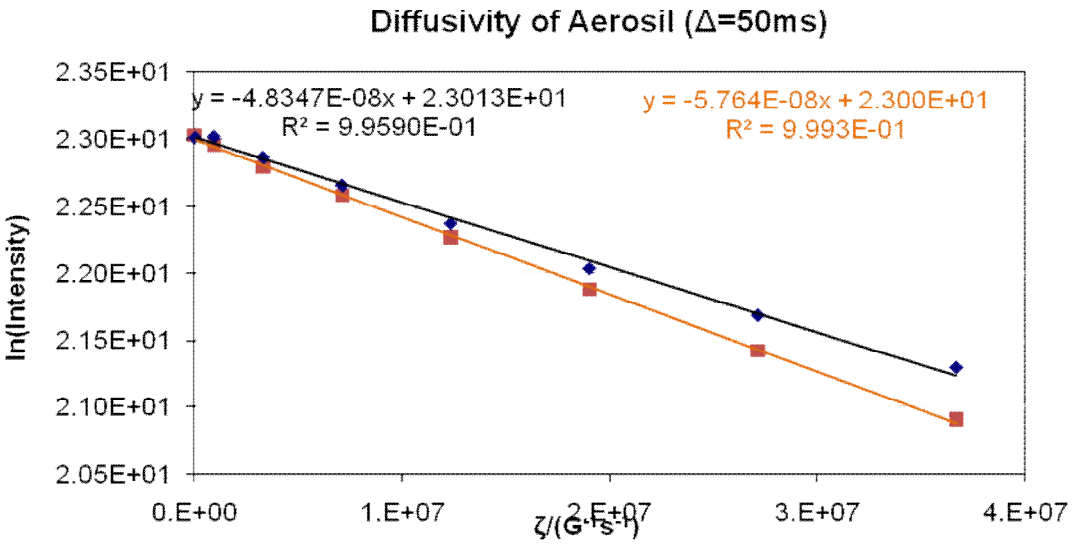

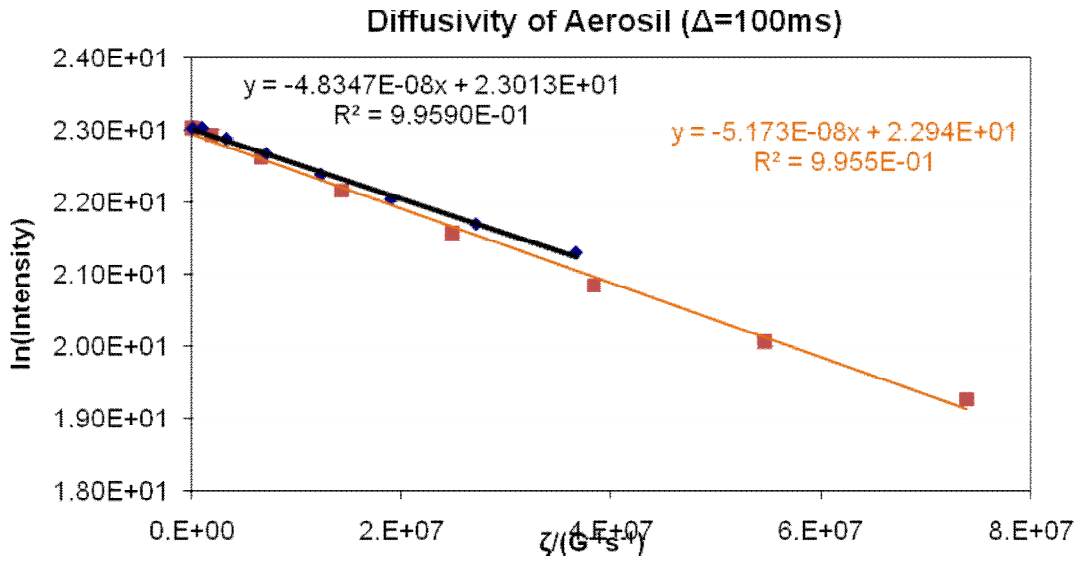
Diffusivity of Aerosil (Δ=100ms)
y = -4.8347E-08x + 2.3013E+01
R² = 9.9590E-01
y = -5.173E-08x + 2.294E+01
R² = 9.955E-01
ln(Intensity)
2.40E+01
2.30E+01
2.20E+01
2.10E+01
2.00E+01
1.90E+01
1.80E+01
0.E+00
2.E+07
4.E+07
6.E+07
8.E+07
ζ/(G⁻¹s⁻¹)

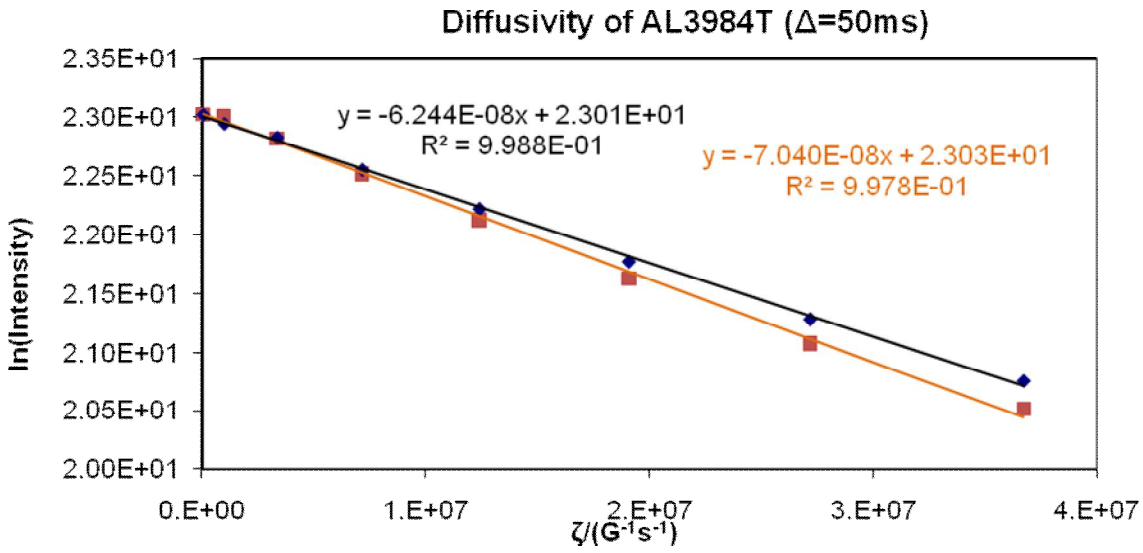
Diffusivity of AL3984T (Δ=50ms)
y = -6.244E-08x + 2.301E+01
R² = 9.988E-01
y = -7.040E-08x + 2.303E+01
R² = 9.978E-01
ln(Intensity)
2.35E+01
2.30E+01
2.25E+01
2.20E+01
2.15E+01
2.10E+01
2.05E+01
2.00E+01
0.E+00
1.E+07
2.E+07
3.E+07
4.E+07
ζ/(G⁻¹s⁻¹)

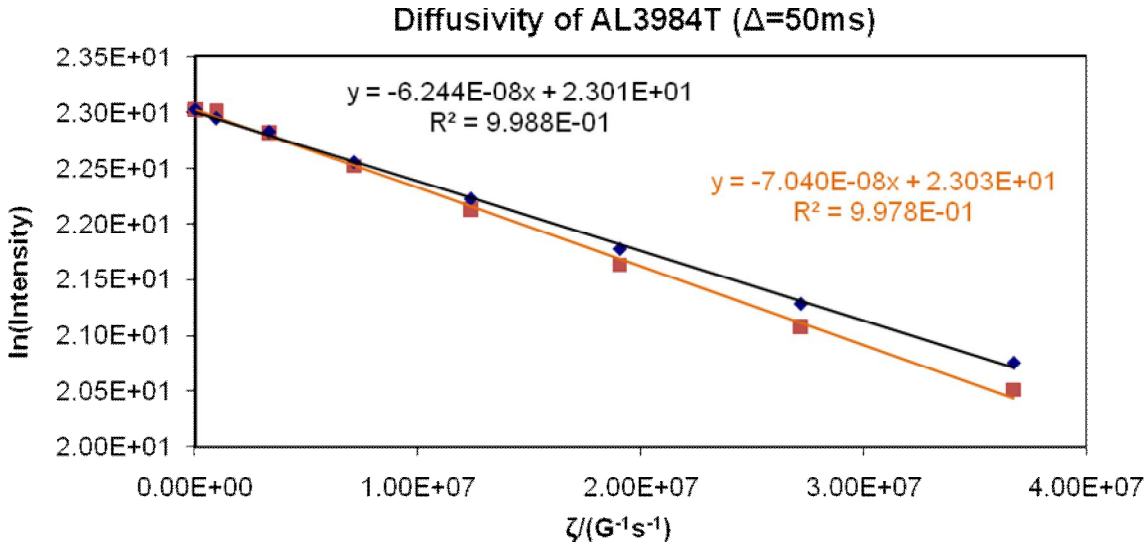
Diffusivity of AL3984T (Δ=50ms)
y = -6.244E-08x + 2.301E+01
R² = 9.988E-01
y = -7.040E-08x + 2.303E+01
R² = 9.978E-01
ln(Intensity)
2.35E+01
2.30E+01
2.25E+01
2.20E+01
2.15E+01
2.10E+01
2.05E+01
2.00E+01
0.00E+00
1.00E+07
2.00E+07
3.00E+07
4.00E+07
ζ/(G⁻¹s⁻¹)

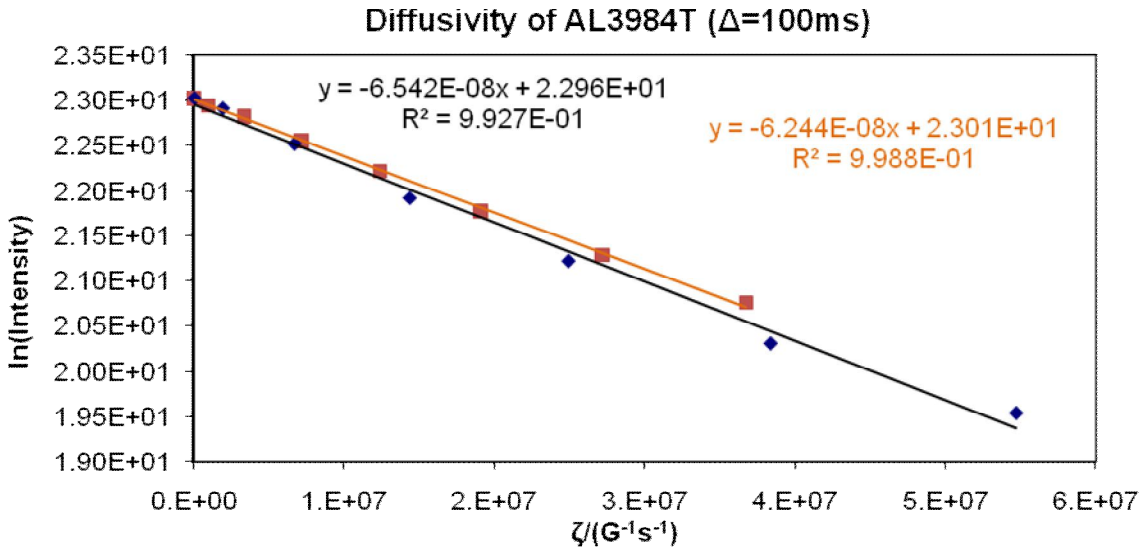
Diffusivity of AL3984T (Δ=100ms)
y = -6.542E-08x + 2.296E+01
R² = 9.927E-01
y = -6.244E-08x + 2.301E+01
R² = 9.988E-01
ln(Intensity)
ζ/(G⁻¹s⁻¹)
2.35E+01
2.30E+01
2.25E+01
2.20E+01
2.15E+01
2.10E+01
2.05E+01
2.00E+01
1.95E+01
1.90E+01
0.E+00
1.E+07
2.E+07
3.E+07
4.E+07
5.E+07
6.E+07

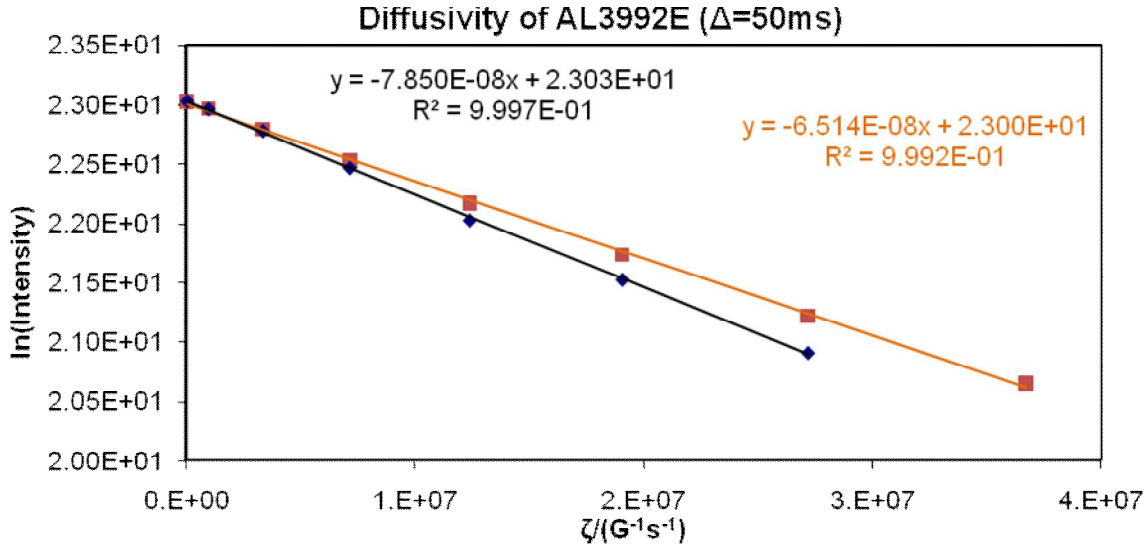
Diffusivity of AL3992E (Δ=50ms)
y = -7.850E-08x + 2.303E+01
R² = 9.997E-01
y = -6.514E-08x + 2.300E+01
R² = 9.992E-01
ln(Intensity)
ζ/(G⁻¹s⁻¹)
2.35E+01
2.30E+01
2.25E+01
2.20E+01
2.15E+01
2.10E+01
2.05E+01
2.00E+01
0.E+00
1.E+07
2.E+07
3.E+07
4.E+07

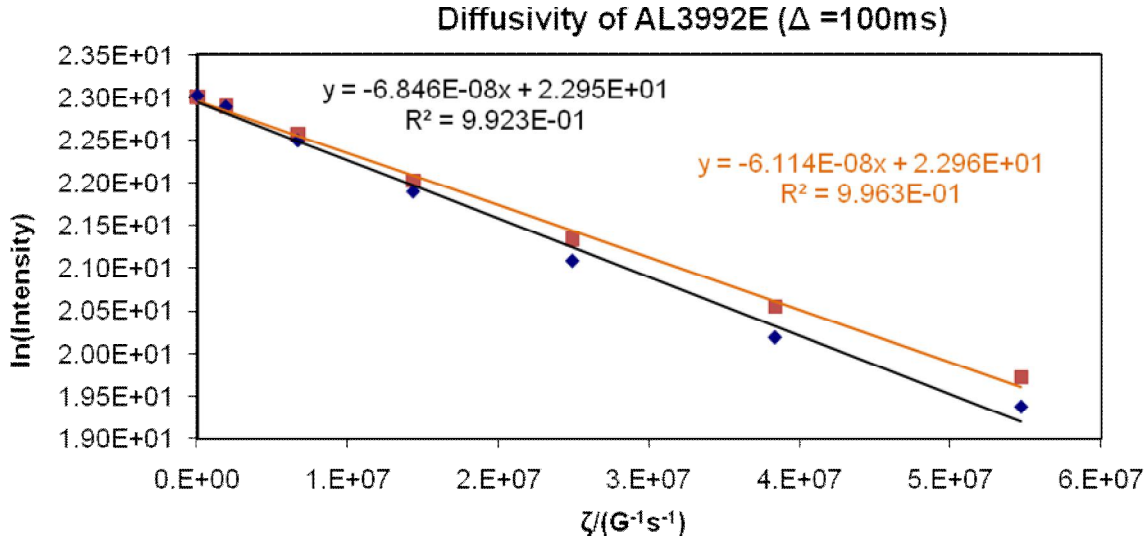
Diffusivity of AL3992E (Δ =100ms)
y = -6.846E-08x + 2.295E+01
R² = 9.923E-01
y = -6.114E-08x + 2.296E+01
R² = 9.963E-01
ln(Intensity)
ζ/(G⁻¹s⁻¹)
2.35E+01
2.30E+01
2.25E+01
2.20E+01
2.15E+01
2.10E+01
2.05E+01
2.00E+01
1.95E+01
1.90E+01
0.E+00
1.E+07
2.E+07
3.E+07
4.E+07
5.E+07
6.E+07

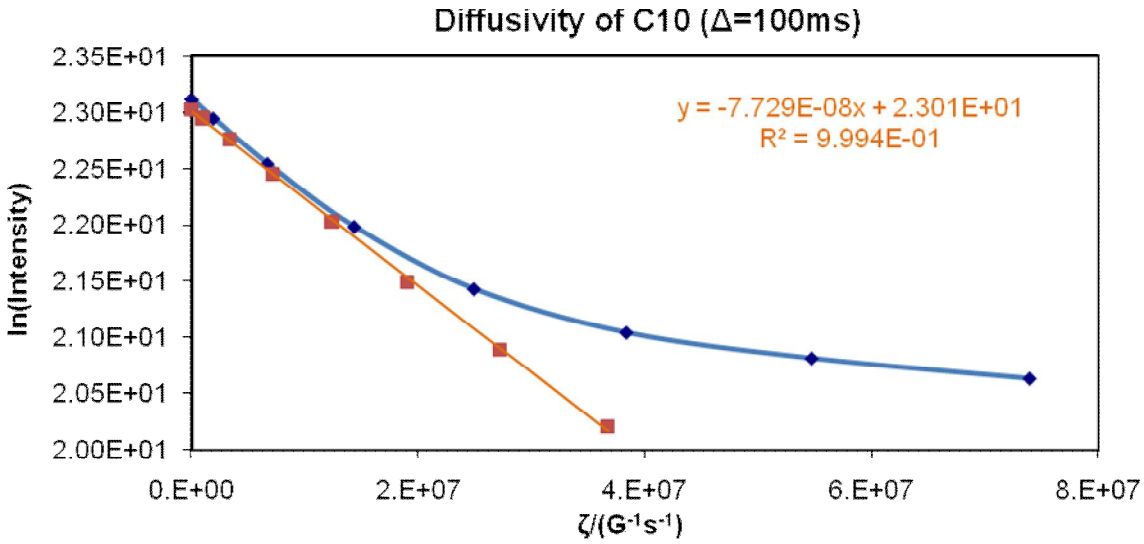
Diffusivity of C10 (Δ=100ms)
y = -7.729E-08x + 2.301E+01
R² = 9.994E-01
ln(Intensity)
2.35E+01
2.30E+01
2.25E+01
2.20E+01
2.15E+01
2.10E+01
2.05E+01
2.00E+01
0.E+00
2.E+07
4.E+07
6.E+07
8.E+07
ζ/(G⁻¹s⁻¹)

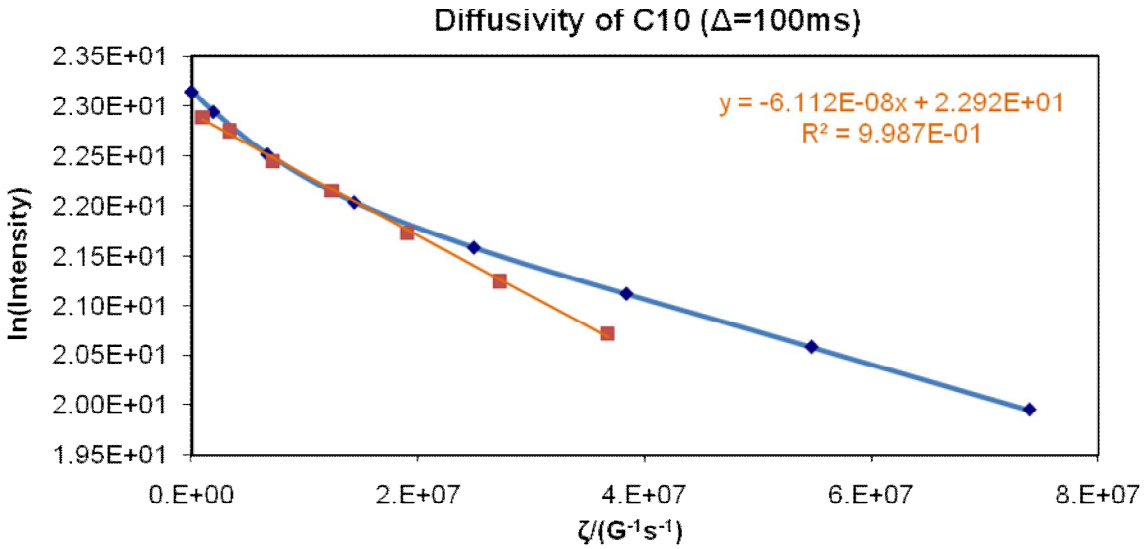
Diffusivity of C10 (Δ=100ms)
y = -6.112E-08x + 2.292E+01
R² = 9.987E-01
ln(Intensity)
2.35E+01
2.30E+01
2.25E+01
2.20E+01
2.15E+01
2.10E+01
2.05E+01
2.00E+01
1.95E+01
0.E+00
2.E+07
4.E+07
6.E+07
8.E+07
ζ/(G⁻¹s⁻¹)

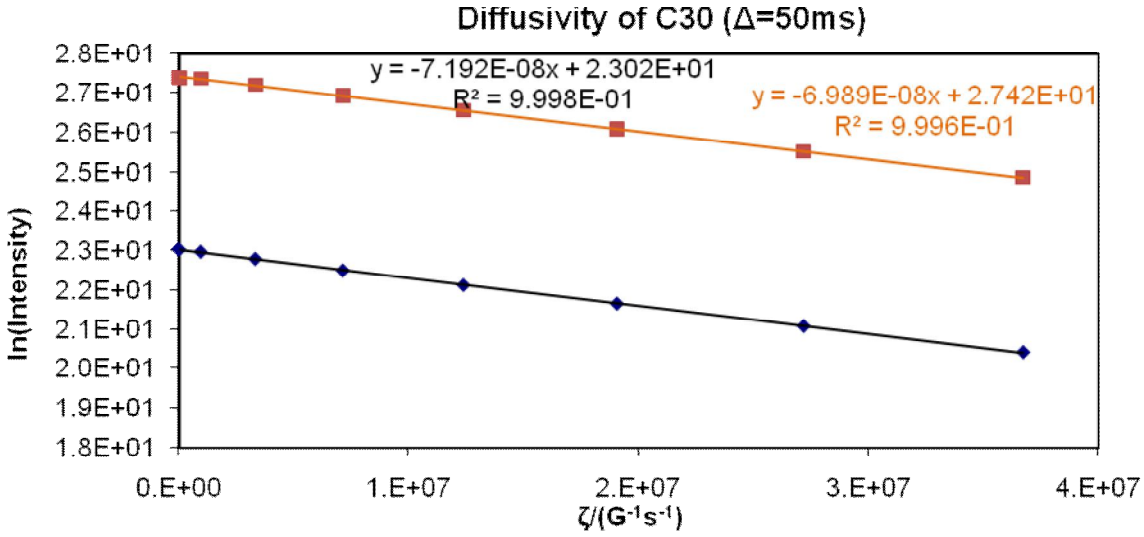
Diffusivity of C30 (Δ=50ms)
y = -7.192E-08x + 2.302E+01
R² = 9.998E-01
y = -6.989E-08x + 2.742E+01
R² = 9.996E-01
ln(Intensity)
2.8E+01
2.7E+01
2.6E+01
2.5E+01
2.4E+01
2.3E+01
2.2E+01
2.1E+01
2.0E+01
1.9E+01
1.8E+01
0.E+00
1.E+07
2.E+07
3.E+07
4.E+07
ζ/(G⁻¹s⁻¹)

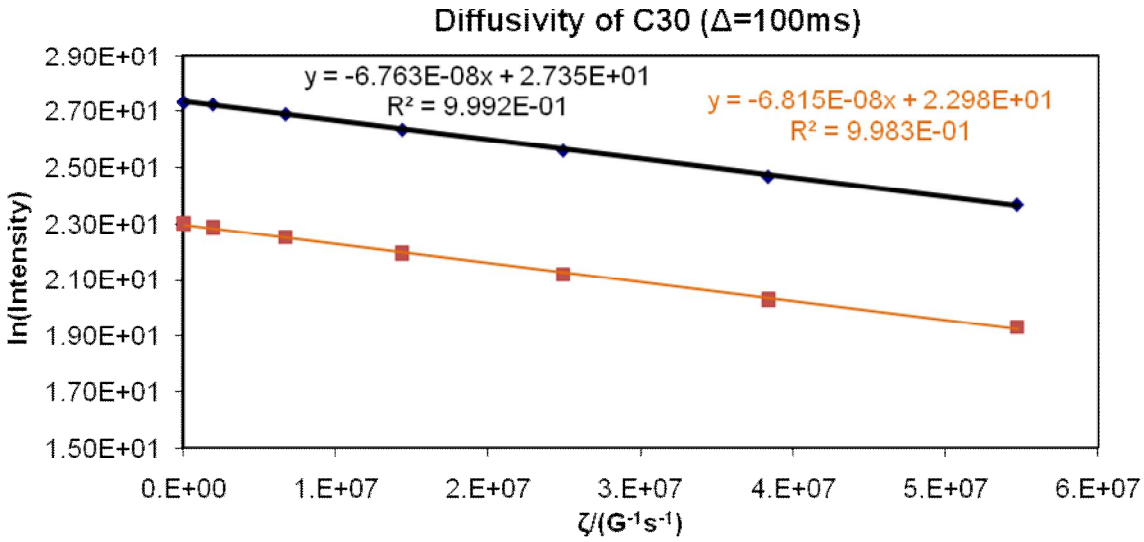
Diffusivity of C30 (Δ=100ms)
y = -6.763E-08x + 2.735E+01
R² = 9.992E-01
y = -6.815E-08x + 2.298E+01
R² = 9.983E-01
ln(Intensity)
2.90E+01
2.70E+01
2.50E+01
2.30E+01
2.10E+01
1.90E+01
1.70E+01
1.50E+01
0.E+00
1.E+07
2.E+07
3.E+07
4.E+07
5.E+07
6.E+07
ζ/(G⁻¹s⁻¹)

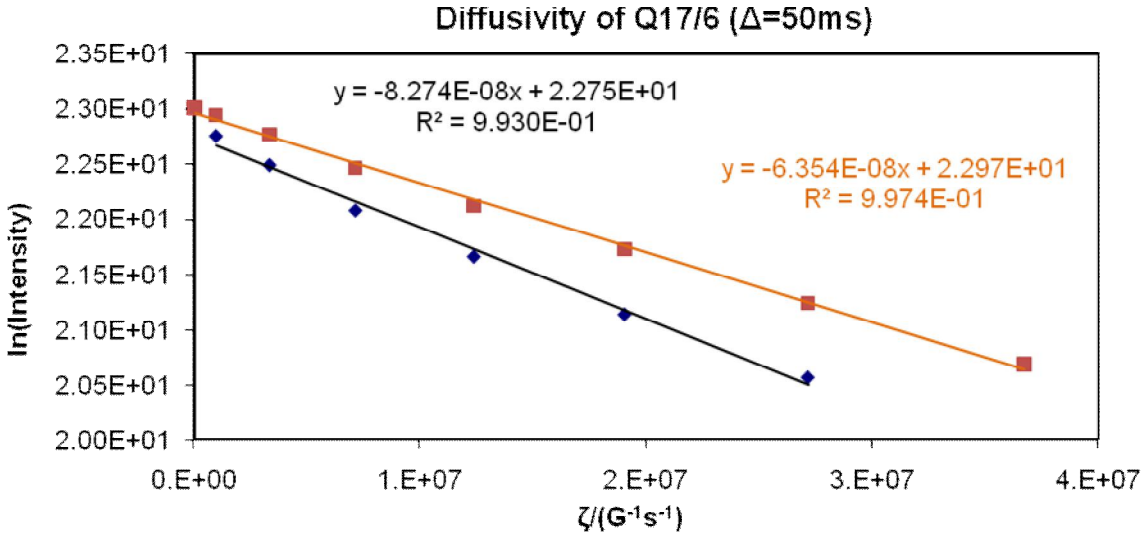
Diffusivity of Q17/6 (Δ=50ms)
y = -8.274E-08x + 2.275E+01
R² = 9.930E-01
y = -6.354E-08x + 2.297E+01
R² = 9.974E-01
ln(Intensity)
2.35E+01
2.30E+01
2.25E+01
2.20E+01
2.15E+01
2.10E+01
2.05E+01
2.00E+01
0.E+00
1.E+07
2.E+07
3.E+07
4.E+07
ζ/(G⁻¹s⁻¹)

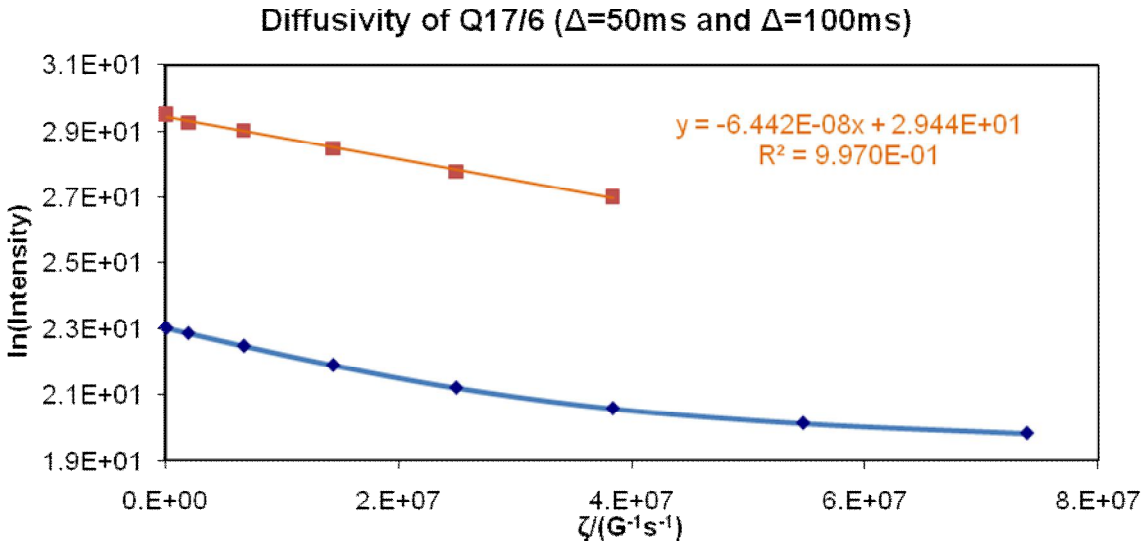
Diffusivity of Q17/6 (Δ=50ms and Δ=100ms)
y = -6.442E-08x + 2.944E+01
R² = 9.970E-01
ln(Intensity)
3.1E+01
2.9E+01
2.7E+01
2.5E+01
2.3E+01
2.1E+01
1.9E+01
0.E+00
2.E+07
4.E+07
6.E+07
8.E+07
ζ/(G⁻¹s⁻¹)

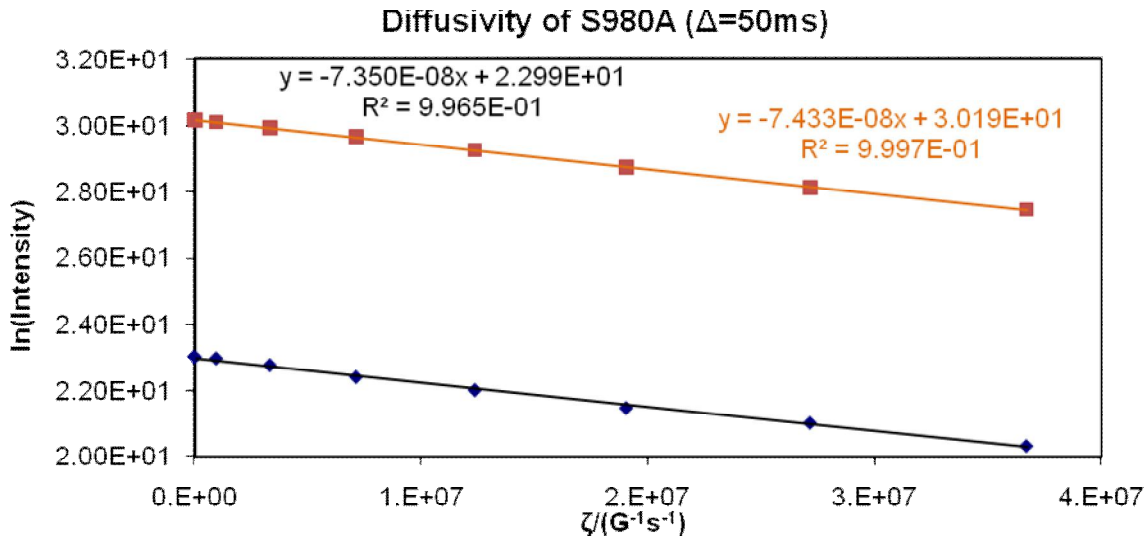
Diffusivity of S980A (Δ=50ms)
y = -7.350E-08x + 2.299E+01
R² = 9.965E-01
y = -7.433E-08x + 3.019E+01
R² = 9.997E-01
ln(Intensity)
3.20E+01
3.00E+01
2.80E+01
2.60E+01
2.40E+01
2.20E+01
2.00E+01
0.E+00
1.E+07
2.E+07
3.E+07
4.E+07
ζ/(G⁻¹s⁻¹)

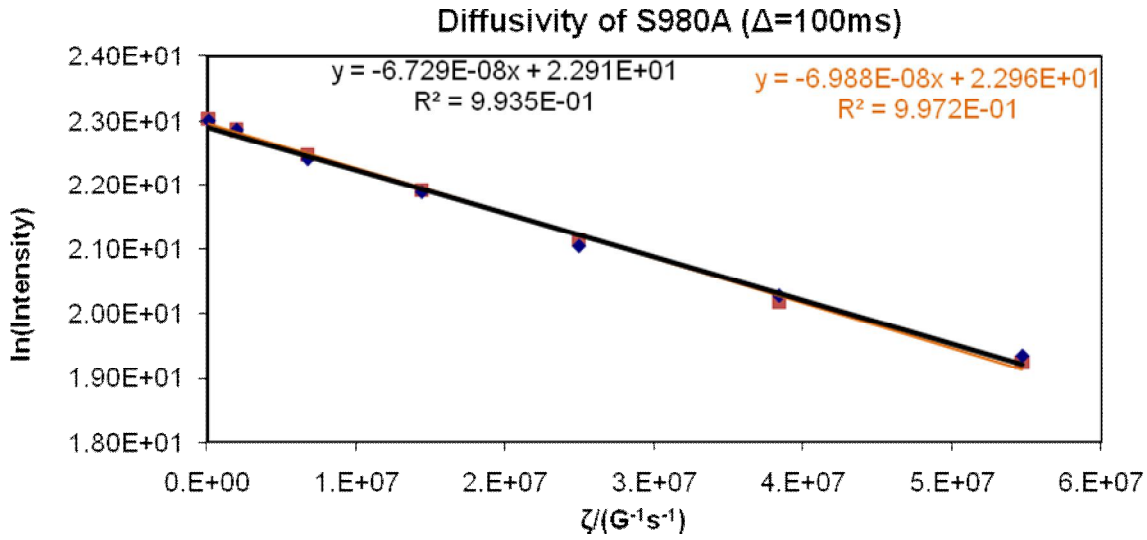
Diffusivity of S980A (Δ=100ms)
y = -6.729E-08x + 2.291E+01
R² = 9.935E-01
y = -6.988E-08x + 2.296E+01
R² = 9.972E-01
ln(Intensity)
2.40E+01
2.30E+01
2.20E+01
2.10E+01
2.00E+01
1.90E+01
1.80E+01
0.E+00
1.E+07
2.E+07
3.E+07
4.E+07
5.E+07
6.E+07
ζ/(G⁻¹s⁻¹)

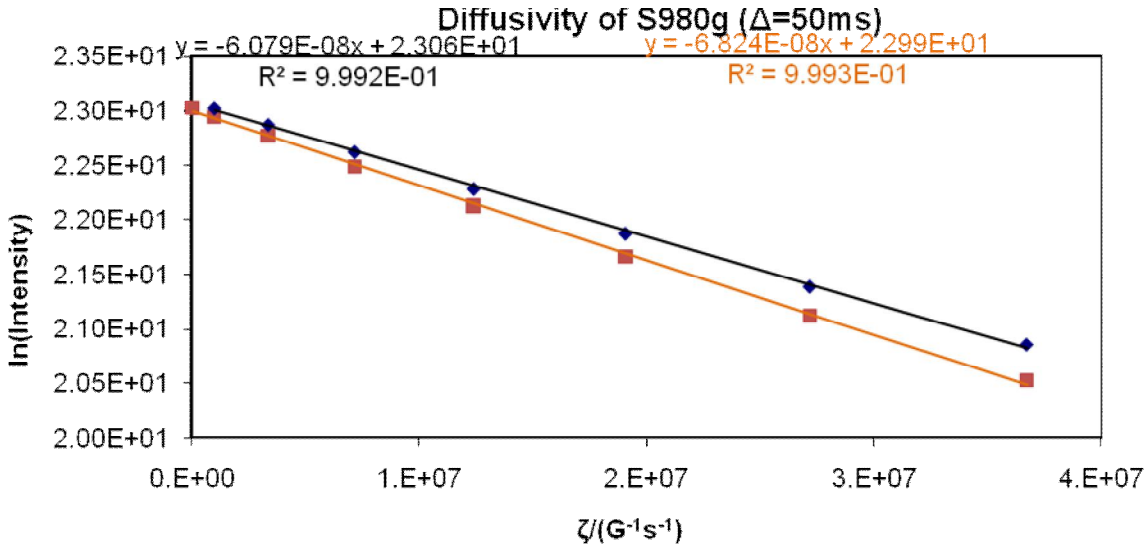
Diffusivity of S980g (Δ=50ms)
y = -6.079E-08x + 2.306E+01
R² = 9.992E-01
y = -6.824E-08x + 2.299E+01
R² = 9.993E-01
ln(Intensity)
2.35E+01
2.30E+01
2.25E+01
2.20E+01
2.15E+01
2.10E+01
2.05E+01
2.00E+01
0.E+00
1.E+07
2.E+07
3.E+07
4.E+07
ζ/(G⁻¹s⁻¹)

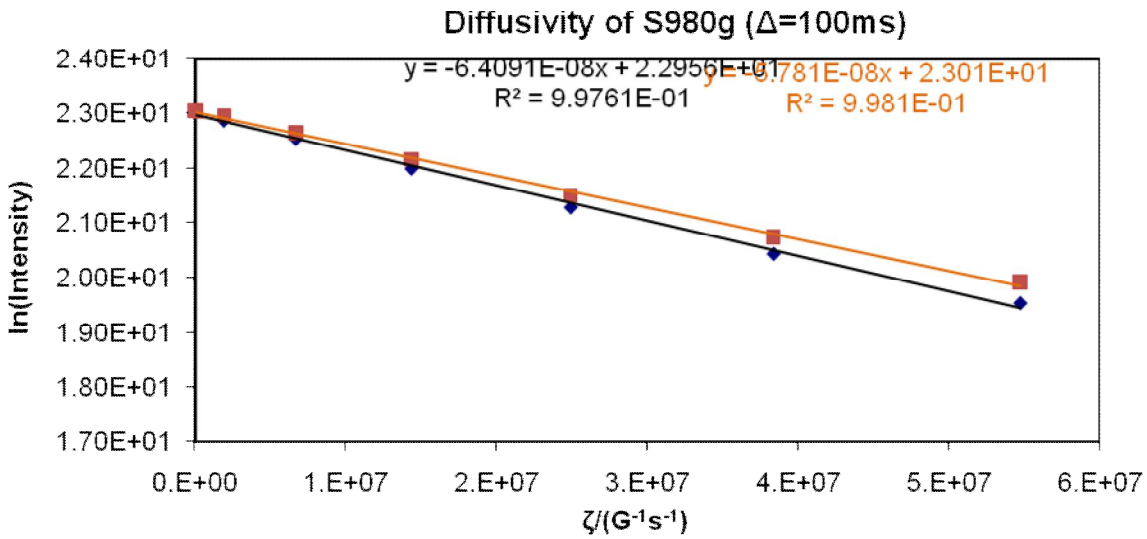
Diffusivity of S980g (Δ=100ms)
y = -6.4091E-08x + 2.2956E+01
R² = 9.9761E-01
y = -6.781E-08x + 2.301E+01
R² = 9.981E-01
ln(Intensity)
2.40E+01
2.30E+01
2.20E+01
2.10E+01
2.00E+01
1.90E+01
1.80E+01
1.70E+01
0.E+00
1.E+07
2.E+07
3.E+07
4.E+07
5.E+07
6.E+07
ζ/(G⁻¹s⁻¹)

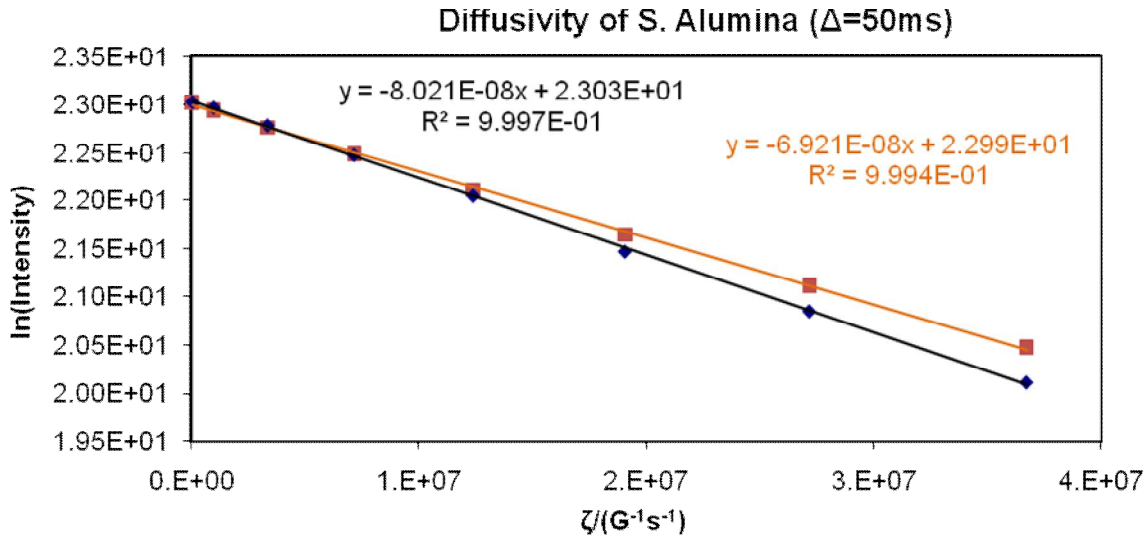
Diffusivity of S. Alumina (Δ=50ms)
y = -8.021E-08x + 2.303E+01
R² = 9.997E-01
y = -6.921E-08x + 2.299E+01
R² = 9.994E-01
ln(Intensity)
2.35E+01
2.30E+01
2.25E+01
2.20E+01
2.15E+01
2.10E+01
2.05E+01
2.00E+01
1.95E+01
0.E+00
1.E+07
2.E+07
3.E+07
4.E+07
ζ/(G⁻¹s⁻¹)

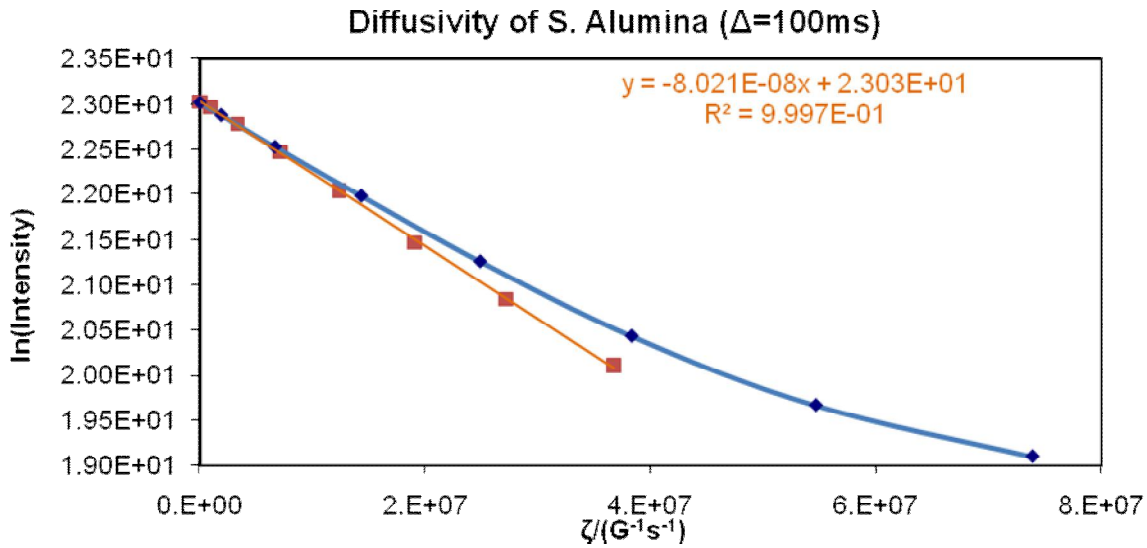
Diffusivity of S. Alumina (Δ=100ms)
y = -8.021E-08x + 2.303E+01
R² = 9.997E-01
ln(Intensity)
2.35E+01
2.30E+01
2.25E+01
2.20E+01
2.15E+01
2.10E+01
2.05E+01
2.00E+01
1.95E+01
1.90E+01
0.E+00
2.E+07
4.E+07
6.E+07
8.E+07
ζ/(G⁻¹s⁻¹)

Partially saturated samples with 1.5M Na_2CO_3 reservoir (Case IV)

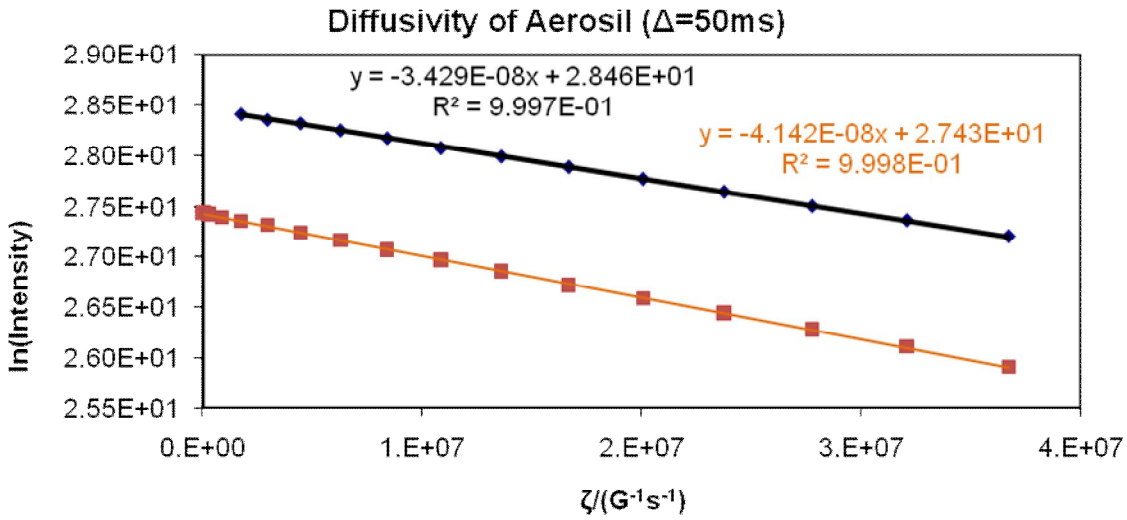

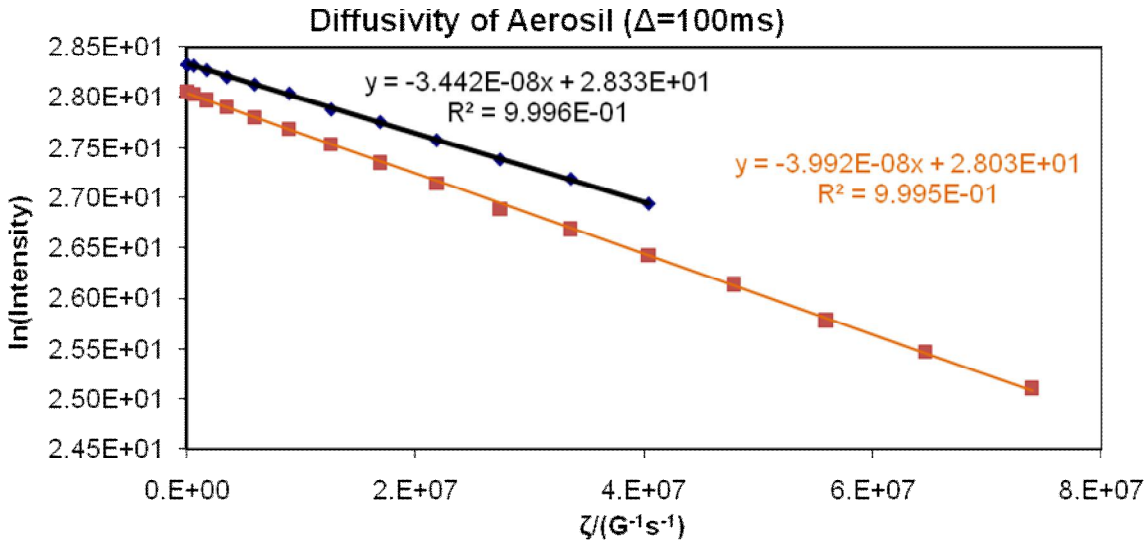

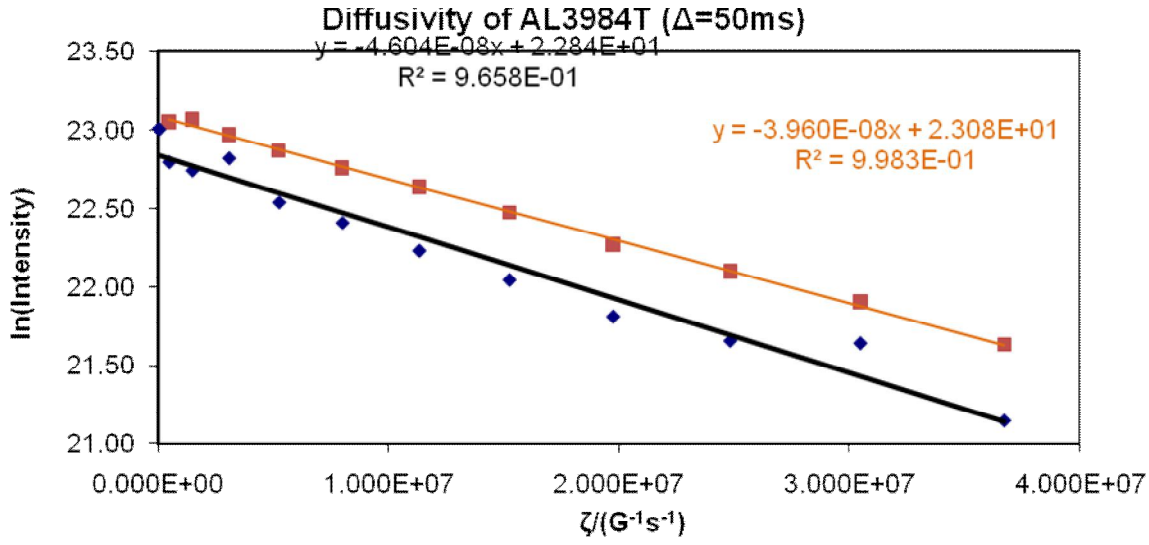

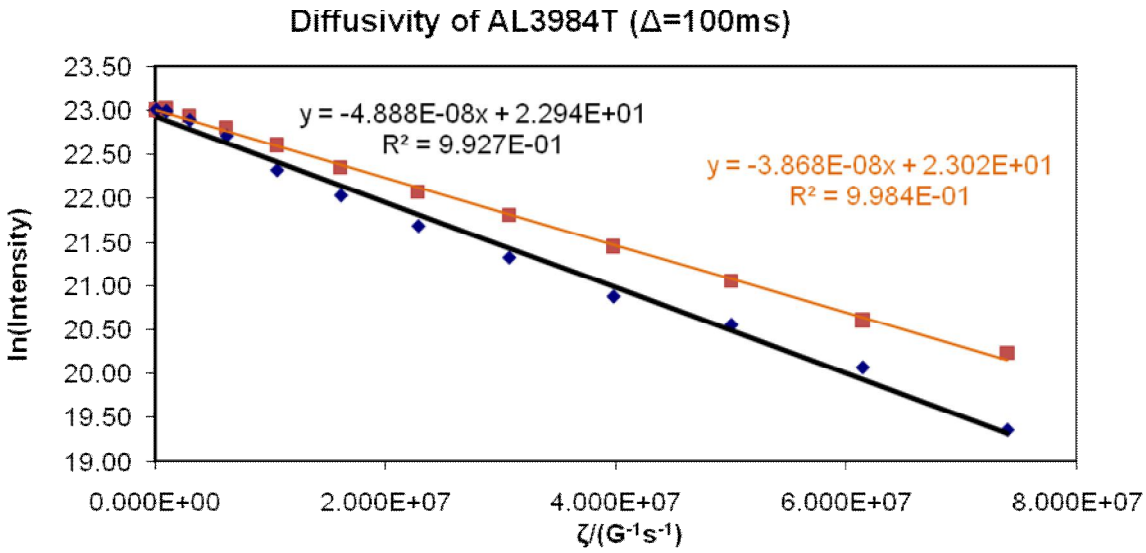
Diffusivity of AL3984T (Δ=100ms)
y = -4.888E-08x + 2.294E+01
R² = 9.927E-01
y = -3.868E-08x + 2.302E+01
R² = 9.984E-01
ln(Intensity)
ζ/(G⁻¹s⁻¹)

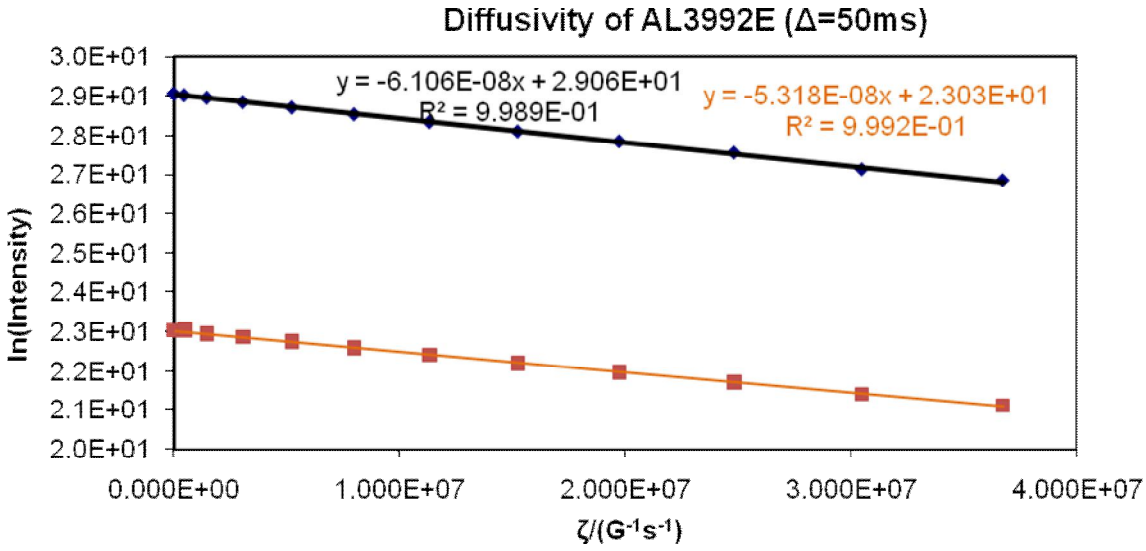
Diffusivity of AL3992E (Δ=50ms)
y = -6.106E-08x + 2.906E+01
R² = 9.989E-01
y = -5.318E-08x + 2.303E+01
R² = 9.992E-01
ln(Intensity)
ζ/(G⁻¹s⁻¹)

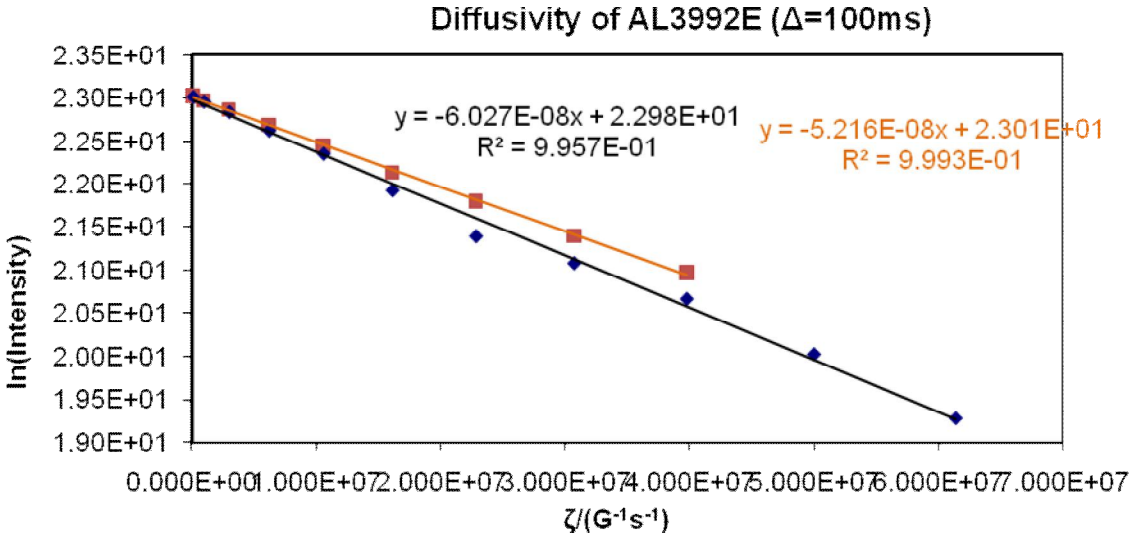
Diffusivity of AL3992E (Δ=100ms)
y = -6.027E-08x + 2.298E+01
R² = 9.957E-01
y = -5.216E-08x + 2.301E+01
R² = 9.993E-01
ln(Intensity)
ζ/(G⁻¹s⁻¹)

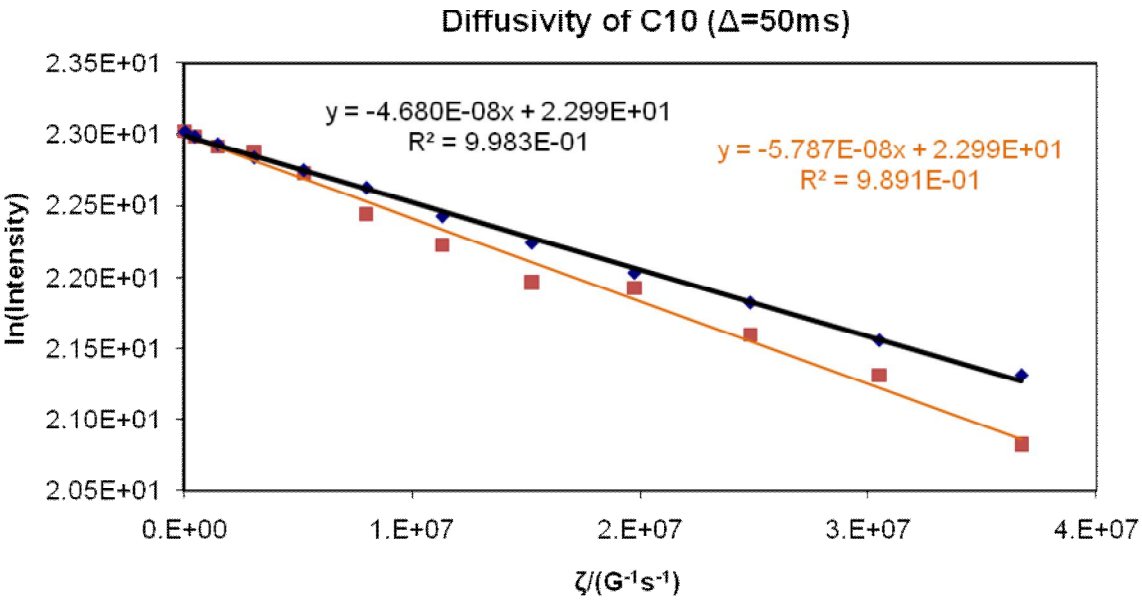
Diffusivity of C10 (Δ=50ms)
y = -4.680E-08x + 2.299E+01
R² = 9.983E-01
y = -5.787E-08x + 2.299E+01
R² = 9.891E-01
ln(Intensity)
2.35E+01
2.30E+01
2.25E+01
2.20E+01
2.15E+01
2.10E+01
2.05E+01
0.E+00
1.E+07
2.E+07
3.E+07
4.E+07
ζ/(G⁻¹s⁻¹)

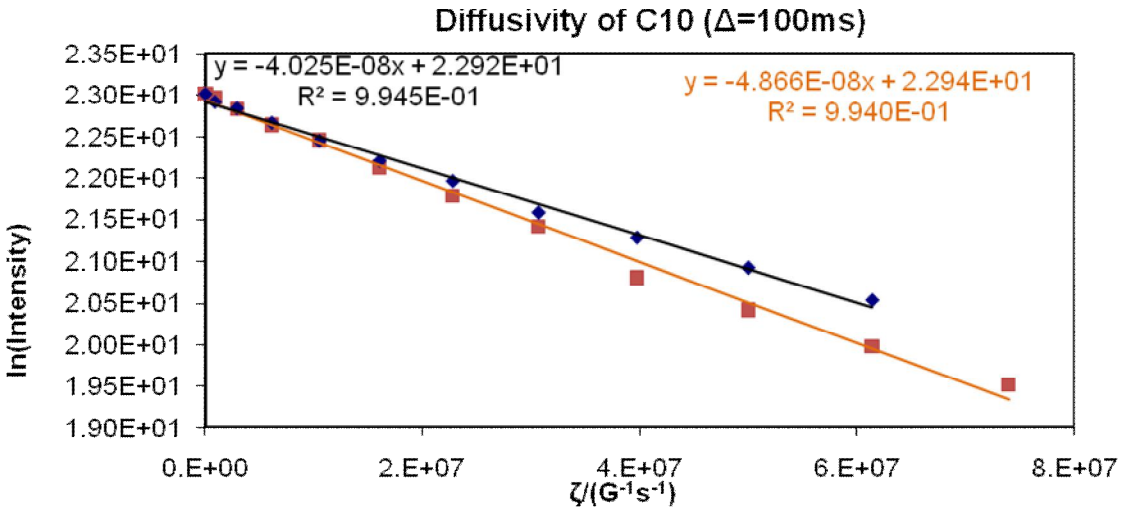
Diffusivity of C10 (Δ=100ms)
y = -4.025E-08x + 2.292E+01
R² = 9.945E-01
y = -4.866E-08x + 2.294E+01
R² = 9.940E-01
ln(Intensity)
2.35E+01
2.30E+01
2.25E+01
2.20E+01
2.15E+01
2.10E+01
2.05E+01
2.00E+01
1.95E+01
1.90E+01
0.E+00
2.E+07
4.E+07
6.E+07
8.E+07
ζ/(G⁻¹s⁻¹)

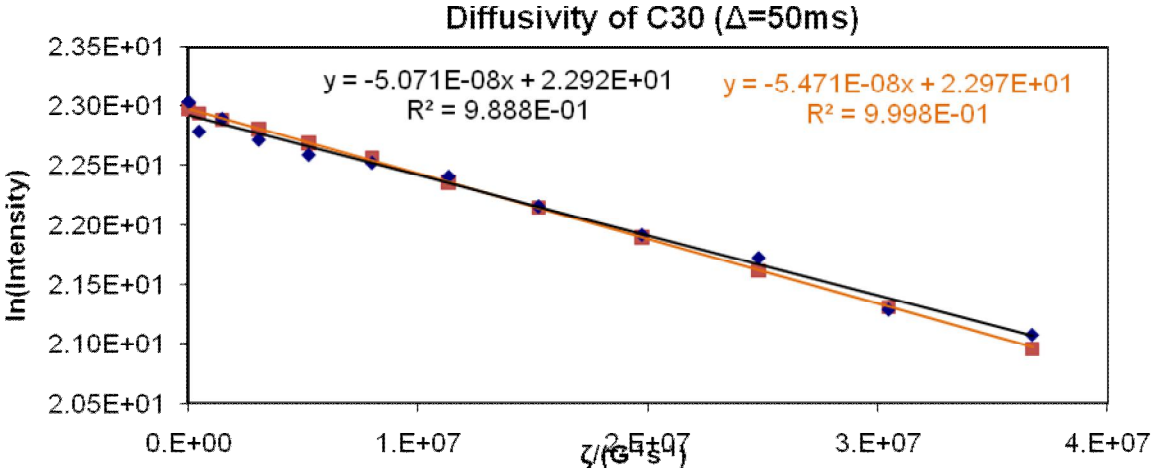
Diffusivity of C30 (Δ=50ms)
y = -5.071E-08x + 2.292E+01
R² = 9.888E-01
y = -5.471E-08x + 2.297E+01
R² = 9.998E-01
ln(Intensity)
2.35E+01
2.30E+01
2.25E+01
2.20E+01
2.15E+01
2.10E+01
2.05E+01
0.E+00
1.E+07
2.E+07
3.E+07
4.E+07
ζ/(G⁻¹s⁻¹)

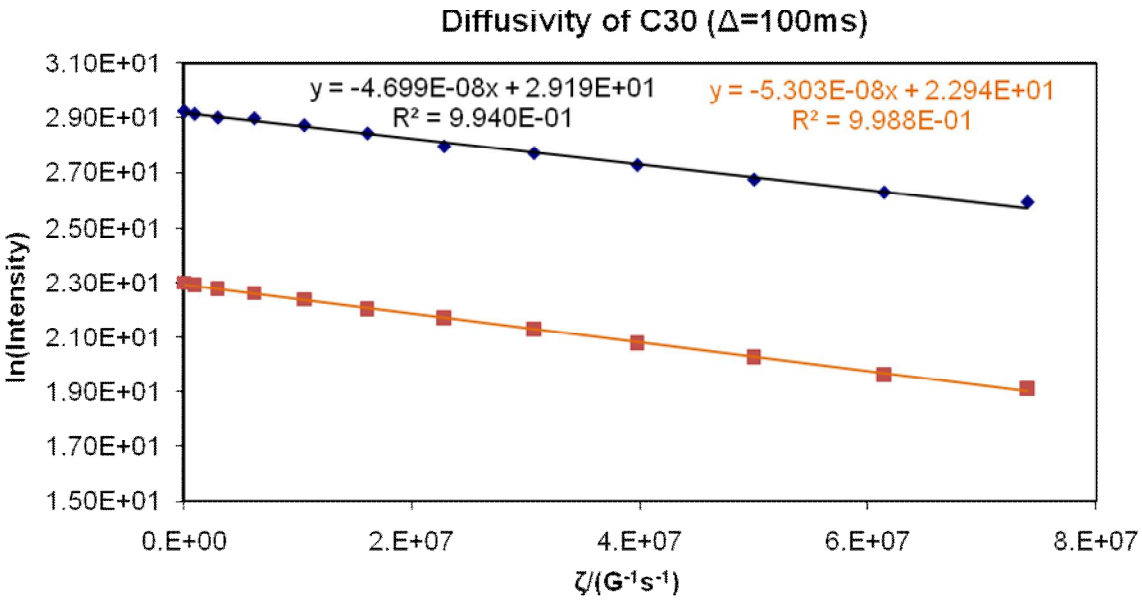
Diffusivity of C30 (Δ=100ms)
y = -4.699E-08x + 2.919E+01
R² = 9.940E-01
y = -5.303E-08x + 2.294E+01
R² = 9.988E-01
ln(Intensity)
3.10E+01
2.90E+01
2.70E+01
2.50E+01
2.30E+01
2.10E+01
1.90E+01
1.70E+01
1.50E+01
0.E+00
2.E+07
4.E+07
6.E+07
8.E+07
ζ/(G⁻¹s⁻¹)

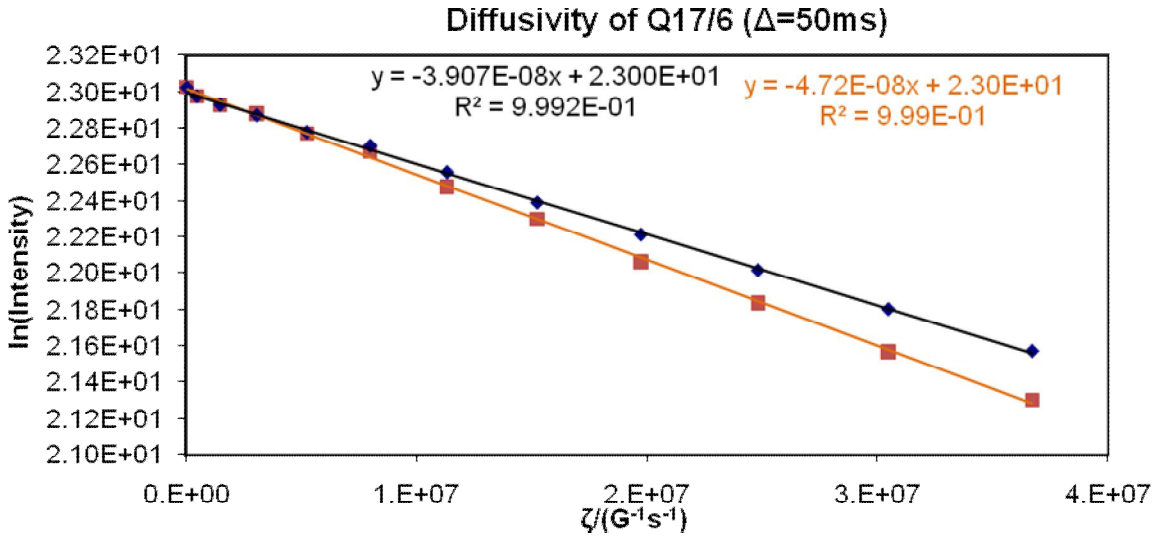
Diffusivity of Q17/6 (Δ=50ms)
y = -3.907E-08x + 2.300E+01
R² = 9.992E-01
y = -4.72E-08x + 2.30E+01
R² = 9.99E-01
ln(Intensity)
2.32E+01
2.30E+01
2.28E+01
2.26E+01
2.24E+01
2.22E+01
2.20E+01
2.18E+01
2.16E+01
2.14E+01
2.12E+01
2.10E+01
0.E+00
1.E+07
2.E+07
3.E+07
4.E+07
ζ/(G⁻¹s⁻¹)

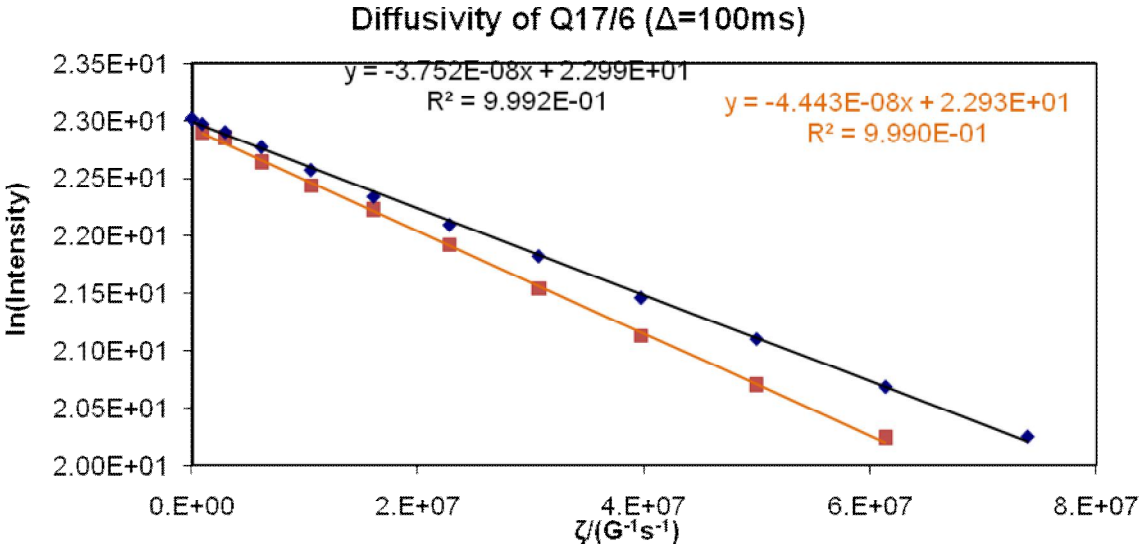
Diffusivity of Q17/6 (Δ=100ms)
y = -3.752E-08x + 2.299E+01
R² = 9.992E-01
y = -4.443E-08x + 2.293E+01
R² = 9.990E-01
ln(Intensity)
2.35E+01
2.30E+01
2.25E+01
2.20E+01
2.15E+01
2.10E+01
2.05E+01
2.00E+01
0.E+00
2.E+07
4.E+07
6.E+07
8.E+07
ζ/(G⁻¹s⁻¹)

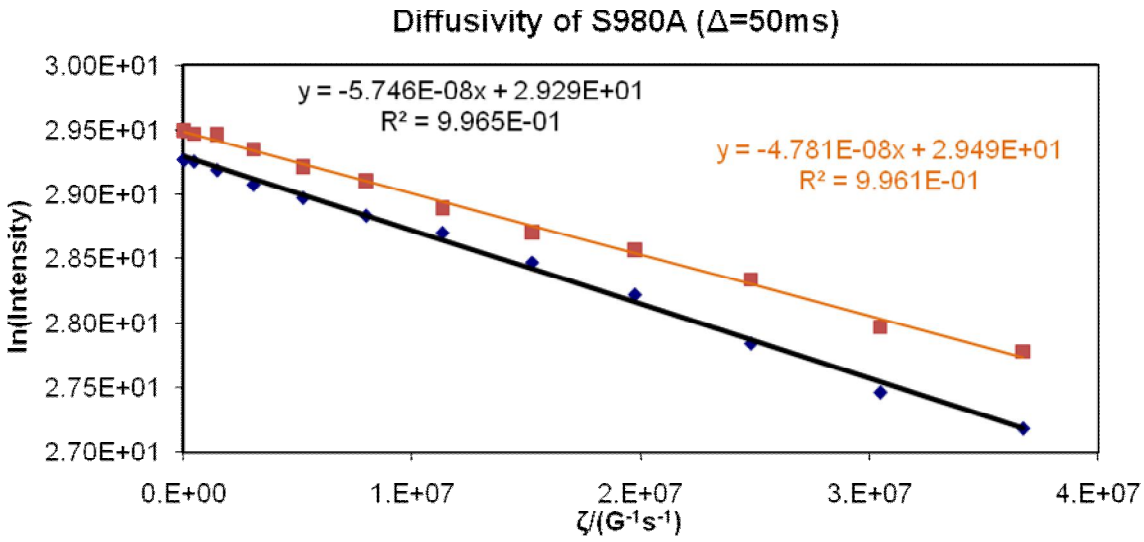
Diffusivity of S980A (Δ=50ms)
y = -5.746E-08x + 2.929E+01
R² = 9.965E-01
y = -4.781E-08x + 2.949E+01
R² = 9.961E-01
ln(Intensity)
ζ/(G⁻¹s⁻¹)
3.00E+01
2.95E+01
2.90E+01
2.85E+01
2.80E+01
2.75E+01
2.70E+01
0.E+00
1.E+07
2.E+07
3.E+07
4.E+07

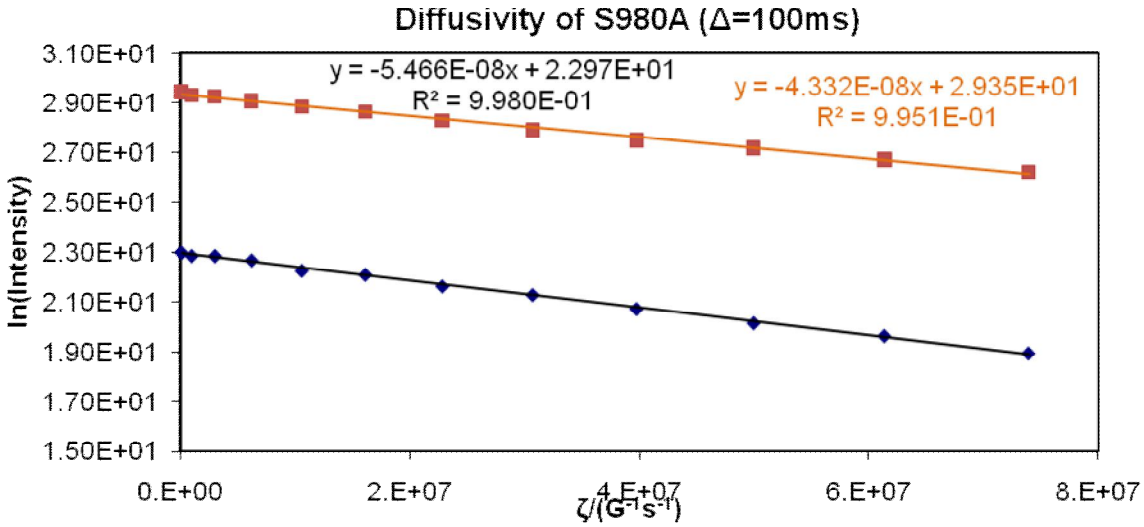
Diffusivity of S980A (Δ=100ms)
y = -5.466E-08x + 2.297E+01
R² = 9.980E-01
y = -4.332E-08x + 2.935E+01
R² = 9.951E-01
ln(Intensity)
ζ/(G⁻¹s⁻¹)
3.10E+01
2.90E+01
2.70E+01
2.50E+01
2.30E+01
2.10E+01
1.90E+01
1.70E+01
1.50E+01
0.E+00
2.E+07
4.E+07
6.E+07
8.E+07

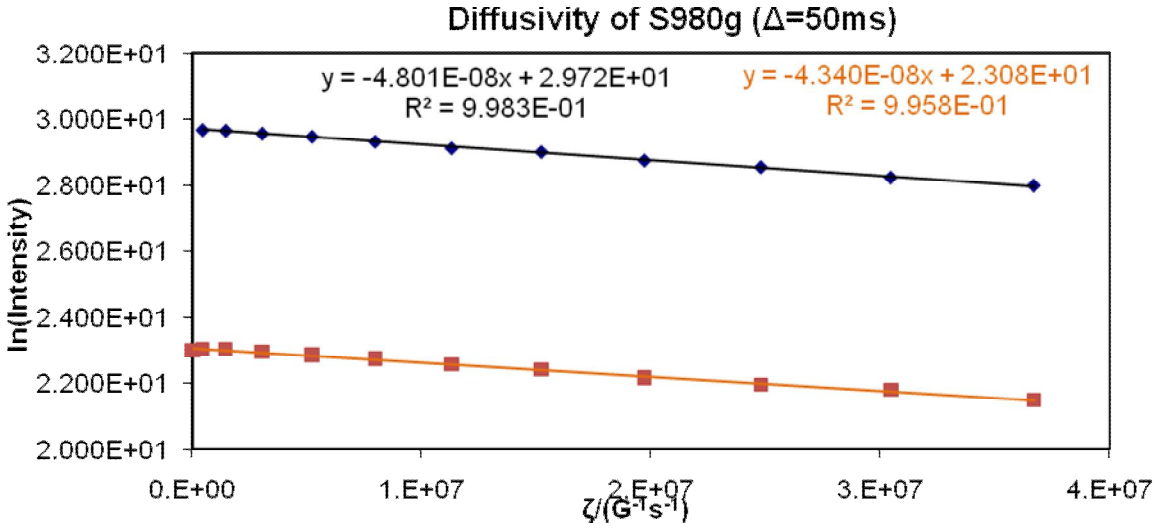
Diffusivity of S980g (Δ=50ms)
y = -4.801E-08x + 2.972E+01
R² = 9.983E-01
y = -4.340E-08x + 2.308E+01
R² = 9.958E-01
ln(Intensity)
ζ/(G⁻¹s⁻¹)
3.200E+01
3.000E+01
2.800E+01
2.600E+01
2.400E+01
2.200E+01
2.000E+01
0.E+00
1.E+07
2.E+07
3.E+07
4.E+07

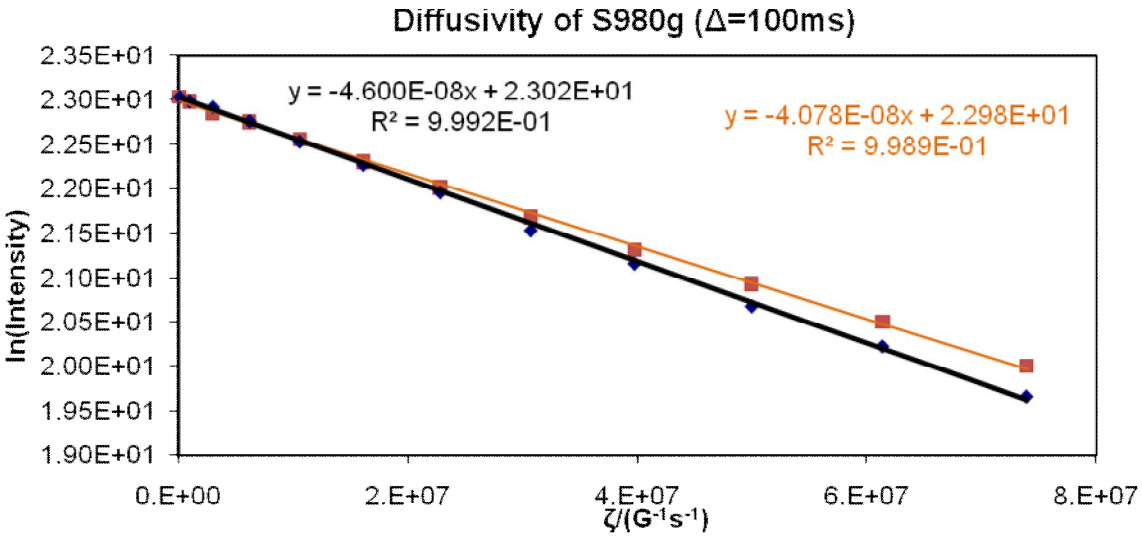
Diffusivity of S980g (Δ=100ms)
y = -4.600E-08x + 2.302E+01
R² = 9.992E-01
y = -4.078E-08x + 2.298E+01
R² = 9.989E-01
ln(Intensity)
ζ/(G⁻¹s⁻¹)

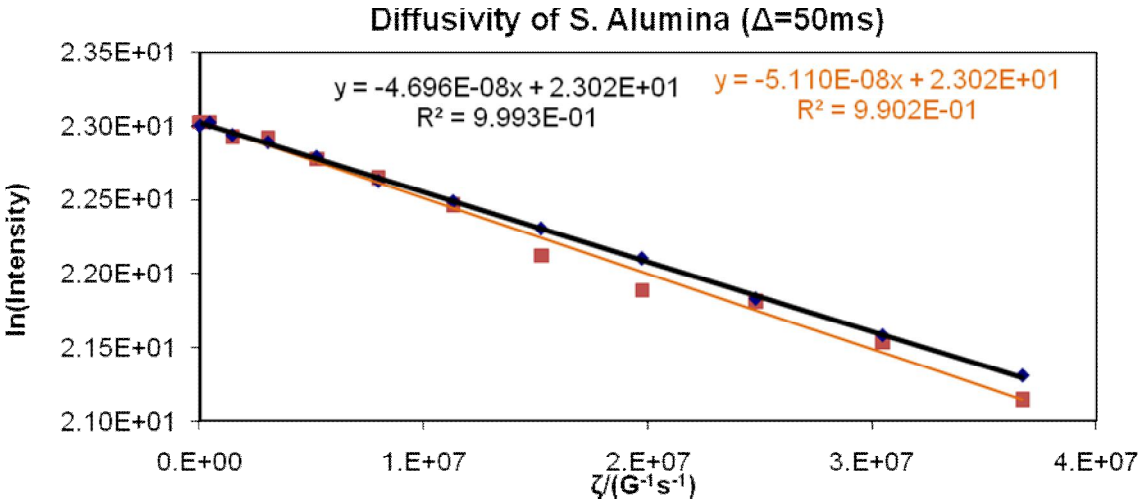
Diffusivity of S. Alumina (Δ=50ms)
y = -4.696E-08x + 2.302E+01
R² = 9.993E-01
y = -5.110E-08x + 2.302E+01
R² = 9.902E-01
ln(Intensity)
ζ/(G⁻¹s⁻¹)

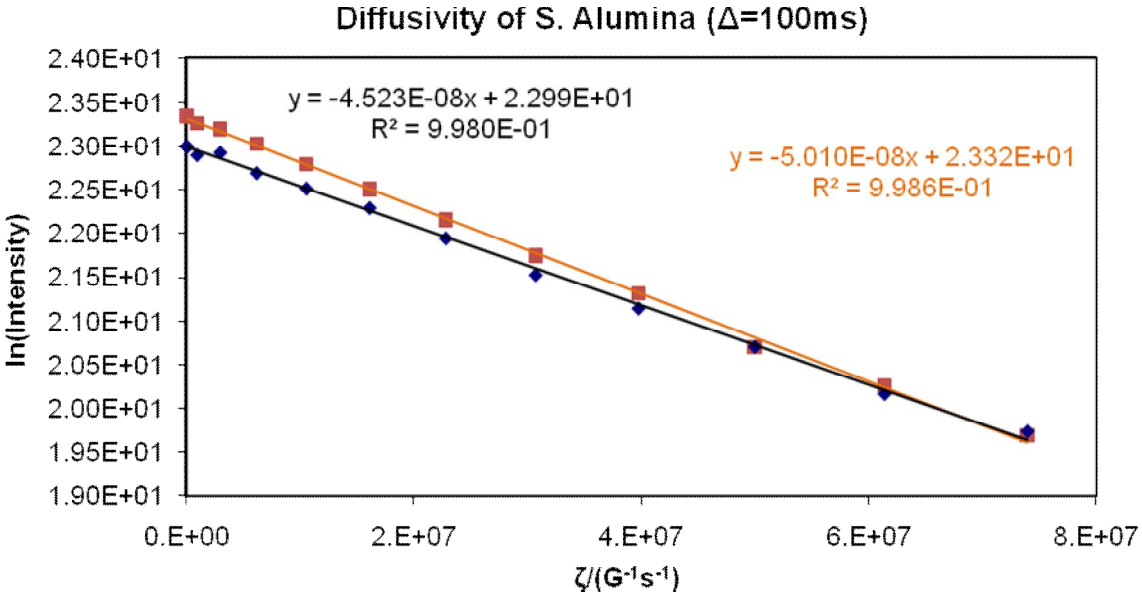
Diffusivity of S. Alumina (Δ=100ms)
y = -4.523E-08x + 2.299E+01
R² = 9.980E-01
y = -5.010E-08x + 2.332E+01
R² = 9.986E-01
ln(Intensity)
ζ/(G⁻¹s⁻¹)

Appendix (A7)

[NMR pulsed gradient spin echo technique II appendix figures]

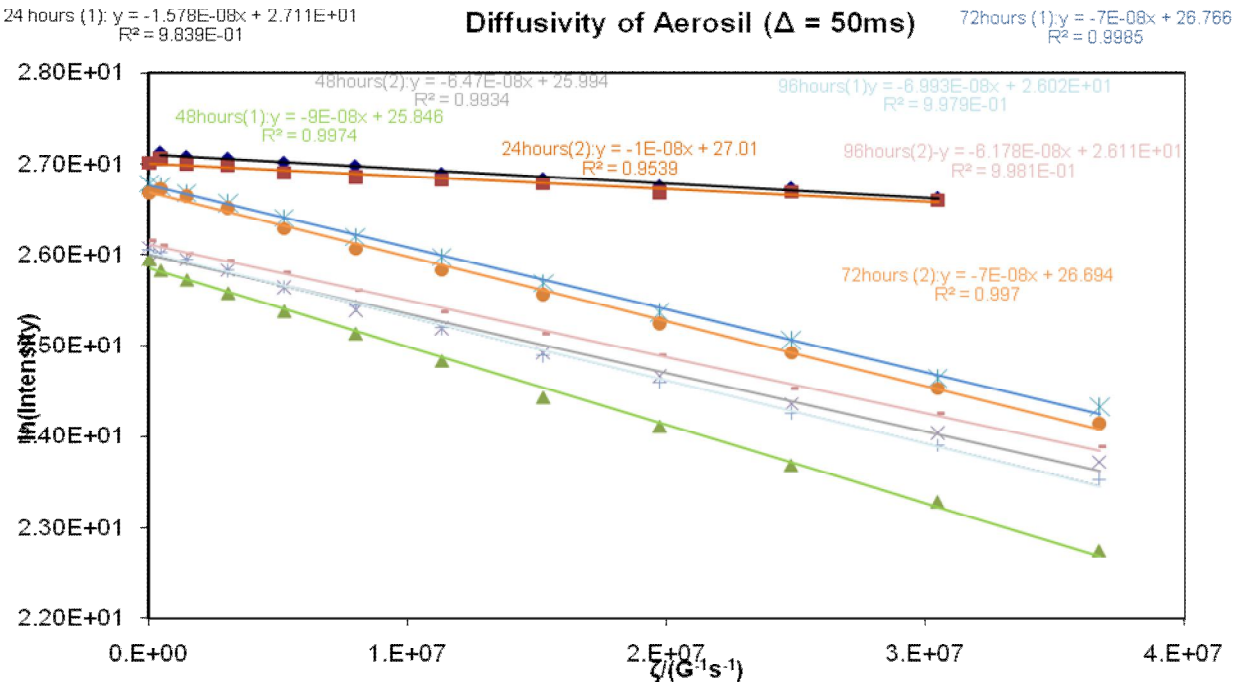

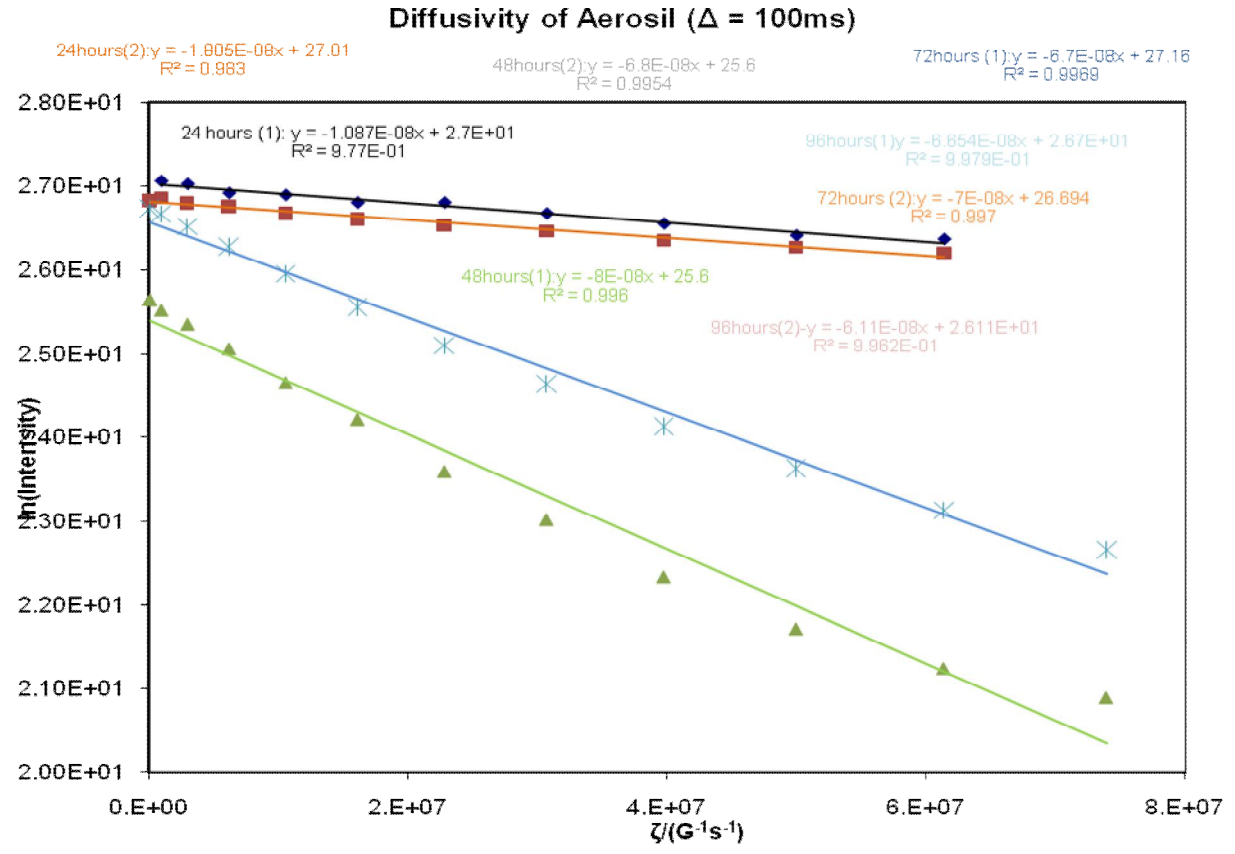

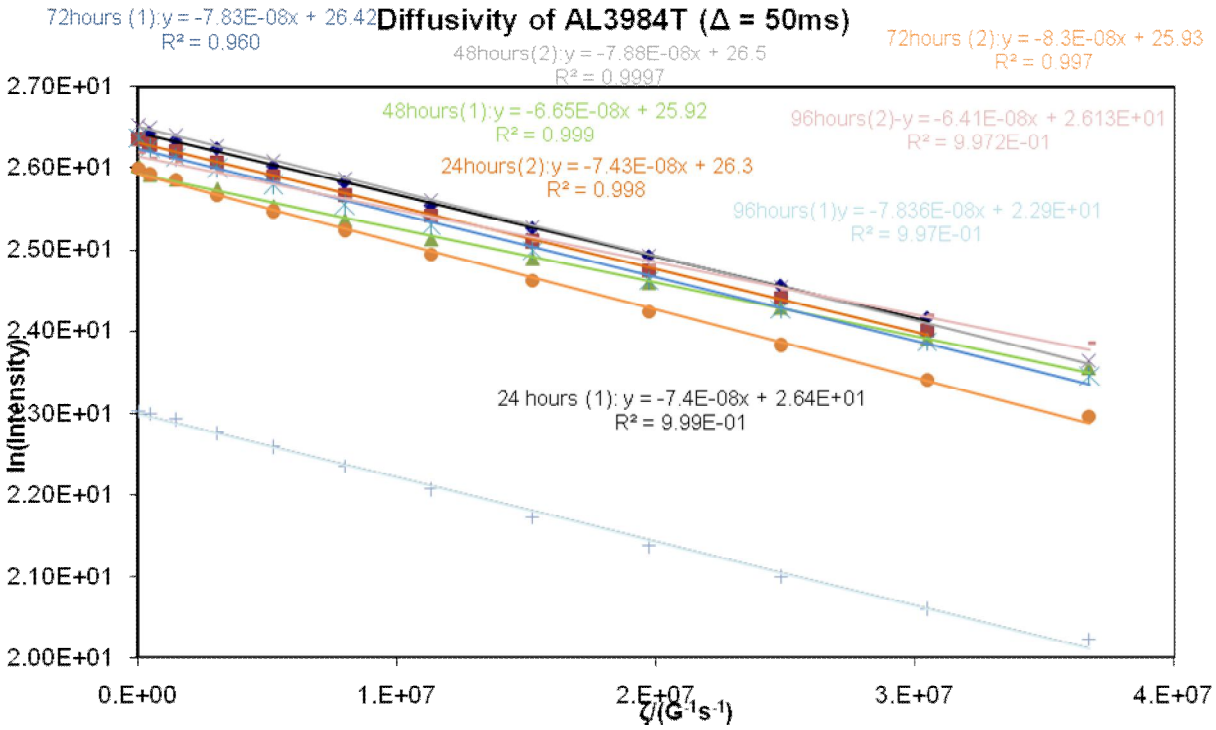
Diffusivity of AL3984T (Δ = 50ms)
72hours (1):y = -7.83E-08x + 26.42
R² = 0.960
48hours(2):y = -7.88E-08x + 26.5
R² = 0.9997
72hours (2):y = -8.3E-08x + 25.93
R² = 0.997
48hours(1):y = -6.65E-08x + 25.92
R² = 0.999
96hours(2)-y = -6.41E-08x + 2.613E+01
R² = 9.972E-01
24hours(2):y = -7.43E-08x + 26.3
R² = 0.998
96hours(1)y = -7.836E-08x + 2.29E+01
R² = 9.97E-01
24 hours (1): y = -7.4E-08x + 2.64E+01
R² = 9.99E-01
ln(Intensity)
2.70E+01
2.60E+01
2.50E+01
2.40E+01
2.30E+01
2.20E+01
2.10E+01
2.00E+01
0.E+00
1.E+07
2.E+07
3.E+07
4.E+07
ζ/(G⁻¹s⁻¹)

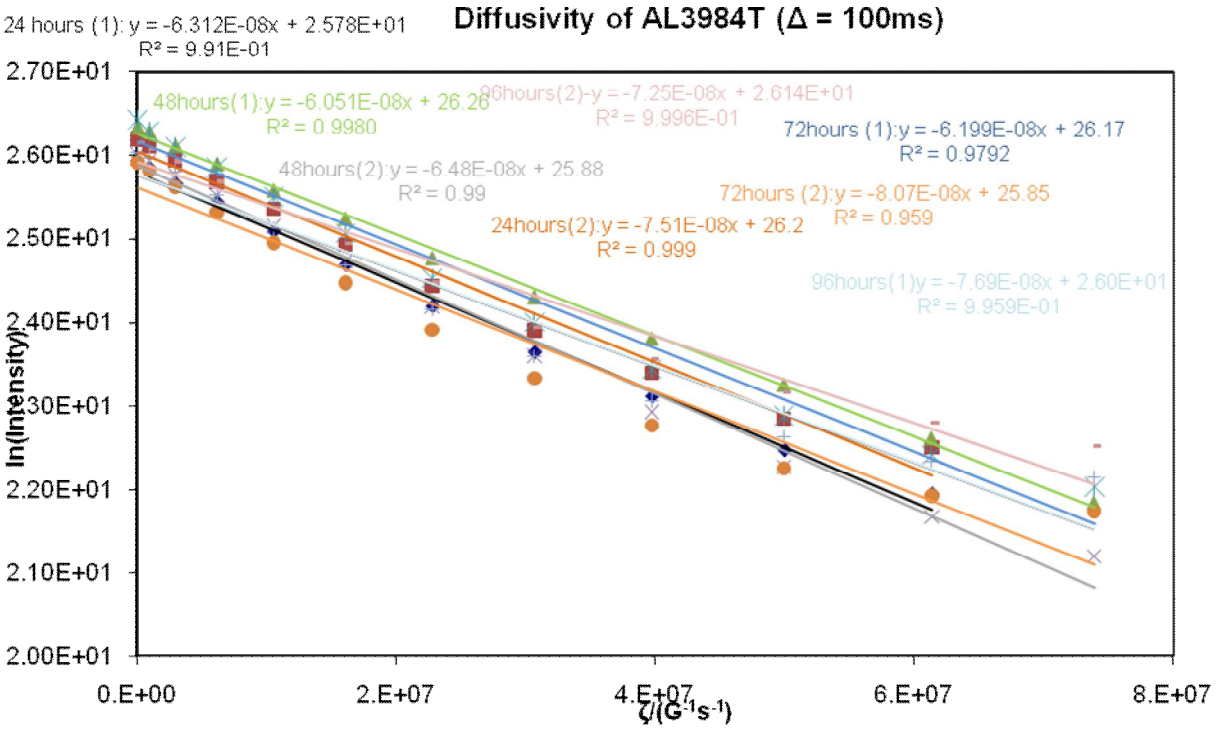
Diffusivity of AL3984T (Δ = 100ms)
24 hours (1): y = -6.312E-08x + 2.578E+01
R² = 9.91E-01
48hours(1):y = -6.051E-08x + 26.26
R² = 0.9980
96hours(2)-y = -7.25E-08x + 2.614E+01
R² = 9.996E-01
72hours (1):y = -6.199E-08x + 26.17
R² = 0.9792
48hours(2):y = -6.48E-08x + 25.88
R² = 0.99
72hours (2):y = -8.07E-08x + 25.85
R² = 0.959
24hours(2):y = -7.51E-08x + 26.2
R² = 0.999
96hours(1)y = -7.69E-08x + 2.60E+01
R² = 9.959E-01
ln(Intensity)
2.70E+01
2.60E+01
2.50E+01
2.40E+01
2.30E+01
2.20E+01
2.10E+01
2.00E+01
0.E+00
2.E+07
4.E+07
6.E+07
8.E+07
ζ/(G⁻¹s⁻¹)

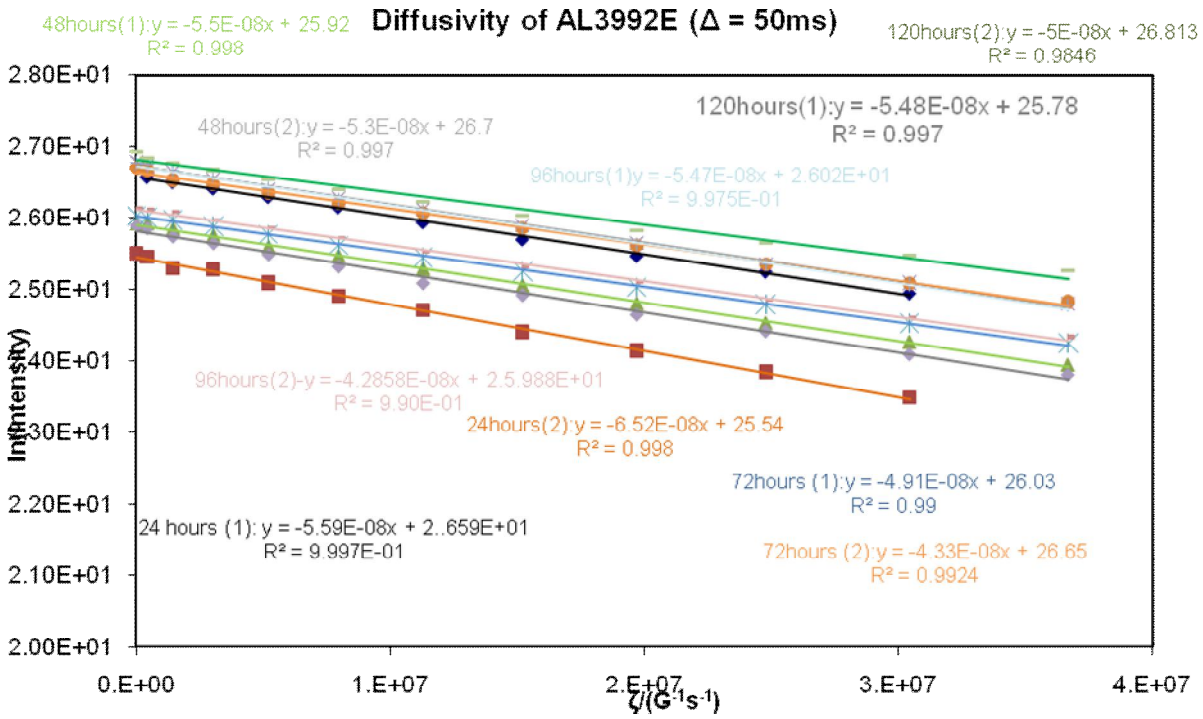
Diffusivity of AL3992E (Δ = 50ms)
48hours(1):y = -5.5E-08x + 25.92
R² = 0.998
120hours(2):y = -5E-08x + 26.813
R² = 0.9846
120hours(1):y = -5.48E-08x + 25.78
R² = 0.997
48hours(2):y = -5.3E-08x + 26.7
R² = 0.997
96hours(1)y = -5.47E-08x + 2.602E+01
R² = 9.975E-01
96hours(2)-y = -4.2858E-08x + 2.5.988E+01
R² = 9.90E-01
24hours(2):y = -6.52E-08x + 25.54
R² = 0.998
72hours (1):y = -4.91E-08x + 26.03
R² = 0.99
24 hours (1): y = -5.59E-08x + 2..659E+01
R² = 9.997E-01
72hours (2):y = -4.33E-08x + 26.65
R² = 0.9924
ln(Intensity)
2.80E+01
2.70E+01
2.60E+01
2.50E+01
2.40E+01
2.30E+01
2.20E+01
2.10E+01
2.00E+01
0.E+00
1.E+07
2.E+07
3.E+07
4.E+07
ζ/(G⁻¹s⁻¹)

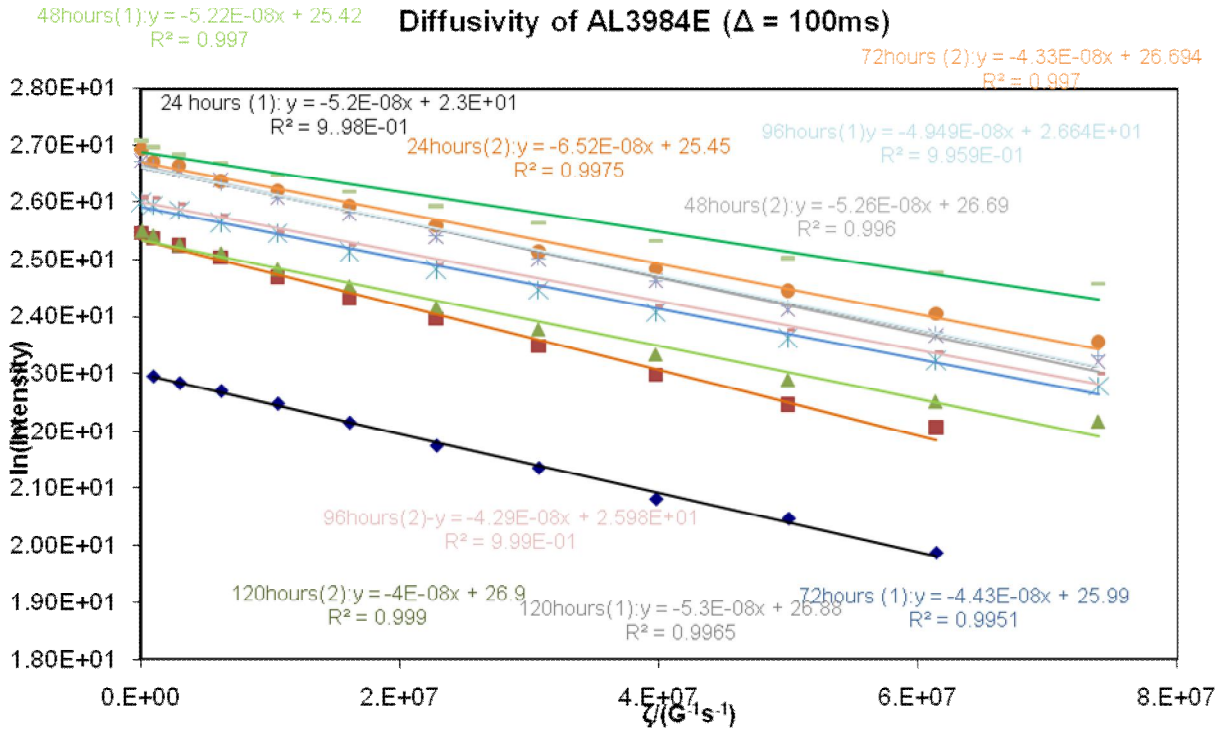
Diffusivity of AL3984E (Δ = 100ms)
48hours(1):y = -5.22E-08x + 25.42
R² = 0.997
72hours (2):y = -4.33E-08x + 26.694
R² = 0.997
24 hours (1): y = -5.2E-08x + 2.3E+01
R² = 9..98E-01
24hours(2):y = -6.52E-08x + 25.45
R² = 0.9975
96hours(1)y = -4.949E-08x + 2.664E+01
R² = 9.959E-01
48hours(2):y = -5.26E-08x + 26.69
R² = 0.996
96hours(2)-y = -4.29E-08x + 2.598E+01
R² = 9.99E-01
120hours(2):y = -4E-08x + 26.9
R² = 0.999
120hours(1):y = -5.3E-08x + 26.88
R² = 0.9965
72hours (1):y = -4.43E-08x + 25.99
R² = 0.9951
ln(Intensity)
2.80E+01
2.70E+01
2.60E+01
2.50E+01
2.40E+01
2.30E+01
2.20E+01
2.10E+01
2.00E+01
1.90E+01
1.80E+01
0.E+00
2.E+07
4.E+07
6.E+07
8.E+07
ζ/(G⁻¹s⁻¹)

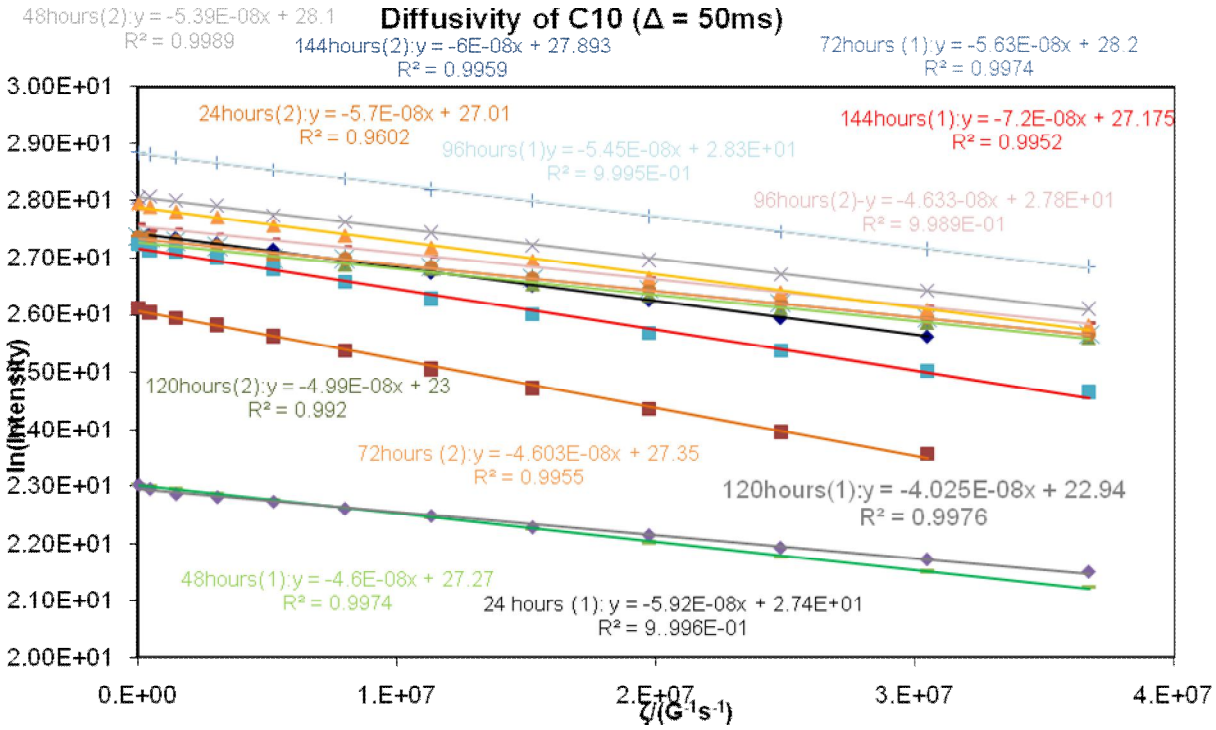
Diffusivity of C10 (Δ = 50ms)
48hours(2):y = -5.39E-08x + 28.1
R² = 0.9989
144hours(2):y = -6E-08x + 27.893
R² = 0.9959
72hours (1):y = -5.63E-08x + 28.2
R² = 0.9974
24hours(2):y = -5.7E-08x + 27.01
R² = 0.9602
144hours(1):y = -7.2E-08x + 27.175
R² = 0.9952
96hours(1)y = -5.45E-08x + 2.83E+01
R² = 9.995E-01
96hours(2)-y = -4.633-08x + 2.78E+01
R² = 9.989E-01
120hours(2):y = -4.99E-08x + 23
R² = 0.992
72hours (2):y = -4.603E-08x + 27.35
R² = 0.9955
120hours(1):y = -4.025E-08x + 22.94
R² = 0.9976
48hours(1):y = -4.6E-08x + 27.27
R² = 0.9974
24 hours (1): y = -5.92E-08x + 2.74E+01
R² = 9..996E-01
ln(Intensity)
3.00E+01
2.90E+01
2.80E+01
2.70E+01
2.60E+01
2.50E+01
2.40E+01
2.30E+01
2.20E+01
2.10E+01
2.00E+01
0.E+00
1.E+07
2.E+07
3.E+07
4.E+07
ζ/(G⁻¹s⁻¹)

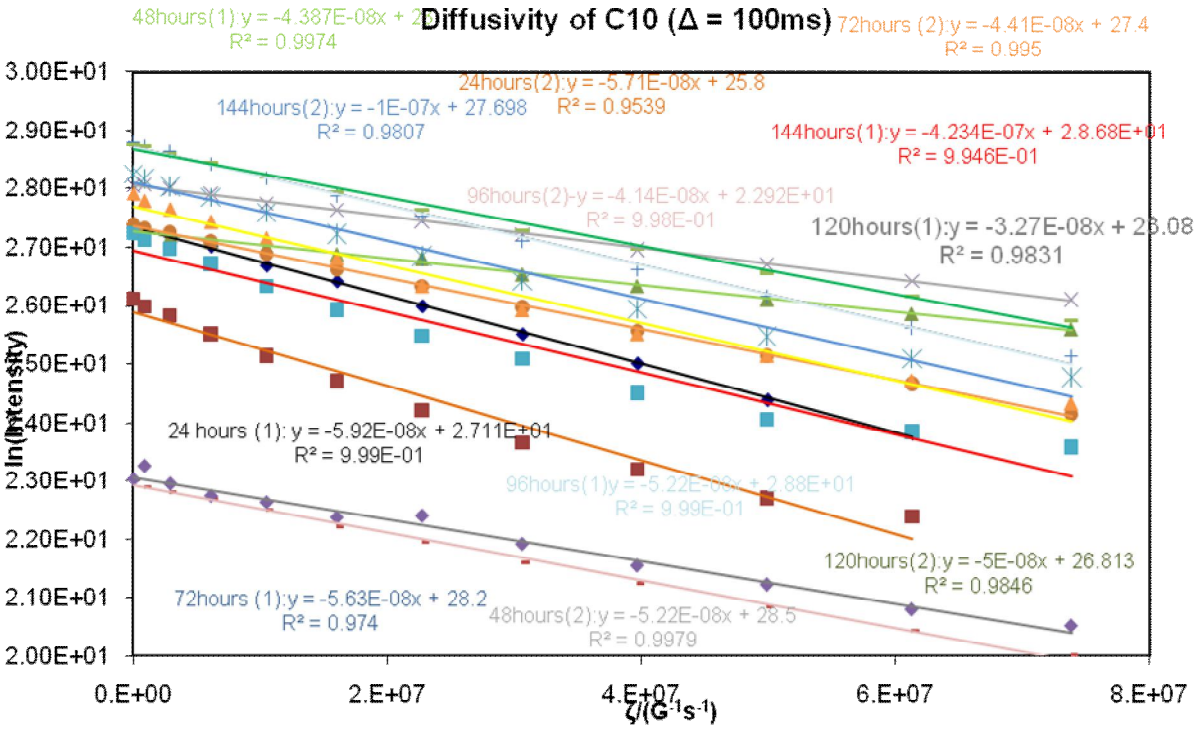
Diffusivity of C10 (Δ = 100ms)
48hours(1):y = -4.387E-08x + 2
R² = 0.9974
72hours (2):y = -4.41E-08x + 27.4
R² = 0.995
24hours(2):y = -5.71E-08x + 25.8
R² = 0.9539
144hours(2):y = -1E-07x + 27.698
R² = 0.9807
144hours(1):y = -4.234E-07x + 2.8.68E+01
R² = 9.946E-01
96hours(2)-y = -4.14E-08x + 2.292E+01
R² = 9.98E-01
120hours(1):y = -3.27E-08x + 28.08
R² = 0.9831
24 hours (1): y = -5.92E-08x + 2.711E+01
R² = 9.99E-01
96hours(1)y = -5.22E-08x + 2.88E+01
R² = 9.99E-01
120hours(2):y = -5E-08x + 26.813
R² = 0.9846
72hours (1):y = -5.63E-08x + 28.2
R² = 0.974
48hours(2):y = -5.22E-08x + 28.5
R² = 0.9979
ln(Intensity)
3.00E+01
2.90E+01
2.80E+01
2.70E+01
2.60E+01
2.50E+01
2.40E+01
2.30E+01
2.20E+01
2.10E+01
2.00E+01
0.E+00
2.E+07
4.E+07
6.E+07
8.E+07
ζ/(G⁻¹s⁻¹)

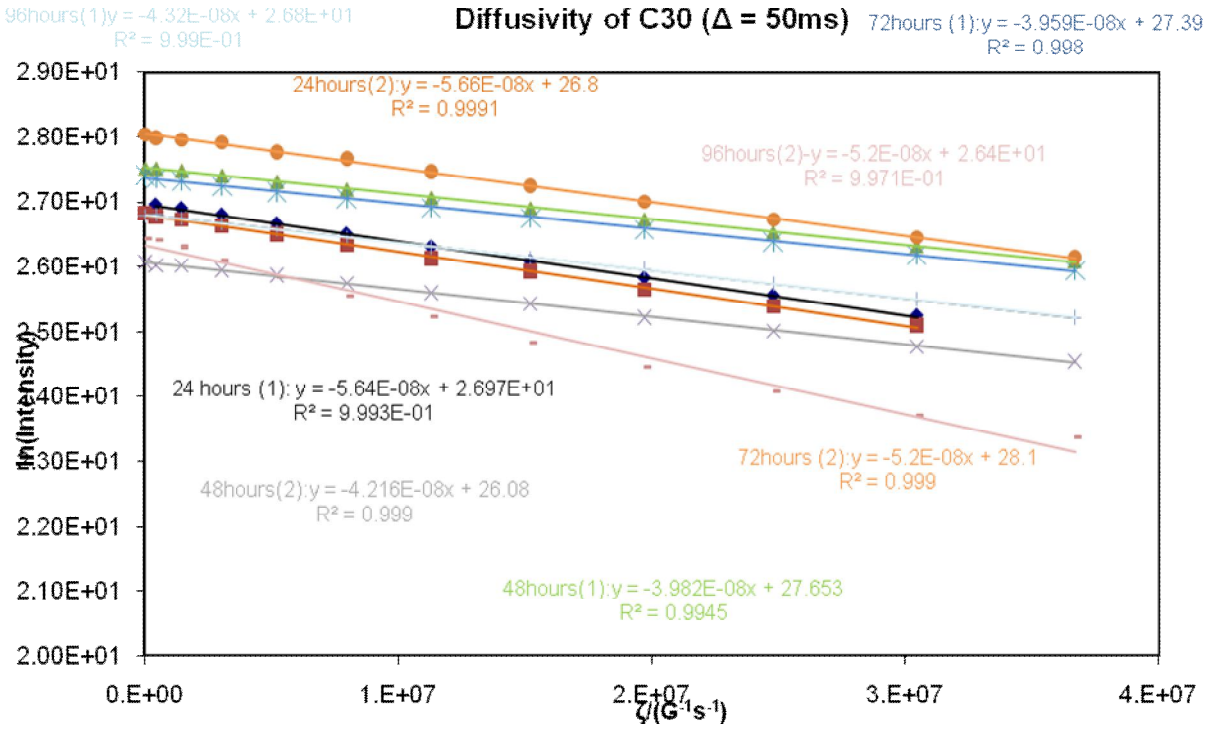
Diffusivity of C30 (Δ = 50ms)
96hours(1)y = -4.32E-08x + 2.68E+01
R² = 9.99E-01
72hours (1):y = -3.959E-08x + 27.39
R² = 0.998
24hours(2):y = -5.66E-08x + 26.8
R² = 0.9991
96hours(2)-y = -5.2E-08x + 2.64E+01
R² = 9.971E-01
24 hours (1): y = -5.64E-08x + 2.697E+01
R² = 9.993E-01
72hours (2):y = -5.2E-08x + 28.1
R² = 0.999
48hours(2):y = -4.216E-08x + 26.08
R² = 0.999
48hours(1):y = -3.982E-08x + 27.653
R² = 0.9945
ln(Intensity)
2.90E+01
2.80E+01
2.70E+01
2.60E+01
2.50E+01
2.40E+01
2.30E+01
2.20E+01
2.10E+01
2.00E+01
0.E+00
1.E+07
2.E+07
3.E+07
4.E+07
ζ/(G⁻¹s⁻¹)

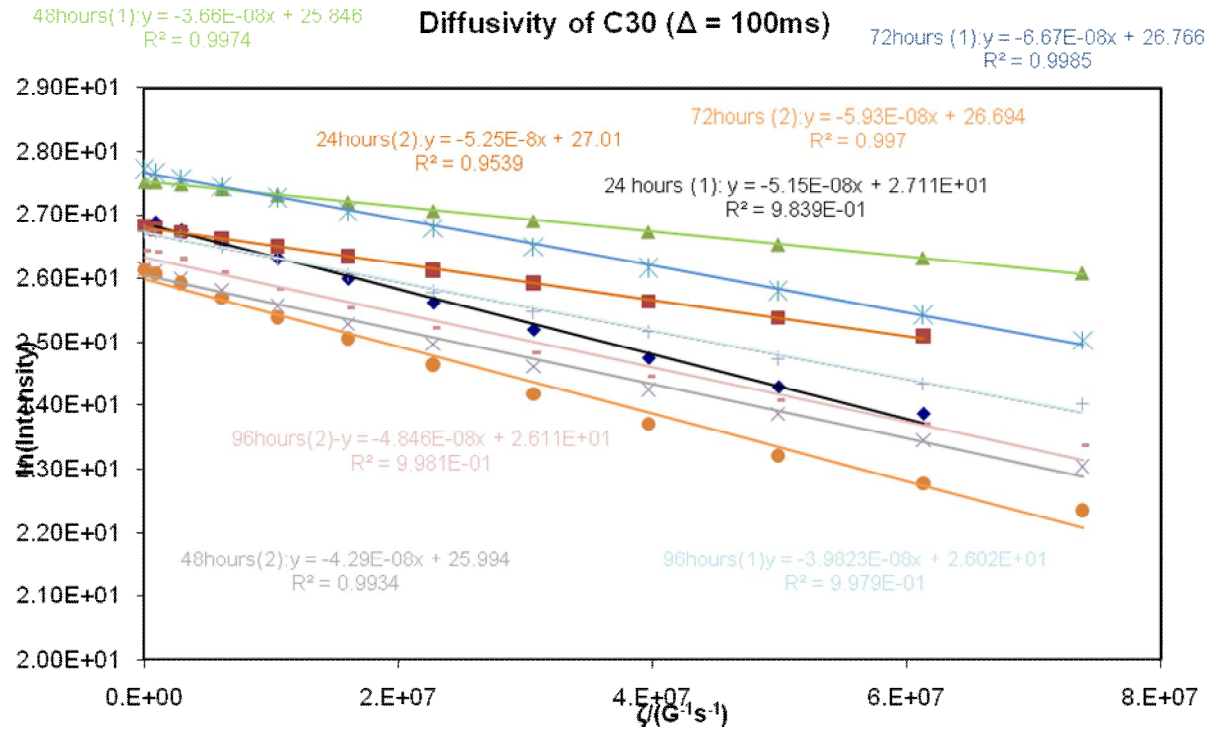
Diffusivity of C30 (Δ = 100ms)
48hours(1):y = -3.66E-08x + 25.846
R² = 0.9974
72hours (1):y = -6.67E-08x + 26.766
R² = 0.9985
72hours (2):y = -5.93E-08x + 26.694
R² = 0.997
24hours(2):y = -5.25E-8x + 27.01
R² = 0.9539
24 hours (1): y = -5.15E-08x + 2.711E+01
R² = 9.839E-01
96hours(2)-y = -4.846E-08x + 2.611E+01
R² = 9.981E-01
48hours(2):y = -4.29E-08x + 25.994
R² = 0.9934
96hours(1)y = -3.9823E-08x + 2.602E+01
R² = 9.979E-01
ln(Intensity)
2.90E+01
2.80E+01
2.70E+01
2.60E+01
2.50E+01
2.40E+01
2.30E+01
2.20E+01
2.10E+01
2.00E+01
0.E+00
2.E+07
4.E+07
6.E+07
8.E+07
ζ/(G⁻¹s⁻¹)

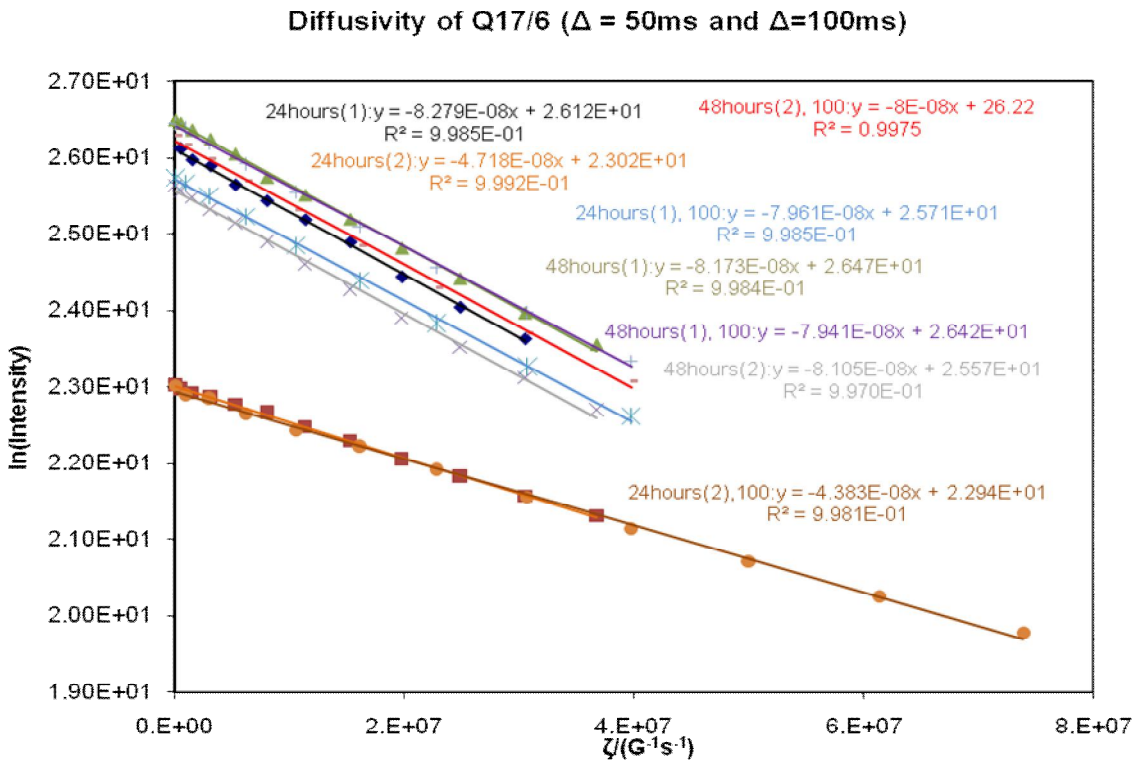
Diffusivity of Q17/6 (Δ = 50ms and Δ=100ms)
24hours(1):y = -8.279E-08x + 2.612E+01
R² = 9.985E-01
48hours(2), 100:y = -8E-08x + 26.22
R² = 0.9975
24hours(2):y = -4.718E-08x + 2.302E+01
R² = 9.992E-01
24hours(1), 100:y = -7.961E-08x + 2.571E+01
R² = 9.985E-01
48hours(1):y = -8.173E-08x + 2.647E+01
R² = 9.984E-01
48hours(1), 100:y = -7.941E-08x + 2.642E+01
48hours(2):y = -8.105E-08x + 2.557E+01
R² = 9.970E-01
24hours(2),100:y = -4.383E-08x + 2.294E+01
R² = 9.981E-01
ln(Intensity)
2.70E+01
2.60E+01
2.50E+01
2.40E+01
2.30E+01
2.20E+01
2.10E+01
2.00E+01
1.90E+01
0.E+00
2.E+07
4.E+07
6.E+07
8.E+07
ζ/(G-1s-1)

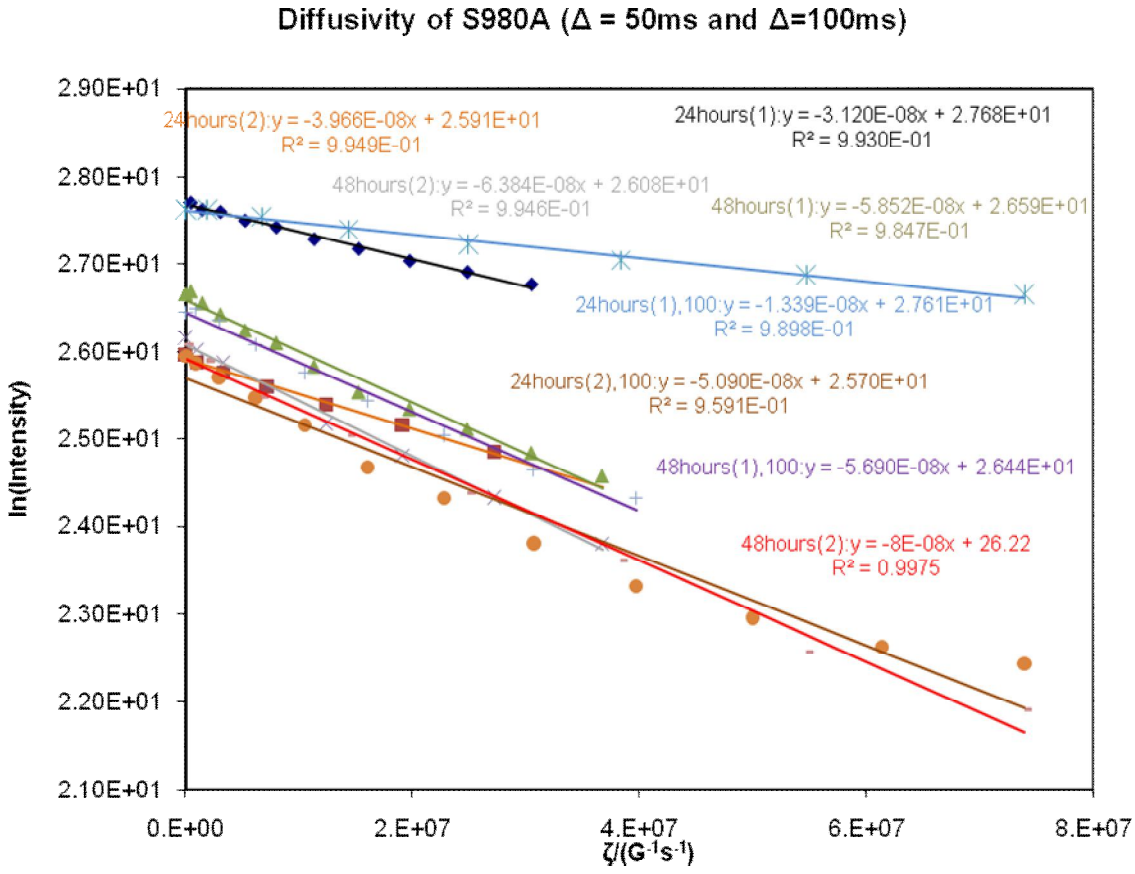
Diffusivity of S980A (Δ = 50ms and Δ=100ms)
24hours(2):y = -3.966E-08x + 2.591E+01
R² = 9.949E-01
24hours(1):y = -3.120E-08x + 2.768E+01
R² = 9.930E-01
48hours(2):y = -6.384E-08x + 2.608E+01
R² = 9.946E-01
48hours(1):y = -5.852E-08x + 2.659E+01
R² = 9.847E-01
24hours(1),100:y = -1.339E-08x + 2.761E+01
R² = 9.898E-01
24hours(2),100:y = -5.090E-08x + 2.570E+01
R² = 9.591E-01
48hours(1),100:y = -5.690E-08x + 2.644E+01
48hours(2):y = -8E-08x + 26.22
R² = 0.9975
ln(Intensity)
2.90E+01
2.80E+01
2.70E+01
2.60E+01
2.50E+01
2.40E+01
2.30E+01
2.20E+01
2.10E+01
0.E+00
2.E+07
4.E+07
6.E+07
8.E+07
ζ/(G-1s-1)

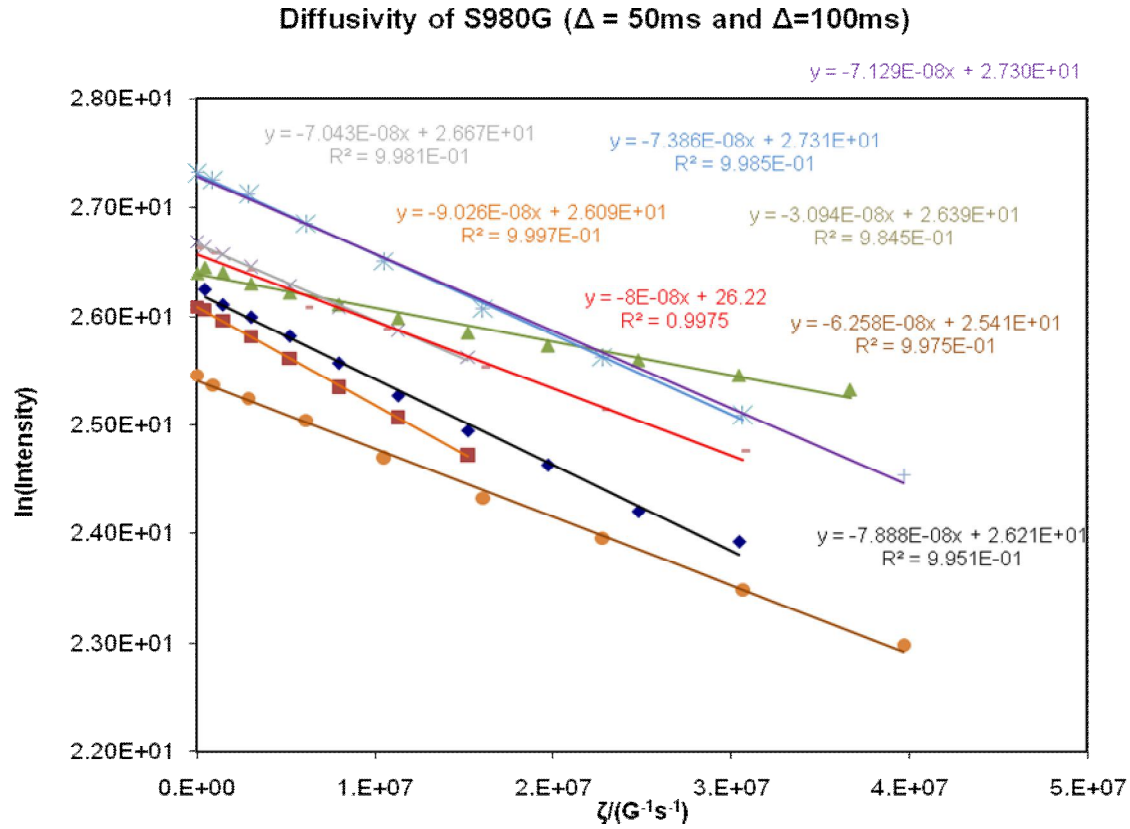
Diffusivity of S980G (Δ = 50ms and Δ=100ms)
y = -7.129E-08x + 2.730E+01
y = -7.043E-08x + 2.667E+01
R² = 9.981E-01
y = -7.386E-08x + 2.731E+01
R² = 9.985E-01
y = -9.026E-08x + 2.609E+01
R² = 9.997E-01
y = -3.094E-08x + 2.639E+01
R² = 9.845E-01
y = -8E-08x + 26.22
R² = 0.9975
y = -6.258E-08x + 2.541E+01
R² = 9.975E-01
y = -7.888E-08x + 2.621E+01
R² = 9.951E-01
ln(Intensity)
ζ/(G-1s-1)

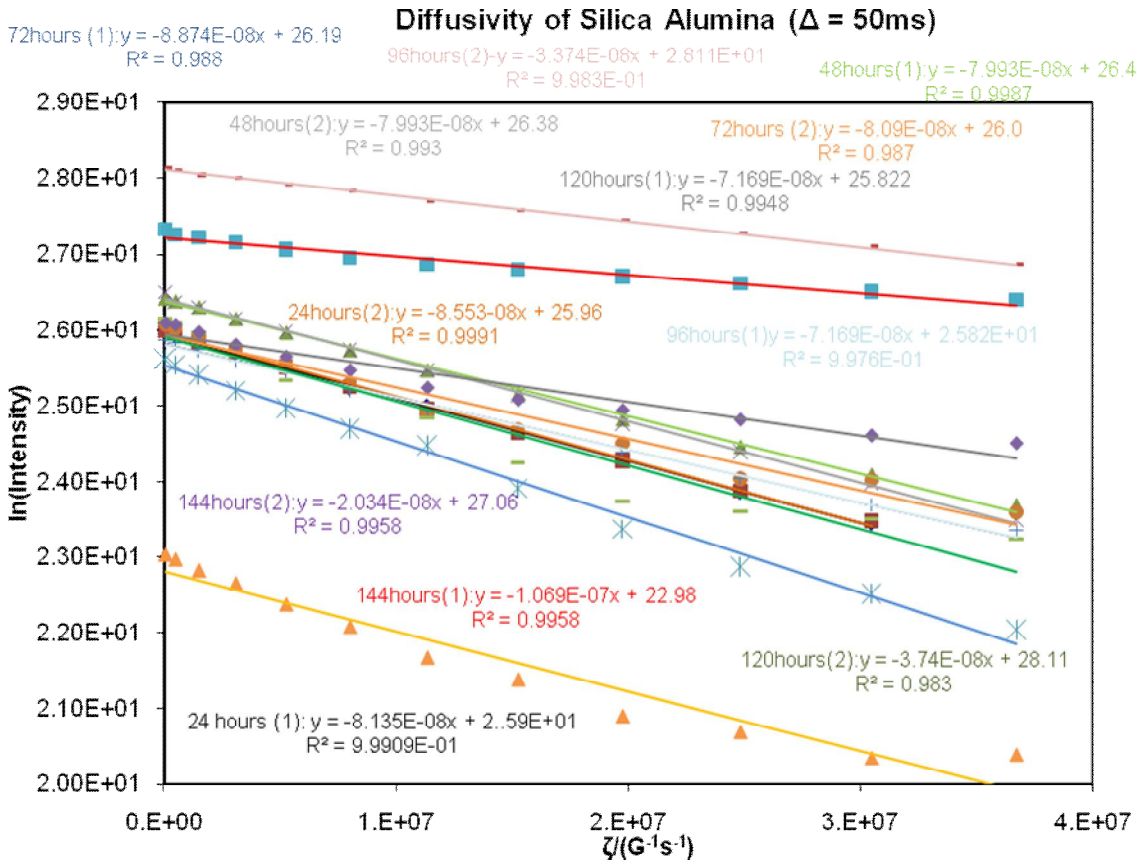
Diffusivity of Silica Alumina (Δ = 50ms)
72hours (1):y = -8.874E-08x + 26.19
R² = 0.988
96hours(2)-y = -3.374E-08x + 2.811E+01
R² = 9.983E-01
48hours(1):y = -7.993E-08x + 26.4
R² = 0.9987
48hours(2):y = -7.993E-08x + 26.38
R² = 0.993
72hours (2):y = -8.09E-08x + 26.0
R² = 0.987
120hours(1):y = -7.169E-08x + 25.822
R² = 0.9948
24hours(2):y = -8.553-08x + 25.96
R² = 0.9991
96hours(1)y = -7.169E-08x + 2.582E+01
R² = 9.976E-01
144hours(2):y = -2.034E-08x + 27.06
R² = 0.9958
144hours(1):y = -1.069E-07x + 22.98
R² = 0.9958
120hours(2):y = -3.74E-08x + 28.11
R² = 0.983
24 hours (1): y = -8.135E-08x + 2..59E+01
R² = 9.9909E-01
ln(Intensity)
ζ/(G-1s-1)

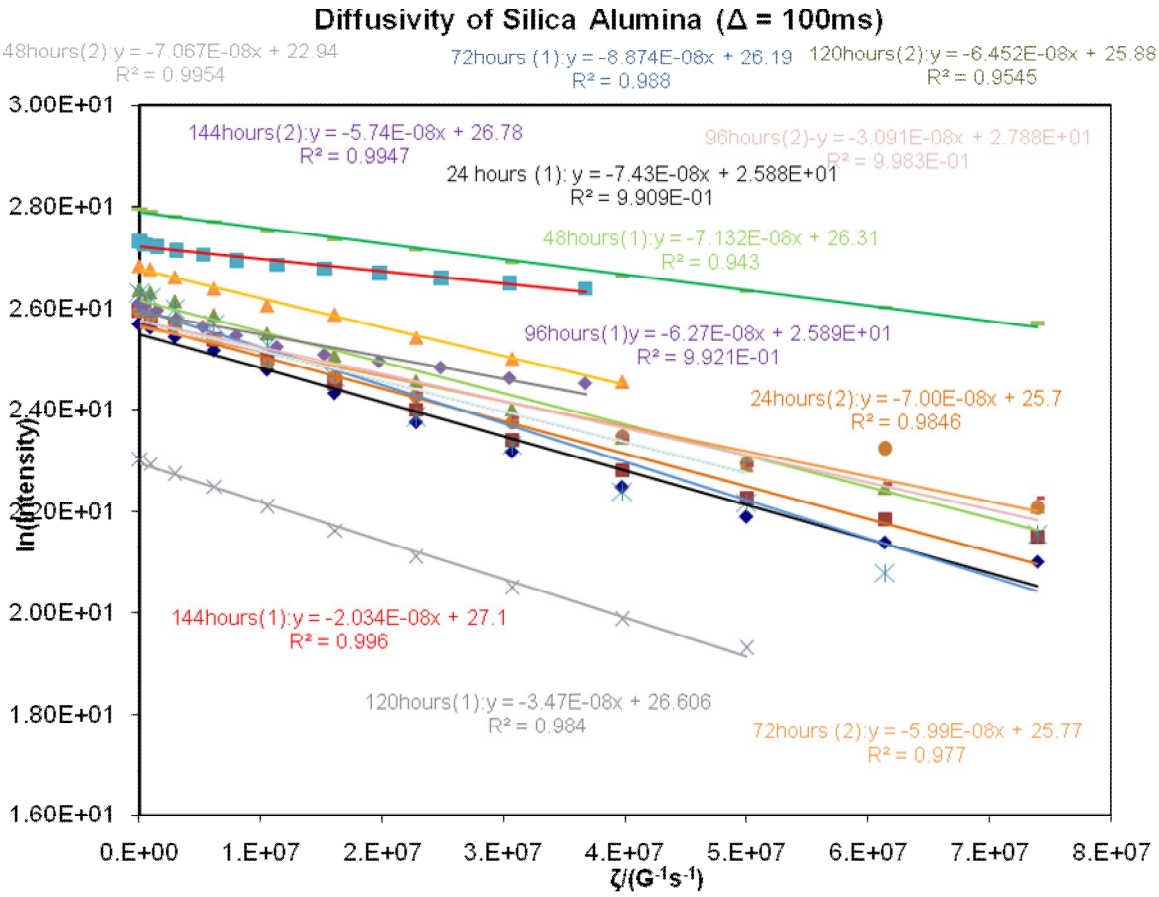
Diffusivity of Silica Alumina (Δ = 100ms)
48hours(2):y = -7.067E-08x + 22.94
R² = 0.9954
72hours (1):y = -8.874E-08x + 26.19
R² = 0.988
120hours(2):y = -6.452E-08x + 25.88
R² = 0.9545
144hours(2):y = -5.74E-08x + 26.78
R² = 0.9947
96hours(2)-y = -3.091E-08x + 2.788E+01
R² = 9.983E-01
24 hours (1): y = -7.43E-08x + 2.588E+01
R² = 9.909E-01
48hours(1):y = -7.132E-08x + 26.31
R² = 0.943
96hours(1)y = -6.27E-08x + 2.589E+01
R² = 9.921E-01
24hours(2):y = -7.00E-08x + 25.7
R² = 0.9846
144hours(1):y = -2.034E-08x + 27.1
R² = 0.996
120hours(1):y = -3.47E-08x + 26.606
R² = 0.984
72hours (2):y = -5.99E-08x + 25.77
R² = 0.977
3.00E+01
2.80E+01
2.60E+01
2.40E+01
2.20E+01
2.00E+01
1.80E+01
1.60E+01
ln(Intensity)
0.E+00
1.E+07
2.E+07
3.E+07
4.E+07
5.E+07
6.E+07
7.E+07
8.E+07
ζ/(G⁻¹s⁻¹)

Appendix (A8)

(Experimental corrections appendix figures)

Effect of pore connectivity on mercury entrapment

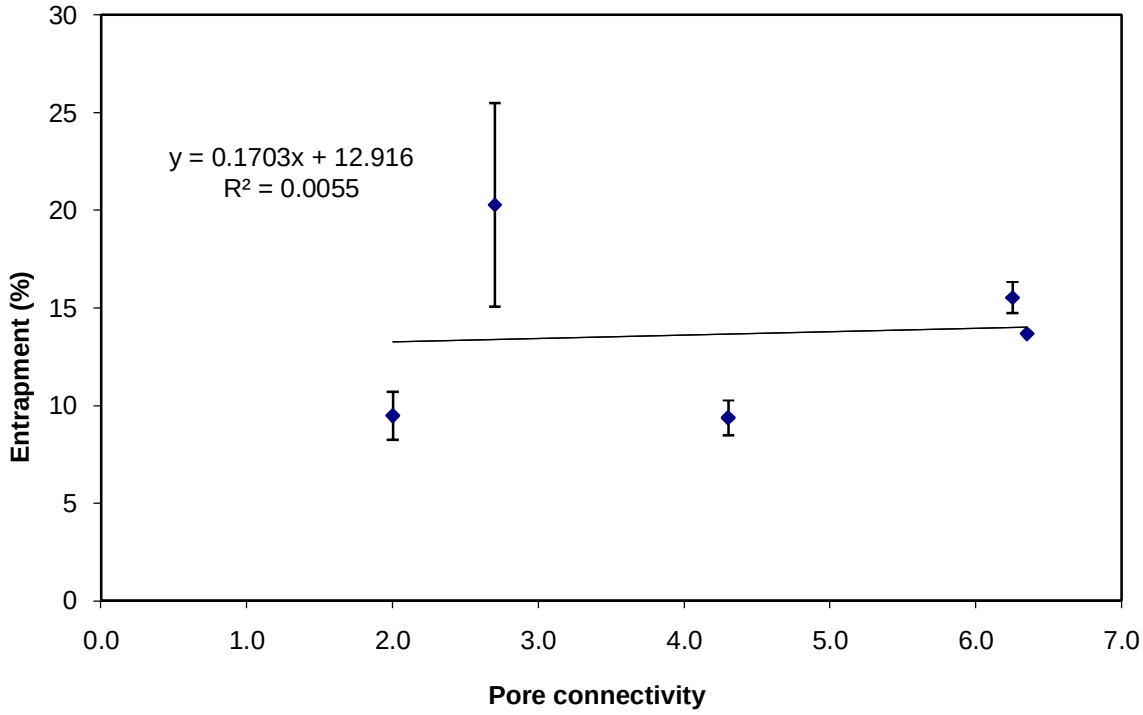

Effect of pore connectivity on tortuosity, Δ = 50 ms in case I

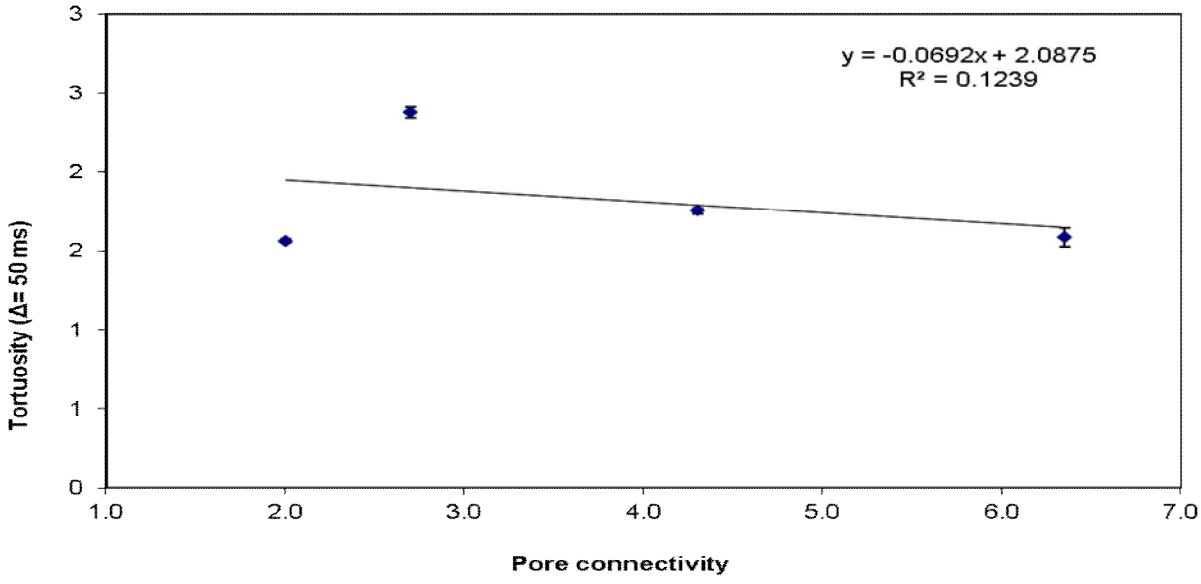

Effect of pore connectivity on tortuosity, Δ = 100 ms in case I

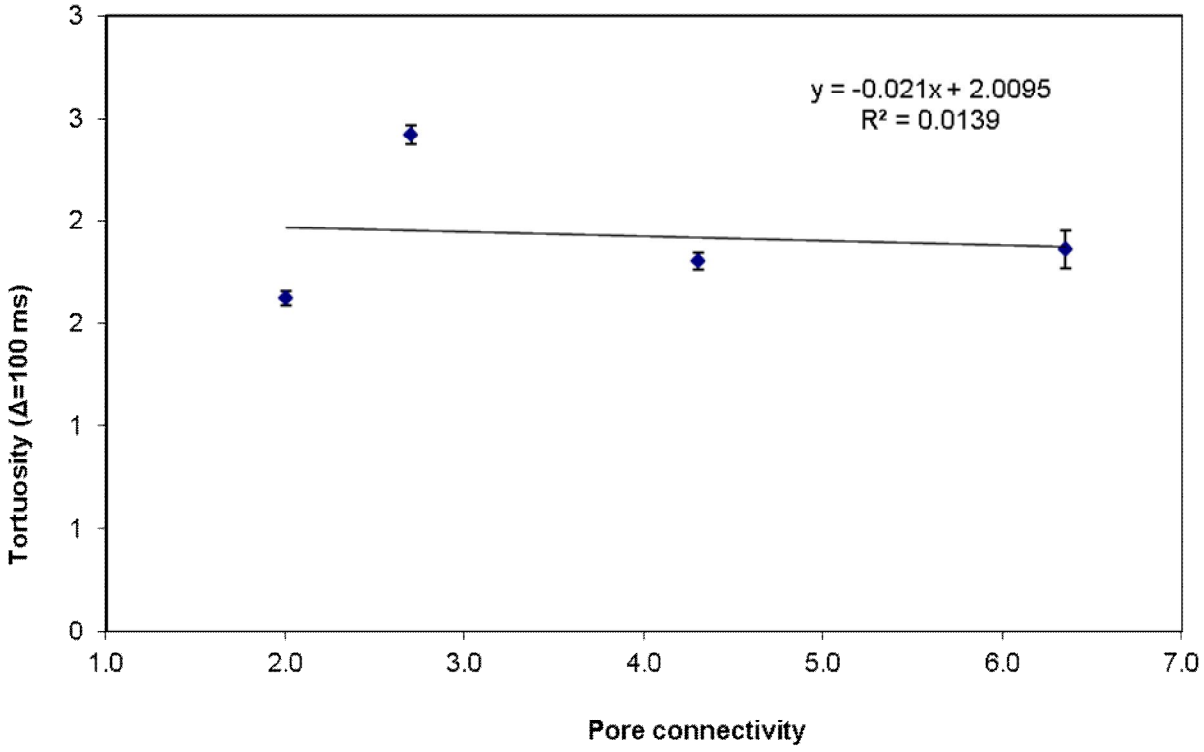

Effect of pore connectivity on tortuosity, Δ = 50 ms in case II

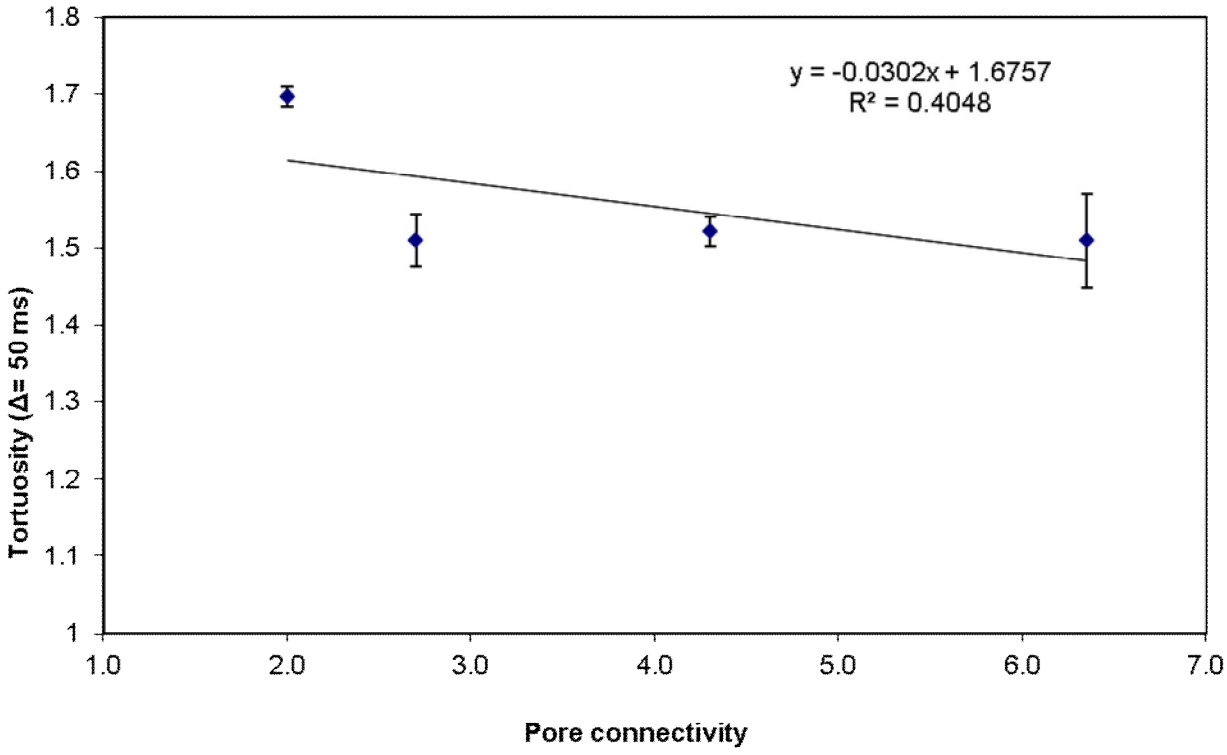

Effect of pore connectivity on tortuosity, Δ = 100 ms in case II

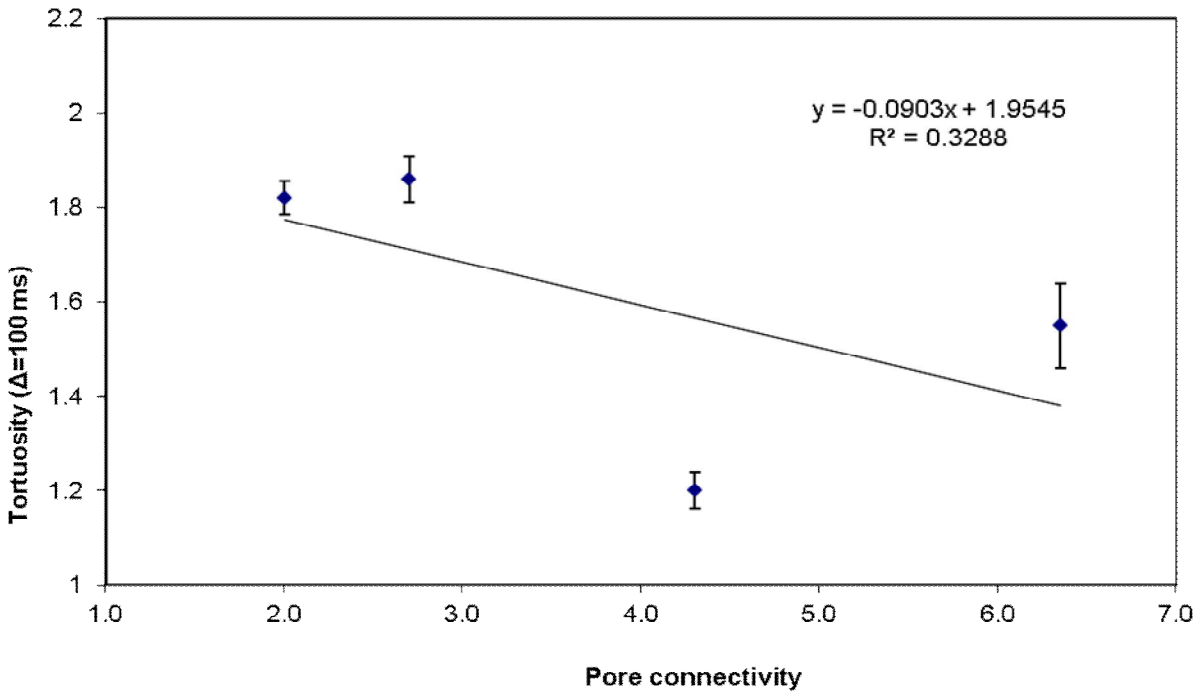

Effect of variance of PSD on tortuosity, Δ = 50 ms in case II

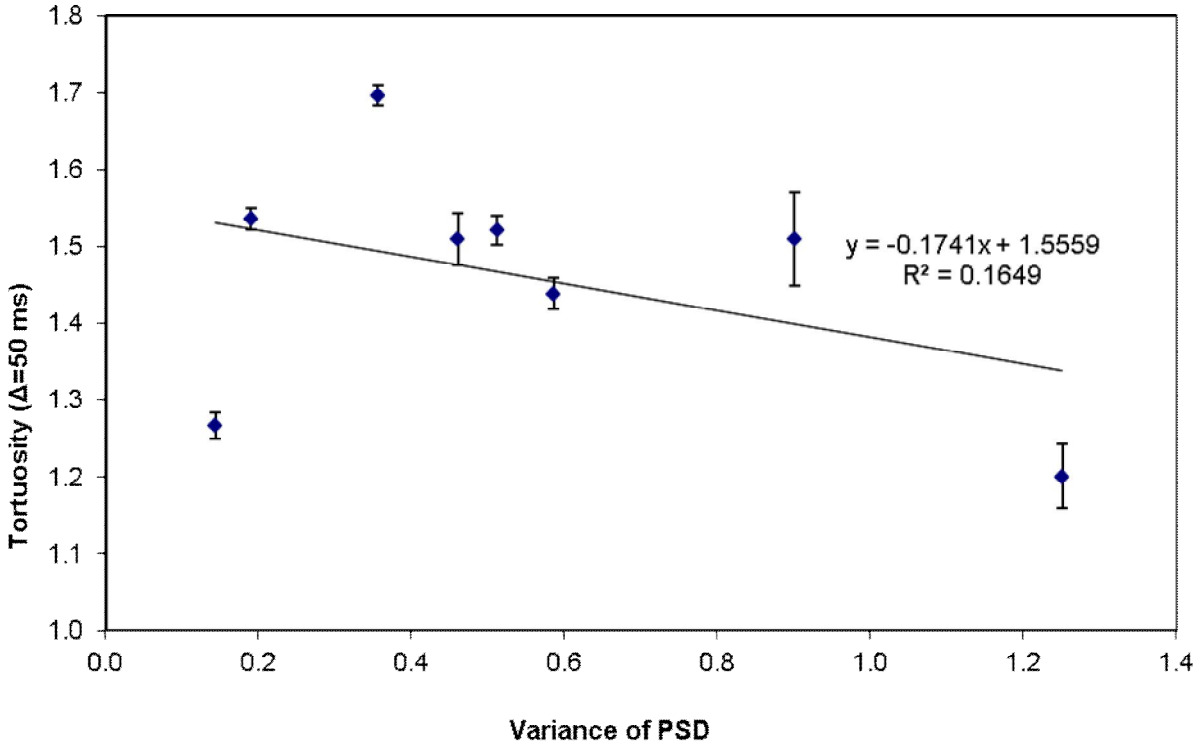

Effect of variance of PSD on tortuosity, Δ = 100 ms in case II

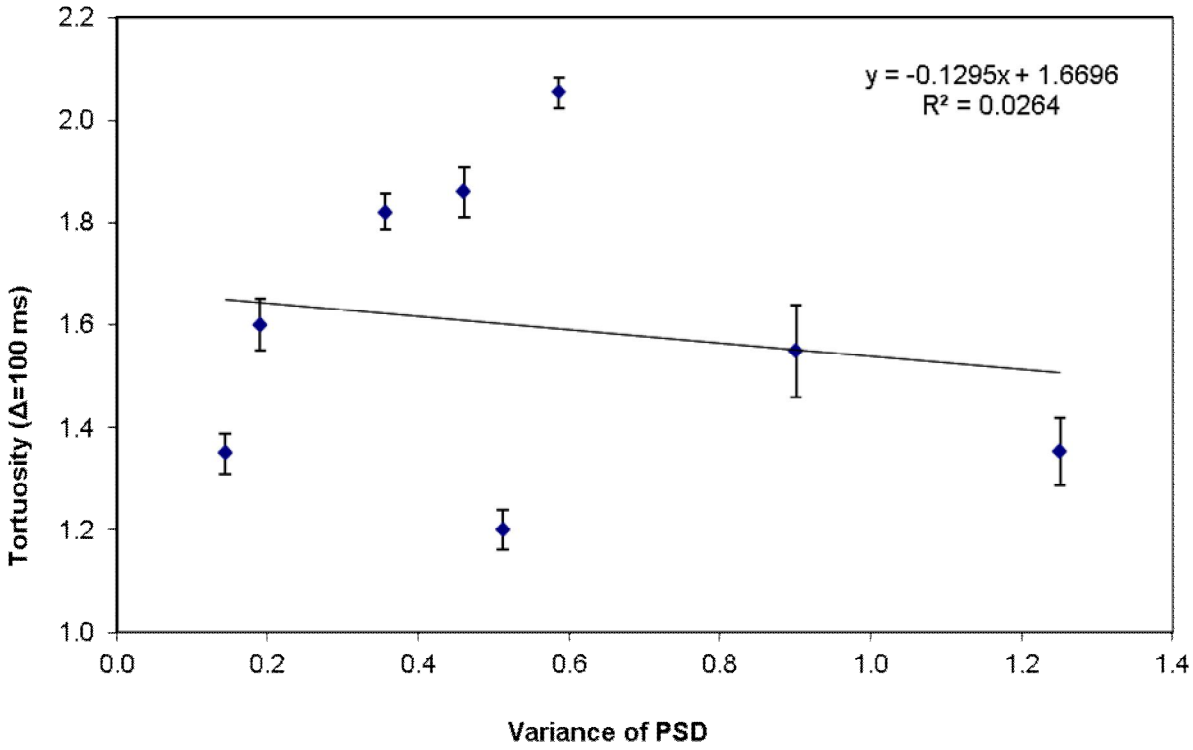

Effect of mercury entrapment on tortuosity, Δ = 50 ms in case II

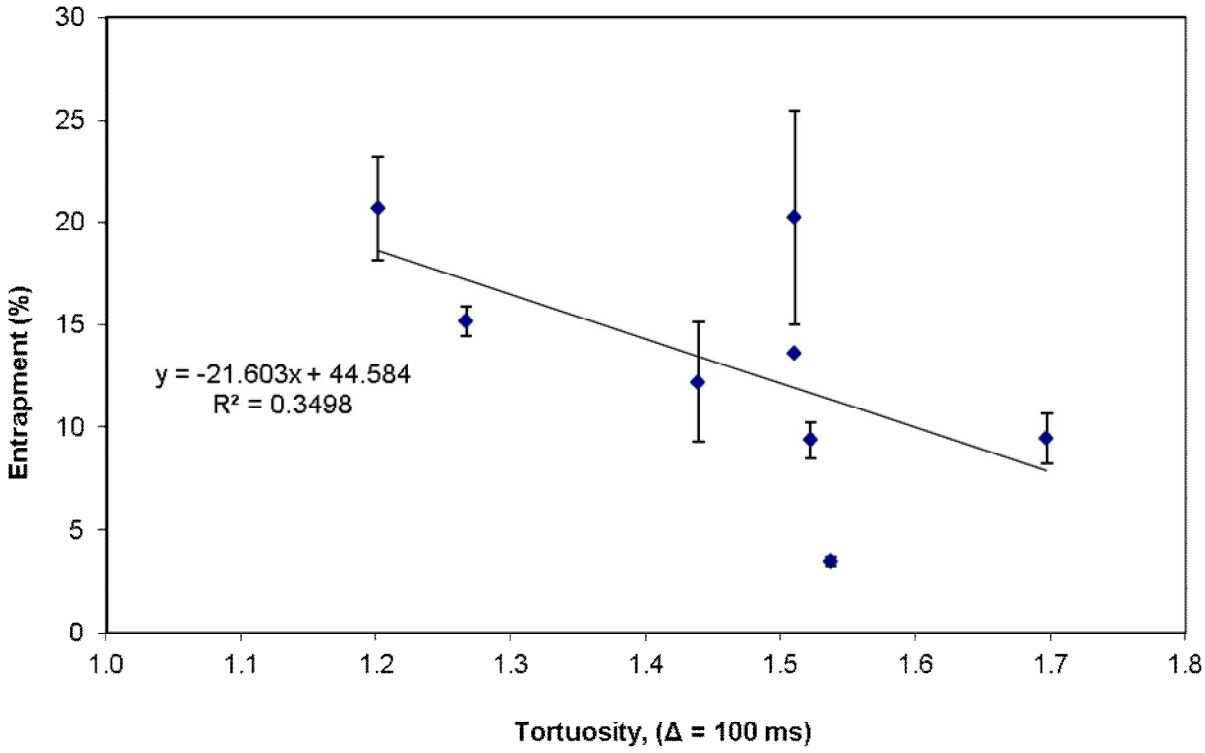

Effect of mercury entrapment on tortuosity, Δ = 100 ms in case II

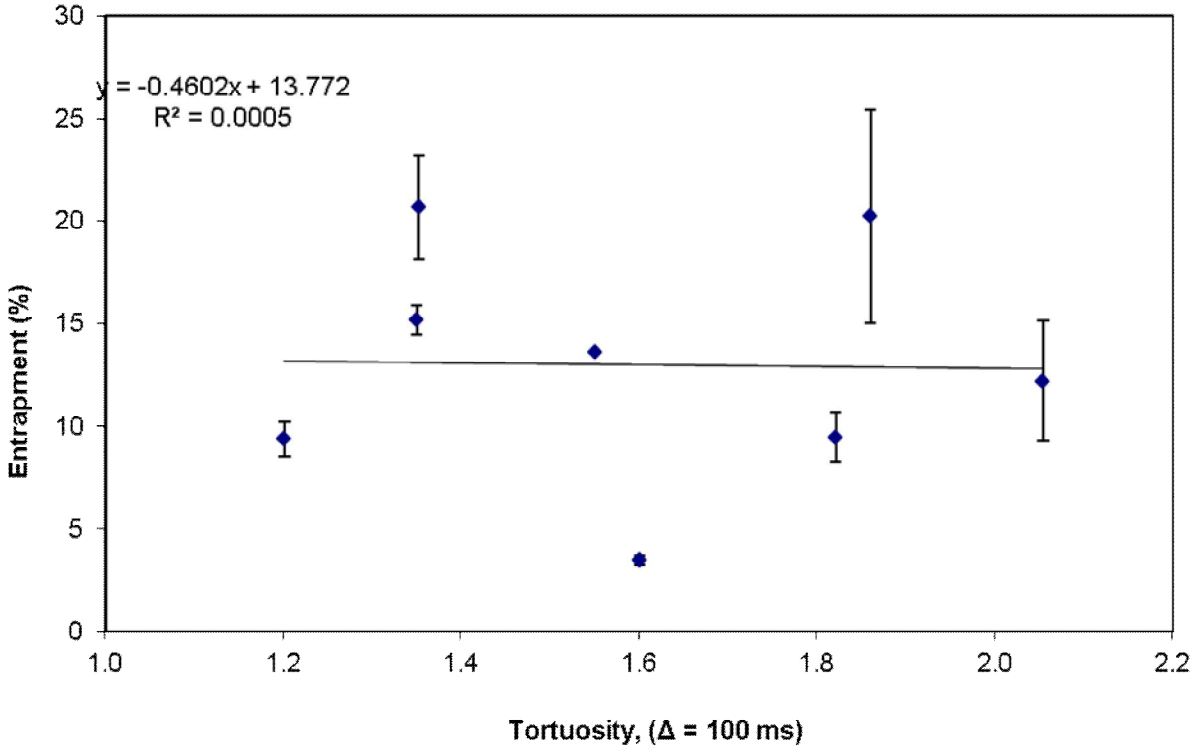

Effect of mercury entrapment on macroscopic tortuosity, Δ = 50 ms, I

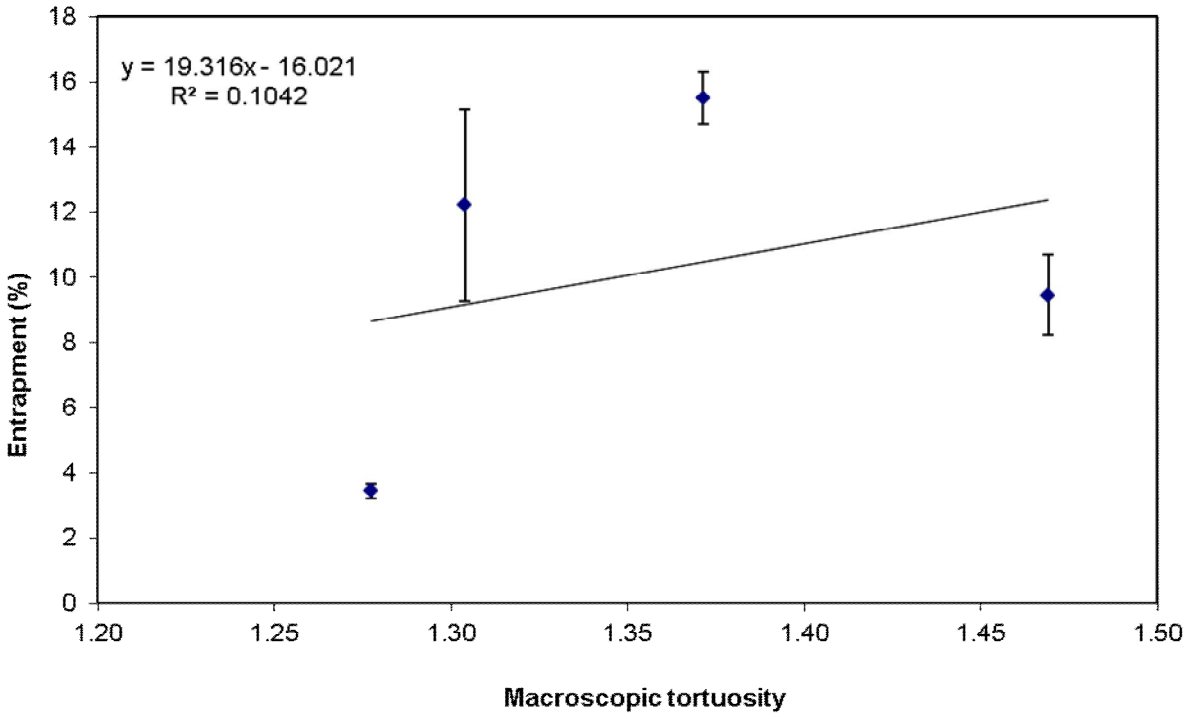

Effect of mercury entrapment on macroscopic tortuosity, Δ = 100 ms, I

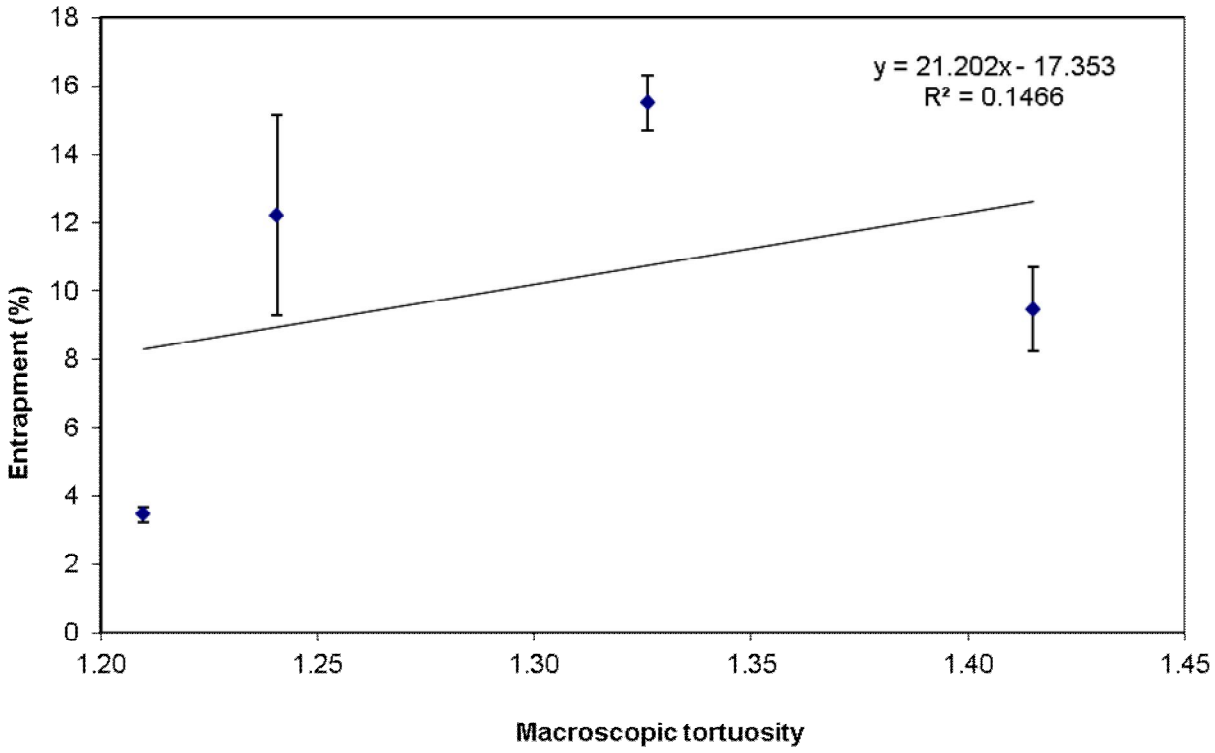

Effect of mercury entrapment on macroscopic tortuosity, Δ = 50 ms, II

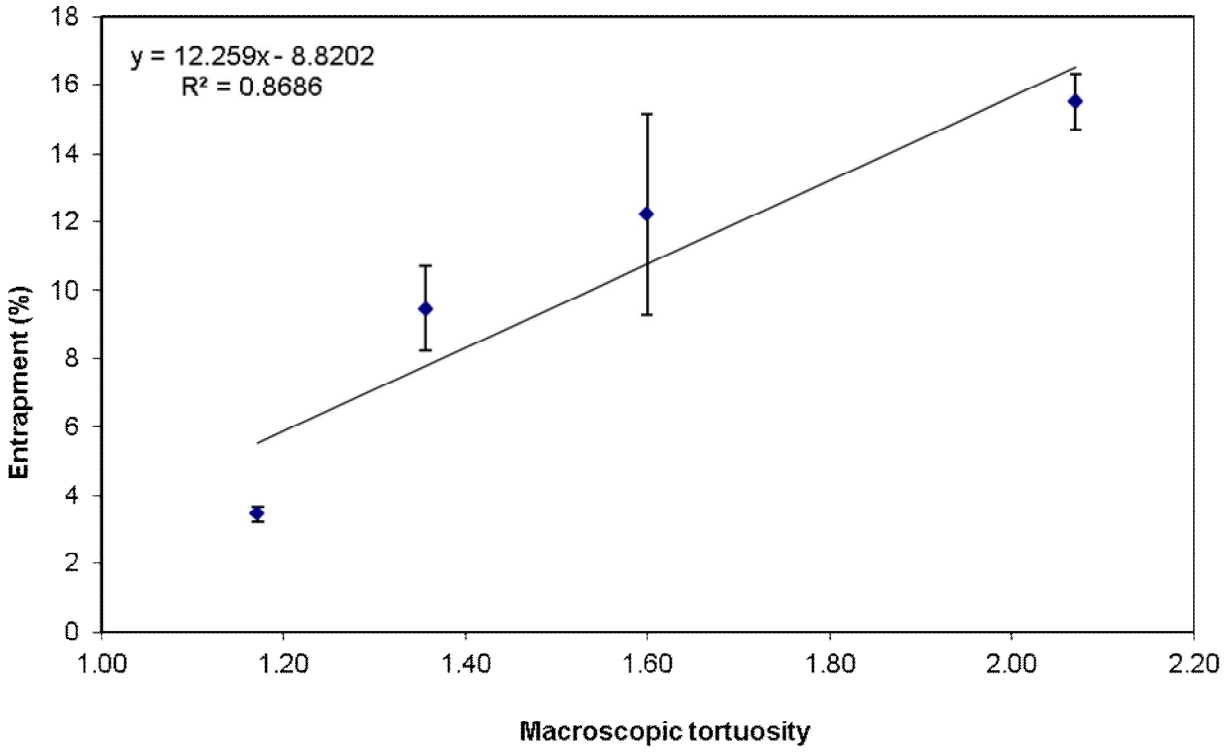

Effect of mercury entrapment on macroscopic tortuosity, Δ = 100 ms, II